Cranfield University

Tim P Bray

A Parametric Study of Vane and Air-jet Vortex Generators

College of Aeronautics

Engineering Doctorate (EngD)

Cranfield University

College of Aeronautics

Flow Control & Prediction Group

Engineering Doctorate

1997-8

Tim P Bray

A Parametric Study of Vane and Air-jet Vortex Generators

Supervisor: Dr. K P Garry

October 1998

Dedication...

That's all you need.

Roy Castle (1932-1994)

Abstract

An experimental parametric sturdy of vane and air-jet vortex generators in a turbulent boundary layer has been carried out. Experiments were carried out in two facilities, one with a free-stream velocity of 20 m/s and a boundary layer thickness (δ) of 41.5 mm, and one in a high speed facility at free-stream Mach numbers of between 0.45 and 0.75 and a boundary layer thickness of 20 mm. Cross-stream data were measured at a number of downstream locations using a miniature five-hole pressure probe, such that local cross-stream velocity vectors could be derived. Streamwise vorticity was calculated using the velocity vector data.

In the low speed study, vortex generator parameters were as follows:

- Vane vortex generators: thin rectangular vanes with a vane aspect ratio of unity ($2h/c = 1$), free-stream velocity = 20 m/s, incidence (α = 10°, 15°, 18°, 20°), height-to-boundary-layer-thickness-ratio (h/δ = 0.554, 0.916, 1.27, 1.639), and streamwise distance from the vortex generator (x/δ = 3.855, 12.048, 19.277, 26.506).
- Air-jet vortex generators: circular jet nozzles, free-stream velocity = 20 m/s, jet nozzle pitch and skew angles (α, β = 30°, 45°, 60°), hole diameter-to-boundary-layer-thickness-ratio (D/δ = 0.098, 0.193, 0.289), jet-to-free-stream-velocity ratio (VR = 0.7, 1.0, 1.3, 1.6, 2.0), and streamwise distance from the vortex generator (x/δ = 3.855, 12.048, 19.277, 26.506).

In the high-speed study, the vortex generator parameters were as follows:

- Vane vortex generators: thin rectangular vanes with an aspect ratio of unity, incidence (α = 15°, 20°), height-to-boundary-layer-thickness-ratio (h/δ = 0.75), streamwise distance from the vortex generator (x/δ = 8.75, 16.25, 23.75), and free-stream Mach numbers of 0.45, 0.6 and 0.75.
- Air-jet vortex generators: jet pitch (α = 30°, 45°), jet skew angle (β = 30°, 45°, 60°), hole diameter-to-boundary-layer-thickness-ratio (D/δ = 0.15, 0.3), jet-to-free-stream-velocity ratio (VR = 1.6), and streamwise distance from the vortex generator (x/δ = 8.75, 16.25, 23.75, 31.25), and free-stream Mach numbers of 0.50, 0.6 and 0.75.

Streamwise vorticity data from the experiment was used to generate prediction techniques that would allow the vorticity profiles, downstream of vane or air-jet vortex generators, to be predicted. Both techniques are based on the approximation of the experimental cross-stream vorticity data to Gaussian distributions of vorticity through the vortex centre. The techniques, which are empirically derived, are simple equations that give the peak vorticity and vortex radius based on the vortex generator parameters. Use of these descriptors allows the assembly of the Gaussian vorticity equation.

Both techniques are compared with the experimental data set and were seen to produce peak vorticity results to within 12% and 20% (for the vanes and air-jets respectively), 15% for the radius of the vortex, and 15% and 20% in vortex circulation (for the vanes and air-jets respectively). The two simple prediction techniques allow good prediction of the vortex structure at extremely low computational effort.

TABLE OF CONTENTS

Table of Figures

Chapter 1 - Project Historical Overview

The topic of this research programme concerns the use of flow control devices called Vortex Generators. These devices are small protrusions from the surface over which a fluid flows, and the devices cause longitudinal vortices to be created. These devices have application to a wide variety of fluid dynamics problems. In the case of this doctoral research programme, the work forms a contractual requirement of an international collaborative concerned with jet engine inlet systems. A brief introduction to this work is presented.

Flow control has been used in a wide variety of forms for many years, including vortex generator, boundary layer suction and blowing and aerodynamic fences. Research at the NASA Lewis Research Center showed that vortex generators could be applied to highly curved S-duct inlet systems using a new philosophy[49]. Vortex generators have been used traditionally to prevent boundary layer separation by increasing skin friction through increased boundary layer mixing. By using the vortices to induce a cross-stream velocity vector at the walls of the inlet, the natural cross-stream pressure gradients in a highly curved inlet could be overcome.

Following from this largely computational study, a Joint Aeronautical Programme (JAP) was set up between the United Kingdom Ministry of Defence (UK MoD) and the National Aeronautics and Space Administration (NASA) to establish some design guidelines for the use of vortex generators in highly curved engine intakes. The first phase of this works was called Task 46. The milestones included the computational design of a vortex generator system for a highly curved inlet geometry (known as M2129) using a Reduced (or parabolised) Navier Stokes CFD code (RNS3D) by NASA, and the experimental testing of the inlet duct by the Defence Research Agency (for the UK MoD). The results of this work showed that an improvement could be seen in the performance of the inlet, but that the parabolised CFD code did not predict the location of the boundary layer separation in the intake.

This work led to an extension of the programme, which was called Task 59. This was a first iteration of the CFD/experimental data, where the experimentally measured separation positions were used to re-design the vortex generator system. Experimental tests revealed that the agreement between the CFD model and the experimental data was very good (when the vortex generators were located upstream of the separation location), and that the improvement in the inlet performance was substantial. At this time, it was decided that air-jet vortex generators could be used in inlet systems, and a simple system was designed for experimental testing.

The CFD code was using a very simple vortex generator pre-processor, which allowed a step input in vorticity to be made for each vortex generator, rather than numerically modelling the generator itself. This was carried out in order to reduce the number of grid cells, thereby reducing the computational complexity of the calculation. It was realised that this model was extremely basic, and that if any improvement in the prediction was to be realised, then a better model needed to be implemented. Further, the basic model was based around simple vane vortex generators, and was incapable of modelling the air-jet vortex generators, which were of growing interest. Thus, as the programme went forward past Task 59, this requirement was written in to the next phase. At this point, the method of international collaborations was changed from the Joint Aeronautical Programme to a Tri-National Collaborative Programme (TTCP). This task was entitled TTCP AER TP-5 'Vortex Flow Control for the Management of Distortion in Compact Inlet Systems'. In this programme, NASA was tasked with the numerical modelling of vane vortex generators in inlets. The National Research Council of Canada (NRC) was tasked with the fundamental numerical modelling of air-jet vortex generators. The Defence Evaluation & Research Agency (DERA) was tasked with experimental evaluation of vortex generators applied to inlet systems. Also, DERA was tasked with the production of a simple empirical model to allow the prediction of the vorticity from a range of vane and air-jet vortex generators. This work was set as an Extra-

mural Research Contract (EMR) to Cranfield University, and is the subject of this doctoral research.

The research programme was undertaken as an Engineering Doctorate degree, which required a response to the aerodynamic problems involved in the research. Further, as fulfilment of the regulations for the Engineering Doctorate programme, a 'non-technical' study was required in addition to the engineering work.

The chosen subject of this non-technical study was a methodology for identifying future research requirements in military programmes, where a monetary cost or benefit was difficult to place on new technology. This methodology was applied to the particular engineering task of the thesis.

Thus, the structure of this thesis starts with the definition of a Technology Strategy Methodology that is proposed for research activities. This methodology is used to demonstrate the engineering research requirement of this doctoral programme, which is addressed in the rest of the thesis.

Chapter 2 - Technology Strategy Methodology

2.1 - Introduction

In a dynamic world, the ability to predict the future is an advantageous, if unrealistic, skill. Nowhere more so than the defence aircraft industry. The nature of combat aircraft is such that the technologies that must be employed on a new system must be the most modern available if the aircraft is to be successful in combat with an enemy aircraft system. However, as the aircraft system becomes more complex, so the development period increases in duration, making the application of 'cutting-edge' technology very difficult. Often, as an aircraft enters service, the employed technologies are almost a decade old.

Not only are the technology aspects difficult to engineer, but they are difficult to predict. Very rarely is an aircraft a *jack-of-all-trades* and master of all of them, and thus the roles or missions that the aircraft must undertake must be carefully selected. Should a mission become obsolete, then the aircraft will ultimately be a poor performer in another role. The mission must be well defined, and the technologies required must be clarified.

It becomes clear that these two compounding problems: the definition of the aircraft role; and the employment of technologies are a significant problem at the aircraft definition phase. As the aircraft is being defined, questions regarding the availability of technologies, and more importantly how to reach technology maturation in technical disciplines, become significant if the aircraft is to be feasible, on-time, and on-budget.

In order to remove some of the uncertainty in the defence aircraft market, *Scenario Planning* can be employed. This section will use the methodology with application to a *Future Advanced Combat Aircraft System* (FACES), which might be expected to have an in-service date of 2030. The methodology consists of the following phases:

- Analysis and Auditing of the External Environment
- Generation of the Key Determinants
- Definition of the Aircraft Attributes
- Definition of the Technology Drivers
- Generation of Scenarios
- Analysis of the effects of the Key Determinants on the Scenarios
- Assessment of the Technology Risks
- Aircraft Attributes and the Technology Driver Probability
- Assessment of the Strategic Importance of Technologies
- Technology Focus: Engine inlet system flow management.

2.2 - Analysis and Audit of the External Environment

Before the aircraft is defined, the environment in which it operates should be studied. This environment is not considered in terms of the flight regime, but rather in the broader non-combat factors which will ultimately define its use: to wit, the world we live in.

The range of environmental factors are wide and might include:

- Time scales,
- Politics,
- Technology.

These factors can be more easily approached using a PEST Analysis

2.3 - Pest Analysis

The PEST analysis is a simple tool that breaks down the environmental factors in to 4 major topics: Political; Economic; Socio-cultural; and Technological[1]. The PEST analysis is a convenient way of taking stock of what the future could be. It is based on a series of assumptions about what will happened in the future, often using trends from history. However, caution must be taken in this analysis. Since it is the future that is being predicted, the use of trends must be considered carefully: trends go on until they stop. Further, since this type of analysis is the foundation of the whole exercise, it should not be taken lightly.

It should be stated here that the PEST analysis presented here is not a heavily researched topic, and is presented more as a vehicle for the discussion of the total Technology Strategy Methodology, rather than a clever analysis of tomorrows society. The results of the whole Methodology should therefore be read *in relation to the assumptions made within*.

2.3.1 - Politics

Looking forward to the year 2030, the political nature of the UK will be quite different. With the current European Union debate raging, it is likely that the UK will fall either completely in to or completely out of the European Union. While this debate is currently far from resolved, it is felt that the pull from Europe is inevitable on a number of fronts, not least an economic one. Thus, it is suggested that the next 30 years will see significant levels of European integration, not only economically, but also politically, and militarily. This final point could be argued on an economic basis alone, since the costs of operating a number of different armed forces to the same end is extremely inefficient. This factor will widely affect the purchase, manufacture and operation of a combat aircraft greatly.

The further integration of the European nations would also give rise to congruence in defence policy. Thus, not only would it be economically inefficient to have a number of different armed forces within an integrated continent, but also since they would be providing the same service, a second inefficiency would arise.

Since the breakdown of the Cold War, the stability of the world has changed. Under the Cold War regimes, an arms race was built up over fear between the Western Nations and the Warsaw Pact countries. While this situation brought rise to significant tensions on a major scale, stability between smaller nations was witnessed. In the last 10 year, since the end of the Cold War, a number of smaller wars and conflicts have occurred, including the breakaway of some of the former Soviet states (all of which involved armed uprisings), wars in Africa (most notably Somalia and Zaire), and wars in the Middle East, including the Gulf War. Most of these wars have involved either the United Nations or the North Atlantic Treaty Organisation (NATO) to provide some policing or stabilising power. The military presence in NATO and the UN comes from individual nations, and it is therefore suggested that there is a shift from domestic defence to

commitments to global policing. The nature of the conflicts around the world is changing the requirements for new weapons and armaments. Rapidly deployable vehicles are required, which are flexible and easy to support away from base.

As well as the operational requirements for a new aircraft, the design and build of the aircraft creates its own political issues. The cost of the aircraft design process is becoming too expensive for any one country to consider alone (with the exception of the United States of America. International collaborations are already a significant part of the military aircraft production reality, and it is believed that further rationalisation is likely. Indeed, it is believed that by the year 2030, there will only be four or five aircraft manufacturers in the military business: one or possibly two in the United States, one in the CIS (as a rationalisation of the Sukhoi, Tupolev and Mikoyan-Gurevich design bureaus), one in Europe (through integration of British Aerospace, DASA, Dassault, Alenia, CASA, and Saab), and possibly one in the Far East (as an expansion of IPTN). This had wide and sweeping implications. Firstly, since the number of aircraft types will become less, the political ability to buy a range of aircraft will become more difficult. Exports will become a difficult market, since it would become difficult to sell aircraft abroad that the exporting nations are using as their front line aircraft. Within the collaborative nations, the work-share agreements may become difficult to agree upon, since it is difficult for a nation to give up on an industry that is seen as being so important to the country's strength. Further, the employment consequences are significant. It is believed within the UK that the number of jobs involved within the Eurofigther programme directly is around 40,000. This figure does not include the secondary jobs through wealth creation. Cancellation of a single project alone can create significant domestic political problems.

2.3.2 - Economics

Whilst being less significant that the political aspects, the economic factors underlie the whole project simple due to the cost of military hardware. It is the economic climate that ultimately defines the volume/quality of the product, regardless of the defence requirements. Therefore, prediction of future defence budgets (which will be related to the Gross Domestic Product) is a very significant point. In the insightful and witty text by Augustine[2], trends in the unit cost of aircraft were correlated with the year of initial operation, and an alarming exponential curve is noted (see graph below).

When the US defence budget is superimposed on this graph, Augustine generates his IX law, which states:

> ***In the year 2054, the entire defence budget will purchase just one tactical aircraft. This aircraft will have to be shared by the Air Force and Navy 3½ days each per week except for the leap year, when it will be made available to the Marines for the extra day.***

Whilst a little flippant, the significance of this is apparent. Assuming the extension of the current trends, the cost of new military aircraft is set to become prohibitive. While over the last century performance was all, affordability must now takes precedence.

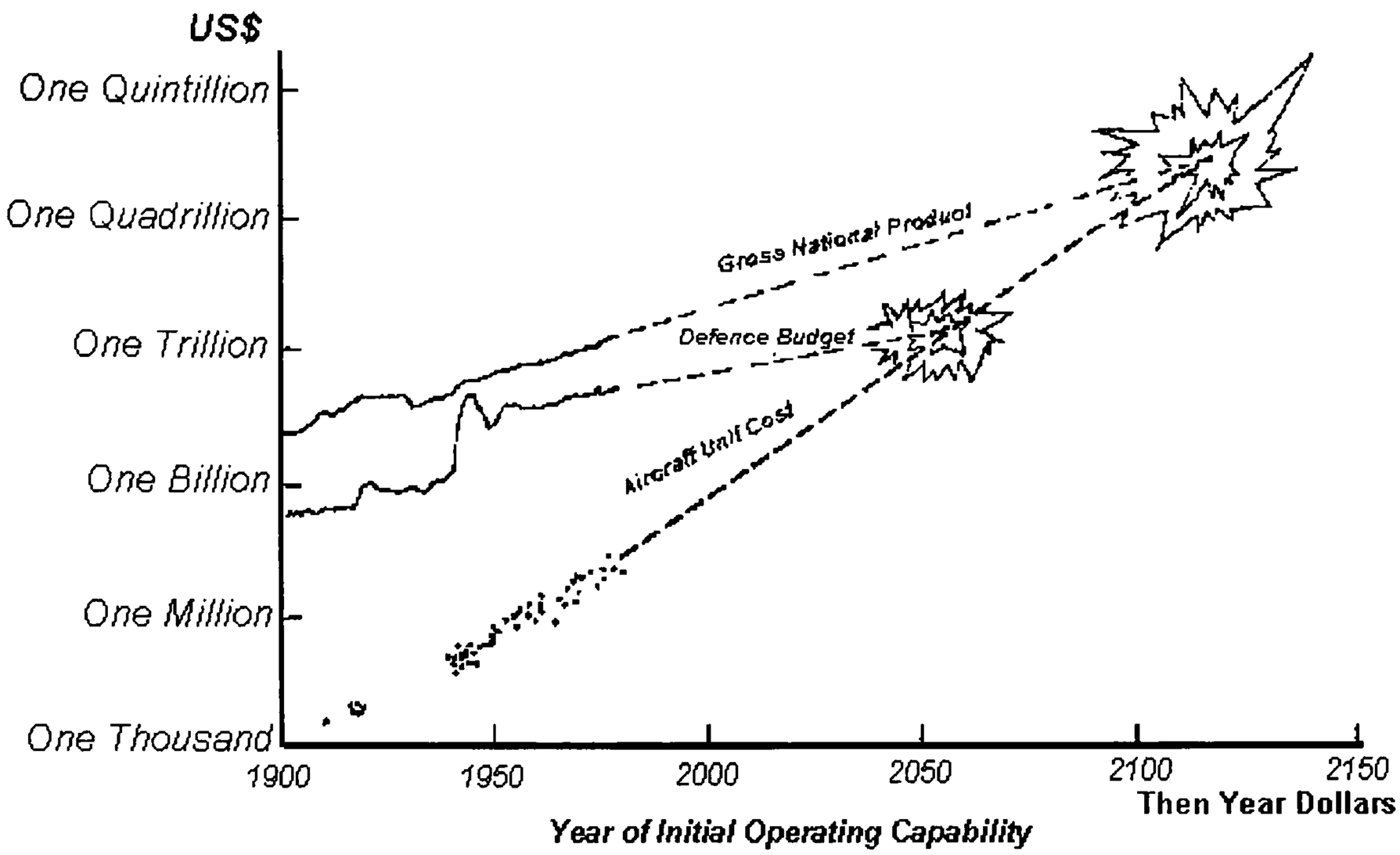

Figure 1: Aircraft Acquisition Cost Projections (ref. 2)

2.3.3 - Socio-culture

In the strict sense of a PEST analysis, the socio-cultural environment is perhaps the least significant of the PEST aspects. Such factors do include the levels of education of those expected to operate and maintain the proposed aircraft. It is important to note that the current state of civil aviation is already suffering from this point. LOT Polish Airlines decided not to purchase Airbus airliners (which incorporated significant levels of composite materials and a sophisticated fly-by-wire system), since it felt that its maintenance staff were not sufficiently well trained to successfully maintain the aircraft[2]. As technology levels increase in complexity, the military may encounter a problem whereby the air forces may not be able to attract maintenance engineers and technicians with sufficient training and expertise.

Another significant fact to be accounted for is the change in culture towards conflict. A graphic example of this is the post-Second World War Culture of Japan, where the country became largely pacifistic (albeit in revulsion to the war time activities, and under international political pressure). Also, as the nature of war is forgotten by new generations, there is perhaps less of a tendency to consider defence in such a grave light, and the perception of the cost of defence changes. In short, the population considers that the price of maintaining peace reduces. While this may manifest itself in a political manner, changing cultures and the demand for peace from the culture must be considered.

The 'cost of life' is another socio-cultural influence to consider. During both the major World Wars of this century, young men have been expected to go to war against the oppressor. Even in the case of the United States of America (which was under no serious threat of invasion), many millions of troops were sent abroad to fight. However, only twenty years after the Second World War, the culture of the country had changed, and mass demonstrations were staged to show revulsion at sending troops to Vietnam to fight a conflict there. The cost-of-life had risen, and it was not considered that the Vietnam War was worth fighting. Thus, in some conflicts, there is a reluctance to risk assets.

It should also be remembered that, while some political rationalisation might take place in Europe, other non-European nations might do the same. Most significant integration might come from the

Middle East or the Far East, where the culture opinion to armed confrontations differs greatly from those in the West. Therefore, socio-cultural factors of potential enemies must be considered when analysing the needs of the military.

2.3.4 - Technology

Along with politics, the technology aspects of the environment are the most significant. While it is the politics that brings about the need for defence, it is the technology that realises that defence.

When talking about technology, there are currently two key phrases that shape its use. These are: technology *maturation*, and *technology transfer*.

Technology maturation is concerned with ensuring that engineering solutions are available. Aerospace history is littered with examples of aircraft types that tried to employ technologies which were not ready for use, and which ultimately caused delays in the in-service dates, and often caused project cancellation. The case of the British Aircraft Corporation TSR-2 is a high profile example of this fact. The aircraft was to have been unrivalled in terms of performance, but was extremely ambitious. Delays followed, and cost increased. While it is still debated today as to whether the technical problems were overcome, the time and financial aspects eventually brought about the project's cancellation on political grounds. Had the technology been more mature prior to design, build and test, politicians would have had far less grounds for cancellation, the project may well have succeeded.

Technology transfer is concerned with cost reduction and information exchange, by ensuring that work is not duplicated, and also by introducing novel ideas from outside the traditional aerospace industry. The most high profile cases of technology transfer come from the US/NASA Apollo space program, which aimed to place man on the moon. The revenue generated from the transfer of technologies, as wide and diverse as materials through to pharmaceuticals, was around six times the Apollo program budget. The technology transfer does not necessarily have to go out from the selected program however. Indeed, the aerospace industry has gleaned considerable data on the use of composite materials from the racing car industry, for example.

As suggested earlier, as technology dominates, costs increase: that is, technology has an inevitable cost associated with it. This fact alone has wide reaching influences. As the costs go up, the expectations for the product go up, and inevitably, the development cycle and the service life increases. This further increases the lead times, and makes the technology definition for the future more difficult.

2.3.5 - PEST Analysis Matrix

Taking the points that have been made above, they can be quickly summarised. The PEST analysis which would impact on a future aircraft programme as follows:

Table 1: PEST Analysis Matrix

1. ***Political*** ✈ Government Defence Policies and Budgets ✈ Changing aircraft requirements ✈ Export Sales Policy ✈ Domestic Employment Rate ✈ Foreign Policy and International Relations ✈ Commitments to Treaties and Allies (e.g. UN, NATO) ✈ Domestic Manufacturing Industry ✈ Integration with Continental Interests ✈ International Collaborations ✈ Rationalisation of International Defence Contractors	3. ***Socio-cultural*** ✈ Education Levels ✈ Attitudes to conflict/war
2. ***Economic*** ✈ GDP Trends ✈ National/Continental Defence Budgets ✈ Interest & Borrowing Rates for Defence Contractors	4. ***Technological*** ✈ National Research & Development Expenditure ✈ Speed of Technology Maturation ✈ Speed of Technology Transfer ✈ Rates of Obsolescence ✈ Wide Diversity of Technology ✈ Length of Lead Times ✈ Length of Service Life ✈ Cost of technology

2.4 - Environment Summary

From the PEST analysis, the important influences become apparent, and these are called the Key Determinants. These are listed below:

1. Rationalisation of defence contractors: therefore fewer aircraft producers
2. Change in International defence policies and commitments
3. Change in 'customer requirements' from performance at any price to Survivability, Affordability, Effectiveness, Technology
4. Trend of increasing costs and times of new equipment purchase
5. Increased equipment life-cycles
6. Resistance to commit military assets.

With the environment defined, it is possible to go on and look at the aircraft role, and possible aircraft that could fulfil that role.

2.5 - Aircraft Definition

For the purposes of this study, the aircraft role has been chosen as a future air-combat aircraft, to be known as the *Future Advanced air-Combat Engagement System* (FACES). It is assumed that this aircraft will be a replacement for the current generation of aircraft in this role: Boeing F-22, Eurofighter 2000, Dassault Rafale, Mig-35, Sukhoi-35/7.

For this study, the role of this aircraft is assumed to be a platform with the capability to shoot down enemy aircraft in the Beyond-Visual-Range (BVR) and In-Visual-Range (IVR) encounters, and to provide a Combat Air Patrol (CAP) type role as well as the fighter escort role. Whether this definition of an aircraft role is necessarily applicable in tomorrow's force structure is not known, and is beyond the scope of this work, but this role provides a convenient vehicle for discussion.

2.5.1 - Aircraft Scenarios

In order to fulfil this role, there are a wide number of potential aircraft designs that could be considered. For a 'real' case, it is prudent to select a wide number in order to allow for the wide differences that subtle changes in aircraft design can make on the mission fulfilment. However, choosing too many designs is a waste of resources, since many design philosophies may stem from the same basic design feature. For a real case, some ten designs may give a complete set of choices. Some of these may be aircraft, some may be missile systems. However, in order to reduce the work package to a more manageable size, three very different aircraft solutions are proposed in this study.

FACES-A: The Stealthy Aircraft

The FACES-A aircraft is proposed as a crewed, highly stealthy design, which would achieve excellent BVR offensive capability, whilst proving to be a challenging target. Fairly manoeuvrable, it would not employ any thrust vectoring technology, as this would compromise the stealth aspects. The aircraft would use internal weapons storage, and would be optimised to reduce, not only the Radar Cross Section (RCS) signature, but also the InfraRed (IR) signature, the acoustic noise, and the visual signature.

FACES-B: The Agile Aircraft

The FACES-B aircraft is proposed as a crewed/un-crewed, highly agile aircraft, probably employing Thrust Vectoring Technology (TVT) to achieve excellent point-and-shoot capability. Whilst employing a high quality radar system for good BVR capability, this aircraft design would be an extremely effective dog-fighting machine. Some stealthy attributes would be employed to help reduce the RCS, but not at the expense of manoeuvrability.

FACES-C: The Weapons Platform

The FACES-C aircraft system would be a weapons platform which employs existing technology as the aircraft, but is re-fitted with a complete avionics/weapons suite using new technology to achieve increased kill probability. Emphasis on the airframe would be towards weight and cost reduction. This aircraft might use airframes such as Eurofighter 2000, Dassault Rafale, Saab JAS39 Gripen, or depending on the political climate, Boeing F-22, Mig-35, Sukhoi-35/7.

In the real case, each of these aircraft systems would undergo some preliminary design studies in order to bring about designs that can be assessed formally.

2.5.2 - Application of the Key Determinants to the Scenarios

With the aircraft defined, it is then possible to apply the Key Determinants (from the environment audit) to each of the aircraft scenarios. This is simply done in some broad-brush manner, in order to simply assess each impact.

Table 2: Scenario Matrix

Key Determinants	Scenario A Stealthy Aircraft	Scenario B Agile Aircraft	Scenario C Weapon Platform
Survivability	Hard to target from range. Low manoeuvrability makes close combat less certain.	Has potential for targeting from any range. Manoeuvrability allows evasion of missiles & good close combat performance.	Can be more easily targeted from any range. Low manoeuvrability makes close combat less certain.
Affordability	High price of stealth technology in: • design & test • maintenance • acquisition	High price of technology in: • design & test • maintenance	Aircraft price is low. Weapons price is high.
Effectiveness	? Requires detailed analysis of aircraft design	? Requires detailed analysis of aircraft design	? Requires detailed analysis of aircraft design
Technology	High (Stealth technology is not desperately mature, and requires a great deal of technology input)	Medium/High (Thrust vectoring has been used on existing aircraft types, and a number of experimental programmes are currently expanding the knowledge base)	Low/Medium Weapons technology gives rise to some risk
Development times **(compared with current new aircraft projects)**	Increased	Increased	Reduced
Equipment Life Cycles	Long	Long	Short/Medium
Resistance to Commit Military Assets	Very High	Medium	Low

As can be seen from the table above, the impacts are stated. It should be noted here that specialists in the field using techniques such as the UK MoD Joust simulation code must carry out the analysis of the aircraft performance. The preliminary design studies would be the subject of simulations with possible future threats, and the results assimilated.

From this table, the 'technology' aspects can be investigated further in terms of the Technology Drivers, and these are listed in the next section.

2.5.3 - Technology Drivers

The aircraft can be divided in to a number of technology categories, each of which have a number of more specialised sub-sets or *technology drivers*. The basic aircraft can thus be dissected thus:

1. Aerodynamics

1.1. Configuration
1.2. Wing
1.3. Control surfaces/jet reaction control
1.4. High Lift Devices
1.5. Air inlet system
1.6. Engine exhaust treatment

2. Propulsion

2.1. Compressor
2.2. Combustion chambers
2.3. Turbine
2.4. Reheat
2.5. Advanced engine control

3. Weapons System

3.1. Radar System/IR/EO
3.2. Radar/missile interface
3.3. Missile system
3.4. Weapon Carriage System
3.5. Identification-Friend-or-Foe (IFF)
3.6. Integrated information management system with other assets

4. Stealth

4.1. Shape
4.2. Materials
4.3. Surface finish
4.4. Surface coating
4.5. Conformally mounted sensors (CMS)
4.6. Air-data systems
4.7. Emissions

5. Manufacturing

5.1. Technology maturation
5.2. Composite techniques
5.3. Standardisation
5.4. Flexible tooling/jigging
5.5. Quality/Reliability
5.6. Application of stealth materials & paints

6. Maintenance

6.1. Repair of coatings & paints
6.2. Treatment/repair of materials
6.3. Standardisation
6.4. Reduction in complexity

7. Flight Control Systems

7.1. Non-linear aerodynamic modelling
7.2. Fly-by-wire/light (FBW)
7.3. Integrated FBW system with engine control
7.4. 'Carefree' handling
7.5. Electrical/hydraulic system

8. Crew Operations

8.1. Piloted/Remotely-piloted
8.2. Virtual Cockpit (360°/360° viewing arc)

8.3. Thrust Vectoring Technology display systems (Track and attitude)
8.4. Direct Voice Input (DVI) & Direct Brain Links
8.5. Environmental systems
8.6. Training
8.7. Safety

9. Materials

9.1. Composite Materials (Carbon and Metal composites)
9.2. Single crystal materials
9.3. 'Smart' materials
9.4. Heat resistant materials
9.5. Increased strength-to-weight materials

10. Structures

10.1. Mass reduction
10.2. Dynamics tolerance
10.3. Health Monitoring (HUMS) integration with the control systems
10.4. Battle damage tolerance
10.5. Mission-adaptable structures (buffet alleviation, high 'g' wing modifications)

These are considered to be the basic broad-brush areas that are of some technology concern for any proposed aircraft design. These drivers will impact on a specific design in a unique way, and this impact needs some assessment.

The method employed is similar in nature to Quality Function Deployment (QFD). Since the thrust of this work is to identify areas that require significant research effort, these technology drivers need to be assessed principally on two parameters: the *Technology Risk* and the *Technology Driver Probability.* The two parameters for each Technology Driver can be plotted on a graph called the *Technology Strategy Matrix.* This is useful as a 'quick reference' tool as to the relative importance and risk involved with certain technologies. Further, it helps to make the choices as to which technologies should be invested in, and of which awareness is needed.

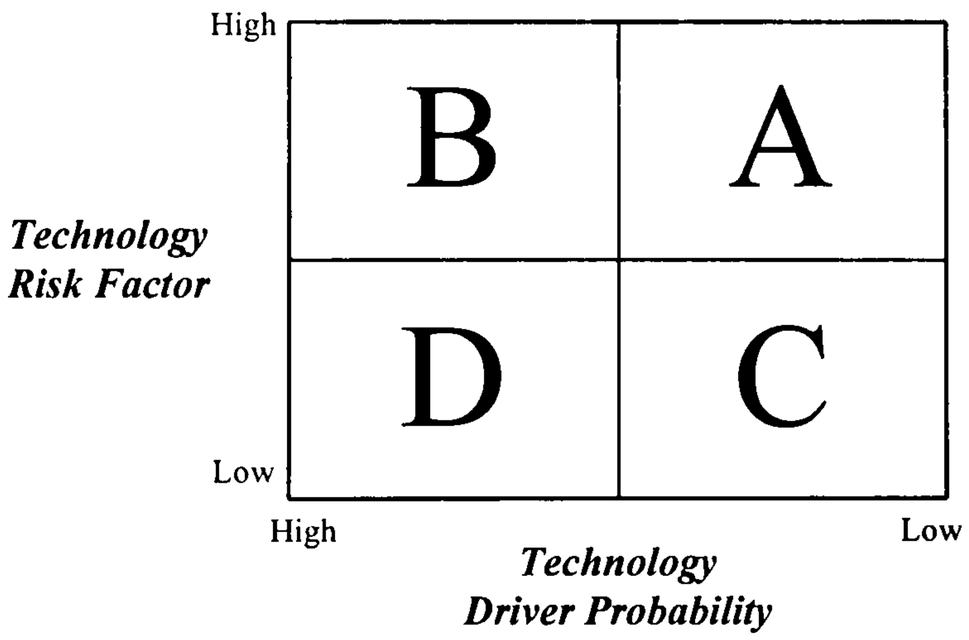

Figure 2: Generic Technology Strategy Matrix

The two parameters are described below, allowing the generation of the *Technology Strategy Matrix*,

2.5.4 - Technology Risk

The *Technology Risk* is defined as being the technology leap over existing aircraft technology to achieve a mature technology capable of being applied to FEACES. The Technology Risk will be a function of such things as:

- required effort,
- technical maturity,
- obsolescence,
- complexity,
- possible acceptance of failure.

Cost should not be considered as part of this Technology Risk. While cost is a significant factor, the Technology Risk is concerned with the technical problems which may be overcome, should fair and reasonable funding be made. The cost aspect would be taken in to account in the *Affordability* Key Determinant, and thus double counting should be avoided.

When evaluating the Technology Risk, expert knowledge should be sought in the specific area of concern. In the case presented here, this was done through a questionnaire given to some experts in industry and academia, and the questionnaires are given in the Appendix. Each subject was asked to rate the Technology Drivers for the Technology Risk on a scale from 1 to 9. A result of 1 would imply that no work needed to be done in an area, and that a solution was available. A result of 9 would imply that serious fundamental research was needed in a given area.

The results from the expert analysis were averaged across each category, in order to compromise where disagreement was raised.

2.5.5 - Technology Driver Probability

The *Technology Driver Probability* is a factor that looks at the contribution that each of the Technology Drivers makes to the fulfilment of the aircraft mission attributes. The attributes would come from the performance studies at the time of the aircraft role definition, and cover a broad range of areas. These would be factors primarily associated with the drive for Leathality, Survivability and Supportability. A series of these attributes may be drawn up, and a ranking can be produced for their relative importance. Again, in a real situation, this would be achieved through a computer simulation and design optimiser (such as the UK MoD JOUST code), but for this exercise, experts in aircraft conceptual design were used to produce the ranking. The attributes and the average results from the experts are given below.

Table 3: Aircraft Attributes Ratings

Attributes		Mean Ranking	Performance Attributes Rating
Lethality	Multi-role Capability	23	0.31
	Flexibility of Mission	25	0.25
	Stores Carriage Flexibility	18	0.47
	Navigation Capability	21	0.38
	Mission Quality Assessability	26	0.22
	Payload	13	0.63
	Range	11	0.69
	Target Acquisition	4	0.91
	Payload Delivery Accuracy	7	0.81
	Target Discrimination	5	0.88
	All-Weather/Night Capability	8	0.78
	Weapons/Sensor Integration	14	0.59
Survivability	Mission Planning	27	0.19
	Information Management	9	0.75
	Situational Awareness	12	0.66
	Low RCS	3	0.94
	Low IR	10	0.72
	Low Acoustic Signature	30	0.09
	Low Visual Signature	15	0.56
	Low Electronic Emissions	15	0.56
	Speed	15	0.56
	Manoeuvrability	6	0.84
	Countermeasures	19	0.44
	Hardware Protection	28	0.16
	Systems Redundancy	29	0.13
Maintainability	Systems Commonality	22	0.34
	Maintainability	1	1
	Reliability	2	0.97
	Interoperability	31	0.06
	Carrier Suitability	32	0.03
	Basing Flexibility	20	0.41
	Logistics Support 'Footprint'	23	0.31

The attributes are plotted in the following graph, which gives an easy quick reference. The values plotted are the *Performance Attributes Rating* which is a fraction of the ranking order (as defined: *PAR* = (33-Ranking)/32). A *PAR* value of I denotes the most important attribute.

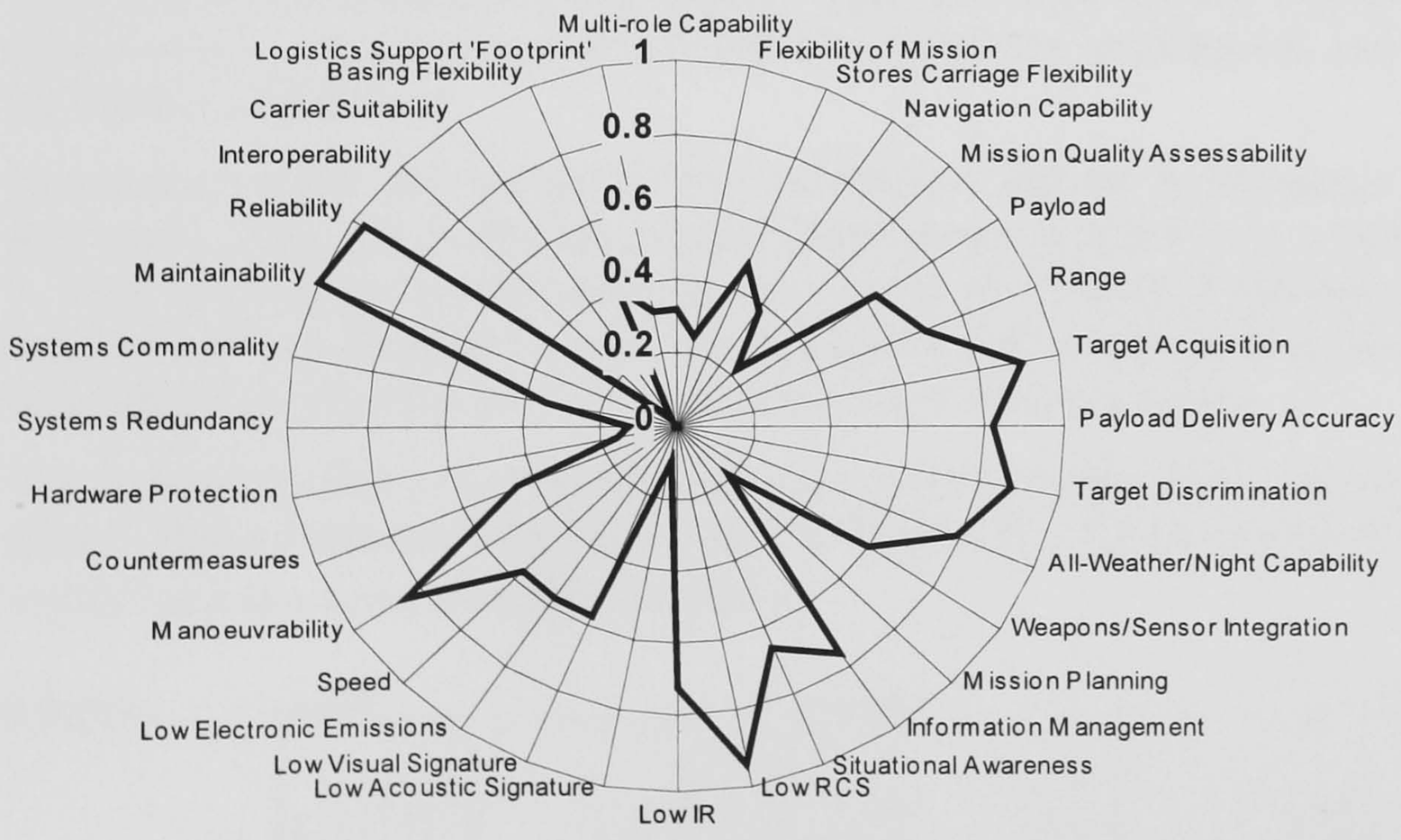

Figure 3: FACES Performance Attributes

Each of the attributes above refers to some aspect of the total system performance, and the ranking places emphasis on certain aspects more than others. For example, the most important attribute of future military aircraft is on the life cycle cost aspects (attributes with a *Performance Attribute Rating* close to 1). Hence, factors such as *maintainability* and *reliability* are considered to be the

highest priority. Also, a low radar cross-section is considered to be very important for future aircraft.

In order to assess the effects of the *Technology Drivers* on the *Performance Attributes*, each *Technology Driver* was assessed in terms of the effective contribution that that *Technology Driver* made to the *Attribute*. This *Technology Driver Contribution* was ranked from 1 to 5, where a score of 1 suggested no contribution, and a score of 5 suggested a major contribution. This assessment was made for each aircraft separately, and was made with respect to each aircraft design individually. Thus, the *Technology Driver Contribution* is given by the following formula:

$$TDP = \frac{\sum (TDC_N x PAR_N)}{N}$$

Where *TDP* is the *Technology Driver Probability*
TDC is the *Technology Driver Contribution*
PAR is the *Performance Attribute Ranking*
and *N* denotes each Performance Attribute.

Technology Driver Probability Calculation Example

In order to fully illustrate this concept, the calculation for a single TDP value will be described. Using the Wing Technology Driver from the aerodynamics category as applied to the FACES-B (agile) aircraft (Technology Driver B. 1.2), the data is applied as follows:

1. All of the Attributes for the aircraft are listed, together with *the Performance Attributes Rating* values (first row of numbers in the table below). These are the values from the spider diagram above.

2. The *Technology Driver* (in this case the wing) is applied to each attribute in turn, and the contribution which that driver makes to the achieving that aircraft's ability within that attribute is rated. In the case given, the aerodynamics concerns of the wing does not contribute significantly to the lethality or supportability aspects, but does contribute significantly to the speed and manoeuvrability of this design. Thus these aspects score highly. The rating here is scored from I to 5, where a score of I signifies the lowest contribution, and a score of 5 shows the highest contribution.

3. The product of the *Technology Driver Contribution* and *the Performance Attribute Rating* is then made. Here, the *Technology Driver Contribution* is turned in to a fraction by division by 5. Thus, the highest contribution becomes a value of 1, and multiplication by the *PAR* value (which itself is a fraction) would yield a value of I for the most important Attribute. All of these values are displayed in the second data row in the table below.

4. The *Technology Driver Probability* value of then the average of the products found in step (3) above. These values are found for all the attributes, for the three aircraft types.

Table 4: FACES Technology Driver Probability Calculations

FAECES-B: Agile Aircraft	*LETHALITY*												*SURVIVABILITY*												*SUPPORTABILITY*							***Average(TDC_N x PAR_N)***
Attribute	Multi-role Capability	Flexibility of Mission	Stores Carriage Flexibility	Navigation Capability	Mission Quality Assessability	Payload	Range	Target Acquisition	Target Discrimination	Payload Delivery Accuracy	All-Weather/Night Capability	Weapons/Sensor Integration	Mission Planning	Information Management	Situational Awareness	Low RCS	Low IR	Low Acoustic Signature	Low Visual Signature	Low Electronic Emissions	Speed	Manoeuvrability	Countermeasures	Hardware Protection	Systems Redundancy	Systems Commonality	Maintainability	Reliability	Interoperability	Carrier Suitability	Basing Flexibility	Logistics Support 'Footprint'	
FAECAS Attribute Ranking Factor	0.31	0.25	0.47	0.38	0.22	0.63	0.69	0.91	0.81	0.88	0.78	0.59	0.19	0.75	0.66	0.94	0.72	0.09	0.56	0.56	0.56	0.84	0.44	0.16	0.13	0.34	1.00	0.97	0.06	0.03	0.41	0.31	
Technology Driver Contribution 1.2. Wing *(TDC_N x PAR_N)*	1 0.06	1 0.05	2 0.19	1 0.08	1 0.04	2 0.25	4 0.55	1 0.18	1 0.16	1 0.18	1 0.16	1 0.12	1 0.04	1 0.15	1 0.13	2 0.38	1 0.14	1 0.02	1 0.11	1 0.11	4 0.45	4 0.68	1 0.09	1 0.03	1 0.03	1 0.07	1 0.2	1 0.19	1 0.01	1 0.01	1 0.08	1 0.06	0.16

2.6 - The Technology Strategy Matrix

With the *Technology Drivers* assessed in terms of the 'risk' and the 'probability' of need, this information can be plotted on a graph as the *Technology Strategy Matrix*.

In the following plots, the *Technology Drivers* are numbered using the key in the listing above, and the prefix letters refer to each of the three scenarios.

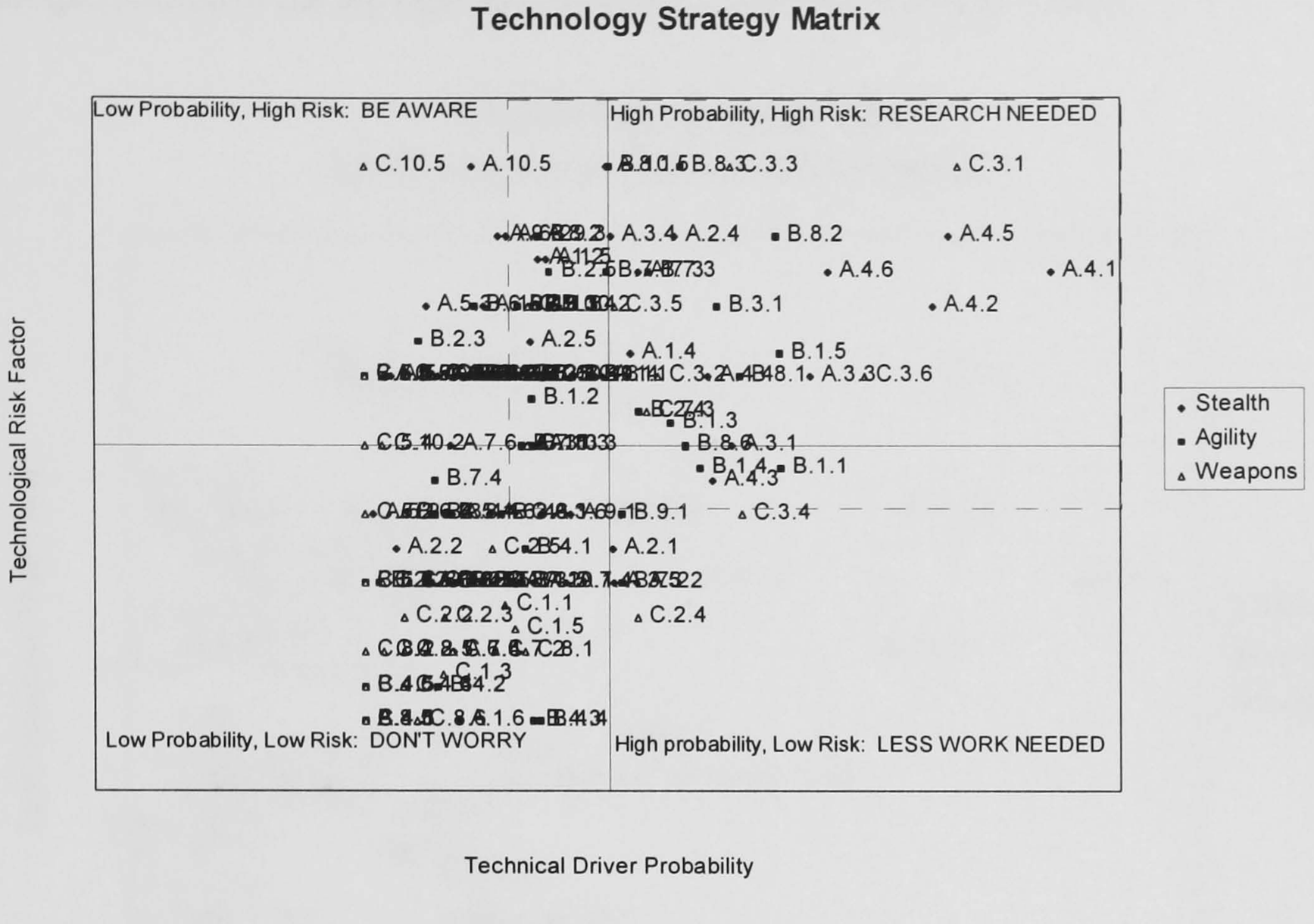

Figure 4: Complete FACES Technology Strategy Matrix

Using the Technology Strategy Matrix, the technology drivers can be roughly broken down into four categories:

1. High Technology Risk Factor, High Technology Driver Probability,
2. High Technology Risk Factor, Low Technology Driver Probability,
3. Low Technology Risk Factor, High Technology Driver Probability,
4. Low Technology Risk Factor, Low Technology Driver Probability.

The exact differentiation between these categories is fairly subjective, and it is good to ensure that there is a fair spread of results between categories.

In the case where both parameters are high, the probability that technology research is needed is high, and that a considerable amount of research effort must be done. These would be the technologies that must receive research attention.

Where the risk is high, but the probability is low, the chance that the technology will be needed is less. However, research should still be carried out in to some of these programmes, since, if it turns out that this is a problem area, a great deal of work needs to be done. Awareness is therefore needed of fundamental research, and risk reduction studies should be carried out.

Where the risk is low but the probability is high, it is most likely that engineering solutions are needed, rather than fundamental research, and therefore effort is needed in this area.

If the risk is low, and the probability is low, it suggests that, if in the event that it turns out that the

technology is required, it is only the application of that technology that is needed.

The full Technology Strategy Matrix is rather cluttered due to the high number of data points, some 168 for all three aircraft. The area of real interest is that where significant work is needed, and the following chart enlarges this area. As stated earlier, the four classifications are rather subjective. In order to allow for this, it is usual to focus attention not just in the top right of the matrix, but also around some of the borders that overlap with other regions. The graph below is an enlarged portion of the top right section of the Technology Strategy Matrix.

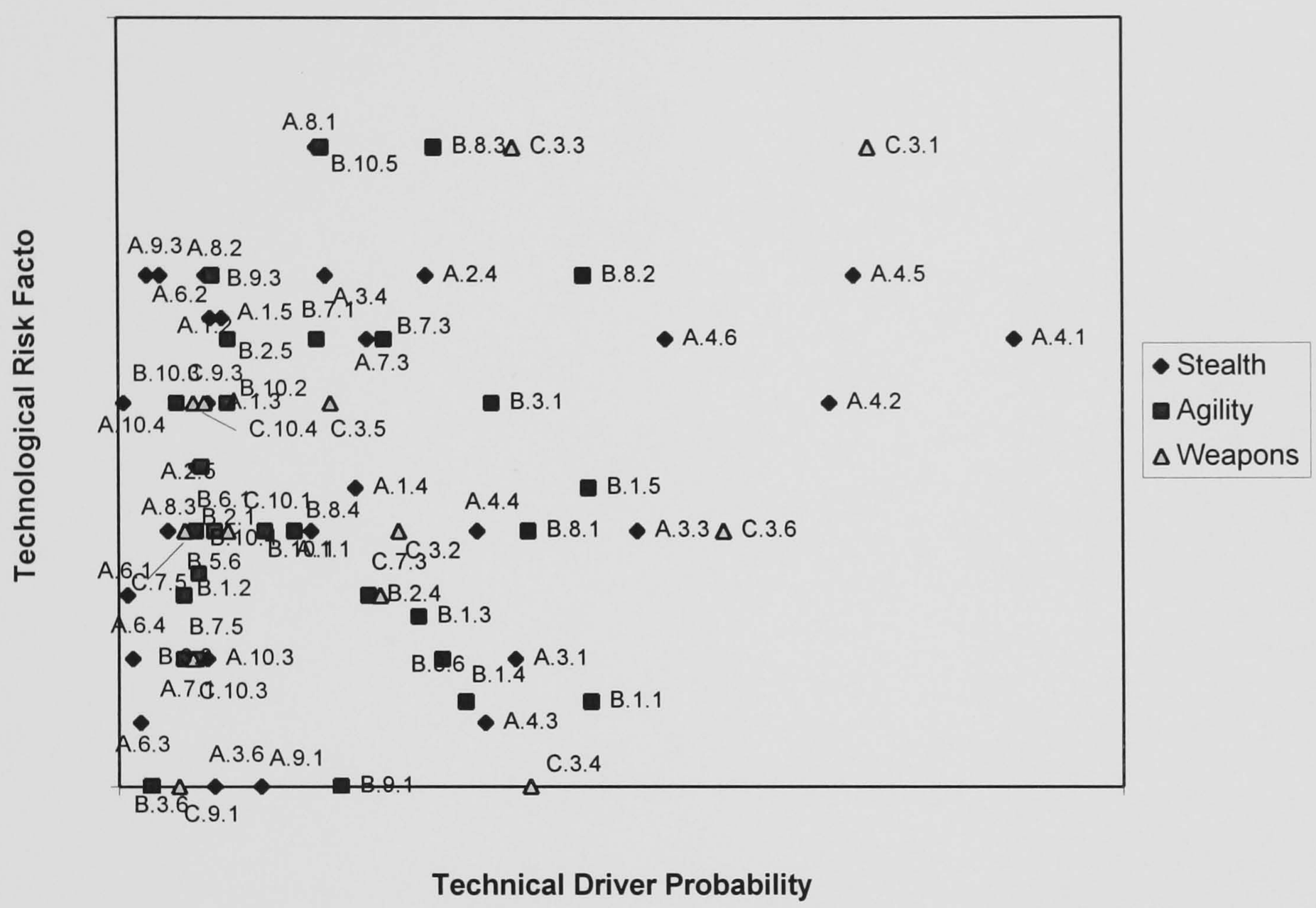

Figure 5: High Risk/High Probability Portion of the Technology Strategy Matrix

2.7 - Significant Technologies Drivers

The technologies of significance in the Zoomed Technology Strategy Matrix can be reordered in terms of the list of Technology Drivers for each of the scenario designs. Referring to the diagram below, the technologies that are 'dark-greyed' in the grid below are those that are of significance. Also checked in the grid are the technologies which are of less strategic importance, but which are still of a high risk (that is the top left quarter of the Technology Strategy Matrix). These are the technologies that are not, as yet, considered vital. However, changing the initial assumptions may make them vital, and hence an awareness is desirable.

Using this diagram, it becomes apparent where research is needed, and to a degree, the diversity of the research that is needed. If the same *Technology Driver* shows work that is needed for more than one of the FACES designs, that work may not be in a related area and may need many parallel programmes. Conversely, the same technologies may be applicable across the designs, in which case, the importance of those research programmes becomes more acute. For example, a stealthy aircraft may have a required *Technology Driver* to treat the engine exhaust (in order to lower the IR signature). An agile aircraft also requires engine exhaust treatment, but to provide

thrust vectoring. Clearly, different research in needed to fulfil the *Technology Driver* demands.

If some technology areas are vital (dark grey) for some designs, and need awareness (light grey) for other designs, prudence would dictate that the research areas be widened to take account of the possible needs. This approach therefore allows the strategic view of research whereby 'all-bases-are-covered' to the appropriate depth.

In order to take this methodology a stage further, it is worth taking an example of one of the *Significant Technology Drivers* to the next stage. This will be the aircraft engine inlet system.

Table 5: Significant technology Drivers Matrix

	FEACAS		
	A	B	C
1. Aerodynamics Technology Drivers			
1. Configuration Performance	■	■	
2. Wing	■	■	
3. Control Surfaces/Jet Reaction control	■	■	
4. Air Intake Design	■	■	
5. Engine Exhaust Treatment	■	■	
2. Propulsion Technology Drivers			
1. Compressor		■	
2. Combustion chambers			
3. Turbine		▒	
4. Reheat (Afterburner)	■	■	
5. Advanced Engine Control	■	■	
3. Weapons System Technology Drivers			
1. Radar System	■	■	■
2. Radar Missile Interface		▒	■
3. Missile System	■	■	■
4. Weapon Carriage System	■	▒	■
5. Identification-Fried-or-Foe			■
6. Integrated information management	■	■	■
4. Stealth Technology Drivers			
1. Shape/Configuration	■		
2. Materials	■		
3. Surface Finish	■		
4. Surface Coatings	■		
5. Conformally Mounted Sensors	■		
6. Air-data Systems	■		
5. Manufacturing Technology Drivers			
1. Technology Maturation	▒	▒	
2. Composites Techniques		▒	
3. Standardisation	▒		
4. Flexible Tooling/Jigging	▒	▒	▒
5. Assembly Techniques	▒		
6. Quality/Reliability	▒	■	▒
6. Maintenance Technology Drivers			
1. Quality & Reliability	■	■	▒
2. Repair of Coatings & paints	■	▒	▒
3. Standardisation	■	▒	
4. Fatigue	■	▒	
5. Reduction in Complexity	▒	▒	
7. Flight Control Systems Technology Drivers			
1. Non-linear aerodynamic Modelling	■	■	
2. Fly-by-Wire (FBW) -Light			
3. Integrated FBW System with other Systems	■	■	■
4. Carefree Handling		▒	
5. Electrical/Hydraulic Systems	▒	■	■
8. Crew Operations Technology Drivers			
1. Piloted/Remote Pilot	■	■	
2. Display Concept	■	■	
3. Display Issues	■	■	
4. Man-Machine Interface	▒	■	▒
5. Environmental Systems			
6. Training		■	
9. Materials Technology Drivers			
1. Composites	■	■	■
2. Single Crystal Materials	▒	▒	▒
3. 'Smart' Materials	■	■	■
10. Structures Technology Drivers			
1. Mass Reduction		■	■
2. Dynamics Tolerance	▒	■	▒
3. Health Monitoring	■	■	■
4. Battle-Damage Tolerance	■	■	■
5. Mission-Adaptable Wing	▒	■	▒

Chapter 3 - Significant Technology Example: The Air Inlet System

The air inlet system was highlighted in two of the scenarios as being an area of significant interest. The two aircraft were the -A and -B variants: the stealthy design and the agile design. Analysis of the two requirements is needed to investigate any overlap in requirements.

3.1 - FACES-A Inlet Requirements

The inlet requirements for a stealthy design centre on the reduction in the Radar Cross-Section (RCS) of the complete inlet side of the engine installation. Good quality airflow to the engine is of paramount importance, but all of the RCS reduction techniques reduce the airflow quality.

The RCS issues associated with the inlet system design centre on two basic design problems.

1. The intake lip on a conventional aircraft would be rounded in some manner. If the lip is too sharp, any incidence or sideslip of the aircraft might cause the flow inside the inlet to separate, thereby reducing the flow quality to the engine. This is further exasperated by the range of flow conditions which the engine must operate over: if the engine inlet conditions were the same over the entire thrust range, then the inlet could be optimised. However, in the practical case, the air mass entering the engine changes with many different parameters, and thus is never at one design point. The result is that it is the intake lip that would normally be designed to cope. For a stealthy aircraft, curved surfaces are good sources of radar energy reflectors, and the radar return will be sent in a wide spread of directions, increasing the detection arc of the aircraft. Thus there is a direct conflict between the intake performance and the RCS performance.

2. Because of the curvature and the relatively large surface area of the compressor blades of the engine, its radar reflection is high. Further, radar return can also reveal the aircraft type, since the type and rotation speed of the compressor blades are unique for each engine/aircraft installation. Thus, not only does the enemy know the presence of an aircraft, but also the aircraft type. This information then reveals possible mission tactics. Thus it is imperative to hide the engine face. This is achieved by burying the engine deep within the airframe, and by employing an inlet duct that is curved, thereby removing the direct line of sight. The curvature introduces a significant reduction in the flow quality at the engine face, which can be increased by flow control devices. Other means include the use of screens and baffles, but these greatly reduce the efficiency of the intake, thereby reducing the thrust which the engine can produce.

3.2 - FACES-B Inlet Requirements

The requirements of the agile aircraft are such that good quality air is received at the engine face thought the range of violent manoeuvres that the aircraft might pull. These may include the sustained high incidence/side-slip manoeuvres, or the dynamic manoeuvres that use high-pitch rate moves. These would be the types of manoeuvre such as the much-publicised 'Cobra' manoeuvre practised by the Russian Sukhio-27 airshow display pilots. It is expected that future combat manoeuvres will be more severe. As with the problems of the stealth intake lip, the highly manoeuvrable aircraft will have similar issues due to the extreme flight angles. However, since this aircraft will operate at more extreme angles than the stealthy aircraft, and it will do so more often, the problem is more significant. Designs for the intake lip could be made to reduce the problems here, and flow control within the intake could help to reduce the effects of any problems caused by lip separation.

Another issue for these designs is the reduction in weight of the inlet system, as highlighted by the requirements of the US Air Force for the next generation of aircraft[3]. Weight reductions of 65% over the current designs are sought, with reductions in length of 50%. Since current aircraft use

very gently curved ducts to channel the air from the side of or below the cockpit to the engine face, the reduction in length increases the relative severity of the bend, thereby reducing the air quality at the engine face. Flow control can help to alleviate this problem.

3.3 - Conclusion of Predicted Problems

In light of the discussion above, it is clear that there are some regions of overlap between the requirements of the stealth and agile aircraft, and hence it would be prudent to research in to these areas.

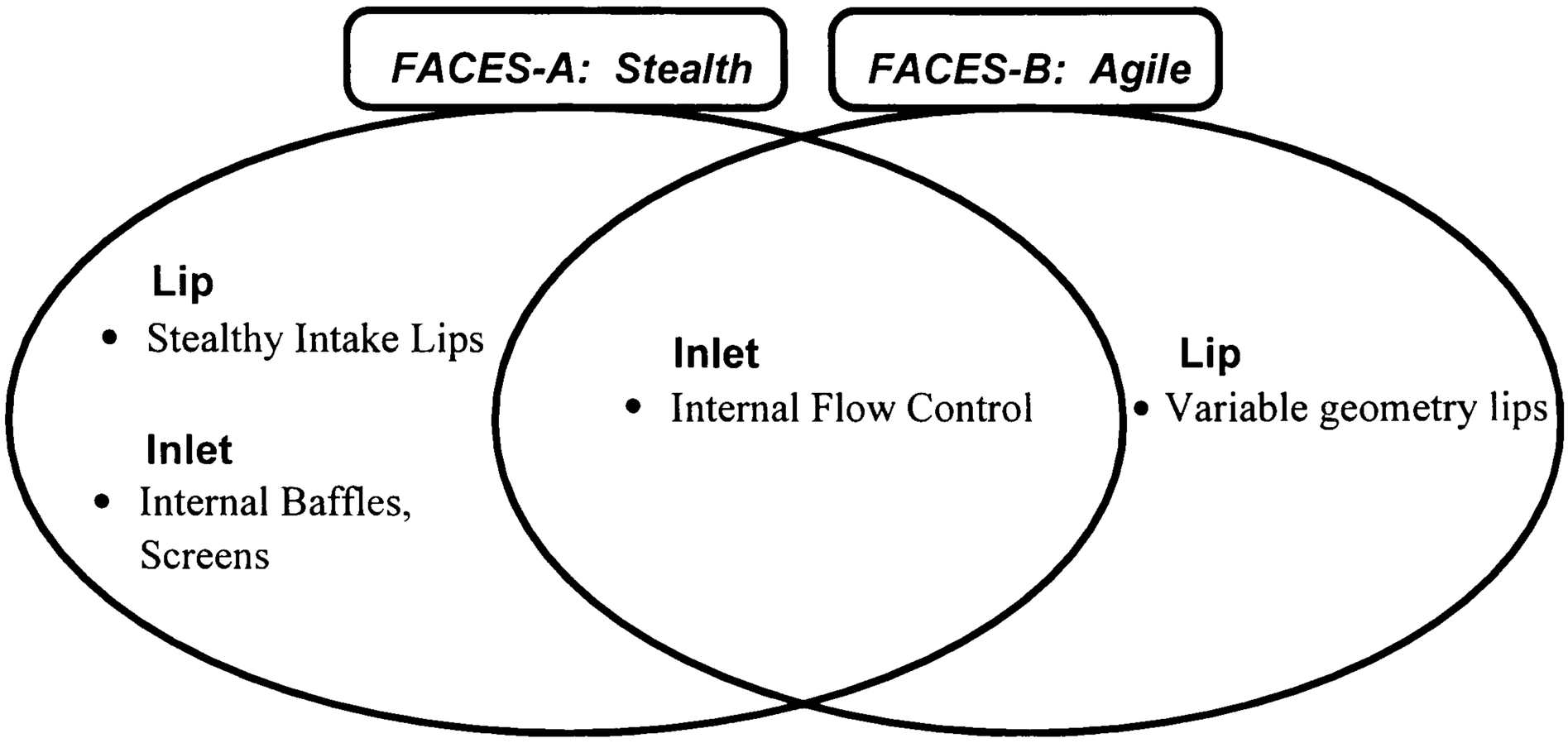

Figure 6: Overlap of Technology Requirements

The flow control in the intake duct is therefore an interesting and important area to investigate. While the Technology Drivers are different (that is, the stealth requirement and the agility requirement), the problem to be overcome is the same: the airflow to the engine is distorted aerodynamically, and the flow control can provide a correction.

In it important to take a system approach to the flow control devices in order to successfully assess their contribution. While it is relatively easy to measure the aerodynamic benefits of flow control, there are a number of other factors to be taken in to account.

3.4 - Intake Problems

Without delving too deeply in to the field of flow control, there are a few choices for controlling the flow in engine intakes that will help to improve the flow quality at the engine face. The two most serious problems are *total pressure distortion* and *swirl*.

Total pressure distortion is a non-uniformity of pressure over the engine face. This leads to increased fatigue of the compressor blades, and the possibility of engine surge. While the first problem is concerned with maintenance and life-cycle costs, the second problem is flight critical. If the distortion becomes too great, the engine surge occurs, whereby the compressed air which has just passed through the compressor reverses direction, and is forced back through the compressor blades with an explosive force. This causes a large loss in power, and possibly destruction of the engine. The distortion can be caused by a number of factors including:

- Intake lip separation (for example with the agile aircraft)
- Fuselage boundary layer ingestion
- Wake ingestion from stores release
- Hot gas ingestion (from missile release, gun firing, engine exhaust)

- Duct geometry (for example in the stealth configuration)

Swirl is characterised by the core of air in the intake rotating about the duct axis. This too can lead to engine surge, but is generally less of a problem. Swirl is largely caused by the geometry of the duct, but can be reduced using simple means.

3.5 - Flow Control Devices

A number of options are available to cure some or all of the flow problems encountered. These are listed in the table form below:

Table 6: Flow Control Device Options

Flow Control Technique	Problem Overcome
Optimum duct design	Lower distortion, but only around a single design point. Not flexible
Variable Lip Geometry	Reduces the chances of lip separation. Only of real benefit at high flow angles
Boundary Layer Bleed	Removal of boundary layer fluid that reduces the problems of fuselage boundary layer fluid ingestion.
Slot Blowing	Blowing of 'sheets' of air parallel to the duct wall. Allows some restructuring of the flow in the duct. High mass flow of air needed.
Vortex Flow Control	Use of vortex generators to restructure the flow in the duct. Reduction in flow distortion, and some reduction in swirl.

Some framework is needed in order to assess each of these technologies in some objective manner. Choosing the last technology 'Vortex Flow Control', the framework will be described.

3.6 - Vortex Flow Control Assessment

The flow control described here is that using vortex generators. These are small devices that create a vortex (or column of rotating fluid) with its axis in the flow direction. The rotation of the vortex at the wall of the duct induces a cross-stream motion that can be used to re-order the duct flow.

Devices that could be used include vane vortex generators; air-jet vortex generators; Micro-Electro-Mechanical-System Devices.

It should be said here that MEMS technology is a new and exciting field. These devices are very small active devices, which can be of a vane or air-jet type. The mechanisms for vortex production are the same, but the ancillary technologies are novel, and address some of the failings of the other two. In terms of the aerodynamics, the effects may be similar to the other devices, albeit on a smaller scale (therefore possibly requiring more devices). They should be seen as competitors to the conventional vanes and air-jets. However, due to their wide-ranging form, then will not be dwelt upon in this illustrative exercise.

Assessing the total vortex generator system, it can be looked at using the following categories:

In this assessment, it is very difficult to state unconditionally that one system is *better* than another. All engineering decisions are compromises, and in the case of flow control for engine intakes, it will very mush depend on the application as to which sort of flow control should be applied. Thus, rather than a using a methodology which provides a black and white answer, a series of statements should be made which would help the designer to choose the most appropriate system.

3.6.1 - Quality Function Deployment Approach

The best selection for a flow control system is made with quantitative data. In order to provide this data, many more man-hours are needed than can be provided here within the scope of this study. However, this methodology does provide the framework on which that assessment can be made.

The quantitative aspects would be brought in through the use of Quality Function Deployment. As with the technology Strategy Matrix described earlier, data can be generated based on a performance rating and a mission significance factor (compared with the Technology Risk Factor and Technical Driver Probability respectively).

In this case, each of the categories can be broken into a number of issues, and a performance rating can be applied which may be rated between large negative contribution through to large positive contribution. Also, the significance of that issue can be rated with respect to the mission performance, thus allowing the systems to be assessed in relation to each other, *based on what is important for the particular use intended.*

The system that scores with most of its factors in Part A of the matrix becomes the most attractive system, while the system with most of its factors in Part D of the matrix becomes the least attractive. Therefore, this technique thus allows the optimum choice to be made at time the technologies are considered.

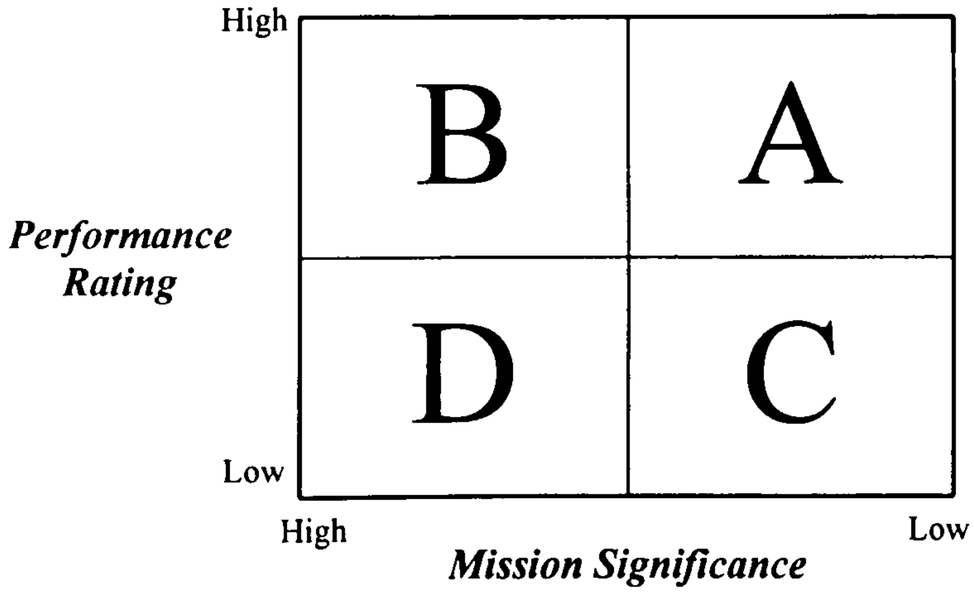

Figure 7: Quality Function Deployment Matrix

In order to use this technique, the performance ratings must be achieved from test data, and applied in the context of the flight envelope, and the mission significance. This is not possible in

the scope of this study, since the time required is high. A further technique is proposed which allows less time for an experienced aircraft designer to choose the required system.

3.6.2 - Concurrent Data Display

The concurrent display of information in this manner is more preferable than the conventional SWOT technique. In the SWOT case, one technology would be considered at a time, and then the relevant issues would be split in to the Strengths, Weaknesses, Opportunities and Threats (hence SWOT) of the system. This is less preferable, since it is important to look at the benefits and drawbacks of each system in relation to the other systems. The SWOT analysis tends to segregate each technology and restricts comparison. The concurrent technology statements are made below.

From this table, a designer can then look at *all* of the relevant factors that may influence their choice in system selection. By considering the system as a whole, or more importantly the impact of that system on the total aircraft package, the optimum choice can be made.

Category	***Vane Vortex Generator Systems***	***Air-Jet Vortex Generator Systems***
Aerodynamic Performance	Vast improvement over a poorly designed S-Duct • Intake Efficiencies of 4% demonstrated • Total Pressure Steady-state Distortion reduced by up to 70% • Further optimisation to be demonstrated • Passive devices. Effects cannot be controlled • Less effective if intake suffers from a lip separation • Good performance over all speed range	Vast improvement over a poorly designed S-Duct • Intake Efficiencies of 4% demonstrated • Total Pressure Steady-state Distortion reduced by up to 70% • Further optimisation to be demonstrated • Active device. Flow control can be optimised in flight • Good performance even with lip separation • Performance reduces as speed become very high
Design Implications	Intake can be dramatically shortened for little aerodynamic problem: • Large weight saving • Application to ASTOVL aircraft • 1% increase in efficiency = 2% increase in installed thrust • 1% increase in efficiency = 10% reduction in fuel burn for a typical mission of a Harrier type aircraft.	Intake can be dramatically shortened for little aerodynamic problem: • Possible weight reduction due to high-pressure pipework, control valves, etc. • Some mass flow loss from engine needed to drive air-jets (0.5% duct flow typically) • Application to ASTOVL aircraft • 1% increase in efficiency = 2% increase in installed thrust • 1% increase in efficiency = 10% reduction in fuel burn for a typical mission of a Harrier type aircraft.
Manufacture	Simple system • Small rectangular thin plates mounted perpendicular to surface • Use of composites to reduce RCS	Complex System • Air-jets are simple circular holes drilled at an angle in surface: possible difficulty in drilling holes accurately (diameter approx. 1 mm). • Pressurisation required air bleed from engine, ducting, control system for air, integration with flight control system

Maintenance	Foreign Object Damage (FOD) Hazard in event of failure: • Inspection needed to ensure no cracks/damage • Reduction in intake access, since vanes are sharp, and are all around the duct wall. • In-flight failure is serious for FOD reasons	Complex system: • Monitoring needed • Difficult to access especially in the stealth aircraft where inspection hatch numbers are reduced. • In-flight failure reduces flight envelope
Safety/Certification	In-flight failure is potentially very dangerous Icing in intakes is a serious issue. Vanes require de-icing elements/warm air bleed. Possible aid to gun integration (hot gas ingestion)	In-flight failure will limit flight envelope performance (speed, incidence/sideslip angle). Not flight critical. Icing in intakes is a serious issue. Jets require duct heating to ensure no ice build up. Possible aid to gun integration (hot gas ingestion)
Crew Operations	Little impact on crew performance until failure occurs. Pilot must have direct control over heating devices in the inlet system (Def. Stans.) Issues on alerting the pilot, and modifying the envelope	Integration with the flight control system should allow a 'hands-free' operation. Failure should be fail-safe though flight control limits of the envelope
Cost of Ownership	Reduced on baseline duct: • Penalty on engineering of system • Penalty on maintenance of vanes • Saving on compressor fatigue • Saving on fuel burn • Saving on aircraft weight (and hence more fuel) • Saving due to increased survivability (stealth/agility)	? on baseline duct: • Penalty on engineering of system • Penalty on maintenance of system • Saving on compressor fatigue • Saving on fuel burn • ? on aircraft weight (reduced duct size vs. weight of system) • Saving due to increased survivability (stealth/agility) even over vanes • Saving due to optimised performance

3.7 - Conclusion

A methodology has been proposed which allows the formulation of a Technology Strategy. This methodology encompasses aspects of conventional management business strategy tools, and applies them to the area of technology.

The methodology uses PEST analysis to assess the technology needs or Technology Drivers, and uses Scenario planning coupled with Quality Function Deployment (QFD) in order to try to remove some of the uncertainty in predicting the future. The use of QFD allows some objectivity to be applied to an area in which subjectivity rules supreme. The objective of this exercise is to produce a list of the areas that are of strategic importance, and this is successfully demonstrated.

Following on from this, one area of importance is expanded upon, in order to highlight the need to examine the required technologies at a systems level. The use of QFD can again be employed to help rate the effectiveness of systems, but in the absence of hard numerical data, an awareness table can be drawn up, which can highlight the benefits and drawbacks of the systems.

Chapter 4 - Notation

Symbol	*Definition*	*Units*
C_f	Skin friction coefficient	
D	Air-jet context: Diameter of Air-jet Orifice	(m)
	Vane context: Spanwise distance between vanes	(m)
h	Height of the vortex	(m)
i	complex operator	
P	Total pressure	(Pa)
p	Static pressure	(Pa)
q	Dynamic pressure	(Pa)
q_t	Tangential velocity (also given as v_θ)	(m/s)
r	Radial distance from vortex centre	(m)
t	Time	(s)
U	Free-stream velocity (in the x-axis direction)	(m/s)
u	Velocity component in the x-axis direction	(m/s)
VR	Air-jet velocity ratio	
v	Velocity component in the y-axis direction	(m/s)
v_θ	Tangential velocity (also given as q_t)	(m/s)
W	Free-stream velocity (in the z-axis direction)	(m/s)
w	Velocity component in the z-axis direction	(m/s)
x	Cartesian co-ordinate axis	
y	Cartesian co-ordinate axis	
z	Cartesian co-ordinate axis	
Γ	Vortex Circulation	(m^2/s)
α	Pitch angle	(degrees)
β	Skew angle	(degrees)
δ	Boundary layer thickness	(m)
γ	Vortex helix angle	(degrees)
μ	Absolute Coefficient of viscosity	(kg/ms)
ν	Kinematic Coefficient of viscosity	(m^2/s)
ρ	Density	(kg/m^3)
τ	Wall shear stress	(N/m^2)
ω	Vorticity - where $\omega = f(\xi,\eta,\zeta)$	(s^{-1})
ξ	Vorticity component in the x-axis	(s^{-1})

η	Vorticity component in the y-axis	(s^{-1})
ζ	Vorticity component in the y-axis	(s^{-1})

Subscripts

avg	Average
j, jet	Jet
min	Minimum
∞, 0	free stream

Chapter 5 - Literature Survey – Vortices & the Vortex Generator

The following chapter is a literature survey that discusses the structure of vortices, and documents the important features of the vortices. With the vortex flow features fully discussed, previous investigations on the generation of the vortices will be discussed, including studies on vane and air-jet vortex generators.

The vortex is a flow in which the fluid particles form a rotating chain and is carrying with it a swirl of particles that flow around in circles with one common axis. It is worth noting that as this flow is in the most part inviscid, each fluid particle has no rotation about its own axis, merely a circular translation about the rotational centre. This leads to the treatment of the vortex as a mostly inviscid potential flow problem.

5.1 - Vortex Production

5.1.1 - Vorticity

The formation of a vortex is achieved through the reorganisation of the vorticity within a fluid flow. The vorticity is simply defined as one of the two motion types available to a fluid particle, which allows it to rotate about its three axes. (The other type of motion is translation along the three particle axes). Since the rotation of the fluid molecule can be about one of the three axes, the vorticity must be defined in a manner that allows the orientation of the rotation to be identified. Thus, for a fluid element, the vorticity is denoted as ω where:

$$\omega = f(\xi, \eta, \zeta) \qquad \textit{Equation 1}$$

ξ, η, ζ are the vorticity components about the *x, y & z* axes respectively, also denoted as ω_x, ω_y and ω_z.

It may be shown[5] that the vorticity is equal to twice the rotational spin of the element. For most cases involving a vortex whose rotational axis is in the streamwise (usually denoted as x) direction (also called a longitudinal vortex), the vorticity components η & ζ are usually small, and so the major portion of the vorticity comes from the component in the x direction, ξ.

The vorticity is mathematically defined as the curl of the velocity vector, as follows:

$$\vec{\omega} = \nabla x \vec{u}$$

or

$$\omega_x = \frac{\partial w}{\partial y} - \frac{\partial v}{\partial z} \qquad \textit{Equation 2}$$

$$\omega_y = \frac{\partial u}{\partial z} - \frac{\partial w}{\partial x}$$

$$\omega_z = \frac{\partial v}{\partial z} - \frac{\partial u}{\partial y}$$

Further, the total vorticity enclosed within a boundary is called the circulation, Γ, and is defined as follows:

$$\Gamma = \int \omega.dA$$

or in cartesian co - ordnates for a streamwise vortex

Equation 3

$$\Gamma = \iint \omega_x.dy.dz = \iint \left[\frac{\partial w}{\partial y} - \frac{\partial v}{\partial z}\right] dy.dz$$

Following the work of Morton[6], the Helmholtz vorticity equation for a homogeneous fluid is given as:

$$\frac{\partial \omega}{\partial t} + (v.\nabla)\omega = (\omega.\nabla)v + \nu\nabla^2\omega$$

Equation 4

The term $(\omega \cdot \nabla)v$ is described as the vorticity processing term which concerns the local amplification of vorticity by vortex filament stretching. The term $\nu\nabla^2\omega$ represents the viscous spread of vorticity. It is interesting to note that there is no term representing the generation of vorticity, and thus no new vorticity can be introduced into the flow. Vorticity can then only be created at the boundaries of a homogeneous fluid, and not within it.

The vortex filament term warrants a further statement. It may be proved that the vorticity is divergence-free, that is:

$$\nabla.\omega = \frac{\partial \omega_x}{\partial x} + \frac{\partial \omega_y}{\partial y} + \frac{\partial \omega_z}{\partial z}$$

Equation 5

Integrating this over a finite volume and with the Divergence Theorem applied:

$$\int_V \nabla.\omega \, dV = 0 \Rightarrow \int_S \omega \cdot n \, ds = 0$$

Equation 6

In the same manner as a streamline may be defined for all the points along the tangent to the velocity vector, a vorticity line can be defined for all points lying along the tangent of the vorticity vector. If a vortex tube is the area surrounding a cluster of vorticity lines (in the same manner as a stream tube surrounds stream lines), then we can apply the above equation at different points along the vortex tube. On the enclosing surface of the vortex tube, the vorticity out of the plane of the vortex tube must be zero (compare with the velocity in the cross-stream plane of a stream tube). Thus:

$$\int_{S_1} \omega \cdot n \, dS + \int_{S_2} \omega \cdot n \, dS = 0$$

Equation 7

and,

$$\Gamma_1 = \Gamma_2$$

Thus, the circulation within a vortex tube is constant. If the vortex tube is reduced in cross-sectional area, then the average vorticity is increased, and vice versa. This result is known as Helmholtz's 1st Law.

In investigating vorticity at boundaries, Morton[6] sets up initial boundary conditions in two dimensions.

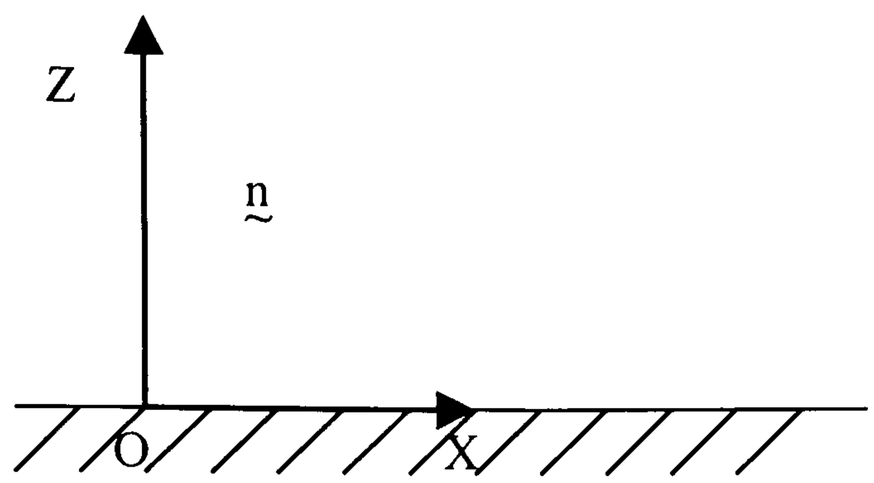

Figure 8: The Co-ordinate System in the Neighbourhood of a Boundary

$$V_{x=0} = (u, w)_{x=0} = 0 \qquad \textit{Equation 8}$$

It follows that for all values of x and t:

$$\frac{\partial (u, w)_{x=0}}{\partial x} = 0 \qquad \textit{Equation 9}$$

$$\frac{\partial^2 (u, w)_{x=0}}{\partial x^2} = 0$$

By satisfying the incompressible continuity equation when $\partial u/\partial x = 0$, on $z = 0$ and for all values of x and t,

$$\frac{\partial u}{\partial x} + \frac{\partial w}{\partial z} = 0$$

then

$$\frac{\partial w}{\partial z} = 0 \qquad \textit{Equation 10}$$

By relating the velocity gradient at the wall to the wall shear stress, we get the relation:

$$\tau_x = \mu \frac{\partial u}{\partial z} \qquad \textit{Equation 11}$$

Recalling that $\partial w/\partial x = 0$, then:

$$\omega = (\xi, \eta, \zeta) = \left\{0, \left(\frac{\partial u}{\partial z} - \frac{\partial w}{\partial x}\right), 0\right\} = \left\{0, \frac{\tau_x}{\mu}, 0\right\} \qquad \textit{Equation 12}$$

This implies that the wall shear stress is at 90° to the vorticity filaments in the boundary layer, and this is also true for the three dimensional case. Morton states that this is an important result, since it is a clear indication that wall shear stress cannot generate vorticity.

Further from this, Morton applies the Navier-Stokes equations at a boundary, and gives a reduced equation as:

$$0 = -\frac{1}{\rho}(\nabla p)_0 + \nu(\nabla^2 v)_0 \qquad \textit{Equation 13}$$

Rearranging this equation gives:

$$\frac{\partial^2}{\partial z^2}(u, w) = \frac{1}{\mu}\left(\frac{\partial}{\partial x}, \frac{\partial}{\partial z}\right) p \qquad \textit{Equation 14}$$

Applying this at z = 0, and remembering the result relating the vorticity to the wall shear stress, we

get:

$$-v\left(\frac{\partial w}{\partial z}\right)_0 = -\frac{1}{\rho}(n \times \nabla)p \qquad \textit{Equation 15}$$

This is equivalent to the result obtained by Lighthill[7], and is noted as the 'diffusive flux density' of positive vorticity outwards from the wall. Morton notes that this is important, but the balance of positive and negative vorticity generated, lost or gained cannot be determined without a physical understanding of the flow, which this relationship does not provide.

Morton does go on to state that the generation of vorticity is instantaneous, and is carried out by the wall imparting an impulse to the fluid particles directly above the wall as the wall accelerates relative to the fluid. At time t = 0, the molecules will have a velocity, but will not have moved, and hence the vorticity will be infinite, and confined to the fluid particles directly above the wall. This process is inviscid. However, at any time after t = 0, the vorticity will now be diffused away due to the viscous nature of the fluid*, and this process occurs immediately after generation. Viscosity plays no part in the generation of vorticity, which is due only to the inertial forces of the fluid.

The decay of vorticity is another area to which Morton extends his work to. He states that the circulation inside a contour is a measure of the gross vorticity in that region and that if the boundary is at rest, then the gross circulation must always be zero. Further, vorticity is not lost by diffusion through a solid surface, unless vorticity of the opposite sign is being generated there. Thus the cross-diffusive annihilation of vorticity in the fluid interior is the sole cause of the decay of vorticity fields. Thus for Morton's cup-of-tea, if the cup is stirred, the bounding cup is at rest, so the overall circulation is zero. While the centre of the cup may have negative vorticity (generated by the spoon), the effect of the initial acceleration is to produce (inviscidly) a positive layer of vorticity at the cup surface, which will cancel out through cross-diffusion with the negative region to reduce the vorticity to zero.

5.1.2 - Linking of Vorticity to the Vortex

As summarised by Bushnell[8], in most general cases, transverse pressure gradients are responsible for the formation of vorticity (through the transverse acceleration of the flow). Typical cases are (a) wing tip flows; (b) delta wings at incidence; and (c) axi-symmetric bodies at incidence. In the case of a wing tip, vortex filaments (in the boundary layer and the separated wake) created by this spanwise pressure gradient and are oriented in a streamwise direction. Due to their rotational nature, they roll-up behind the wing tip as each one interacts with the next, i.e. as in Prandtl's lifting line model. Due to the large strength of the pressure gradient close to the wing tip, it is logical to suggest that the strength of the vortex filament close to the tip will be stronger than that further inboard, and will induce the other vortex filaments to roll around it.

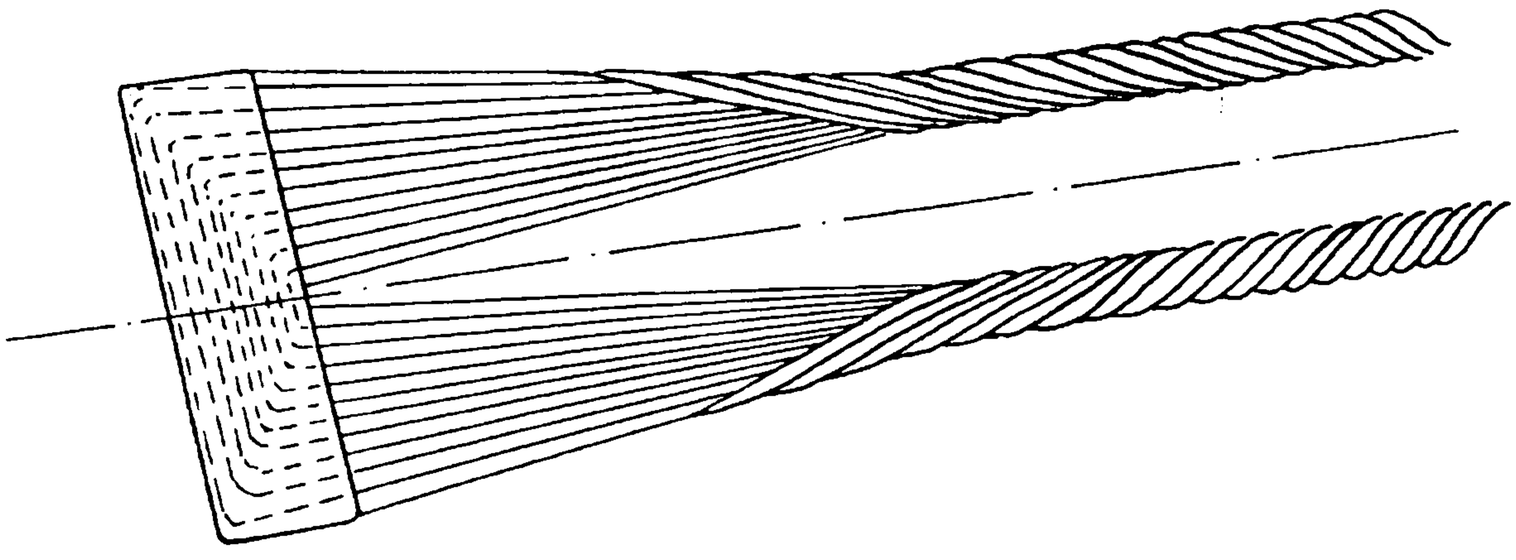

Figure 9: Prandtl Lifting Line Theory Model of the Vortex Formation (Diagram from Houghton & Carruthers[1])

* remembering Helmholtz's equation and the term $\nu\nabla^2\omega$ representing the viscous diffusion of vorticity

Experimental investigation by Iverson[9] on free vortices has shown that the vortex will pass through three major phases of structure. The first is the vortex establishment process described above (i.e. that on or immediately behind the aerofoil surface) that is highly three-dimensional. In the second stage, the vortex develops to an inviscid roll-up region described by Iverson as the 'plateau region' in which the decay of the vortex is negligible, which would be the region where the vortex is recognisable in Figure 9. It is shown that the plateau region is determined by a number of factors: (a) the axial velocity of the vortex; (b) the non-equilibrium turbulence; and (c) that the presence of the plateau is due to the viscous core. The third stage is the decay of the vortex, where the circulation strength of the vortex reduces with streamwise distance from the point of generation. The inviscid model does not model this observation.

5.1.3 - Streamwise Velocity of the Core

The axial velocity of the core of the vortex will, in almost all cases, not be at the free stream speed[10] but will have a velocity either higher or lower. In the case of the core having a lower axial velvety, the core is referred to as being a *wake* like core, and in the case of a higher axial velocity, the core is described as being *jet* like. Typical variations are given below. U is the streamwise velocity component, and r is the radial distance from the centreline of the vortex.

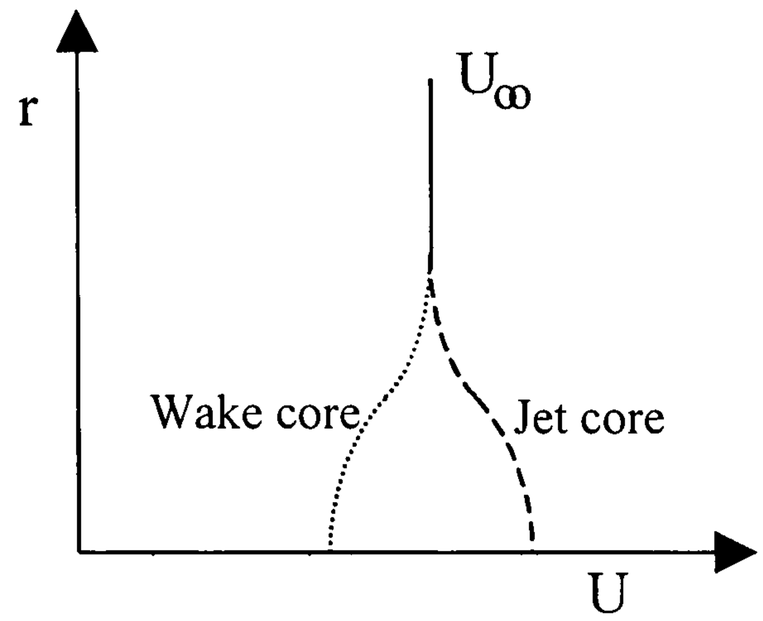

Figure 10: Vortex Core Velocity Profiles

It is noted that the two differing axial velocity states in the core are present, depending on the nature of the vortex induced. The wake-like core tends to be associated with the weaker vortex case of a trailing vortex (where the deficit is small) or in the case of a three-dimensional breakdown of the flow. The jet-like wake is associated with the strong, intense vortices that are formed on the upper surface of a delta wing at incidence, where the axial velocity at the centre of the core can reach as much as three times the free-stream speed.

It was noted by Batchelor[11] that there must be a link between the radial and axial motion in the vortex core which would be provided by the pressure terms: that is that the radial pressure forces are balanced by the centrifugal forces due to the rotation. Further, it was noted that any change in the vortex motion in the axial direction would have an implication in the radial motion since the conservation of mass in the vortex centre must hold. Thus, if the vortex were to undergo a favourable pressure gradient, then the axial velocity would tend to increase with a reduction in the vortex core diameter. Similarly, if the vortex negotiated an adverse pressure gradient that would tend to reduce the axial velocity, then the vortex core size would grow to allow for this fact. This would then help to explain the increase in vortex decay rate, a point that will be discussed in Section 5.2.5.

Clearly, the axial velocity of the vortex will depend on how the vortex core has been accelerated during the production phase, and the pressure gradients that develop downstream. It is therefore reasonable to suggest that in the case of a wing-tip type flow, the vortex which is produced does not undergo an appreciable favourable pressure gradient capable of increasing the axial component

of velocity of the vortex while tightening the extent of the vortex core. However, for the separation seen in the case of a sharp edged delta wing, it may be expected that the flow undergoes a large favourable pressure gradient. This would increase the axial velocity of the core, hence leading to magnitude of axial velocities (as compared with the free-stream velocity) noted above.

5.1.4 - Vortex Core Turbulence Modelling

Analysis of the turbulence levels in the vortex core by Shabaka *et. al.*[12] has shown that the simple empirical correlation used in current turbulence models does not accurately represent the actual turbulence, and hence are unlikely to correctly predict the flow features in any great detail. Considering that the eddy viscosity levels are significantly higher than the laminar viscosity†, it will be clear that the eddy viscosity will play an important role in the modelling of turbulent vortices. Shabaka *et al.* showed that the eddy diffusivity of Reynolds stresses are 'ill-behaved' either side of the core. Thus the only way that an empirical model can be used is if the eddy viscosity is related to the cross-plane co-ordinates around the vortex, which would have limited application in other vortex cases. A better calculation method could be used, but the level of modelling (of the triple products of velocity fluctuations) would be immense. Clearly though, an improvement in the numerical modelling of the viscous part of the vortex core requires a more sophisticated turbulence model.

5.1.5 - Free Vortex Breakdown

The following development of the vortex is very dependent on where the vortex is placed. If the vortex is free (i.e. outside any boundary layers), then the vortex will decay or burst. Delery[10] describes this bursting as a rapid dilatation of the vortex structure. When breakdown occurs, the core of the vortex undergoes rapid expansion (usually due to a large deceleration of the core in the streamwise direction), and flow visualisation of the vortex gives the impression of a large jump between two well-defined flow types. Experiments by Sarpkaya[13] have suggested that there are three types of vortex breakdown, which depend on the swirl intensity of the vortex. However, Delery suggests that there is even some doubt if even some of Sarpkaya's classifications of vortex breakdown actually exist, as some of the different classifications could be different observations of the same phenomenon. Vortex breakdown does not tend to occur in vortices embedded in a turbulent boundary layer. Either the pressure gradients which cause the core deceleration do not tend to occur, or the vortices tend to be decayed by the presence of the wall before the natural burst point.

5.1.6 - Embedded Vortex Development & Mixing

As mentioned in the introductory chapter, it is often advantageous to deliberately introduce a vortex into a flow close to a boundary layer region. Taylor at the United Aircraft Corporation first published this idea[16]. Much of this initial work was used in applications such as diffusers and fuel-air mixing devices, but in all cases, the principle of operation was the same.

The vortex provides a local rotation to the flow in a cross-stream sense. If the vortex is then placed in a region where fluid with two differing properties is trying to mix, the rotation of the fluid enhances the mixing process. Thus, for the fuel-air-mixing device (which was applied to a ramjet pre-combustion chamber), the streamwise length for efficient mixing could be reduced.

---

† It should be noted that the relative magnitude of the turbulent viscosity over the laminar viscosity for the vortex core is not clear in current literature. Wendt, Greber & Hingst[14] indicate that the turbulent viscosity is about 35 times larger than the laminar viscosity, while Shabaka[12] uses the figure of 70, and Schubauer & Spangenberg[15] refer to the order of 100 times. Clearly all these figures are the same order of magnitude, but no more can be inferred.

Similarly, in the region of a thickening boundary layer where the boundary layer fluid becomes of particularly low momentum‡, the vortex can be encouraged to mix higher momentum flow from outside the boundary layer with lower momentum flow in the boundary layer. This mixing is well described in the figure below[17].

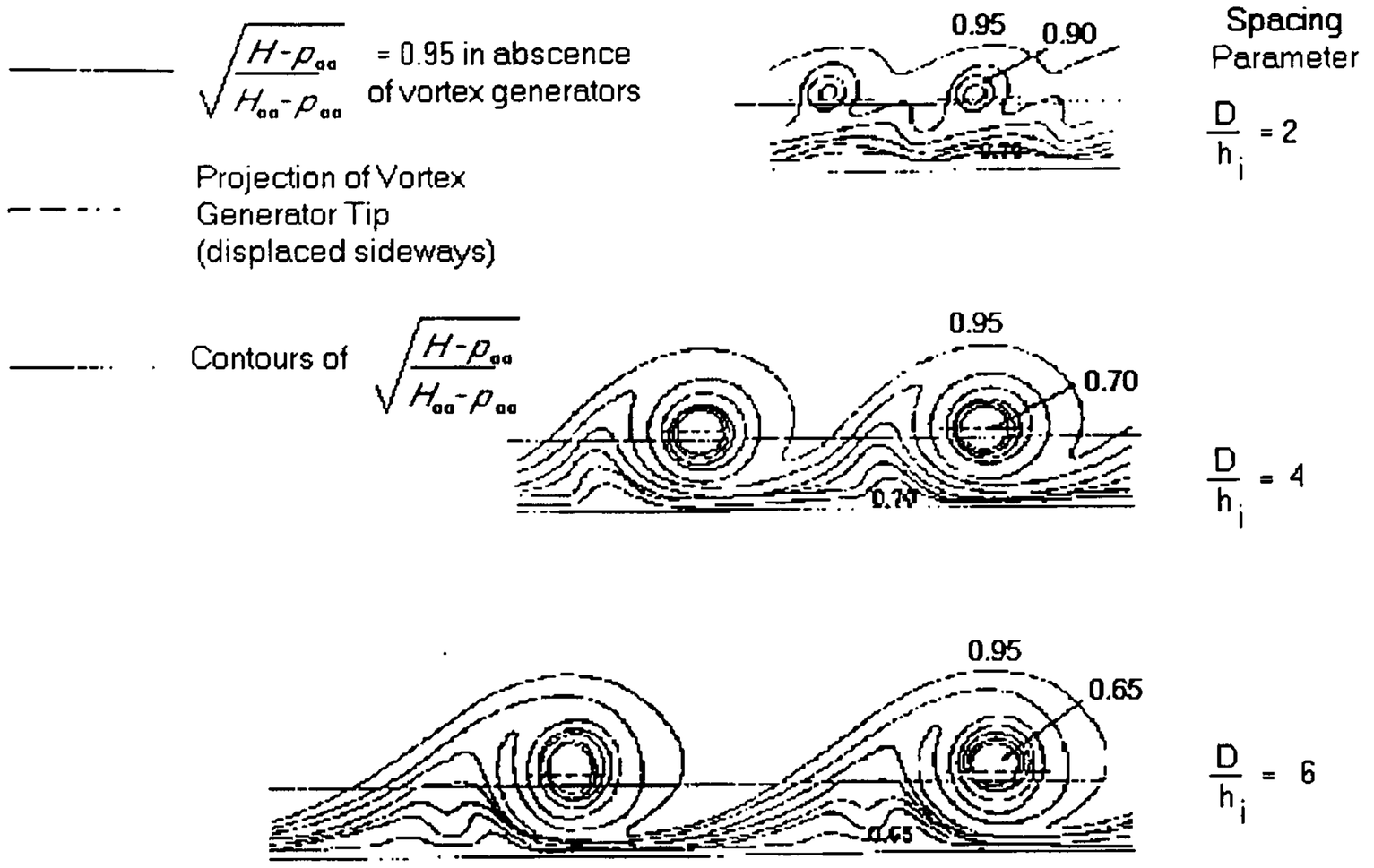

Figure 11: Boundary Layer mixing with Streamwise Vortices (Diagram from ESDU 93024[17])

For the two vortices pictured (rotating in a clockwise sense), it may be seen that the vortex sweeps the higher momentum fluid (i.e. higher values of $\sqrt{[(H-p_{\infty})/(H_{\infty} - p_{\infty})]}$) down towards the surface on the right hand side of the vortex, and sweeps lower momentum fluid up from the surface towards the free-stream. Thus it may be seen that the thickness of the boundary layer is considerably less on the right-hand (flow-towards-the-wall side) and thicker on the left-hand side.

As noted by Wendt & Greber[14], the quality of the vortex mixing will depend on the characteristics of the vortex set in the boundary layer. Four factors are highlighted as:

1. The Circulation, as a measure of the strength of the vortex.
2. Peak streamwise vorticity - as an indication of the concentration of the vortex. The larger this value takes, the thinner and more concentrated the vortex will be.
3. & 4. The spanwise and normal location of the peak vorticity that locates the centre of the vortex in the cross flow plane.

‡ The reader will recall that the separation of a boundary layer will occur when the velocity gradient away from the wall is zero, and hence will be due to the loss of momentum of the flow immediately above the surface.

Clearly, if the vortex circulation is large, then the amount of fluid swept around the vortex will be greater. As the vortex strength increases, so will the induced velocity at a given distance from the centre.

The peak streamwise vorticity, ω_{peak}, will have implications as to the growth of the vortex core. In the absence of all else, the vortex should remain at a constant circulation (with a control volume at the extent of the vortex boundary) until some mechanism is encountered through which decay can take place. Freestone[18] suggests that, following on from the work by Wendt and Greber, the decay rate of the single vortex is small, being related to the surface skin friction through the expression:

$$\frac{d\Gamma}{\Gamma} = -k\frac{c_f}{h}dx$$

Equation 16

Γ is the vortex circulation, k is a constant, c_f is the coefficient of skin friction, h is the height of the vortex core from the wall, and x is the streamwise distance.

Clearly, the decay in vortex strength will be affected directly by the local surface skin friction, which will in turn be affected by the Reynolds number of the flow. Thus the skin friction will provide a mechanism for circulation strength reduction. For the single vortex, this reduction will be small.

Vortex decay is a significant aspect in the use of embedded vortices. The effects of cross-diffusive annihilation can also significantly reduce vortex strength. It has been highlighted that as the vortex grows downstream, the vortex core will increase in size. If the vortex is placed in such a way that it is close to other vortex cores, the vorticity in the cores could cross diffuse, with the result that vorticity of opposite signs will cancel each other out, with a significant reduction in the level of circulation of the vortex. Even in the case of the single embedded vortex, due to the 'no-slip' condition at the wall, the central boundary layer must contain vorticity of the opposite sign to the vortex situated above it, which is induced by the transverse pressure gradient caused by the vortex induced motion. Thus as the vortex develops downstream, this region of opposite vorticity will be eventually drawn out from the boundary layer and into the vortex core, with a resulting reduction in the circulation of the vortex[19]. If the vortex is sufficiently strong, the transverse acceleration of the boundary layer can be so great as to cause a separation underneath (and to the upwash side) of the main vortex. This secondary vortex is driven by the secondary vorticity (of opposite sign to the main vortex) created in the boundary layer[20, 21].

The exact distance from the point of generation where the reduction in circulation strength occurs (i.e. the length of Iverson's plateau region) will depend on a great number of variables, not least the height of the vortex core at generation, and the number of other vortex cores in the vicinity. There appears to be little absolute data on these distances.

5.2 - Modelling of a Single Embedded Vortex

5.2.1 - Potential Flow Method

A simple, but useful model to use in order to track the downstream development of a vortex is the inviscid theory as used for the modelling of the single free vortex. In the two dimensional case (where the axis which is ignored is that which forms the rotational axis) of a free vortex, the flow is simply modelled using complex potential theory. Using this idea, it may be seen that the velocities induced around the vortex are dependent on the radial distance from the centre of the vortex in a logarithmic variation. Further, if the vortex is defined as having strength Γ at the centre, then the tangential velocity can be defined as:

$$v_t = \frac{\Gamma}{2\pi r}$$

Equation 17

v_t is the tangential velocity, Γ is the vortex circulation, and r is the radial distance from the centre of the vortex where the tangential velocity acts.

In this case though, the vortex has to be introduced above a flat plate in order to represent the wall. This two-dimensional representation would be a realistic assumption if the flow were considered far downstream where the vortex is well developed.

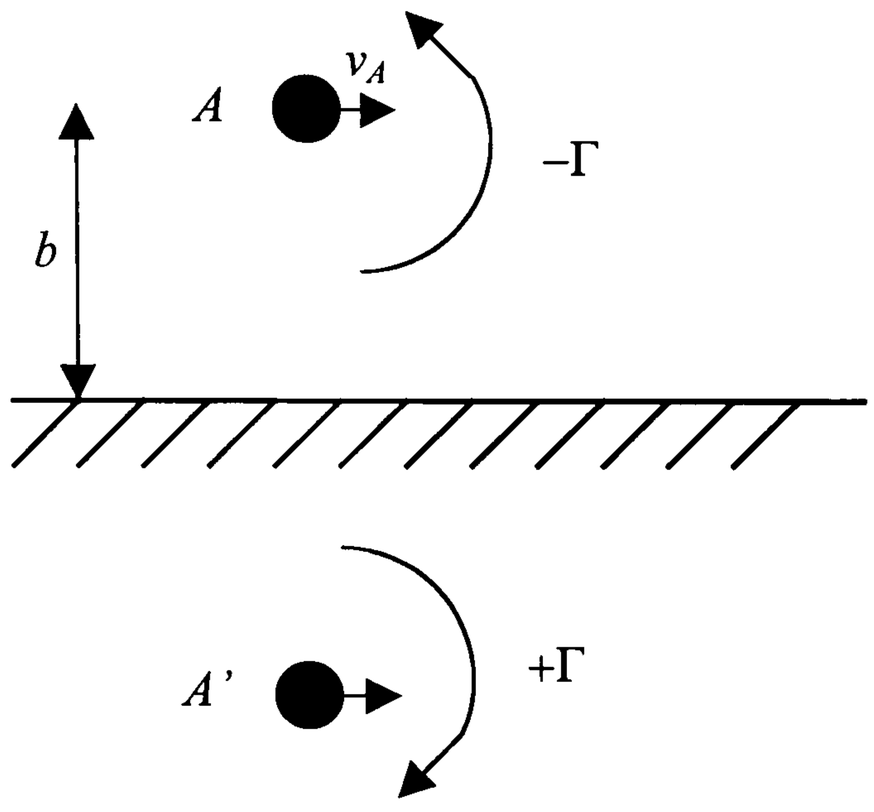

Figure 12: Potential Flow Model of a Real and Image Vortex

The treatment consists of using an image vortex (A') which reflects the modelled vortex (A) in the solid surface (see diagram above). Then considering the centre of A, it will have a lateral motion induced at it by the image vortex given by complex potential theory. Hence the first two terms represent the effects of the true vortex and image vortex (respectively):

$$\omega(z) = -\frac{i\Gamma}{2\pi}\ln(z - ib) + \frac{i\Gamma}{2\pi}\ln(z + ib) \qquad \textit{Equation 18}$$

In this equation, $z = x + iy$, where x and y are the ordinates of the co-ordinate system. Differentiating this expression gives the u and v velocity components in the cross-flow plane:

$$\frac{d\omega(z)}{dz} = u - iv = \frac{\Gamma b}{\pi}\frac{1}{z^2 + b^2} \qquad \textit{Equation 19}$$

To evaluate the effect on the vortex A due to the image, it is necessary to find the velocity components at A, u_A and v_A. This would take place when $x = 0$ and $y = b$, hence $z\ (= x + iy) = ib$. Using just the complex potential for the image vortex, since the point vortex A will induce no velocity at its own centre), the velocities at A become:

$$u_A = \frac{\Gamma}{4\pi b} \qquad \textit{Equation 20}$$

$$v_A = 0$$

Thus for the vortex which is established far downstream of its source (and neglecting the effect of decay) it may be seen that the vortex is expected to move parallel to the wall in the positive x-direction. There is no movement of the vortex perpendicular to the wall, for the co-ordinate system shown here, since the velocity perpendicular to the wall must be zero at the vortex centre. It should of course be noted that this is an extremely simple model that neglects several factors including the effect of the boundary layer, the viscous cores, and the decay of the vortex.

While this model is a good approximation for the flow away from the centre of the vortex in two dimensions (i.e. sufficiently far downstream that the vortex formation process can be ignored), it incorrectly models the flow at the centre of the vortex. Indeed, referring to Equation 17, if

Γ is a constant, then as $r \rightarrow 0$, $v_t \rightarrow \infty$. This is clearly impossible in fluid motion. Studies have shown that the true flow in the centre of the vortex consists of an area where the flow rotates as a solid body centre. This region is known as the vortex core, and will therefore not be modelled by the potential model. It is worth noting that this approach was taken by Jones[22] who modelled the movement of a counter-rotating vortex generator array, and while he did not model the vortex cores (which would not affect the vortex movement), the effect of slow decay was included through a simple vortex strength reduction. These modelled results compared favourably with the observed case.

In the viscous core, the fluid particles are not only translated around the axis of rotation, but each particle also rotates about its own axis. Thus the core of the vortex will contain vorticity. Introducing a model which would account for this would be most advantageous, but better still would be a model which could more accurately allow for the growth of a vortex from its generation to a fully developed vortex. This is achieved in the 'Oseen' model, developed from that proposed by Squire[23].

5.2.2 - Viscous Core Modelling - the 'Oseen' Vortex Model

Squire's work, extended from that of Lamb[24], considers the potential vortex, and incorporated a time dependant viscous decay of the vortex strength that grows from the vortex centre. This gives a Gaussian distribution of vorticity that represents the vortex core and is merged with a potential model of the vortex in the cross flow plane. Thus, if we consider an initial vortex concentrated at the centre of the streamwise axis, the outward growth of the core can be integrated to give the vorticity at any point by:

$$\omega_x = \frac{\Gamma}{4\pi\nu t} e^{-r^2/4\nu t} \qquad \textit{Equation 21}$$

ω_x is the streamwise vorticity component, Γ is the vortex circulation, ν is the coefficient of kinematic viscosity, r is the radial distance from the centre-line of the vortex, and t is the time (in seconds) from the generation of the vortex.

Similarly, the velocity (in the viscous core and the inviscid outer flow) is given as:

$$v_t = \frac{\Gamma}{2\pi r}\left(1 - e^{-r^2/4\nu t}\right) \qquad \textit{Equation 22}$$

Both these equations are devised for laminar flow (as indicated by the laminar kinematic viscosity, ν). Part of Squire's work was to extend this by adding a turbulent eddy viscosity term. However, turbulence models are notoriously difficult for extremely accurate modelling of real flows. Squire overcomes this by applying a very simple model, which he reasons will yield reasonably accurate results. Moreover, the model is based on terms already in the equation: the size of the eddies is set as directly proportional to the circulation of the line vortex ($\varepsilon = a.\Gamma$) and thus the term ν is replaced by $(\nu + \varepsilon) = (\nu + a.\Gamma)$. Quoted values for the turbulent kinematic viscosity vary in range from 30 to 100 times the laminar value[8,15], and must be found empirically. If the vortex is now considered as growing downstream, then the streamwise velocity component[§] $w = w_0 + w'$ rather than $w = w'$. At a sufficiently large distance downstream, w_0 will be large compared with all other velocities, and will be nearly equal to U_0. This is the equivalent of saying that for the vortex that has just been generated, the vortex core is of zero radius. As the vortex grows downstream, the timing of the core growth can be related to the free-stream speed and the distance from the vortex

§ Squire uses an axis system with the z-axis defined in the streamwise sense. This system will be used to discuss this work.

origin (as far from the vortex origin, the core growth will be more linear). Therefore, U_0/x could be substituted for t, giving:

$$\omega_x = \frac{\Gamma}{4\pi(\nu + a\Gamma)x}\exp\left[-\frac{r^2 U_0}{4(\nu + a\Gamma)x}\right] \qquad \textit{Equation 23}$$

$$v_t = \frac{\Gamma}{2\pi r}\left[1 - \exp\left(\frac{r^2 U_0}{4(\nu + a\Gamma)x}\right)\right] \qquad \textit{Equation 24}$$

The result is a model which is useful (to a fair approximation) for the three-dimensional growth of a vortex. However, there will be more significant errors due to two major areas: (a) it is still assumed that the streamwise velocity of the core is that of the free stream; and (b) the turbulence model in not sufficiently good to accurately model the cross-stream diffusivity.

The Oseen model takes this work a stage further by evaluating the velocities in the cross-flow plane from any number of real and image vortices, and by combing these velocities, the velocity field can be established. The rationale is given below[25]. Remembering:

$$v_t = \frac{\Gamma}{2\pi r}\left(1 - e^{-r^2/4\nu t}\right) \qquad \textit{Equation 25}$$

This can be re-written in terms of the Cartesian co-ordinates for a vortex, i, located with the centre at (y_i, z_i), giving cross-plane velocities, v_i and w_i, (with the bracketed term as F_i):

$$v_i = -\frac{\Gamma_i(y - y_i)}{2\pi R_i^{\,2}}F_i$$

$$w_i = \frac{\Gamma_i(z - z_i)}{2\pi R_i^{\,2}}F_i \qquad \textit{Equation 26}$$

where

$$R_i^2 = (y - y_i)^2 + (z - z_i)^2$$

$$F_i = 1 - \exp\left\{-\frac{\pi\omega_{peak}}{\Gamma}R_i^2\right\}$$

The same approximations that were made earlier can be applied again. If the vortex is sufficiently far downstream then the time dissipation of the vorticity is directly proportional to the free-stream speed. Further, a laminar and turbulent viscosity can replace the laminar viscosity of Lamb in order to represent the turbulent flow that the vortex is situated in. The function F represents the decay of the vorticity of the vortex core, which can be better represented by substituting the maximum (or peak) vorticity in the core. Since the vorticity and the circulation strength are related, the peak vorticity can be found in terms of the circulation strength:

$$\omega_x = \frac{\Gamma}{4\pi\nu t}e^{-r^2/4\nu t} \qquad \textit{Equation 27}$$

and

$\omega_x = \omega_{peak}$ when $r = 0$:

$$\omega_{peak} = \frac{\Gamma}{4\pi\nu t}$$

The peak vorticity can be calculated (the peak value being that at the centre of the vortex**). Thus the function F_i can be written as:

$$F_i = 1 - \exp\left\{-\frac{\pi\omega_{peak}}{\Gamma} R_i^2\right\} \qquad \textit{Equation 28}$$

This result now gives the whole expression in terms of meaningful quantities that relate to the vortex, as highlighted by Wendt & Greber[14]. This will also allow an easier comparison with experimental data, since the peak vorticity can be measured with relative ease, whereas the turbulent viscosity will be more troublesome.

This model has proved to be useful, since the velocities for each vortex, whether it be real or image, can be summed to give the total velocity flow field, as can the streamwise vorticity, which can be evaluated in a similar fashion. Comparisons with experimental data[14] have shown that the secondary velocity is modelled to within 5% of the experimental value in all regions except the upwash region, where the deviation can be as much as 40%. The model does not represent the effects of core and secondary vorticity convection on the structure of the vortex, and as these effects become larger with downstream location, the model deviates from the real case far downstream.

This model is difficult to implement in its published form, since it does require considerable empirical data. This data is not published in sufficient detail in this paper, and there is relatively little data in the literature that would allow the model to be used practically.

Even still, this model is a two dimensional one where the streamwise influences on the vortex are ignored, most notably the reduction in the circulation strength of the vortex (due to a reduction in vorticity), and the axial velocity of the core. The problem with the circulation reduction is that the viscous forces that control the diffusion of the vorticity are not accurately modelled. Also, the problem of the axial core velocity is that this is very much dependant on the type of vortex initiation (as to whether the vortex will be a weak or a strong vortex), and therefore dependant on the vortex generator type.

5.2.3 - Improvements to the Oseen Model

The logical extension to the Oseen vortex is to take the two-dimensional model and to inset features which would allow the third dimension to be modelled. Since Wendt et al. had defined the Oseen model in terms of the vortex descriptors which they considered defined the behaviour of the vortex, imposing assumptions about the streamwise development of these descriptors allowed the vortex model to be extended. This was done in a simple manner by applying Euler based equations to step between spatial locations.

The cross-plane locations of a single vortex are modified in the stream-wise development due to the effect of other vortices imposing a velocity field around it. If the motion is taken as being in one time step, then the cross-stream position gradients (dx/dz and dy/dz) are approximately equal to the ratio of the cross-stream velocity to the free-stream velocity (u/W_0 & v/W_0) if the time steps are small enough. The axial flow of the vortex at this point is treated by the similarity method proposed by Batchelor[11].

The variation in peak vorticity was carried out by extracting an empirical relationship from experimental data. It was found that the peak vorticity was dependant on two things: (a) the axial location a variable parameter; and (b) an adjustable decay rate parameter. While the axial location

---

** Some investigators have suggested that there are instances where the peak vorticity location and the centre of rotation of the vortex do not coincide[41]. The data on this is rather inconclusive, since measurements were taken using a 5-hole probe system where a probe offset angle could have been present.

is an easy parameter to decide, the decay rate parameter appears to be a weak link in the chain of this analysis, and it is unclear how the correct value can be chosen without prior knowledge of the real vortex.

The circulation of the vortex will be reduced by two factors: (a) the effect of wall skin friction; and (b) the cross-diffusive annihilation of vorticity within the fluid. This first part assumes that the skin friction applies a retarding torque to the vortex with the result that angular momentum is lost. It is assumed that the angular momentum is proportional to the circulation, and hence the circulation is directly related to the wall shear stress. Again, a degree of empiricism is necessary to allow the relation constant to be evaluated. The cross-diffusive annihilation is achieved by remembering that the reduction in circulation between two vortices of opposite sign will be due to the circulation interchange between them, that is, the reduction in positive vorticity from one vortex will be due to a reduction in negative vorticity from the second vortex. Thus relations between the vortices can be achieved in terms of the distance between the vortex cores. Clearly, this should have little effect for far-spaced vortices, and a much greater effect for closer spaced vortices.

This model produces some good results for single vortices and groups of vortices in arrays. However, there are still some short falls.

- The problems of the difference in observed and calculated results on the upwash regions are unresolved,
- For the case of stronger vortices, the generation of secondary vorticity at the wall (which would cause cross-diffusive annihilation) cannot be modelled,
- The model relies on significant empirical data.

Despite these limitations, this model is one of the more computational efficient models for a vortex that produces results of a good agreement with the real case.

5.2.4 - Vortex Strength

The discussion so far has considered only the effect of the general vortex. However, it will be apparent to the reader that the strength of the vortex is not fixed at formation, and is dependent on the type of vortex production. It has been mentioned that the rolling up of the vortex filaments provides the mechanism through which the discrete vortices form. However, there exist a number of different vortex formation methods by which the rolling up can take place. These are listed by Delery[10] as: (a) the tornado-like vortex; (b) the horseshoe-like vortex; and (c) the delta-wing vortex.

The tornado-like vortex is a common vortex structure where the separation surface (the three-dimensional equivalent of a separation streamline) is located where the vorticity tends to congregate, and the vortices which form are a rolling up of the separation surface. The ends of the separation surface form two foci that form the centre of the vortex at formation.

The horseshoe vortex occurs when the force sustaining the vortex occurs in the line of symmetry of the vortex, and the vortex pair that would be seen downstream is actually two 'arms' of the same vortex.

The delta-wing vortex is caused by the separation surface being coincident with the sharp leading edge of the wing. Because of the separation, the vorticity which migrates from the boundary layer to the outer flow concentrates at the centre of the vortex, and the vortex is fed from the whole of the separated boundary layer, or from the down stream wake.

The types of vortices generated by these methods are usually categorised as being either weak vortices or strong vortices. While the definition of weak and strong vortices is hazy, the vortices formed by of the tornado- and horseshoe- types are almost always weak, while the vortices

produced by a delta wing may be either weak or strong. It is inferred in a number of texts that the definition of the strength may be achieved through the comparison of the maximum cross-plane velocity vector ($v_{\theta max}$) to that of the free-stream (U_∞). This can be thought of as a direct comparison between velocity vectors, or as the flow angle induced by the vortex from the free-stream direction, γ. Typical values of $v_{\theta max}/ U_\infty$ which are used to describe weak vortices are up to 0.5, which gives a corresponding angle $\gamma = 25°$, while strong vortices appear to be refereed to as having values of $v_{\theta max}/ U_\infty$ typically of 0.85, with flow angles $\gamma = 40°$.

5.2.5 - Further Factors Increasing the Decay of Vortices

As highlighted above, the decay of vortices will be dependent on the cross-stream annihilation of the vorticity in the core. This will occur when vortices of opposite sign interact (for example in the case of the secondary vortex induced by the primary vortex), or by absorption at the core of opposite signed vorticity from the boundary layer. However, the decay can also be influenced by some further factors.

It has been shown that by imposing an adverse pressure gradient on an embedded vortex in a boundary layer, the decay rate of a vortex will increase[14]. It was seen that a vortex core would increase in diameter approximately in proportion with the boundary layer thickness in which it is embedded. The result for the adverse streamwise pressure gradient is that the boundary layer will thicken considerably faster than in the zero pressure gradient case, and hence the vortex core will also thicken in a similar way. This increase in the vortex size is due to the linking of axial and radial motions through the conservation of mass. As the adverse pressure gradient retards the flow, the core must grow in a radial direction, thus leading to a thicker and more diffuse vortex.

The decay of the vortex is expected to increase if the vortex is in a three-dimensional boundary layer[26]. It was seen that, while the initial peak vorticity for a vortex in two- and three-dimensional boundary layers are very similar, the decay rate for the three-dimensional case is two to three times higher than that of the two-dimensional case. It was stated that the difference in boundary layers gave striking differences between the mean velocity fields, which also lead to differences in the turbulence intensity.

With the development of the vortex now covered, the methods of vortex production will now be discussed.

5.3 - The Vortex Generator

The vane vortex generator was first used as a flow-mixing device by Taylor at the United Aircraft Corporation[16]. The devices used were very low aspect ratio wings of a standard profile, placed at incidence in the boundary layer of a wind tunnel diffuser. For this case, some design characteristics for the counter-rotating vortex generator array were considered, including:

- streamwise location from the point of boundary layer separation,
- the height of the vortex generator,
- aerofoil tip chord length,
- generator spacing in the array,
- aerofoil profile.

While values for the design criteria are suggested, it will be shown through a review of subsequent work, that the results obtained by Taylor were rather 'raw', and that the design criteria can be significantly refined such that a vortex generator array can be designed within much tighter limits. Taylor also suggested that the vortex generator should perhaps have a variation in chord along its length. Since the vortex generator would be submerged in a boundary layer (which would have a variation of streamwise velocity with height from the surface), it was suggested that in order to

provide the correct conditions for the optimum vortex, the chord of the vane should be reduced towards the tip. This point will be discussed later.

Further work by Valentine & Carroll[27] extended these design criteria for the use of counter-rotating vortex generators in diffuser. Rectangular planform generators were used with a NACA 0012 profile, and the effects were assessed relative to the flow improvement in the diffuser. The results from this analysis were:

- The optimum incidence for high and low speeds were 14° & 20° respectively,
- The optimum spacing between vanes in the array is about two span lengths,
- the optimum aspect ratio should be no more than ½††,
- Ratio of span-to-boundary-layer-displacement-thickness should be about 6.

Concurrent with this latter work in the United States, investigations were underway in England, most notably at the National Physical Laboratory. A preliminary report by Tanner, Pearcey and Tracy[28] investigated the effect of static pressure rise in front of a spoiler downstream of different vortex generator configurations. This work was aimed towards the alleviation of shock induced separation on transonic aerofoils, but experimentation was limited to low speed work due to scaling problems with the N.P.L. high speed tunnel facility. During this investigation, a complete parametric study of vortex generators was undertaken in which the following conclusions were made (as summarised by Pearcey[29].

5.4 - Vane Vortex Generator

Pearcey notes that the vane type vortex generator of Taylor can be set in two basic ways: (a) the co-rotating array where the vortices which are shed are all of the same rotational direction; and (b) counter-rotating arrays where the rotational sense of the vortices alternate along the array. He also notes the biplane arrangement where vortex generators are essentially in the counter-rotating type, but with the rotational sense of the vortices alternating for every 2 vortex generators.

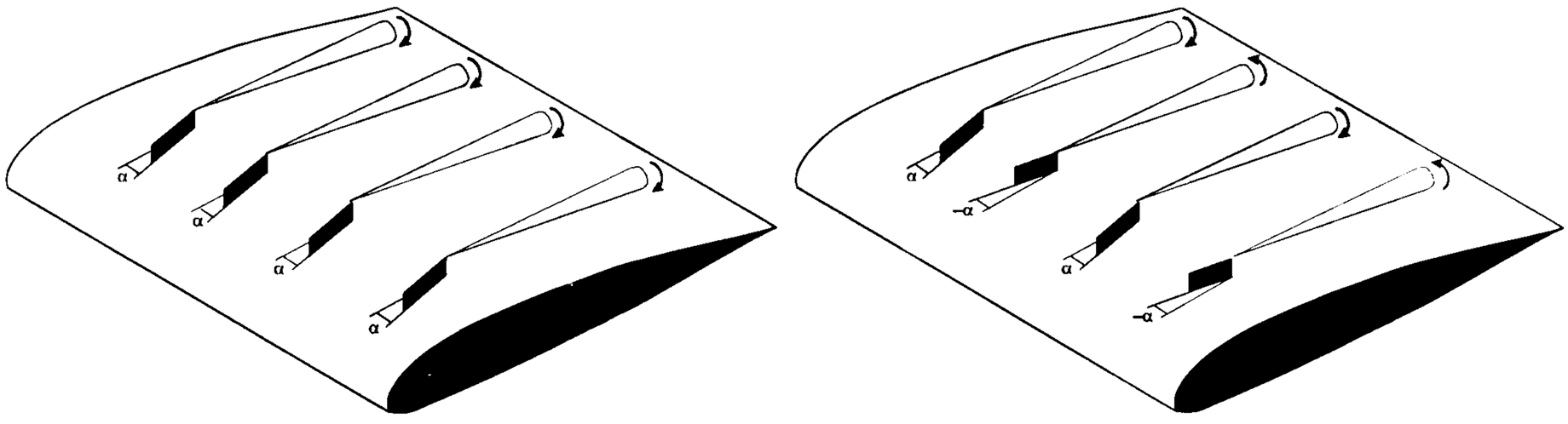

Figure 13 (a) Co-rotating Vortex Generators, (b) Counter-rotating Vortex Generators

It is noted that the positioning of the vortex generator should be ahead of the region of adverse pressure gradient which will lead to the separation of the boundary layer, and also that the spanwise path of the vortex must be considered in choosing the location point. This will depend on the initial spacing of the vortex generators, and the height, strength and rotational sense of the vortices.

Further, it is noted that once the effects of separation have been taken in to consideration, other aspects of the use of vortex generators must be taken in to account, and any adverse effects should be minimised. These may include: (a) supersonic effects from local shock waves generated by the

---

†† The aspect ratio of a vortex generator is usually defined to include the image area of the vortex generator that is created by 'reflection' of the wetted area of the vortex generator. Aspect Ratio = $2S/c^2 = 2h/c$, where S is the physical vanes area, h is the height, and c is the chord.

vortex generators; (b) local boundary layer thickening or separation; and (c) the induced drag of the vortex generators.

5.4.1 - Co-rotating Arrays

It has been mentioned already that the effect of vortex spacing is most important in the design of the optimum vortex generator array. For the early work concerning arrays, the effect from the co-rotating array was found to be much poorer than the counter-rotating array[28]. However, closer inspection through the use of total pressure traverses (for example) have shown that the effect of the boundary layer mixing is very different for the same spacings between these two types of arrays. If the co-rotating vortices are located too close together (D/h = 2, say), the result is that the fluid being swept up by one vortex is immediately swept back down by the next generator along, with the effect that the boundary layer is not significantly thinned (see previous diagram from ESDU 93024[17]). Further, the high velocities that would be induced by the vortex are damped out, and the vortex strength quickly decays. This was the result which lead to the early (but incorrect) conclusion that the co-rotating vortex array was worse than the counter-rotating array. As the spacing increases (D/h = 4), the level of mixing increases, and it was noted[29] that the increase in mixing as the spacing was increased from D/h = 4 to D/h = 8 was small. It was therefore concluded that for the co-rotating vortex generator array, a spacing of D/h $\cong$ 6 was the optimum. As the vortices become more widely spaced, the mutual interference will become less, and it is suggested that for such large spacings (although there is a lack of experimental data) the use of single vortex data be used[14].

From the potential vortex model, it was noted, for the single fully established two-dimensional vortex, that the height of the vortex would not change due to the influence of the image vortex at the wall. Similarly, for the infinite array of co-rotating vortices, the velocity induced at the centre of a given vortex by the sum of the vertical velocities on one side of that vortex will be balanced by the velocities induced in the opposite direction on the other side of the vortex. Thus, all the vortices should remain at the same height. However, for the finite array, the vortices at the end of the array will not be balanced in terms of induced velocities at the vortex centres, and the one end of the array will tend to move towards the surface, while the other end will tend to move away. These end vortices will eventually tend to roll-up around each other on either side of the array.

It will be clear that the vortices will also move laterally across the solid surface in a manner described by the potential flow model. Since all the vortices are rotating in the same direction, the motion will be identical across the array, and all the vortices will crab sideways, always remaining at the same initial vortex spacing.

The streamwise location of the vortex generator array is clearly important, and should be placed upstream of the location of the adverse pressure gradient (for the control of shock induced separation). It was noted that for the case of the co-rotating array, suitably strong vortices can be produced which remain at the surface, and sufficiently un-damped back to about 100 generator heights downstream (assuming the vortices are properly spaced). In fact, the position of the vortex generator array is recommended as being located between 10 generator heights and 75 generator heights for full effectiveness. Streamwise distances of up to 100 generator heights will give good mixing[29].

5.4.2 - Counter-rotating Arrays

The movement of the counter-rotating vortices in an array is far different to those of the co-rotating array. It will be appreciated from the potential flow model that the effect of locating two vortices of opposite rotation next to one another has two major effects on the location of the vortex centres.

Firstly, the spanwise location of the vortices will change relative to one another. From the potential model of the single vortex, it is clear that the lateral direction of travel (induced by the

image vortex) is dependent on the rotational sense. As the two vortices will have different sense of rotation, they will move in different directions - either towards or away from each other depending on their locations.

If this movement occurs in an array, vortices along the array will tend to 'pair-up'. However, as this happens, the 'infinite array' effect, which holds all the vortices at the same height for the co-rotating array, will not hold, and the second effect occurs: vortices will tend to move away from the surface. Due to this effect, the streamwise location of the counter-rotating vortex generator array becomes more critical, and it is suggested that in some circumstances that the vortices could lift of at about 20 generator heights downstream of the array.

The effect of lift off of the vortices will mean a reduction in the ability of the array to control the boundary layer on two fronts. Most noticeably since the vortices will be physically moved out of the boundary layer, but also due to the mutual damping caused by vortices (and hence vorticity) of opposite senses interacting.

It was noted in early investigation that the counter-rotating vortex generator spacings gave better results that the co-rotating generators. In fact, the spacings of the vortex generators for the counter-rotating array can be variable, since the effect of spacing between vanes of the same and opposite rotations can be altered. If the common-flow-down distance between two vortices is minimised, then the vortices will be closer to the surface for a longer downstream distance.

Increasing the distance between generators of the same rotational sense causes the velocity component normal to the surface to be reduced, with the velocity parallel to the surface being almost unchanged. It is noted that it is desirable to minimise the number of vortex generators over a given array length, and Pearcey concludes that it is as useful to use a spacing of vortex generators of the same rotation of $D/h_i = 10$ as it is to use $D/h_i = 5$.

5.4.3 - Vane Design Criteria

Angle of Incidence of the generator should be such as to provide a well-defined vortex over the anticipated range of operating incidence. For the applications that are linked to aircraft wings[17], the local incidence at the vane may change considerably in flight, and so an incidence that will produce the desired vortex over this range should be used. While no specific value is recommended by Pearcey[29], values commonly used in the cited successful design are in the range 15° to 20°, thus agreeing with previous work. It should be realised that in cases where the drag of the vortex generators is critical, it may be desirable to optimise the vortex not for the vortex strength parameter ($\Gamma/h_i U_\infty$), but for the Vane Performance Parameter (the vortex strength parameter / the device drag).

Aspect Ratio of the vane should be kept low. It is desirable to keep the vortex core as small as possible to reduce the possibilities of dissipation. Large aspect ratios are known to produce weak vortices (due to the largely two-dimensional nature of the flow except near the tip), and as the aspect ratio is reduced, it is known that the vortex strength will increase. However, due to the viscous nature of the formation of the vortex at the tip, it is suggested that the larger the chord (and hence downstream region of the vane), the larger the core will be, which is undesirable. Hence some balance between high and very low aspect ratio is needed. It is suggested[30] that generators as low in aspect ratio of 0.5 have proved successful.

Planform of the vane will affect the stability of the vortex if the tip chord is of zero length. The stability will be defined in terms of steadiness of strength and position relative to changing flow conditions. Pearcey notes that Taylor suggests reducing the chord length of the vane towards the tip. Further, the choice of planform, and incidence for that matter, will very much depend on the nature of the flow in which the vane is to be located, since the vortex may break down (and hence be unstable), at certain Mach number or incidence values. The choice of planform will certainly be influenced by Mach numbers of greater than 1, since it will be desirable to have the vane free

from shock wave effects at the tip (i.e. have a very swept vane). Referring back to the vane performance parameter, the drag of the vane can also be reduced by the application of some sweepback, but the increase in taper will result in a reduction in vortex strength.

Vane Profile is most often simple, since most vortex generators are simple flat plates, giving a thickness to chord ratio of about 0.05. It is stated that no aerodynamic data is found for the effect of thickness added to these flat plate designs. As noted earlier, aerofoil designs are often used in wind tunnel diffusers, although this is probably as much to do with the need for thickness for structural purposes. In the United States, the use of a half-NACA 0012 profile is common as a vortex generator[31], although these devices are usually of a large scale, and are unsuitable for the easy manufacture required for small scale applications. In the main, the flat plate is far more common, principally due to the sheer simplicity of the design and manufacture.

Vortex Generator Height (when used for shock-induced separation control) is suggested as being dependant on the streamwise location of the vortex generators when installed father than on the relation to the local boundary layer height at either the vortex generator position of the shock position[14]. Through the use of the vortex strength parameter (which should be about 1 for good mixing), the position of the vortex height above the surface can be derived, if the vortex is to be generated closer than 100 generator heights from the shock location. While this may be so for shock induced separation control, several other investigators have reasoned that the vortex centre should be located at about the boundary layer height, indeed, some have even reasoned that the ratio of vortex generator height to boundary layer thickness (h/δ) should be 1.3 to 1.4.

5.4.4 - Other Types of Mixing Devices

While the majority of the section has dealt with the idea of the vane vortex generator, being the most common flow mixing device, there are a great number of other designs which are generally less successful than the simple vanes.

Schubauer & Spangenberg[16] highlighted a number of mixing devices (including the standard vane vortex generator) which were designed to draw higher momentum fluid from the free stream towards the surface, while pushing the low momentum air up and away. Devices are shown in below, and are all essentially scooping devices. It is interesting to note that the effect of the shields on some of the devices was to reduce the tailing vortex strength thus reducing the induced drag. The devices gave a mixed degree of effectiveness, but probably due to their complex nature, are not used today.

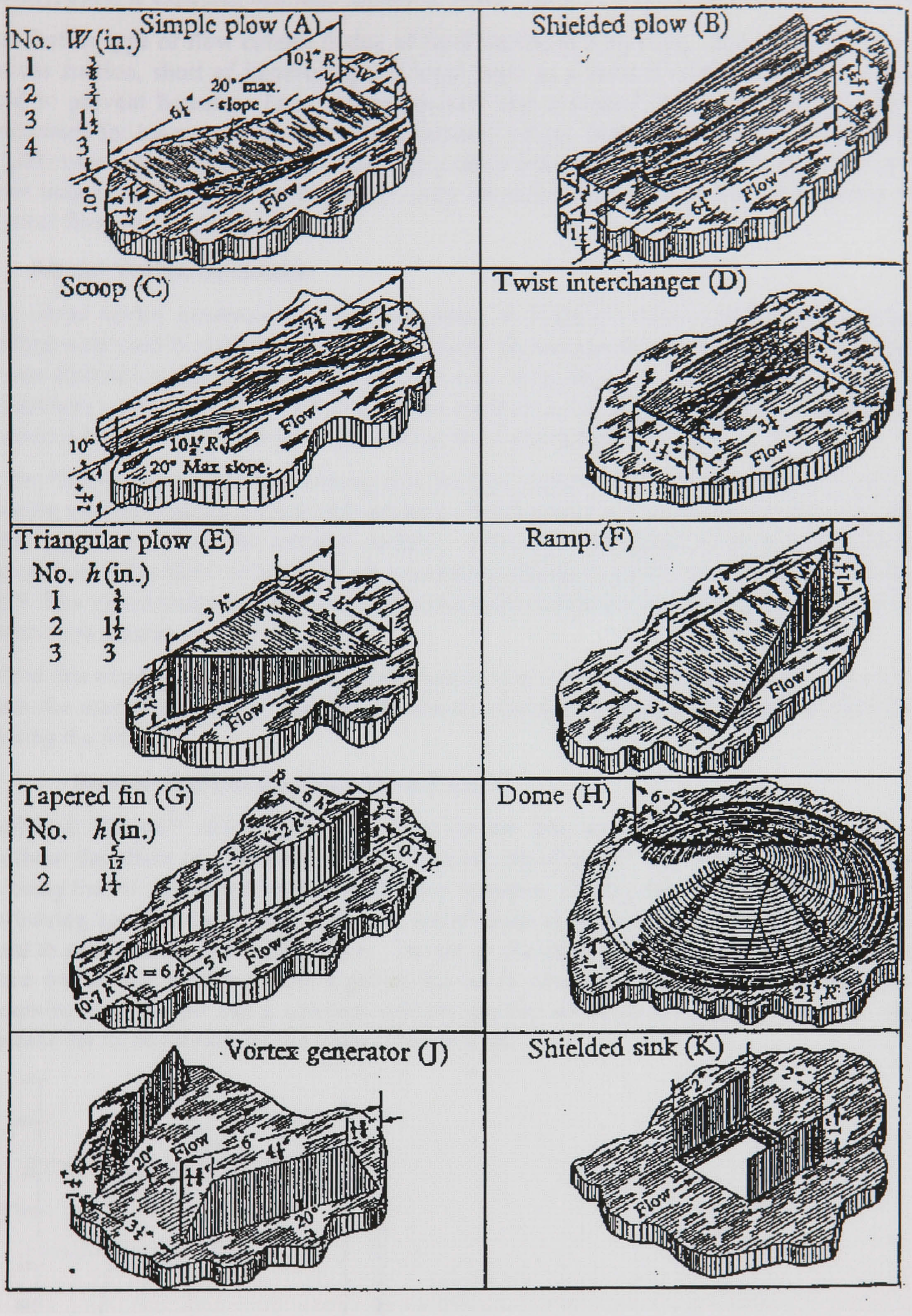

Figure 14: Other Vortex Generator Designs (Diagram from Schubauer & Spangenberg[16])

Pearcey[29] highlighted further designs, including the use of small wings which are placed above the aerofoil surface on stings, and the use of leading edge discontinuities such as leading edge notches, wing fences and fairings. Other devices of interest are the so-called Sub-Boundary-Layer devices such as the Wheeler[32] and 'Wishbone'[25] vortex generators. In these cases, a single generator produces a counter-rotating pair of strong vortices (with centre flow upwards) at a location well within the boundary layer (e.g. $h/\delta \approx 0.3$). These vortices lift off the surface quite

quickly, but it is expected that their influence would last for a considerable distance downstream.

One further type of flow control is that of fluid suction and blowing. The intention here is not to discuss suction, short of identifying this large topic as a method of removal of low momentum fluid to prevent boundary layer separation, and also a method by which laminar flow may be maintained for longer periods than would naturally occur. Blowing is another very large topic that would cover all aspects of forced blowing control from small jets set in the surface up to large sheet tangential blowing. In this report, only the topic of jets blown from the surface to induce vortical flow will be discussed.

5.5 - Air-Jet Vortex Generator

The air-jet vortex generator was first suggested by Wallis[33] where circular jets issuing from a surface were used to produce 'persistent vorticity' for the purpose of delaying turbulent separation. It was discovered that inclining and pitching a jet at an angle to the free-stream could produce a streamwise vortex. It was noted that for the vorticity to be produced, the jet momentum must be introduced to give a significant component in the cross-stream direction.

It was known that a normal jet issuing into the free stream would produce a pair of weak counter-rotating vortices that would pass downstream. Wallis chose a cross-stream jet that was angled at a pitch angle of 45° to the aerofoil surface. This was considered to give a suitable spanwise component to the flow while giving the penetrating ability to pierce up through the boundary layer. Both flow visualisation and boundary layer traverses confirmed that for each jet, a single persistent vortex was present.

While this result shows that vortices are present, it is worth considering the formation of vortices from the normal jet issuing into the free-stream, and then considering the effects of pitching and yawing the jet.

5.5.1 - Normal Jets Issuing in to a Free-Stream

Keffer & Baines[34] discussed the problem of the free jet issuing into a uniform free-stream (without the effect of a boundary layer). The mixing of the jet and the cross-flow are considered as being that of two irrotational potential flow streams. Firstly, the free jet with no cross-flow, the jet issuing up from the surface causes an entrainment of fluid around the jet, causing the external fluid to accelerate in the jet direction. The jet on the other hand is retarded by the external flow, since the kinetic energy at the edges of the jet is dissipated out into the external flow. Thus assuming that the jet had a uniform velocity profile at the jet nozzle, the velocity profile will become far more rounded at the sides of the free jet.

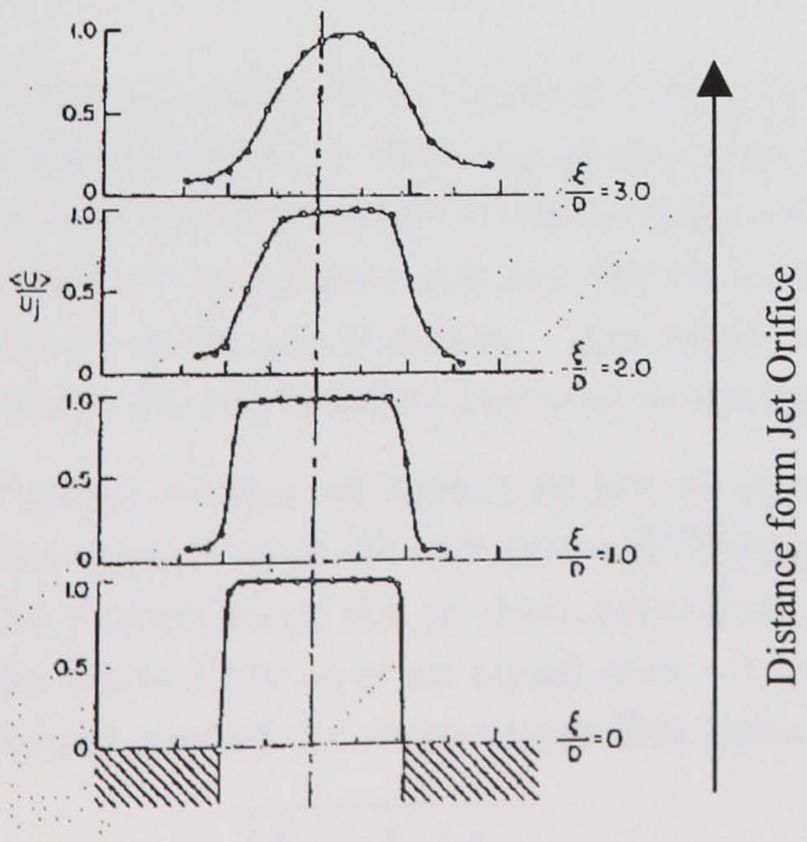

Figure 15: Normal Jet Velocity Profile (Diagram from Kamotani & Greber[35])

The addition of the free-stream component complicates the flow further. As well as the reduction in the jet velocity profile, the lateral effect on the jet must now be considered. Due to the reduction in velocity at the edge of the jet, there will be a corresponding increase in static pressure. As the flow passes around the jet, there will be lateral shearing stresses induced. At the rear of the jet, the free-stream flow will separate at either side of the jet, causing a low static pressure wake region to be formed. This initial period of the interaction is known as the Zone of Establishment. During this stage, the maximum velocity in the jet is still equal to the maximum velocity in the jet at the nozzle. Thus the transfer of kinetic energy from the sides of the jet has not yet lead to a complete reduction in the magnitude of the jet nozzle velocity profile.

Once the transfer of turbulent kinetic energy (which reduces the maximum velocity in the jet to a value below that at the jet nozzle) has affected the potential core of the jet, the jet is said to enter the Zone of Established Flow. The jet is highly turbulent in this region, but the effect on the free-stream is now much smaller, so that variations in mean velocities and pressures can be neglected.

From this simple description above, it may be expected that the length of these zones will be dependent on the ratio of jet velocity to free-stream velocity. This idea will be explored later on, but it is interesting to note that Keffer & Baines suggested that at low velocity ratios, the jet is deflected more by the cross-stream, and so the 'virtual' tip of the decaying jet shifts downstream. At higher velocity ratios, it is noted that the potential core of the jet is conical in shape, with the point of the cone almost above the jet exit. It is also noted that the effect of the cross-stream at the higher velocity ratios is to turn the, originally circular, jet cross-section in to a characteristic kidney shape.

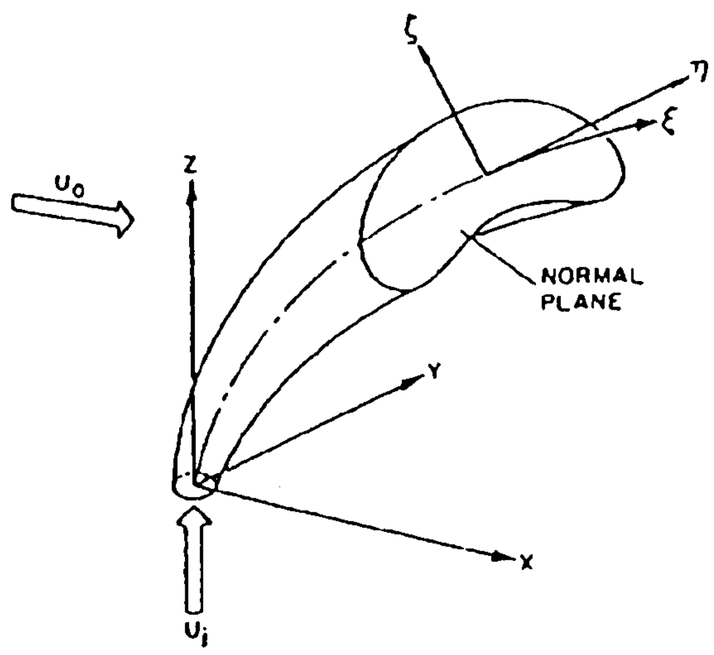

Figure 16: 'Kidney-Shaped' Jet Profile

Since the sides of the kidney shape (i.e. the extremities of the jet in the *y* direction) have been subjected to large shearing stresses, they will contain particularly low momentum fluid. The result is that the free-stream fluid passing around the jet will separate at the sides the jet. Due to the effect of the jet entrainment, the return flow in the wake region at the rear of the jet will be rapidly drawn in the jet direction. This leads to the formation of a weak pair of counter-rotating vortices, which are expected to increase in strength through the zone of established flow.

Further studies on turbulent jets in cross-flows have been undertaken by Kamotani & Greber[35], Karagozian et al.[36] and Fearn & Weston[37]. It is noted that for the jet issuing in to a free-stream, the properties of the jet once issued are dependant on the ratio of the jet momentum flux to that of the cross-flow over an equal area. A more common way to display this equation is by taking the square root of the momentum flux ratio, and writing it as the velocity ratio (VR)[37]:

$$VR = \sqrt{\frac{\int s_0 \rho_j V_j^2 d\sigma}{\rho_0 U_0^2 S_0}} \qquad \textit{Equation 29}$$

Suffices j and 0 represent the jet and cross-stream conditions respectively, and s_0 and S_0 represent suitable areas in order to directly compare the momentum fluxes. Now, if the jet velocity, U_j is constant across the jet, and the pressure at the jet is equal to that of the free-stream, then this equation simplifies to the Mach number ratio (MR):

$$MR = \frac{M_j}{M_0} \qquad \textit{Equation 30}$$

Also, if the density of the jet fluid is equal to that of the cross-stream ($\rho_j = \rho_0$), then:

$$VR = \frac{V_j}{V_0} \qquad \textit{Equation 31}$$

Thus, in the simplest case, the evolution of the jet may be expected to depend, in part, on the ratio of the jet velocity to the cross-stream velocity, the result which Keffer & Baines stated above.

Kamotani & Greber[35] suggest that the qualitative idea of the of the jet deflection being directly over the top of the jet exit (as made by Keffer & Baines and others) is not helpful, since it has lead to the idea of an 'effective source of jet deflection'. Measurements taken by Kamotani & Greber suggest that the jet deflects close to this point, but propose a 'better' relationship. Measurements of the vorticity were also made, and it was seen that the jet core is drawn in to a crescent shape (similar to the kidney shape of Keffer & Baines), and that far downstream, the jet core is untraceable, while the vortices remain. It was noted that the effect of increasing the velocity ratio was to increase the strength of the vortices, but that this substantially reduced the streamwise extent of the crescent region.

The normal jet is modelled by Fearn & Weston[37] using two two-dimensional vortex models in which a small amount of experimental data is used to fully describe the two-dimensional span-wise representation of the counter-rotating vortices. In the first model, a simple vortex filament idea is used which, while being very simple (in that the effects of the viscous vortex core are ignored), does not require a significant amount of experimental data. The second model assumes a Gaussian distribution of vorticity in the vortex core, and is an extension the first model. Fearn & Weston[37] also show an unexpected relationship concerning the circulation of each vortex, at the range of velocity ratios tested here ($3 < VR < 8$): the circulation is suggested as being proportional to the diameter of the jet orifice and to the velocity of the jet.

From this basic description of the normal jet, the discussion will now be extended to work carried out for air-jets that are pitched and skewed.

5.5.2 - Pitched and Skewed Air-Jets

As highlighted by the work by Wallis, the rotation of an air-jet in both yaw and pitch provides a spanwise component of momentum to the flow from which the generation of a single persistent vortex results.

The Vortex Mechanism

A suggestion as to the mechanism behind the skewed air jet vortex generator was given by Pearcey[29], and was explained further by Pearcey, Rao, & Sykes[38]. For the jet piercing through a boundary layer, the presence of the jet also causes the deflection of the boundary layer streamlines, leading to the production of vorticity in the boundary layer. This vorticity is entrained by the jet, which sweeps the vorticity away from the surface. The effect of skewing the jet is then to strengthen one of the counter-rotating vortices (produced by the jet with no skew angle), while weakening the other. It was further noted in this work that experiments by Rao had shown that above a certain skew angle, the pair of counter-rotating vortices is replaced by a single persistent, stronger vortex, but that the critical value of skew also depends on the jet velocity ratio. It is also

suggested that for any skew angle above the critical, the vortex strength then increases.

Flow visualisation studies by Barberopolous[39] have shown that the vortex structure around the jet is quite complicated. At the edge of the jet, a horseshoe vortex is present which is quite weak and remains very close to the wall. At the rear of the jet, the separation either side of the jet is similar in nature to that behind a circular cylinder. However, the effect of the jet entrainment is to draw the separated wake region away from the surface, enhancing the vortex roll-up. The resulting vortex system is similar in nature to the 'tornado-type' vortex structure described by Delery. However, in this case, the vortices are generated either side of a jet, and the vortices are rapidly oriented in the free-stream direction as the jet is deflected. With the vortices now under the jet core, the core is entrained in to the vortex, rather than the vortex being formed around the core. Increasing the skew angle of the jet causes the separation points to move around the jet, with the separation moving forward on the leeward side of the jet, and moving rearward on the windward side of the jet. The resulting shift in the separation points then affects the size of the vortex that results, increasing the strength of the leeward vortex, and reducing the strength of the windward vortex. As the vortices develop downstream, the smaller of the two vortices is quickly entrained and becomes lost in the resulting flow field.

5.5.3 - Investigation of the Vortices

Johnston & Nishi have examined the air-jet vortex generator in more depth[40]. Their approach was to extend the limited knowledge as to the effects of air-jets by choosing a number of simple cases to assess the effects of the vortices, most noticeably on skin friction in the mixed boundary layer and also velocity profiles. In all cases, the pitch angle (α) on the jet was set to 45°, and different skew angles (β) were used to simulate co- and counter-rotating arrays by setting the skew angles at ±90°. The free-stream speed was 15 m/s.

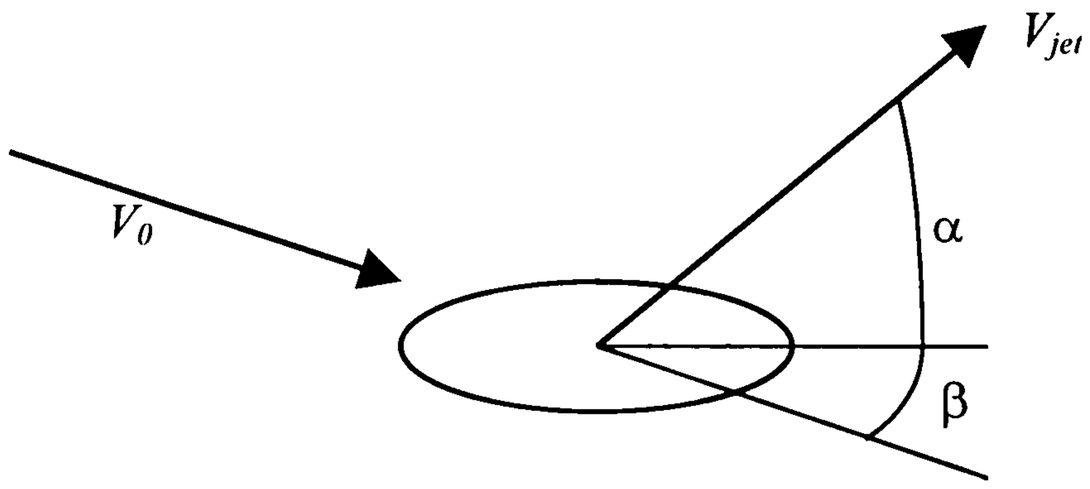

Figure 17: Air-jet Geometry Definitions

The skin friction was measured in order to assess the effect on the boundary layer‡‡, and it was noticed that the effect of the vortices was similar to that noted from vane vortex generators. It was also noted that as the vortices moved in the spanwise direction, the motion could have resulted from both the image vortex (reflected in the solid surface) and the convection of the core due to residual spanwise momentum from the jets. Some variation in the jet velocity ratio was investigated, mostly in order to prevent separations. It was noted that an increase in blowing ratio above 1 would not give any greater separation control benefits. While this may be true for this particular experiment, it is felt that this is a dangerous statement to make, since this could be interpreted as saying that the vortices do not get stronger, which this fact neither proves of disproves.

A further problem with this study was in the measurement system. A five-hole probe was used to derive the vorticity in a cross-flow plane. However, the scale of the vortex compared to the size of

‡‡ The effect of reducing the thickness of the boundary layer is to increase the skin friction. Similarly, as the boundary layer thickens (and grows closer to separating) the skin friction reduces.

the probe and the sampling grid was quite small. As a result, it was not possible to sample the vorticity in the region where the vortex was close to the wall (since the probe would have fouled on the wall), and thus a good deal of the vortex information was lost.

As well as the velocity ratio of the jet, and the pitch and skew angles, several other parameters are important to consider in using an air-jet vortex generator. These include: (a) the dimensional relation between the jet and the boundary layer, which is given as δ/D; (b) a jet Reynolds number, perhaps given by $R_j = \rho V_j D/\mu$; and (c) a Mach number relationship, perhaps evaluated in terms of that suggested earlier in this paper.

A study by Compton and Johnston[41] extended earlier work by measuring the flow velocities in the cross-flow plane for a variety of skew angles and blowing ratios for a single air-jet. Again, the free-stream speed was 15 m/s. It was noted that, even for the strongest case tested, the vortex was only weak, classified as such due to the low induced secondary velocity.

This air-jet was qualitatively compared with the vortex produced from a vane. It was noted that the dissipation of the vorticity from the core occurs at a much greater rate for the air-jet case, and that the peak vorticity appeared to occur very close to the wall. The secondary velocities were much lower than those obtained from the vane generators. Further, the low velocity cores created by the boundary layer lift off for the vanes were not present for the air-jet cases. It was concluded that the vortices produced by the air-jets were radically different to those from vanes. This was principally due to the fact that the centre of secondary circulation of the vortex does not coincide with the location of the centre of the core of minimum axial velocity, or the centre of the core of maximum vorticity. However, it must be stated that this investigation was made using a 5-hole pressure probe, which may have had an offset angle associated with it. This would give the same result.

Selby, Lin & Howard[42] made a complete parametric study of air-jet vortex generators in arrays. The four major descriptors that control the vortices were varied independently over a wide range, these being:

- Pitch angle: $15° < \alpha < 90°$
- Skew angle: $0° < \beta < 90°$
- Orifice diameter: 0.8 mm → 4.8 mm (actually quoted as a ratio with the boundary layer momentum thickness)
- Velocity ratio: 0.6 → 6.8

The results were measured against the ability to control separation on a rearward-facing ramp at a free-stream speed of 40 m/s, and are listed as follows:

- With the pitch and skew angles held constant, and with a constant mass flow through the jets, the greatest pressure recovery was noted with the highest velocity ratio (i.e. when the hole jet hole diameter was as small as possible).
- With the pitch and skew angles held constant, and with a constant jet hole diameter, the greatest pressure recovery was noted with the highest velocity ratio (or highest jet mass flow rate).
- The effect of jet pitch angle was investigated (with the skew angle at 90°), and it was noted that the maximum pressure recovery was noted between 15° to 20°, and some positive effect was noted at 45°, but very little effect was noted above this.
- The effect of jet skew angle was investigated (with the pitch at 15° and 45°), and it was noted that the maximum pressure recovery was to be found with $\beta = 60°$ when $\alpha = 15°$ and with $\beta = 90°$ when $\alpha = 45°$. It is concluded that the dominant member of the vortex pair is strongest when $60° < \beta < 90°$.

Zhang & Li[43] have carried out some parallel work and have provided some comparative results. It was noticed that while the effect of increasing the velocity ratio was to increase the vortex strength, the height of the vortex from the surface also increased, and thus must be considered in the vortex generator application. In this investigation, it was suggested that the strongest vortex was produced when the skew angle was 30°. This is in contradiction to all previous work that suggests that the strongest vortex is seen at a skew angle of 60° or more. The reason why this result is achieved is not known, although the accuracy of the vortex strength measurement system is questionable. This study used a fluorescent thread technique, where the thread was positioned in the vortex core using a rod mounted to a three-axis traverse system. The thread would be rotated to describe the surface of a core by the vortex, and measurement of the cone base circle would be an indication of vortex strength. This system is potentially subject to great errors in estimation of the distances involved, and makes no allowance for the differing velocity profiles of the core of the vortex, which could cause the tuft to behave differently regardless of the vortex strength. Lastly from this work, it was seen that by using a crescent shaped jet, the area of the jet could be reduced to about 25% of that of the round jet, while 85% of the vortex strength would remain (for the same velocity ratios).

5.5.4 - Computational Models of Air-Jets

Computational Fluid Dynamics (CFD) modelling of the air jet vortex generator has been attempted, and results of Zhang[44] were compared with the experimental results of Compton and Johnston[41], and some fair comparisons were seen. However, it is of worth to note that the differences may be due to either (a) the differences in the air jet velocity profiles; or (b) the poor turbulence model used in the computational work (in this case, the k-ε model)§§.

Henry & Pearcey[45] and Akanni & Henry[46] have undertaken further modelling studies. Both of these studies modelled the effects of rectangular jet orifices that, according to Freestone[47], produce stronger vortices than round jets. The experimental validation of the models was acceptable, and some analysis of the computational data was said to show the production of the two counter-rotating vortices of differing strengths, and that the weaker vortex was quickly consumed by the stronger vortex, until its presence was undetectable.

5.5.5 - The Effect of Mach Number

It is noticeable that the majority of work concerned with the use of air-jet vortex generators has been at low subsonic speeds where the effects of compressibility can be neglected. This is with two noticeable exceptions: (a) work by Rao[48]; and (b) work carried out concerning the use of air-jet vortex generators in engine intakes and diffusers[49,50]. However, in both of these cases, the assessment has been in terms of an aerodynamic performance improvement, either of an aerofoil, or of an intake duct. An obvious extension to the work would be to examine the performance of the air-jets by measuring the flow in the jet/vortex stream, with a view to producing an empirical model of the air-jet that could be used to predict air-jet performance more accurately.

A series of investigations into small inclined air-outlets at transonic Mach numbers was carried out by Dewey[51] and Nelson & Dewey[52]. In these cases, air was discharged through small circular holes in the wall of a transonic tunnel, at pitch angles of 30°, 45° and 60°, with 0° skew angle. The velocity ratios were all less than unity. These experiments were carried out to assess the effect of the shape inside the jet nozzle. Since the upstream side of the jet orifice had a plenum, the contouring between the plenum and the jet was altered from a simple hole in a flat plate to a curved 'bell-mouth' entrance to the jet orifice. The purpose of the tests was to investigate the discharge coefficient of each of the jet configurations at a number of jet mass flow rates. This

§§ It will be recalled that the turbulence models used in the modelling of vortices from vanes greatly affected the results, and that no current turbulence model would suffice.

work demonstrated the importance of jet efficiency. This would have particular relevance to the practical case of air-jets, where the driving pressure of the jet would need to be bled from the engine compressor. It was seen that the discharge coefficient tends to be relatively independent of Mach number. This study has little application to the work on air-jet vortex generators (since the velocity ratios are too low to generate sufficiently strong vortices), and it highlights the lack of measurement of vortices at high subsonic Mach numbers.

5.6 - Summary of the Literature Survey

The historical view of the use of vane and air-jet vortex generators has highlighted that there are some simple design parameters which can be considered for each vortex generator. While parameter guidelines are available for the use of vortex generators for separation control, very few studies have made any significant measurements of the vortices produced in relation to the vortex generator parameters. Further, most studies have been carried out at Mach numbers less than 0.1, and hence the Mach number effects are not well understood.

5.7 - Proposed Programme of Investigation

In order to produce vortex measurements from vortex generators, and experimental parametric study of both vane and air-jet vortex generators is proposed. The study will use devices which are representative of practical designs, and will investigate the production and decay of vorticity.

In the case of the vane vortex generators, simple rectangular plan form devices will be used, and the variable parameters will be:

- Vane Incidence,
- Vane Height-to-boundary-layer-thickness ratio
- Downstream distance

In the case of the air-jet vortex generator, circular jets will be used. The variable parameters will be:

- Hole diameter
- Jet-to-free-stream velocity ratio
- Jet pitch angle
- Jet skew angle
- Downstream distance

Using the experimental results, it is proposed that simple empirical equations will be produced which will predict the vorticity signatures downstream from the point of generation.

Chapter 6 - Low-Mach Number Tests

6.1 - Introduction to Low-Mach Number Tests

The low-Mach number tests were so called, since the Mach number for all of these tests was set at 0.06 (or 20 m/s). The low Mach number was chosen so as to provide a proving ground where data could be obtained at low cost, since the running costs of a wind tunnel will increase significantly with Mach number. Thus the parametric study would use as much low speed data as possible in order to understand the trends in air-jet performance, and then to carry out a study to investigate the effect of Mach number on some selected test cases.

6.2 - Low-Mach Number Tests Experimental Arrangements

6.2.1 - Wind Tunnel & Boundary Layer Studies

All low Mach number tests were carried out in the Cranfield College of Aeronautics 2'x2' (0.61 m x 0.61 m) 'Brough' open return low speed wind tunnel, at a free-stream speed of 20 m/s.

The Brough wind tunnel has a 9:1 contraction ratio, giving a turbulence level of around 0.25%. The wind tunnel working section is 2.4 m long and the natural boundary layer on the floor of the wind tunnel is turbulent at the entrance to the working section, having passed through transition in the contraction cone. A station was chosen for the vortex generators where the boundary layer would be turbulent, and sufficiently thick for accurate measurements, leaving a reasonable distance downstream for measurements to be taken. This position was to be 0.8 m from the leading edge of the working section floor. The natural boundary layer at this point was confirmed as being a turbulent boundary layer with a $1/7^{th}$-power law profile, and a thickness of 18 mm. However, this boundary layer was considered to be too small for sufficiently accurate measurements. Therefore, the boundary layer was artificially thickened using three 2-mm diameter wires running across the entrance to the working section. These wires were placed with a streamwise separation distance of approximately 50-mm. The result was a thickened boundary layer of 41.5 mm 800-mm from the entrance to the working section, with a $1/7^{th}$-power law profile. This geometry is depicted in the Figure below:

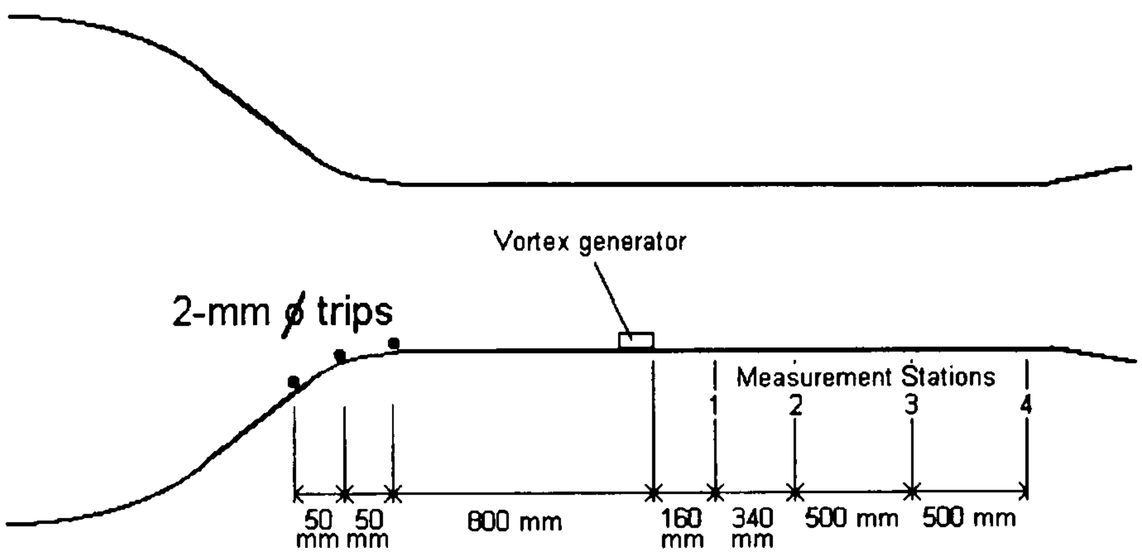

Figure 18: Schematic of the Brough Wind Tunnel Working Section

Streamwise static pressure measurements were also made to ensure that the wind tunnel static pressure gradient was zero. This gradient was observed as being slightly negative, translating to an increase in flow speed of approximately 0.5% (at 20 m/s) over the 2.4 m long working section.

6.2.2 - Vortex Generators & Mounting

The vortex generators used in this study were both vanes and air-jets. These were all mounted on a turntable that was used to change incidence for the vanes and skew angle for the air-jets. The centre of rotation was located 0.8 m from the entrance to the working section, and was mounted

centrally in the cross-stream sense. The turntable was 196 mm in diameter. The top plate of the turntable was interchangeable to allow both the vanes and the air-jets (with plenum) to be mounted.

Vane Vortex Generators

The vane vortex generators were designed using the guidelines laid down by Pearcey[29]. The details of the tests are given in the Table 1. Each vane was constructed from 1.5-mm aluminium sheet, and was black anodised to aid with flow visualisation. The largest of the vanes was fractionally larger than the radius of the turntable, and thus to keep the whole chord on the turntable, the rear of the vane was placed 6 mm behind the centre of rotation. As a result, all the other vanes were similarly mounted, so that the trailing edges of all the vanes were mounted at the same point.

The four vanes were tested at 4 incidence values over the expected useful range, and at four downstream stations. Thus a total of 64 data points were taken.

Table 7: Vane Vortex Generator Test Configuration

Chord, c (mm)	Height, b (mm)	Downstream Distances, x (m)	Vane height-to-Boundary Layer Thickness ratio, h/δ	Incidence Range, α (°)
46	23	0.16	0.55	10
76	38	0.5	0.90	15
106	53	0.8	1.25	18
136	68	1.1	1.62	20

Air-jet Vortex Generators

The air-jets were designed using the guidelines of Selby[42], and were adapted to model the expected range of results in an intake duct. The holes were of circular bore, and the diameters were scaled to give diameter to boundary layer height ratios (D/δ) of 0.096, 0.193 and 0.289 (4 mm, 8 mm, and 12 mm respectively).

Plugs were manufactured to serve as the surface through which the hole would be made. The plugs were 114 mm in diameter, and were 22.5 mm thick. This thickness is representative of a wall thickness which may be used on an intake wall. The holes were made though plugs that fitted to the turntable plate. Three plugs were made for each of the three hole sizes, where the pitch angles were 30°, 45°, and 60°. Skew angles were altered by rotation of the turntable.

Velocity ratios of 0.7, 1.0, 1.3, 1.6 & 2.0 were used. The air was introduced to the wind tunnel by means of a throttled centrifugal compressor. The air was ducted to a plenum chamber through 50-mm diameter pipe. Total pressure, static pressure and total temperature in the pipe was measured, as was static pressure in the plenum.

Air-Jet Calibration

Initial measurements of the jet velocity profiles with no cross-flow showed that the jet issuing from the simply drilled hole did not give a sharp edged jet - indeed, they did not even give an axi-symmetric jet. While this configuration may have been representative of a practical engineering solution, it would make the development of an empirical model difficult, since the exact nature of the asymmetry may have been dependant on a number of factors which were not quantifiable. Thus, is seemed more prudent to attempt to use a flat-topped, sharp-edged jet profile, and then to develop some correction for the effect of 'real' jets.

The reason for the asymmetry was thought to be due to the oblique angle on the jet entrance. Since the air in the plenum was at a very low dynamic pressure, at the entrance to the jet, the flow would undergo a very rapid acceleration to the jet velocity. With the oblique angled side of the jet being sharp edged in nature, the combination of the rapid acceleration around the sharp edge may cause a separation analogous to that at the trailing edge of an aerofoil at moderate incidence in a viscous flow. Thus in order to improve on these characteristics, a number of bell-mouth nozzles were made which were inserted into the entrance of the jets. Further measurements of the jets showed a marked improvement in the jet characteristics, which made them more suitable for a baseline to the air-jet work. The effect of the bell-mouth on the jet profile is demonstrated below.

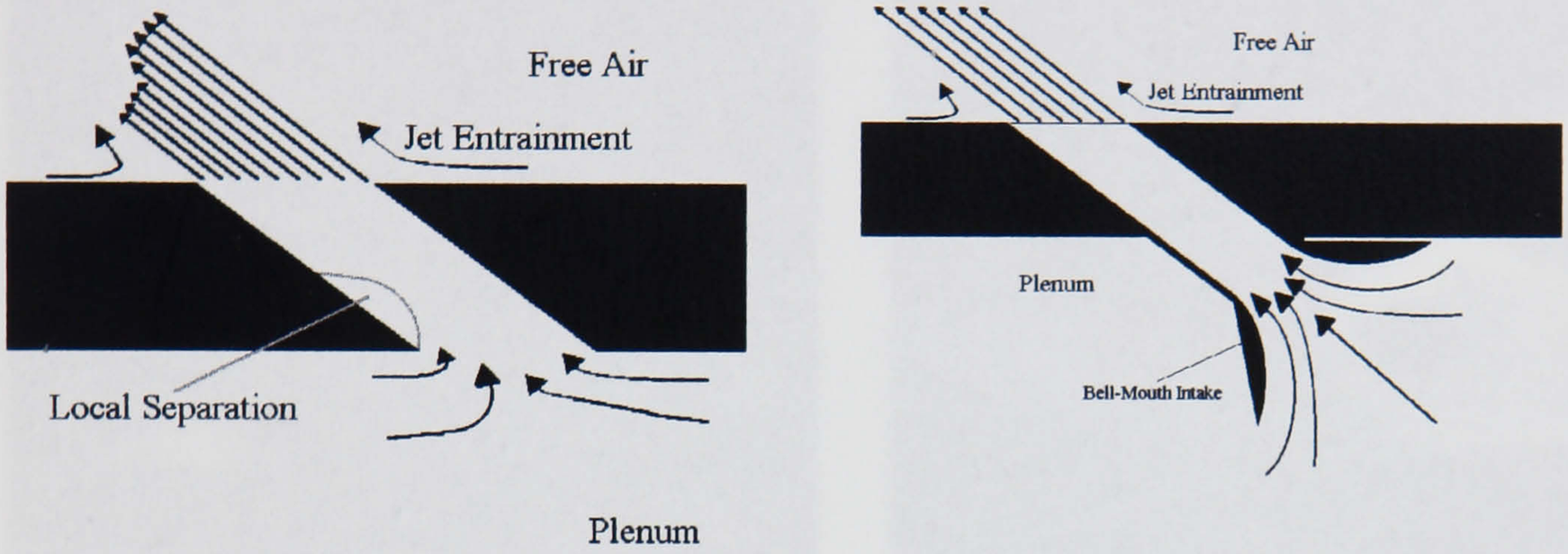

Figure 19: Deduced Internal Jet Flow for un-modified and Modified Jets

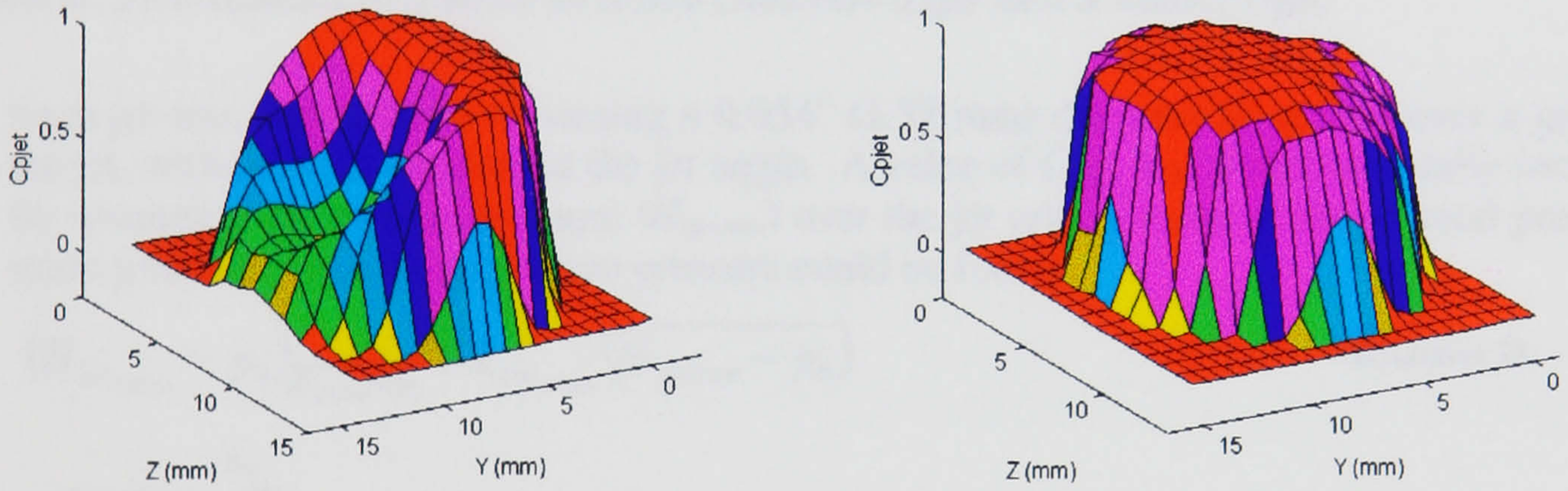

Figure 20: Jet Pressure Coefficient Plots for the un-modified and modified jets (D = 12 mm, $\alpha = 60°$)

Initially, in order to set the flow characteristics of the jet with the cross flow, the volumetric flow of air to the air-jet plenum was to be measured. However the flow rates were so small, that satisfactory measurements could not be made without significant pressure losses in the system.

As an alternative, it was decided to relate the jet dynamic pressure to the total pressure in the plenum chamber through a series of calibration constants. Thus, for each jet configuration, a series of jet velocities were tested and calibration constants, k_{jet}, were produced:

$$k_{jet} = \frac{H_{jet} - p_0}{H_{plenum} - p_0} \qquad \textit{Equation 32}$$

The coefficient k_{jet} is a measure of the efficiency of the jet to provide total pressure, but also allows an indication of the jet velocity. Since the air in the free-stream is at a static pressure, p_∞, the dynamic pressure of the jet, q_{jet}, can be estimated as the difference between the jet total pressure and the free-stream static pressure. This approximation assumes that the jet exit static

pressure and the free-stream static pressure are equal. While this is extremely difficult to measure accurately, some estimation was made which suggested that the difference was less than 0.5 mm H_2O at all jet velocities. This was reinforced by smoke flow visualisation. 'Disco Fog' was introduced to the plenum chamber, which coloured the jet. On exit, the jet plume was seen to remain at the same diameter as the jet orifice, suggesting that the pressure difference across the jet boundary was negligible.

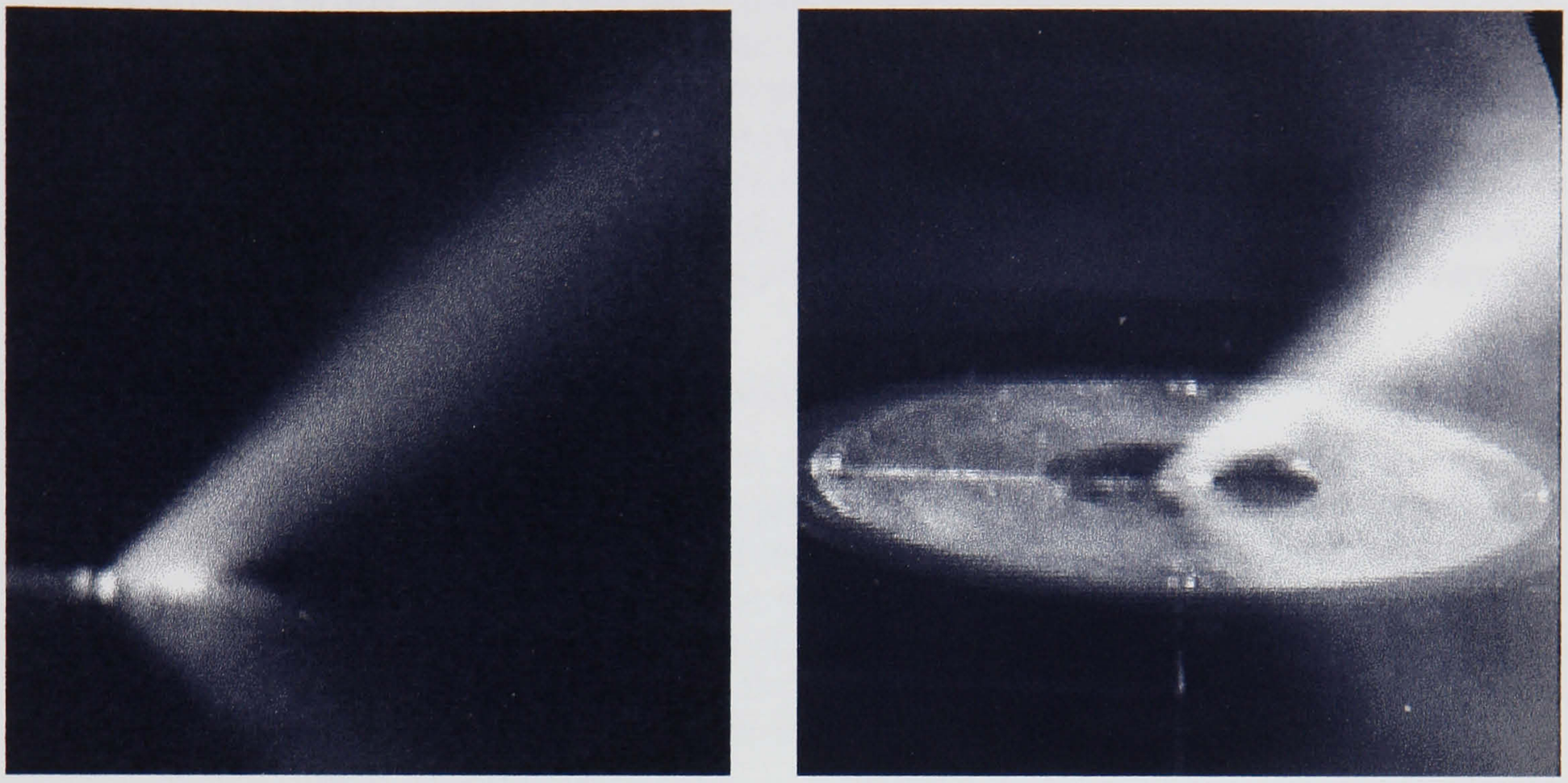

Figure 21: Flow Visualisation of the Air-jet in Zero Cross-Flow (Light Sheet & Ambient Light)

Each jet was measured by traversing a 0.054" (1.37 mm) diameter Pitot tube over a grid through the jet, with the tube inclined at the jet angle. A value of Cp_{jet} was obtained locally over the grid. By averaging the plenum pressure (H_{plenum}) over the jet grid, a value of the jet total pressure (less static pressure) for a given plenum pressure could be found:

$$\left(H_{jet_{LOCAL}} - p_0\right)_{\overline{H_{plenum} - p_0}} = k_{jet_{LOCAL}} \left(\overline{H_{plenum} - p_0}\right) \qquad \textit{Equation 33}$$

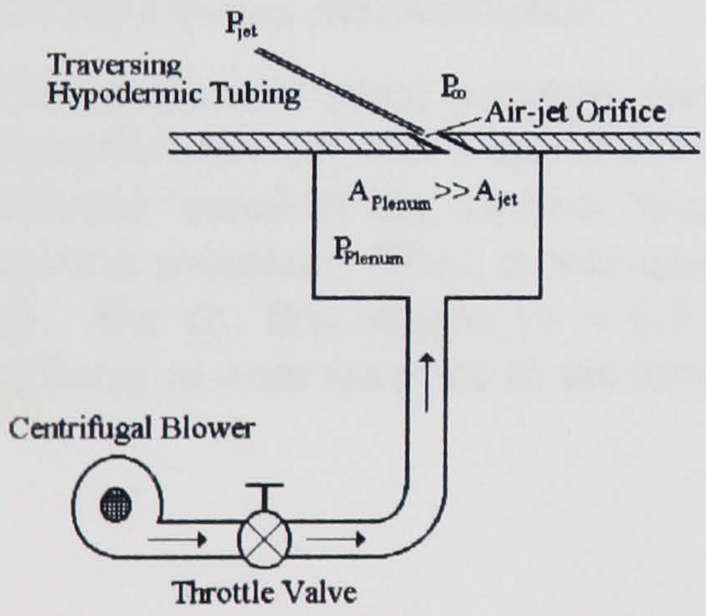

Figure 22: Schematic of the Apparatus for the Measurement of the Jet Profile

This averaged value is essentially a non-dimensionalised value which is referred back to a given jet strength condition. Using this pressure, and assuming a zero static pressure gradient across the jet boundary, the local jet velocity can be found. Using this and the measurement grid position references, the local mass flow can be found:

$$\dot{m} = \int \sqrt{\left[\frac{\left(H_{jet_{LOCAL}} - p_0\right)_{(H_{plenum} - p_0)}}{\frac{1}{2}\rho}\right]} \rho a.da \qquad \textit{Equation 34}$$

Thus, the mass flow can be related to the plenum pressure through the jet calibration.

It was interesting to note in the jet calibration process how the difference in the grid spacing could affect the velocity profile. While it is clear that too few points will not give sufficient resolution to the profile, when the grid spacing was dropped below the Pitot diameter, the flat top to the profile appeared larger than was previously measured. It appears that if the probe is too large in diameter, then an average process results. This implies that while the probe centreline may have been free of the jet, the outer lip was in the high plateau region of the jet, and thus the pressure at a position nominally outside the jet was averaged over an area containing the jet. Thus care was needed in this process.

1.1.1 - Measurement Methods - 5 Hole Pressure probe

In order to measure the flow behind the vortex generators, a 5-hole pressure probe was selected. The probe can be calibrated to yield the local values of pitch and yaw angle (θ and ϕ respectively) as well as the local total and static pressure. From these values, the local flow velocity vector can be calculated (with an appropriate temperature measurement), and hence the velocity vectors in the defined co-ordinate system can be calculated. Traversing the probe over a grid, a slice though the flowfield can be taken, and a plane of local flow velocity vectors can find found. For details on the calibration and data reduction of the five-hole pressure probe, refer to the Appendices.

1.1.2 - Traverse Gear & Installation Tests

The traverse mechanism that was to be used was a *y-z* (cross-stream) traverse consisting of two vertically mounted screw-thread linear slides, with a horizontally mounted linear slide attached to the carriages of the vertical slides. Stepper motors, which were driven by a PC based control system, controlled the motion.

While the traverse could only give motion in the y and z directions, the downstream station measurements were achieved by moving the traverse within the wind tunnel. Since the blockage of the traverse would be relatively high, checks were made to verify the effects of the traverse of the wind tunnel characteristics.

The streamwise static pressure gradient was used as a benchmark for the empty wind tunnel characteristics. It was found that by mounting the probe on a rigid arm that placed the probe tip 450-mm ahead of the traverse feet, the static pressure at the probe tip was unaffected by the traverse presence. Thus, it was assumed that the effect of the traverse was minimal at the probe tip. For the first station (x = 0.16 m), the boundary layer profile was also checked, and no differences were seen due to the traverse position.

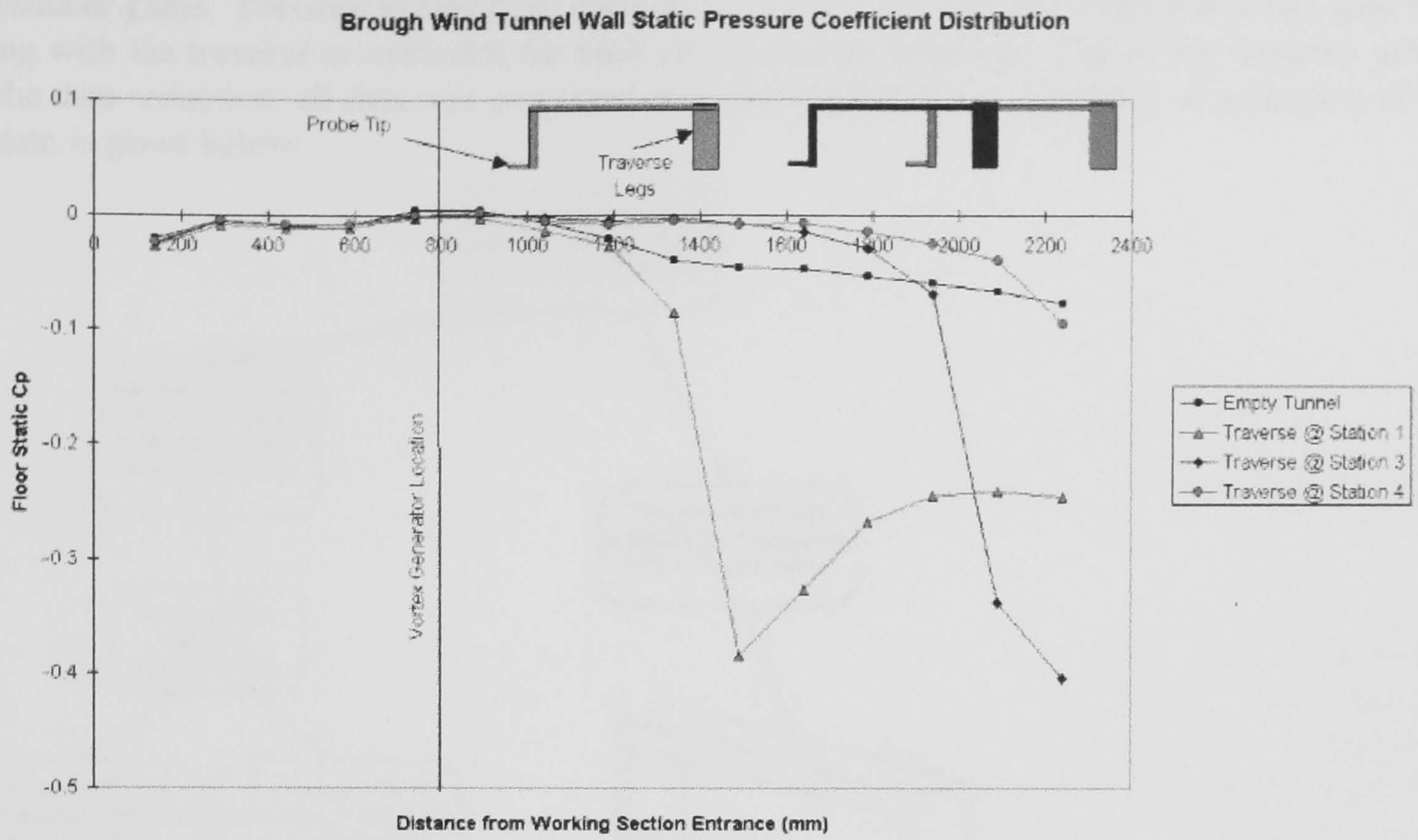

Figure 23: Brough Wind Tunnel Wall Streamwise Static Pressure Coefficient Distribution

1.1.3 - Data Acquisition

The data acquisition system was PC based using custom written software running under Microsoft Windows. The data acquisition controlled both the movement of the traverse and the reading of data to a text file.

Pressures were read using pressure transducers. A single Furness FCO 16 ±200 mmH_2O differential micro-manometer (Serial Number 9601308) was used to measure the dynamic pressure, and was connected to a Pitot-static probe which was located in the free-stream above the vortex generator. Five Furness FCO 44 ±100-mmH2O micro-manometers (Serial Numbers 9509141 to 9509145), were used for the 5 hole probe, with one transducer used per hole. These transducers were differential in nature, and were referenced to the free-stream static pressure given by the Pitot-static probe mounted over the vortex generator and on the wind tunnel centre-line. The pressure transducers were calibrated together with the amplifiers using a Druck DP 601 pressure calibrator.

The electrical output of the pressure transducers was single-ended in nature, and was therefore susceptible to electrical noise. Examination with an oscilloscope revealed a sinusoidal oscillation superimposed over the output signal, and this was filtered using a 0.01 kHz filter. Also, a large amplitude random spike was seen on the output trace, and this was traced to the stepper motors. It proved difficult to remove this noise, since it appeared to be transmitted in part through the PC. Therefore an amplifier was used to increase the signal to noise ratio, and by averaging the data over the three-second-time period, the effect of the noise was dramatically reduced.

Controlling software (called Generation neXt) was written, using Microsoft Visual Basic, which would address an internally mounted Analogue-to-Digital Converter (ADC), and which would control the traverse via a second piece of software: Compumotor's Motion Architect. Thus, a grid could be mapped out, and then data were taken at each grid point, with the motion being carried out automatically. For a grid of around 300 data points, a run time of about 1-hour was required. Data were sampled at 100 Hz, over a three-second period, and the values were averaged.

Data were converted from the raw voltages read from the ADC board to corresponding pressures

in the data acquisition, the program allowing for the effect of wind off zero offsets, and the transducer gains. Pressure values from each of the transducers was then stored in a text data file, along with the traverse co-ordinates for each set of pressure readings. Due to the complex nature of the data reduction, all data was processed once the run had been completed. A schematic of the system is given below:

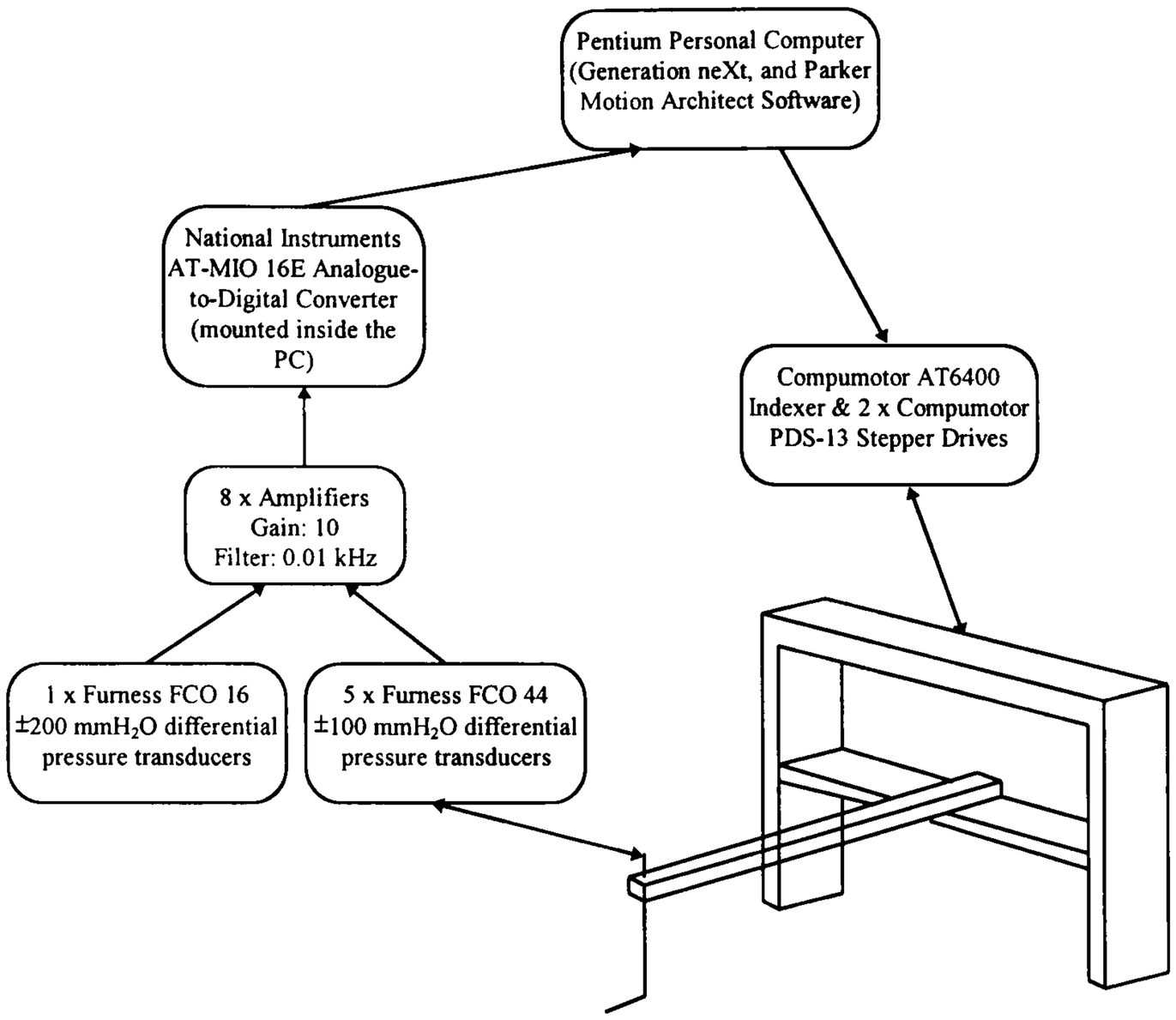

Figure 24: Schematic of the Data Acquisition Methodology

6.2.6 - Data Reduction

Data reduction and data presentation was carried out using Math Works Inc. MATLAB. Data were read in from the text files supplied by the Generation neXt software. The data were re-arranged into two-dimensional matrices (with the same dimensions as the experimental grid), the matrices being y co-ordinate in mm; z co-ordinate in mm; dynamic pressure in Pascals; and P1 to P5 in Pascals (these being the pressure read from probe tubes 1 to 5 respectively). The pressure data were then non-dimensionalised to coefficient form as follows:

$$Cp_\theta = \frac{P_3 - P_1}{P_5 - P_{avg}}$$ *Equation 35*

$$Cp_\phi = \frac{P_2 - P_4}{P_5 - P_{avg}}$$ *Equation 36*

$$Cp_5 = \frac{P_5 - P_0}{H_0 - P_0}$$ *Equation 37*

$$Cp_{avg} = \frac{P_{avg} - P_0}{H_0 - P_0}$$ *Equation 38*

P_{avg} is defined as the average of the pressures in tubes 1 to 4 and all the pressures (P_n) correspond to the pressures from the probe tubes as illustrated below.

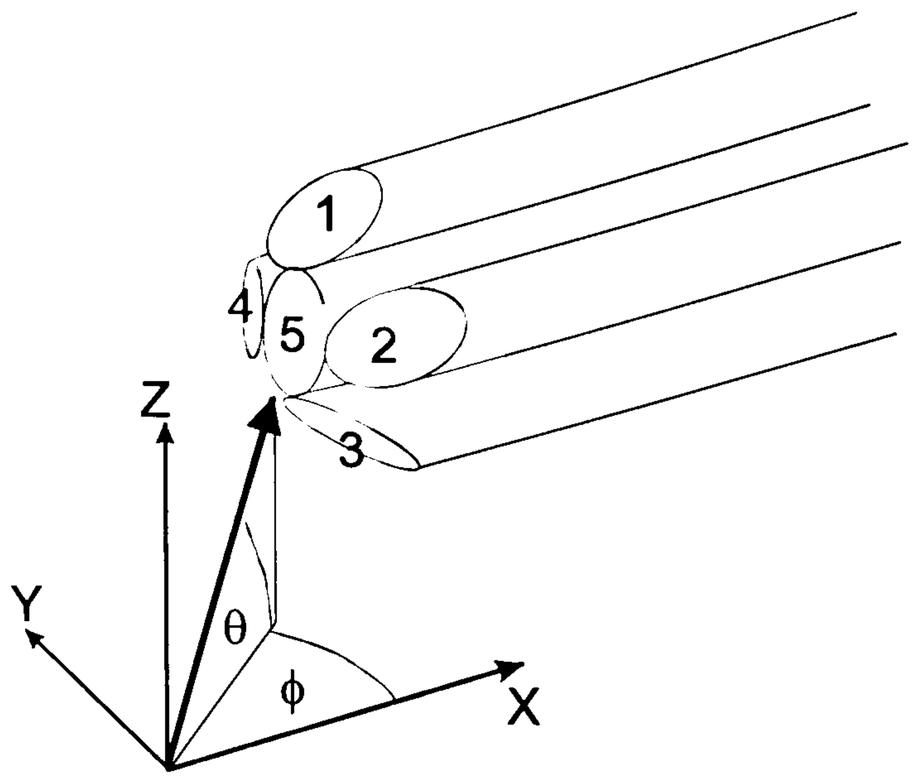

Figure 25: 5-Hole Probe Co-ordinate System

It may be seen in the equations above that the pressure coefficients in pitch and yaw (respectively) are defined using pressures sampled at the probe tip, i.e. they are self-contained. Essentially, the numerator of each equation corresponds to the pitch or yaw angle, and it is non-dimensionalised by a probe tip response that is analogous to dynamic pressure. The pressure sampled at tube five is essentially the Pitot pressure (or total pressure), and the average of the four outer-tube pressures is a combination of total and static pressures. In fact, the calibration method relates P_5 to the total pressure and P_{avg} to the static pressure.

A graphical interpolation was then used to find the pitch and yaw angles, obtained in calibration, which corresponded to the experimental values of Cp_θ and Cp_ϕ (see Figure below). Initially, the calibration matrices were searched to find the calibration values of Cp_θ and Cp_ϕ (corresponding to four pitch-yaw combinations - labelled 1 - 4) which were located around the experimental values (labelled as 'e'). Each value of Cp_θ and Cp_ϕ was associated with unique values of pitch and yaw angles from calibration. Thus, a bi-linear interpolation could be performed in the following manner:

$$Cp_\theta = a_\theta\theta + b_\theta\phi + c_\theta\theta\phi$$
$$Cp_\phi = a_\phi\theta + b_\phi\phi + c_\phi\theta\phi$$

Equation 39

In the equation above, a, b and c are coefficients which can be found by solving at the calibration data points. Thus it should be possible to solve for θ and ϕ, the values of pitch and yaw. However, due to the cross-product term, this is not possible. Thus, a second interpolation must be performed.

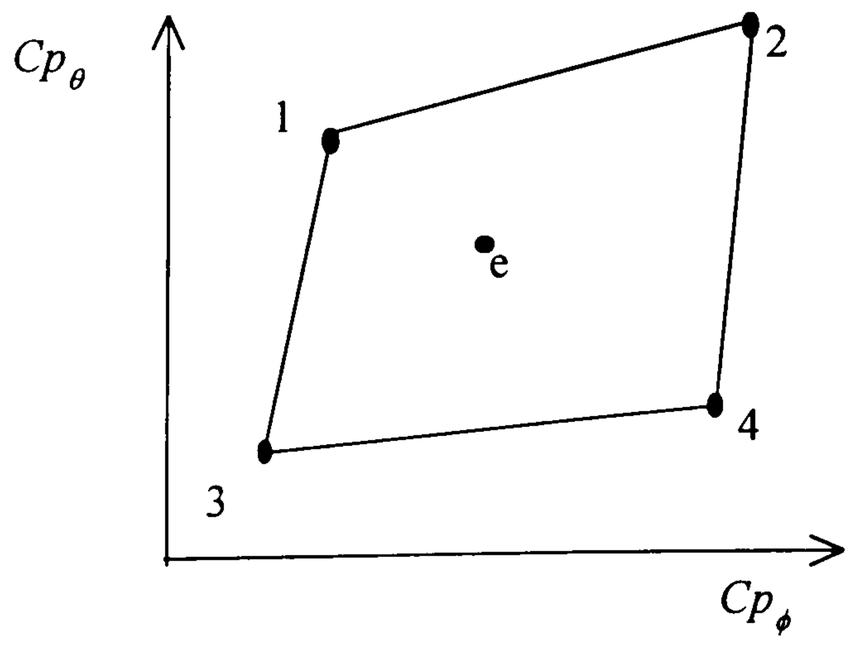

Figure 26: Graphical Interpolation of Pitch and Yaw Coefficients

The calibration data can be graphically interpolated between to obtain approximated values of Cp_θ and Cp_ϕ at a desired angular resolution. In the current method, this was carried out over 0.1° steps. These approximated values were then compared with the experimental values using a least-squares method, in order to find the nearest pitch-yaw combination.

Once the pitch and yaw angles have been determined, the total pressure and static pressure can be determined from calibration data. Again a bi-linear interpolation is used of the following form:

$$Cp_5 = a_{Total}\theta + b_{Total}\phi + c_{Total}\phi\theta$$
$$Cp_{avg} = a_{Static}\theta + b_{Static}\phi + c_{Static}\phi\theta \qquad \textit{Equation 40}$$

While this method appears rather tortuous, the nature of the data lends itself to this approach. The bi-linear approximation works well, since the magnitude of the cross product in each case is small. This is in part due to the response of the probe, but also aided greatly by a reasonably close angle spacing in calibration. The largest angle spacing for the calibration data set was 4°, and the spacings were chosen to be in the areas where the probe response changed least with a change in angle. The results were seen to be most favourable and are discussed below.

6.2.7 - Calculation of Vorticity

Once the data for pitch/yaw angles and local total and static pressure have been obtained from the probe data reduction, the local dynamic pressure can be derived, and hence the local velocity vector can be found.

$$\overline{V_{LOCAL}} = \sqrt{\left.\frac{H_0 - p_{LOCAL}}{\frac{1}{2}\rho}\right|_{LOCAL}} \qquad \textit{Equation 41}$$

Since the pitch and yaw angles of the probe-tip response to the free-stream are known, the local velocity vector can be decomposed to form the three vector components in the chosen axis co-ordinate system. The equation below shows such a decomposition using a *pitch-yaw* system.

$$u = \overline{V}\cos\theta\cos\phi$$
$$v = \overline{V}\cos\theta\sin\phi \qquad \textit{Equation 42}$$
$$w = \overline{V}\sin\theta$$

Once the cross-stream velocity vectors (v and w) have been found at all points over a grid, the velocity derivatives can be calculated to give vorticity:

$$\omega_x = \frac{\partial w}{\partial y} - \frac{\partial v}{\partial z} \qquad \textit{Equation 43}$$

The gradients were calculated using a built-in MATLAB function that calculates the approximate gradient using a curve fitting approach.

In order to calculate the total circulation of the vortex, the vorticity must be integrated.

$$\Gamma = \oint(v dy + w dz) = \iint\left(\frac{\partial w}{\partial y} - \frac{\partial v}{\partial z}\right)dy.dz \qquad \textit{Equation 44}$$

It is clear that a simple but effective way to integrate is to use a 'two-dimensional trapezium rule' where the vorticity value is assumed to act over an area, and thus the circulation becomes the area sum of the vorticity-area product.

6.3 - Repeatability & Error Analysis

6.3.1 - The Effect of Grid Spacing

The use of fine grids for planar measurements is most desirable, and the limit of practicality needs to be established. As such, a series of tests was conducted which compared the effect of reducing the grid spacing. Two comparisons were made, one of the effects between 10-mm and 5-mm grid spacing, and one for the effects between 5-mm and 3-mm grid spacing. The results are given below:

Table 8: First Case - 10 mm and 5 mm Grid Spacing

Grid Spacing (mm)	Γ (m^2s^{-1})	ω_{max} (s^{-1})	$y_{\omega max}$ (mm)	$z_{\omega max}$ (mm)
10	0.2831	735.7655	20	20
5	0.2957	1278	15	20

Table 9: Second Case - 5 mm and 3 mm Grid Spacing

Grid Spacing (mm)	Γ (m^2s^{-1})	ω_{max} (s^{-1})	$y_{\omega max}$ (mm)	$z_{\omega max}$ (mm)
5	0.3511	1381.4	20	19
3	0.3544	1602.1	18	18

It can be seen in Table 2 that the maximum vorticity measured (ω_{max}) for the 10-mm spaced case is considerably smaller than for the 5-mm case. Also, the position of this peak vorticity is very different as highlighted by the co-ordinates $y_{\omega max}$ and $z_{\omega max}$: the widely spaced grid was not of a sufficient resolution to pick up enough of the flow features in the vortex.

From the second comparison of grid spacings, when the grid spacing has been reduced by 40% in each direction, an increase in the time for the run by a factor of 3 is seen. This increase in resolution leads to an increase in circulation strength (Γ) of 1% between the grid spacing of 5-mm to 3-mm, compared with an increase of 4% from the reduction of grid spacing from 10-mm, to 5-mm. Also, it may be seen that while the magnitude of the peak vorticity for the 3-mm grid is still higher in the case of the fine grid, the positions are now much closer as given by the co-ordinates for peak vorticity.

In choosing the grid spacing to be used, an appreciation for the accuracy of the runs is needed, and the time constraints involved. Clearly, the most number of data points in the area in which the vortex lay would aid the better evaluation of the vortex parameters. It was seen that using the 5 mm grid spacing allowed sufficient resolution to achieve an accurate interpolation of the data while using as low a run time as possible.

6.3.2 - Repeatability

Two separate vortex generator test cases were carried out to assess repeatability. The data for these vortices are presented below.

Table 10: Repeatability Test (Rectangular Vane, $\alpha = 15$, $h/\delta = 0.55$)

Run N°	Γ (m^2s^{-1})	ω_{max} (s^{-1})	$y_{\omega max}$ (mm)	$z_{\omega max}$ (mm)
t08	0.2220	1134.8	15	19
t09	0.2284	1109.8	15	19
112	0.2260	1099.1	15	19

Table 11: Repeatability Test (Rectangular Vane, $\alpha = 15$, $h/\delta = 0.90$)

Γ (m^2s^{-1})	ω_{max} (s^{-1})	$y_{\omega max}$ (mm)	$z_{\omega max}$ (mm)
0.3844	1114.4	30	30
0.3865	1112.1	30	30

The repeatability in these results is extremely encouraging. It may be seen that in Table 4, the peak vorticity is spread about the central case (t09) by +2.25/-0.96%, and that the circulation strength, Γ, is -2.08/+1.1% about the middle case value. The results from the second case are equally good with a difference of 0.5% in circulation and 0.2% in peak vorticity.

6.3.3 - Errors

An estimation of errors has been carried out, and a statement of the magnitude of these errors for all measured values will be made. However, in the case of the derived quantities (such as vorticity and circulation), the effect of the measurement errors on these values is difficult to quantify. Where possible the error analysis is carried out using a statistical analysis of a sample[53], with the error being quoted with a 95% certainty level.

Five-Hole Probe Results

The 5-hole probe was calibrated over a range of expected pitch and yaw values that would allow sufficient resolution to achieve a good degree of accuracy for graphical interpolation. Once the calibration data had been collected, more 'check' data points were taken immediately after calibration. The 'experimental values' of these data points were then entered into the data reduction scheme, and it was seen that the maximum angular errors in all cases was 0.1°. These 'experimental points' are compared with the measured values in Table 6 below:

Table 12: 5-Hole Probe Measurement Error Analysis

$\theta_{measured}$	$\phi_{measured}$	P_5 (Pa)	P_{avg} (Pa)	Cp_ϕ	Cp_θ	$\theta_{experiment}$	$\phi_{experiment}$	Error in θ	Error in ϕ
22.8°	13.0°	165.51	48.90	1.1726	1.672	22.8°	12.9°	0.0°	0.1°
15.9°	-18.0°	149.07	54.58	-1.889	1.500	15.8°	-18.0°	0.1°	0.0°
-8.7°	-26.0°	109.37	30.52	-3.708	-0.597	-8.7°	-25.9°	0.0°	0.1°
-18.5°	-4.0°	157.85	56.82	-0.4965	-1.981	-18.5°	-8.9°	0.0°	0.1°

Following from these angular errors, an estimation of the error in the measurement of the local dynamic pressure was made. It was seen that the maximum error was to be less than 3.0%.

Free-Stream Velocity

Statistical analyses of a number of randomly chosen runs were carried out, and it was seen that the mean wind tunnel velocity could be set to within 0.1 m/s (or 0.5% @ 20 m/s) with a scatter of ±0.15 m/s (or 0.75% @ 20 m/s).

Velocity Ratio

Statistical Analyses of the velocity ratio as measured for the air-jet vortex generators was carried out for a number of randomly chosen runs. It was seen that the mean air-jet velocity ratio could be set to within 0.005 of the desired value (0.4% @ $VR = 1.3$, and 0.25% @ $VR = 2.0$), with a scatter

of ±0.013 (1% @ $VR = 1.3$, 0.65% @ $VR = 2.0$).

Empty Wind tunnel Tests - Estimation of 'Ghost Vorticity'

Before measuring the vortices that are produced by the vortex generators, empty working section tests were carried out to assess the wind tunnel boundary layer, and to investigate the effect of the probe in regions of high cross-stream total pressure gradient.

Since the probe is of finite size, it will measure the local flow conditions over a small volume, rather than at a point. If the flow conditions change significantly over this volume (for example the high velocity gradient close to the wall in a boundary layer), the probe will sense the corresponding pressure gradient as the effect of a local flow angle. The effect of the pressure data reduction to vorticity is that a small amount of 'ghost' vorticity is observed close to the wall. Therefore in the subsequent analysis of the vortex flows, any vorticity at a point below the peak 'ghost' vorticity should be ignored.

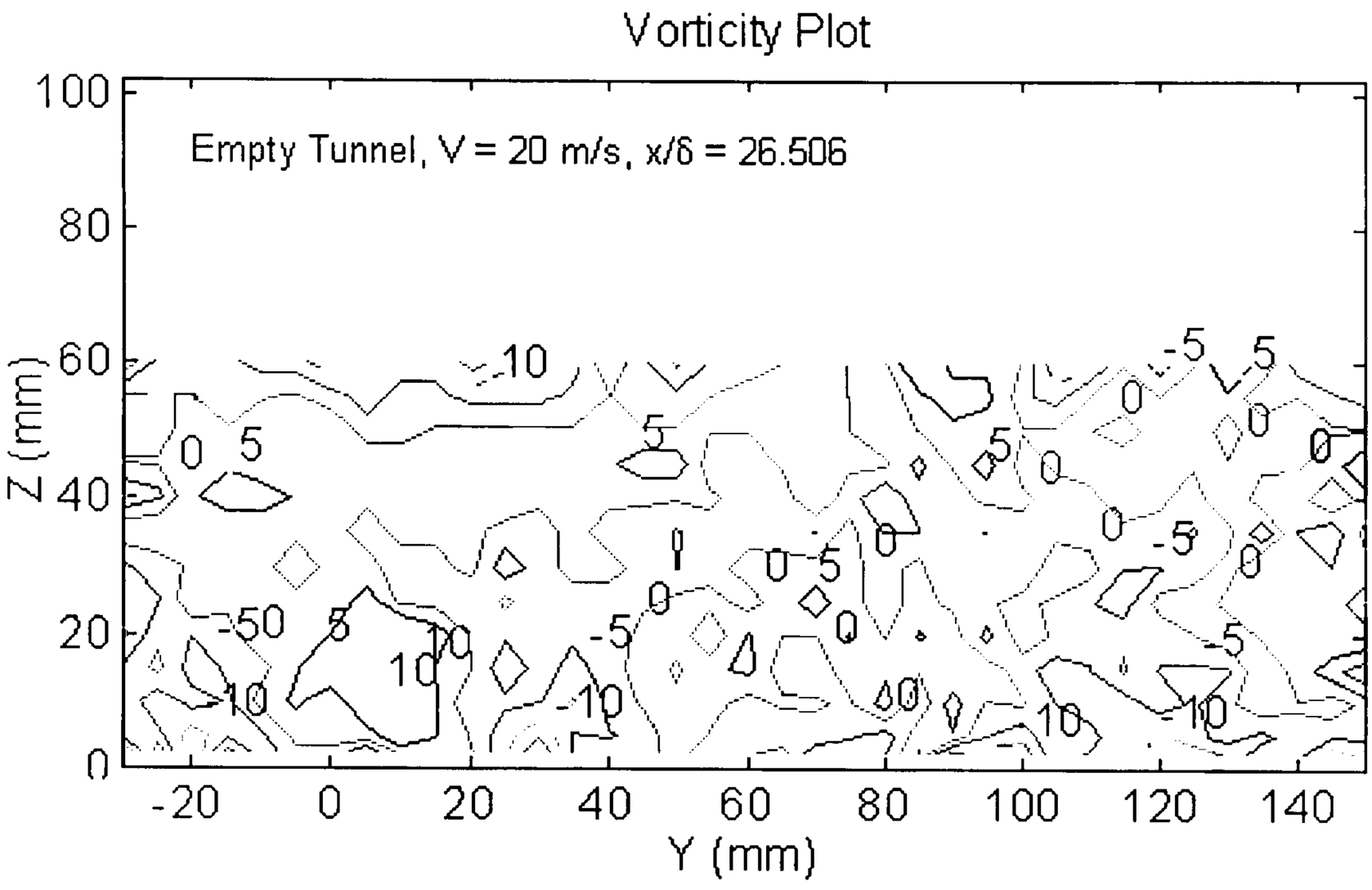

Figure 27: 'Ghost Vorticity' in the Empty Wind Tunnel

The graph above shows the empty wind tunnel vorticity plot, and in the main, it is clear that the vorticity in the main region of the flow field is very low (between -5 s^{-1} and 5 s^{-1}). However, very close to the working section floor (at $z = 0$), the vorticity levels achieve a higher order of magnitude, with vorticity levels reaching -20 s^{-1}. Due to the nature of the pressure gradient, the 'ghost' vorticity is mostly negative in sign close to the wall. However, in order to reduce its effect, a cut of in vorticity is applied as so:

Ghost Vorticity Cut-off Level = +25 s^{-1}

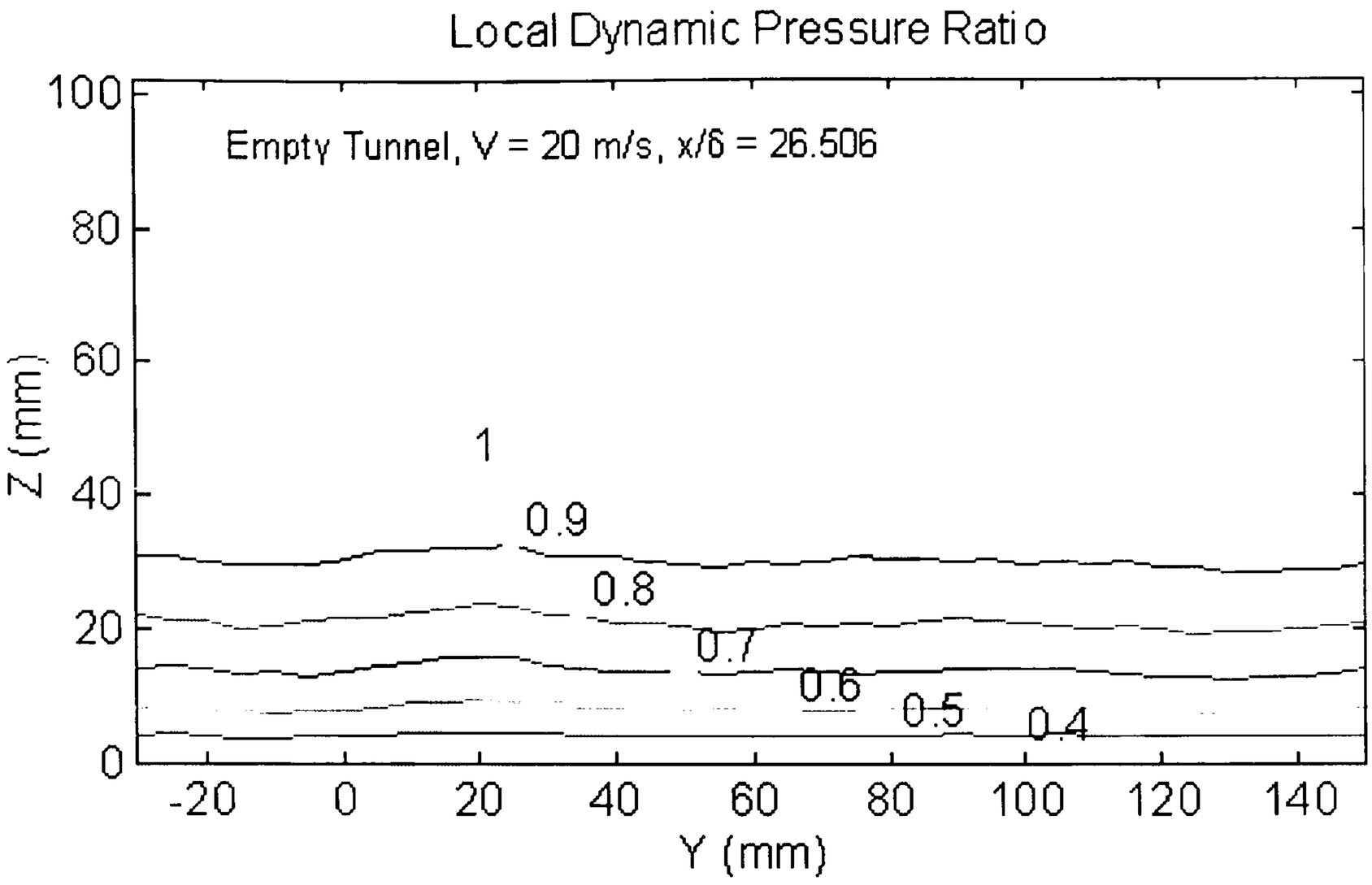

Figure 28: Local Dynamic Pressure Ratio of the Empty Wind Tunnel

As noted earlier, this 'ghost' vorticity is generated in the region of high shear in the boundary layer, which is evident from the close spacing of the isobars directly above the wind tunnel floor (Figure above). This information is translated into a false pitch angle reading above the floor, highlighted by the pitch angle contours in the Figure below.

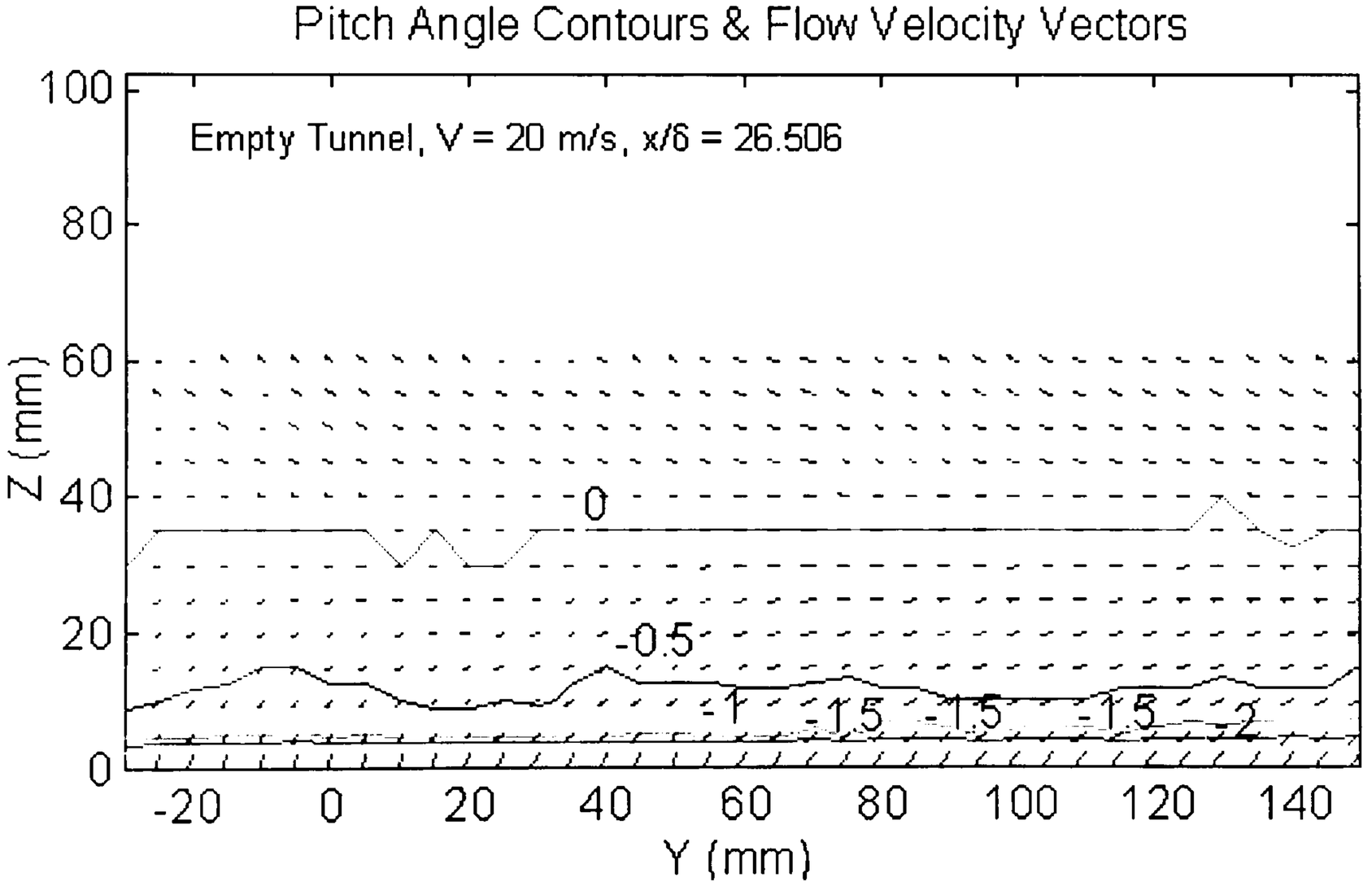

Figure 29: Empty Wind Tunnel Local Cross-stream Velocity Vectors (with Pitch Angle Contours Superimposed)

6.1 - Low Mach Number Tests Results

From the initial considerations, the appearance of the vortices from the vane and air-jet vortex generators was quite different in nature. Although the vortices from each generation method are essentially a column of rotating flow that is largely inviscid, but with a central viscous core, some of the parameters associated with the vortex are markedly different. Thus, the results are presented as two separate sections, even though the experimental procedures were identical.

6.1.1 - Basic Low Mach Number Vane Results

For the low Mach number tests, three parameters were varied: vane incidence (values of 10°, 15°, 18° and 20°); vane height-to-boundary-layer-thickness ratio (h/δ of 0.544, 0.916, 0.1277, 1.639); and streamwise distance ratio (x/δ = 3.855, 12.048, 19.277 and 26.506). The three-dimensional matrix of test data points is presented in Figure 30, revealing the 64 individual test cases.

Using the five-hole pressure probe, the local flow angles and the local total and static pressures were measured, from which the flow velocity vector and the vorticity could be derived. Plots of the local dynamic pressure coefficient (defined as *the local dynamic pressure/free-stream dynamic pressure*) and the vorticity profiles are presented. Since the total number of data points is rather large, rather then display all of this data, the trends are shown, by altering one parameter for only one case of the other two. The effect of height ratio is demonstrated at an incidence of 15° and a streamwise distance ratio of 3.855 (Figure 31). Plots are presented which show the effect of the variation in incidence at a height ratio of 0.916, and a streamwise distance ratio of 3.855 (Figure 32). Also, the streamwise decay of the peak vorticity is demonstrated for a height ratio of 0.916 and a vane incidence of 18° (Figure 33).

Dynamic Pressure Plots

The dynamic pressure ratio plots give an indication as to the distortion or mixing which occurs in the boundary layer (Figure 31 (a), (c), (e) & (g)). The effect of the vortex in the boundary layer is that on one side, the free-stream fluid is swept down on the surface, while on the other side, the boundary layer fluid is swept up in to the free-stream. In the field of separation control, the net effect is that the local skin friction at the wall is increased by the interchange between the boundary layer and free-stream fluids. Since the vortex is generated as the rolling up of the flow in the wake of the vortex generator, the centre of the vortex tends to have a dynamic pressure that is less than that of the free-stream value. This type of dynamic pressure profile through the vortex core is termed as a wake type core (as opposed to a jet type core, where the core dynamic pressure is higher than the free-stream value). As stated in the Introduction section, the pressure gradient in which a vortex is placed will affect the development of the vortex through the vortex-stretching phenomenon. Thus the local dynamic pressure is an important parameter not just in understanding the extent of the mixing, but also in understanding the development of the vortex core.

Vorticity Plots

Referring to Figure 31 (b), (d), (f) & (h), clearly, the magnitude of the distortion to the undisturbed boundary layer will be dependent on the strength of the vortex. If the vortex has a high rotational velocity (i.e. high vorticity), the extent to which the fluid is swept around the vortex centre in a circumferential sense will be larger. Further, if the physical size of the vortex is large, then the radial extent of the deformation of the boundary layer will be greater. Thus, while vortices are very often defined in terms of the circulation (or the area integral of the circulation), classification in terms of the vorticity and the radius yields a clearer picture of the vortex characteristics. It is therefore advantageous to consider the effect of the varied parameters in terms of these two aspects.

Vortex Location

The vertical position of a vortex generated by a vane is largely fixed by the geometry of the vane, and previous investigators have noted that the centre of the vortex is formed at approximately 95%

of the height of the vane. This observation may be seen from the dynamic pressure ratio and vorticity profile plots, where for a vane of height ratio (h/δ) = 0.916 (a vane height of 38 mm), the centre of the vortex tends to occur at a height of approximately 35 mm, or 92% of the vane height. This observation is consistent across the data set. Clearly, the larger the span of the vane, the further from the surface the vortex will occur.

Comparison of a Vane with a Conventional Lifting Wing

The vorticity is shed from the vortex generator in a similar manner as that from a conventional lifting wing, with the tip vortex the result of the rolling up process. Thus, parallels can be drawn.

As the planform area of the vortex generator is increased (in this case, the aspect ratio was held constant, thus an increase in area in achieved by an increase in vane height), a stronger vortex would be expected. As the vane is increased in height, the velocity at the tip will increase towards the free-stream value (due to the boundary layer profile), and therefore the magnitude of the pressure difference between the windward and leeward surfaces of the vane would increase. Further, the streamwise length which the vortex would roll up over would increase, and it may be expected that the strength of the vortex would increase accordingly. This observation is borne out in the results presented (Figure 31 (b), (d), (f) & (h)), where the peak vorticity is seen to increase with h/δ, and the amount of boundary layer deformation increases as well. It may be seen that the radius of the vortex core is similar in all the cases presented (varying h/δ, at a constant incidence and streamwise position). Clearly, at generation, the size of the vane does not significantly affect the physical size of the vortex, suggesting a similar initial size of the viscous core in the vortex. This idea is therefore consistent with the much-cited idea of a vortex core growing from an infinitely small point vortex, even if the physical scaling is not actually infinitely small. What is apparent from the full set of vorticity plots is that vortex radius grows as a function of the peak vorticity gradient (or the 'steepness' of the vorticity profile). Thus is will be shown that while the height of the vane does impact on the peak vorticity produced, it does not affect the size of the vortex at generation. It does impact on the size of the vortex downstream though, as the increased level of peak vorticity of the vortex increases the decay rate and therefore the cross-stream diffusion of vorticity.

While the aspect ratio was not altered, its effect on the vortex is not significant as long as the aspect ratio is less than a value of about 2. Above this value, the strength of the vortex drops considerably in a similar manner as that on a high aspect ratio wing[54].

As with a conventional lifting wing, the pressure difference across the vane increases with incidence, and hence the strength of the vortex will increase. This manifests itself as an increase in the value of the peak vorticity, as well as an increase in the physical size of the vortex (Figure 32). However, increasing the incidence too far also results in a parallel with the conventional wing stall: for a vane vortex generator, a situation occurs where the peak vorticity is reduced by up to 40%, and where the physical size of the vortex increases. The result is that the circulation (the area integral of the vorticity profile) is reduced, a result which for a conventional wing would signify a loss in lift. Thus in the 'post-stall' regime, a weaker and more diffuse vortex is apparent. The incidence at which the stall occurs is not independent of the height of the vane: at a small value of the height ratio (h/δ), the vane appeared not to stall over the range of incidences tested (up to 20°). However, for the largest vane, the stall occurred at about 12°. The dynamic pressure ratio plots reveal that the increase in incidence increases the mixing in the boundary layer, and the magnitude of this is easily seen (Figure 34). Also of note is the fact that the height of the vortex from the surface does not change with incidence, but again remains at about 92% of the height of the vane (Figure 32 (b), (d), (f) & (h)). The vorticity plots reveal both an increase in the peak vorticity and an increase in the physical size of the vortex core, thus revealing the importance of the pressure difference across the vane in increasing the vortex strength.

The effect of streamwise distance is also demonstrated for the same vortex at four different streamwise stations. As the vortex develops downstream, the vortex grows in the cross-stream

direction. This is clearly demonstrated in the dynamic pressure profiles (Figure 33), where the boundary layer becomes significantly more distorted downstream. From Figure 33 (b), (d), (f) & (h), the peak vorticity of any vortex would decay with streamwise distance from the point of generation. This decay will be due principally to the diffusion of vorticity away from the centre of the core. As the core becomes close to the solid surface, the vorticity in the core will be destroyed due to the cross-diffusive annihilation with the image vorticity produced by the image vortex. This will decrease the vorticity level at the edge of the vortex, thus increasing the vorticity gradient. Thus, it will be demonstrated that the closer the vortex to the solid surface, the greater the decay in peak vorticity. The streamwise factor is of considerable significance to the use of vortex generator arrays. If the lateral spacing between generators is too close, the upwash from one vortex will be destroyed by the downwash from a second vortex. While the plots for the last downstream station reveal that the vortex core has a diameter of about the vane height, the influence of the distortion of the boundary layer is much greater, an extends to around two vane heights either side of the vortex centre for this isolated vortex. Thus, if the generators were placed within 4 generator heights spacing, the interaction between adjacent vortices would have a similar effect on decay as the proximity of the wall.

The deformation of the boundary layer is very much a function of the three main parameters, the peak vorticity, the core radius, and the height of the vortex from the surface. The boundary layer is deformed by the sweeping effect of the vortex, drawing free-stream fluid around on one side, while pushing boundary layer fluid out on the other side. The amount of sweep is dependent on the strength of the rotational sense of the vortex core, but this can also be affected by the height of the vortex from the wall. If the vortex is close to the wall, the amount of fluid swept under the core is reduced, and the vortex decay will be more significant. The interaction between the wall and the core is another important factor, and thus the distance from the wall relative to the core radius is also important.

6.1.2 - Derived Low Mach Number Vane Results

Peak Vorticity data, vortex radius data, and lateral positions of the vortex centre from all of the low-Mach number tests was extracted, and reduced to a series of plots describing the effect of the varied parameters on the vortices.

The peak vorticity was found by interpolating the experimentally measured data, thereby finding a peak value and also its location in the experimental grid co-ordinate system. Interpolation was carried out in order to find interpolated vorticity values over a 0.5-mm grid using the 5-mm grid spacing from the experimental data.

The radius of the vortex was also investigated. It was found that, in the main, the vorticity fitted well to a Gaussian distribution. The only significant difference was seen in the region far from the centre of the vortex. In order that a radius could be measured accurately, a 'half-life' radius was defined, where the half-life radius was the radial distance from the centre of the vortex core where the local vorticity was equal to half the peak vorticity. In this region, there was no difference between the experimental trends and the Gaussian distribution shape. Thus in the following discussions, the radius of the vortex is actually the 'half-life' radius of the vortex. This half-life radius will be discussed further in the vortex-modelling Chapter.

Derived Data: Effect of Vane Height Ratio, h/δ

It should be noted here that the response of the largest vane (h/δ) was quite unexpected with respect to the peak vorticity values measured. It was seen that the measured values of peak vorticity would increase with streamwise distance – a result that could not physically occur in this experiment. However, it all other regards, the data sampled was consistent with the expected results. The vortex, which was produced, was observed to be outside the boundary layer - an observation that did not occur for any of the other cases. It was considered that the interaction

between the edge of the boundary layer and the free vortex might have caused this unexpected behaviour.

The effect of vane incidence is demonstrated using the 'lift-curve' slope approach in Figure 34. It is clear from this figure that the smallest vane ($h/\delta = 0.554$) provided a linear increase in peak vorticity with increasing incidence, hence suggesting that this vane did not stall over the range tested. As the size of the vane was increased ($h/\delta = 0.916$), there appeared to be a levelling in the maximum value of peak vorticity measured at between 18° and 20°. As the vane height was increased beyond the boundary layer thickness ($h/\delta = 1.277$), the vane appeared to stall within the test range on incidence, at a value of about 14°. As the size of the vane was further increased, the vane appeared to stall at around 12°. Thus the peak vorticity was a product function of peak vorticity and vane incidence.

Figure 35 shows the effect of the vane height ratio, h/δ, on the streamwise development of the vortex. For any given vane height, it is clear that the decay performance is similar regardless of the vane incidence (Figure 35 (a)-(d)). Curve fitting to the experimental data revealed that, to within experimental accuracy, the slopes of the curve were exponential in nature, and varied as a function of h/δ. In order that the plots for all the cases would collapse on to one graph, the vortices needed to be scaled in a similar manner, and following Wendt [14], the streamwise distance was divided by the vane height.

Referring to the plots of core radius (Figure 35 (e)-(h)), it is clear that the increase in core radius is most significant for the smallest vane, where the increase in vortex radius is greatest. As the height of the vane in increased, this increase in vortex radius becomes less great. Since the vortex is larger, and it is suggested that the helix angle of the vortex is approximately the same, then the effective streamwise length is less than that for the smallest vane case. While is might be argued that the wrong non-dimensionalising parameter has been used (i.e. that the vane height rather than the boundary layer thickness should have been used), it is important to remember that it is the effect of placing a vortex generator in a given flowfield which is important. Thus the governing parameters should be investigated in terms of the flowfield; in this case, the streamwise distance ratio based on the boundary layer thickness. Again then, it is noted that as the vane height is increased to $h/\delta = 1.277$, the increase in radius becomes smaller again, as essentially, the early part of the vortex is focussed upon. The diagram in Figure 36 is a graphical representation of this description.

Figure 35 (i)-(l) shows the position of the vortex core laterally. Remembering the inviscid vortex and its image vortex from the Introduction section, the image is the real vortex's reflection in the solid surface. The rotation of the image vortex causes a lateral velocity to be imposed upon the centre of the real vortex and *vice versa*, causing the vortex pair to crab sideways. The speed of the sideways movement is proportional to the strength of the vortices. Therefore, as the vortex strength is increased, it would be expected that the vortex would move sideways at a faster rate. As the vortex decays sufficiently, and the circulation becomes reduced, the sideways movement will decrease, and the vortex will curve towards the free-stream direction. This is apparent for the smallest vane ($h/\delta = 0.544$) at an incidence of 20° (Figure 35 (i)).

Derived Data: Effect of Incidence, α

Reviewing the plots of the effect of incidence on peak vorticity production (Figure 37 (a)-(d)), it becomes apparent that the decay rate is not the same for all height ratios. For example, the reduction in peak vorticity for the smallest vane ($h/\delta = 0.544$) at 10° incidence is much greater than for the $h/\delta = 1.277$ vane at the same incidence (Figure 37 (a)). The former sees a reduction of around 75% over the streamwise distances tested, while the latter looses around 50%. This highlights the statements earlier to this effect. It must therefore be the size and distance of the vortex from the solid surface that becomes the significant factor in the decay of the vortex. A similar trend is observed for all of the other incidence cases. Thus, while the decay rate appeared

not to be a function of incidence (as indicated by the previous set of plots), the decay rate was seen to be a function of the vane height.

In the plots for the growth of the vortex radius (Figure 37 (e)-(h)), the observation made with respect to the previous plots (variation of incidence for constant vane height) that the relative observation length for the smallest vortex generator was much larger than for the largest vortex generator. With reference to the two plots where the vanes were not stalled (α = 10°, 15°), it is clear that the increase in the radius is by far the greatest for the smallest vane, and that the largest vane barely increases in radius at all. As the vanes increase in incidence, they all appear to increase in radius at a similar rate, with the larger two vanes increasing their radius more in line with the smaller two vanes. This suggests that as the vanes approach the stall angle (for that particular vane), the vortex radius becomes larger and will diffuse more quickly, suggesting that the growth of the vortex downstream is a complex function of incidence and vane height.

Again with the lateral core positions, the spanwise crabbing of the vortices is apparent. In this representation of the data (at a constant incidence) it appears that, close to the vanes at least, the spanwise movement is at the same velocity, since the core position lines are parallel. This fact does not necessarily imply that the vortices are of equal strength. In this case, the different vane heights mean that the real vortex and its image will be further apart. Since the tangential velocity of a vortex decays exponentially with distance from the vortex, the same velocity can be imparted by a stronger vortex that is further away from the surface. Also of note is the fact that each of the different vortices created at one incidence appears to have originated at a different lateral location. The origin of the lateral position is at the trailing edge of the vortex generator, and this implies that the position of the vortex at the point of generation changes with the vane height. The effect of decay of the vortex strength is apparent from the plots at α = 15°, 18°, 20° (Figure 37 (i)-(l)), where the change in the smallest vane spanwise location becomes smaller far downstream. As the vortex decays sufficiently, the image vortex imparts a reduced velocity on the real vortex, and hence the spanwise velocity is reduced in magnitude. In the α = 20° case (Figure 37 (l)), the same effect can be seen for the next largest vane, where the vortex strength is reduced far downstream from the point of generation.

Comparison with ESDU Empirical Results

Simple predictions of the circulation strength of the vortex can be made using ESDU Data Item Number 70015[55]. This item uses experimental data of measurements of forces made on flat plates to predict the normal-force coefficients for a variety of plate configurations.

Since the vane at low incidence produces a lift (or normal) force, the force can be equated to the circulation about the plate:

$$L = \tfrac{1}{2}\rho V^2 S C_L = \rho V b \Gamma$$

$$Thus:$$

$$\Gamma = \tfrac{1}{2} V c C_L$$

If the circulation about the vane is shed as a trailing vortex, then the circulation strength of the vortex (close enough to the vane so that the vortex has not decayed in strength) is equal to the bound circulation over the vane.

The ESDU data item does not include data for plates close to a surface at a very low incidence. However, if the vane is considered as a plate of twice the vane span (i.e. a vane reflected in the solid surface), then an approximateion can be made accordingly. Also, the vanes are embedded in a boundary layer, and therefore an effective velocity is defined by the ESDU item, where the effective velocity is equal to 7/9 x free-stream velocity for a $1/7^{th}$ power law boundary layer.

Further corrections can be made to allow for the turbulence of the boundary layer*, allowing the lift (or normal) force coefficients to be calculated. The ESDU predictions for the vortex circulation strength are compared with the area-integrated experimental vorticity profiles. Results are plotted in the graph in Figure 38.

From these results, it is clear that the basic agreement is quite good, although there is a tendancy to underpredict the circulation at 18° incidence, and then as the vane 'stalls' (assuming that the vane does stall) at 20°, the circulation strength is over-predicted. Thus, allowing for the non-linearity with incidence of the vane vortex generator case, the prediction methods using simple flat plate data is remarkably good. At the incidences under consideration, the ESDU prediction method suggests that the variation of circulation with incidence is approximately linear. At incidences under ten degrees, the behaviour becomes non-linear, allowing the ESDU method to predict zero circulation at zero incidence (as must physically be the case).

The benefit of this comparison is that it demonstrates that the only effect of the vane height ratio (other than as a direct scaling parameter) is in the effect of the vane stall behaviour, where a small vane will stall at a much higher incidence than a large vane.

Mach Number Thoughts

With the trends established, it was possible to analyse the results, and design an experiment to account for the effect of Mach number. Rather than testing all of the current 64 data points at a number of different Mach numbers, it was decided that only one vane height and two incidences should be selected, but tested at three Mach numbers, and three downstream distances. A vane of height-to-boundary-layer-thickness ratio of 0.75 was chosen, and it was to be tested at incidences of 15° and 20°, thereby allowing some correlation with the low-Mach number test. This experiment will be discussed in the next Chapter.

6.1.3 - Basic Low Mach Number Air-jet Results

As with the vane results presented above, the presentation of the air-jet results consists of contour plots of both dynamic pressure ratio (defined as *local dynamic pressure/free-stream dynamic pressure*) and the streamwise vorticity.

The matrix of experimental data points was five dimensional in nature, with the varied parameters being: jet pitch angle; jet skew angle; jet hole diameter ratio (D/δ); jet Mach number ratio (*MR*); and, streamwise distance ratio (x/δ). The range of parameters was varied as follows:

Table 13: Parameter Variation at the First Streamwise Station

PARAMETER	RANGE	NUMBER OF CASES
Pitch Angle, α	30°, 45°, 60°	3
Skew Angle, β	30°, 45°, 60°	3
Hole Diameter Ratio, D/δ	0.096, 0.193, 0.289	3
Mach Number Ratio, *MR*	0.7, 1.0, 1.3, 1.6, 2.0	5
Streamwise Distance Ratio, x/δ	3.855	1
TOTAL NUMBER OF TEST DATA CASES		135

* An empirical factor is used where $C_{N(Turbulent)} = C_{N(Smooth)} (1+k_1k_2)$, where k_1 is 0.04, and k_2 ranges from 0.06 to 0.18 for the vane cases presented here.

Table 14: Parameter Variation at the Final Three Streamwise Stations

PARAMETER	RANGE	NUMBER OF CASES
Pitch Angle, α	30°, 45°, 60°	3
Skew Angle, β	30°, 45°, 60°	3
Hole Diameter Ratio, D/δ	0.096, 0.193, 0.289	3
Mach Number Ratio, *MR*	1.3, 2.0	2
Streamwise Distance Ratio, x/δ	12.048, 19.277, 26.506	3
TOTAL NUMBER OF TEST DATA CASES		162

Therefore, the total number of low-Mach number test configurations was (135+162 =) 297. In order to display some of the cross-stream data, typical results have been chosen where only one parameter at a time is varied. These results are discussed below.

Effect of Incidence, α

Displayed in Figure 39, is a series of data points showing the increase in incidence (from 30° through 45° to 60°) of an air-jet with a skew angle of 45°, a hole diameter ratio of 0.193, and a Mach number ratio of 2.0 at the first streamwise measurement station ($x/\delta = 3.855$).

With reference to the dynamic pressure plots (Figure 39 (a), (c) & (e)), it is apparent that the physical deformation of the boundary layer in the normal-to-surface direction is small, but increases with pitch angle. This fact is, of course, no surprise, as it would be expected that increased boundary layer deformation would occur as the jet is issued with a greater component of velocity in that direction. Two other points are more significant, however.

The first is the location of the core: at a low incidence, the jet has a greater lateral component of velocity, and therefore the effective position of the point of vortex generation is transposed sideways. The difference in the lateral position from the maximum and minimum incidence cases is quite large, at around 20 mm (or 0.5δ). However, the height of the vortex from the wall does not actually change a great deal, even though the boundary layer distortion does change. Between the maximum and minimum incidence values, the height of the core increase by about 5 mm with incidence (or about 0.15δ). Thus the height of the vortex from the wall is not a strong function of incidence. This is likely to be due to the jet, at low incidence, passing through the low momentum region of the boundary layer to a similar height as the higher inclined jet that is injected directly in to the higher momentum regions of the boundary layer.

The second point concerns the magnitude of the dynamic pressure at the centre of the vortex. Unlike the vane-produced vortex, the core of the air-jet-produced vortex has an input of momentum supplied by the jet, and thus the dynamic pressure tends to be higher. There is considerable momentum loss between the point where the jet is issued, and the point where the core is established, presumably involved in the turning of the jet from its initial issue direction to that of the vortex axis. However, the dynamic pressure in the centre of the jet is much higher that for a vane-produced vortex. This is important, since it suggests that a vortex produced by an air-jet would be able to withstand a greater streamwise pressure gradient immediately after generation than a vane vortex. This point will be discussed in more detail later.

Turning to the vorticity plots (Figure 39 (b), (d), & (f)), careful scrutiny reveals that it is the lowest incidence value that yields the highest peak vorticity value. Also, the smallest incidence gives a much tighter vortex with a smaller radius. As the pitch angle is increased, the peak vorticity is reduced, and the vortex radius is increased, thus leading to a weaker and more diffuse vortex. In

terms of achieving a persistent vortex, it is therefore more advantageous to lower the pitch angle as much as possible, within the engineering manufacturing constraints available. However, caution should be heeded, since reducing the incidence too far will result in a vortex very close to the wall that may decay more quickly, and thus not persist downstream.

Effect of Skew, β

The same air-jet parameters case is now discussed, but with the pitch angle, α, held at 45°, while the skew angle was varied from 30°, through 45°, to 60°. Plots are show in Figure 40.

A skew angle of 0° indicates that the jet is pointing downstream, and the skew angle increases as the jet is rotated to one side. From the dynamic pressure plots (Figure 40 (a), (c) & (e)), it may be seen that the lowest skew angle case gives the highest dynamic pressure in the centre of the vortex. Clearly, with the jet having the highest streamwise velocity component, less momentum is lost in the realignment of the jet velocity vector, and so the jet momentum contributes more to the dynamic pressure in the centre of the vortex.

As the skew angle is increased, the streamwise velocity component of the jet is reduced as a sinusoidal function of the skew angle, and hence a greater drop is seen between the 45°-60° cases than the 30°-45° cases. The deformation of the boundary layer is not significantly affected by the skew angle, although the centre of the vortex does move laterally, due to the increased spanwise of component with increasing skew angle. The height of the vortex from the surface does not change appreciably. Skewing the jet would not have any direct effect on the height of the vortex. However, it may be expected that presenting more of the jet profile to the free-stream might cause the jet to degrade more quickly, thereby fixing the point of generation of the vortex at a lower level. Whether this point is true can not be adequately justified from the data presented herein.

Investigation of the vorticity profiles (Figure 40 (b), (d) & (f)) reveals that the effect of increasing the skew angle is to increase the value of the peak vorticity. Further, it may also be seen that the radius of the vortex in not significantly affected rather the vorticity gradient across the profile increases in magnitude.

Effect of Diameter Ratio, D/δ

The effect of hole diameter ratio (Figure 41) is one of the very significant parameters concerning the vortex production. As may be expected increasing the diameter of the hole will increase the mass-flow rate and the scale of the jet. This will have the effect of creating a larger jet profile around which the flow will split and form the vortex, and since the jet is of increased diameter, it may be expected that it will penetrate further into the free-stream.

The evidence from the dynamic pressure plots (Figure 41 (a), (c) & (e)) reveals that, for the α = 45°, β = 45°, *MR* = 2.0 jet, the smallest jet (D/δ = 0.096, Figure 41 (a)) provides only a small distortion to the boundary layer profile. The centre of the vortex located at a low height (z/δ = 0.25), and laterally transposed by only a relatively small distance. For this case, the effect of the vortex barely makes an impression on the dynamic pressure at the edge of the boundary layer, and most of the mixing is carried out well within the boundary layer itself.

As the hole diameter ratio is doubled (to 0.193, Figure 41 (c)) the distortion of the boundary layer increases in size, and the centre of the vortex moves away from the surface to a position at about 0.45δ. With a further increase in hole diameter (to D/δ = 0.289, Figure 41 (e)), the distortion to the boundary layer becomes very significant, and the boundary layer in the 'swept-down' side of the vortex is reduced in thickness by a factor of 2. It may be seen that the increase in the boundary layer thickness on the other side of the vortex is relatively small in comparison, highlighting the benefit for separation control. It may also be seen that the local dynamic pressure in the centre of the vortex is less than that for the smaller jet diameters. This highlights the rather bluff-body nature of the separation around the jet that generates the vortices in the first place. Further, it tends to highlight that the centre of the vortex is not actually the core of the jet, but that the jet core is eventually entrained in to the core of the vortex.

The vorticity plots (Figure 41 (b), (d) & (f)) highlight the effect of the diameter ratio on the physical size of the vortex, and it may be seen that the radius of the vortex is not as affected as would be initially thought. There is a slight trend to increase the radius of the vortex with increasing jet diameter, and again this suggests that the vortex does not form around the jet core. It is clear from these plots that the peak vorticity increases significantly with the hole diameter ratio, and that this increase is greater than that which is possible with the geometric angles of the jet.

Effect of Mach Number Ratio

As with the hole diameter ratio, the Mach number ratio is a very significant parameter when producing vortices with air-jets (Figure 42). With the Mach number ratio as low as 0.7, only a very small disturbance is apparent for the hole diameter ratio of 0.193 (Figure 42 (a)). As highlighted above, this disturbance (the vortex) can be increased in size and scope by increasing the hole diameter. By increasing the Mach number ratio, the vortex can be increased in size as well. For this diameter of hole, only with the Mach number ratio over unity does the boundary layer see any appreciable deformation (Figure 42 (e), (g) & (i)).

From the vorticity plots (Figure 42 (b), (d), (f), (h) & (j)), a great deal more information can be inferred. Initially, with a Mach number ratio of 0.7, the vortex is quite weak, and very low in the boundary layer. At this point, the jet has little momentum, and the jet is quickly turned parallel to the surface. The vortex core interacts with the surface, and the vortex will decay very quickly as it progresses downstream. As the Mach number ratio is increased, the size of the vortex does not increase considerably, but the peak vorticity does, and the vortex lifts away from the surface. With a further increase in Mach number ratio, the trends continue, with the vortex core being located further away from the surface, and the peak vorticity increasing further.

Effect of Streamwise Distance

The effect of the growth of the vortex downstream, and the streamwise decay of the vortex is described in Figure 43. Close to the point of generation, the vortex causes a moderate distortion to the boundary layer, and as the vortex grows downstream, the size of this distortion becomes more significant. With reference to the dynamic pressure ratio plots, it may be seen that the initial dynamic pressure ratio in the core is around 0.75, but this value increases with downstream distance to around 0.8. Thus the core of the vortex is accelerated by the entrainment of the core axial velocity. Plots of the vorticity profiles (Figure 43 (b), (d), (f) & (h)) reveal that at a close distance to the jet, the vortex is moderately high, and the diameter is quite small. However, with only a short distance downstream, the peak vorticity level reduces in this case by around 50%, and the radius increases by around 40%. With further increases in distance, these trends level out. However, it is clear that the vortex decays quite rapidly, and that the peak vorticity reduces very quickly. This fact will be discussed, in relation to the vortices produced by vanes, in a later section.

6.1.4 - Derived Low Mach Number Vane Results

From each of these sets of data (and the other data sets not presented), values for the peak vorticity and vortex radius have been extracted and plotted, allowing the trends in the behaviour of the vortices to be followed qualitatively. The experimentally derived values are given in the Appendix.

As with the vane data, the true radius of the vortex was not used in the presentation of the data. The vorticity compares well with the Gaussian distribution, but the agreement breaks down far from the vortex centre line. The reasons for this will be discussed later. However, this does mean that the measurement of the vortex radius is difficult. As such, a half-life radius is defined, where the half-life radius is the distance from the vortex centre line where the local vorticity is half the peak value. In the following discussion, the term radius in place of the term 'half-life radius' in order to be concise.

Derived Data: Effect of Pitch and Skew Angles

The first series of plots (Figure 44) reveal the effect of the pitch and skew angles of the jets. In the first two plots, the effect on the peak vorticity of varying the skew angle is depicted for the three pitch angles tested. It has been previously demonstrated[34, 35, 36, 37] that a jet with a skew angle of zero produces a pair of counter-rotating vortices. As the skew angle of an air-jet is increased from zero, one of the vortices will increase in size, while the other reduces, and eventually, the smaller is lost by wrapping around the major vortex. This fact has been demonstrated using flow visualisation techniques, and is demonstrated quantitatively here. For any given pitch angle (Figure 44 (a)), increasing the skew angle increases the peak vorticity (and hence strength) of the single strong vortex, with the rate of increase being a function of the jet pitch angle. For the 30° pitched jet, an increase in peak vorticity of around 75% can be gained by increasing the skew angle from 30° to 60°, while for the 60° pitched jet, the same increase in skew gives an increase in peak vorticity of some 10%.

The effect of increasing the pitch angle (Figure 44 (a)) is that, at least for the two higher skew angles, the peak vorticity reduces. With the pitch angle very high (as 60°), the jet is close to issuing as a surface-normal jet. As stated above, a normal jet produces two weak counter-rotating vortices. It is therefore reasonable to expect that as the pitch angle is increased towards the normal, the vortex produced by the skewed jet will reduce in strength. By reducing the pitch angle, the component of lateral velocity in the jet is increased. This will increase the tendency for the jet core to persist and to cause the free-stream fluid to be drawn around the core forming the vortex. However, if the vortex is relatively weak (in the case of a skew angle of 30°), and the pitch angle is quite low (30°), then the vortex will be formed close to the wall. As a result, the vortex will decay very quickly, hence giving the very low peak vorticity value for the 30° pitch, 30° skew case.

It should be noted that the optimum pitch angle for a given yaw angle varies with yaw angle. Thus, for a skew angle of 30°, the optimum pitch angle will rest at about 40°, but as the skew angle increases to 45°, the optimum pitch angle decreases to around 30°. A further increase of skew angle to 60° pushes the optimum pitch angle to a value lower than was tested in this investigation.

Referring to the half-life radius plots (Figure 44 (c) & (d)), it may be seen that the radii of the vortices were, to within experimental uncertainty, the same, except for the high pitch angle case where the radius increased slightly with skew angle. The uncertainty involved in the assessment of the radius will be discussed in the Model chapter, but it is suggested that the radius† can be measured to within 0.5 mm, or 0.012δ.

In order to check whether these trends change significantly with hole diameter ratio, a second series of plots is shown with the hole diameter ratio increased to 0.289 (Figure 45). The basic trend in these plots are identical to those presented for the smaller hole diameter, with the exception of the 30° pitch, 30° skew case. Since the jet core has a higher diameter, the jet will tend to penetrate slightly further in to the free-stream, and therefore the vortex will form further from the surface. Thus the decay on this vortex will be less, and the peak vorticity value will be increased relative to the smaller hole diameter, such that there is no significant difference in peak vorticity for a skew angle of 30°.

The effect of the jet parameters is shown in the next series of plots (Figure 46). The effect of increasing the hole diameter ratio is that the peak vorticity increases in a linear fashion. This demonstrates that it is the streamwise profile (or footprint) of the jet that must be an important factor, rather than the cross-sectional area of the jet which is important. The physical streamwise

† It will be shown that the radius used is actually the 'half-life' radius of the vortex, which is defined as the radius of the vortex at the point where the local velocity is half the peak value.

depth of the jet is less important, and the jet could be reduced in this dimension, helping to reduce the mass flow of air required to produce the same size of vortex. Previous investigators have noted that using a jet of crescent[43] or rectangular[47] shape can have this effect, but these observations were made on the measurement of the circulation of the vortex, rather than on the vorticity profile. This fact leads to the conclusion that the jet mass flow is not an important parameter for the production of vortices. In terms of driving the air-jets (by using a compressor which provides a given mass flow), mass-flow may be significant, but careful tailoring of the jets for a given mass flow will provide more significant vortices.

Extrapolation of the best-fit lines reveals that the hole diameter ratio could be reduced to zero with a linear variation in peak vorticity. This may be true up to a point, but as the physical hole becomes small, the viscous losses inside the jet orifice may become significant, reducing the characteristics of the jet velocity profile significantly.

The effect of the Mach number ratio is also shown for the different hole diameters tested (Figure 46 (b)), and it may be seen that the variation in peak vorticity with Mach number ratio (with all else held constant) is a straight-line fit. In the case where the temperature of the jet and the free-stream are the same (as is the case from this experiment), the speed of sound will be the same, and therefore the Mach number ratio can be described as the velocity ratio. Clearly then, if the free-stream is held constant, then the jet velocity is an important parameter. Again, this is not the same as the mass flow from the jet, since that is dependent on the jet orifice area. It may also be seen that the vortex radius appears to be fairly insensitive to the Mach number ratio. However, the radius is sensitive to the hole diameter ratio, since the increase in the physical size of the vorticity production area must increase the radius of the vortex (Figure 46 (d)).

Important Parameters For Vortex Production

The important parameters given above are the pitch angle, α, the skew angle, β, the hole diameter ratio, D/δ, and the Mach number ratio, *MR*. In order to maximise the peak vorticity at the point of generation, it is important to set up the parameters such that the maximum 'attached flow' around the jet orifice is achieved. As the free-stream passes around the jet, there will be a point on the surface where free-stream splits either side of the jet. The flow then passes around the jet and is entrained away from the surface. At the rear of the jet, there will be some point where no more fluid is entrained, and gives a surface oil-flow pattern that is similar to a wake behind a cylinder[39]. If the distance that the free-stream flow is drawn around the jet is maximised, then the peak vorticity will be maximised too. This distance will be termed the arc-separation length. This is depicted in Figure 47.

However, as discussed previously, using a pitch angle which is very low will cause a vortex to be generated close to the surface, where the core of the vortex quickly interferes with the surface, resulting in a reduction in vortex strength, and increased streamwise decay. Similarly, excessive use of skew angle beyond about 85° results in a more diffuse vortex. Simple flow visualisation was carried out using a disco fog generator to fill the jet with a white fog. As the jet was oriented to point upstream, the vortex meachnism appeared the same, but the vortex core grew rapidly in size.

Streamwise Decay

The decay of the vortices is depicted in Figure 48. It can be seen that the peak vorticity decay (Figure 48 (a)) is similar for the cases shown, and that the decay is relatively high. The growth of the vortex tends to be similar for the cases presented (effect of increased diameter), and therefore, unlike the vane vortex cases, the decay of the vortex is not dependent on the scale of the vortex generator (Figure 48 (b)).

The lateral movement of the vortex follows a similar trend to the vane case (Figure 48 (c)), with the air-jet which produces the strongest vortex moving sideways at the greatest rate, if the vortices are located at the same height from the surface. However, it must also be remembered that if the

vortex is further from the surface (which the strongest vortex, which will invariably come from the largest hole is), then the velocity induced by the image vortex will be reduced. As with the vane case, when the weakest vortex decays significantly, its sideways movement is greatly reduced.

Referring to the height of the vortex core (Figure 48 (d)), it may be seen that the larger the jet diameter, the further the vortex is from the surface. This result is fairly unsurprising: a larger jet will carry more momentum, and therefore will be able to pierce in to the cross-flow to a greater distance. A similar effect has been seen for the effect of Mach number ratio, highlighted above. Thus the height of the vortex is related not just to the angles which the jet is angled, but also the 'speed' of the jet, and its persistence. It was suggested above that the peak vorticity is dependant on the arc-separation length, and that the streamwise depth of the jet is far less relevant. It has been demonstrated that this is the case for a jet with a significant depth, but is the jet is reduced in depth, then the jet will carry less momentum, and therefore its velocity profile will decay more quickly. Thus mass flow will be reduced for a similar level of vorticity production, so long as the jet does not loose its persistence.

The use of an air-jet vortex generator should be carefully considered in order to obtain the correct mix of vortex strength and decay rate for the desired application. Many factors can change the effectiveness of the jet to produce a sustainable vortex, and thus the flowfield in question needs to be carefully considered before the application of air-jet flow control.

Comparison with Other Investigations

In order to assess the agreement with other work, similar investigations are needed. There are only a small number of studies which have carried out similar work: although there are a number of investigators who have carried out air-jet vortex generator studies, only one other study (that of Compton & Johnston[41]) carried out measurements in planes of data though a vortex.

Compton & Johnston[41] used a circular jet with a hole diameter ratio of 0.45, which is outside the current study, but all other parameters are comparable: $\alpha = 45°$, $\beta = 45°$, $MR = 1.3$. Figure 49 shows the data for this configuration, together with the data for the three hole diameter ratios tested in the present study.

While the hole diameter ratio is not within the range tested, this data does show that the trends for the hole diameter hold very well, and that the decay characteristics are not facility dependant. Thus, it is felt that the present study compares well.

Comparison Betwen Vane and Air-jet Produced Vortices

With both vanes and air-jets producing vortices, it may be expected that there are similarities and differences between the fundamental characteristics of the vortices. While it is clear that the formation process is radically different and the vortex has a significant structure, comparisons are possible. While it is difficult to pinpoint the exact distance from the generator where the vortex is fully developed, a rough rule of thumb can be applied. A streamwise distance of one chord length from the trailing edge of the vane, and about 3 hole diameters from the centre of an air-jet, can be assumed to be the roll up distances.

With the vortex formed, the vorticity profiles are very similar in nature, with both types approximating well to a Gaussian distribution. The vorticity values can be non-dimensionalised in order to allow all of the profiles to collapse well on to one another. The non-dimensionalising parameters are best defined as the peak vorticity (ω_{peak}), and a suitable radius. The true definition of the radius of the vortex is the radial distance in which all of the vorticity is contained. However, due to inaccuracies in the measurement system, the edges of the vortex become difficult to define. Thus, a half-life radius is proposed, and is defined as the radial distance from the centre of the vortex (where the local vorticity is equal to the peak vorticity), where the local vorticity is equal to half the peak vorticity. This location is much easier to measure than the core radius, and is subject to less error.

Comparison plots are given for the vane (Figure 50) and air-jet (Figure 51) produced vortices, and the data is displayed as lateral slices (in the *y*- axis) though a series of vortices. The data is given in a non-dimensionalised format.

From the plot of the vane-produced vortices (Figure 50), it may be seen that the distribution of vorticity is very close to Gaussian in nature, with the only significant error being in the outer radius of the vortex core, where the agreement breaks down. This tends to be in the region where the local vorticity is approximately $0.1\omega_{peak}$. Since the peak vorticity for this set of data is of the order of 1000 1/s, the error occurs when the local vorticity is less than 100 1/s.

For the case of the air-jet produced vortices (Figure 51), The majority of the vorticity distribution is seen to be Gaussian in nature. Again though, agreement breaks down in the region where the local vorticity is less than $0.1\omega_{peak}$. In the case of the air-jet produced vortices, the vorticity outside this radius is negative, and as the radial distance is increased further still, the vorticity drops to zero. While these regions look significant, the actual levels of vorticity measured (i.e. the values prior to non-dimensionalisation) are relatively small, at between 0 and 16 1/s on the (-)*y* side of the vortex, and between 24 and 62.4 1/s on the (+)*y* side of the vortex. It is suggested that the values on the (-)*y* side are measuring errors, since these values are relatively small. However, on the (+)*y* side of the vortex, the negative vorticity is probably due to the sweeping of opposite sign vorticity which is generated at the surface by the vortex inducing a strong cross flow. That negative vorticity is swept up as a tongue around the side of the vortex, thereby cancelling some of the positive vorticity from the main vortex core. The value of the peak vorticity in the opposite-sign region is generally of the order of 0.1 ω_{peak}. Similar observations have been made for a select few of the vane cases, where a particularly strong vortex was located close to the wall. However, in the main, the vane vortices were located further from the wall, and thus this was not a serious consideration.

The distortion effect on the boundary layer close to the vortex generator was very similar in both cases. The distortion is a function of the velocity vectors rotating about the vortex core, and therefore should not be vortex-type specific. The amount of distortion is of course dependent on the magnitude of the vortex strength, and on the height of the vortex above the wall. In the case of the vanes, the size of the vortex was controlled by the size of the generator and the incidence of the vane. Its height was controlled only by the height of the vane. By comparison, the size of an air-jet vortex generator is a very weak function of most of the variables, but the hole diameter does reveal a trend of increasing the size of the vortex with increasing hole diameter. The height of the vortex from the wall is a function of the persistence of the jet length, which is determined by the hole diameter and the Mach number ratio of the jet. In general though, the height of an air-jet vortex generator (with the parameters tested in this study) was considerably less than for the vane cases, with the height being from 0.1 δ to 0.25 δ for the air-jet cases while the vane heights ranged from 0.5 δ to 1.5 δ. However, the physical size of the vortices was similar in nature. Thus, in order to increase the height of the air-jet produced vortices, either the diameter of the Mach number ratio of the jets needed to be increased. This would also change the vortex strength as well, and thus it is very difficult to generate exactly similar vortices using the two different methods.

With reference to the dynamic pressures within the core, Figure 52 shows the streamwise change in the dynamic pressure coefficient of the core centre-line for the smallest vane ($h/\delta = 0.554$) over the range of vane incidences. It may be seen that the dynamic pressure of the core after generation is very low. As the vortex develops downstream, the core is accelerated, presumably by free-stream entrainment of the core. Since the vortex is produced by the roll-up of the flow from the vane, the structure of the vortex will be largely wake dominated. As the vane incidence is increased, the magnitude of the wake will be increased, and it is reasonable to expect that the magnitude of the dynamic pressure coefficient will decrease with increasing incidence.

These results may be compared with the air-jet results given in Figure 53. For the case of the air-jets, it may be seen that the change in core dynamic pressure does not change as much as for the vane case. Indeed, it is interesting to not that as the Mach number ratio is increased (which will increase the peak vorticity), the core dynamic pressure is enhanced by the extra jet momentum, and thus the change in dynamic pressure is reduced still further. This is the opposite result from the vane case, where the highest peak vorticity occurs with the lowest core dynamic pressure. (It should be stated that the vortices compared in these two plots are the closest cases that could be found for comparison between vanes and air-jets. Vortex strengths and heights of the vortices were all comparable). The fact that a strong vortex is produced with a high momentum core is of benefit in regions where the vortex will be subjected to a large adverse pressure gradient. The effect of an adverse pressure gradient on a vortex is that the slowing down process causes the vortex to grow in cross-sectional area, and (for a free vortex, at least) the onset of vortex burst may occur. For the vortex generator, the pressure gradient will see a large reduction in peak vorticity as the vortex stretching process takes effect in reverse (i.e. vortex compression where the cross-sectional area increases, and the vorticity level reduces). This suggests that for applications in which the flow speed is reducing (i.e. rear of an aerofoil profile, engine intakes) the air-jet will have less decay characteristics. This is a very significant result, since it demonstrates that the characteristics of the vortices are different, even after generation.

Extension to the Experimental Data Base

This study was set at only one free-stream velocity. Since the vortex generators were to be used at potentially high subsonic Mach numbers, it was important to extend the study to in Mach number. So as to limit the number of Mach number varying cases, cases which were of practical use, or which produced strong vortices were considered, at the expense of the less productive cases. From the discussion above, the following choices were made:

The optimum pitch angle of those tested was 30°, and so this was chosen. In the practical case, 45° may also be used, so this pitch angle was selected as well;

Since the skew angle of the air-jet will depend on the local flow conditions which may change in operation, skew angles of 30°, 45° and 60° were considered;

Two hole diameter ratios were selected to cover the range of the low speed test. These were D/δ = 0.15, 0.3;

A single nominal Mach number ratio of 1.6 was chosen, which would produce strong vortices capable of being measured accuractely;

One streamwise distance was chosen for all of the above cases, at a value of $x/\delta = 8.75$. Further measurements were made for only one geometry ($D/\delta = 0.3$, $\alpha = 45°$, $\beta = 45°$) at three ofther streamwise distance ratios of 16.25, 23.75, and 31.25,

Three Mach number values of 0.5, 0.6 and 0.75 were selected to meet the requirements of the practical application and the capabilites of the proposed experimental facility.

6.2 - Vane Plots

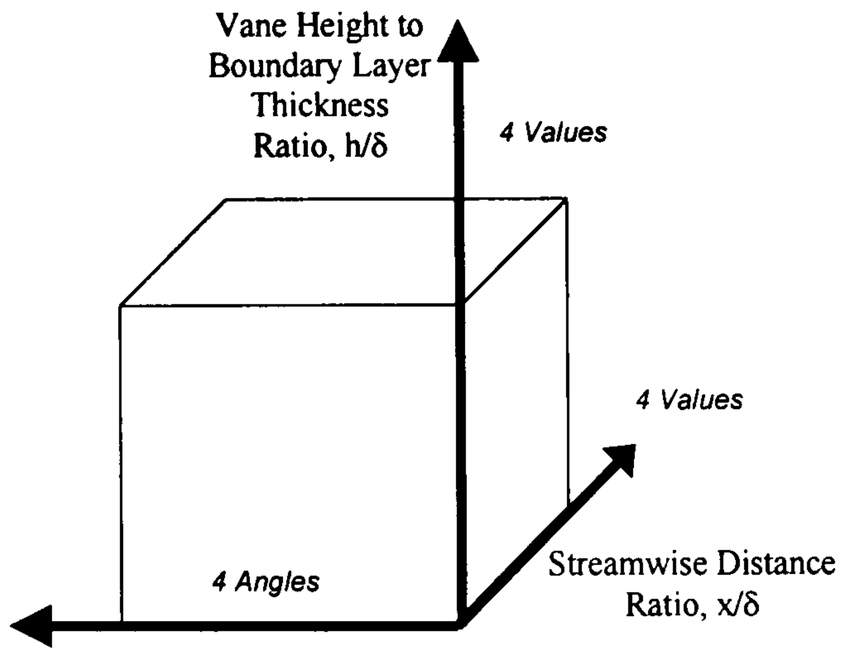

Total Number of Data Points = 4 angles x 4h/δ x 4 x x/δ = 64 Total

Figure 30: Vane Vortex Generator Test Parameters

Figure 31: Effect of Vortex Generator Height Ratio: Dynamic Pressure & Vorticity Plots

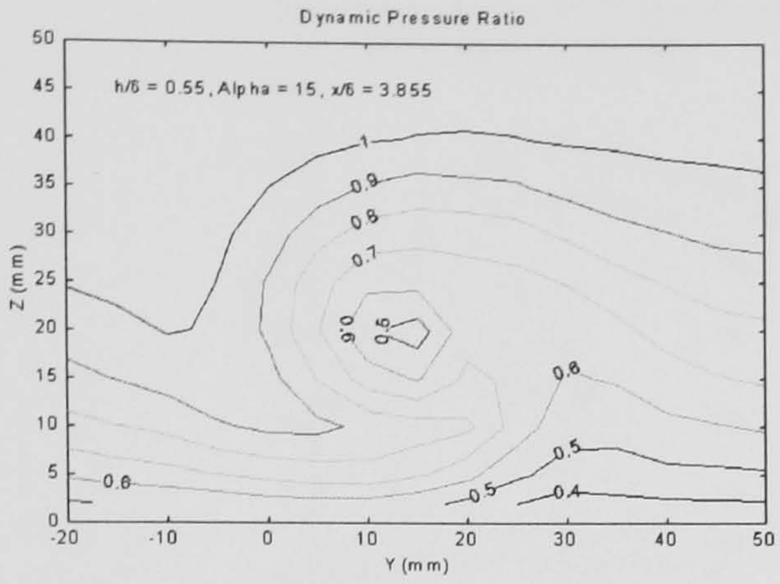

(a) h/δ= 0.55

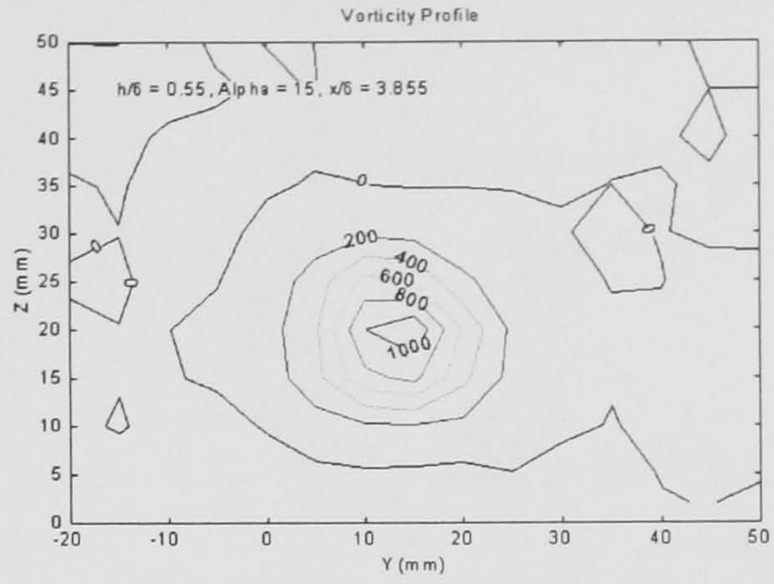

(b) h/δ= 0.55

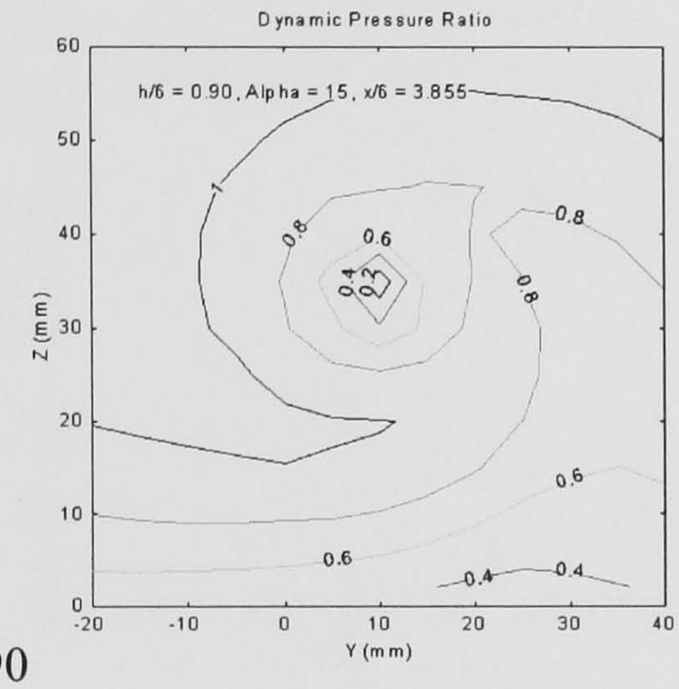

(c) h/δ= 0.90

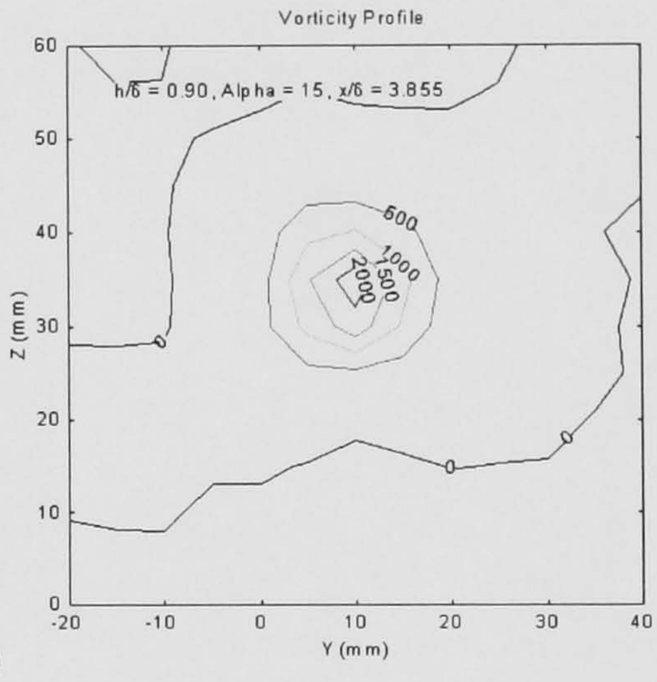

(d) h/δ= 0.90

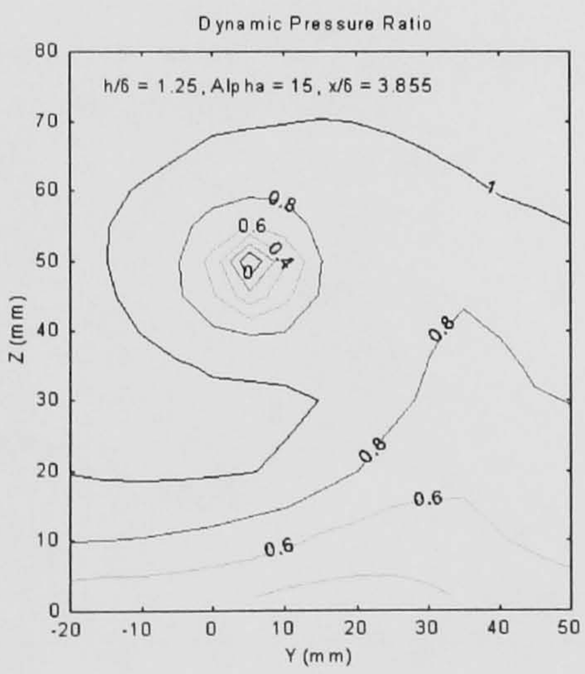

(e) h/δ= 1.27

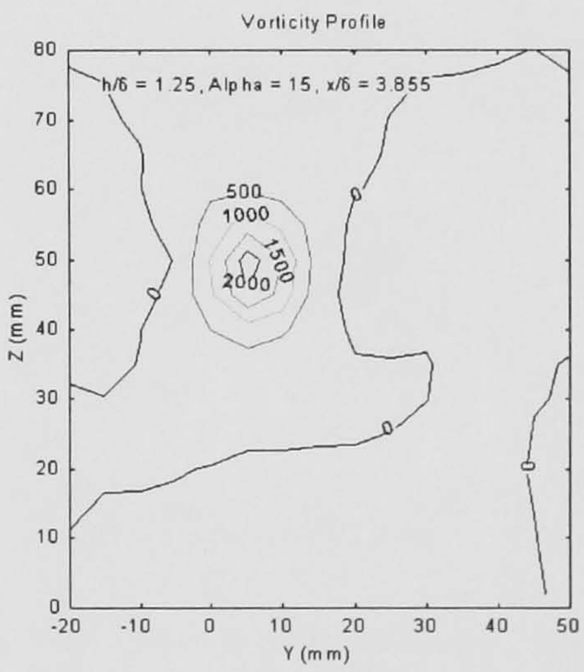

(f) h/δ= 1.27

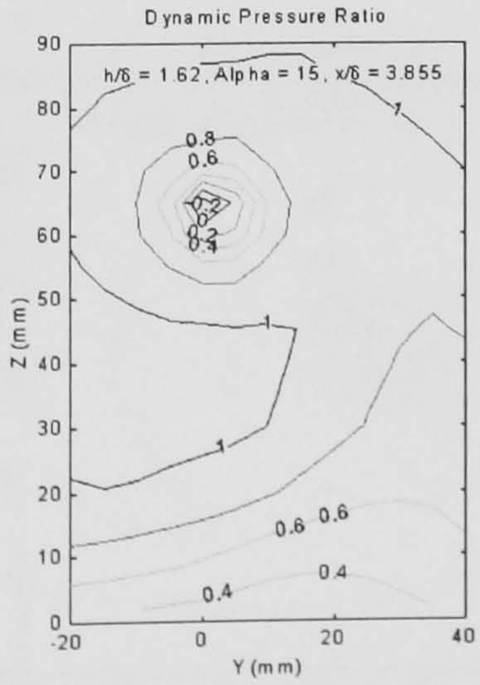

(g) h/δ= 1.63

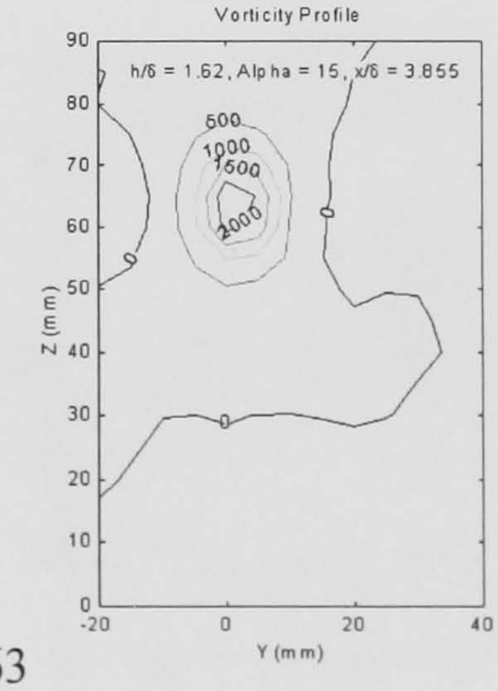

(h) h/δ= 1.63

Figure 32: Effect of Vane Incidence: Dynamic Pressure & Vorticity Plots

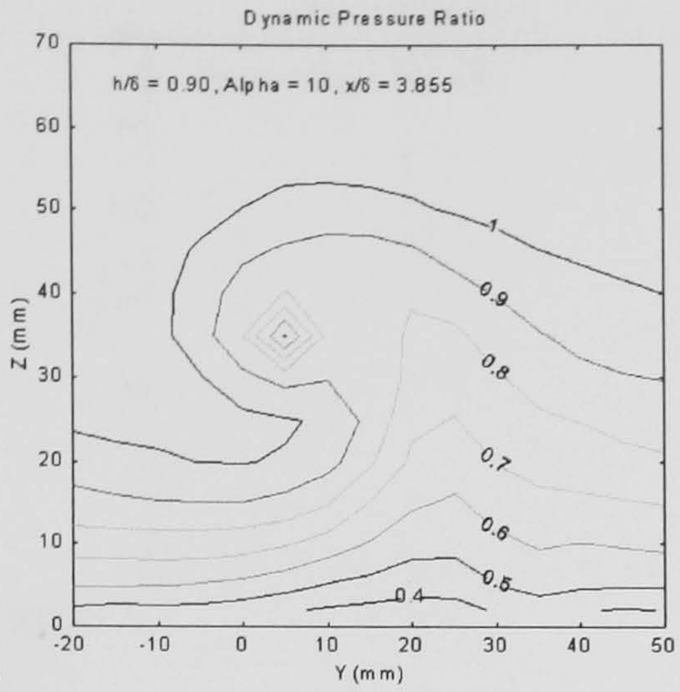

(a) $\alpha = 10°$

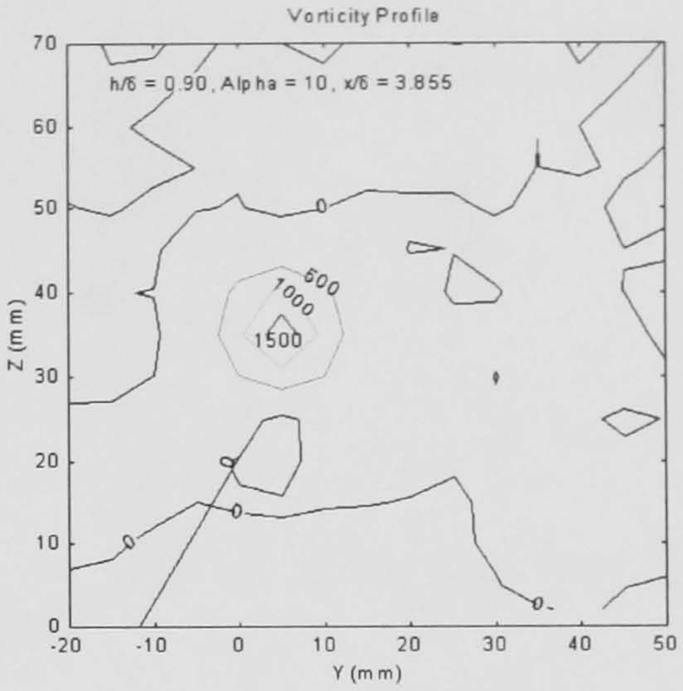

(b) $\alpha = 10°$

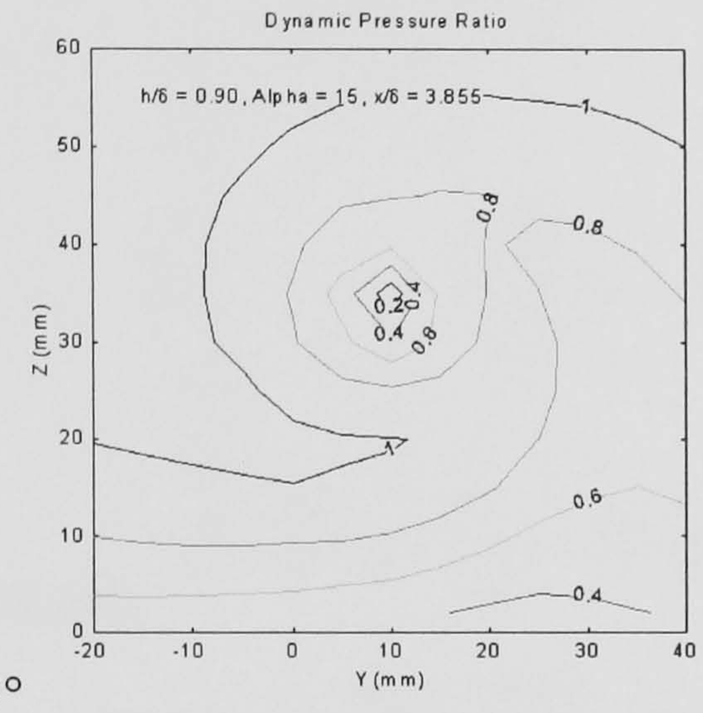

(c) $\alpha = 15°$

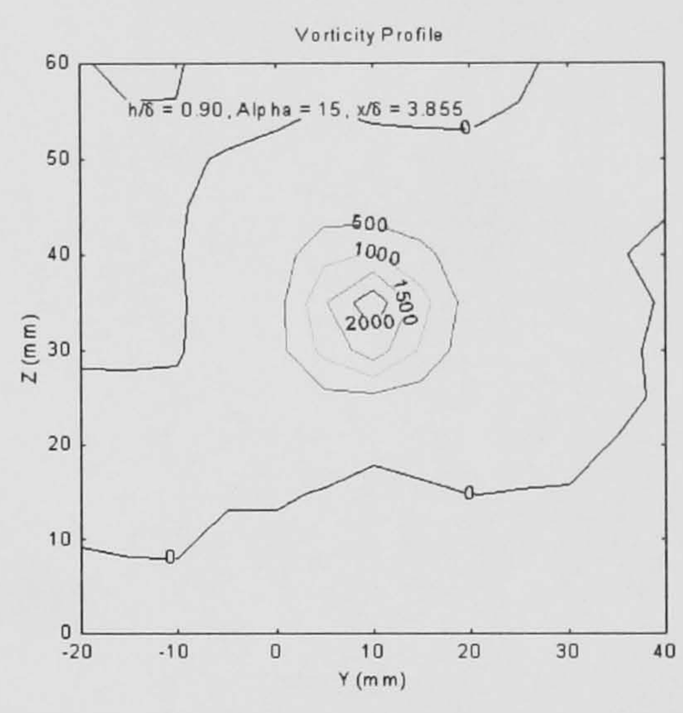

(d) $\alpha = 15°$

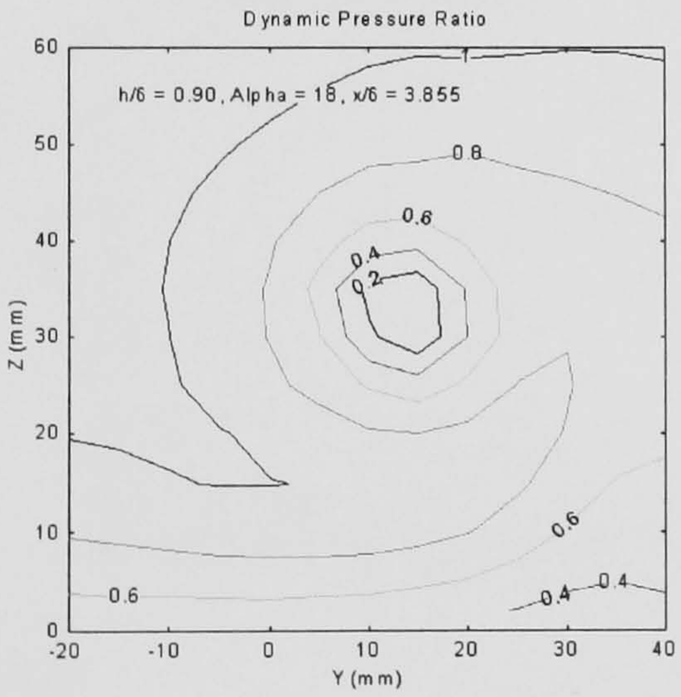

(e) $\alpha = 18°$

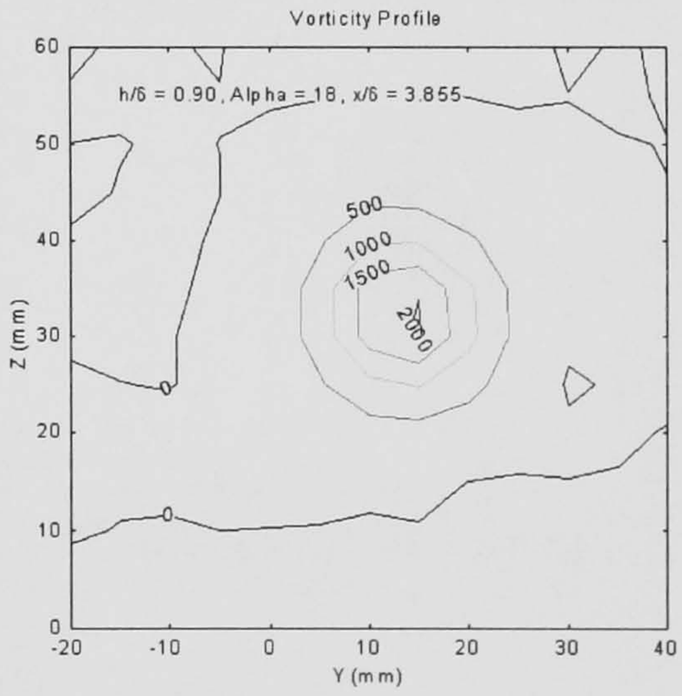

(f) $\alpha = 18°$

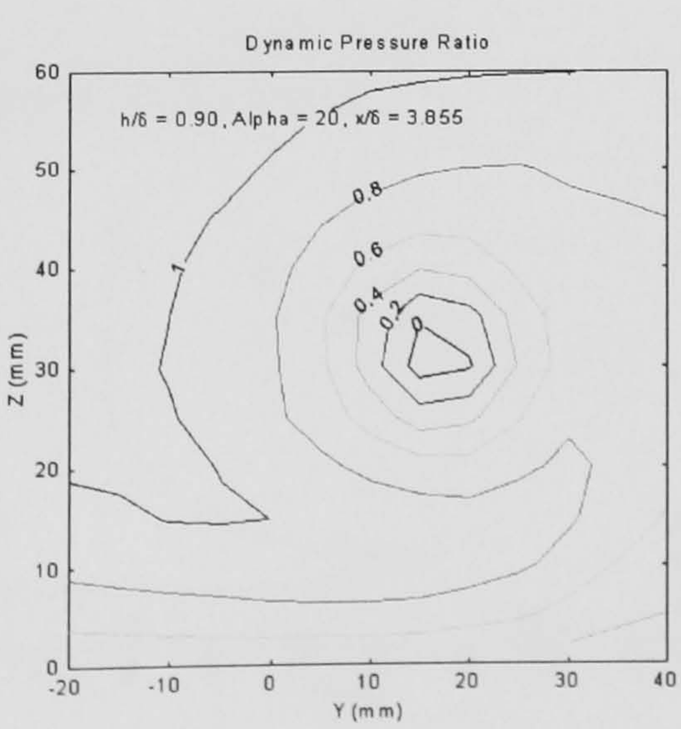

(g) $\alpha = 20°$

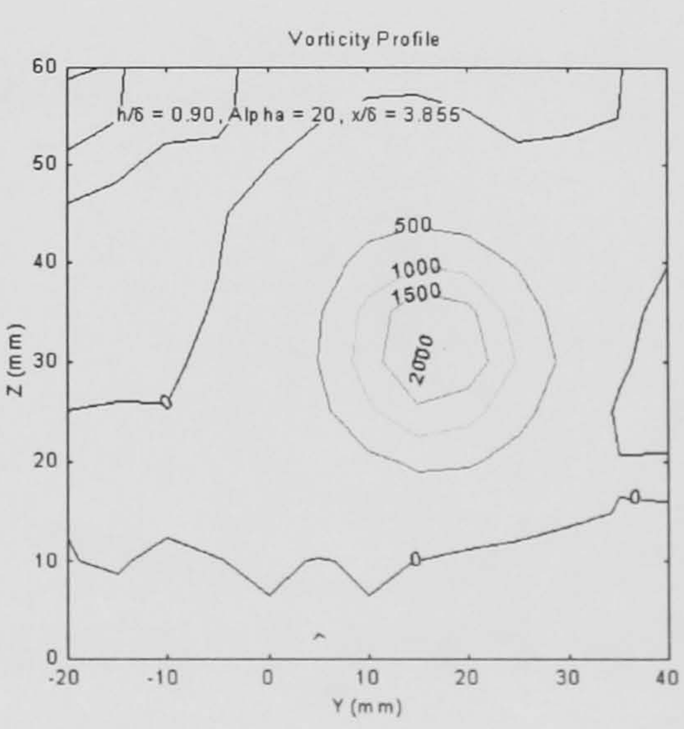

(h) $\alpha = 20°$

Figure 33: Effect of Streamwise Distance: Dynamic Pressure & Vorticity Plots

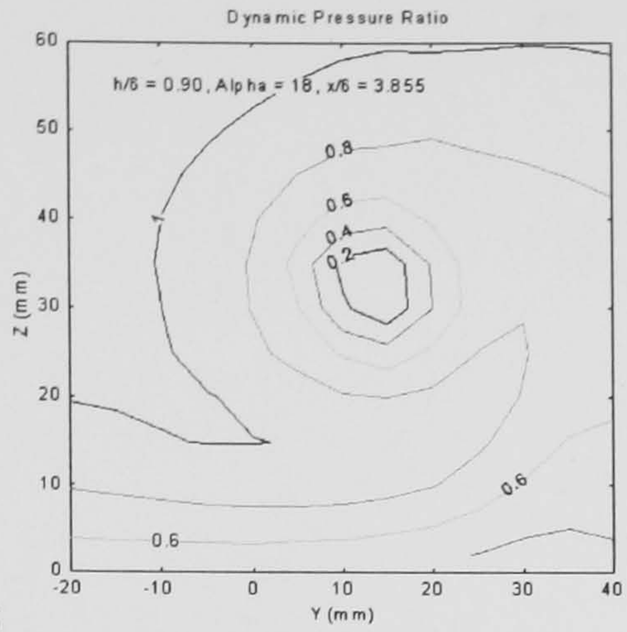

(a) x/δ= 3.855

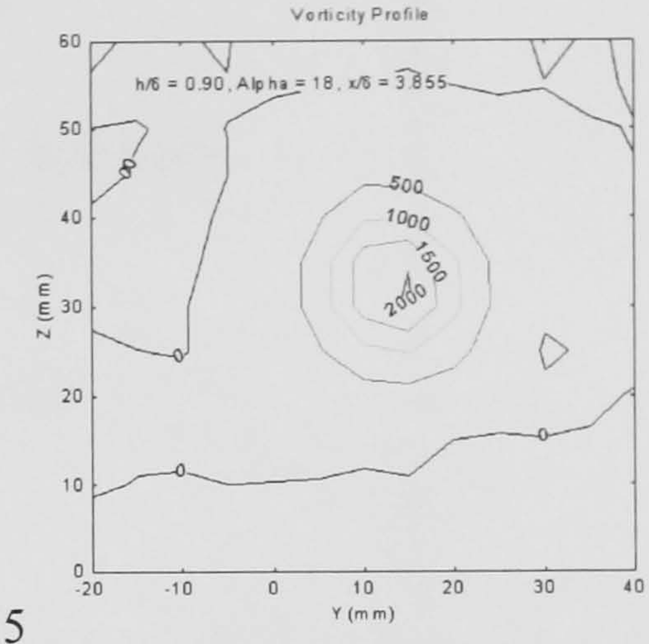

(b) x/δ= 3.855

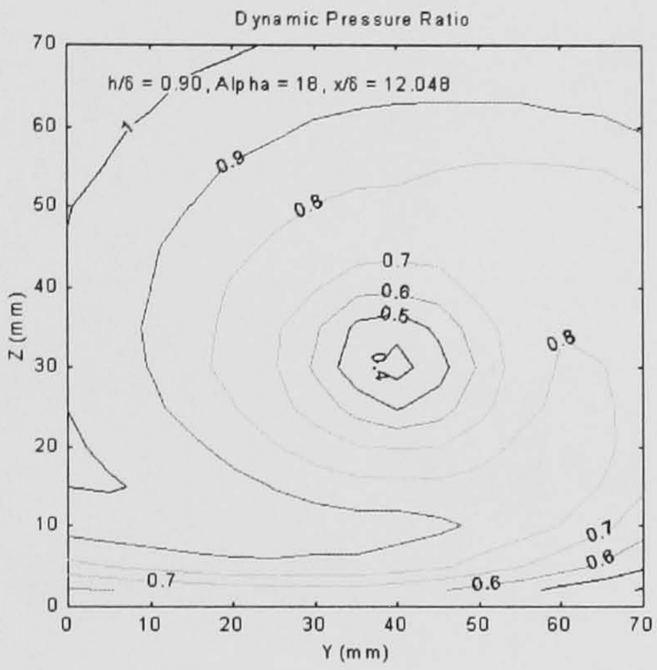

(c) x/δ= 12.048

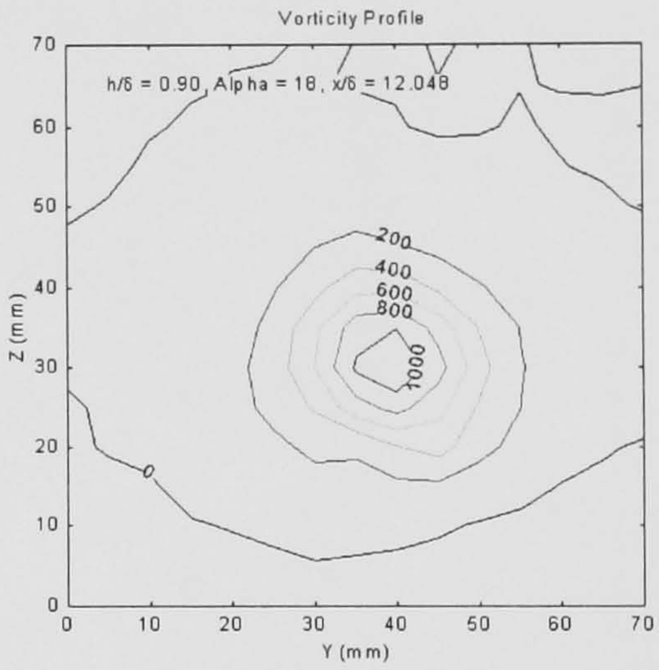

(d)x/δ= 12.048

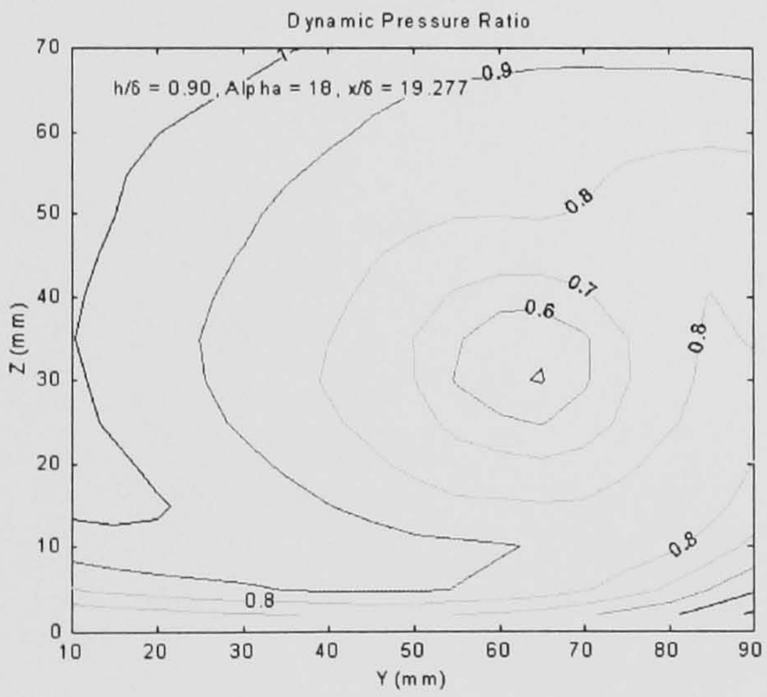

(e) x/δ=19.277

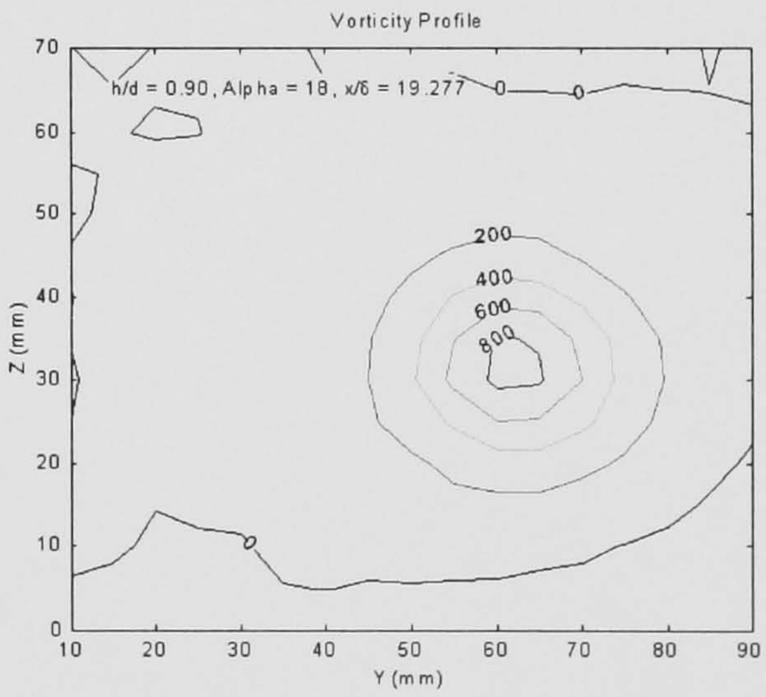

(f) x/δ=19.277

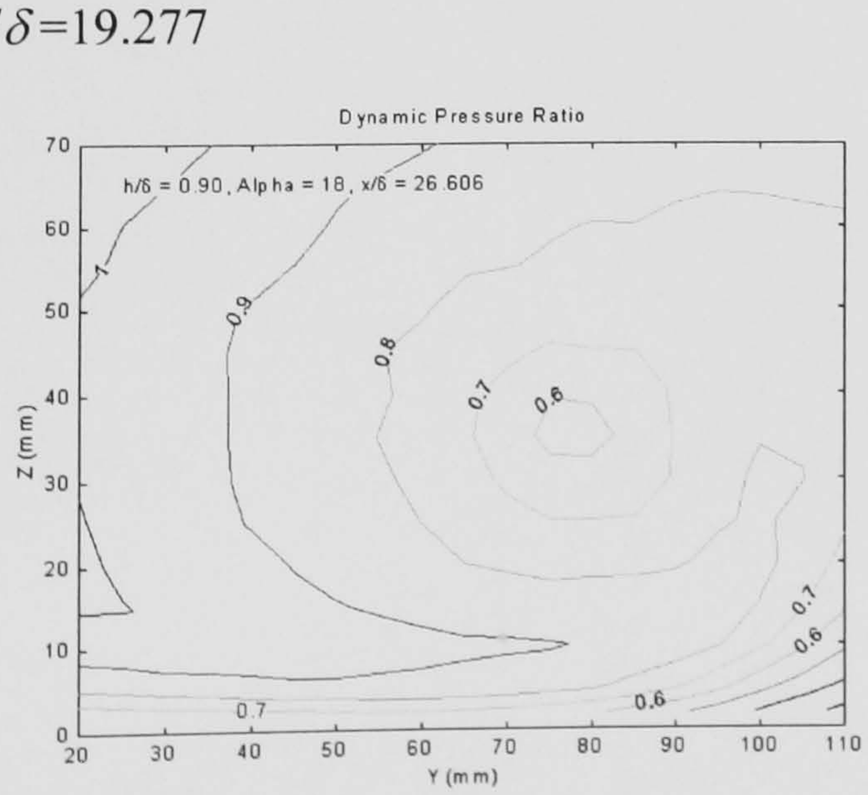

(g) x/δ= 26.506

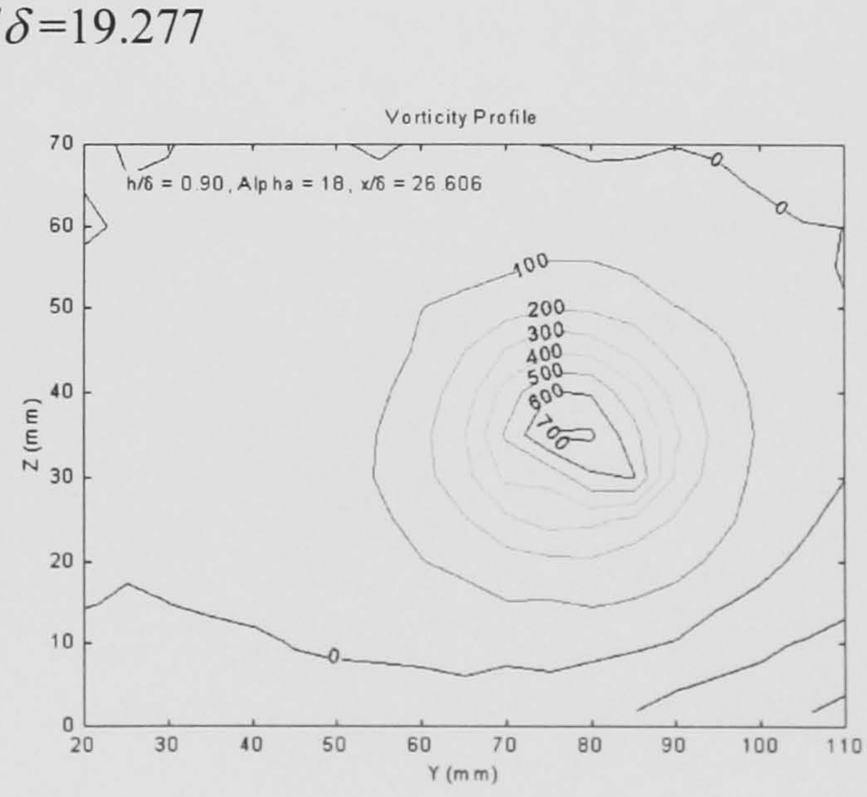

(h) x/δ= 26.506

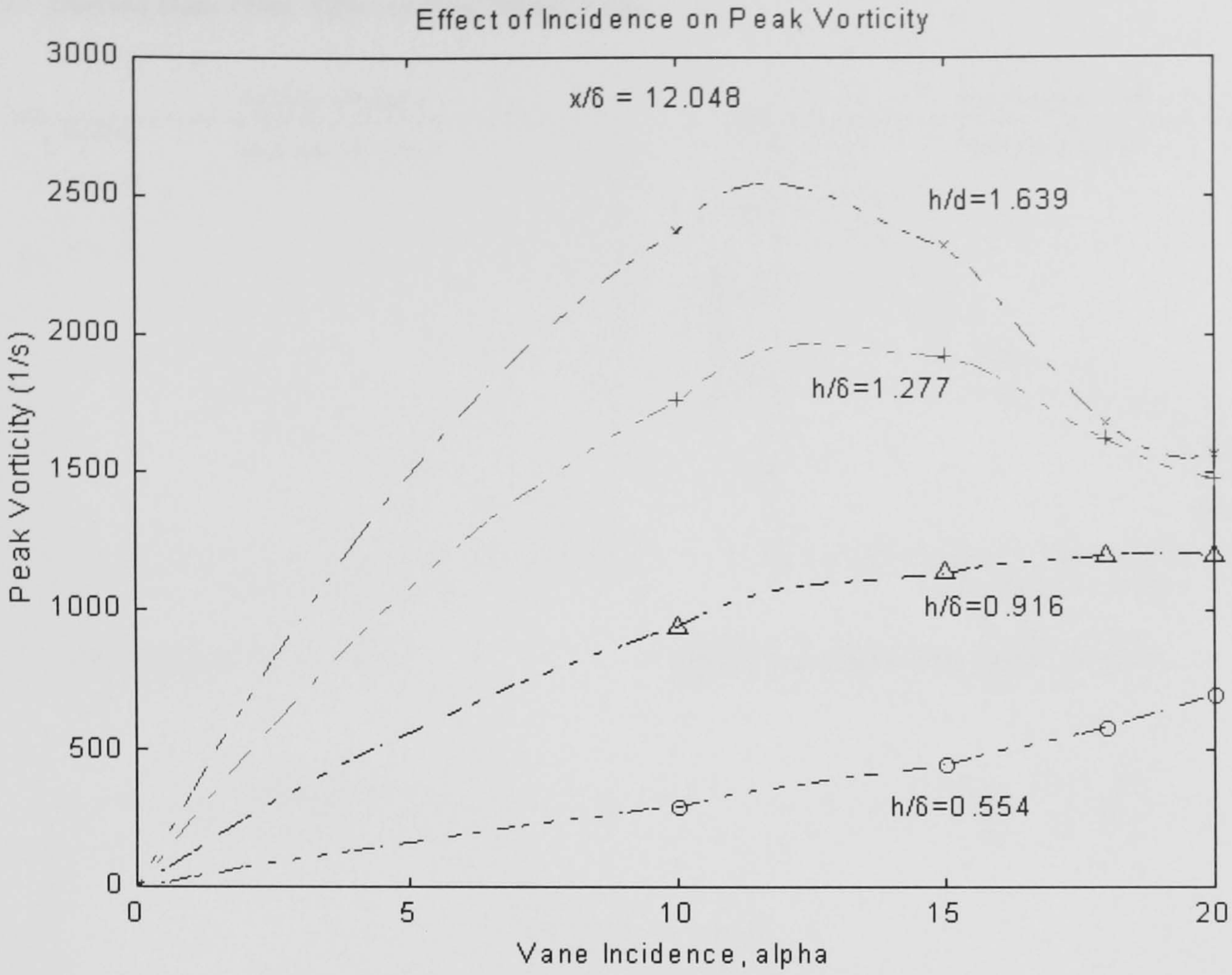

Figure 34: Vane Vortex Generator 'Lift-Curve Slopes'

Figure 35: Derived Data Plots: Effect of Vane Height Ratio

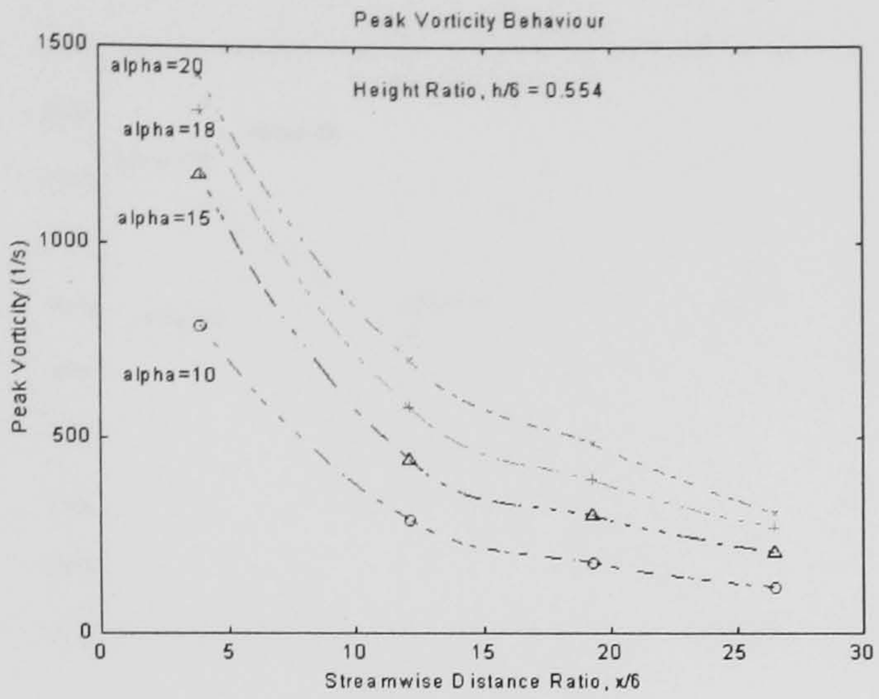

(a) Peak Vorticity, $h/\delta = 0.554$

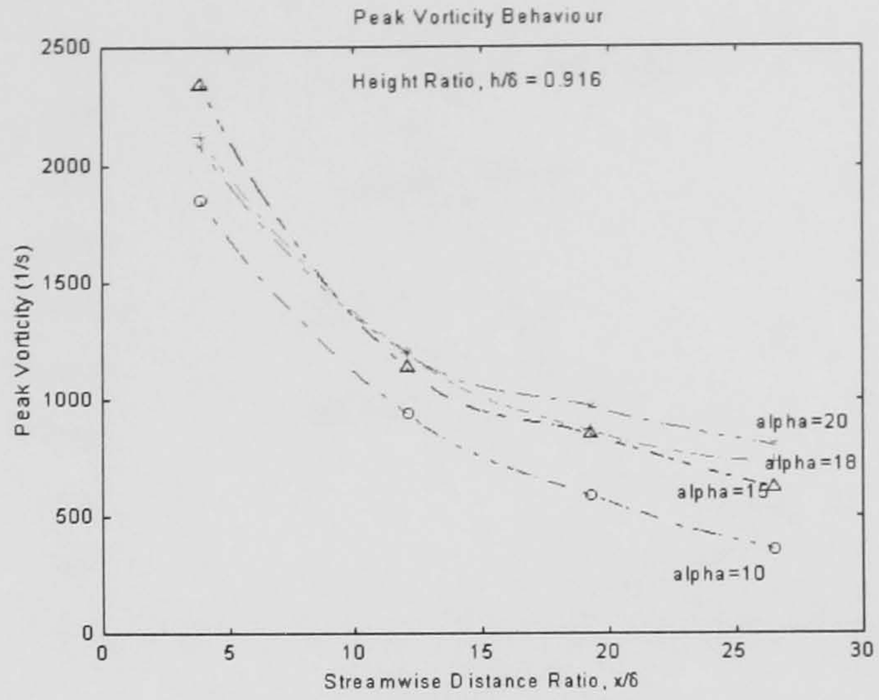

(b) Peak Vorticity, $h/\delta = 0.916$

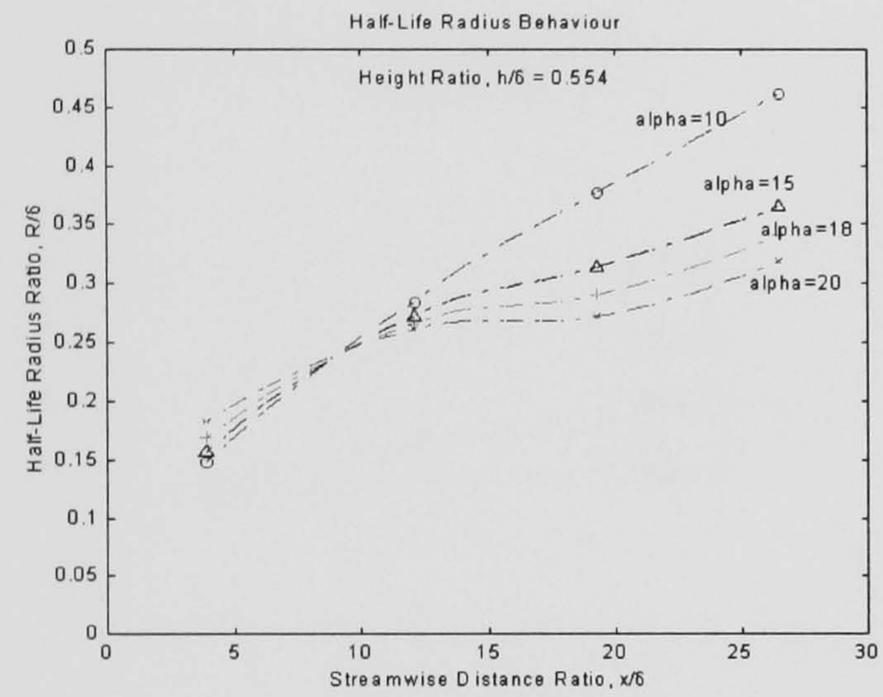

(e) Half-Life Radius, $h/\delta = 0.554$

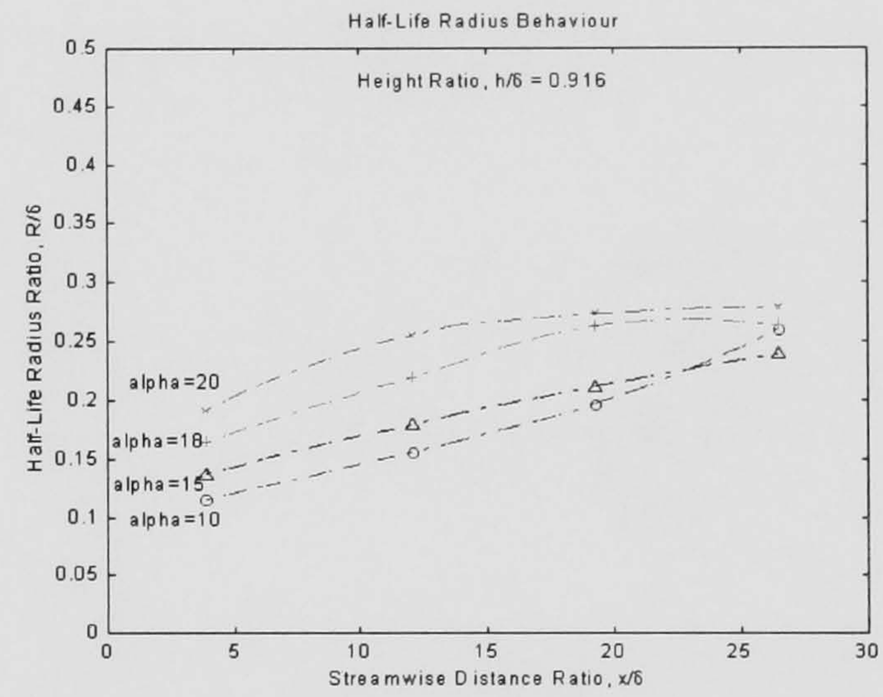

(f) Half-Life Radius, $h/\delta = 0.916$

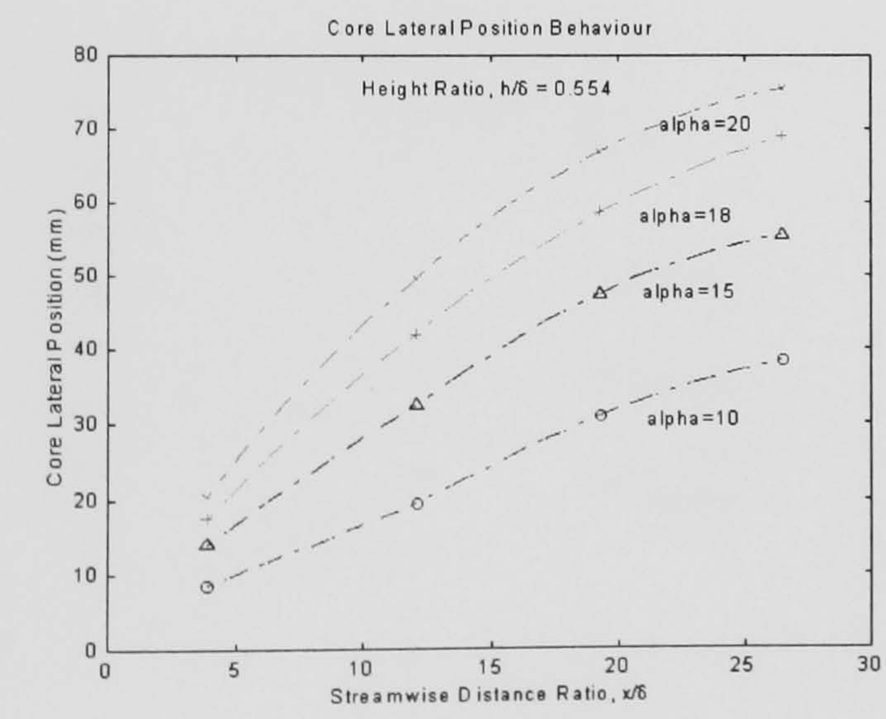

(i) Lateral Core Position, $h/\delta = 0.554$

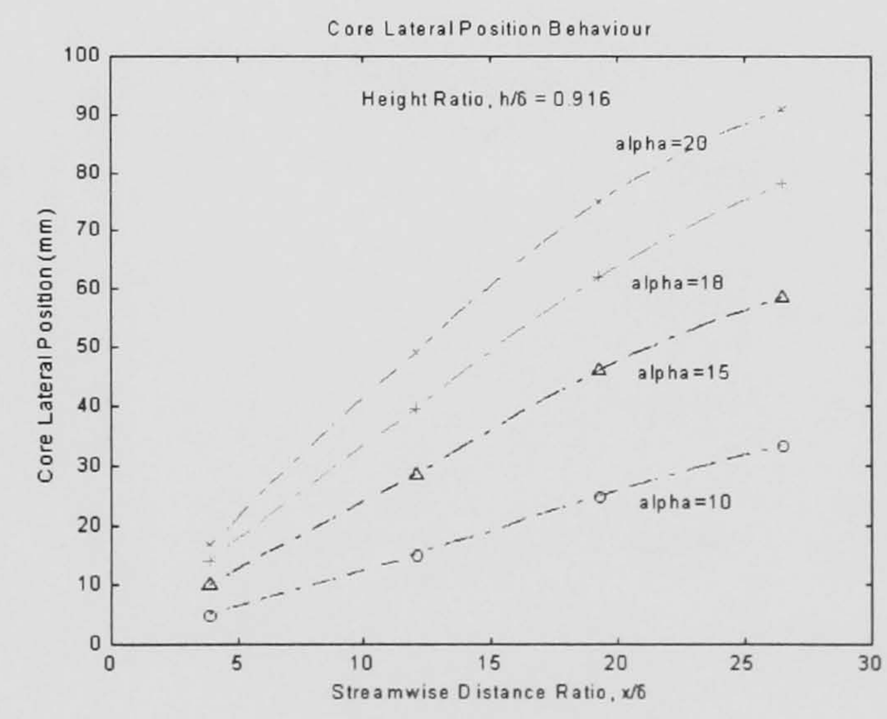

(j) Lateral Core Position, $h/\delta = 0.916$

Figure 35: Derived Data Plots: Effect of Vane Height Ratio (Cont.)

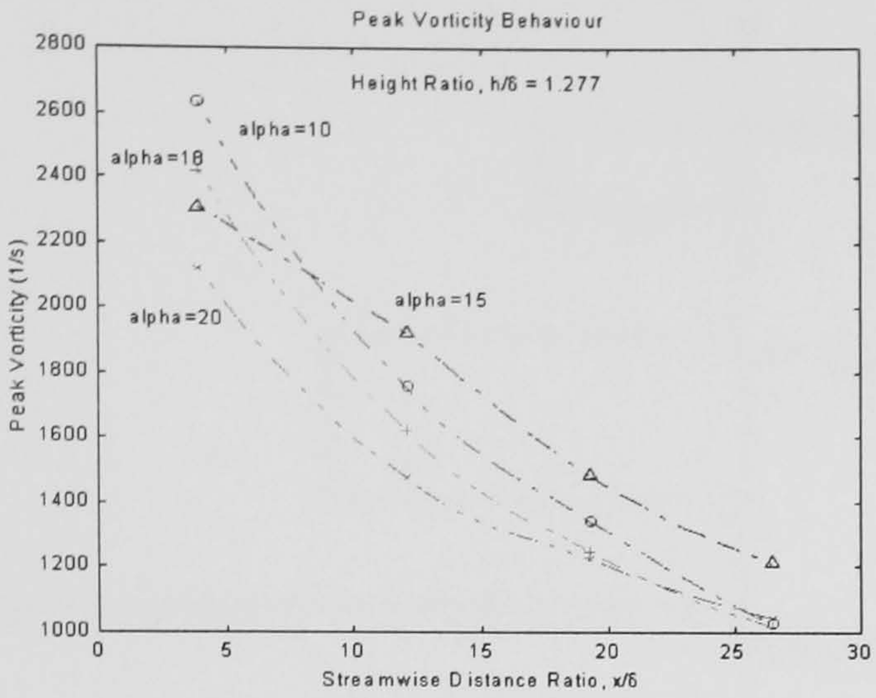

(c) Peak Vorticity, $h/\delta = 1.277$

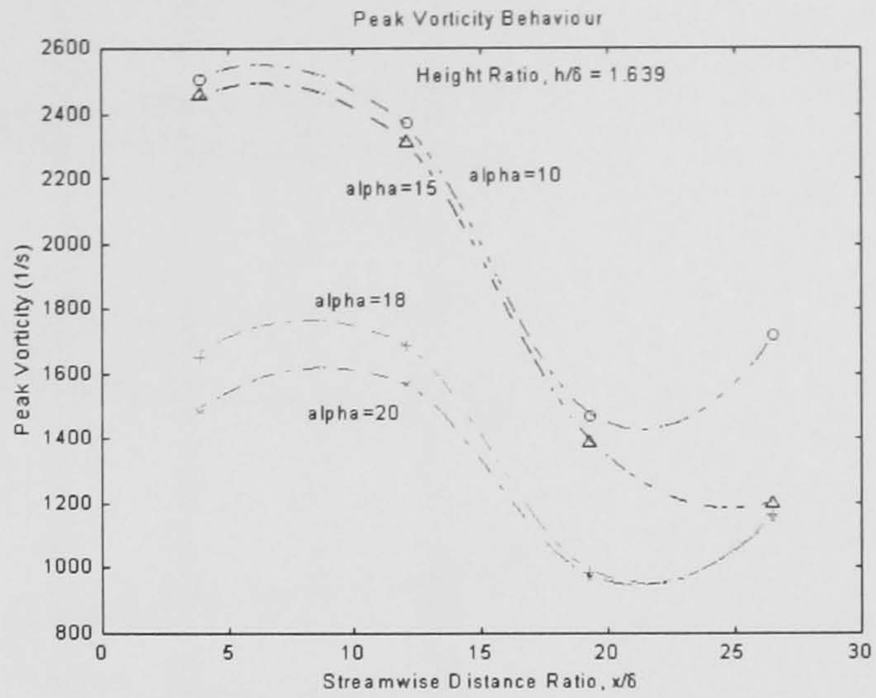

(d) Peak Vorticity, $h/\delta = 1.639$

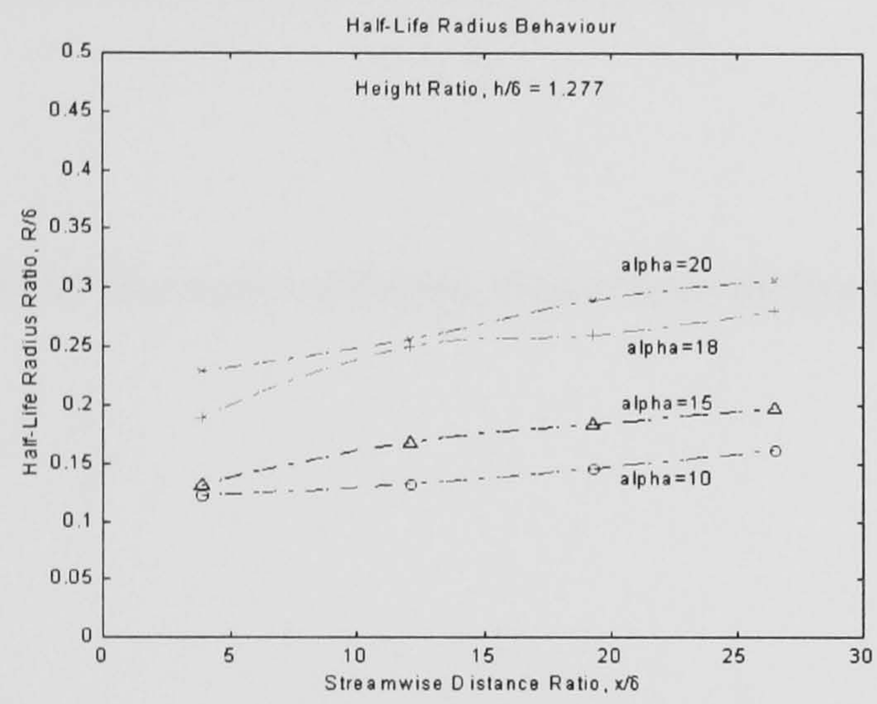

(g) Half-Life Radius, $h/\delta = 1.277$

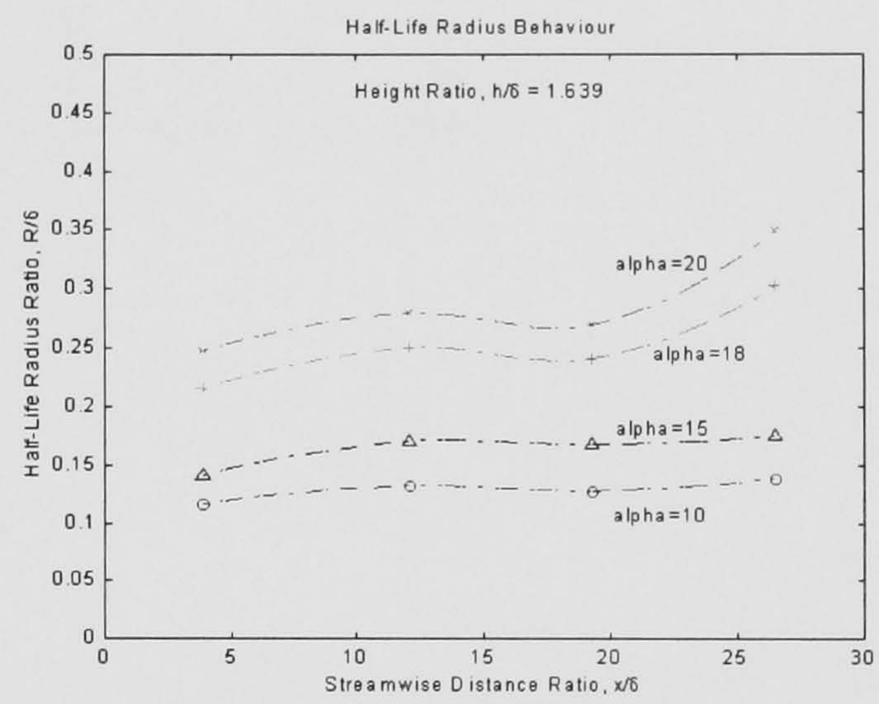

(h) Half-Life Radius, $h/\delta = 1.639$

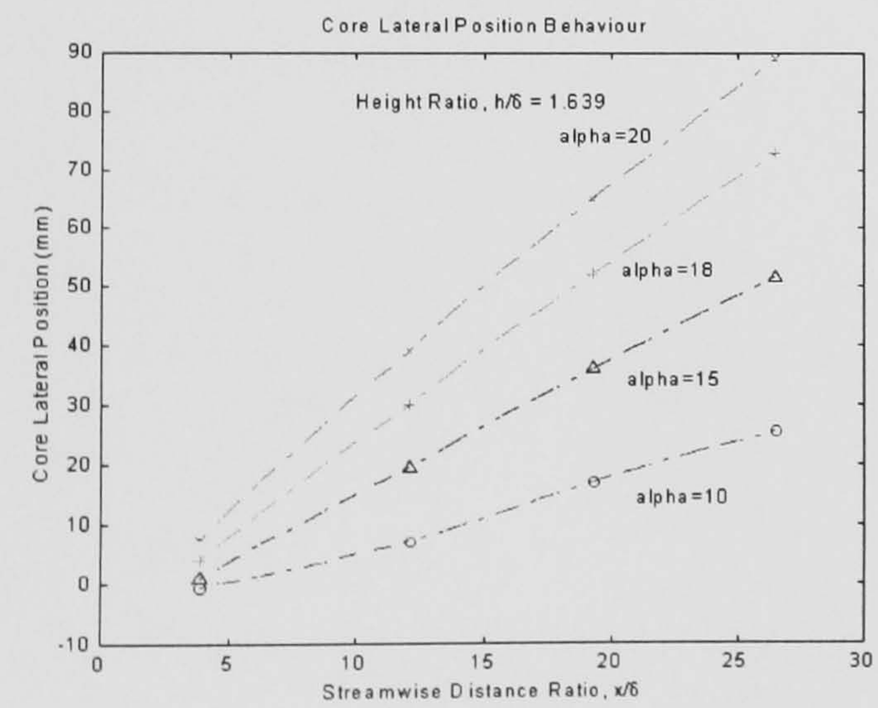

(k) Lateral Core Position, $h/\delta = 1.277$

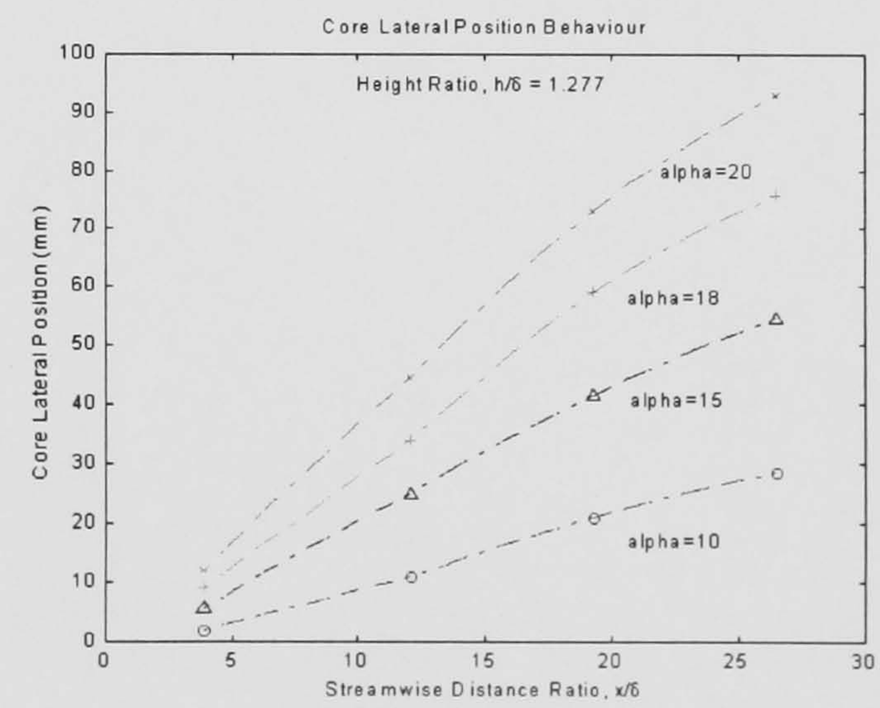

(l) Lateral Core Position, $h/\delta = 1.639$

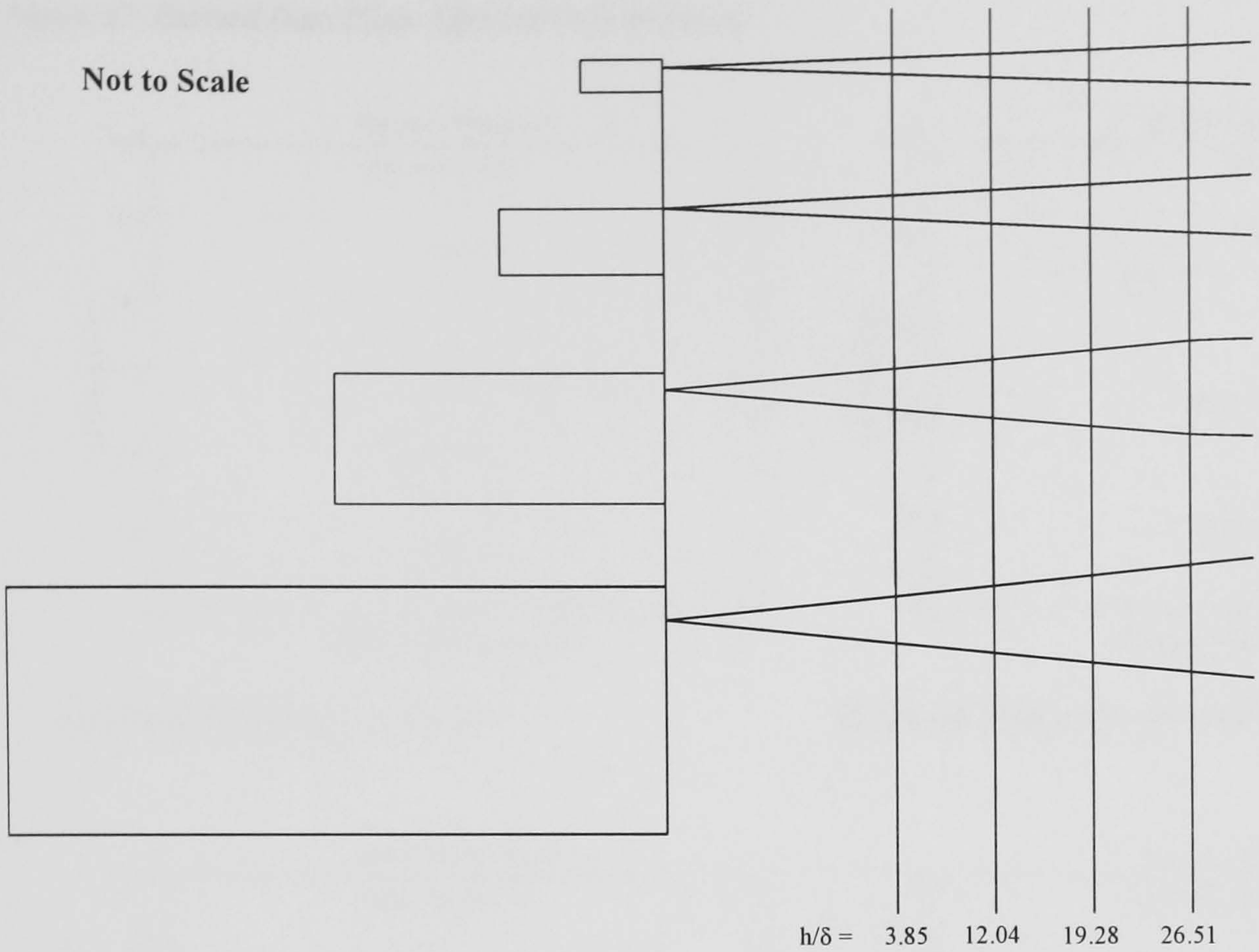

Figure 36: Illustration of Relative Vortex Generator Scaling

Figure 37: Derived Data Plots: Effect of Vane Incidence

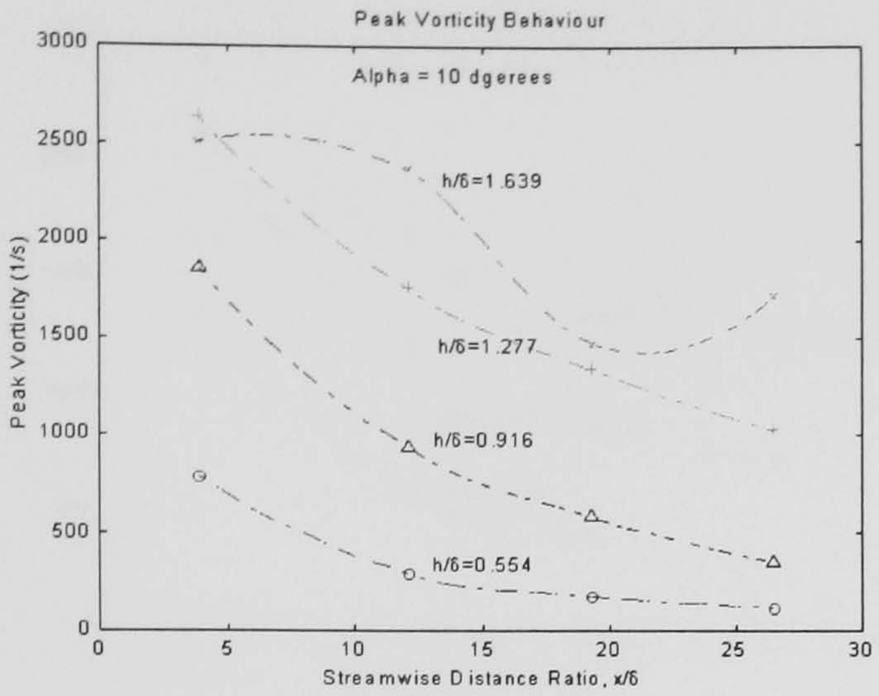

(a) Peak Vorticity, $\alpha = 10°$

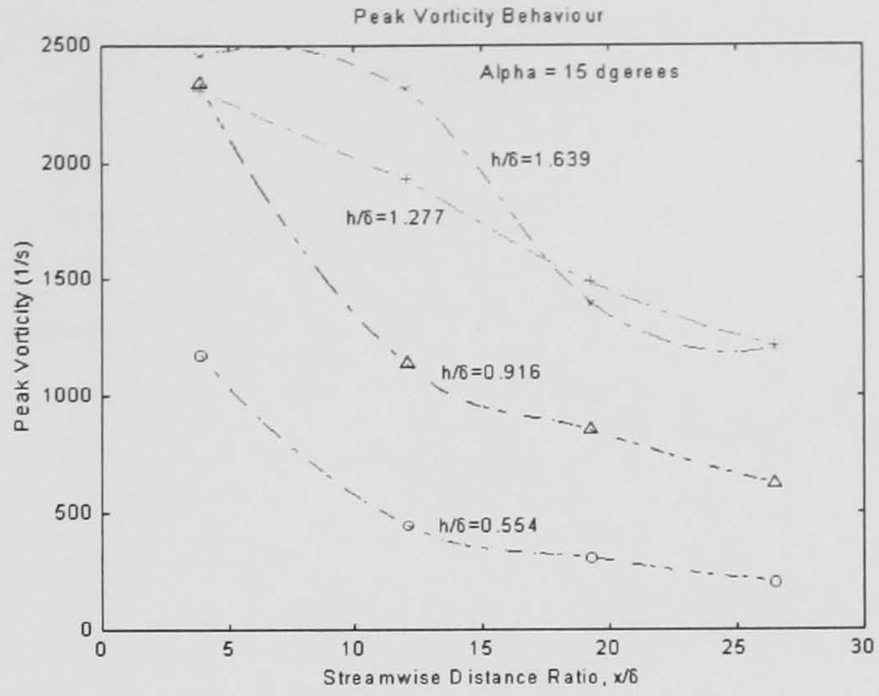

(b) Peak Vorticity, $\alpha = 15°$

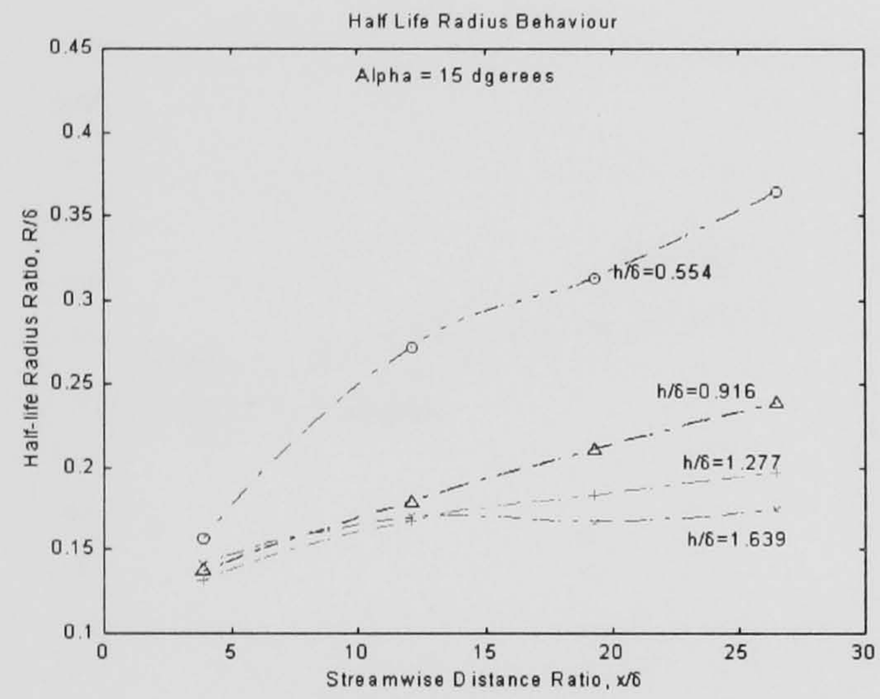

(e) Half-Life Radius, $\alpha = 10°$

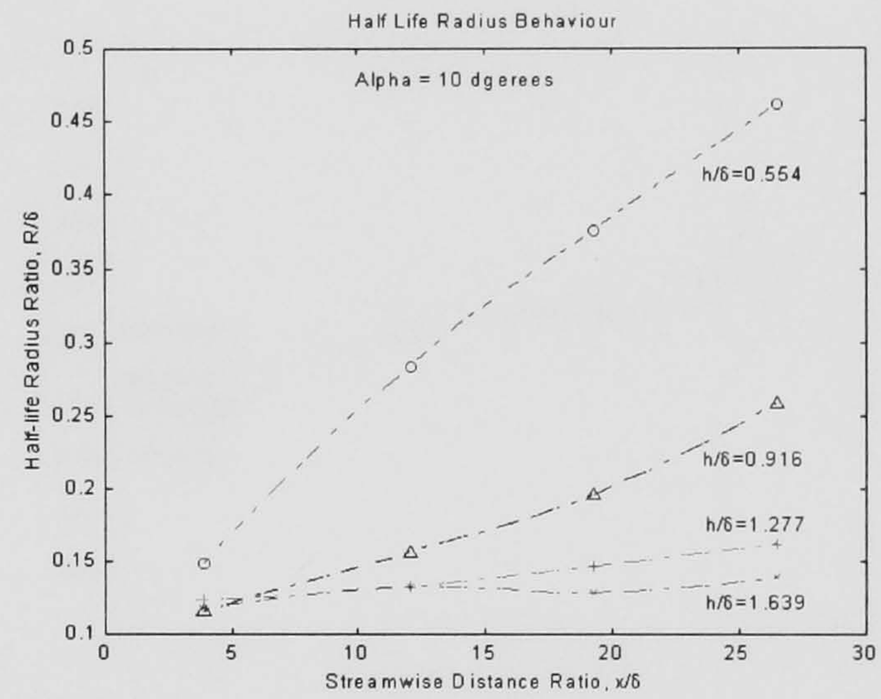

(f) Half-Life Radius, $\alpha = 15°$

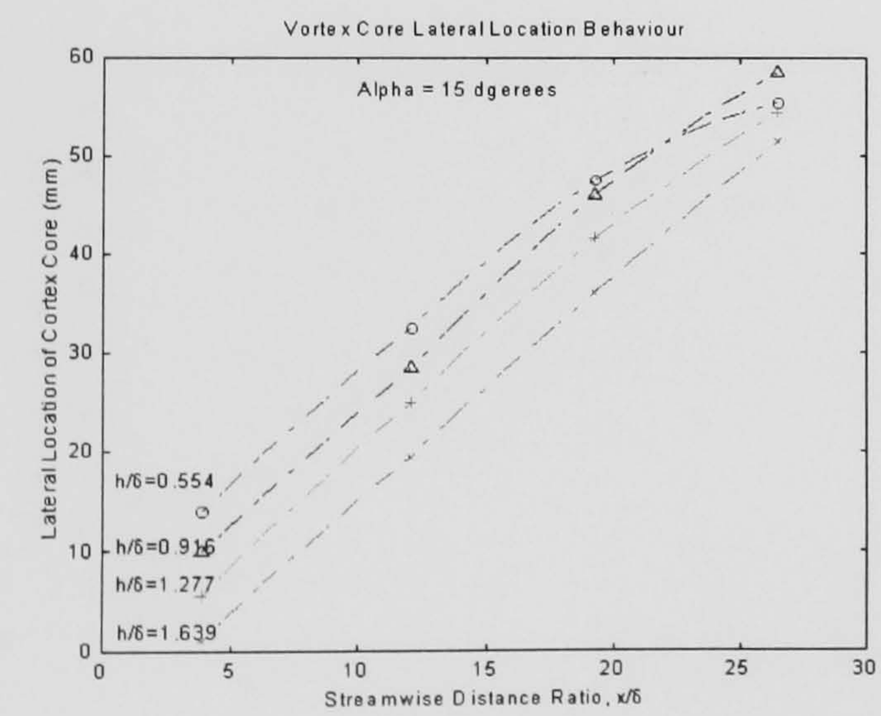

(i) Lateral Core Position, $\alpha = 10°$

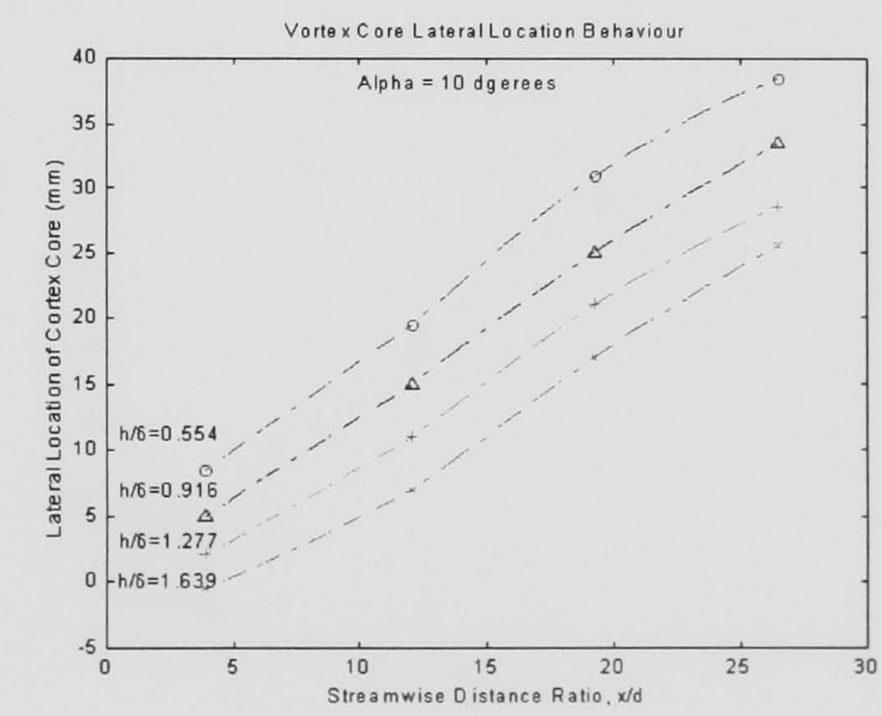

(j) Lateral Core Position, $\alpha = 15°$

Figure 37: Derived Data Plots: Effect of Vane Incidence (Cont.)

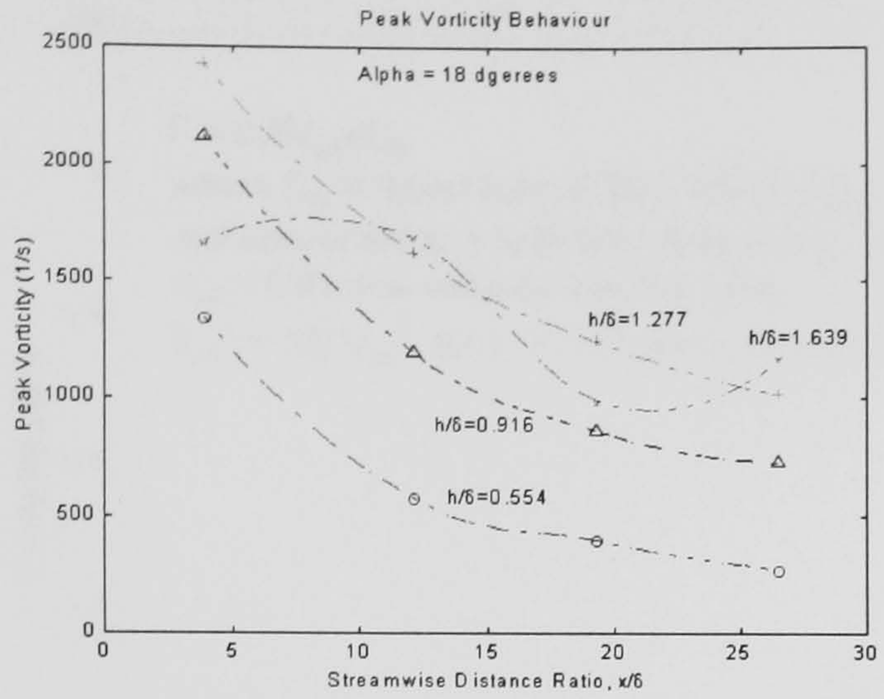

(c) Peak Vorticity, $\alpha = 18°$

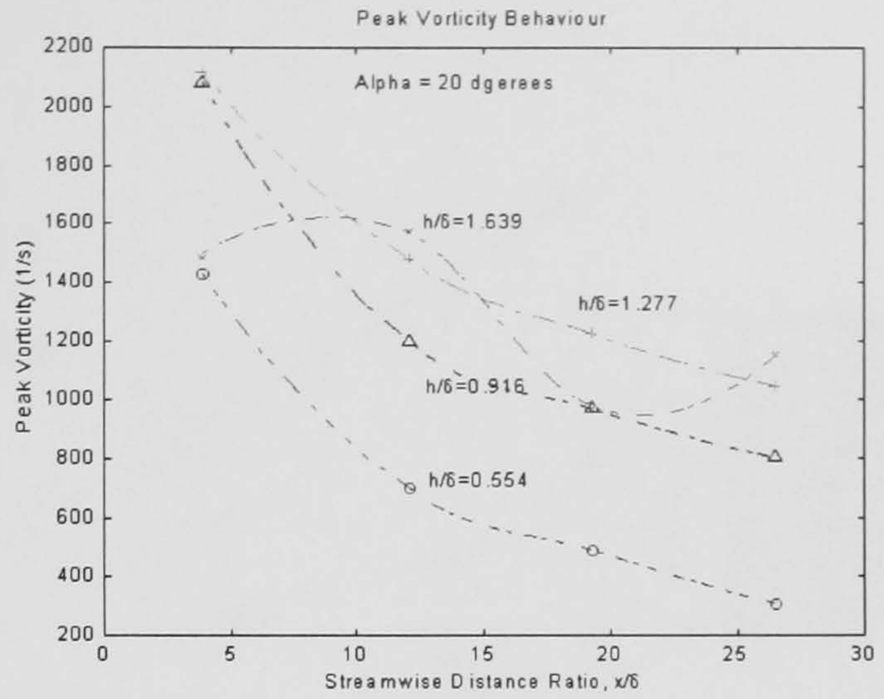

(d) Peak Vorticity, $\alpha = 20°$

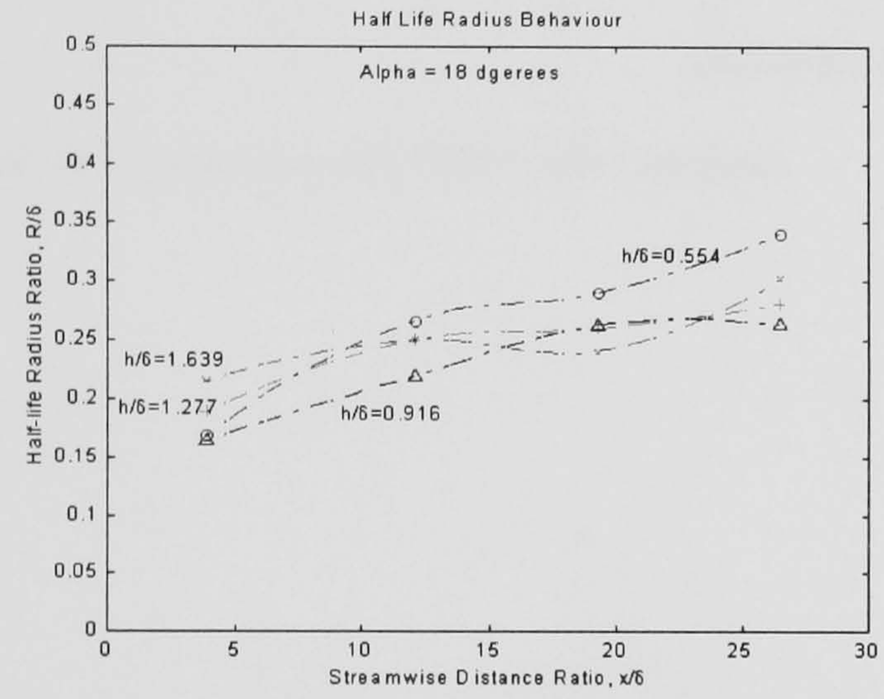

(g) Half-Life Radius, $\alpha = 18°$

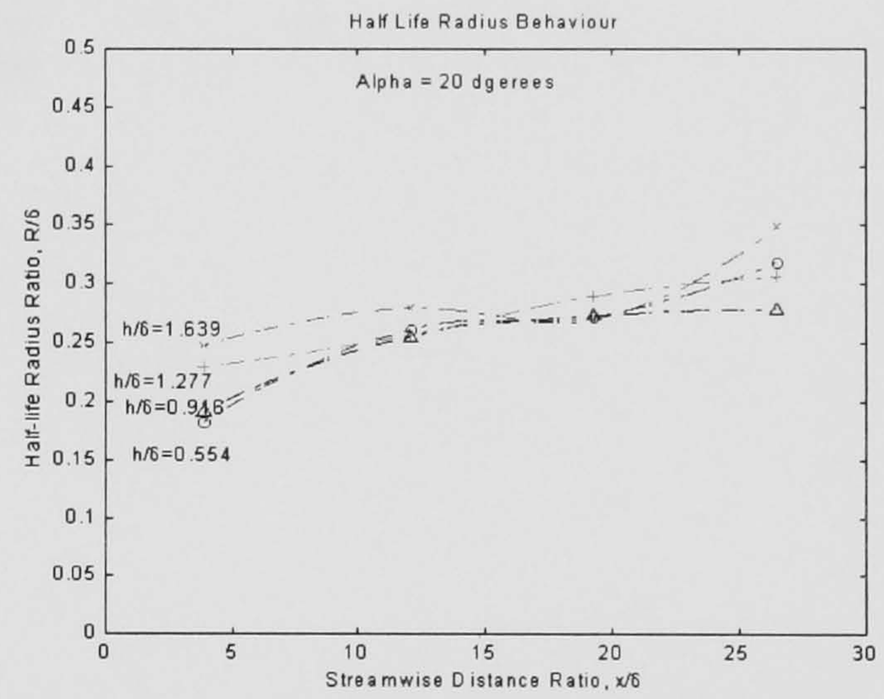

(h) Half-Life Radius, $\alpha = 20°$

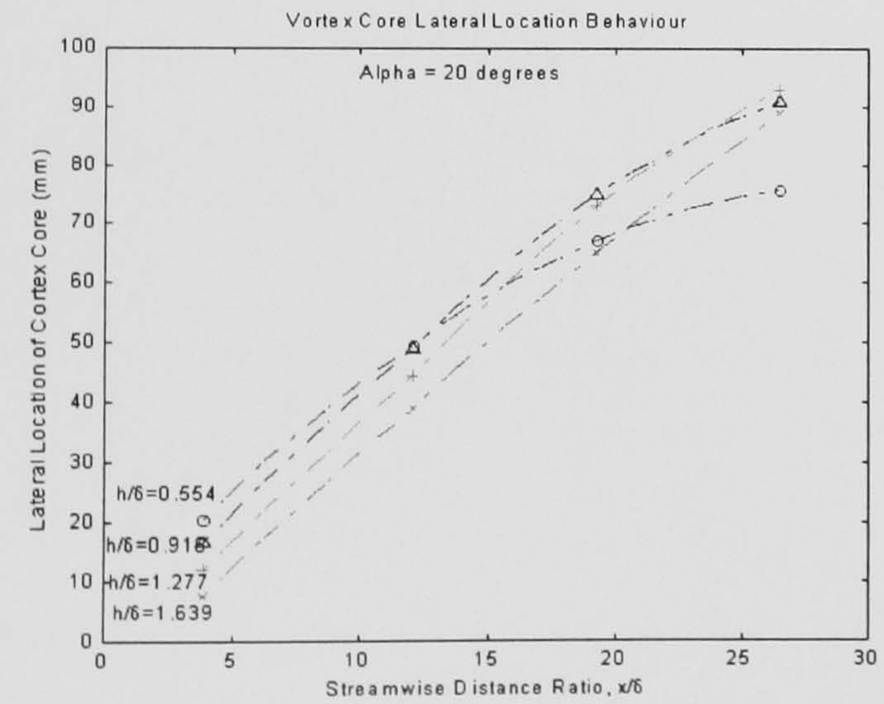

(k) Lateral Core Position, $\alpha = 18°$

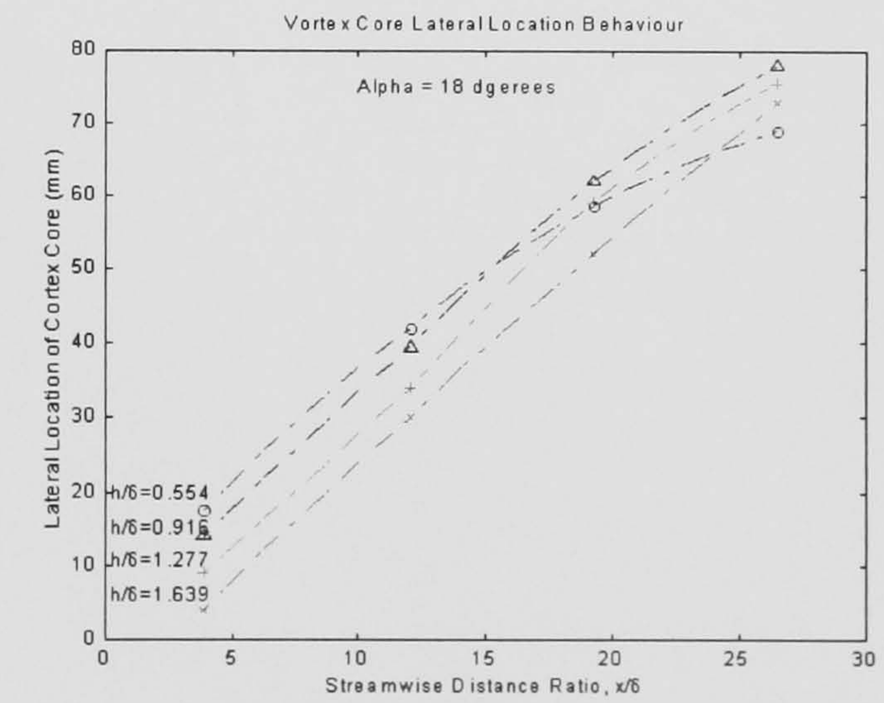

(l) Lateral Core Position, $\alpha = 20°$

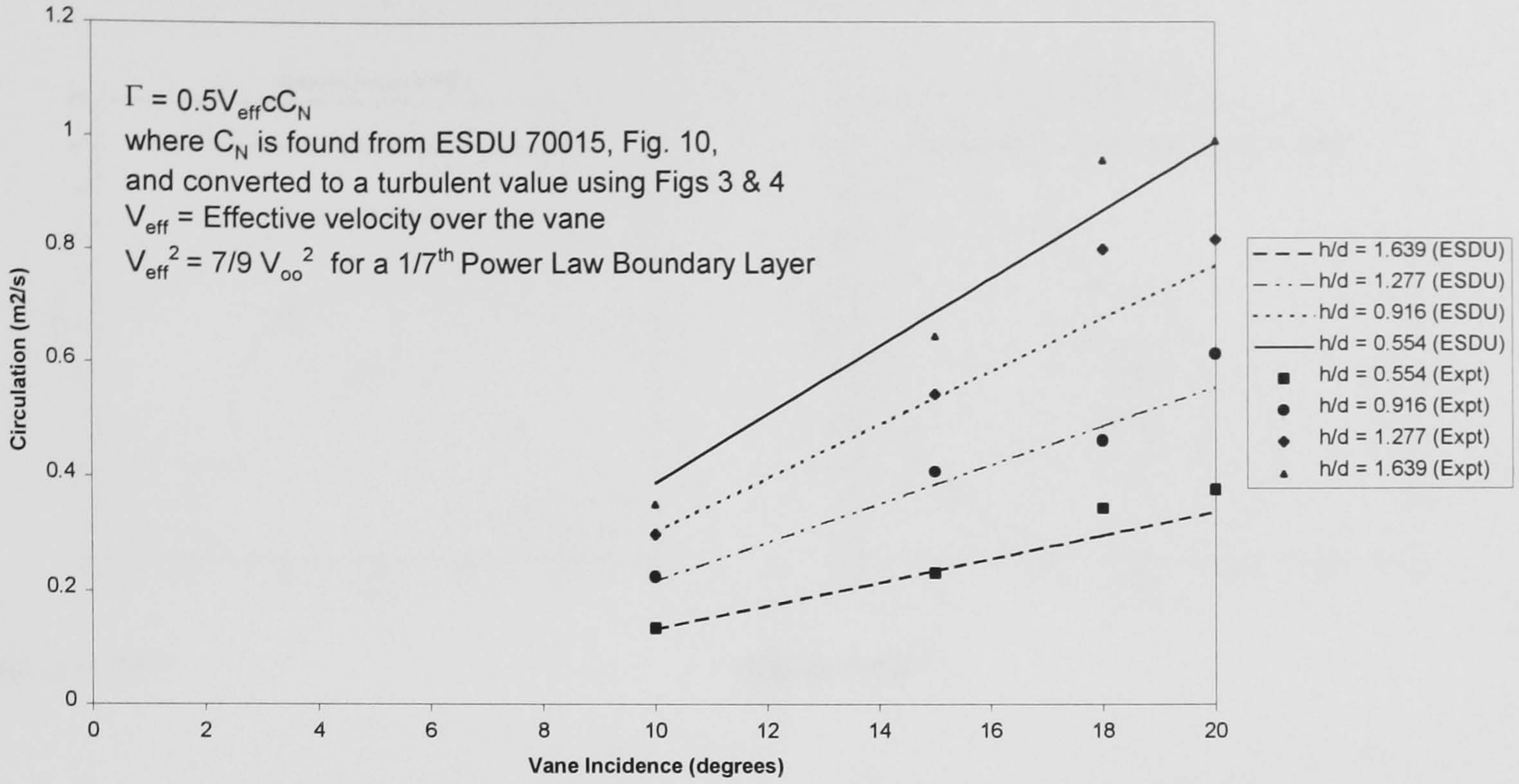

Figure 38: Comparison with ESDU 70015 Methods

6.3 - Air-jet Plots

Figure 39: Effect of Incidence: Dynamic Pressure Ratios & Vorticity Profiles

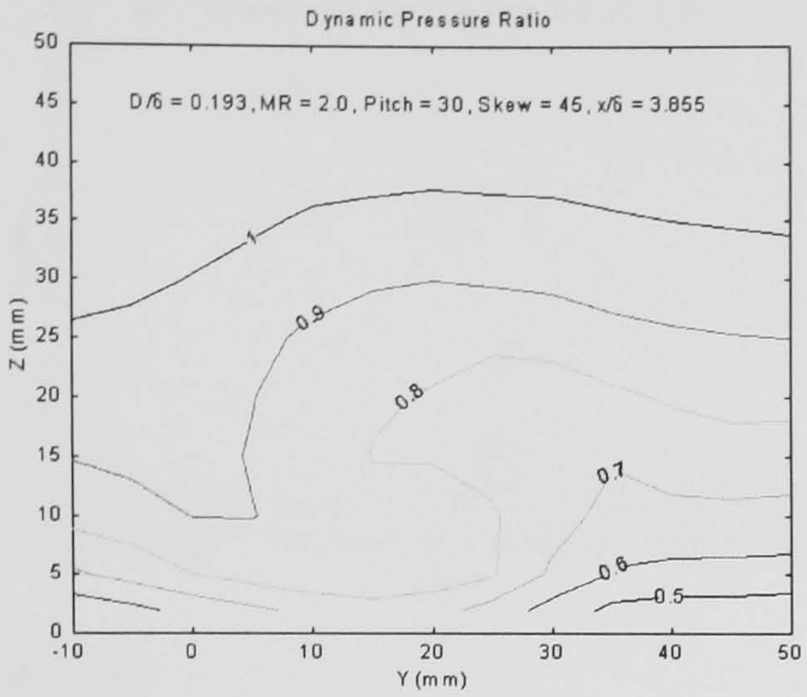

(a) $\alpha = 30°$

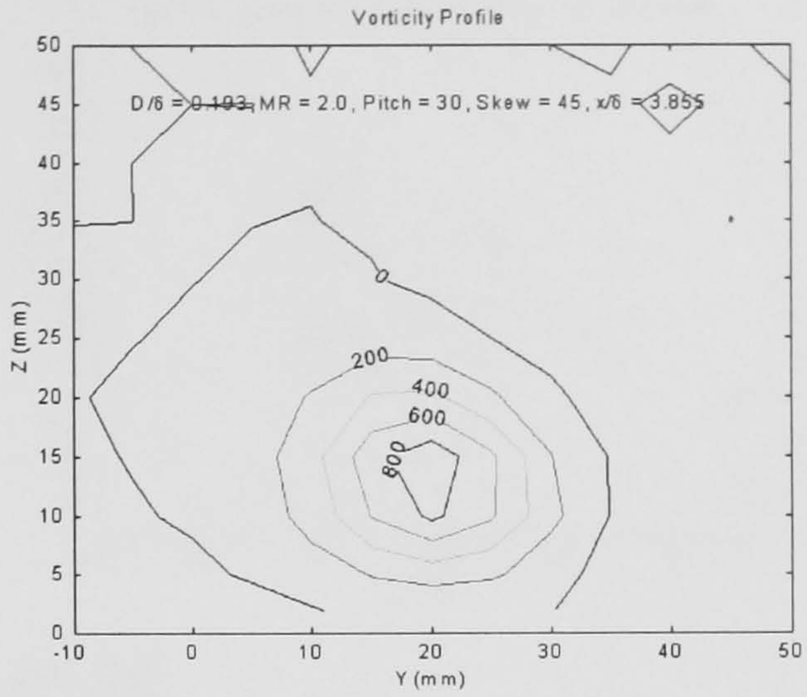

(b) $\alpha = 30°$

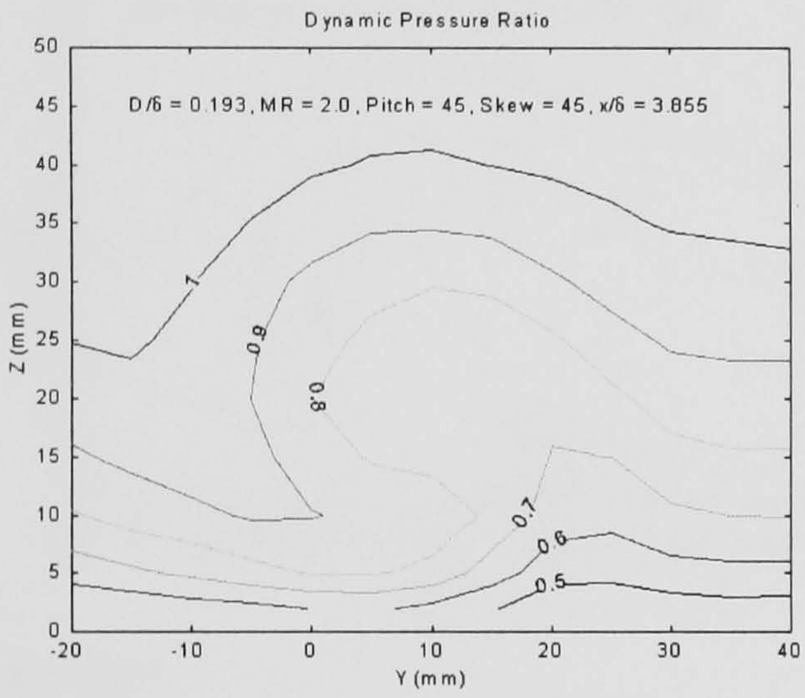

(c) $\alpha = 45°$

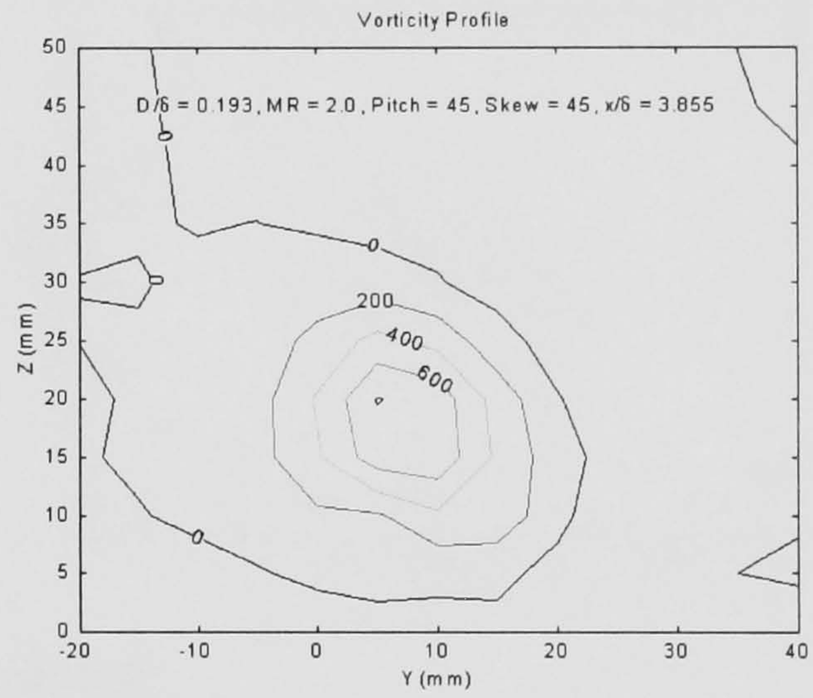

(d) $\alpha = 45°$

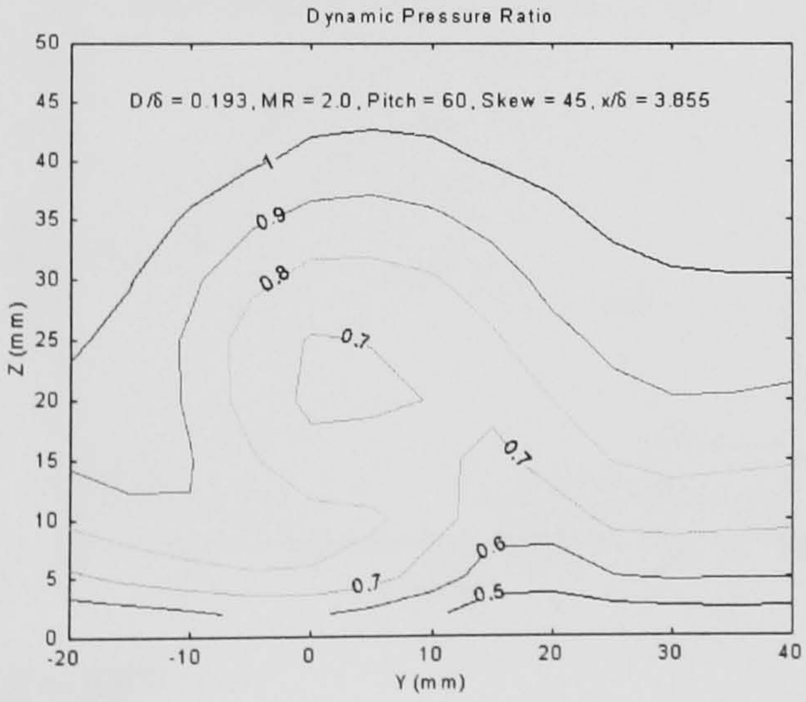

(e) $\alpha = 60°$

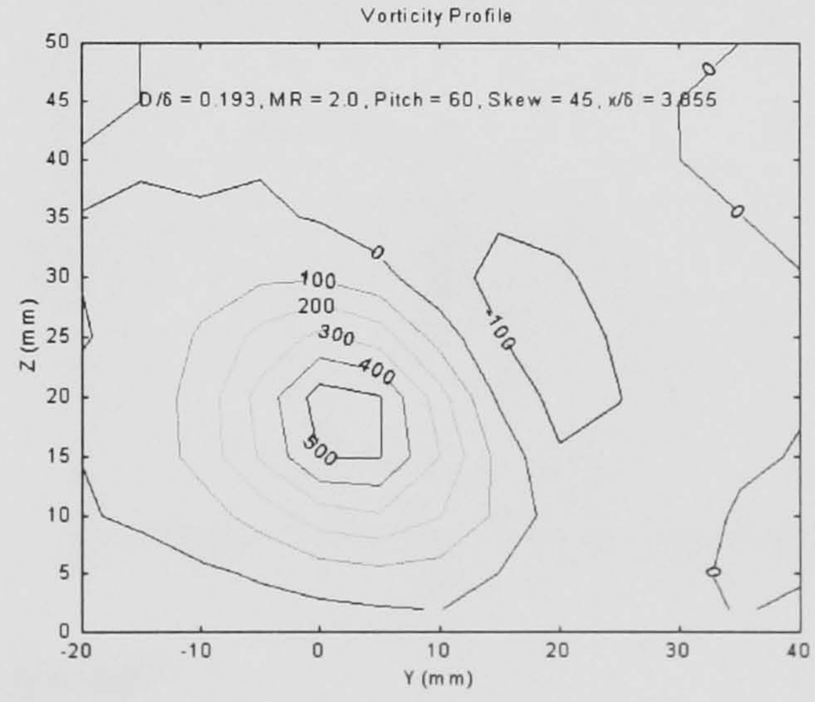

(f) $\alpha = 60°$

Figure 40: Effect of Skew: Dynamic Pressure Ratios & Vorticity Profiles

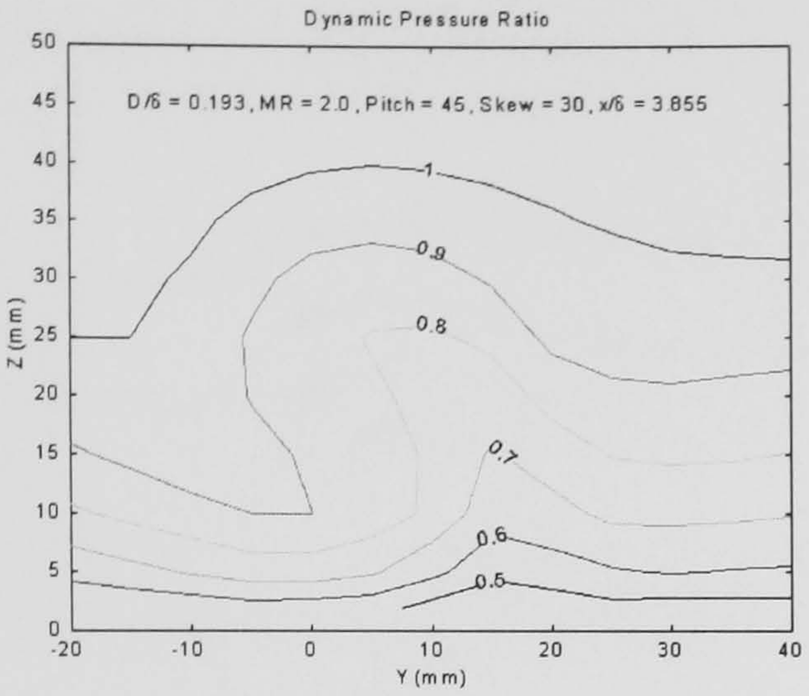

(a) $\beta = 30°$

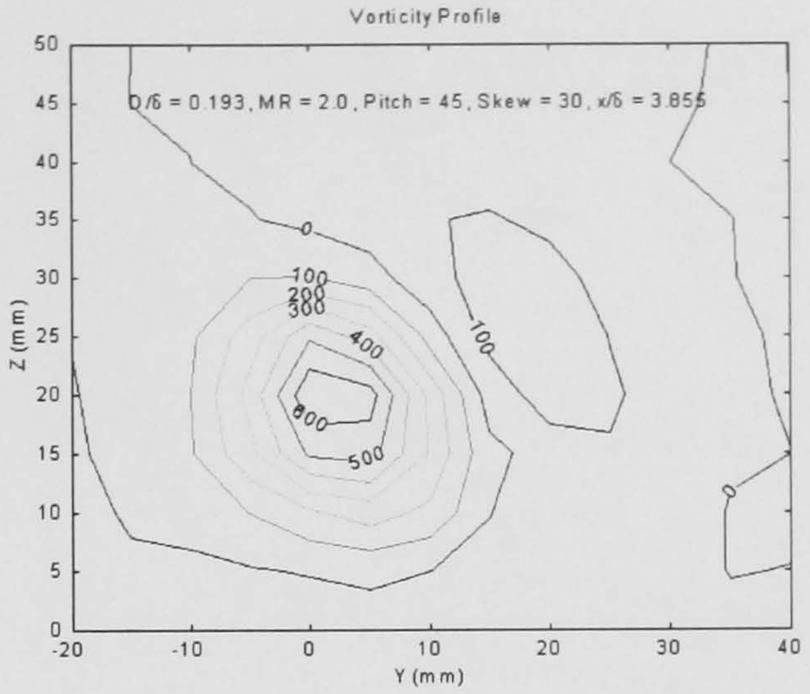

(b) $\beta = 30°$

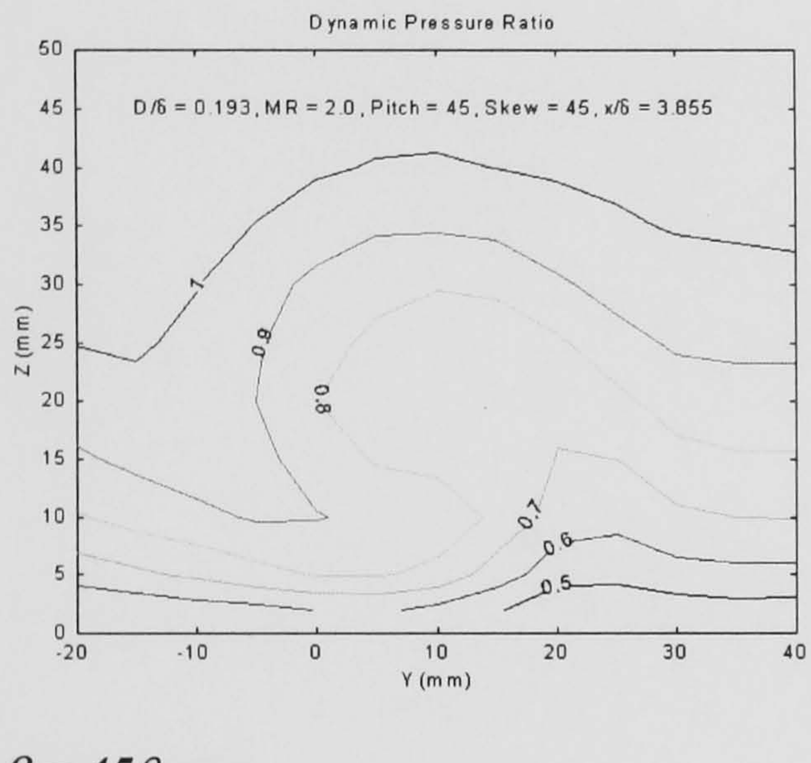

(c) $\beta = 45°$

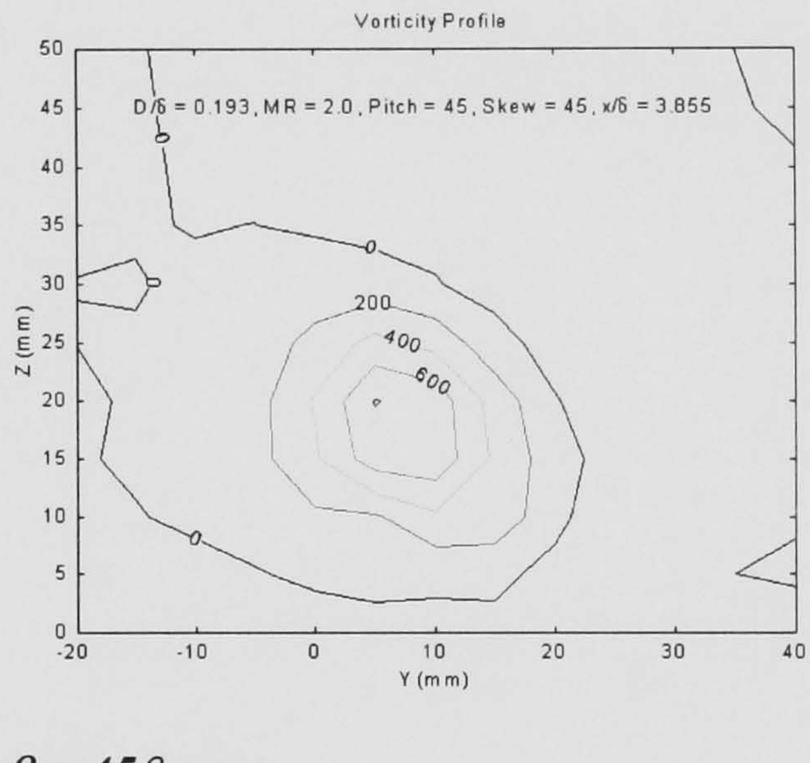

(d) $\beta = 45°$

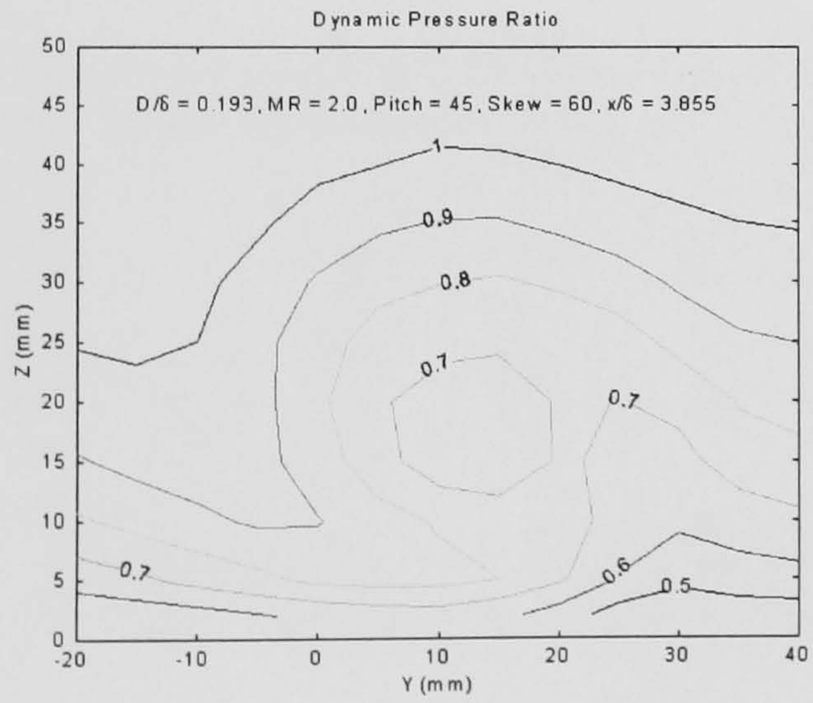

(e) $\beta = 60°$

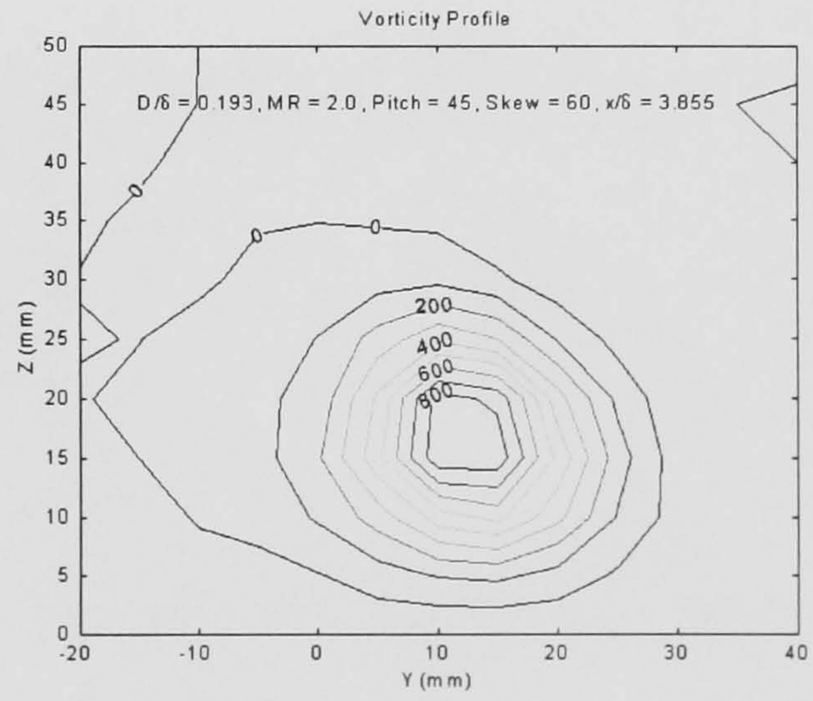

(f) $\beta = 60°$

Figure 41: Effect of Jet Diameter Ratio: Dynamic Pressure Ratios & Vorticity Profiles

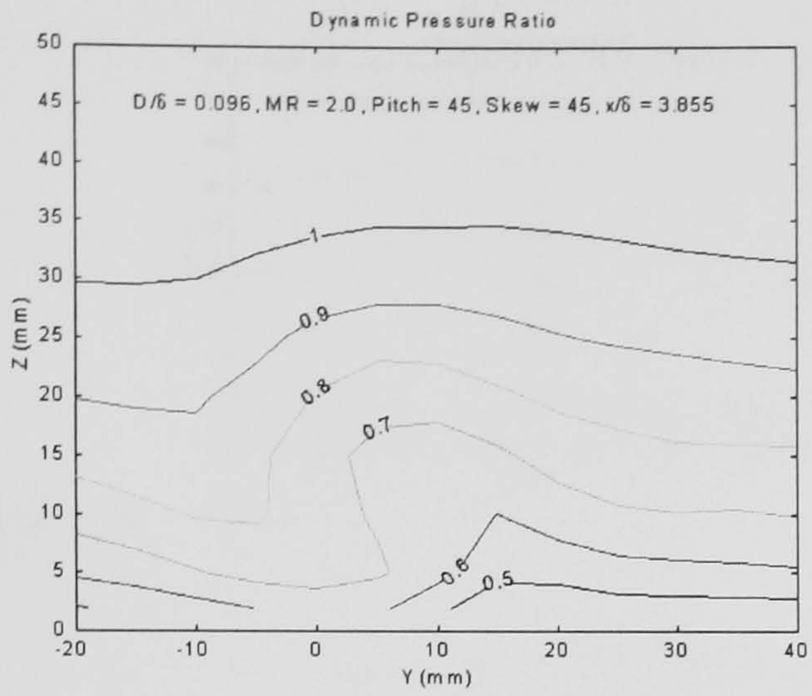

(a) D/δ = 0.096

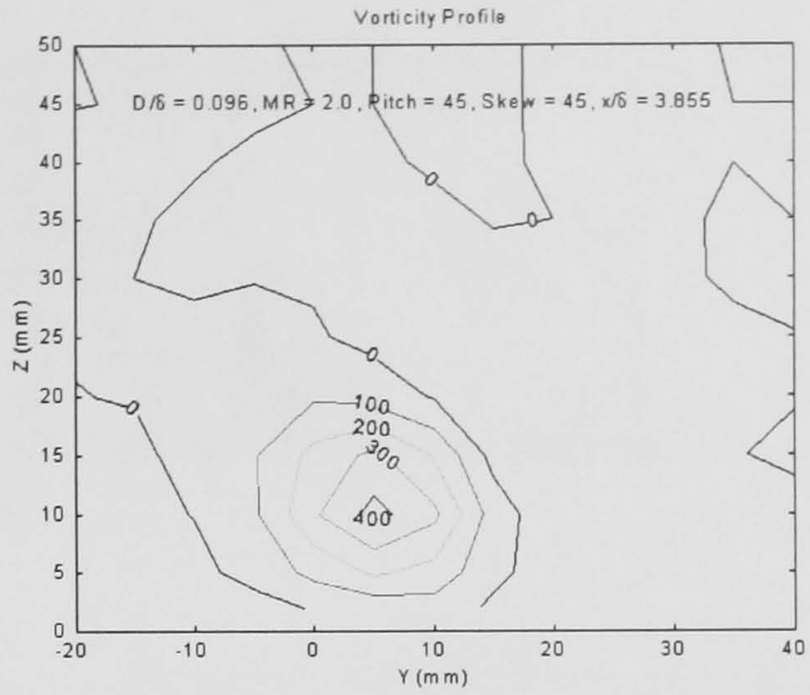

(b) D/δ = 0.096

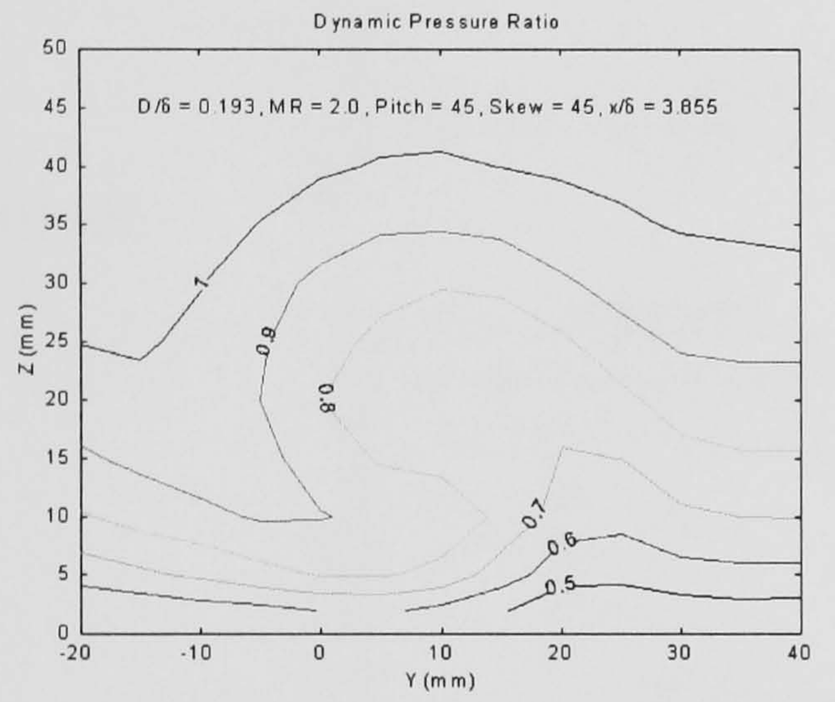

(c) D/δ = 0.193

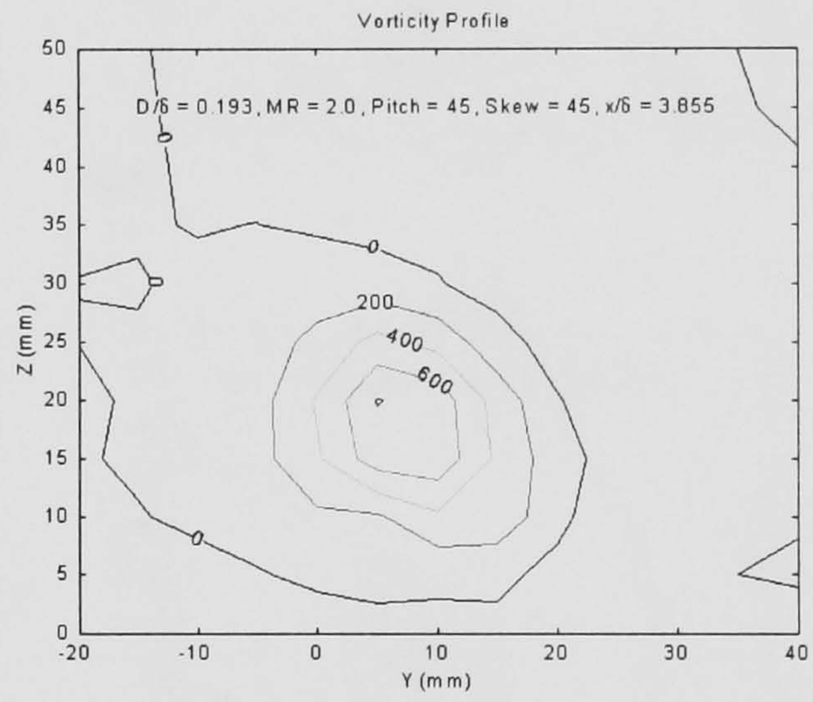

(d) D/δ = 0.193

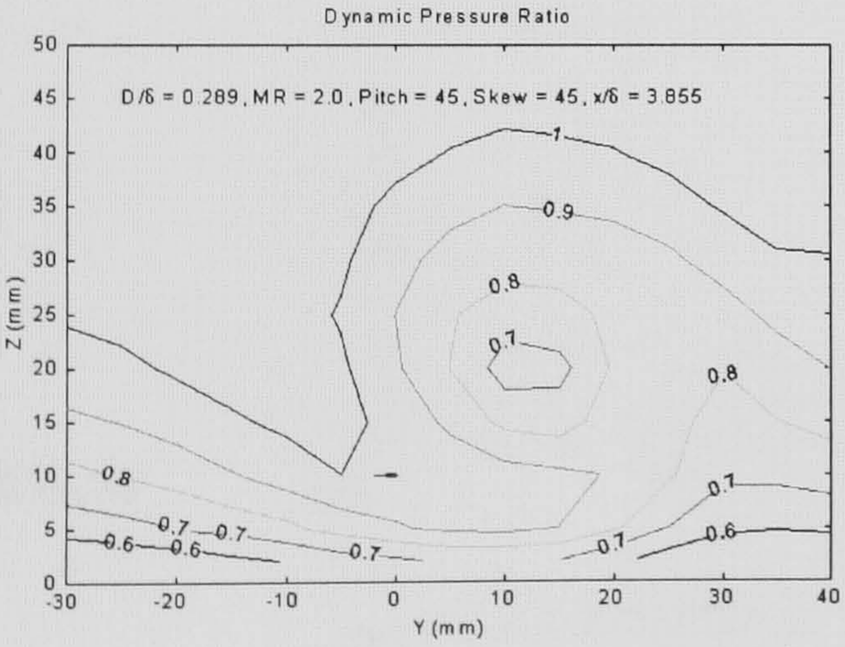

(e) D/δ = 0.289

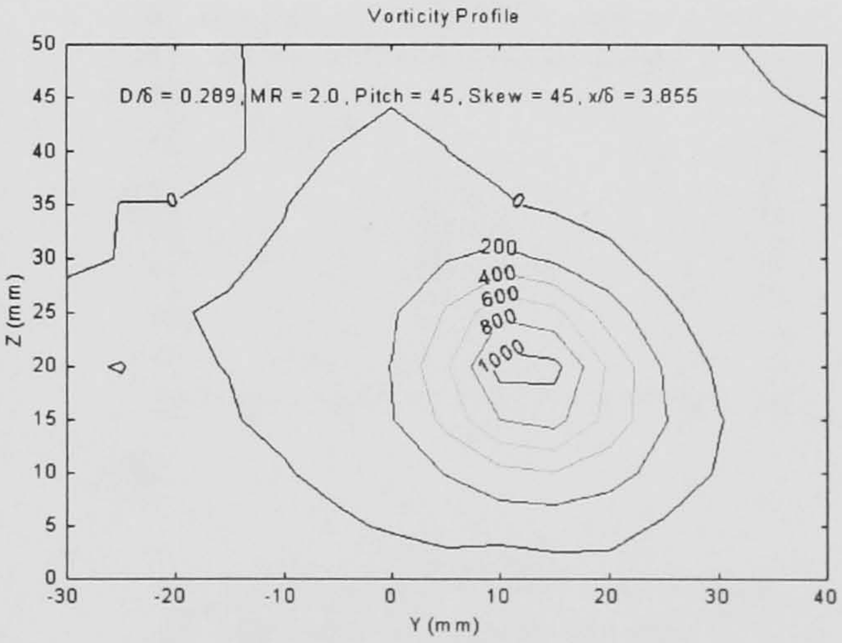

(f) D/δ = 0.289

Figure 42: Effect of Mach Number Ratio: Dynamic Pressure Ratios & Vorticity Profiles

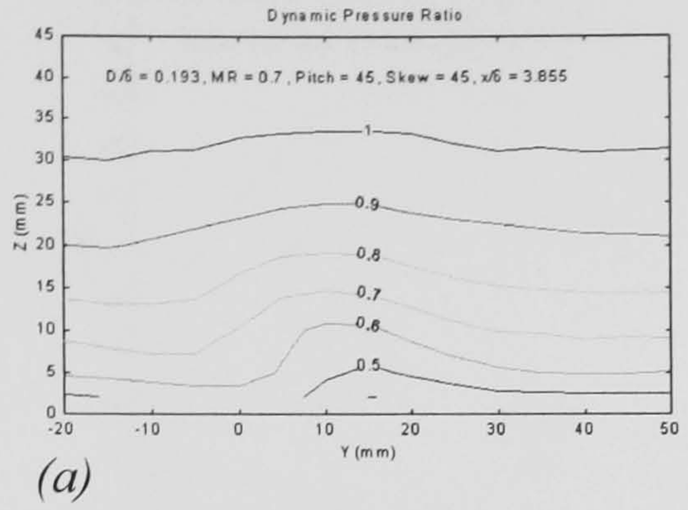

(a)

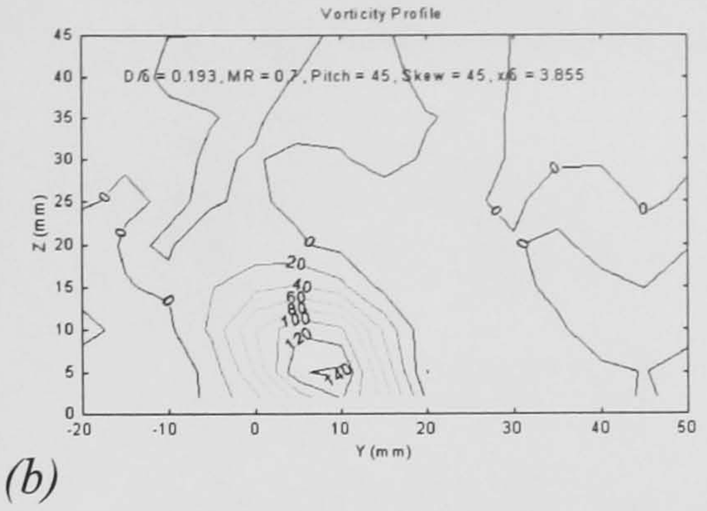

(b)

MR = 0.7

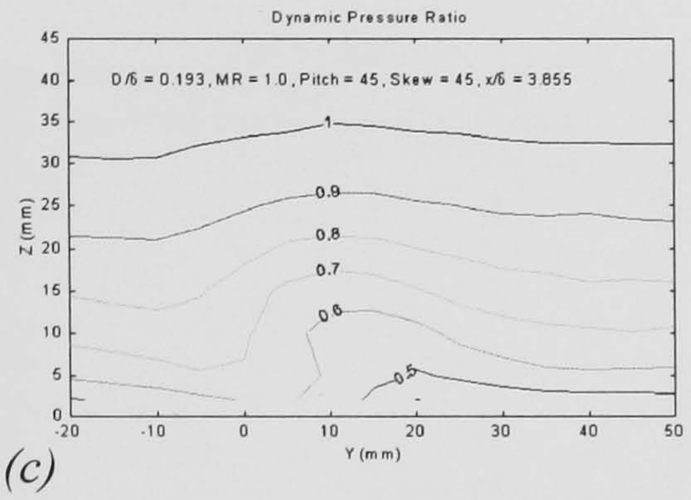

(c)

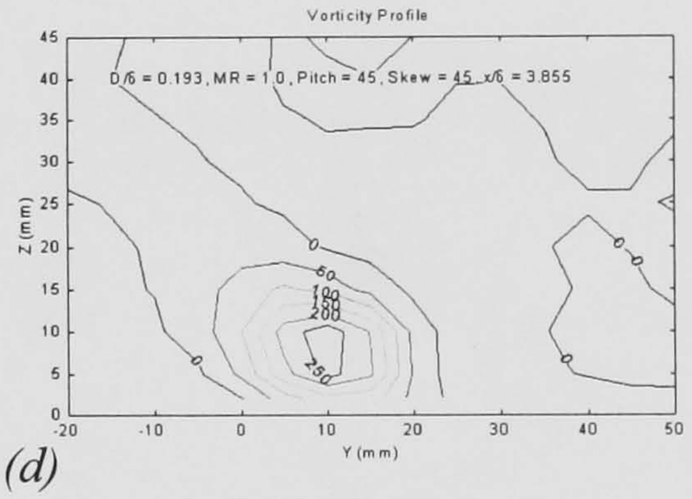

(d)

MR = 1.0

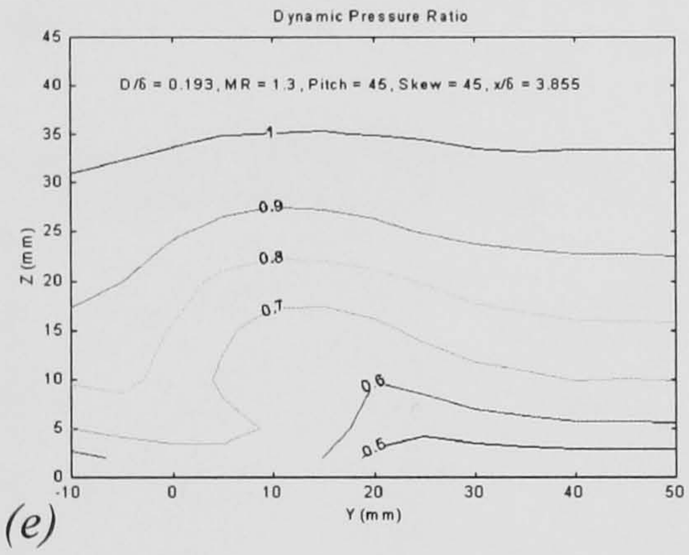

(e)

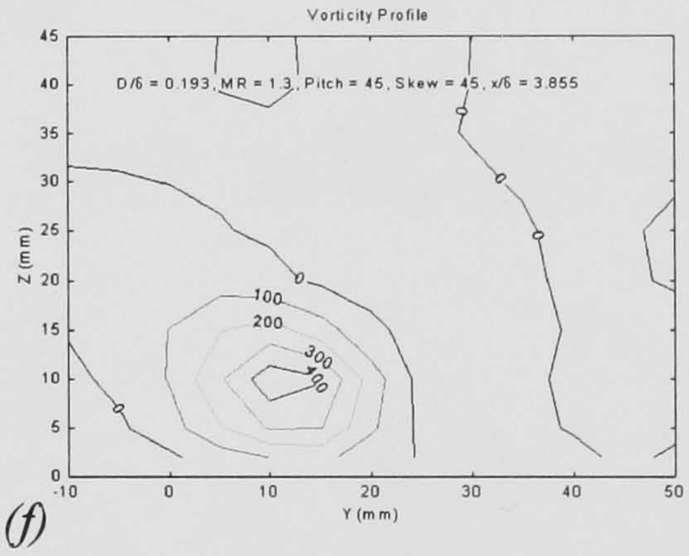

(f)

MR = 1.3

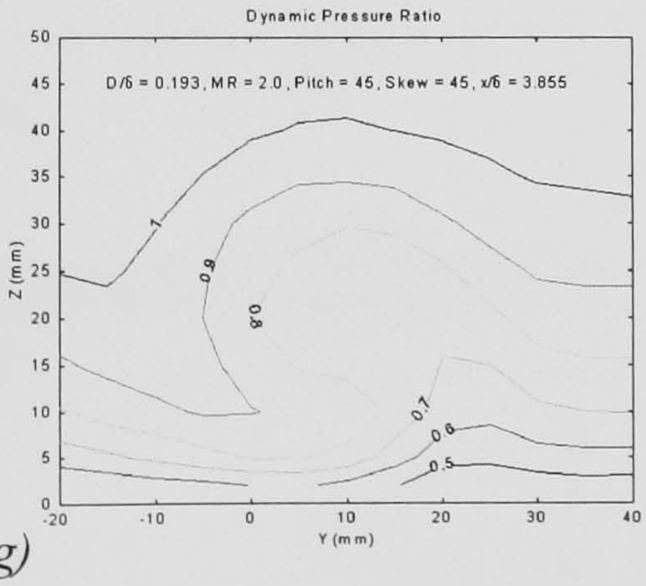

(g)

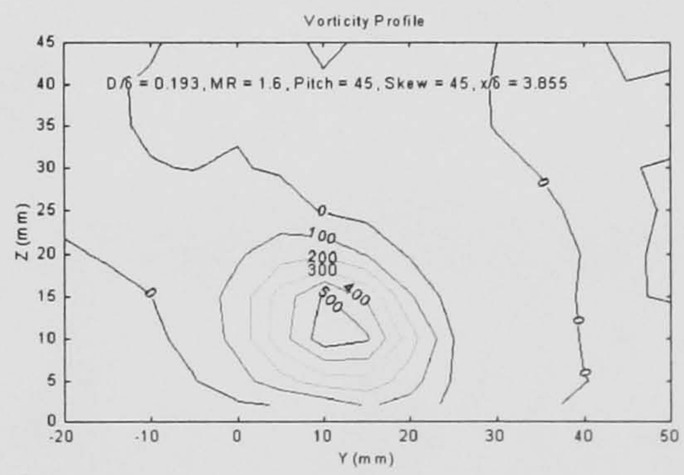

(h)

MR = 1.6

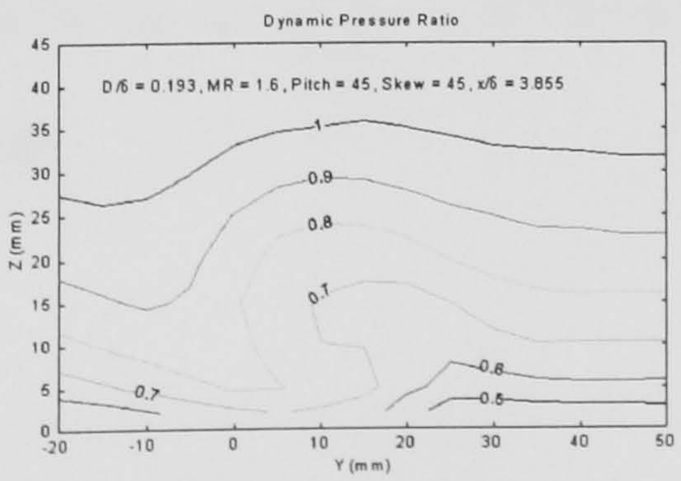

(i)

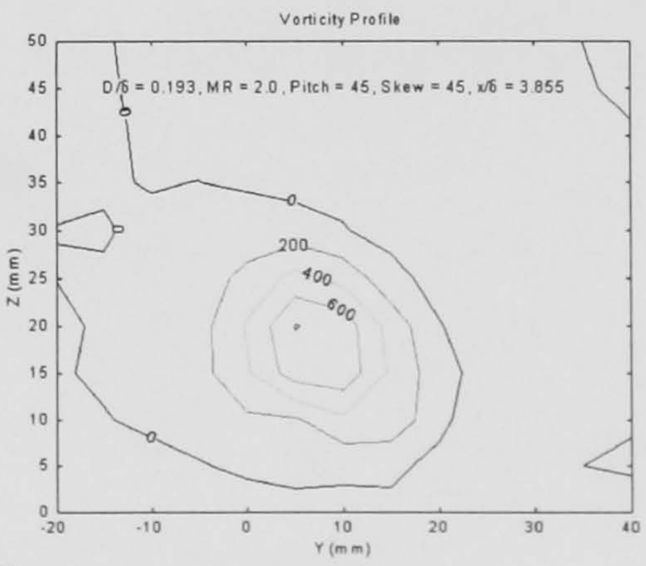

(j)

MR = 2.0

Figure 43: Effect of Streamwise Distance Ratio: Dynamic Pressure Ratios & Vorticity Profiles

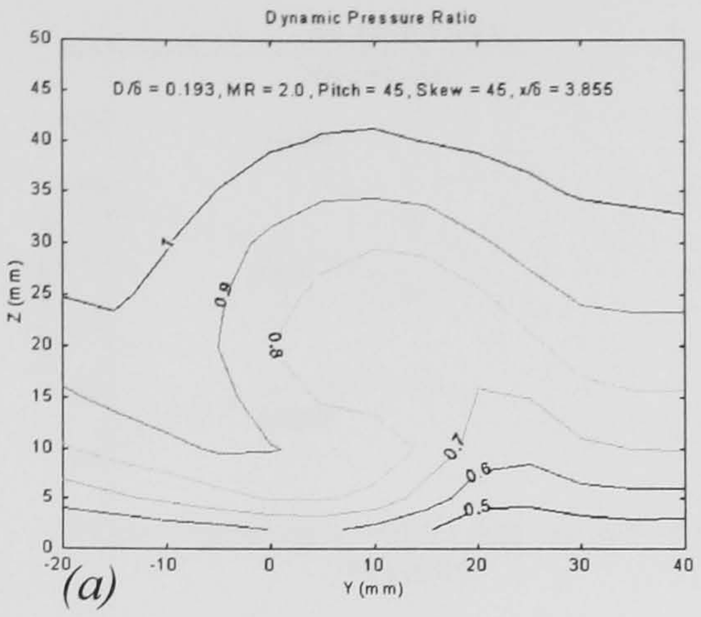

x/δ = 3.855 *(a)*

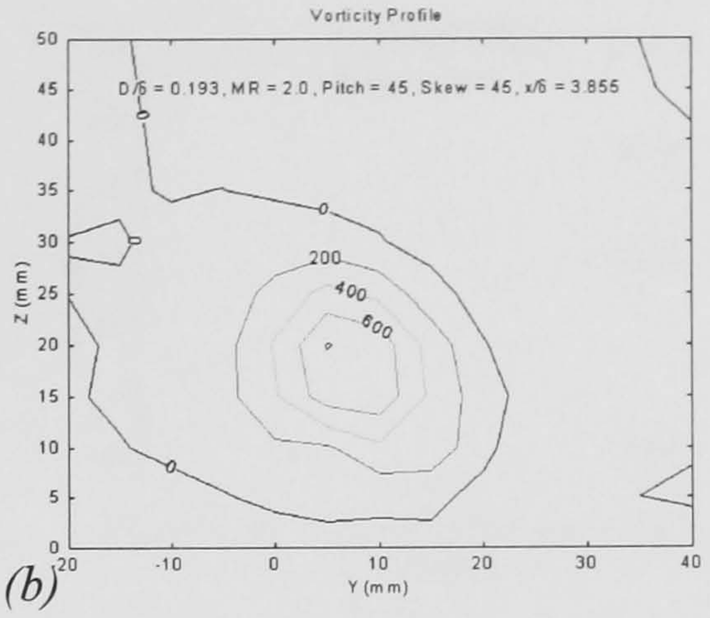

(b)

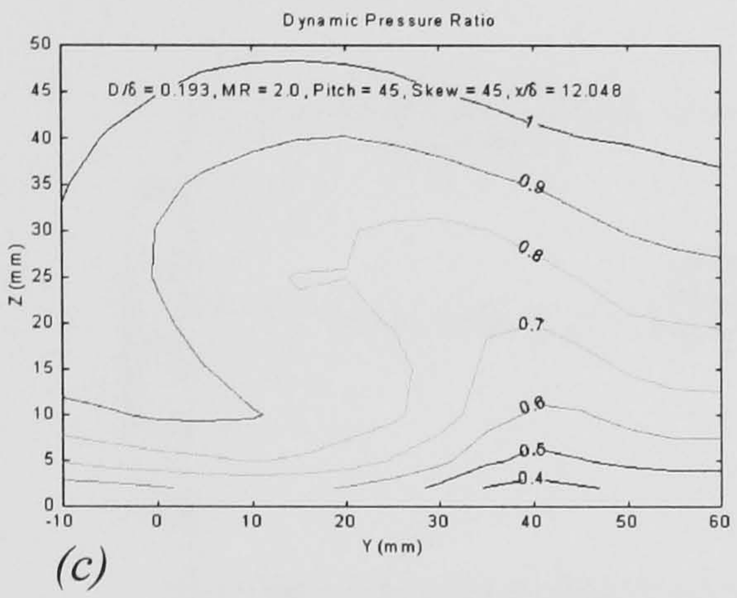

x/δ = 12.048 *(c)*

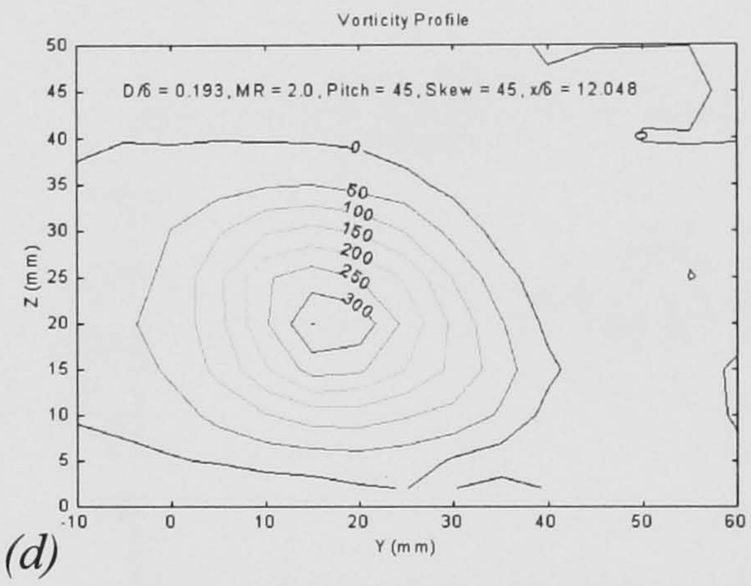

(d)

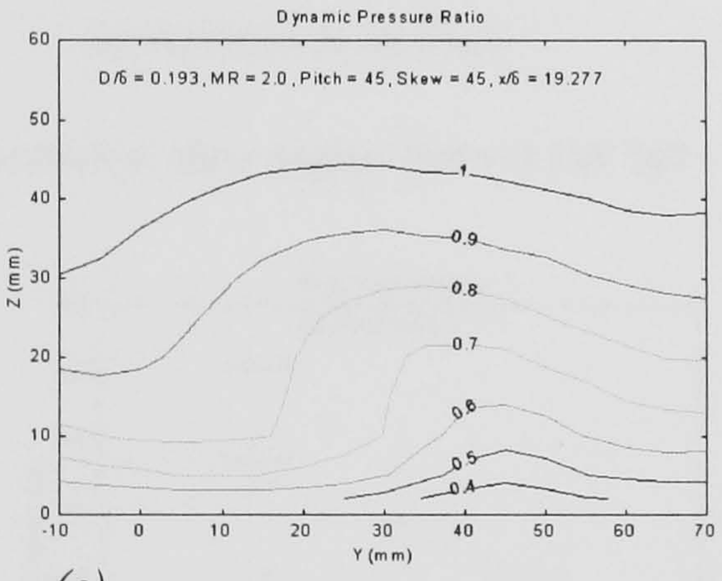

x/δ = 19.277 *(e)*

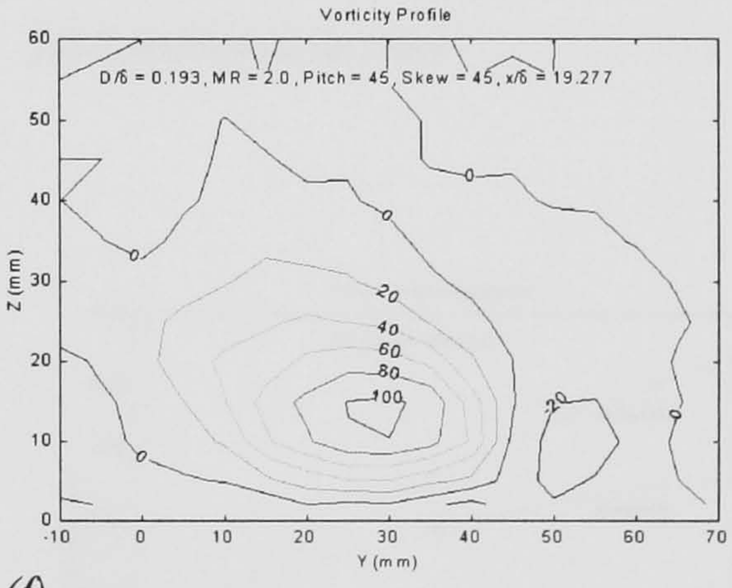

(f)

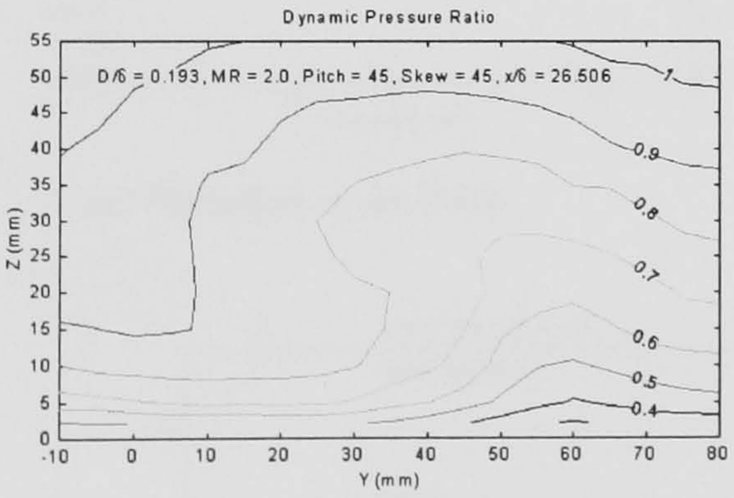

x/δ = 26.506 *(g)*

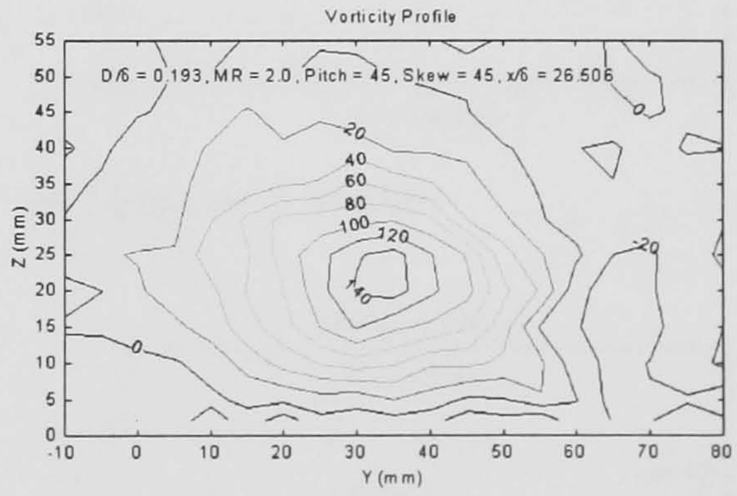

(h)

Figure 44: Effect of Jet Pitch & Skew Angles: $D/\delta = 0.193$, MR = 2.0

Peak Vorticity

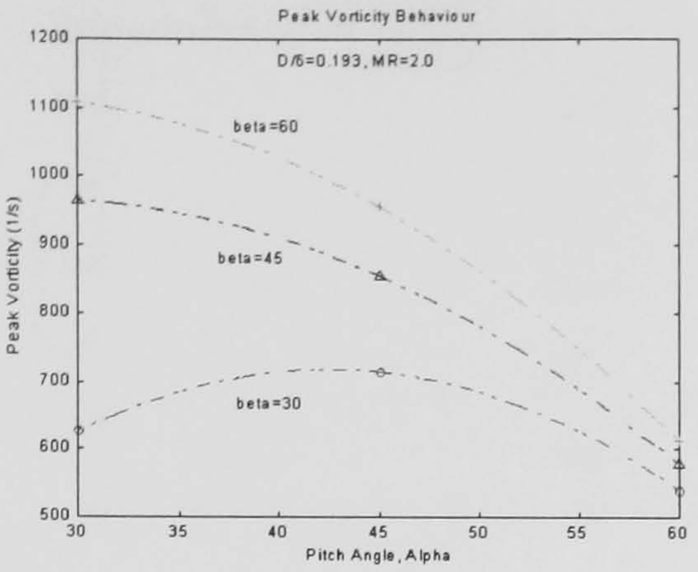

(a) Variation in Jet Pitch

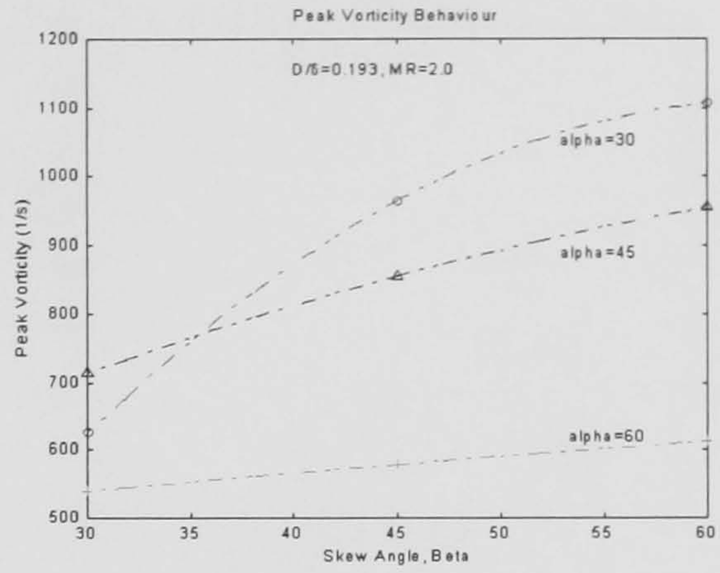

(b) Variation in Jet Skew

Half-Life Radius

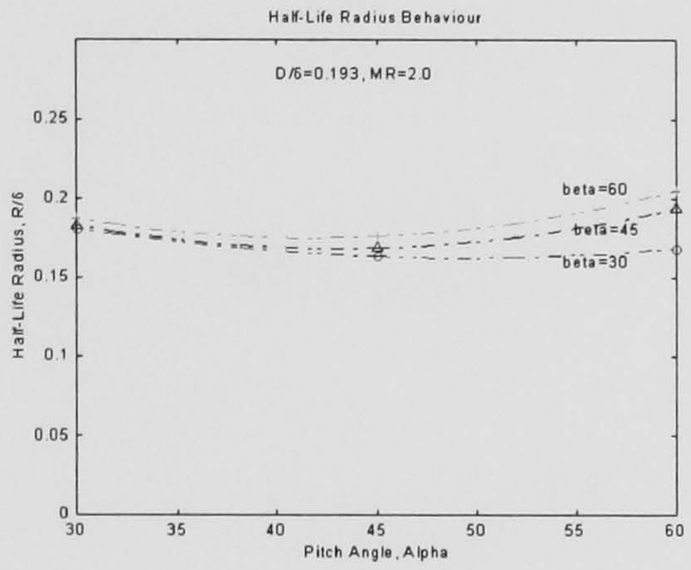

(c) Variation in Jet Pitch

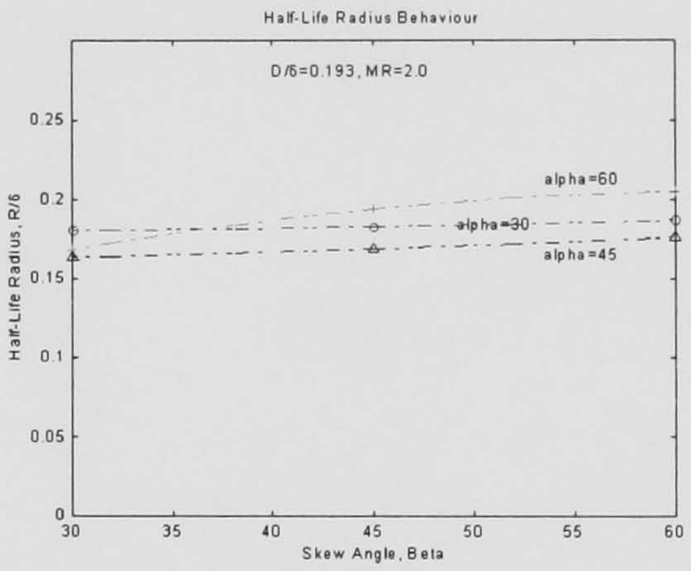

(d) Variation in Jet Skew

Figure 45: Effect of Jet Pitch & Skew Angles: $D/\delta = 0.289$, MR = 2.0

Peak Vorticity

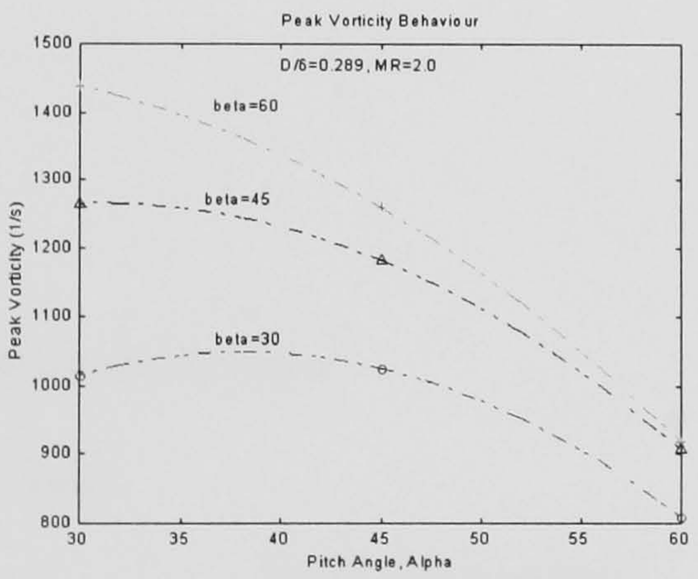

(a) Variation in Jet Pitch

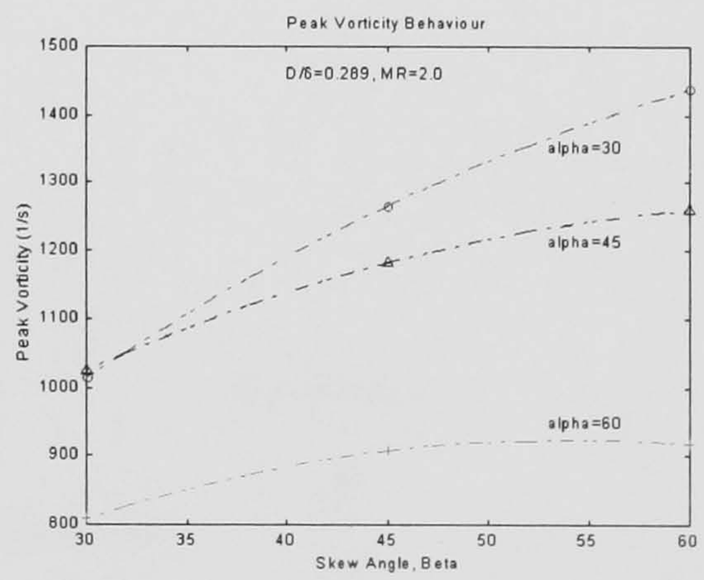

(b) Variation in Jet Skew

Half-Life Radius

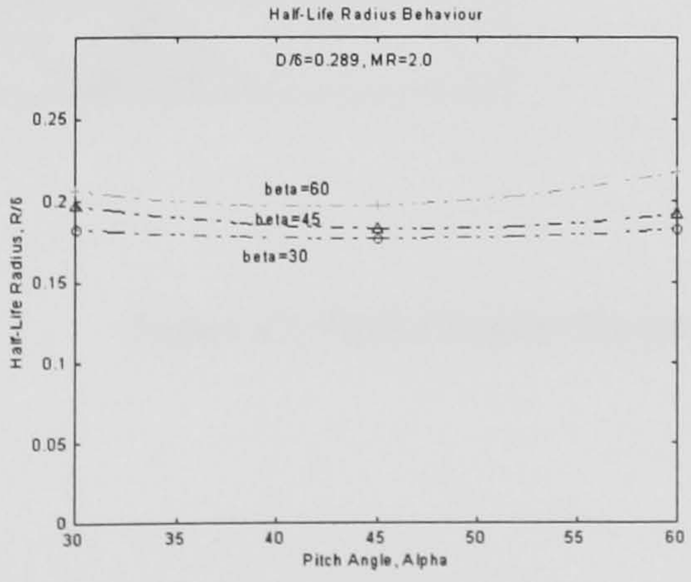

(c) Variation in Jet Pitch

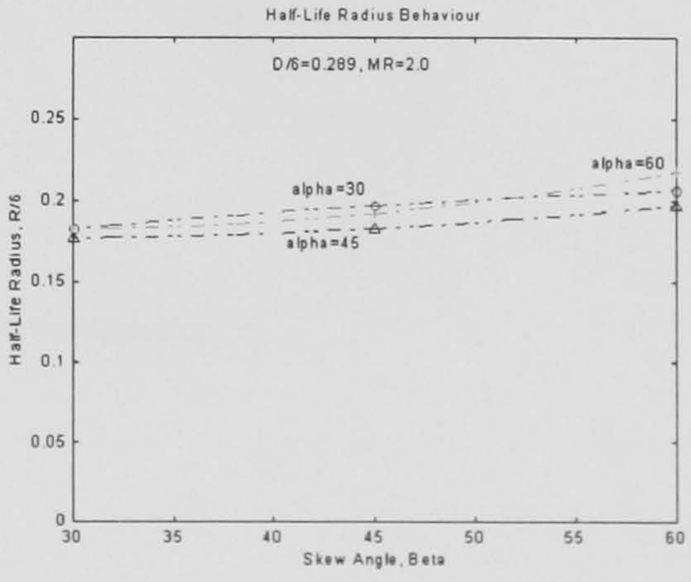

(d) Variation in Jet Skew

Figure 46: Effect of Hole Diameter Ratio & Mach Number Ratio: $\alpha = 45°$, $\beta = 45°$

Peak Vorticity

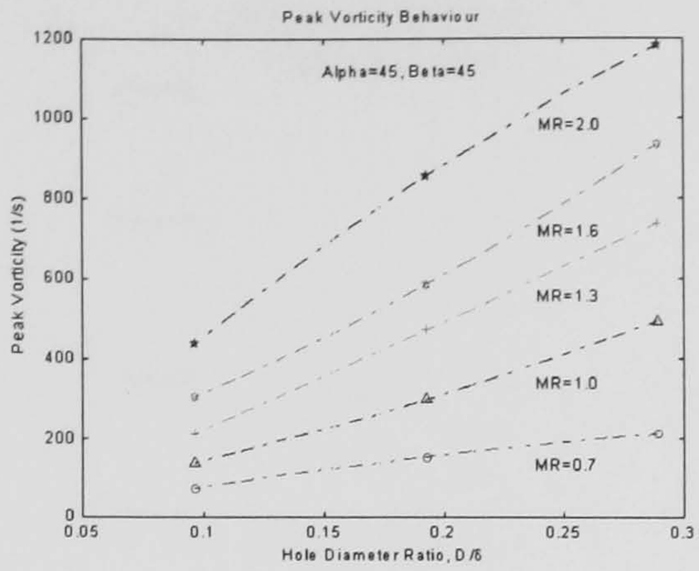

(a) Variation in Hole Diameter Ratio

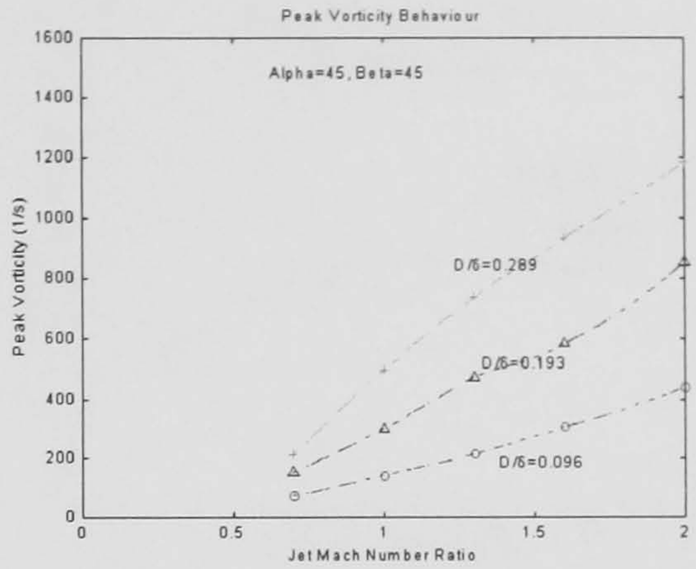

(b) Variation in Mach Number Ratio

Half-Life Radius

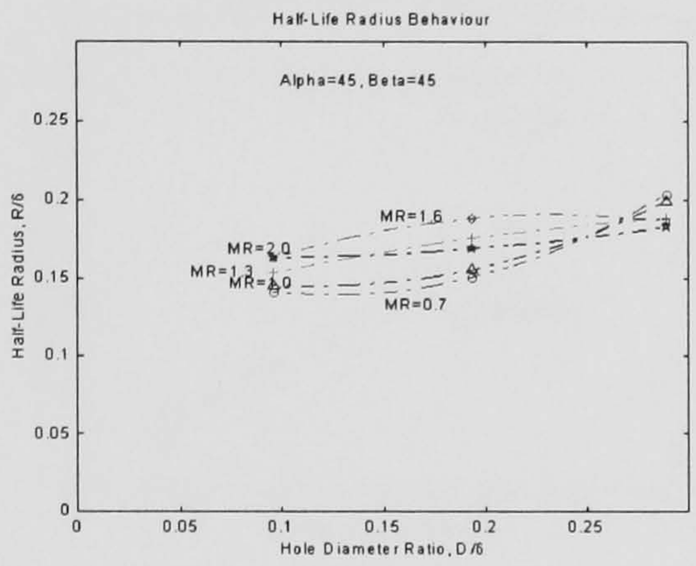

(c) Variation in Hole Diameter Ratio

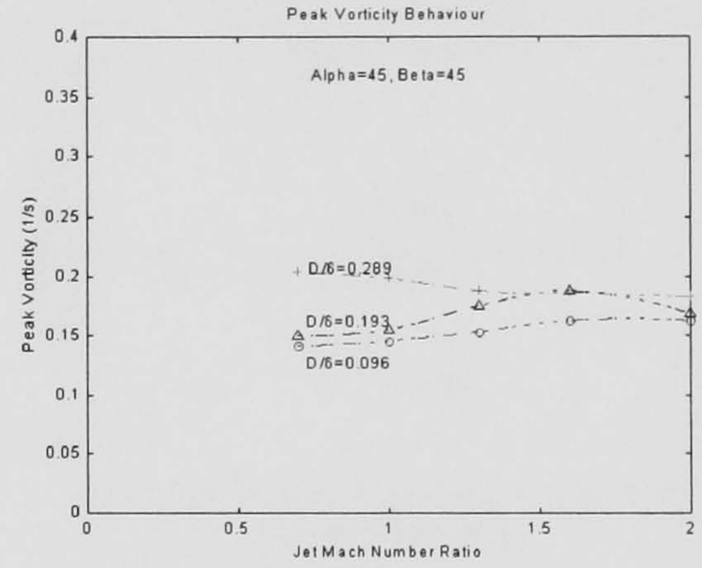

(d) Variation in Mach Number Ratio

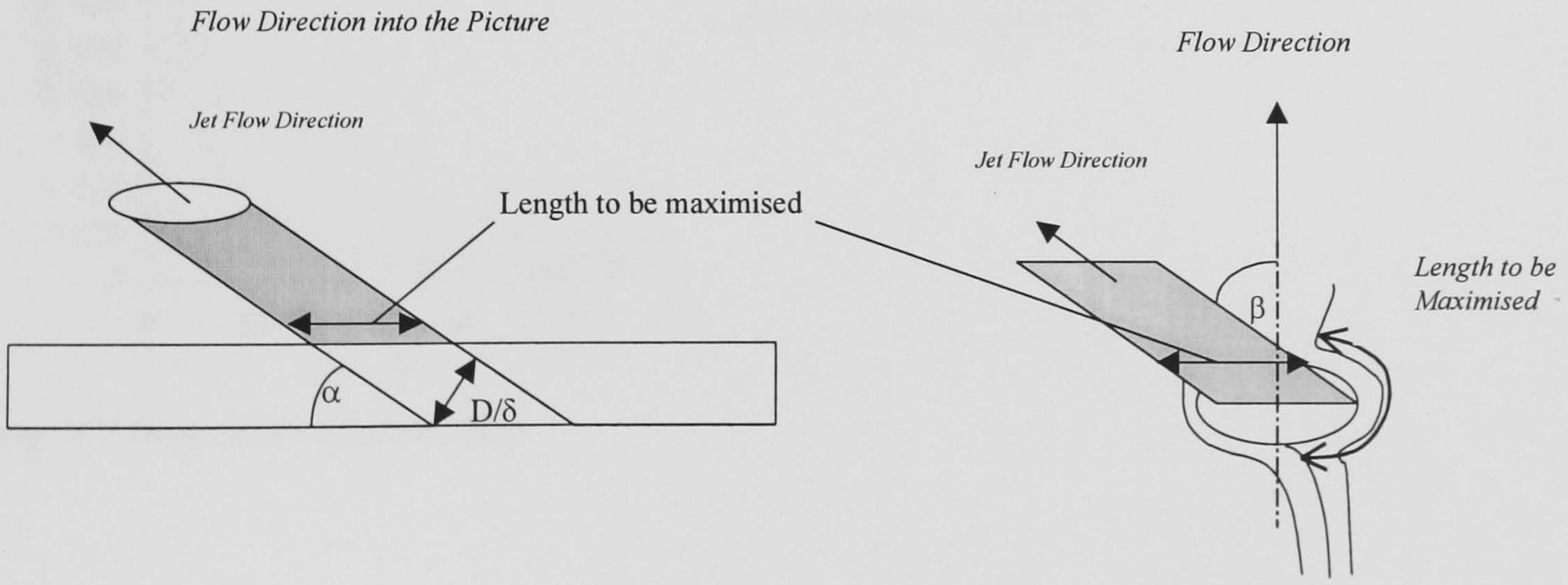

Figure 47: Peak Vorticity Maximisation Parameters

Figure 48: Effect of Streamwise Distance Ratio: $\alpha = 45°$, $\beta = 45°$

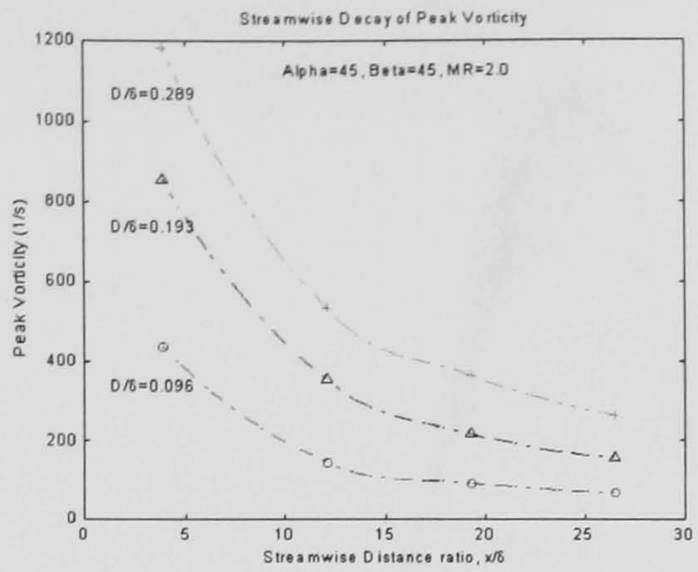

(a) Peak Vorticity

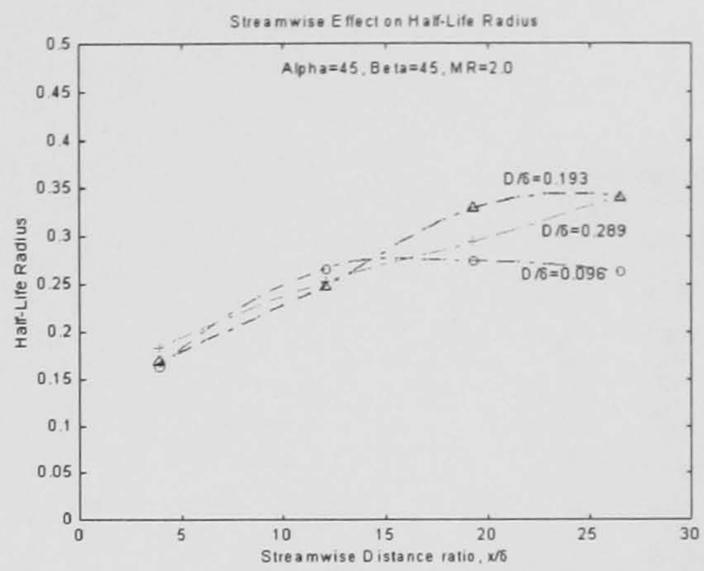

(b) Half-life Radius

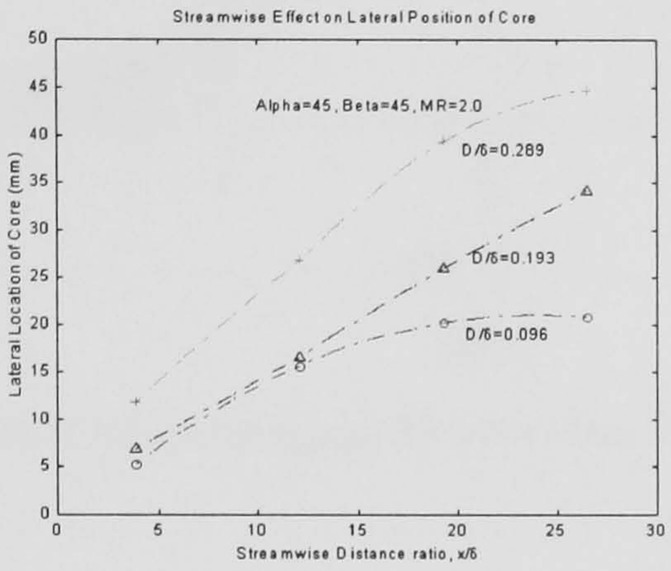

(c) Lateral Position

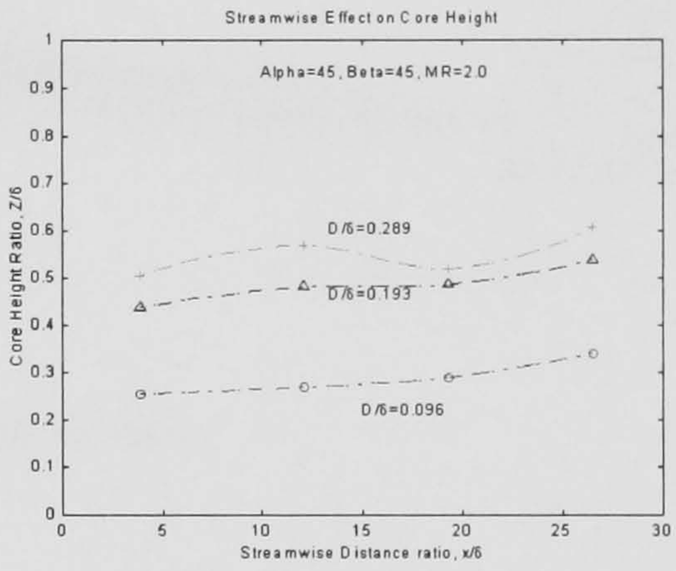

(d) Vortex Height From Wall

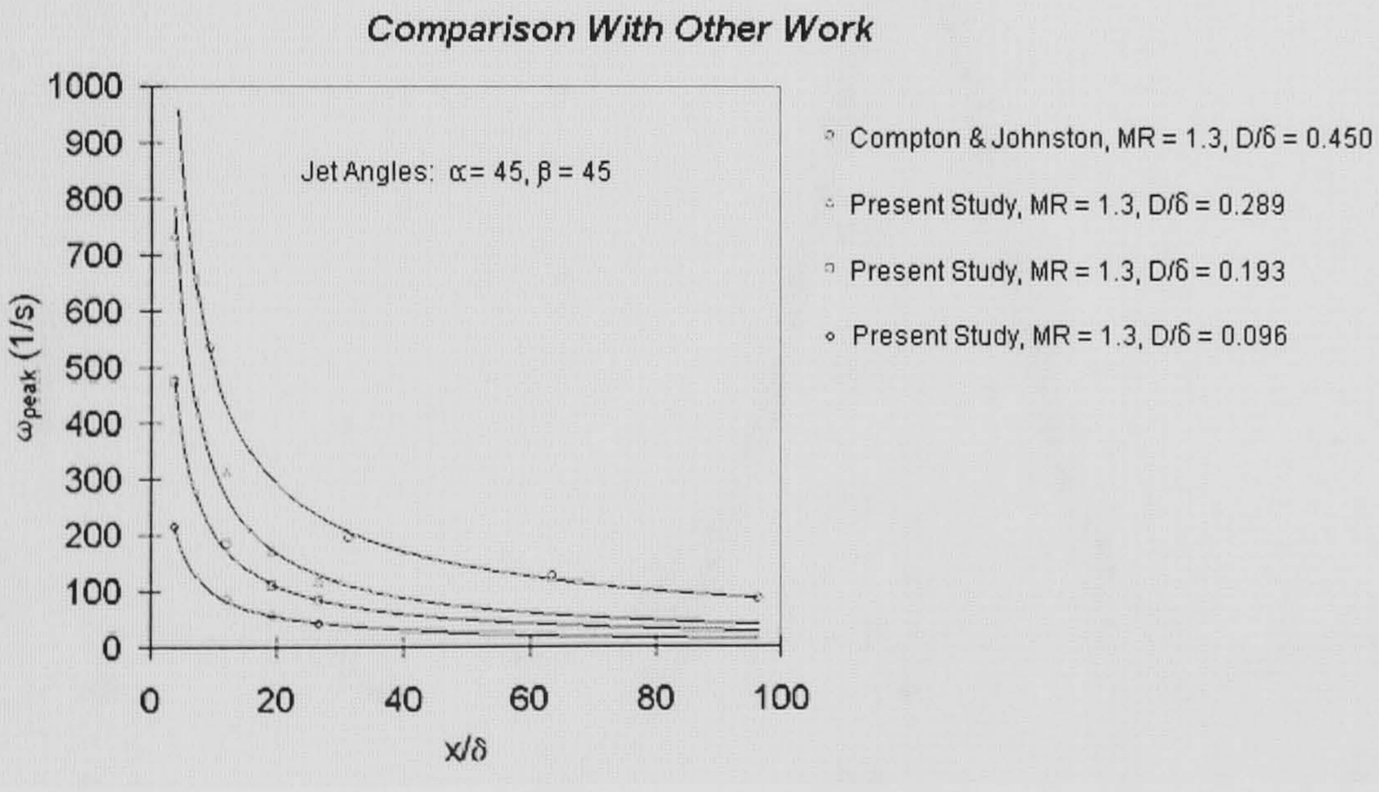

Figure 49: Comparison with Other Work

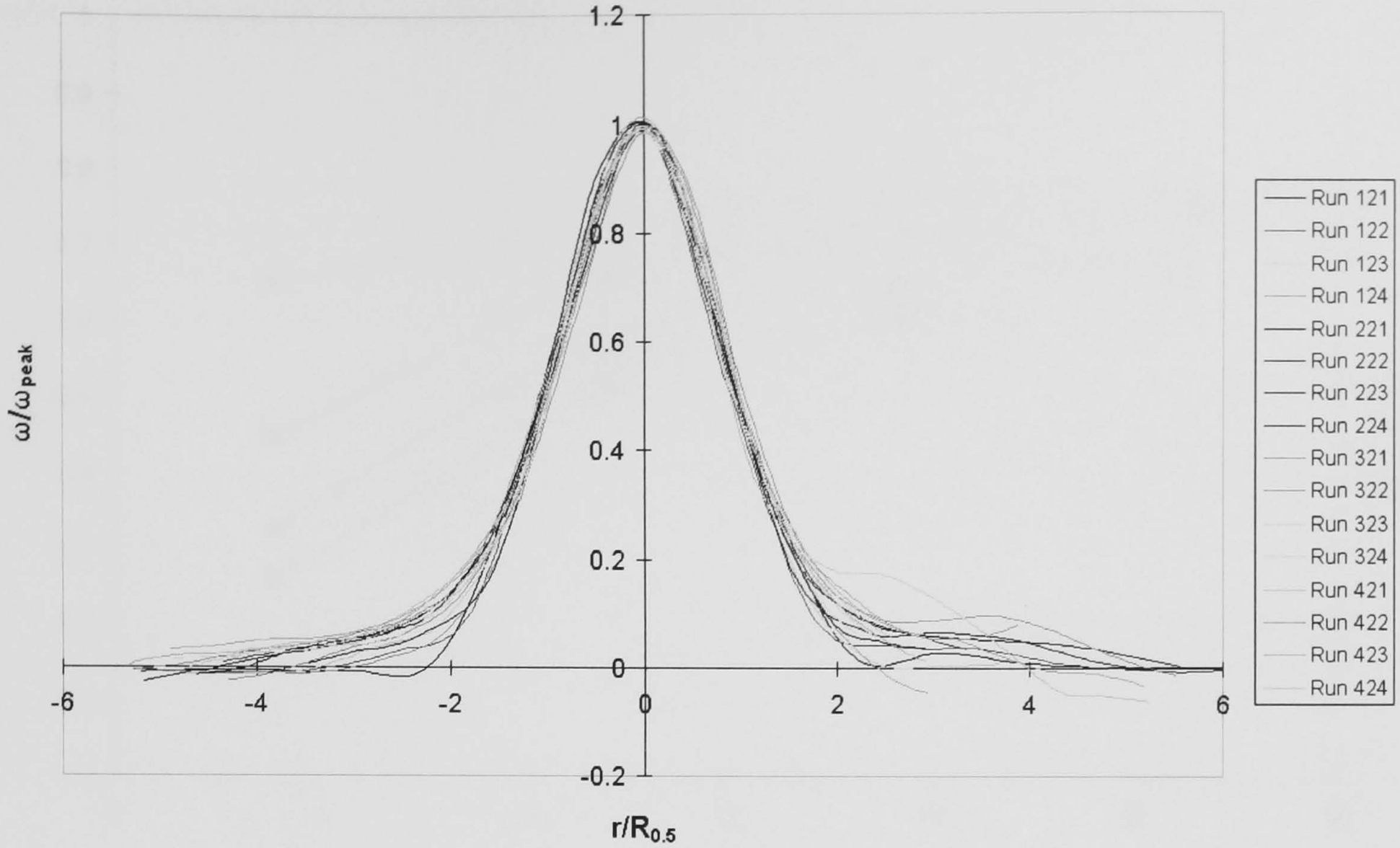

Figure 50: Non-dimensionalised Vorticity (ω/ω_{peak}) for some Vane-Produced Vortices

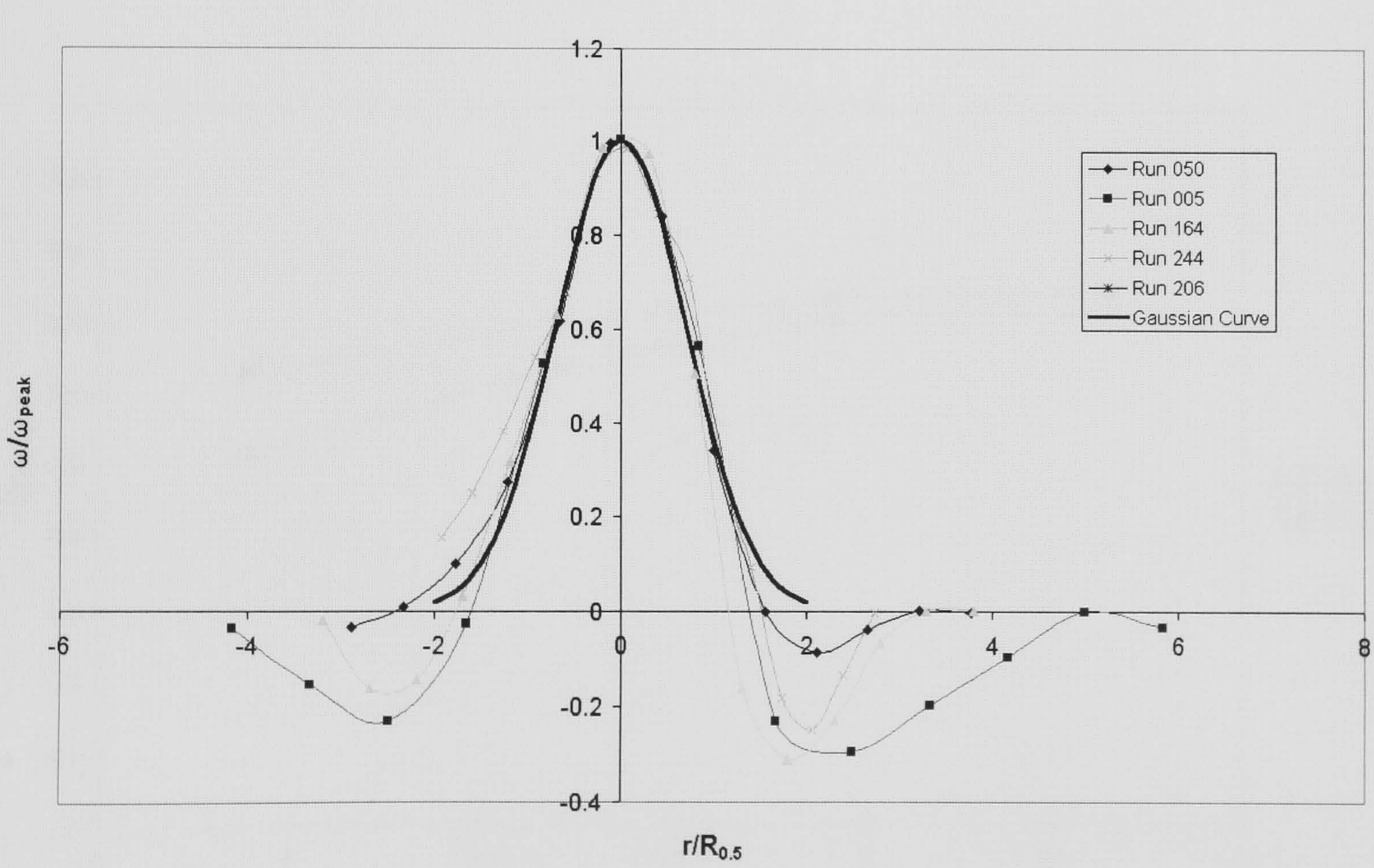

Figure 51: Non-dimensionalised Vorticity (ω/ω_{peak}) for some Air-jet-Produced Vortices

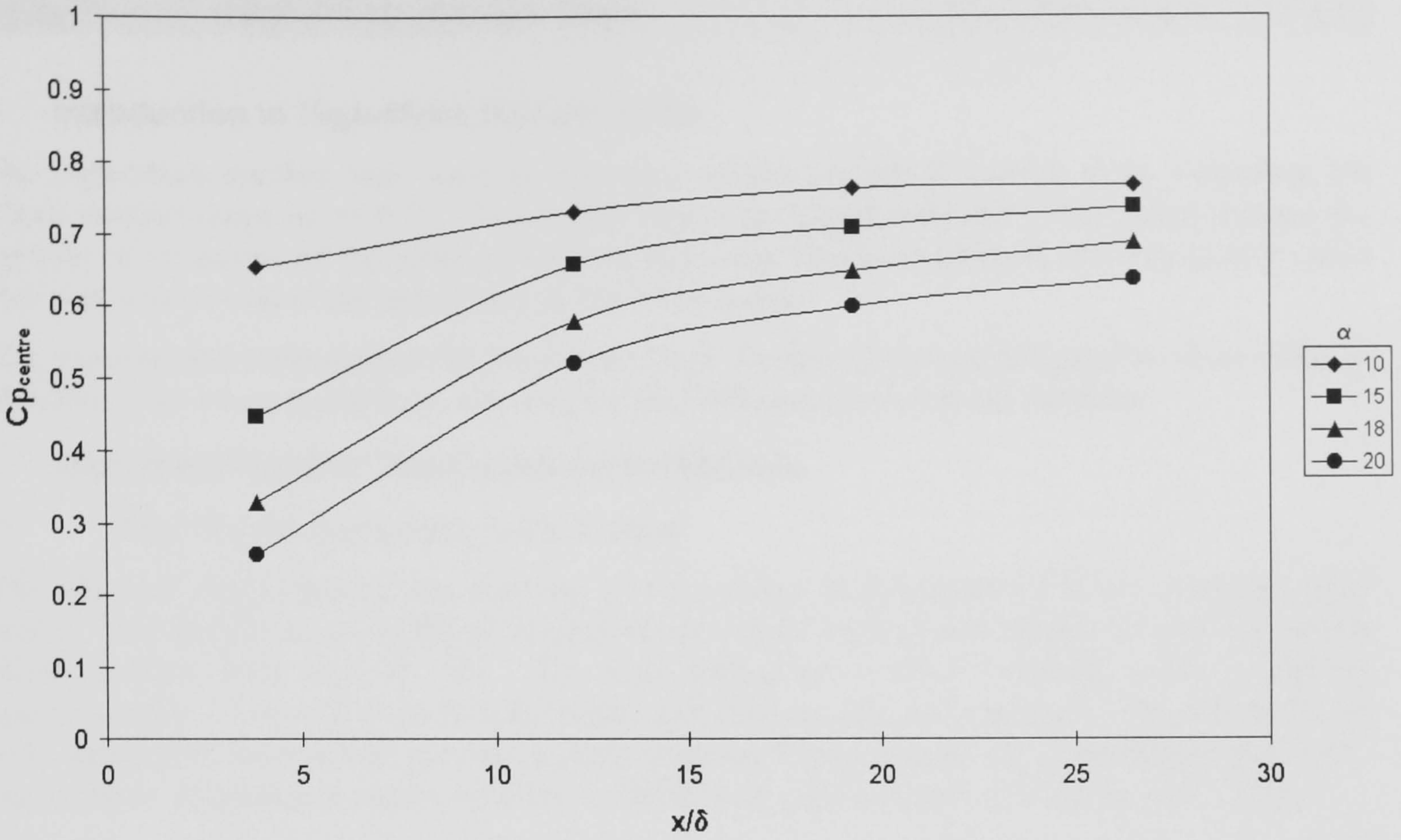

Figure 52: Vortex Centre-line Pressure Coefficients for Vane-Produced Vortices ($h/\delta = 0.554$)

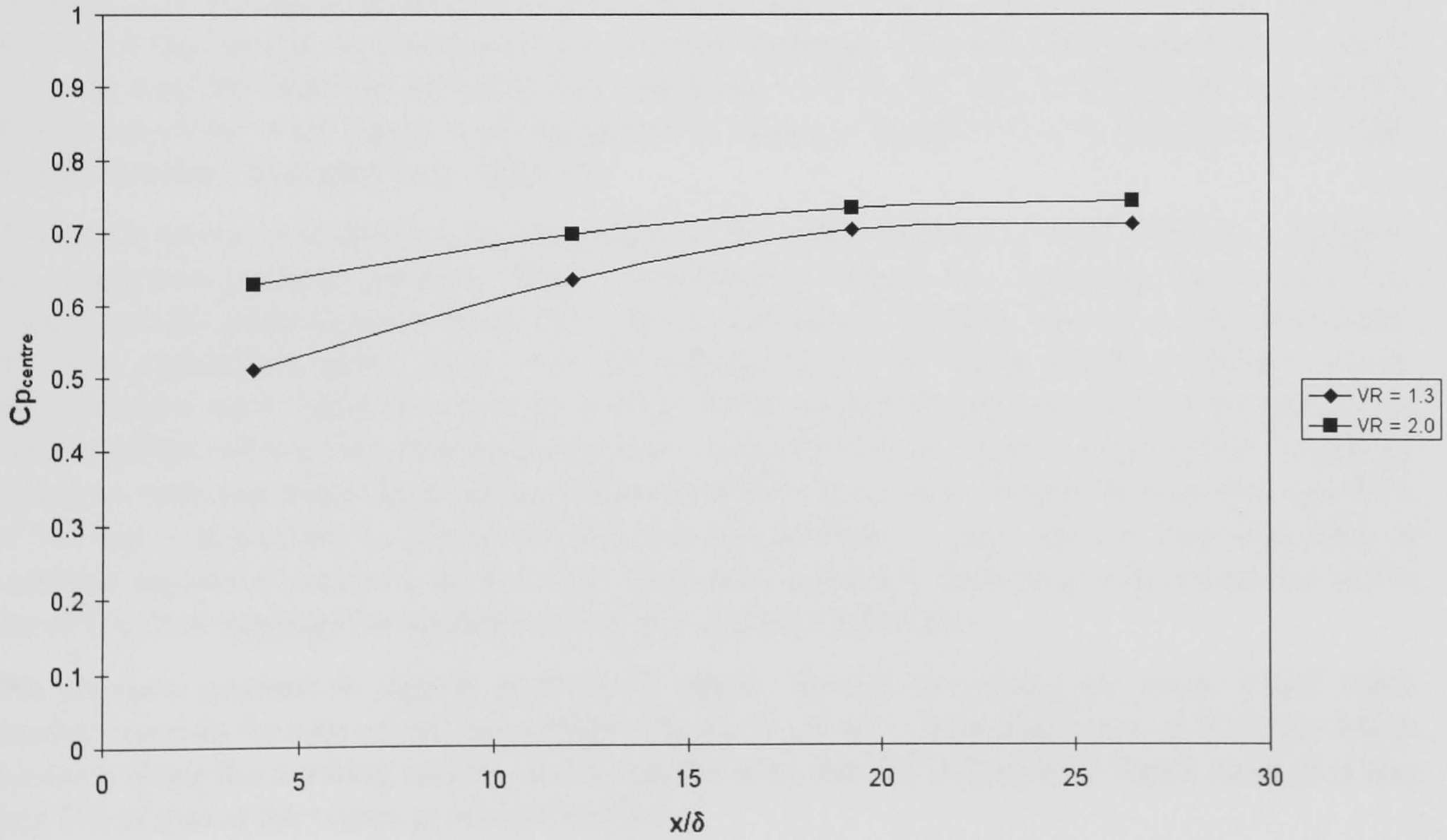

Figure 53: Vortex Centre-line Pressure Coefficients for Air-jet-Produced Vortices ($D/\delta = 0.193$, $\alpha = 30°$, $\beta = 60°$, $M = 0.0588$)

Chapter 7 - High-Mach Number Tests

7.1 - Introduction to High-Mach Number Tests

The high-Mach number tests were an extension of the low-Mach number tests, extending the Mach number range up to 0.75. Due to the high cost of high-subsonic wind tunnel testing, the number of variations of the other parameters was more closely controlled, and this higher speed data was used to extend the trends seen at the lower speed.

The experimental arrangement for the higher Mach number tests was designed to be as close as possible to the lower speed tests, allowing for the differences between the facilities.

7.2 - High-Mach Number Test Experimental Methods

7.2.1 - Wind Tunnel & boundary Layer studies

The effect of Mach number was assessed in the College of Aeronautics 9"x7½" transonic wind tunnel. This facility is a continuous running closed-circuit wind tunnel capable of working section Mach numbers from 0.45 to 1.05. The wind tunnel has a usable working section length of approximately 1.5 m, and is fitted with slotted wall liners on the roof and floor. The side walls are solid removable doors which may be of either glass or metal construction. This facility has a sub-atmospheric stagnation pressure, which is variable from 3 psi to 12 psi (20.7 kPa to 82.7 kPa).

An existing wind tunnel wall was modified for these tests, and this determined the position of the vortex generator station. The wall was fitted with a turntable window, with the centre of rotation being located at 478 mm from the end of the contraction cone curvature. Preliminary boundary layer studies showed that the natural boundary layer at this location was 8 mm with a turbulent $1/7^{th}$ power law profile (measured at M = 0.6, and a stagnation pressure, H_0 = 6 psi (41.4 kPa). In order to increase the boundary layer thickness (to make the experimental scaling larger), a 2 mm diameter wire was taped against the wall of the contraction cone at a distance of 75 mm before the end of the contraction cone curvature (i.e. 553 mm upstream from the vortex generator location). This trip wire increased the boundary layer thickness to 20.0 mm with a $1/7^{th}$ power law profile. A diagram of the wind tunnel working section is shown in Figure 54, as is the vortex generator station boundary layer profile in Figure 55.

Wall static pressure measurements were made in the empty working section in order to quantify the streamwise pressure gradient. Data is presented in Figure 56. Since there were only four tappings on the sidewall (over which the vortex would pass), measurements were also taken along the floor centre-line where there were 20 tappings along the length of the working section. Measurements were taken over a range of wind tunnel stagnation pressures and at the middle test Mach number. shows the streamwise pressure measurements at varying wind tunnel stagnation pressures, with one result showing the tripped boundary layer case. It may be seen that the effect of the trip is negligible on the streamwise pressure gradient. It may also be seen that there is excellent agreement between the wall and floor static pressures, thereby giving confidence in the use of the floor tappings for streamwise pressure gradient definition.

The pressure gradient is slightly positive in nature, thereby decreasing the wind tunnel Mach number towards the rear of the test section. Figure 57 shows a normalised plot of the floor Mach numbers along the working section, and it may be seen that the reduction in Mach number is less than 5% of that at the vortex generator location.

7.2.2 - Vortex Generators and Mounting

The vortex generators under consideration were both of the vane and air-jet type. The devices were mounted at the centre of a turntable window. Since the wind tunnel would be operating at a

sub-atmospheric pressure, to allow the turntable to rotate during a run, the turntable was mounted on thrust bearings, and had a mechanical chain drive to allow rotation.

The turntable was 300 mm in diameter, and the centre section allowed the positioning of plug that contained the vortex generator models.

Vane Vortex Generator

Following from the low speed experiments, fewer experimental data points were chosen, since the task was to extend the existing database, rather than to define a new database. One vortex generator height was chosen, $h/\delta = 0.75$. Similarly, only two incidence values were chosen, 15° and 20°. Three downstream distance ratios were chosen: $x/\delta = 8.75$, 16.25, 23.75. These configurations were tested at free-stream Mach numbers of 0.45, 0.60, and 0.75.

Air-jet Vortex Generators

As with the vanes, the air-jet database was to be extended by choosing fewer data points. Hole diameters of 3 mm and 6 mm ($D/\delta = 0.15$, 0.3) were chosen with pitch angles of 30° and 45°, and skew angles of 30°, 45°, and 60°. The jet Mach number ratio was set at 2.0, and the free-stream Mach number was set at 0.50, 0.60, and 0.75. These configurations were tested at one downstream station ($x/\delta = 8.75$).

Further downstream tests were made, but with fewer generator variables being changes. Tests at the downstream distances of $x/\delta = 16.25$, 23.75 and 31.25 were carried out with: $D/\delta = 0.15$, 0.3; pitch angle, $\alpha = 45°$; skew angle, $\beta = 45°$; Mach number ratio = 2.0; free-stream Mach number = 0.5, 0.6, 0.75.

Air-jet Calibration

As with the low speed tests in the previous Chapter, the air-jets were calibrated to give an accurate knowledge of the air-jet total pressure profile. This would allow the definition of a velocity ratio (or Mach number ratio) to be defined. Since the low speed test had shown that the entrance to the jet orifice was critical to the profile of the jet, the jets for the high-speed test were designed with bell-mouth intakes.

Following on from the low speed tests, the total pressure profiles of the air-jets were measured with a variety of jet plenum pressure, such that calibrations could be obtained which were independent of jet Mach number. The total pressure was measured with a piece of 0.5 mm hypodermic tubing that was traversed across the jet exit plane. Calibrations were obtained which were independent of Mach number. These calibrations are presented below:

Table 15: Air-jet Nozzle Calibration Constants

Air-jet	k_{jet}
$D/\delta = 0.15$, $\alpha = 30°$	**0.82167**
$D/\delta = 0.15$, $\alpha = 45°$	**0.89075**
$D/\delta = 0.30$, $\alpha = 30°$	**0.90700**
$D/\delta = 0.30$, $\alpha = 45°$	**0.88567**

Using these values, and by measuring the plenum total pressure and free-stream static pressure, the jet Mach number can be found as follows:

$$M_{jet} = \sqrt{\frac{2}{(\gamma - 1)}\left[\left(\frac{H_{jet}}{p_0}\right)^{\gamma - 1/\gamma} - 1\right]}$$

where

$$H_{jet} = k_{jet} H_{plenum} + \left(1 - k_{jet}\right) p_0$$

Equation 45

so:

$$MR = \frac{M_{jet}}{M_0}$$

7.2.3 - Measurement Method - 5 Hole Pressure probe

As with the low speed test, the vorticity was calculated using the cross-stream velocity vectors measured by a 5-hole pressure probe. A new 5 hole pressure probe was designed and built for the high speed test, with a probe tip diameter of 1.7 mm. This allowed greater accuracy when used in the smaller scale of this test (compared with the 2.5 mm probe which was used for the low speed test).

The 5 hole probe was calibrated in the DERA Bedford 0.1016 m (4") wind tunnel. This wind tunnel is capable of free-stream Mach numbers from 0.1 to 0.75[56]. A gimbal fitting is mounted in a section behind the working section that allows the simultaneous pitch and yaw of a probe while the probe tip is kept in the same location in the flow. The probe was calibrated over a wide Mach number range (0.2 to 0.7 in 0.1 increments), and over a wide pitch and yaw range (± 25° simultaneous pitch and yaw). A full description of the calibration method, together with the calibration data, is given in the Appendices.

When used for taking data, the probe was traversed over a cross-stream grid of locations, and the pressures at each location were sampled.

7.2.4 - Traverse Gear Installation

Due to the tight confines of the 9" x 7½" wind tunnel working section, the traverse could not be mounted in the same manner as for the low-Mach number tests. The addition of the traverse within the working section would have increased the wind tunnel blockage to a point that the achievement of the high Mach numbers needed would have become questionable.

As a result, it was decided that the traverse mechanism should be mounted externally from the wind tunnel working section, and that the probe should pass through lateral slots in the wind tunnel wall. When the slots were not being used, they were filled with airtight plugs. In order that the wind tunnel be operated below atmospheric pressure, the traverse was encased in a plenum chamber. This is shown in Plate 1 below.

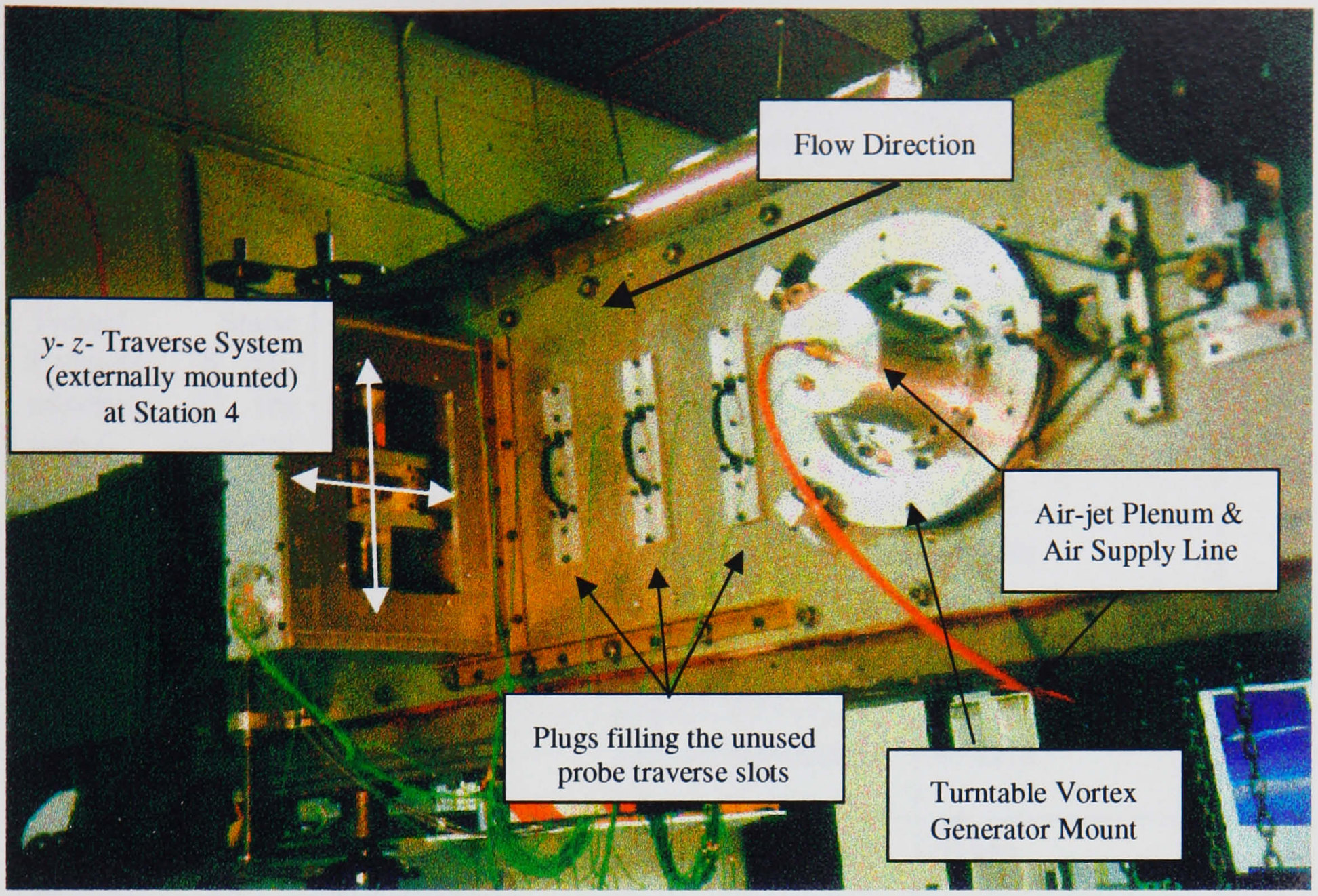

Plate 1: 9"x7½" Transonic Wind Tunnel fitted with 2-Axis Traverse and Vortex Generator turntable

7.2.5 - Data Acquisition

Data acquisition was carried out using a Personal Computer (PC) based system that carried out both the traverse motion control and the Analogue-to-Digital conversion of the readings from pressure transducers.

Transducers

The transducers were used to sample all pressures/temperatures in the wind tunnel. The transducers are listed in the following table.

Table 16: High Mach Number Test Transducer Details

Flow Parameter	Transducer Type	Transducer Range	Serial Number
Tunnel Stagnation Pressure (measured in the settling chamber)	Druck PDCR10	15 psi absolute	199579
Tunnel Static Pressure (16 mm upstream of the vortex generator station)	Druck PDCR10	15 psi absolute	199578
5-Hole Probe Port No. 1	Druck PDCR10/35L	±350 mbar differential	362546
5-Hole Probe Port No. 2	Druck PDCR10/35L	±350 mbar differential	492108
5-Hole Probe Port No. 3	Druck PDCR10/35L	±5 psi differential	472353
5-Hole Probe Port No. 4	Druck PDCR10/35L	±5 psi differential	23882
5-Hole Probe Port No. 5	Druck PDCR10/35L	±5 psi differential	783401
Air-jet Plenum Pressure	Druck PDCR 820-0800	7 bar gauge	316258
Total temperature (settling chamber)	National Semiconductors LM35CZ	-40°C - 110°C	-

As listed above, the wind tunnel stagnation pressure was measured by an absolute pressure transducer, which was connected to a Pitot tube in the wind tunnel settling chamber. The wind tunnel reference static was taken from the floor static pressure tapping that was closest to the vortex generator model location. The wind tunnel total temperature was measured using a temperature transducer located with the Pitot tube in the settling chamber.

The pressures from the 5-hole probe were measured using differential transducers. The pressure measurements were all to be made with reference to the wind tunnel static pressure. However, since it would have been bad practice to interfere with the wind tunnel static pressure connection, the next wall static pressure tapping was used, and a calibration made to allow for the difference in pressure reading between the two tappings.

The signals from the transducers were passed though voltage amplifiers with gains that would give the optimum voltage level for the PC to read, thus using as much of the sensitivity of the analogue-to-digital converter as possible. The amplifiers were fitted with frequency filters, and 100 Hz cut-off filters were applied to help reduce the electrical noise on the transducer channels.

Transducers were calibrated using a vacuum chamber system to which an accurate Druck transducer was connected.

Acquisition Control

A stated earlier, the data acquisition was PC based, where a single program was used to sample the outputs from the pressure transducers, and to move the traverse mounted probe between data points. The grid of data was set by user input, and the program looped until all the measurements had been taken.

The analogue-to-digital converter was a National Instruments AT-MIO-16E-10 PC mounted card with a 12-bit resolution. Data were sampled at a frequency of 300 Hz, over a time period of 5 seconds. The 1500 samples per channel were then averaged to reduce the effect of any noise. The transducers were connected using a 1 mm bore flexible tubing, and it was found that, over the lengths in use (about 4 m), a time period of around 6 seconds was needed to allow the pressures to stabilise before any samples were taken.

Motion of the traverse was achieved through a PC operated stepper-motor drive system. Two axes could be controlled simultaneously, allowing fully automated movement in the *y*- and *z*- axes.

The controlling program was a purpose-written code in Microsoft Visual Basic, running under the Microsoft Windows environment. This program not only controlled the motion, and sampled the data, but gave on-line wind tunnel reference data (Mach number, stagnation pressure, stagnation temperature), and location of the probe. Also, basic conversion of the raw voltage data to pressure, temperature and Mach number was also carried out, allowing this derived data to be written to disk (along with the raw data). With this data saved to disk, the more computationally demanding post-processing could be carried out off-line after the test run.

7.2.6 - Data Reduction

All off-line data reduction was carried out using the MathsWorks Matlab maths software. Data could be read in from data files, and Matlab could execute a script type code which would perform all of the mathematical analysis needed.

The data, which formed the input to the code, included: the probe *y*- and *z*- co-ordinates; the wind tunnel stagnation and static pressures; the wind tunnel stagnation temperature; the five pressures measured from the 5-hole probe; and in the case of the air-jet vortex generators, the air-jet plenum pressure.

The 5-hole probe had been calibrated at Mach numbers from 0.2 to 0.7 in 0.1 intervals. Initially, software was written which selected the most appropriate calibration data set for each individual data point. However, the computational effort required was immense, and the code took too great a time to execute. It was noticed that the Mach number effect on the probe calibration was very small, and it was decided that a more computationally efficient manner of reducing the data would be to use a calibration data set, which corresponded to the free-stream Mach number. The data reduction was then similar to that carried out for the low speed test. However, rather than dealing with velocity vectors, the calibration was made in terms of Mach number vectors, with a conversion from mach number to velocity based on the local speed of sound.

Thus, the first set was to find the free-stream Mach number at the vortex generator station using the formula:

$$M_0 = \sqrt{\frac{2}{\gamma - 1}\left[\left(\frac{H_0}{p_0}\right)^{\frac{\gamma-1}{\gamma}} - 1\right]}$$

Equation 46

With the free-stream Mach number calculated, the calibration data set could be chosen, and thus the pressure data was reduced to coefficient form for the comparison. Pitch and Yaw coefficients were defined as follows:

$$Cp_\theta = \frac{p_2 - p_4}{p_5 - p_{avg}}$$

$$Cp_\phi = \frac{p_3 - p_1}{p_5 - p_{avg}}$$

Equation 47

Where θ and ϕ represent the pitch and yaw angles respectively, p_n refers to the pressure from each of the n tubes of the 5-hole probe, and p_{avg} refers to the average of the four outer tubes (i.e. p_1 to p_4).

As with the low-Mach number case, the experimentally obtained values of Cp_ϕ and Cp_θ were compared with the data obtained in calibration, in order to find the actual pith and yaw angles of the flow at the probe tip. This was achieved by a fine interpolation of the relatively coarse (as large as 5° between calibration data points) calibration data. The experimentally obtained values of Cp_ϕ and Cp_θ could then be compared with the closest pair of calibration data values to find the pitch and yaw angles to within 0.5°.

With the pitch and yaw angles found, these values could be used to find the remaining two pressure coefficients in the calibration process, which relate the centre tube pressure and the pressure average of the outer tube to the local total and static pressures:

Equation 48

$$Cp_5 = \frac{p_5 - p_o}{H_{local} - p_{local}}$$

$$Cp_{avg} = \frac{p_{avg} - p_0}{H_{local} - p_{local}}$$

With the values of Cp_5 and Cp_{avg} being read from the calibration data and the values of p_5 and p_{avg} being measured experimentally, these equations can be solved simultaneously to yield the local stagnation and static pressures.

$$\begin{bmatrix} p_5 \\ p_{avg} \end{bmatrix} = \begin{bmatrix} Cp_5 & 1 - Cp_5 \\ Cp_{avg} & 1 - Cp_{avg} \end{bmatrix} \begin{bmatrix} H_{local} \\ p_{local} \end{bmatrix}$$

Equation 49

$$\begin{bmatrix} H_{local} \\ p_{local} \end{bmatrix} = \frac{\begin{bmatrix} 1 - Cp_{avg} & Cp_5 - 1 \\ -Cp_{avg} & Cp_5 \end{bmatrix}}{Cp_5 - Cp_{avg}} \begin{bmatrix} p_5 \\ p_{avg} \end{bmatrix}$$

Using the values of local stagnation and static pressure (H_{local} and p_{local} respectively), the magnitude of the Mach number vector can be found at the probe tip. Since the flow was adiabatic, the total temperature of the flow at the probe tip would be the same as the total temperature of the wind tunnel in the settling chamber. Thus, the local static temperature can be found (knowing the total temperature and local Mach number), and thus the local speed of sound can be calculated. Thus the Mach number can be converted to a flow velocity.

Equation 50

$$M_{local} = \sqrt{\frac{2}{\gamma - 1}\left[\left(\frac{H_{local}}{p_{local}}\right)^{\frac{\gamma-1}{\gamma}} - 1\right]}$$

Equation 52

$$T_{local} = \frac{T_0}{1 + \frac{\gamma-1}{2} M^2}$$

Equation 51

$$\overline{V_{local}} = M_{local} a_{local} = M_{local} \sqrt{\gamma R T_{local}}$$

With the local velocity vector and the pitch and yaw angles, the velocity vector can be decomposed in to the three components of velocity: the streamwise component, u; and the two cross-stream components, v and w.

$$u_{local} = \overline{V_{local}} \cos\theta \cos\phi$$

$$v_{local} = \overline{V_{local}} \cos\theta \sin\phi$$

$$w_{local} = \overline{V_{local}} \sin\theta$$

The vorticity is then defined as the curl of the velocity vector or, the spacial differentiation of the cross-stream velocity vectors.

The differentiation above was carried out in the Matlab programming environment, using pre-written function libraries.

Equation 53

$$\omega_x = \frac{\partial w}{\partial y} - \frac{\partial v}{\partial z}$$

7.3 - Repeatability & Error Analysis

7.3.1 - Grid Spacing

Since this experiment was closely modelled from the low-Mach number test, it was decided that a grid spacing of similar scale should be used. Where as the low-Mach number grid spacing had been set to 5 mm in both ordinates (in a boundary layer of 41.5 mm), for the higher-Mach number tests, it was decided that a 3 mm grid spacing should be used (in a boundary layer of 20 mm).

The scaling philosophy was chosen since, it was important to try to capture a similar amount of data within the vortex. Since the vortex was scaled with the boundary layer thickness, it was reasonable that the 3 mm spacing should give sufficient data to allow interpolation without increasing the run time significantly.

7.3.2 - Effect of Selecting A Single Calibration Data Set

It has been stated that, in order to reduce the time needed for data reduction, the calibration data set was chosen as that for the experimental free-stream Mach number. In order to assess the effect of this decision, and the insensitivity of the probe to Mach number, a single data point was processed with a number of different Mach number calibration data sets. Results are presented in Figure 58.

Choosing an air-jet generated vortex (from a 6 mm jet at 45° pitch, 45° yaw, $MR = 1.6$, $M_\infty = 0.5$), data reduction was carried out using three calibration data sets, one at $M_\infty = 0.2$, one at $M_\infty = 0.5$, and one at $M_\infty = 0.7$). This spread of Mach number calibration data sets spans the entire range of calibration data.

It can be seen in the plot that the interpolated contour lines lie almost on top of each other, with the significant part of the difference being due to the interpolation process, rather than the raw data itself. Based on the results of this analysis, the data reduction method was deemed valid.

7.3.3 - Repeatability

A repeat run was made in order to assess the repeatability of the technique. Using an air-jet generated vortex (using a 3 mm jet, 45° pitch, 45° yaw, $M_\infty = 0.75$, $MR = 1.6$), the two runs were reduced, and the data is presented in Figure 59.

While the size of the vortex is relatively small, it may be seen that the interpolated contour lines lies within 0.5 mm of each other, highlighting the excellent degree of repeatability in this case. It is suggested that any difference in the interpolated vorticity result be derived from the tendency of

the wind tunnel and the air-jet to wander in velocity. It was therefore important that the operator was careful in monitoring the test conditions.

7.3.4 - Errors

The errors can be traced to a number of different areas, which can be broadly defined as those associated with the process of data acquisition and those with data reduction.

Data Acquisition Errors

The acquisition errors are sourced from the equipment errors.

Transducers – Pressure transducer calibrations were found to be consistent and repeatable to within 0.25%. Using a 12-bit analogue-to-digital converter, which could read to an precision of 1 mV, an reading error on each transducer (assuming a sufficiently long settling time had been allowed for) of ±100 Pa . Typical readings were in the region of 50,000 Pa, giving an error in the order of 0.1%.

Traverse Positioning – The positioning error of the traverse was linked to the resolution of the positioning system. The traverse mechanism used a 0.5 mm pitch lead screw to drive the traverse carriage, thus one rotation of the stepper motor would yield 0.5 mm of travel. The motors were 200 step/rev motors, thus giving the motion system a nominal precision of 0.0025 mm. The carriages were fitted with anti-backlash nuts, through which this effect could be reduced. While not all of the backlash could be successfully removed (since the nuts would then pitch too hard on the lead screw), backlash was reduced to a measured value of 0.02 mm. Since the traverse was repositioned at the beginning of each run, and the traverse was moved in an S pattern, the maximum error in positioning is considered to be no more than this backlash error value.

Data Reduction Errors

As stated earlier, all the off-line data reduction was carried out using the MathWorks Inc. Matlab software. The package uses pre-written libraries to carry out certain mathematical functions. Those used for the data reduction include: the **`interp2()`** function and the **`gradient()`** function.

The interp2 function carries out the two dimensional interpolation of each data run, in order to increase the effective resolution of the data set. This allows the peak vorticity to found, and also helps to define the physical size of the vortex more accurately.

The gradient function carries out the two dimensional differentiation of the data set values, which allows the calculation of the vorticity.

While the accuracy of these functions has been accepted as excellent, the introduction of data points which include a significant error (maybe due to varying wind tunnel or air-jet conditions) will introduce and error.

Quantification of this error was not made, since the repeatability of the data set was excellent, and thus the effect of rogue data points could be viewed in this manner.

7.4 - High Mach Number Test Results

Qualitatively, the effect of Mach number on the vortices is small, except that the rotational speed of the vortex varies linearly with Mach number. The vortices still have the same appearance: an essentially inviscid line of rotating fluid, with a viscous core. It will be shown that the basic trends are similar, and the quantitative results for the vortices are presented.

7.4.1 - High Mach Number Vane Results

In the low speed study, the effect of the vane-height-to-boundary-layer-thickness ratio (h/δ) was demonstrated, and it was seen that the effect on the peak vorticity and the half-life radius was easy to predict. Thus, in order to limit the number of data points in the higher speed test, only one value was chosen. Incidence values of 15° and 20° were chosen. The basic trends in incidence had been determined, and thus values were needed at high Mach number to adjust these trends. The vortices were measured at three downstream stations in order to assess the decay characteristics. In total, (1 x 2 x 3 x 3 =) 18 data points were taken.

Effect of Mach Number

The local dynamic pressure ratios (i.e. the measure of physical distortion of the boundary layer) and the vorticity plots are similar in nature to the low-speed results. So as to be concise, they will not be displayed. However, the derived data from these planes of data are displayed in Figure 60 (a)–(d).

Referring to the effect on peak vorticity (Figure 60 (a)), it is clear that the peak vorticity increases with increasing Mach number, but that the relationship is non-linear. As Mach number is increased, the peak vorticity follows a line that can be approximated by a power law series, with the exponent taking a value of about 1.3. It may be expected that peak vorticity would be enhanced with increasing free-stream Mach number. As the free-stream Mach number increases, the pressure difference across the vortex generator will increase, and hence the strength of the vortex would increase. As the free-stream Mach number is increased linearly, it may be expected that the vorticity (or the fluid elemental rotational velocity) may increase linearly as well. The implication of the power law agreement is that as the compressibility effects become stronger, the peak vorticity is enhanced. Green[57] notes that as the effect of compressibility becomes stronger, the rotation of a vortex may cause the fluid particles to the 'thrown-out' from the centre of the vortex with more force, thereby reducing the density of the fluid in the core. This, too, would reduce the pressure gradients in the core, thereby increasing the vorticity levels. The effect of compressibility is to stretch the vortex, yielding higher levels of vorticity. Since the exponent of the power law appears to be constant for all of the results (to within experimental error), this suggests that the results at low speed can be extrapolated (so long as the basic trends are not Mach number dependant) with Mach number. This is an important result for the measurement of vorticity from other types of vortex generators: lower speed facilities can be used to understand the trends, thereby reducing the cost of testing. This may have particular influence in the field of Micro-Electro Mechanical System (MEMS) devices, in which future vortex generators may employ very different types of geometries.

The effect of compressibility on the vortex half-life radius may be seen in Figure 60 (b). It has been established that variable density causes a reduction of the pressure gradients in the core. The reduced pressure gradient would then lead to a lower diffusion of the vorticity from the centre of the vortex outward, thereby reducing the effective radius of the vortex core. The basic trends in Figure 60 (b) demonstrate this fact, although it must be stated that the actual values of the change in radius with Mach number are quite small. For the vortex from a vane at 15° incidence, the half-life radius ratio at a point $x/\delta = 8.75$ downstream from the vane is about $R_{0.5}/\delta = 0.20$ at 0.50 Mach. As the Mach number is increased to 0.75, the half-life radius ratio reduces to $R_{0.5}/\delta = 0.18$, a percentage reduction of 10%. With the experimental boundary layer of 20 mm, this equates to a physical distance of 0.4 mm, which is close to the accuracy of the experimental

method. However, all of the results do indicate the decrease, suggesting that the basic trend is probably valid.

The effect of the Mach number on the lateral position of the core is depicted in Figure 60 (c). It would be expected that, as the free-stream Mach number (and therefore the total vortex strength) is increased, then the lateral velocity of the vortex would increase with Mach number. Using the simple inviscid model of two vortices (one 'real' and one 'image' vortex), the velocity imparted by the image vortex on the real vortex is given by:

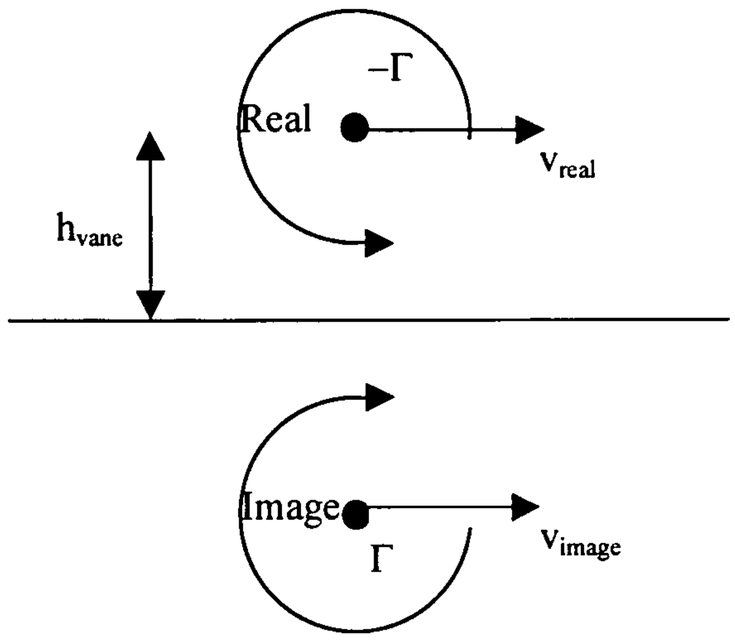

$$v_{real} = \frac{\Gamma_{image}}{4\pi h_{vane}}$$

Since the circulation of the vortex increases fairly linearly with Mach number‡, then the velocity imparted by the image vortex on the real vortex will vary linearly with Mach number. As a result, the angle between the free-stream and the axis of the vortex will be the ratio of the sideways motion of the vortex and the free-stream Mach number.

$$\frac{M_{real}}{M_{\infty}} = \tan\gamma$$

and

$$M_{real} = kM_{\infty}$$

Thus :

$$\tan\gamma = \frac{kM_{\infty}}{M_{\infty}} = k$$

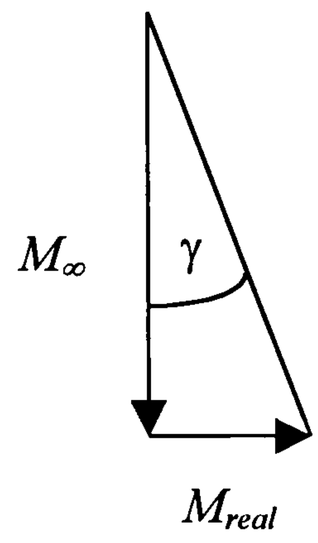

‡ The peak vorticity varies as a power law with Mach number due to the vortex stretching effect. However, the total circulation strength with vary approximately linearly as the vortex core radius growth is reduced by stretching. The linear relationship between the vortex circulation strength and the free-stream Mach number is noted by Wendt[54]

Thus, the angle through which the vortex path (or the lateral movement of the vortex for any given streamwise distance) must be independent of the free-stream Mach number. This is exactly the case from the experimental results. The constant k will depend on the parameters in the equation above, most notably the circulation set up by the vortex generator (without the effect of the free-stream speed, Γ/V_∞) and the height of the vortex core from the surface.

Figure 60 (d) demonstrates the effect of Mach number on the height of the core of the vortex, and it may be seen that (within experimental error), the height of the vortex remains constant with Mach number. Again, the vortex is shed from about 90% of the vane height, but due to the smaller scale of this experiment (compared with the low speed test) the height measurements of the vortices will have an increased error. With data points being taken every 3 mm on the experimental grid, accuracies of better that 1 mm (0.05 δ) would be difficult to achieve.

Streamwise Vortex Decay

The effect of the streamwise decay on the vortex parameters is given in Figure 61. Parameters are plotted for the vane at 15° incidence, and for 20° incidence.

Regarding the peak vorticity plots (Figure 61 (a) & (b)), it may be seen that the basic decay of the vortices is very similar in nature to that for the low speed test. In the case of the 15°-incidence vane (Figure 61 (a)), the decay follows an exponential path, with the exponent following a similar trend to that at low-speed. At the higher incidence of 20° (Figure 61 (b)), the decay of the vortex appears to be far more linear than exponential. In this case, the measurements taken at the furthest downstream station appear to be lower than might otherwise be expected, thereby suggesting that the decay rate for the 20° vane is higher at this far downstream station.

At the higher incidence, the vortex that is produced will have a larger momentum deficit in the core. This observation was not made at low speed, and thus it is suggested that compressibility plays its part. It was noted earlier (by Green[57]) that the effect of compressibility could be to stretch the vortex core, through the change in density in the core, thereby increasing the vorticity at the point of generation. For a vane at a higher incidence, the core of the vortex would have a larger momentum deficit, thereby reducing the velocity in the core. This would increase the static pressure in the core, thereby increasing the pressure gradient through the core, with the effect that the vortex is not stretched as much as the lower incidence case. The impact of this is that as the vortex moves off downstream, the core accelerates, thereby stretching the vortex through the compressibility factor, revealing a different decay rate than the lower incidence case.

With reference to the vortex half-life radius (Figure 61 (c) & (d)), this last point is reinforced. For the 15°-incidence case, the core of the vortex will not be accelerating as much as for the 20° case. Thus, the changing effect of the core compressibility will be less, and the vortex grows downstream. In the 20° case, the acceleration of the core will be more pronounced, and therefore the vortex stretching will increase with distance downstream. As a two-dimensional vortex is stretched, its radius would decrease. Thus for the case of a vortex which would otherwise grow in radius, the effect of the compressibility stretching is to reduce the radius growth to a rate of almost zero (Figure 61 (d)). Also of note from these plots is the effect of Mach number on the actual values of the radius of the core. In all cases, it is evident that the vortex radius reduces with increasing Mach number.

Figure 61 (e) & (f) show the lateral position of the vortex cores. As demonstrated earlier, the lateral position of the vortex is independent of Mach number, to within experimental accuracy. In the case of the 20°-incidence vane (Figure 61 (f)), the lateral motion tends to curve back towards the streamwise direction far downstream. This suggests that either the circulation strength of the vortex decreases far downstream, or the vortex lifts off the surface.

Figure 61 (g) & (h) show that far downstream, the vortices do indeed tend to lift away from the surface. With reference to the inviscid case of the vortex pair, there is no mechanism by which the vortex can lift off the surface. The reason for the vortex lifting is either due to viscous effect which cause the vortex to lift when the core becomes significantly large, or the proximity of the walls to the vortex far

downstream. Since the walls were slotted in nature (either side of the vortex), their reflective qualities will be reduced significantly, such that the effect will be very small. Since the lifting was also noted at low speeds (where the walls were relatively much further away), it must be concluded that this lifting is due to viscous considerations.

Summary

The effect of Mach number on the vortices produced by vanes can be summarised as follows:

The level of peak vorticity in the core of the vortex is affected by the effect of compressibility. These effects manifest themselves as a stretching of the vortex, resulting in an increase in peak vorticity, and a reduction in the growth of the vortex radius with downstream distance. These compressibility effects are affected by the free-stream Mach number, and the velocity deficit in the core of the vortex at the point of generation. In general, the peak vorticity varies as a power law curve fit with respect to Mach number, the power law exponent approximating to a value of about 1.3.

The growth of the vortex core is a function of Mach number; the vortex being of a smaller radius as the Mach number is increased.

The lateral position of the vortex is not dependent on the free-stream Mach number. The position is only a function of the ratio of the vortex strength-to-free-stream velocity ratio, Γ/V_∞, and the height of the vortex from the wall. This is because the vortex circulation strength is a function of Mach number.

The vertical position of the vortex from the wall does not change significantly, until the vortex radius grows downstream. Then, the viscous effect in the boundary layer coupled with the larger core combine to push the vortex from the wall.

7.4.2 - High Mach Number Air-Jet Results

For the high Mach number test of air-jets, fewer parameter choices were made (compared with the low speed test), in order to reduce the number of possible data points. Since the variation in peak vorticity with jet velocity ratio (or Mach number ratio) was linear at low speeds, it was considered that this effect should not change significantly with increasing free-stream Mach number, and so only one ratio was chosen. Similarly, the hole diameter was considered to be a physical scaling parameter, rather than a method of changing the fundamental flow physics, and thus only two sizes of jet were tested. It was considered that the effect of varying the angles of the jet might change the trends in peak vorticity (as the angle relationships were more copmlex in nature), since the presence of compressible effects or shock/expansion waves might influence the development of the vortices. Thus, the three skew angles, which were tested in the low speed tests, were used, since it would be advantageous to measure the vortices over the range of values that would be used in practice. The two lowest pitch angles (30° and 45°) were chosen. Since the 60° pitch angle produced relatively weak vortices (and would therefore not be practically used), and the local pitch angle in any flow would not change to warrant a wide range of experimental data. The four streamwise stations were used to investigate the streamwise decay of the vortices. In total, 1 (*MR)* x 2 (D/δ) x 3 (β) x 2 (α) x 4 (x/δ) = 48 individual test conditions were measured.

Effect of Mach Number with Hole geometry

The effect of free-stream Mach number on the development of the vortices is shown in Figure 62 to Figure 64. Initially, the effect of the Mach number on different jet orifice diameters is shown (Figure 62). The variation of peak vorticity with Mach number (for jets with $\alpha = 30°$, $\beta = 60°$) is in close approximation to a power law series, with the exponent taking a value of about 1.3. This illustrates that, as with the vane vortex generators, the vortex that is produced is subjected to the same compressibility issues, which stretch the vortex. As the vortex rotates, the reduction in density in the core (due to the centripetal acceleration on the core) causes the pressure gradients to be reduced in the core, thereby reducing the radial spread of the vortex and reducing the cross-stream diffusion of vorticity. Similar results are noted for other jet angle cases.

The reduction in the vortex radius with Mach number is depicted in Figure 62 (b). It is shown that as the Mach number is increased, the vortex radius decreases, thereby reflecting the effect of compressibility on the stretching of the vortex. The accuracy of these measurements is to about 0.4 mm (0.02 δ), and thus the effect on the larger of the two hole diameter ratios is less pronounced.

The effect on the lateral spacing of the vortex is demonstrated in Figure 62 (c). In common with the vane case, the air-jet produced vortices do not change in the lateral position (at any downstream station) with Mach number. As described above, the effect of increasing the Mach number not only increases the streamwise velocity, but also the vortex circulation strength. Thus the ratio of the velocity induced laterally to the free-stream velocity remains constant. For the same streamwise distance travelled, the same lateral distances are also covered.

It will be remembered that the basis for the above discussion is that the vortex circulation strength increases linearly, and that the height of the vortex above the solid wall does not increase with Mach number. In the case of the vanes, this was a very reasonable assumption, since the point of formation of the vortex was largely fixed by the vane geometry. In the case of the air-jet, this point will be dependent on the penetration of the jet, i.e. the hole diameter ratio and the Mach number ratio. Keeping these parameters constant, it will be seen that the height of the vortex does indeed remain constant (Figure 62 (d)) to within the measuring accuracy of the technique.

Effect of Mach Number with Jet Angles

The trends associated with air-jet vortex generator performance with respect to angles are shown in Figure 63. Since only two jet pitch angles were tested, data is presented with respect to skew angles, where more meaningful conclusions may be drawn from the more complete data set.

With regard to peak vorticity (Figure 63 (a)), the trends in vorticity production are demonstrated with Mach number, pitch angle, and skew angle. It is clear that for pitched jets at 45°, the increase in peak vorticity is fairly linear, regardless of Mach number. Thus, aside from the observation that increasing Mach number causes an increase in the level of peak vorticity as a power law trend (as has already been noted), the trend in peak vorticity with skew angle holds well. Similarly, the basic shape of the three Mach number results at a pitch angle of 30° shows that the same trend is seen with skew angle (i.e. a curve with a maximum value of peak vorticity at a skew angle of between 50° and 55°). Again, the Mach number would scale the actual value of the peak vorticity, but the trend is similar when altering the skew angle. Since the pitch angle curves are very similar in shape, it is reasonable to assume that the effect of pitch is similarly consistent with Mach number (although there is not sufficient data to prove this allowing for experimental error).

The trends in the vortex half-life radius are depicted in Figure 63 (b). It may be seen that half-life radius of the 30° pitched jet does not increase significantly with increasing skew angle, where as the 45° pitched jet does have some cross-coupling in the vortex growth. However, the trends are independent of free-stream Mach number (to within experimental error).

The lateral variations of the vortices (Figure 63 (c)) do not change appreciably with Mach number (allowing for experimental error), although there is a trend for the vortices to be displaced laterally in the negative sense at the point of generation. The slopes of these lines show that the previous hypothesis concerning the lateral movement of the vortices being based on the vortex strength holds here. Clearly, the jet pitch and 30° is transposed laterally by a greater distance that the 45° pitch jet. This is due to the larger injection of momentum in the cross-stream (y direction) sense.

For the height of the vortices from the wall (Figure 63 (d)), there is little variation in height with Mach number for the 30° case. For the 45° pitched jet, there is more of a variation in height with Mach number, and the height of the vortex from the wall reduces with increasing skew angle. Also of note is that the 30° pitched jet results show that the vortex is produced at a lower height in the boundary layer than the 45° pitched jet cases. This is due to the penetration in to the boundary layer by the higher pitched jet.

Effect of Mach Number with Streamwise Development

The effect of the Mach number on the streamwise development of the vortex is presented Figure 63 for an air-jet of diameter ratio 0.3, at pitch and skew angles of 45° and 45° respectively.

From the graph in Figure 63 (a), the streamwise decay in peak vorticity may be seen where similar trends in the decay are noted. Analysis reveals that the decay can be approximated to a power law series in the same manner as the low-Mach number tests. The effect of Mach number on the decay constant is negligible to within experimental error, and is independent of the parameters varied in this test.

The streamwise decay of the vorticity will be largely related to the turbulent eddies in the vortex (the turbulent transfer of vorticity being two orders larger than the laminar transfer[12,14,15]), and the radius of the vortex relative to the height of the vortex from the wall. The streamwise growth in the radius of the vortex is shown to be largely independent of the free-stream Mach Number (Figure 64 (b)), and varies between 0.3 and 0.5 time the boundary layer height (δ) from the wall. With the vortex remaining at a height of around 0.6 δ, the interaction between the core and the wall over the streamwise range tested is very small, and hence there is no mechanism by which a significant difference should be seen in the decay rate of the peak vorticity. The decay rate of the vortices would also depend on the dynamic pressure in the core of the vortices. Unlike the vane produced vortices (where there were large changes in velocity in the core with different geometries) the core dynamic pressure of the air-jets was free from large changes, which would add a further compressibility effect to the development of the vortices.

The lateral position of the core is shown in Figure 64 (c) and the height of the vortex from the wall is shown in Figure 64 (d). The lateral position of the vortices at M = 0.5, and M = 0.6 are very similar as discussed earlier. However, the vortex produced at M = 0.75 appears not to move laterally as far. Referring to Figure [ ], and allowing for experimental error, it may be seen that the vortex at M = 0.75 is higher in the boundary layer, and thus, while the vortex may be at a proportionally higher strength, its height would reduce the lateral velocity imparted by the image vortex. Scrutiny of the graphs shows that the vortex is displaced laterally by about 2 mm, while in height, the vortex is displaced by 1.5 mm. Extrapolation of the lateral movement of the vortex with streamwise distance reveals that all cases have the same origin. Thus the difference in the lateral movement is due to the vortices being placed at different heights in the boundary layer as shown in Figure 64 (c).

Summary of the Effect of Mach Number of Air-jets Vortex Generators

The principle effect of Mach number on the air-jet vortex generators is that the peak vorticity is increased as a power law series, with the exponent taking a value of about 1.3. This agrees with the vane results, suggesting that this is the effect of compressibility vortex production.

There appears to be no significant cross coupling of Mach number with other air-jet parameters. Trends that are seen in the change in peak vorticity are seen regardless of the Mach number, although the Mach number does alter the numerical value of the peak vorticity levels measured. This suggests that the flow physics of the problem does not change significantly with Mach number.

The streamwise decay of the vortices follows a similar trend regardless of the Mach number. The decay of peak vorticity appeared largely independent of the free-stream Mach number, as did the growth of the vortex. The lateral position of the vortex followed the predicted trends, however, an anomoly was noted for a high Mach number vortex as discussed above.

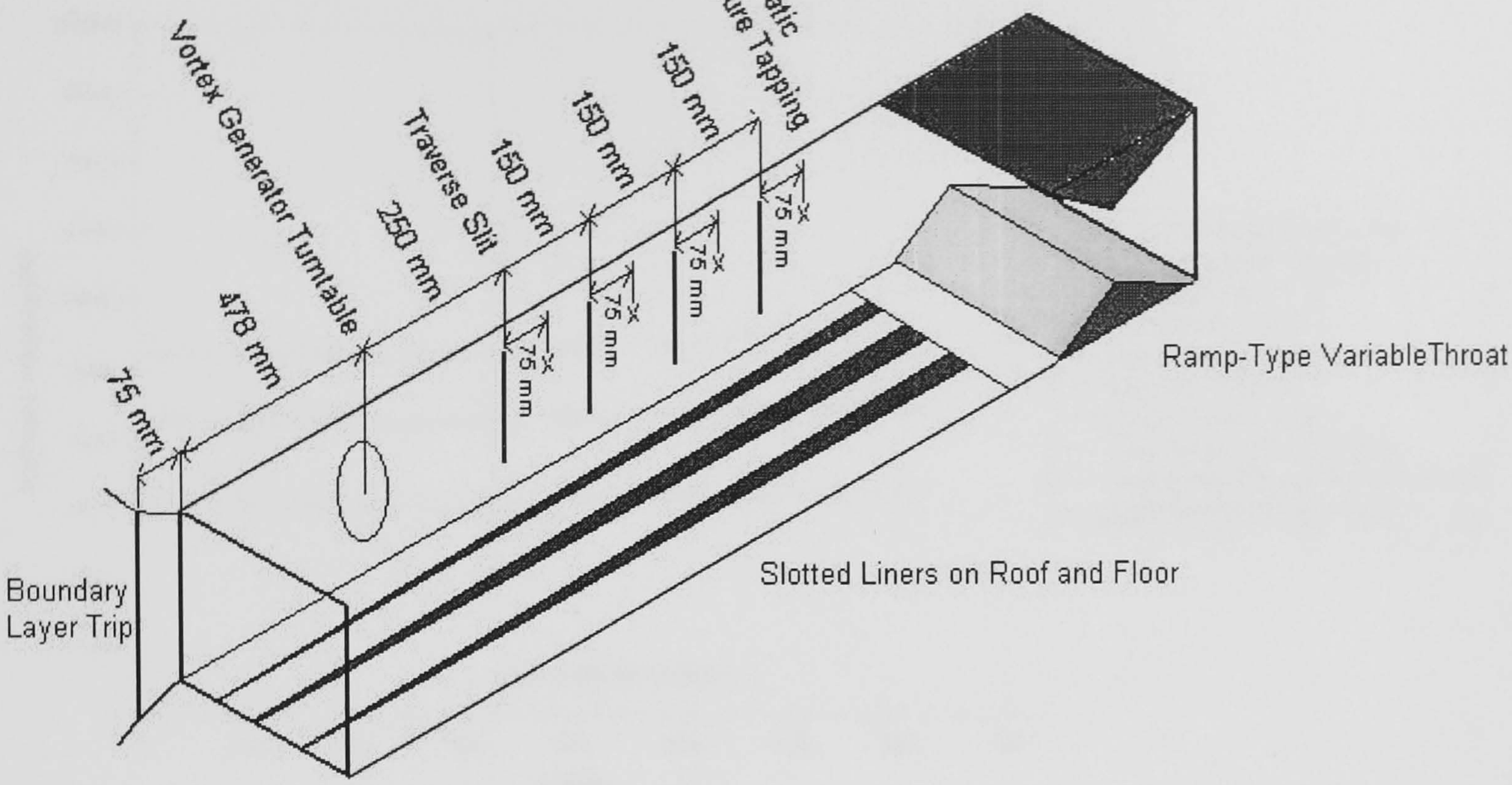

Figure 54: Schematic of the 9"x7½" Working Section

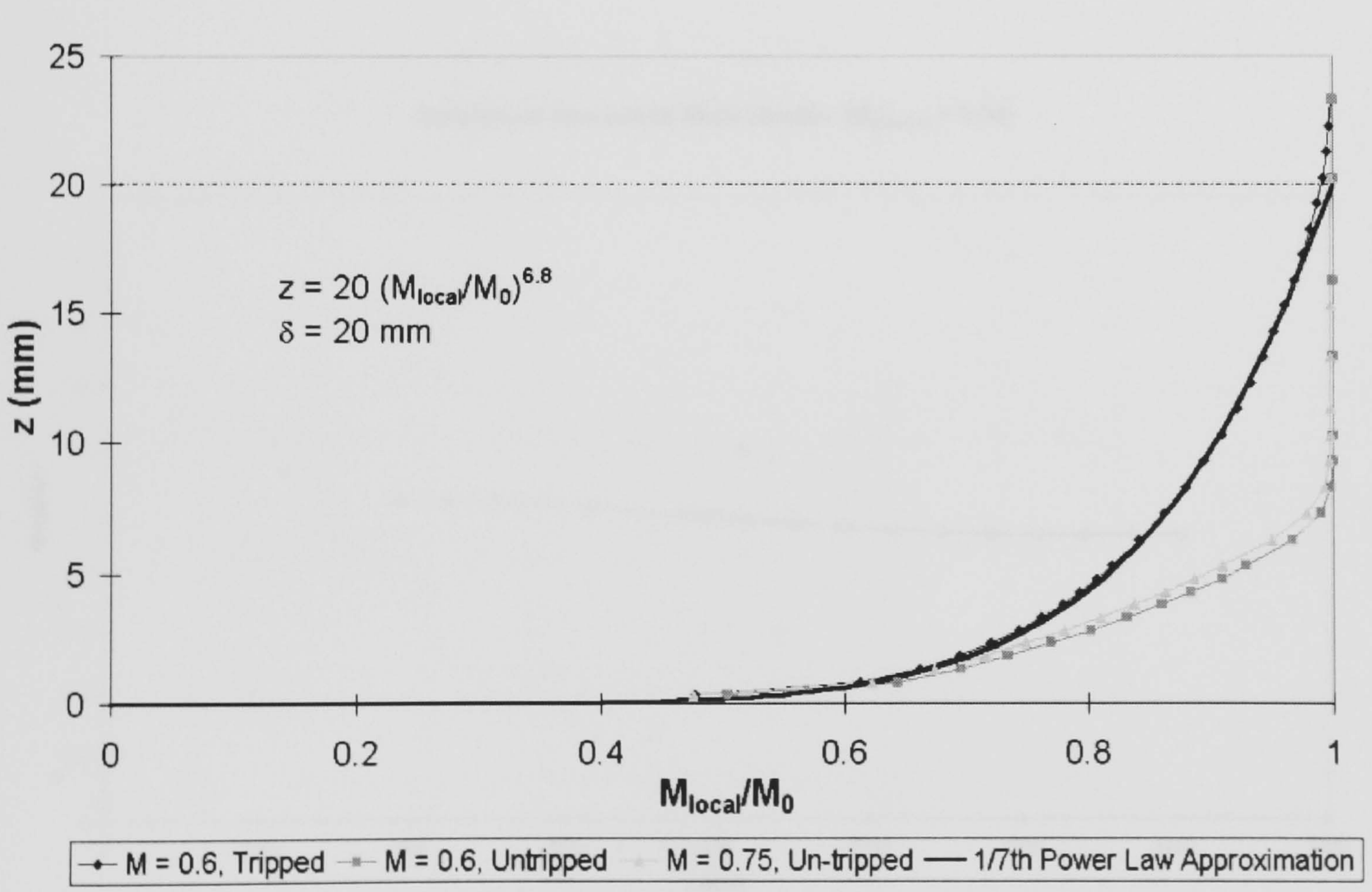

Figure 55: Boundary Layer Thicknesses at the Vortex Generator Location

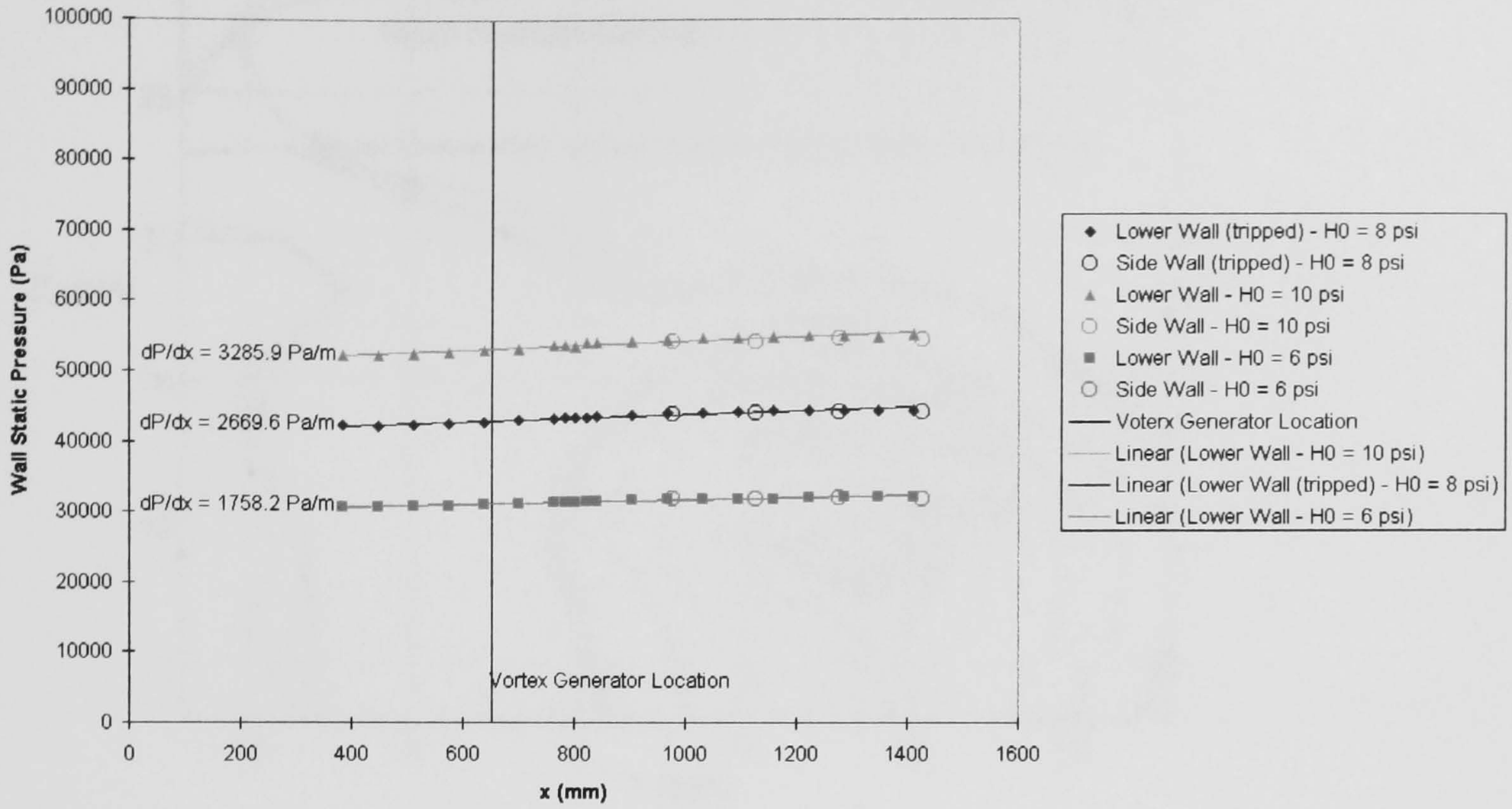

Figure 56: 9" x 7½" Wind Tunnel Wall Static Pressure Distributions

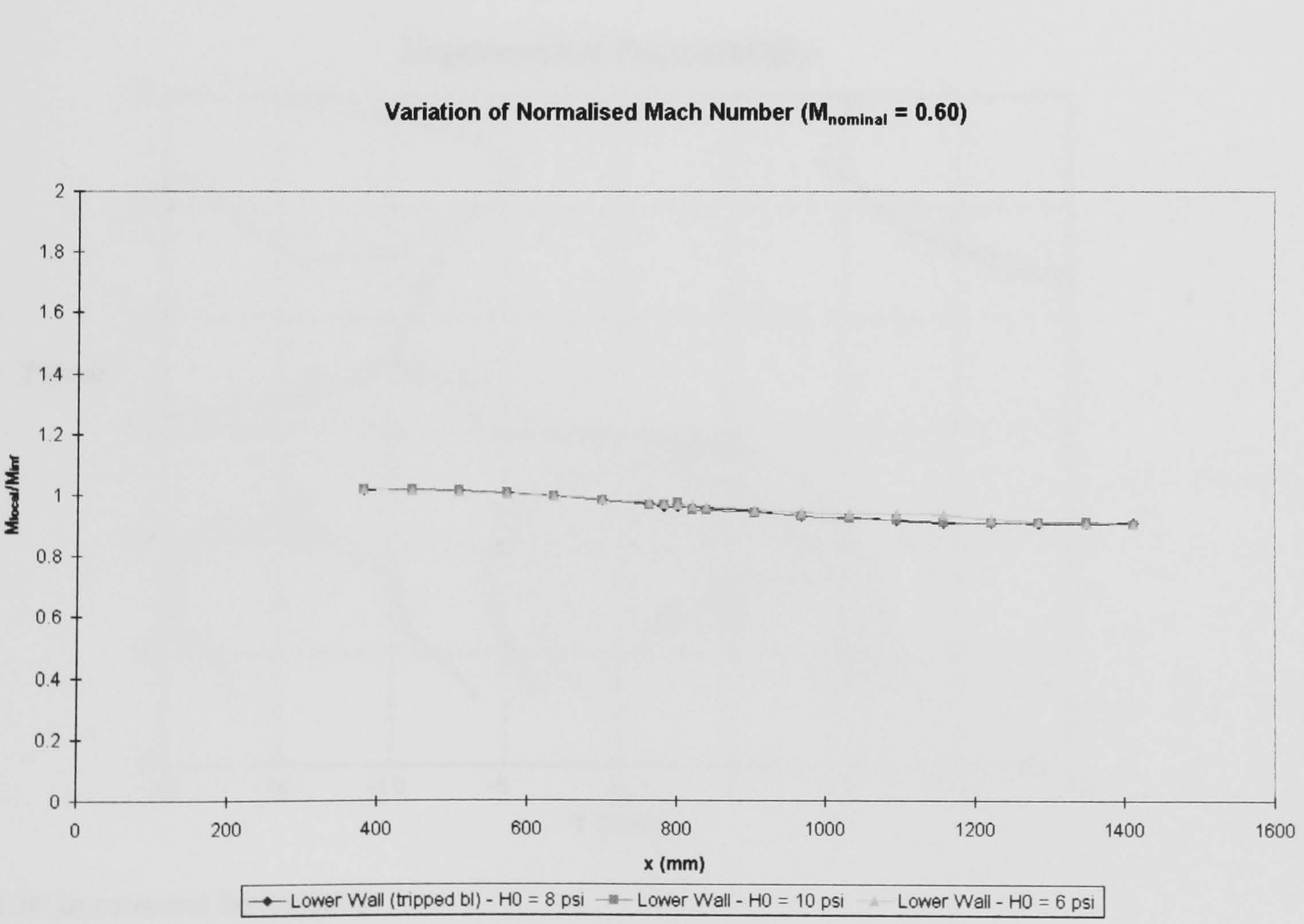

Figure 57: 9" x 7½" Wind Tunnel Normalised Mach Number Distribution

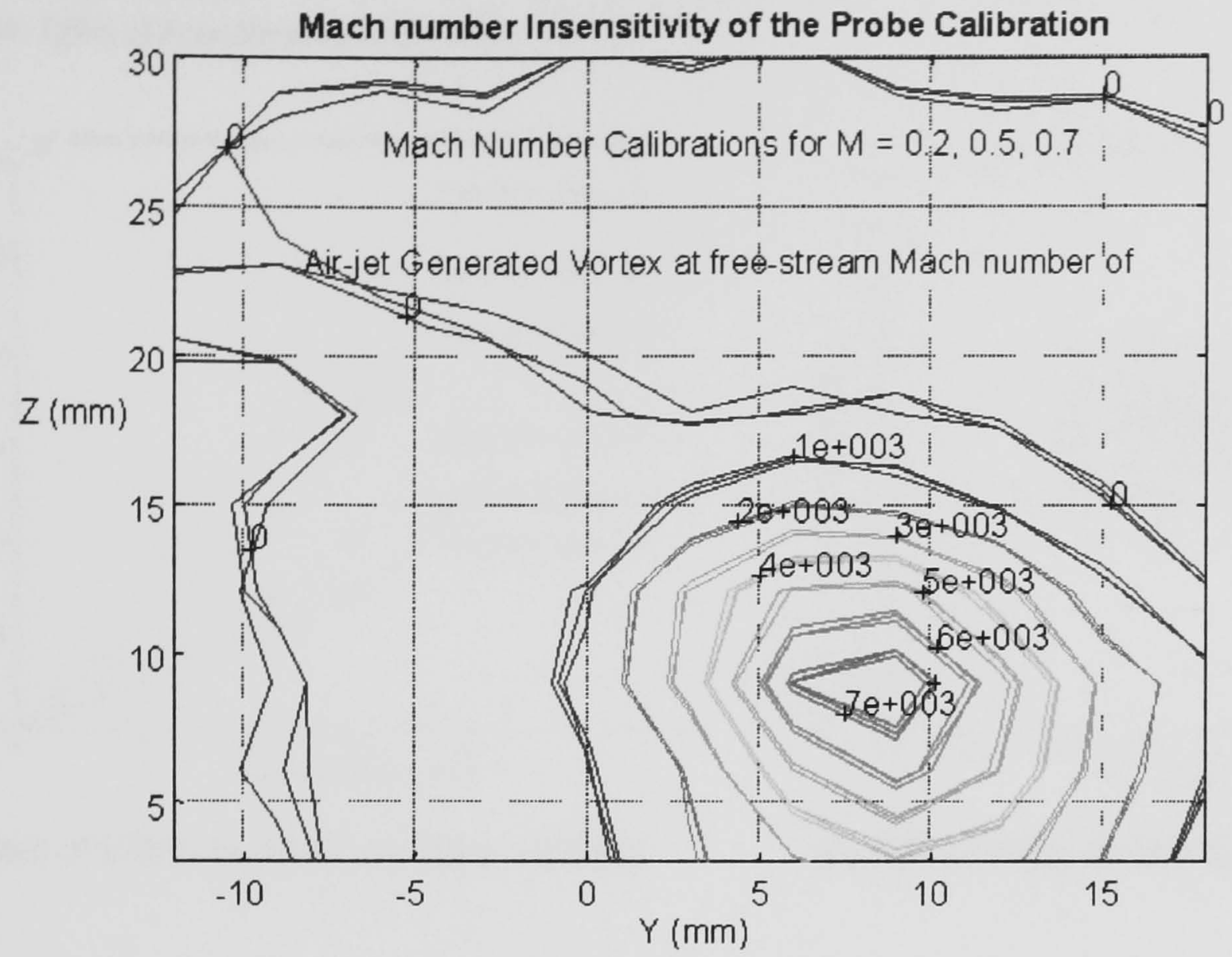

Figure 58: Mach Number Insensitivity of the Five-Hole Probe Calibration

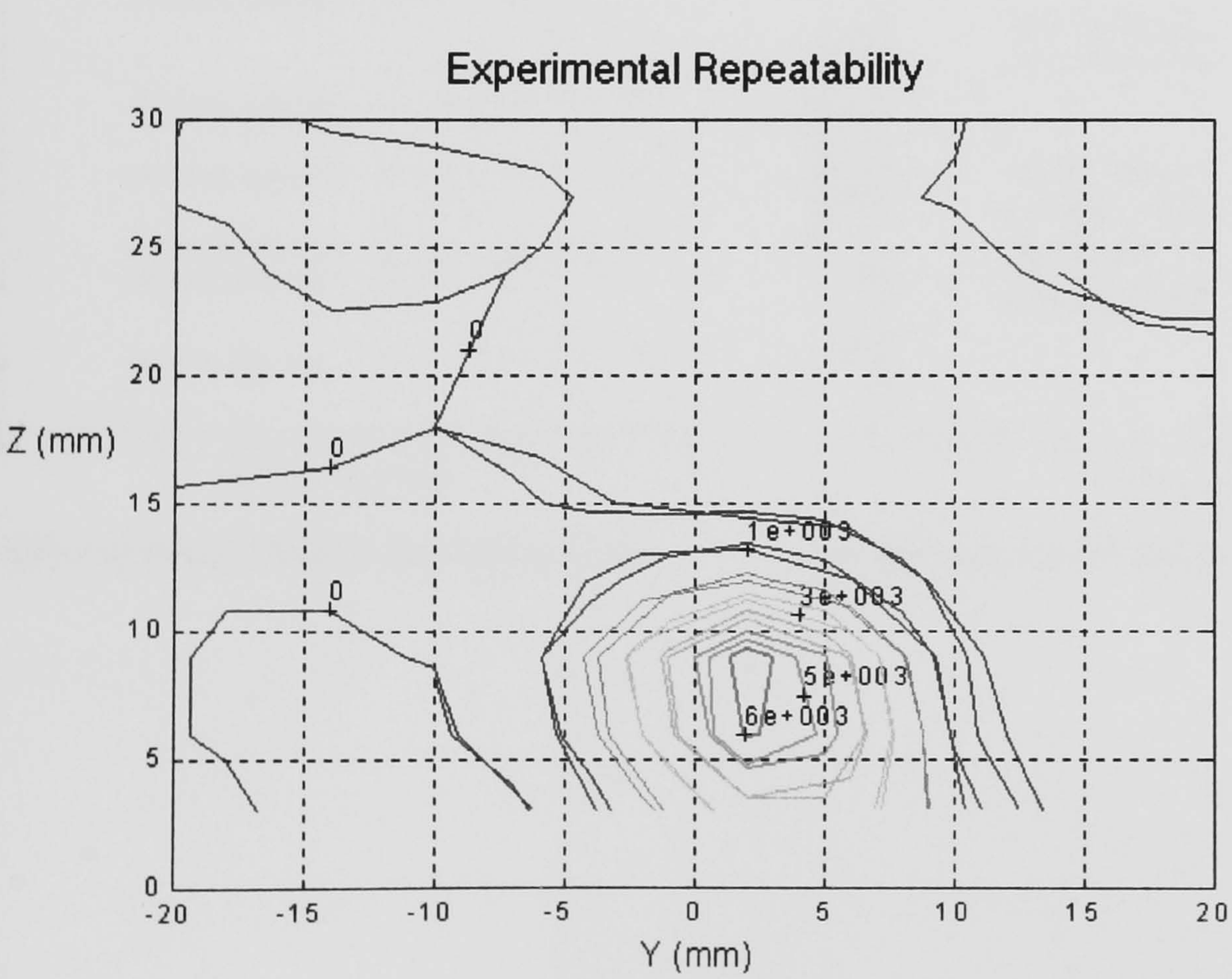

Figure 59: Experimental Repeatability

7.5 - Vane Results

Figure 60: Effect of Free-Stream Mach Number

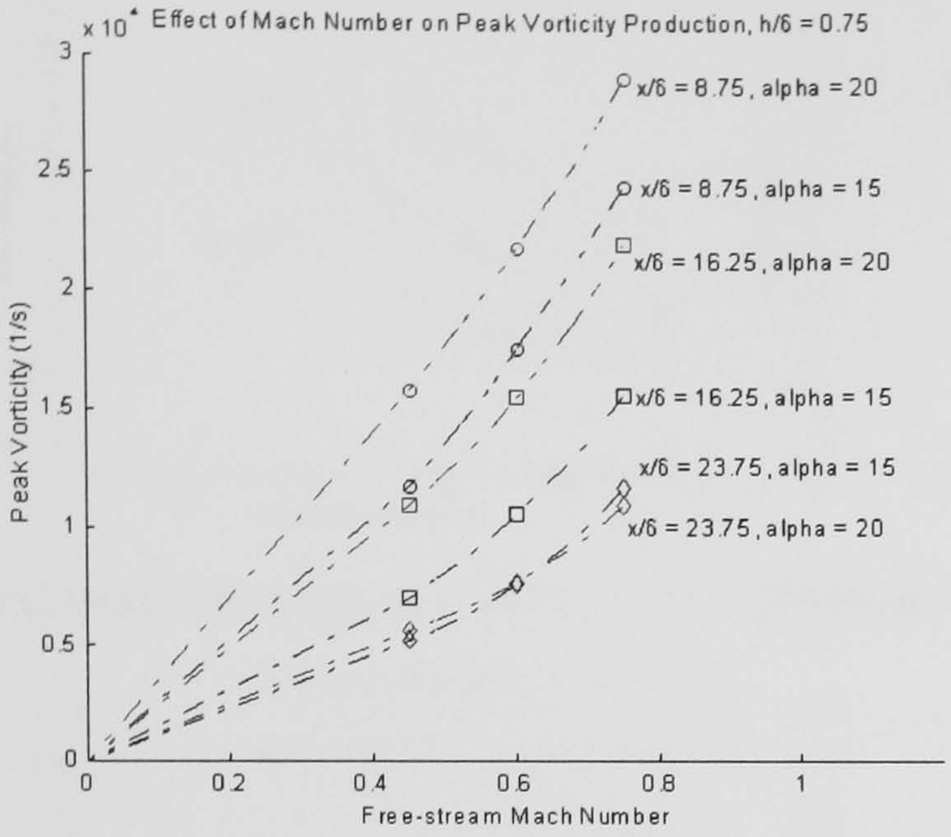

(a) Effect of Mach Number on Peak Vorticity

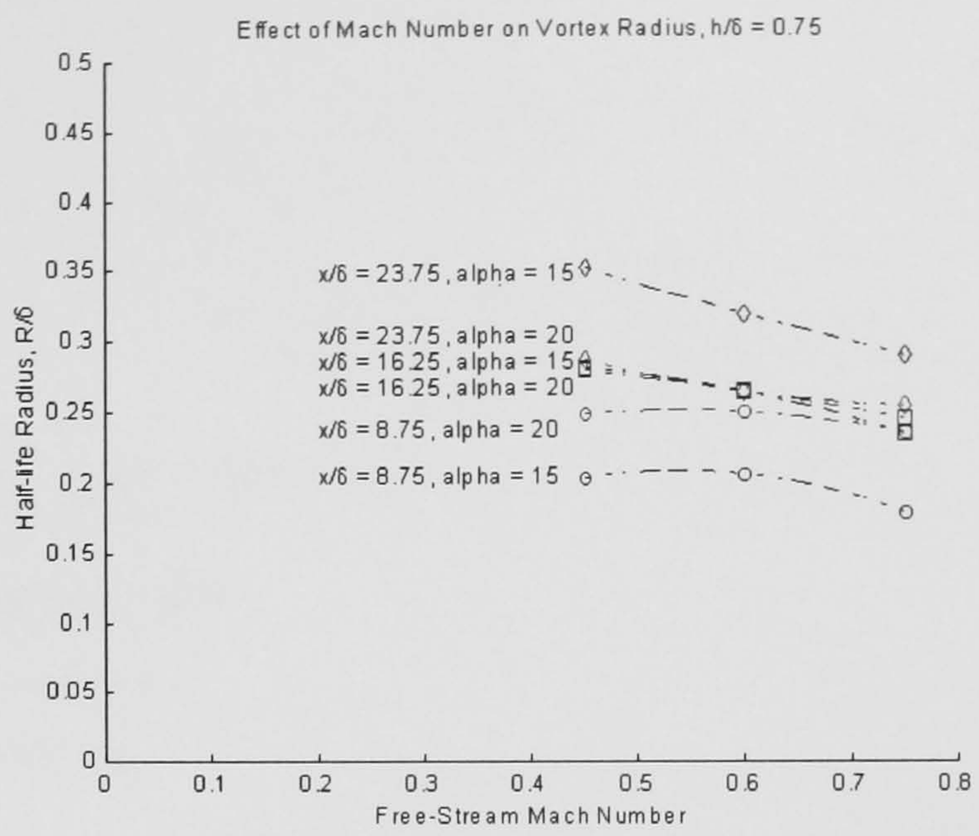

(b) Effect of Mach Number on Half-life Radius

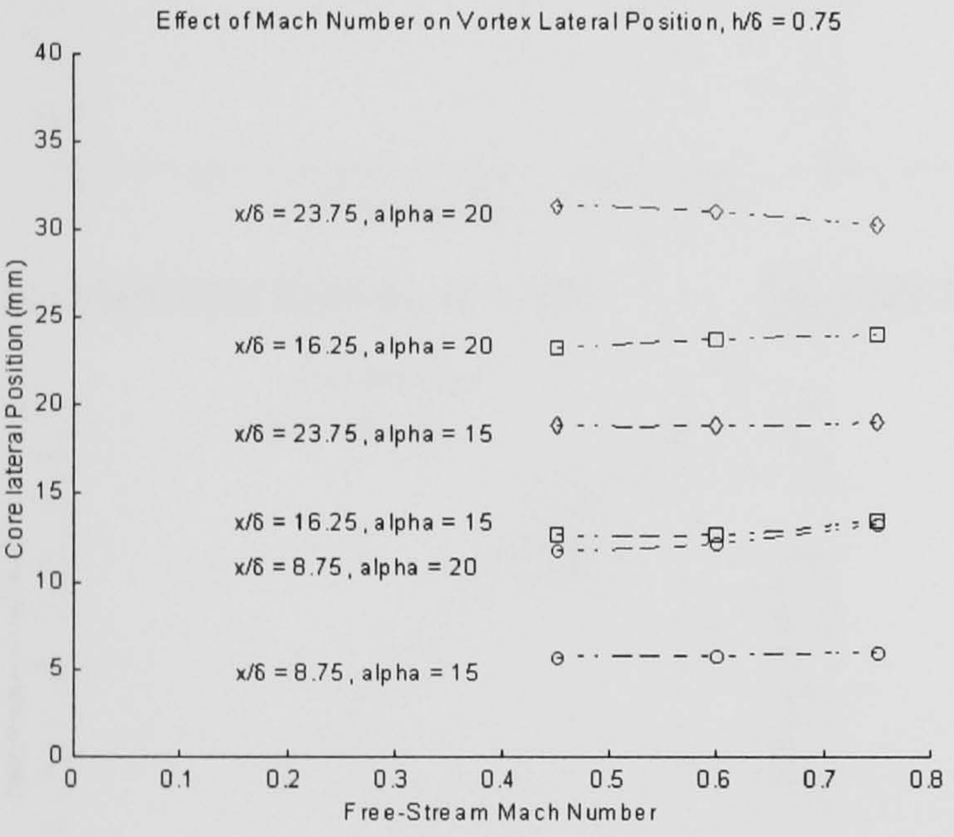

(c) Effect of Mach Number on Lateral Core

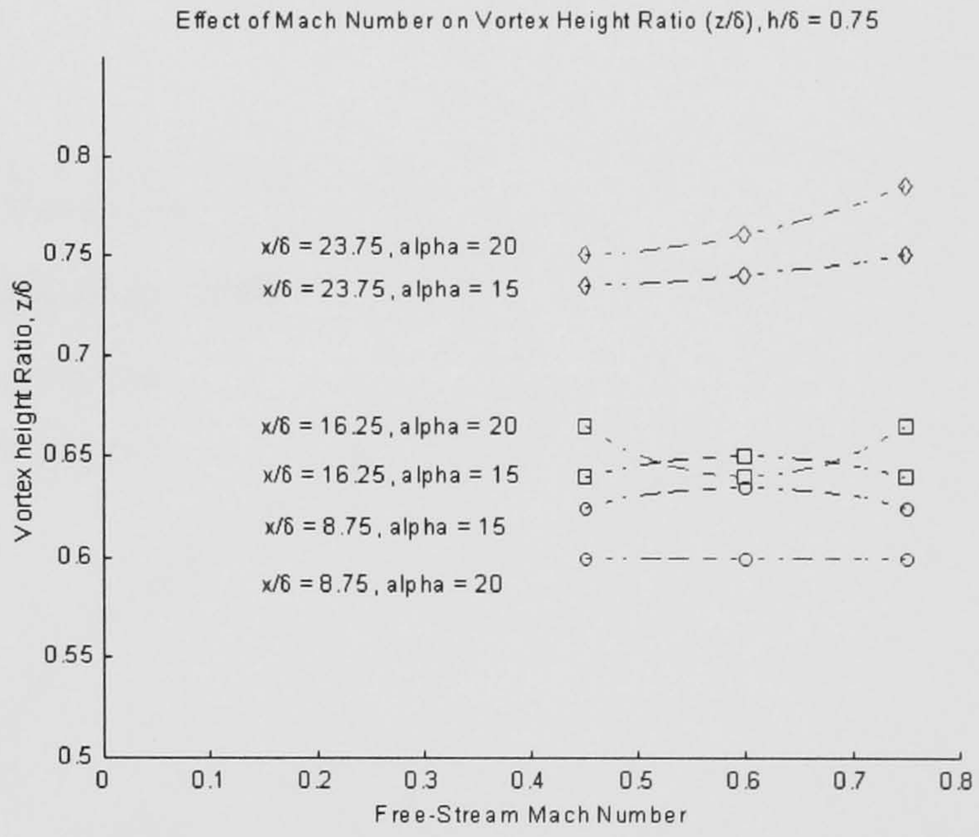

(d) Effect of Mach Number on Vortex Height

Figure 61: Streamwise Vortex Decay: Effect of Free-Stream Mach Number

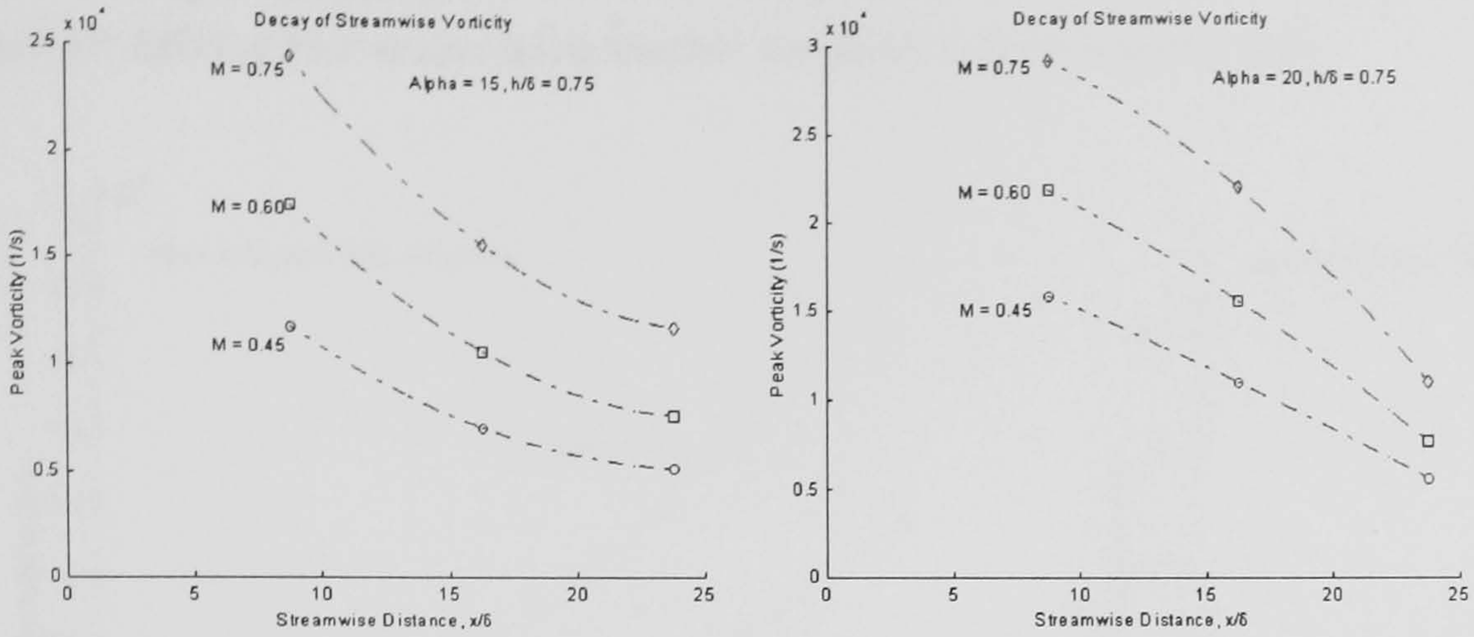

(a) Peak Vorticity, $\alpha = 15°$

(b) Peak Vorticity, $\alpha = 20°$

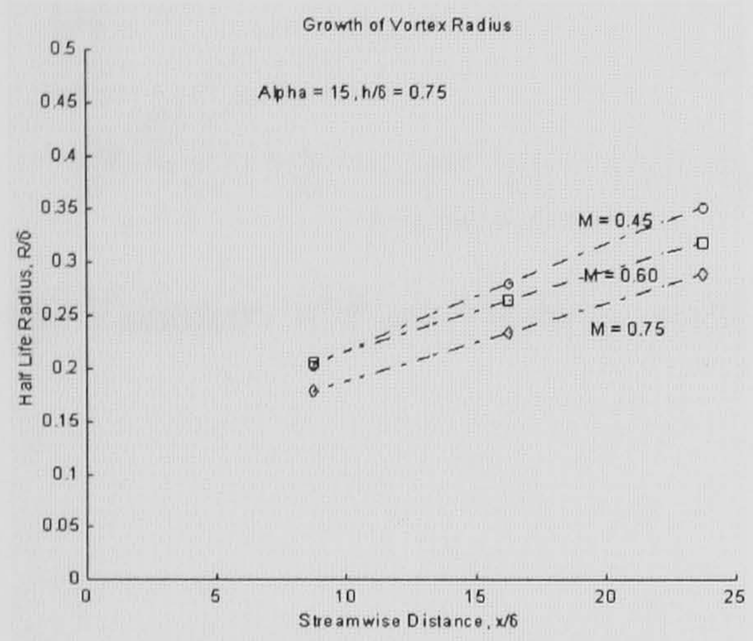

(c) Half-Life Radius, $\alpha = 15°$

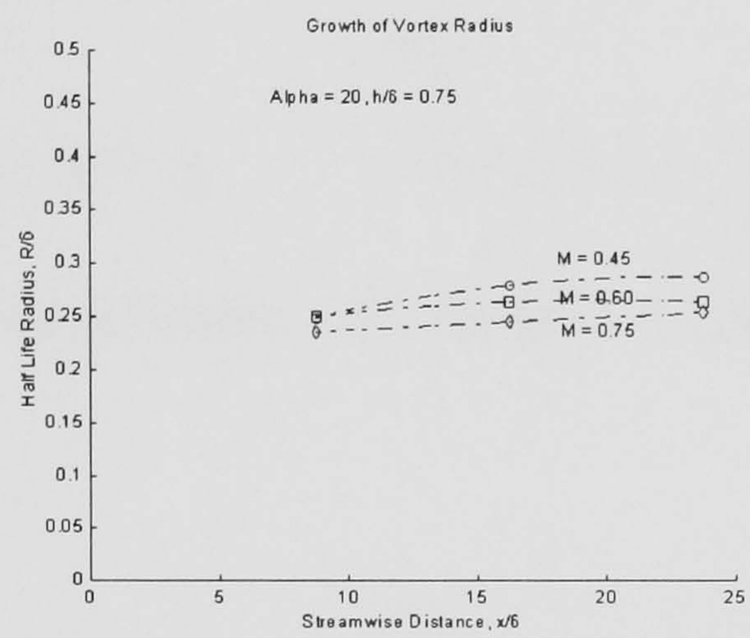

(d) Half-Life Radius, $\alpha = 20°$

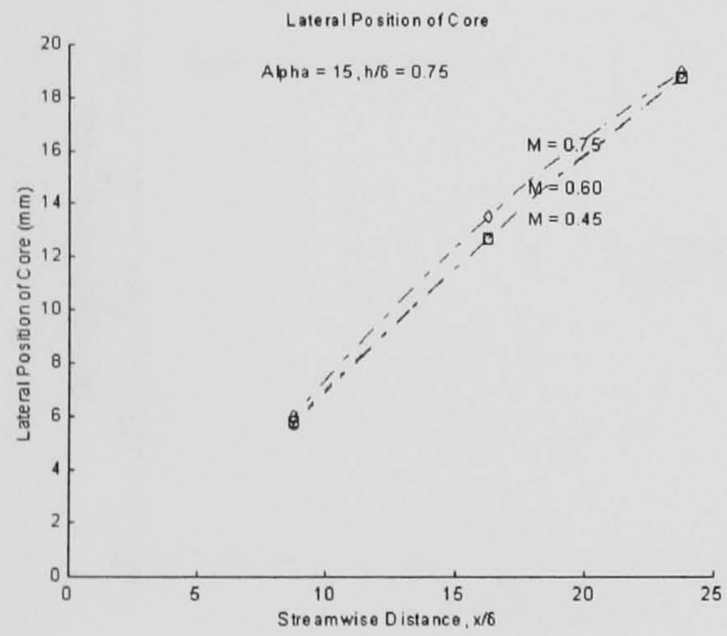

(e) Lateral Position, $\alpha = 15°$

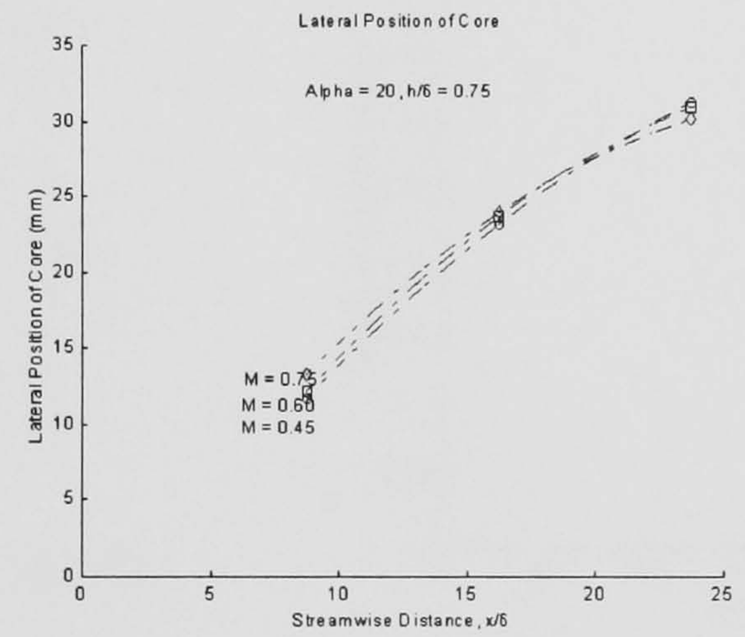

(f) Lateral Position, $\alpha = 20°$

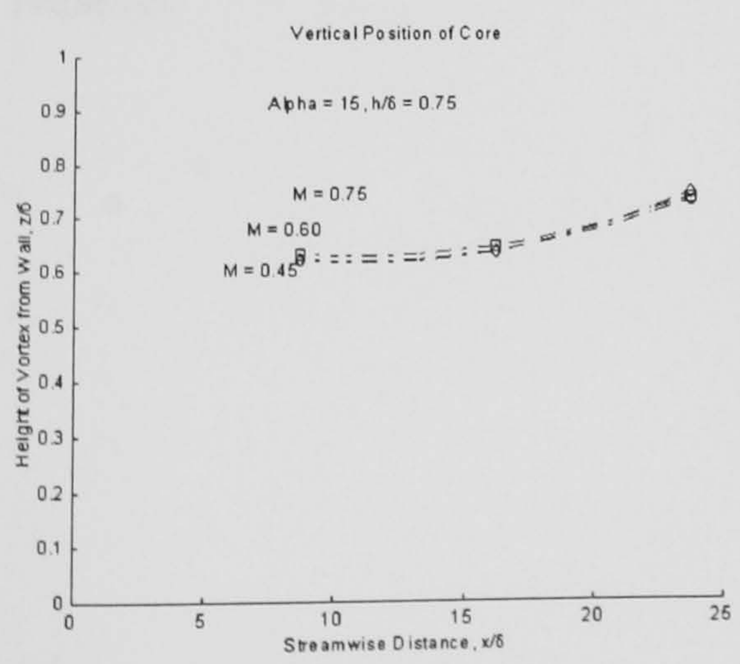

(g) Height Ratio, $\alpha = 15°$

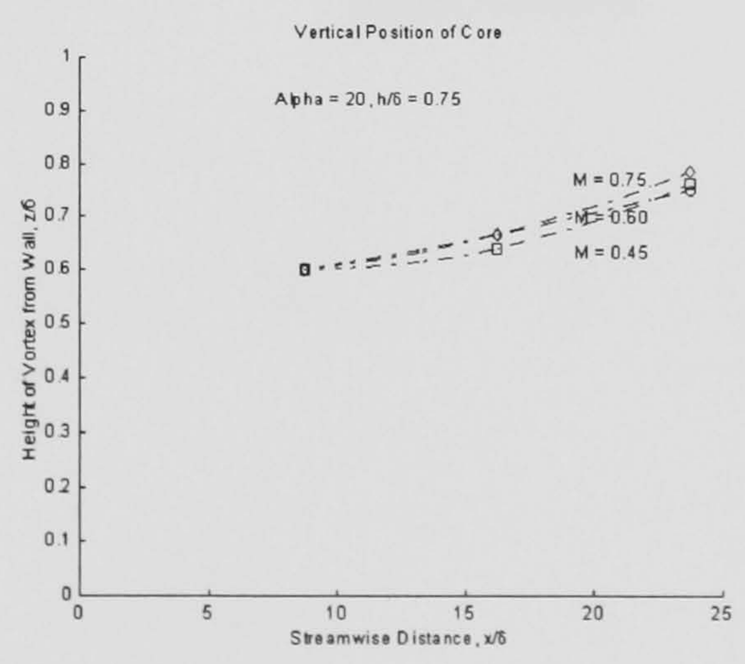

(h) Height Ratio, $\alpha = 20°$

7.6 - Air-jet Results

Figure 62: Effect of Free-stream Mach Number: Variation in Hole Diameter Ratio

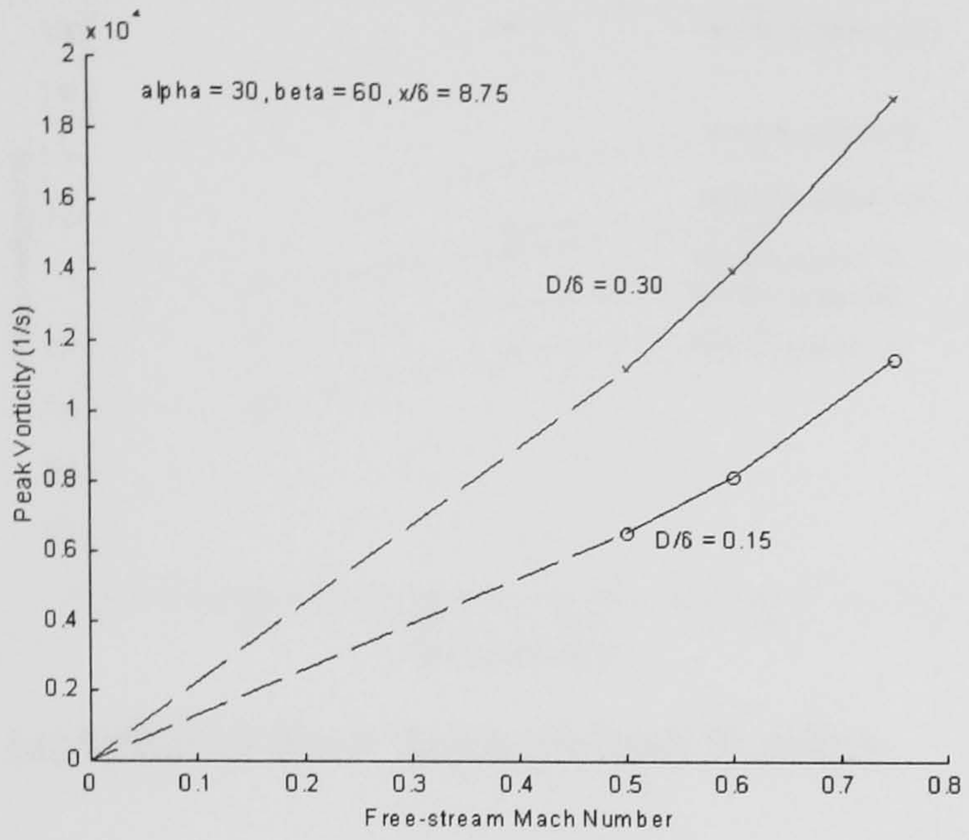

(a) Variation of Peak Vorticity with *Mach Number*

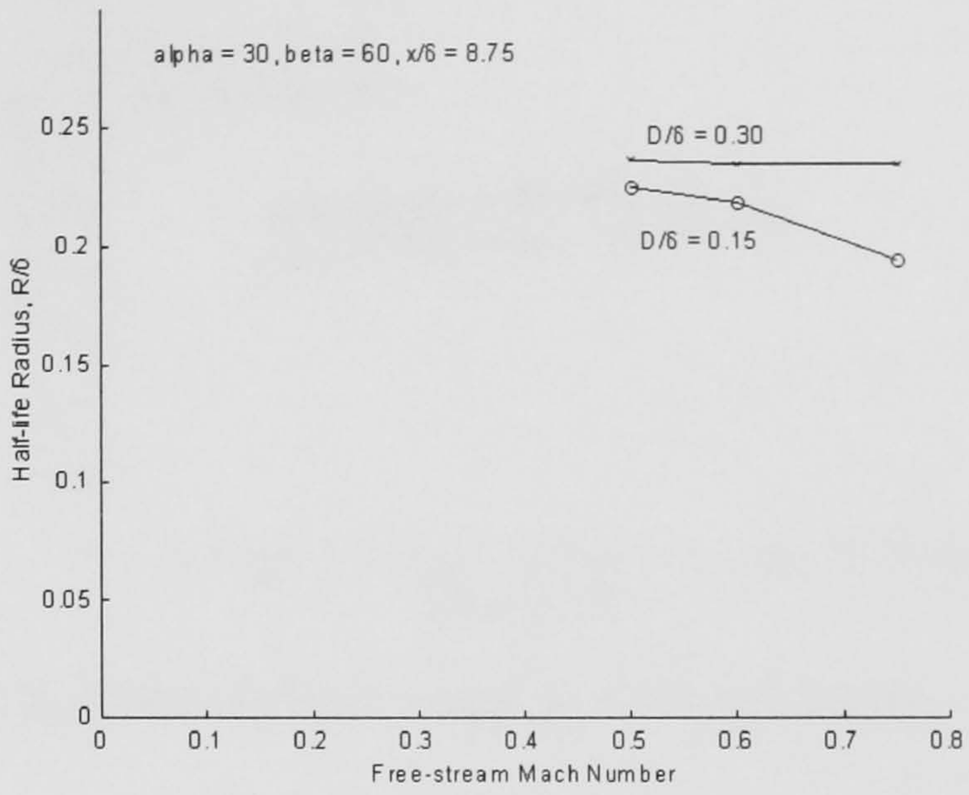

(b) Variation of Half-life Radius with Mach No.

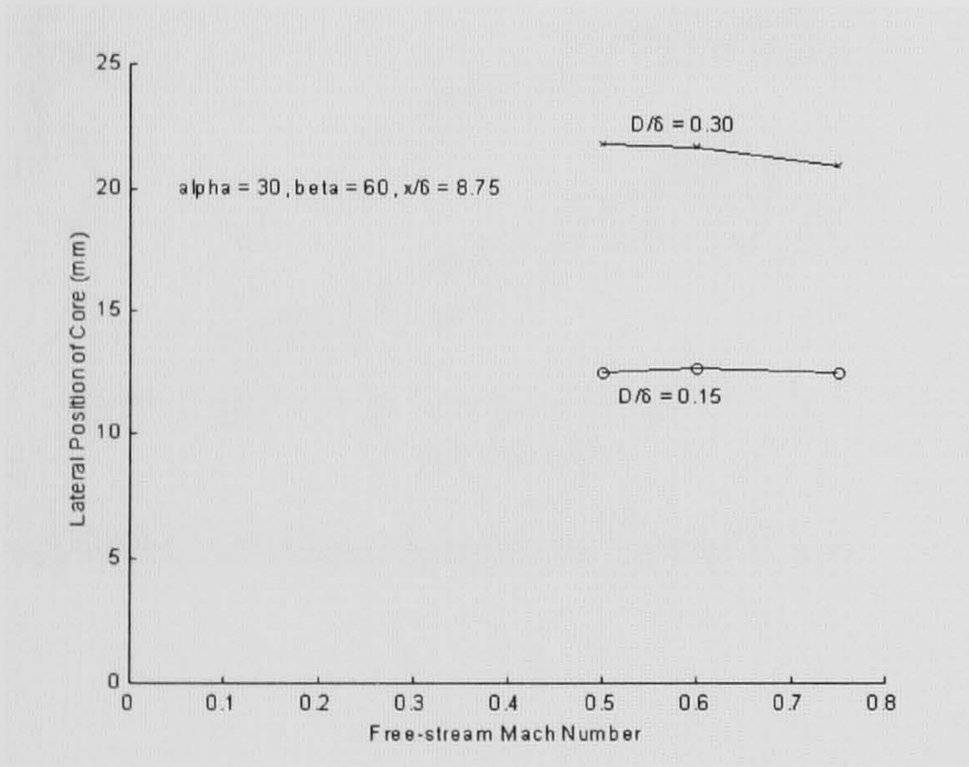

(c) Variation of Lateral Distance with Mach Number

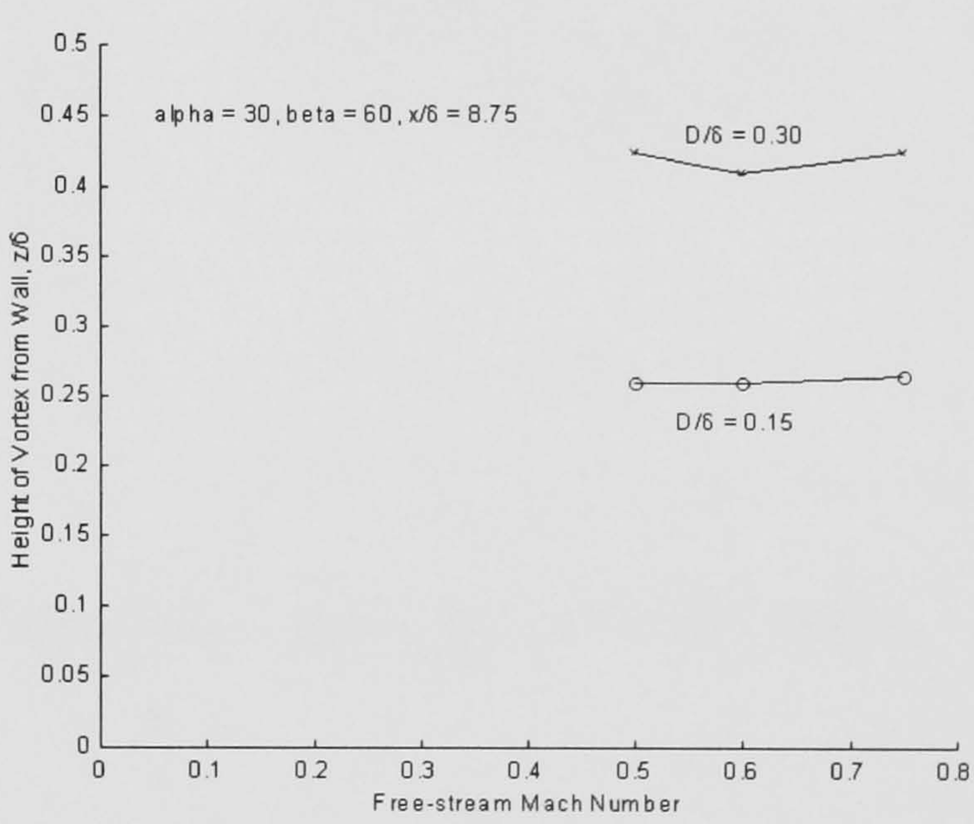

(d) Variation of Vortex Height Location with Mach Number

Figure 63: Effect of Skew Angle

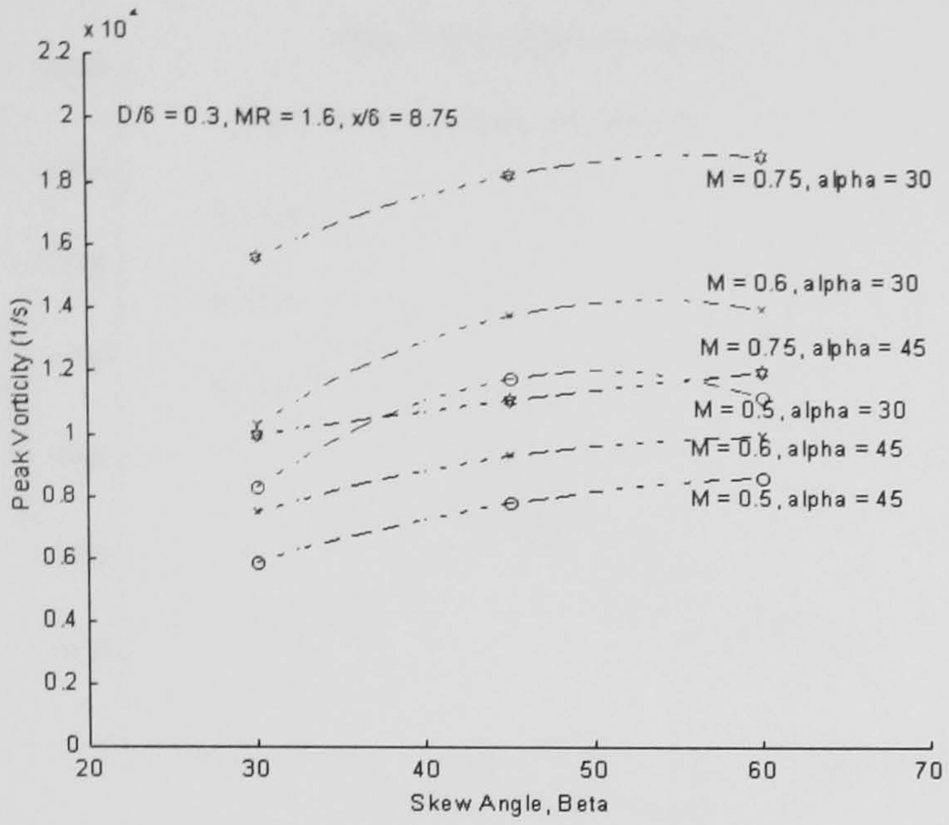

(a) Effect of Skew Angle on Peak Vorticity

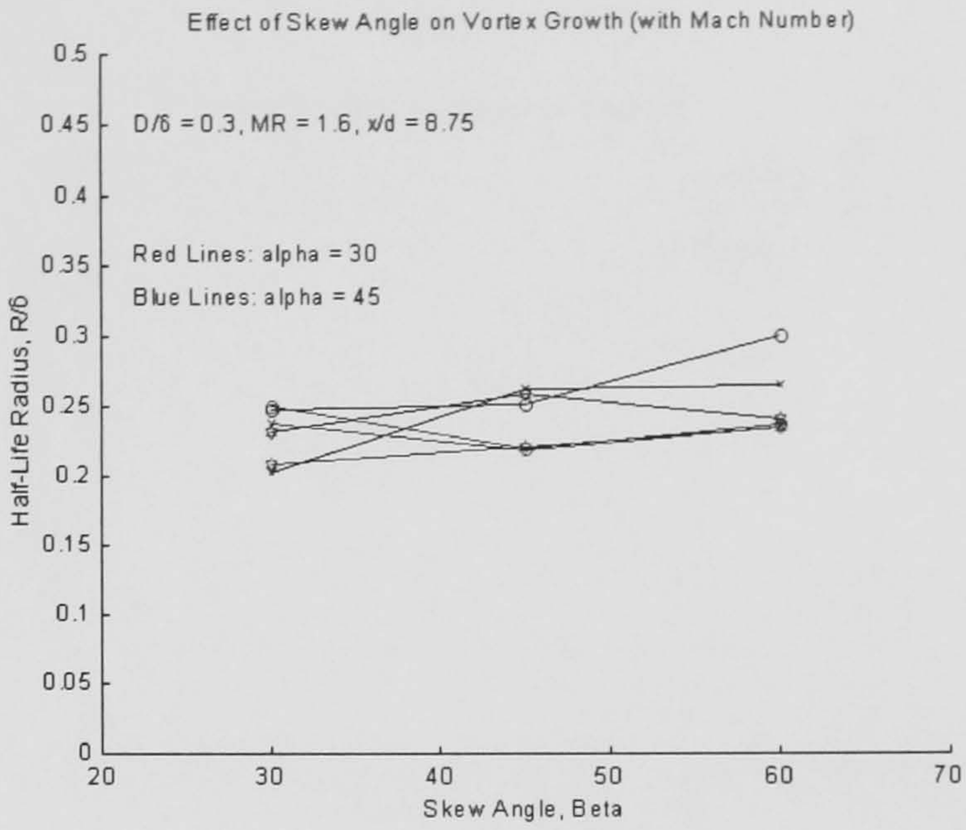

(b) Effect of Skew Angle on Half-Life Radius

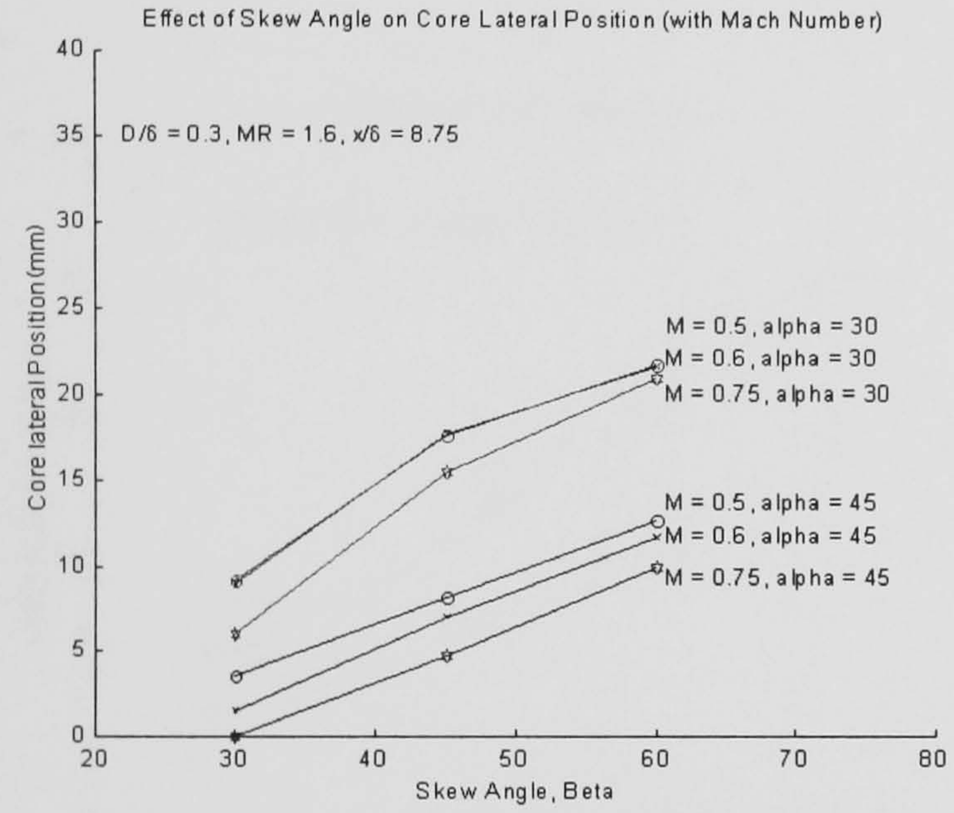

(c) Effect of Skew Angle on Lateral Core

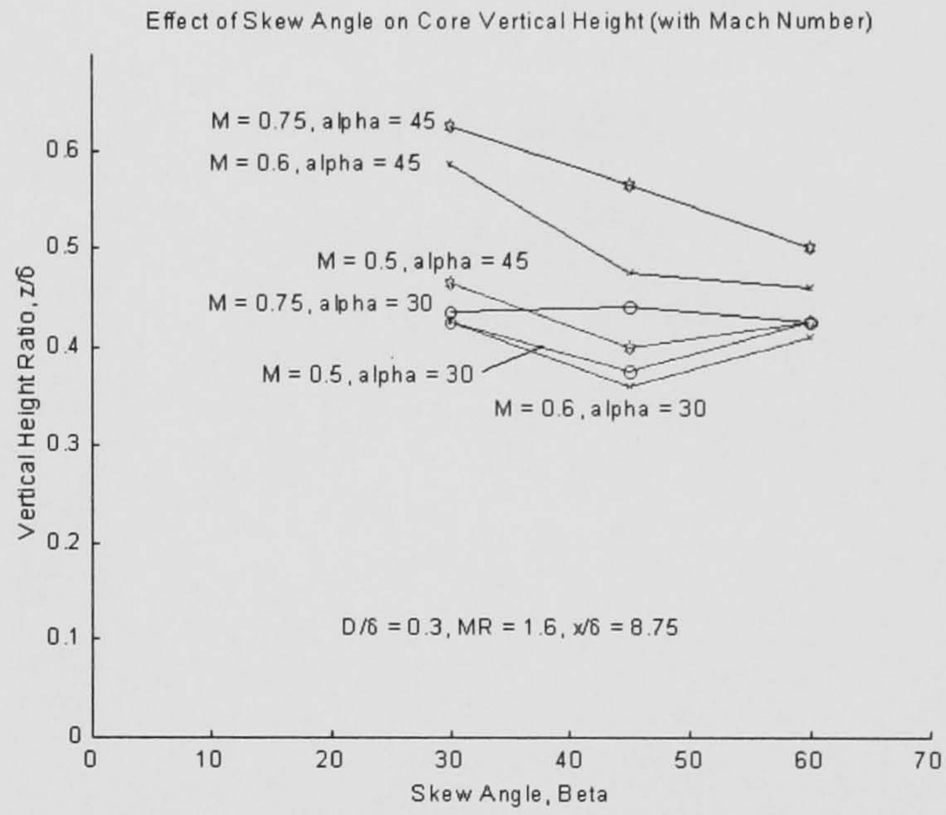

(d) Effect of Skew Angle on Vortex Height

Figure 64: Streamwise Decay of Vortices: Effect of Free-Stream Mach Number

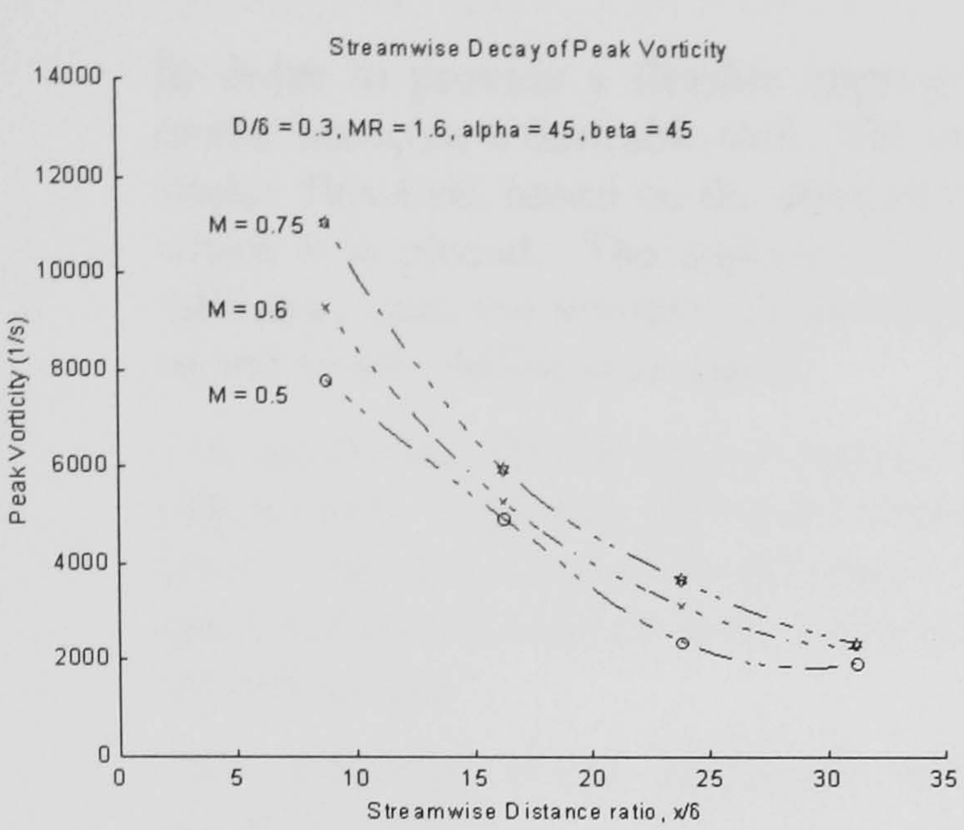

(a) Streamwise Decay of Peak Vorticity

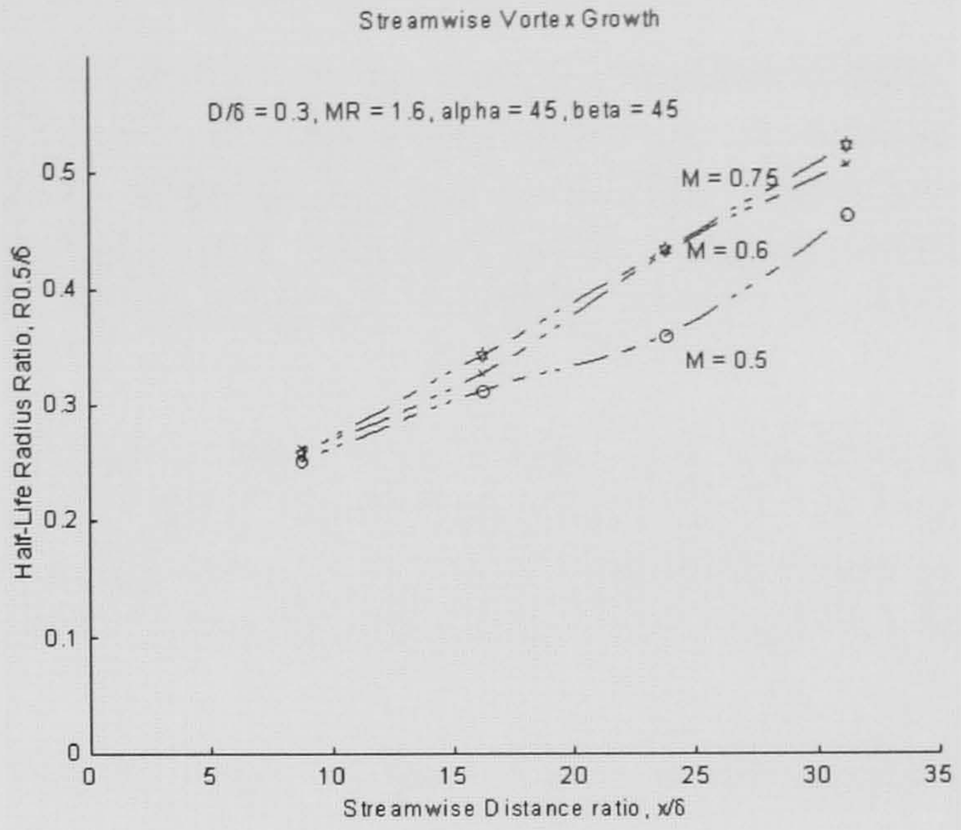

(b) Streamwise Vortex Radius Growth

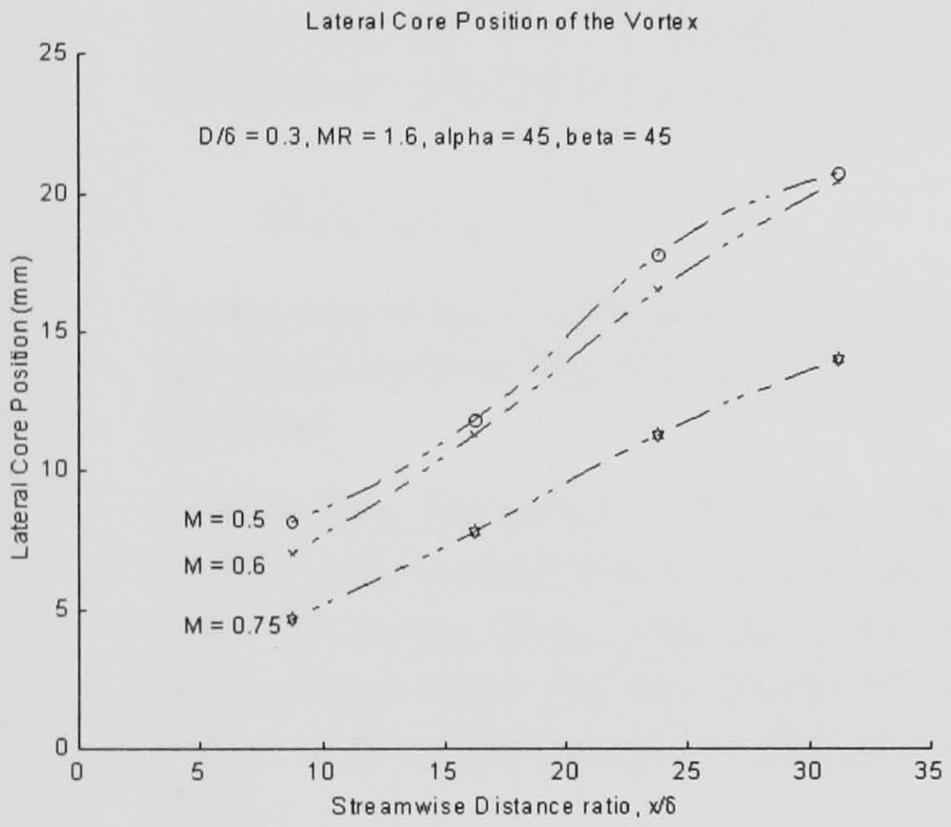

(c) Lateral Position of Vortex Core

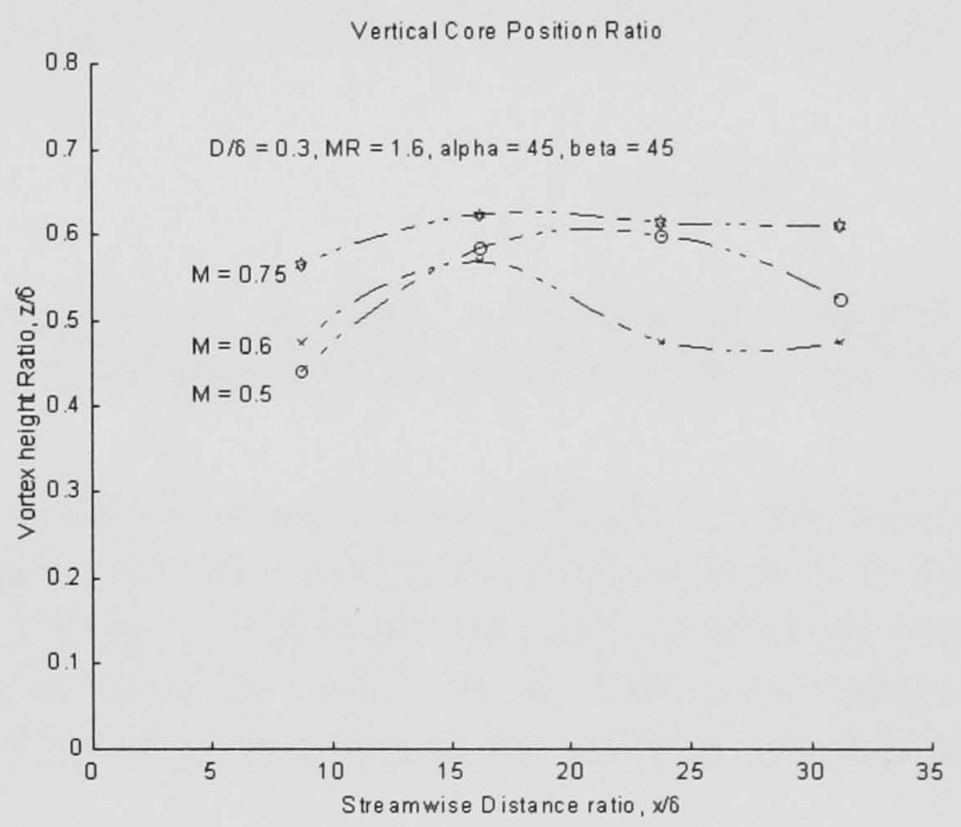

(d) Vortex Core Wall-Height Ratio Downstream

Chapter 8 - Empirical Predictions of Vorticity

In order to provide a flexible approach to the prediction of the vortex generator effects, a model becomes a desirable tool. The ideal tool would allow the prediction of the characteristic vortex flowfield based on the geometric properties of the device, and of the flow properties in which it is placed. The approach for vane-produced- and air-jet-produced- vortices must be different, since the vortices are produced by very different means. Further, the vortices tend to be physically different in nature.

The prediction should have a sound theoretical basis, which would agree with experimental observation. However, this is not always strictly possible if the model is to be kept to a simple level. The use of experimental data to provide empirically derived approximations becomes a good technique, since in very complex flowfields, the correct analytical solution may become unmanageable.

The generation of an empirical prediction tool for each of the vortex generator types is presented here.

8.1 - Modelling Approach

As noted by other investigators[23,24], the experimental data demonstrated that the vorticity profiles of the vortices were, to a large extent, Gaussian in nature. Thus, the vorticity in a cross-stream plane would be dependent on three parameters: the distance from the centre of the vortex; the radius of the vortex; and the peak vorticity in the plane of interest. The Gaussian distribution of vorticity takes the following form:

$$\omega(r) = \omega_{peak} e^{-k(r/R)^2} \qquad \textit{Equation 54}$$

In this equation, constant k would take a value of unity. In order to estimate the vorticity at any distance from the centre of the vortex, r, only the peak vorticity and the vortex radius need be found.

Establishing the radius of the vortex from experimental data is very difficult. If the vorticity profile were considered to be Gaussian in nature, then the vorticity level would reduce to zero when the radius away from the centre reached infinity. In the real case, this observation is not made, since either the low levels of vorticity far from the centre do not follow the Gaussian curve, or the experimental technique has errors of the same order as the vorticity levels at this point.

A better method is to define a radius of the vortex where the local vorticity is half the peak vorticity. This distance will be termed the '*half-life*' radius. At this point in the experimental data, the errors from the measurement technique are of insignificant, and this point can be found to a good degree of accuracy.

$$\omega(r) = \omega_{peak} e^{k(r/R_{0.5})^2}$$

if $r = R_{0.5}$

and $\omega(r) = 0.5\omega_{peak}$

then

Equation 55

$$k = \ln\left(\frac{\omega(R_{0.5})}{\omega_{peak}}\right) = \ln\left(\tfrac{1}{2}\right)$$

$$\omega(r) = \omega_{peak} e^{\ln\left(\frac{1}{2}\right)(r/R_{0.5})^2}$$

A plot of an experimental run and the Gaussian distribution are plotted in Figure 65, and the difference between the two curves far from the centre of the vortex can be easily seen. Also plotted on the graph is the graphical representation of the 'half-life' radius.

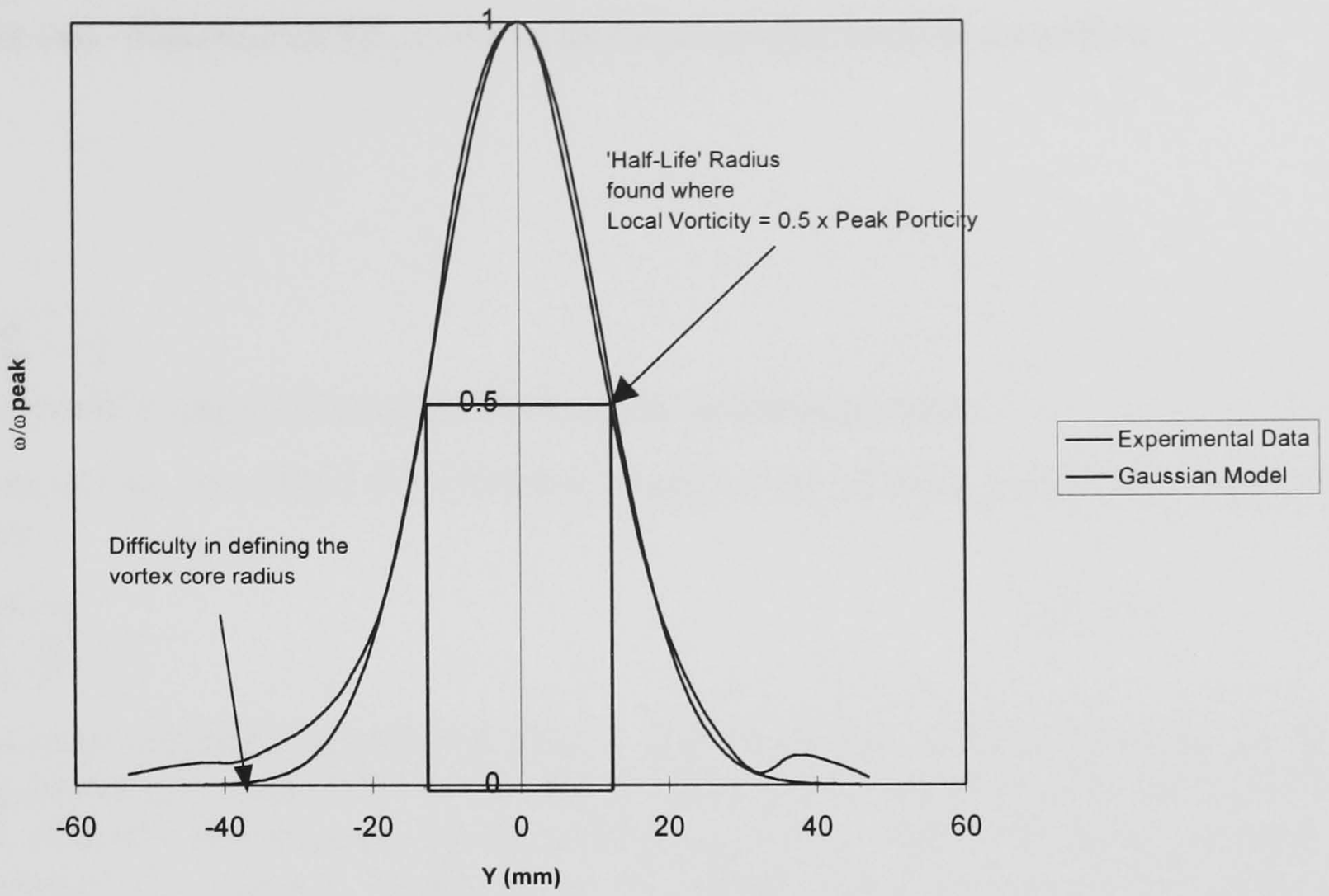

Figure 65: Comparison between the Vorticity through the centre of a Vortex Core, and a Gaussian Distribution of Similar Shape

The model then should concern the behaviour of the peak vorticity, ω_{peak}, and the 'half-life' radius, $R_{0.5}$, as the air-jet parameters are varied.

Therefore, in order to define the vorticity profile through a streamwise vortex, only the peak vorticity at that streamwise location, and the half-life radius at that point are needed. These are the two parameters to which the vortex generator geometries are to be related.

8.2 - Theoretical Approach to the Treatment of Vanes

8.2.1 - Vorticity Prediction: Prandtl's Lifting Line Theory

Prandtl developed a 'lifting line' theory that can be used to relate the lift from an aerofoil to the circulation (Γ) from a bound vortex around that aerofoil. It can be assumed that a vortex generator of rectangular flat plate geometry is a wing at incidence, and thus:

$$L = \tfrac{1}{2}\rho V^2 S C_L = \rho V \Gamma b$$

where

$S = 2hc$ for vane vortex generators

and

$b = span = 2h$ for vane vortex generators

so

$$\Gamma = \tfrac{1}{2} V c C_L$$

Now, the lift coefficient, C_L, can be related to the lift curve slope of the aerofoil and the angle of incidence of the aerofoil in the following fashion:

$$C_L = a\alpha$$

where

$$a = \frac{a_0}{1 + \left(a_0 / \pi AR\right)\left(1 + \tau\right)}$$ *Equation 56*

and a_0 is the two - dimensional lift - curve slope for an aerofoil in an inviscid flow,

where

$$a_0 = 2\pi$$

Therefore,

$$a = \frac{2\pi}{1 + \left(2\pi / \pi AR\right)\left(1 + \tau\right)}$$

where τ is Prandtl's empirical constant to correct for real aspect ratios

Combining these results, we obtain the following result for the circulation around a wing or a vortex generator:

$$\Gamma = \frac{\pi V c \alpha}{1 + \left(2 / AR\right)\left(1 + \tau\right)}$$ *Equation 57*

The circulation from the bound vortex of a wing is shed at the tips in the form of the trailing vortex. Lifting line theory states that the circulation in the bound vortex is equal to that in the trailing vortex, thus the above result can be seen to apply to a vane type vortex generator. Since the circulation of a vortex is defined as the area integration of the streamwise vorticity, the circulation can be related to the peak vorticity by the radius of the vortex core (or the 'half-life radius', $R_{0.5,}$ in this case).

$$\Gamma = \int \omega . dA = \int_0^{2\pi} \int_0^{\infty} \omega \, r . dr$$

but $\omega = \omega_{peak} e^{\ln\left(\frac{1}{2}\right)\left(\frac{r}{R_{0.5}}\right)^2}$ *Equation 58*

$$\Gamma = \omega_{peak} \int_0^{2\pi} \int_0^{\infty} e^{\ln\left(\frac{1}{2}\right)\left(\frac{r}{R_{0.5}}\right)^2} r . dr . d\theta$$

$$\Gamma = \frac{\omega_{peak} \pi {R_{0.5}}^2}{0.693}$$

Therefore:

$$\omega_{peak} = \frac{0.693 V c \alpha}{\left[1 + \left(2 / AR\right)\left(1 + \tau\right)\right] R_{0.5}^2}$$ *Equation 59*

This relationship is for any given slice though a vortex. It does not however take in to account the streamwise change in vorticity, which is brought about by the vortex decay. Since the above relationship is derived from the bound circulation of the wing (i.e. this value is the maximum value from which the streamwise decay will occur), and assuming that the peak vorticity decays as $e^{-k\left(\frac{x}{\delta}\frac{\delta}{h}\right)}$ (from ESDU Data sheet 93024[17]), from the point of generation in the downstream direction, then:

$$\omega_{peak} = \frac{0.693 V c \alpha e^{-k\left(\frac{x}{\delta}\frac{\delta}{h}\right)}}{\left[1 + \left(2 / AR\right)\left(1 + \tau\right)\right] R_{0.5}^2}$$ *Equation 60*

The constants may be written algebraically and the velocity may be substituted with the Mach number and the speed of sound, as below. It has already been shown in the results for the vane

tests that the peak vorticity is a power law function of Mach number: $\omega_{peak} = f(M^k)$. However, it should be remembered that this equation is based on the *circulation*, not the vorticity. Circulation is a linear function of Mach number, and thus in the equation below, k_M *and* k_a should assume a value of unity. In the equation below, the half-life radius is not constant with Mach number, and thus the peak vorticity, as calculated by this equation, will vary with Mach number.

$$\omega_{peak} = \frac{0.693\left(M^{k_M}\right)\left(a^{k_a}\right)c\alpha e^{-k\left(\frac{x}{\delta}\frac{\delta}{h}\right)}}{\left[1+\left(2/_{AR}\right)\left(1+\tau\right)\right]R_{0.5}^2} \qquad \textit{Equation 61}$$

This assumes that the peak vorticity varies linearly with incidence as incidence is increased. The lifting-line theory assumes attached flow over the wing. Empirically, this is not true, as the vane vortex generator appears to 'stall'. Assuming the vorticity curve slope to be approximately quadratic in nature (with an intercept of the ω_{peak} and α axes at (0,0):

$$\omega_{peak} = k_\alpha\left[\frac{\left(M^{k_M}\right)\left(a^{k_a}\right)ce^{-k\left(\frac{x}{\delta}\frac{\delta}{h}\right)}}{\left[1+\left(2/_{AR}\right)\left(1+\tau\right)\right]R_{0.5}^2}\right]\alpha^2 + l_\alpha\left[\frac{\left(M^{l_M}\right)\left(a^{l_a}\right)ce^{-l\left(\frac{x}{\delta}\frac{\delta}{h}\right)}}{\left[1+\left(2/_{AR}\right)\left(1+\tau\right)\right]R_{0.5}^2}\right]\alpha$$

Using a numerical optimiser (such as that found in the Microsoft Excel Spreadsheet Package), the equation can be used to predict values of the peak vorticity for the experimental data by varying the constants in the equation. The optimiser was programmed to vary the constants until the average difference between the experimental and predicted values of the peak vorticity was minimised. Thus, empirically, the constants are found to be:

Table 17: Empirically Derived Constants for the Vane Peak Vorticity Equation

	k	***l***
suffix-α	1.7	0.38
suffix-M	1	1
suffix-a	1	1
suffix-e	0.015	0.015
τ	0.05	0.05

Thus, while the model is based on a simple theory, the empiricism allows the honing of the equation.

8.2.2 - Half-Life Radius Prediction

In order to investigate the variation in half-life radius, $R_{0.5}$, with the vane parameters, the following expression was formulated:

$$\frac{R_{0.5}}{\delta} = f\left(\alpha, \frac{h}{\delta}, M, \frac{x}{\delta}, \text{profile}\right) \qquad \textit{Equation 62}$$

In this investigation, the aerodynamic profiles of the vanes were not varied: only simple thin flat rectangular plates of vortex-generator-aspect-ratio* of unity were tested.

Using the parametric database of experimental results, it was possible to plot graphs varying only one function in turn. It could be seen that, allowing for experimental uncertainty, the

* Vane vortex generator aspect ratio is defined using the span of the physical vane *and* its reflection in the solid surface, divided by the chord: $AR = 2hc$, where h is the height of the vane, and c is the chord.

variation of $R_{0.5}$ (non-dimensionalised by the boundary layer thickness) was approximately linear. By relaxing the linear constraint (by approximating this relationship to a quadratic), a better agreement with experimental data was achieved. Thus:

$$\frac{R_{0.5}}{\delta} = f\left(\alpha, M, \frac{x}{\delta}\right)\left[a_{h/\delta}\frac{h^2}{\delta} + b_{h/\delta}\frac{h}{\delta} + c_{h/\delta}\right]$$

Equation 63

In a similar manner, the variation of $R_{0.5}/\delta$ with Mach number and downstream distance ratio could also be seen. In both cases, the variations were seen to be power law series, with offsets. The variation with streamwise distance shows a clear increase in the radius of the vortex. As with the decay of streamwise vorticity, the variation in vortex core size is related to the streamwise distance-to-vane-height ratio, *x/h*, and is an exponential relationship. Thus in the present terminology, this may be achieved by dividing the streamwise distance ratio by the vane height ratio. This relationship was seen to be of a power law form.

The variation with Mach number is very weak. In the case of peak vorticity, this relationship would be a power law. The circulation is a linear function of Mach number (or a function of Mach number to the power unity). Since it has been seen that vorticity is a function of Mach number to the power *n* (where *n* is not unity), then is follows that the radius of the vortex core must be a function of Mach number to a power, *m* (where *m* is not unity).

Thus, the defining equation becomes:

$$\frac{R_{0.5}}{\delta} = f(\alpha)\left[a_h\left(\frac{h}{\delta}\right)^2 + b_h\left(\frac{h}{\delta}\right) + c_h\right]\left[a_x e^{b_x\frac{x}{\delta}\frac{\delta}{h}} + c_x\right]\left[a_M M^{bM} + c_M\right]$$

Equation 64

The variation with incidence reveals a relation which varies depending on the height of the vortex generator. Analysis revealed that a good approximation could be made using a power law approximation between the radius of the vortex and the incidence when the power index is itself a function of the height ratio of the vane. Thus the complete equation can be expressed in the following form:

$$\frac{R_{0.5}}{\delta} = \left[a_\alpha \alpha^{b_\alpha\frac{h}{\delta}} + c_a\right]\left[a_h\left(\frac{h}{\delta}\right)^2 + b_h\left(\frac{h}{\delta}\right) + c_h\right]\left[a_x e^{b_x\frac{x}{\delta}\frac{\delta}{h}} + c_x\right]\left[a_M M^{bM} + c_i\right.$$

Equation 65

The basis of this equation is not within a theory, merely a convenient way to express observations. This equation is attempting to estimate the radius of the vortex at the point of generation, and then to impose a streamwise term which models the effect of vorticity diffusion. The equation above is essentially a function in vane incidence (as the radius of the vortex is most affected by this parameter) with adjustments to allow for the effects of compressibility and distance from the wall.

The form of this equation was used with an optimiser from the Microsoft Excel Spreadsheet package in order to establish the values of the coefficients. For every experimental configuration, the prediction was compared with the experimentally measured value, and a percentage difference found. The absolute values of these differences were averaged over all of the test cases, and the optimisation was programmed to reduce this average error. The equation then took the following form:

Equation 66

$$\frac{R_{0.5}}{\delta} = \left[0.285\alpha^{0.6\frac{h}{\delta}} + 0.001\right]\left[1.1\left(\frac{h}{\delta}\right)^2 - 0.34\frac{h}{\delta} + 0.9\right]\left[-0.275e^{-0.026\frac{x}{\delta}\frac{\delta}{h}} + 0.45\right]\left[1.24M^{0.16} + 3.28\right.$$

The accuracy of this empirically derived equation will be reviewed in the Discussions chapter.

8.3 - The Approach to the Treatment of Air-jets

The generation of a theoretical basis for the treatment of the air-jet vortices results is significantly more difficult than that for the treatment of the vane-produced vortices. Previous investigators have noted that there are a number of important parameters to consider when investigating the vorticity produced by air-jet vortex generators. These are:

- Free-stream Mach number
- Jet Mach number ratio (Jet Mach number to free-stream Mach number)
- Jet orifice diameter
- Jet pitch angle
- Jet skew angle
- Streamwise distance from the point of generation

As noted in the literature survey in the Introduction Chapter, little attempt has been made to carry out a complete study of air-jet vortex generators by measuring the vorticity profiles in the vortex. Some work has been carried out which shows the structure, but not to demonstrate the trends for the vorticity profile. In contrast, studies have been carried out to assess the trends using air-jet vortex generators, but these studies have looked at the effect of the vortices on some other flow problem (most often flow separation), rather than studying the structure of the vortices themselves. Thus the effect on vortex strength of varying the air-jet parameters have previously been assessed (for separation control), but not in a quantitative manner in terms of vorticity. While separation control is important in its own right, it is not necessarily the only case for using vortex generators, and thus these studies should be used as an indicator for the effects of air-jet vortex generators.

The flow field produced by a pitched and skewed jet in a boundary later is very complex, and no convenient simple theory exists in order to aid modelling. Thus, in order to predict the peak vorticity produced by the air-jet vortex generators, a prediction tool was chosen that uses the trends in the air-jet performance to produce an empirical prediction equation. The process is described below.

8.3.1 - Variation of Peak Vorticity with Air-jet Parameters

The peak vorticity is a function of the various parameters listed above. Thus:

$$\omega_{peak} = f\left(M, MR, {}^{D}/_{\delta}, {}^{x}/_{\delta}, \alpha, \beta\right)$$

(In the equation above, the length parameters are non-dimensionalised by the boundary layer thickness).

Influence of Hole Diameter Ratio

From the low speed test, the variation in peak vorticity could be investigated. It could be seen that the peak vorticity would increase linearly with hole-diameter ratio. Thus, the equation above could be re-written as:

Equation 67

$$\omega_{peak} = a\frac{D}{\delta} + b$$

where

$$a = f\left(M, MR, {}^{x}/_{\delta}, \alpha, \beta\right)$$

$$b = f\left(M, MR, {}^{x}/_{\delta}, \alpha, \beta\right)$$

Influence of Mach Number

Similarly, the peak vorticity was a linear function of Mach number ratio (or velocity ratio, as it was termed in the low-Mach number test). Re-writing the functions a and b in terms of the Mach number ratio, MR:

$$a = cMR + d$$

$$b = eMR + f$$

Equation 68

Therefore:

$$\omega_{peak} = c\left(MR\frac{D}{\delta}\right) + d\frac{D}{\delta} + eMR + f$$

where

$$c = f\left(M, {}^{x}/_{\delta}, \alpha, \beta\right)$$

$$d = f\left(M, {}^{x}/_{\delta}, \alpha, \beta\right)$$

$$e = f\left(M, {}^{x}/_{\delta}, \alpha, \beta\right)$$

$$f = f\left(M, {}^{x}/_{\delta}, \alpha, \beta\right)$$

Plotting the functions c, d, e, f against α and β revealed a more complex relationship. Some of these relationships showed a curved nature, which required some theoretical analysis to increase the understanding. A discussion of these trends follows.

Influence of Pitch Angle

Imagining an air-jet that has a given diameter, Mach number ratio, and skew angle, the influence of the pitch angle, α, can be reasoned. It is well known that if the pitch angle is 90°, the jet is normal to the surface and two very weak vortices are produced. In this case, the peak vorticity will be a minimum. As the pitch angle is lowered, the degree of cross-flow generated locally by the jet increases. The cross-flow is generated by the effective pressure gradient of the jet, and it is the cross-stream pressure gradient that will generate vorticity. The orientation of the jet is critical to the cross-stream pressure gradient, and it can be easily realised that the function is approximately sinusoidal.

Influence of Skew Angle

In a similar manner to the pitch angle, the skew angle can be investigated. Previous investigators have found that in the skew angle range $0° < \beta < 30°$, the air-jet vortex generator produced two weak counter-rotating vortices, one of which becomes larger as the skew angle is increased. By 30°, the larger vortex dominates, and the smaller vortex becomes very small, and insignificant. (Whether the smaller of the two vortices is actually generated in still the subject of discussion in the literature). The peak vorticity generated in the single vortex has a maximum value at 60° - 75° depending on the pitch angle. The trend is not a simple sinusoidal curve, and the functions c, d, e, f tend to vary in a mixture of linear and sinusoidal variations with skew angle.

The relationships of the functions c, d, e, f with pitch and skew angles are summarised below:

Table 18: Trends in the Variation of Peak Vorticity with jet Angles

Function	Function in Pitch, α	Function in Skew, β
c	Sinusoidal	Linear
d	Sinusoidal	Linear
e	Sinusoidal	Sinusoidal
f	Sinusoidal	Linear

This analysis reveals that the equation becomes of the following form:

Equation 69

$$\omega_{peak} = \left\{ \begin{array}{l} \{[a_1 \cos(\alpha - a_2) + a_3]\beta + a_4 \sin(\alpha + a_5) + a_6\}\left(MR\,\frac{D}{\delta}\right) \\ + \{[a_7 \sin(\beta - a_8) + a_9]\alpha + a_{10} \cos(\alpha + a_{11}) + a_{12}\}(MR) \\ + \{[a_{13} \sin(\beta - a_{14}) + a_{15}]\cos(\alpha + a_{16}) + a_{17} \sin(\alpha + a_{18}) + a_{19}\}\left(\frac{D}{\delta}\right) \\ + \{[a_{20} \sin(\beta - a_{21}) + a_{22}]\alpha + a_{23} \sin(\alpha + a_{24}) + a_{25}\} \end{array} \right\} . f\left(M, \frac{x}{\delta}\right)$$

The implication of this equation is that there are no complex relationships which impacts on the peak vorticity between the geometrical parameters of the air-jet, and the boundary layer thickness, the free-stream Mach number, and the streamwise distance. That is, peak vorticity varies with free-stream Mach number as M^k. Also, the vortices decay with streamwise distance ratio, but this is independent of the method of generation. Thus, vortices, once generated, can be decayed in a similar fashion.

Implication of the Free-Stream Mach Number

Analysis of the high Mach number test data reveals that as the Mach number increases, the peak vorticity increases as a power law of Mach number. Further, this power law was independent of all other parameters:

Equation 70

$$\omega_{peak} = f\left(\alpha, \beta, \frac{D}{\delta}, MR, \frac{x}{\delta}\right) M^{k_M}$$

This reveals that the variation of Mach number is less significant in terms of vorticity prediction (since testing can be carried out at low Mach number and scaled). Further, that the effect of compressibility is to cause some stretching of the vortex which increases the peak vorticity of any cross-sectional plane.

Vortex Decay with Streamwise Distance

The streamwise distance ratio has the effect of reducing the peak vorticity at the point of generation with increasing distance from the generator location. Although no vortex strength data could be measured at the vortex generator location itself, measuring the vortex downstream would allow a peak vorticity value to be predicted at the vortex generator location assuming the relationship held at the point where the vorticity was being generated.

Iverson[9] noted that there were three distinct portions in a vortex: the roll-up part where the vortex was generated; a stabilisation zone where the vortex strength was constant; and a decay portion. Extending the decay portion back to the point of generation does not satisfy the physics of the problem (Figure 66), but it does allow a far more simple solution to the modelling problems, particularly since the establishment of the vortex occurs in under five hole diameters downstream of the orifice centre.

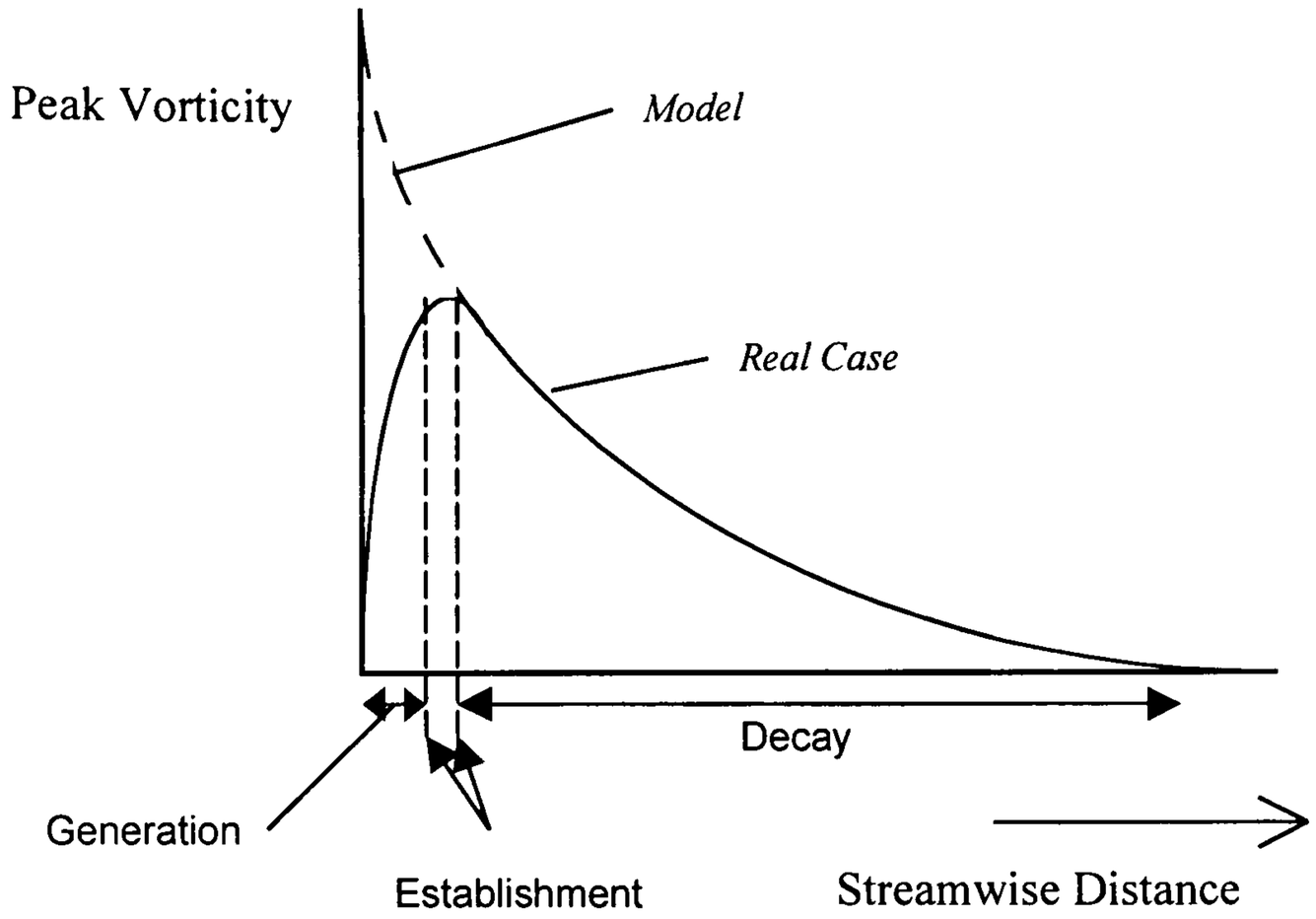

Figure 66: Streamwise Decay of Vorticity

Since the decay of the vortex is not dependent on the geometry of the air-jet (only on the initial *level* of peak vorticity), the decay function is independent of all the other parameters. It may be expected that the decay would be dependent on the height of the vortex at generation, and on the size of the vortex at generation. However, extensive flow visualisation revealed that the turning of the jet in the free-stream direction occurs very close to the orifice, and that regardless of the Mach number ratio, the turning process orients the jet core at a height of approximately one third the boundary layer height. Should the Mach number ratio be significantly larger, the penetration length would be higher. Further, over all of the cases tested, the interaction between the core of the vortex and the surface did not occur until at least 30 boundary layer heights downstream, where upon the proposed decay rate increased.

Analysis of the data revealed an equation of the following form:

Equation 71

$$\omega_{peak} = C\left\{\begin{array}{l}\left\{\left[a_1\cos(\alpha-a_2)+a_3\right]\beta+a_4\sin(\alpha-a_5)+a_6\right\}\left(MR\frac{D}{\delta}\right)\\+\left\{\left[a_7\sin(\beta-a_8)+a_9\right]\alpha+a_{10}\cos(\alpha-a_{11})+a_{12}\right\}(MR)\\+\left\{\left[a_{13}\sin(\beta-a_{14})+a_{15}\right]\cos(\alpha-a_{16})+a_{17}\sin(\beta-a_{18})+a_{19}\right\}\left(\frac{D}{\delta}\right)\\+\left\{\left[a_{20}\sin(\beta-a_{21})+a_{22}\right]\alpha+a_{23}\sin(\beta-a_{24})+a_{25}\right\}\end{array}\right\}.M^{k_M}\left(\frac{x}{\delta}\right)^{k_x}$$

In order to determine the values of the constants a_n, C, k_M and k_x, first guess values were chosen. Values were found using the decomposition method described where the constants were found by curve fitting.

In order to refine the equation, data analysis was carried out using a numerical optimiser from the Microsoft Excel Spreadsheet package. The equation can be programmed in to the spreadsheet, and a prediction can be made for the peak vorticity. This calculation was made for all of the experimental configurations tested.

The task of the optimiser was then to minimise the average of the errors for each of the 350 data points by changing the values of the constants in the vorticity prediction equation.

With this task achieved, the defining equation takes the following form:

Equation 72

$$\omega_{peak} = 5.25\left\{\begin{array}{l}\left\{\left[2230\cos(\alpha-0)-580\right]\beta+1000\sin(\alpha-15)+26700\right\}\left(MR\frac{D}{\delta}\right)\\+\left\{\left[8.4\sin(\beta+15)-19\right]\alpha+2300\cos(\alpha+58)+840\right\}(MR)\\+6100\left\{\left[-6.2\sin(\beta-26)-0.2\right]\cos(\alpha+51)+9.4\sin(\beta+81.5)-11.9\right\}\left(\frac{D}{\delta}\right)\\+\left\{\left[-0.661\sin(\beta+30)+37.7\right]\alpha+2500\sin(\beta-20)-3100\right\}\end{array}\right\}.M^{1.333}\left(\frac{x}{\delta}\right)^{-0.88}$$

It may be seen that the above equation is not dimensionally consistent in the strict sense. The terms on the right-hand-side of the equation are dimensionless, while the vorticity has the units of s^{-1}. This prediction of peak vorticity has not included the effect of the temperature of the flow, which itself affects the local speed of sound (units: m/s). Further, the equation does not take in to account the boundary layer thickness (units: m), and only uses this parameter as a scaling parameter. Thus, the coefficient at the front of the equation must be a function of the boundary layer thickness and the local speed of sound, and take the units of s^{-1}. To investigate these effects further would take a great deal of further experiments.

Thus, an expression has been generated which predicts the peak vorticity at any streamwise location downstream from an air-jet vortex generator. It should be remembered that, as an empirically derived expression, its application should be made carefully. The bounds of the expression are taken from the experimental data parameters:

- $30° < \alpha < 60°$
- $30° < \beta < 60°$
- $0.1 < D/\delta < 0.3$
- $0 < M < 0.75$
- $0.7 < MR < 2.0$
- $0 < x/\delta < 30$

The application of these equations outside these restrictions would most likely be applicable, as long as the basic flow physics does not change. The points where flow physics change include:

- skew angle below about 30°, where the characteristic vortex pair emerge, rather than the single vortex which persists downstream, and skew angles above 90°, where the air-jet becomes very diffuse while pointing upstream,
- pitch angle above about 75°, where the air-jet becomes effectively a normal jet, yielding the weak vortex pair,
- small values of D/δ where the cross-flow jet Reynolds number becomes very low, and different vortex patterns occur on the air-jet wake,
- Mach numbers close to sonic velocity, where the air-jet/cross-flow interaction will be dominated by shock waves,
- Large downstream distances, where the interaction of the vortex core with the solid surface becomes significant and the vorticity decay becomes much greater.

The accuracy of the equation will be investigated in the Discussions chapter, as will its application outside the bounds imposed above.

8.3.2 - Half-Life Radius Prediction

The air-jet produced vortices were assessed for half-life radius in the same manner as the vane produced vortices. An expression was generated which gave an initial size of the vortex radius at generation, and was adapted using a term that modelled the effect of viscosity by increasing the size of the vortex with downstream distance.

$$\frac{R_{0.5}}{\delta} = f\left(\frac{D}{\delta}, MR, \alpha, \beta, M, \frac{x}{\delta}\right)$$

Equation 73

The initial size of the vortex can be thought of as being due to the physical core of the air-jet as it issues from the jet nozzle. It is the core of the jet around which the vortex forms and thus it may be expected that the vortex will increase fairly linearly with the hole-diameter ratio. It is this parameter which gives the greatest contribution to the size of the vortex itself. This linear contribution is observed from the parametric experimental data, and may be expressed as follows:

$$\frac{R_{0.5}}{\delta} = \left[m_{D/\delta}\left(\frac{D}{\delta}\right) + c_{D/\delta}\right] f\left(MR, \alpha, \beta, M, \frac{x}{\delta}\right)$$

Equation 74

Less significant, the Mach number ratio still plays an important part. As the jet is issued, entrainment or the flow around the jet will occur, reducing the momentum at the edge of the jet, thereby reducing the ability of the jet to pierce through the cross-flow. Increasing the momentum (by increasing the Mach number ratio) effectively increases the physical diameter of the jet further away from the surface, and therefore at the point where the vortex wraps around the jet. Therefore increasing the Mach number ratio also increases the vortex radius. Again, the parametric experimental data reveals that this is a linear variation.

$$\frac{R_{0.5}}{\delta} = \left[m_{D/\delta}\left(\frac{D}{\delta}\right) + c_{D/\delta}\right]\left[m_{MR}MR + c_{MR}\right] f\left(\alpha, \beta, M, \frac{x}{\delta}\right)$$

Equation 75

As with the peak vorticity result, the radius of the vortex changes with the pitch and skew angles. As the pitch angle is increased, the effective profile of the air-jet relative to the cross-flow increases, and thus the radius of the vortex which develops also increases. This is quite a weak relationship. The skew angle reveals a more significant variation, where again, increasing the skew angle increases the effective profile of the jet, and hence the radius of the vortex.

Since it is the profile that is important, it may be expected that, as the sine of the flow angle increases, so the radius of the vortex increases. This result is observed in the parametric experimental data.

Equation 76

$$\frac{R_{0.5}}{\delta} = \left[m_{D/\delta}\left(\frac{D}{\delta}\right) + c_{D/\delta}\right]\left[m_{MR}MR + c_{MR}\right]\left[m_{\alpha}\sin(\alpha) + c_{\alpha}\right]\left[m_{\beta}\sin(\beta) + c_{\beta}\right] f\left(M, \frac{x}{\delta}\right)$$

The Mach number function is extremely weak, and serves as a method to reflect the compressibility effects in the equation. The function is basically a linear one, the gradient of which is very small.

Equation 77

$$\frac{R_{0.5}}{\delta} = \left[m_{D/\delta}\left(\frac{D}{\delta}\right) + c_{D/\delta}\right]\left[m_{MR}MR + c_{MR}\right]\left[m_{\alpha}\sin(\alpha) + c_{\alpha}\right]\left[m_{\beta}\sin(\beta) + c_{\beta}\right]\left[m_{M}M + c_{M}\right] f\left(\frac{x}{\delta}\right)$$

The function above contains all of the parameters to which the generation of the vortex can be linked. The final part is to consider the streamwise growth of the core, by introducing a simple expression that allows the vortex to grow, thus mimicking the effect of the viscous diffusion of vorticity. Over the range of streamwise distances tested, this relationship is approximately linear, yielding the final equation, in the following form:

$$\frac{R_{0.5}}{\delta} = \begin{Bmatrix} \left[m_{D/\delta}\left(\frac{D}{\delta}\right) + c_{D/\delta} \right] \left[m_{MR} MR + c_{MR} \right] \left[m_{\alpha} \sin(\alpha) + c_{\alpha} \right] \\ \left[m_{\beta} \sin(\beta) + c_{\beta} \right] \left[m_{M} M + c_{M} \right] \left[m_{x/\delta}\left(\frac{x}{\delta}\right) + c_{x/\delta} \right] \end{Bmatrix} \qquad \textit{Equation 78}$$

As with the other models, estimates for the constants in this equation were made by plotting selected graphs from the experimental data set (varying one parameter at a time). The equation was then used with the optimiser in the Microsoft Excel spreadsheet package in order to predict the vortex half-life radius ($R_{0.5}/\delta$). The predicted values were compared with the measured values to give a prediction error. The sum of the error was then used as the constraint for the optimisation process, where a minimum value was sought. The following equation resulted:

$$\frac{R_{0.5}}{\delta} = \begin{Bmatrix} \left[0.162\left(\frac{D}{\delta}\right) + 0.0893 \right] \left[0.0689 MR + 0.536 \right] \left[1 \sin(\alpha) + 4.51 \right] \\ \left[1.3 \sin(\beta) + 5.16 \right] \left[00059 M + 0.0534 \right] \left[0.0565\left(\frac{x}{\delta}\right) + 1.113 \right] \end{Bmatrix} \qquad \textit{Equation 79}$$

The results and the accuracy of these equations will be analysed in the Discussions Chapter.

8.4 - Summary

From the equations proposed above, whether the vortex generator be a vane or an air-jet, the vorticity profile can be approximated to a Gaussian distribution. The approximation has been well demonstrated in this and other investigations, and appears to hold in all areas of the vortex, except those at the very edge of the vortex core. At this location, the measurement of the very low amounts of vorticity is difficult, and the theory of small amounts of vorticity reaching out to infinity breaks down.

The equations for both vane and air-jet vortex generators allow the prediction of the peak vorticity in any cross-stream plane downstream of the vortex generator location, and the 'half-life' vortex radius. These two parameters allow the Gaussian distribution to be defined, and thus the vorticity at any location downstream of the vortex generator location can be defined, within the limits of these empirical equations.

The accuracy and application of the equations will now be discussed.

8.5 - Discussion of Prediction Tools Agreement

In order to assess the agreement between the experimental data and the predictions available from the two prediction techniques (vane and air-jets), the experimental configuration parameters were used to generate 'predicted' results for the vortices, which could be compared with the experimental. A series of graphs are presented in which the experimental data points are plotted as discrete points, while the predictions are plotted as continuous lines of a given parameter.

8.5.1 - Vane Vortex Generator Equation Agreement

Experimental results are compared with the predictions in Figure 67 to Figure 72. Rather than plotting all of the possible combinations of the 80 individual parameter configurations, plots are shown which illustrate the trends in the equations (compared with the experimental data points), and which highlight the range of errors between the predicted and experimental results.

Figure 67 shows the effect of the incidence in the comparison between the equation and the experiment for the prediction of peak vorticity and half-life radius. With regard to Figure 67 (a), it may be seen that the prediction for the smallest vane ($h/\delta = 0.554$) is very good, where it was previously noted that the increase in peak vorticity with incidence was linear (previously described as a vane which had not stalled). As the vane size is increased, the experimental response of the vane to incidence becomes increasingly non-linear. While the equation was defined with terms to cope with this effect, it may be seen that the equation result over the range $10° < \alpha < 20°$ is quite linear in nature, thereby introducing a source of error into the prediction. The main part of the curvature occurs in the range $0° < \alpha < 10°$, in order to satisfy the equation boundary condition of zero vorticity at zero incidence. Because the variation in peak vorticity with incidence is non-linear, and the effective 'stall' of the vane is difficult to predict, the simple equation must use some degree of curve-fitting to the data, the requirement of which the quadratic equation in α satisfies. If more accuracy were sought, considerably more data would need to be taken in order to allow a more accurate prediction of the 'stalling' behaviour. In Figure 67 (b), the variation in half-life radius is presented for the prediction and the experiment. It may be seen that the variation in half-life radius is quite linear in nature for the smallest vane (i.e. the 'un-stalled' vane). However, as the effect of the breakdown in the inviscid flow over the vane is noted (reducing the level of peak vorticity) the radius of the vortex increases in a non-linear manner. This increase in vortex size is directly related to the stalling effect of the vane, and therefore is difficult to predict in a simple equation form. When considering the differences between the experimental and predictions of the half-life radius, it is important to remember that a variation in half-life radius ratio ($R_{0.5}/\delta$) of 0.01 is equivalent to 0.41 mm at the experimental scale. This magnitude of difference would yield an error of around 5% on a typical value of the half-life radius. Therefore, it must be remembered that the experimental values of the half-life radius are subject to their own errors that could be significant when considering the suitability of the equation. In conclusion, it can be said that the equation holds well up to the maximum experimental incidence of 20°.

In Figure 68 (a) & (b) the variation in vane height ratio is presented for varying incidence cases. In these plots the data from the largest vane ($h/\delta = 1.639$) is also presented. As noted earlier, this vane proved to give unreliable data (inconsistency in streamwise vorticity decay plots). However, in this case, it does illustrate the limit to which this equation can be applied. Figure 68 (a), the variation in peak vorticity is displayed. It may be seen that within the boundary layer (i.e. $h/\delta < 1$), the agreement is very good, with maximum errors between the prediction and the experimental data of about 7%. Outside the boundary layer, the basic trend is followed, in that the smallest vane tends to produce the most peak vorticity (since it has not stalled). However, the errors become increasingly large as the prediction technique breaks down, with errors of 30-50% for the vane of ratio 1.639. Again, this problem with the equation is related directly to the manner in which the vortex strength reduces as the inviscid flow assumptions over the vane break down, and the vane stalls. With regard to Figure 68 (b), the

prediction of half-life radius is good in all cases, although a larger error is again seen for the vane of height ratio $h/\delta = 1.639$. The non-linear nature of the experimental data is duplicated, and results agree well to within experimental error.

The effect of streamwise development of the vortex is depicted in Figure 69 (a) & (b). Figure 69 (a) shows the streamwise reduction in peak vorticity. The reduction is predicted well, particularly in the near field ($x/\delta < 15$), but some error is generated in the far field ($x/\delta = 26.506$). It may be seen that the equation over-predicts the peak vorticity in the far downstream station for the vane at 10° incidence, while the vanes at 15° and 20° have their peak vorticity under-predicted. With reference to the half-life radius prediction (in Figure 69 (b)), it may be seen that in the near field, the radius is very well predicted, and this radius feeds in to the peak vorticity equation, thereby yielding good results. However, the half-life radius model under-predicts the streamwise growth of the smallest vane, and over-predicts the growth of the larger vanes. When the value from the radius prediction is fed to the peak vorticity equation, the error is also imposed on the peak vorticity prediction, thus yielding the error in the far field. Again the problems in predicting the radius of the vortex will be due to the prediction of the stalling of the vane. As the vane stalls, the vortex which is produced becomes quite diffuse, and appears to have a different streamwise development that the less diffuse un-stalled vortex.

It has been noted that the effect of Mach number on vortex production is that the circulation increases linearly with increasing Mach number [ref. Wendt]. This observation has been made with the current data set. Thus the equation was defined such that the circulation was a linear function of Mach number. However, it has been previously noted that the peak vorticity was a function of free-stream Mach: $\omega \propto f(M^{1.33})$. This effective change in the peak vorticity function is achieved through a change in vortex radius prediction that accommodates a significant Mach number function. Thus, so long as the vortex radius is well predicted, then the variation with Mach number should be accommodated.

With reference to Figure 70 (a) & (b), the effect of incidence can be seen for the three different Mach numbers tested*. It may be seen that the shape of the equation curves show the correct trends for peak vorticity production (Figure 70 (a)), but that some error is present. The prediction of the radius of the vortex (Figure 70 (b) reveals that the prediction of the half-life radius is excellent. It is therefore suggested that the difference be due to a weak Mach number function in the peak vorticity equation. The errors in peak vorticity prediction are less than 10%, and are therefore considered to be acceptable without significant complicated expansions of the equations. Further, in light of the excellent agreement with the prediction of the radius of the vortex, the basic equation is quite sufficient to predict the vortices.

This data has also been displayed as lines of constant incidence for varying Mach number (Figure 71 (a) and (b)). Again, it is clear that there is some error in the prediction of peak vorticity, but that the trends are present in the models. Reference to the radius prediction plot (Figure 71 (b)) does show that the prediction of the vortex radius is sensitive to Mach number, and that the radius equation does not give as accurate a prediction of the effect of Mach number as it does the effects of incidence. The error, albeit small, will feed in to the peak vorticity error prediction.

The prediction of the effects of vortex decay are shown in Figure 72 (a) & (b). Again, both equations follow the basic trends well, although both are subject to some error. Since the varying Mach number tests were carried out at a smaller scale ($\delta = 0.20$ m as opposed to $\delta = 0.0415$ m for the $M = 0.0588$ tests) the relative errors in the experimental data for the vortex radius will be larger, and will help to account for the difference displayed here.

---

* The Mach number plots do not involve the low-Mach number test data. This is because the vortex generator parameters did not allow straightforward comparison.

With the peak vorticity and vortex half-life radius predicted, their inclusion in to the final Gaussian model of the vortex is made.

8.5.2 - Comparison of Vane Cross-Stream Vorticity Profiles

The values of peak vorticity and the half-life radius are used to dimension the Gaussian distribution, as follows:

$$\omega(r) = \omega_{peak} e^{-k\left(r/R_{0.5}\right)^2}$$

Using this equation, the vorticity field could be predicted using the simple models that have been proposed. In order to assess their error on the prediction of the vorticity field, plots of the difference between the measured and the predicted profiles are presented.

The difference between results is defined as the percentage difference between the local vorticity of the equation and the experiment, and is defined as follows:

$$Diff\big|_{y,z} = \frac{\left(\omega_{model} - \omega_{measured}\right)}{\omega_{measured}}.100\Bigg|_{y,z}$$

It has already been shown (cross-reference) that the experimental vorticity level at the edge of the vortex shows some small traces far from the centre of the vortex core. At these points, the equation vorticity level would be very close to zero (since the Gaussian distribution moves asymptotically towards zero). As a result, the percentage dfference in these regions would tend towards infinity. Thus, the percentage difference was only calculated in the regions where the vorticity level was greater than +25 s^{-1} (i.e. the 'ghost' vorticity level as described in the Methodology). Outside this region, the percentage difference was set to zero.

Values were calculated at the same location as each experimental data point was measured. Also quoted on each graph are values of the vortex circulation strength calculated from the experiemtnal vorticity distributions and the predicted vorticity distributions, and the peak vorticity by both methods. In order to introduce some physical scale in to each plot, a circle denoting the prediction of the half-life radius is presented. The significance of the half-life radius is that this is the region in which 69.3% of the total vortex circulation lies, and thus a good agreement in this region should help to ensure that the circulation prediction for the vortex is good.

Figure 73 (a) to (j) show the percentage difference in the predictions of the vorticity planes for a wide range of the experimental parameters. For each of these plots, it is possible to see the same trends: the prediction of the peak vorticity is good, with most cases having an error of around 7%. Within the centre of the vortex (i.e. inside the half-life radius ring), the agreement between the experimental and predicted data is very good. Outisde this region, where the vorticity levels are very low, the errors involved with the measurement technique, and the errors involved with the Gaussian distribution assumption cause errors of over 50%. While these errors appear to be large, their significance is very small, since they occur in the regions where the local vorticity contribution to the vortex circulation is very small indeed. With reference to the circulation values displayed, it is clear that the maximum error is 16% in those cases displayed in this data set, with most cases having an error of less than 8%.

Some investigators have noted a degree of ellipticity in the radial structure of the vortex. In the main, this factor was not noted in this experiment, although as the vortex core grows out to touch the wall, this observation becomes likely. In cases such as is shown in Figure 73 (c), the vortex centre is located at about 19 mm above the wall, and the edge of the vortex (which can be estimated using the position of the half-life radius) is close to the wall. In this case, it would be expected that positive vorticity would be cancelled by negative vorticity at the wall, which may account for the overprediction in vorticity at the top and bottom of the vortex. Thus although the peak vorticity is predicted as being less than was measured, the predicted

circulation is more. However, cases of this sort were few, and were constrained to small vane height ratios, and large streamwise didtance ratios.

Summary of the Vane Prediction Equations

In the main, it can be seen that the vane prediction technique reproduces the experimental data to a good degree of accuracy, and therefore the equation can be used successfully. Typical errors in peak vorticity were seen to be around 10%, and maximum errors in circulation were around 7%.

The equation can be used to achieve similar certainty levels so long it is used within the bounds of the experimental data set used to produceit.. Since the equation was generated using experimental data based on a defined parameter set, excursions outside this parameter set will result in significant errors.

The height of the vane in relation to the boundary layer thickness is a tightly defined parameter. If the height ratio is reduced far beyond the minimum value used in generating the equation ($h/\delta = 0.554$), the vortex will be located very close to the wall surface, and will therefore decay far more quickly than will be predicted by the equation. Further, if a vane of very large proportions is used, the vortex will not be fully embedded, and may cause problems of the sort found using the largest experimental vane ($h/\delta = 1.639$). This will also increase errors.

The vane incidence is a difficult parameter to accurately equation, since the vortex generator shows a similar phenomenon to a conventional wing stall. The stalling angle is dependent on the height of the vortex generator in the boundary layer, and thus increases in the vortex generator incidence outside these equation bounds must be treated with caution.

The streamwise decay of the vortices is well described using this equation, so long as the vortex core does not meet the wall. If this does happen, then the vortex decay becomes significantly larger. However, it is usually the case that as the vortex decays, the levels of vorticity far downstream as quite small, and thus will not be significant to the flow field.

The Mach number range tested here is quite wide, and covers from $M_\infty = 0$ to $M_\infty = 0.75$. Again, care must be taken extending the Mach number higher. As the Mach number increases further, some shock effect may be seen that may cause significant distortions to the vorticity profiles.

8.5.3 - Air-jet Vortex Generator Prediction Technique Agreement

Experimental results are compared with the predictions in Figure 74 to Figure 82. There were some 340 individual data points that gave independent variation of 6 parameters. Rather than displaying all of the possible combinations of these parameters, plots are shown which illustrate the trends in the prediction technique (compared with the experimental data points), and which highlight the range of errors between the predicted and experimental results.

Figure 74 (a) & (b) show the effect of a variation in jet skew angle (β) for air-jets at pitch angles of 30°, 45° and 60°. Figure 74 (a) demonstrates that the comparison of the peak vorticity equation with the experimental data is extremely favourable, with the trends in the experimental data being replicated in the equation. Further, the differences between the predicted and the experimental data are small, with only one data point being in any significant disagreement. For the air-jet at a pitch angle of 60°, and a skew angle of 45° (α = 60°, β = 45°) the peak vorticity level is very small (ω_{peak} = 82 s^{-1}), and the equation predicts a higher value (of 98 s^{-1}). While this may be an almost 20% over-prediction, it must be remembered that this level of vorticity is close to the accuracy of the measurement system when combined with the interpolation which must be carried out to find the peak vorticity value. The prediction of the half-life radius ratio with respect to variations in jet skew angle is shown in Figure 74 (b). The difference between the equation and the experimental values is small, showing an excellent level of agreement to within experimental accuracy ($\pm 0.01\ R_{0.5}/\delta$). However, there is a trend, within the bounds of experimental error, for the half-life radius ratio to reduce with increasing skew angle. This change in size is very small, and is not shown in the equation, which tends to increase the vortex radius ratio with increasing skew angle. Attempts to model this decrease merely caused an increase in the error of the agreement between the predicted and experimental data. Since this difference was small, and the trend of reducing radius ratio was very weak, this was accepted in order to reduce the global error of the equation.

Figure 75 (a) & (b) shows the effect of variation in jet incidence for the predicted and experimental results in peak vorticity and half-life radius ratio (varying skew angles, D/δ = 0.096, MR = 1.0, M_∞ = 0.0588, x/δ = 3.855). Referring to Figure 75 (a) for the peak vorticity, the trends seen in the experimental data are repeated in the equation. Differences between the predicted and experimental data may be seen at low values of skew angle, with the agreement being very good at higher angles. This plot (as with all the others presented here) represents only nine separate vortex generator configurations (another 18 were considered for the same jet size/Mach number ratio/Mach number/streamwise distance ratio parameters alone). The maximum differences here represent a 7% difference between the predicted and the experimental data. These differences could have been reduced for this particular plot, but again the global error for the equation as applied to the wide range of other parameter choices would have increased. Thus these differences are considered to be acceptable when modelling such a complex system. The modelling of the half-life radius ratio is presented in Figure 75 (b). Allowing for experimental error, the modelling is very good, and the equation describes the basic trends in the change in the radius ratio.

Figure 76 (a) & (b) shows the effect of the hole diameter ratio (for varying Mach number ratios) on the difference between the predicted and experimental results. The linear trend of the equation follows the experimental data to a good degree of accuracy. The linear increase in peak vorticity with increasing hole diameter ratio is particularly well modelled at low velocity ratios, with the only significant disagreement being at one data point (h/δ = 0.289, MR = 2.0). The radius ratio of the vortex is shown in Figure 76 (b), and it may be seen that the trends are well modelled. The value of the vortex radius ratio is slightly over-predicted, but within the limits of the experimental accuracy.

The effect of Mach number ratio on the prediction of peak vorticity and radius ratio is seen in Figure 77 (a) & (b). The peak vorticity prediction (as highlighted in Figure 77 (a)) using the

equation is seen to have very small differences to the experimental data for all of the hole diameter ratios, and the linear trend is clear. Some difference in the prediction may be seen, but is probably more attributable to the experimental uncertainties, rather than an error in the prediction. The data in this plot is similar in nature to the previous case (Figure 76 (a)) but with lines of constant D/δ, rather than lines of constant *MR*, and for a different set of jet angles. The largest error in the previous case (at D/δ = 0.289, *MR* = 2.0) is not witnessed in Figure 77 (a), thereby suggesting an error in the data point, rather than an error in the trends presented. Figure 77 (b) presents the comparison between the predicted and experimental radius growth. Allowing for the experimental error, there is no significant growth in the vortex core with increasing Mach number ratio. The equation does predict a slight growth, although only by a small amount, and this in itself is not significant enough to generate significant difference. There is some difference in the values of the vortex core radius ratio, which is considered to be due to the hole diameter ratio terms, rather than the Mach number ratio terms. However, this difference is again small, allowing for the experimental error.

Figure 78 (a) & (b) shows the streamwise development of the vortices, in terms of peak vorticity and vortex radius ratio. Figure 78 (a) represents the streamwise decay in peak vorticity, and it may be seen that the agreement between the equation and the experiment is remarkably good, allowing for experimental error[†]. Although these plots were produced for lines of constant hole diameter ratio, similar displays of the vortex decay can be made for all of the other parameters tested. The increase in the vortex core radius is displayed in Figure 78 (b). It is clear that this is the part of the equation that is in the least agreement. The equation predicts a rate of growth consistent with the experimental data (except for the smallest hole diameter at a far downstream distance), but that the radius ratio equation is too strong a function in hole diameter ratio. This is evident from the fact that the difference in the radius of the vortex at very low streamwise distance ratios becomes increasingly larger with hole diameter ratio. However, this plot is an example of a 'worst case scenario' for the radius equation, where the difference presented here is far less than for other cases. Thus accuracy is sacrificed in this case in order to increase the predicted comparison in other cases.

The experimental data taken in the high-speed test has also been compared with the predictions for peak vorticity and half-life radius ratio, and are presented below.

Figure 79 (a) & (b) show the effect of Mach number for the two different jet pitch angles tested. The equation reveals that the differences are small, with the maximum error being about 10% in peak vorticity. The trends follow the experimental data and support the hypothesis of the vortex stretching due to compressibility factors. Similar plots can be achieved by considering different configuration parameters. With reference to Figure 79 (b), it may be seen that the agreement is less good between the experimental and equation values. At a free-stream Mach number of 0.5, the equation under-predicts the radius ratio, but the agreement is better as the Mach number increases. At lower speeds (M_∞ = 0.0588) the agreement was considerably better, leading to the assumption that, either the equation does not work well with Mach number, or the error in the experiment was quite large. The experimental uncertainty was larger, since the scale of the experimental boundary layer was half that used in the low-speed test (thus increasing the uncertainty to ± 0.02 $R_{0.5}/\delta$).

Figure 80 (a) & (b) shows the effect of varying free-stream Mach number for different jet skew angles. The graph for peak vorticity comparison (Figure 80 (a)) shows that the agreement is relatively good, with maximum errors around 10%. The trends are well predicted, and in the main, the levels of peak vorticity are well predicted as well. However, again the radius of the vortex is less well predicted. As with the previous radius prediction plot, the agreement at the lowest Mach number is less good, but improves as the Mach number increases. The effect of

---

[†] The exponential decay of the vortices should give a smooth curve to the model predictions. However, this data was produced using the experimental data configuration parameters, and straight-lines were used to join the data points.

both incidence and skew angle is modelled quite well qualitatively, and the equation predicts on the limit of the experimental error.

Figure 81 (a) & (b) shows the effect of the increase in Mach number at constant hole diameter ratios. The smaller hole diameter ratio is extremely well modelled, and the differences are very small. The larger hole diameter is less well modelled, and while a straight line is observed in the experimental data, it is of a different gradient to the equation. Figure 81 (b) demonstrates that the prediction of the vortex radius is extremely good in the case, allowing for the experimental uncertainty.

Figure 82(a) & (b) shows the streamwise development of the vortex at the three experimental Mach numbers. The basic shape of the vorticity decay curve (Figure 82 (a)) is well modelled, however, the absolute values are not in perfect agreement with the experiment. From the previous graph (Figure 81 (a)) it was seen that there was an over-prediction in the peak vorticity for this vortex generator configuration ($D/\delta = 0.3$, $\alpha = 45°$, $\beta = 45°$). This over-prediction will then impact directly on the downstream vorticity levels, since the equation is based on a prediction of an effective vorticity level at a virtual origin of generation. This vorticity level is then adjusted for Mach number and downstream position. It is clear therefore that if the generation vorticity is over-predicted, then all of the downstream predictions will be too large. Thus, in the cases where the initial generation is good, it can be seen that the agreement will be good. The prediction of the radius ratio growth in the streamwise prediction is well described in Figure 82 (b). It may be seen that the growth of the vortex is approximately linear over the range tested in this study, and that the equation predicts this growth very well in the near field (i.e. the first two measurement stations). Further downstream from this, the agreement is less good, but is on the edge of the limit of the experimental uncertainty, suggesting that the equation is good in this area. It should be remembered that it was in this area at low speed that the equation suffered from its largest difference from the experiment.

8.5.4 - Comparison of Air-jet Cross-Stream Vorticity Profiles

As with the vane vortex generator equations, the final equation to relate the vortex generator parameters to the vorticity field is through the Gaussian relationship combining the peak vorticity and the radius of the vortex:

$$\omega(r) = \omega_{peak} e^{-k\left(r/R_{0.5}\right)^2}$$

where ω_{peak} is the peak vorticity at any downstream location, $R_{0.5}$ is the vortex half-life radius, and r is the radial distance from the centreline of the vortex.

Again, the differences between the prediction and the experimental values are plotted, where the difference is defined as:

$$Diff\big|_{y,z} = \frac{\left(\omega_{model} - \omega_{measured}\right)}{\omega_{measured}}.100\Bigg|_{y,z}$$

at every experimental measurement point in the flow field. It has already been shown (cross-reference) that the experimental vorticity level at the edge of the vortex shows some small traces far from the centre of the vortex core. At these points, the predicted vorticity level would be very close to zero (since the Gaussian distribution moves asymptotically towards zero). As a result, the percentage dfference in these regions would tend towards infinity. Thus, the percentage difference was only calculated in the regions where the vorticity level was greater than +25 s^{-1} (i.e. the 'ghost' vorticity level as described in the Methodology). Outside this region, the percentage difference was set to zero.

Also plotted on each graph is a circle which shows the half-lfe radius of each vortex. As described in the vane discussion, this line gives some indication of the position of the vortex is each plot, as well as a boundary for 70% of the vortex circulation. Thus if the prediction

within the half-life radius is good, then then overall prediction of the vorticity profile should be fair.

The comparisons are made in Figure 83 (a) to (m) and cover the wide range in parameters changing of the 340 individual data points.

Figure 83 (a) shows a vortex, which is quite small, being produced very close to the wall. While the boundary layer thickness (δ) is some 41.5-mm thick, the centre of the vortex from the surface is only 7 mm. With the predicted half-life radius of the vortex being some 6-mm, the predicted circular vortex would pass though the solid surface. In the real case however, the vorticity outside the physical space (i.e. that below he wall) would not be present, and would be cancelled out by the image vorticity. This would lead to a vortex core that would be flattened at the bottom, with a larger vorticity gradient at the bottom of the vortex. It is interesting to note however, that integration of the prediction of vorticity over the 'real' space (i.e. the region above the wall) gives a circulation value very close to that in the measured field. Indeed, reference to the peak vorticity reveals the same size difference in peak vorticity as is seen in circulation strength (4.6% and 4.8% respectively). This suggests that the loss in vorticity under the wall can be accounted for directly by limiting the integration of the vorticity field to the 'real' space region. Exactly the same result is seen in Figure 83 (b), where the vortex again lies very close to the wall. The difference in peak vorticity and circulation strength are again very similar, with values of –3.8% and –3.2% respectively. In both cases, the difference in the predicted and experimental values of the half-life radius ratio ($R_{0.5}/\delta$) were extremely small (less than 2%). Clearly, as with the vane cases, outside the half-life radius, the differences appear to be very large, but due to the very low level of vorticity in these regions, these differences are insignificant in the estimation of the circulation, and in the absolute level of vorticity.

Other cases are presented where the vortex is located at a greater distance from the wall. Figure 83 (c) to (h), similar distributions may be seen. In each case, the equation tends to over predict the circulation strength of the vortex, even though the difference in peak vorticity is very small. This suggests that it is the half-life radius value that is in error. In each case, there is a region where the equation under-predicts the vorticity in the downwash region of the vortex (on the left side of each of the plots presented), and large over-predictions of the vorticity may be seen in very small areas around the rest of the vortex. This suggests that the measured vorticity profile is not axi-symmetric in nature, but that the assumed circular cross-section in stretched on the left side of the vortex centre. An explanation of this occurrence could be reasoned from the proximity of the vortex to the wall. In some of the cross-stream vorticity profiles, it was noticed that low levels of vorticity of the opposite sign to that in the main vortex was swept away from the surface around the vortex. This would reduce the positive vorticity profile around the right side of the vortex, and over the top (if sufficient negative vorticity were entrained). This would then cause the axi-symmetric mature of the vorticity profile, as pictured in Figure 84. The equation is based on the average half-life radius of the experimental vortex, which will help to reduce the difference in the prediction of the overall circulation strength, but increase the relative differences at the edge of the vortex.

This difference in vortex shape was not present for the vane produced vortices. In general, the vanes produced vortices which were higher in the boundary layer, and which were more concentrated at generation, thereby ensuring that there was no significant interplay between the vortex core and the wall until very far downstream. The nature of the air-jets to turn very quickly, and produce a vortex far closer to the surface, causes the axi-symmetric nature of these vortices.

Figure 83 (j) to (m) show the effect of Mach number on the predicted/experimental differences. The same trends are evident. Some difference is noted between the circulation form the predicted and the experimental sources, especially if the vortex is very close to the wall. However, differences in the peak vorticity are very small, highlighting the good prediction of the equation with respect to Mach number. The 'off-centre' shape of the vortex is still present,

and the averaged prediction in the half-life radius ratio is responsible for much of the error in the circulation prediction.

The final plot (Figure 83 (m)) shows a worst case for the prediction of the circulation strength. In this case, a relatively strong vortex is produced using a low-pitched jet ($\alpha = 30°$), and at a high skew angle ($\beta = 60°$). The jet diameter is also quite large ($D/\delta = 0.3$). The large jet diameter combined with the high skew angle yield a large vortex core, which is located close to the surface by the low pitch angle. The high levels of vorticity in the core reflect in the wall and produce a large tongue of negative vorticity that deforms the shape of the vortex. The simple equation cannot easily predict this change in vortex shape, and introduces a significant error into the integration of the vorticity. Thus although the difference in vorticity prediction is 9.2%, the error in circulation prediction is 32%.

Summary of the Air-jet Prediction Technique

The proposed prediction technique of the vorticity profiles from air-jet vortex generators has been shown to have a fair degree of accuracy compared with the experimental data.

The modelling of the vane-produced vorticity is an attempt to model the flow physics in terms of the vortex circulation. This is not the case for the air-jets. The flow field of an air-jet in a boundary layer is a difficult problem to model using simple processes, and unlike the vane case, there is no simple relationship that relates the vortex to the air-jet parameters. As a result, the air-jet equation is an attempt to model the trends in the performance of the air-jet, rather that to model the flow physics. This trend modelling is achieved with the average difference between the experimental and predicted values of peak vorticity being or the order of 10%, while the average difference between the experimental and predicted values of the half-life ratio being around 9%.

Using the equation, it is possible to investigate the trends and boundaries of the equation. The effect of decreasing the pitch angle of the air-jet is to increase the strength of the vortex at the point of generation, but care must be taken: if the pitch angle is very low, the vortex is generated very close to the wall, and significant vortex decay will occur. Thus if a strong vortex is required in the near field, the air-jet should be at a very low incidence (as far as is practical). However, if the vortex should persist downstream, a higher pitch angle should be used. Values for the practical engineering case should be between 30° and 45°.

Increasing the skew angle from 30° upwards increases the strength of the vortex, but extension outside the bounds of the parametric database is dangerous. Rao[48] suggested that below about 30°, the flow physics of the air-jet is different, in that a counter-rotating pair of vortices is produced of approximately the same strength (the difference in strengths increasing with skew angle). At 30°, one vortex dominates, and the other is quickly lost in the entrainment of the flow around a single strong vortex. Clearly, the trends in the air-jet performance would not extend below a skew angle of 30°. As the air-jet skew angle approaches 90°, the vortex becomes diffuse (from flow visualisation observation), and again the trends begin to break down. Thus extension of the equation much over 60° is inadvisable. Optimum values for the air-jet skew angle are between 60° and 75°.

It has already been shown that the hole diameter ratio values agree well with other investigators (see Literature Survey), even though the hole diameter ratios were larger. Thus, as long as the hole diameter ratio is not increased to a significantly greater level, extrapolation outside this database may be acceptable.

Extrapolation of the Mach number ratio trends reveals that reducing the Mach number ratio to a value of 0.4 reduces the peak vorticity to zero, regardless of the hole diameter ratio. Assuming that the linear relationship holds in the extrapolation, this suggests that there is a limiting Mach number ratio for vortex production of 0.4. Below this value, the jet would be entrained in to the free-stream flow without producing significant vorticity.

Using this equation, it has been possible to show a relationship between peak vorticity values measured over a range of free-stream Mach numbers. This is very significant, since it demonstrates that low speed wind-tunnel test results can be extrapolated in free-stream Mach number to a reasonable degree of accuracy. This impacts directly on the cost of testing other vortex generator devices that may be of interest.

8.5.5 - General Comments on Both Prediction Techniques

From the discussion of both the vane and air-jet vortex generator equations, it is clear that uncertainties are of a similar and acceptable level. It has been suggested that extensions outside the experimental database are dangerous, and care must be taken in the use of the equations.

It should be remembered that all of the data were taken in free-stream flow fields with a negligible streamwise pressure gradient. The effect of the pressure gradient is to vary the streamwise velocity (or Mach number), thereby varying the radial growth of the vortex. This in turn varies the level of peak vorticity at any downstream location.

In the case of the vane vortex generator equation, the equation for peak vorticity is really a model of vortex circulation with the allowance for a radius term to convert from circulation to peak vorticity. The streamwise decay of the circulation should not be significantly affected by the pressure gradient, unless the vortex radius increases significantly, causing interference with the wall. It is the radius term that will be the significant factor in the allowance for the streamwise pressure gradient, whereby the streamwise pressure gradient will cause a growth of reduction in the vortex core size. With some empirical data to account for a streamwise pressure variation, this radius equation could be adjusted to account for this variation.

In the case of the air-jet vortex generator equation, alterations would be needed for both the peak vorticity and the radius equations. The adjustment of the equations would most likely be a term that would act as an adjustment factor to the basic peak vorticity equation, in a similar manner to Mach number and streamwise decay terms in the present equation. This adjustment factor would have a value of unity when the pressure gradient was zero. Again, the radius equation would require a similar adjustment to that applied to the vane equation.

8.6 - Comparisons between the Vane Experimental Results and the Vane Predictions

Figure 67: Effect of Vane Incidence

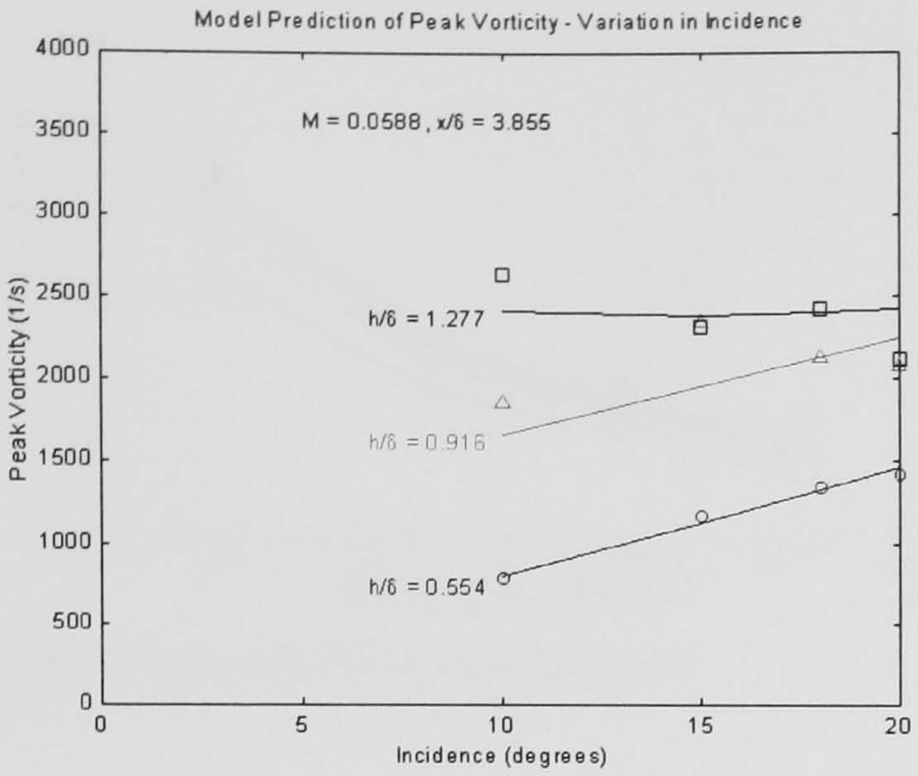

(a) Effect of α on Peak Vorticity Prediction

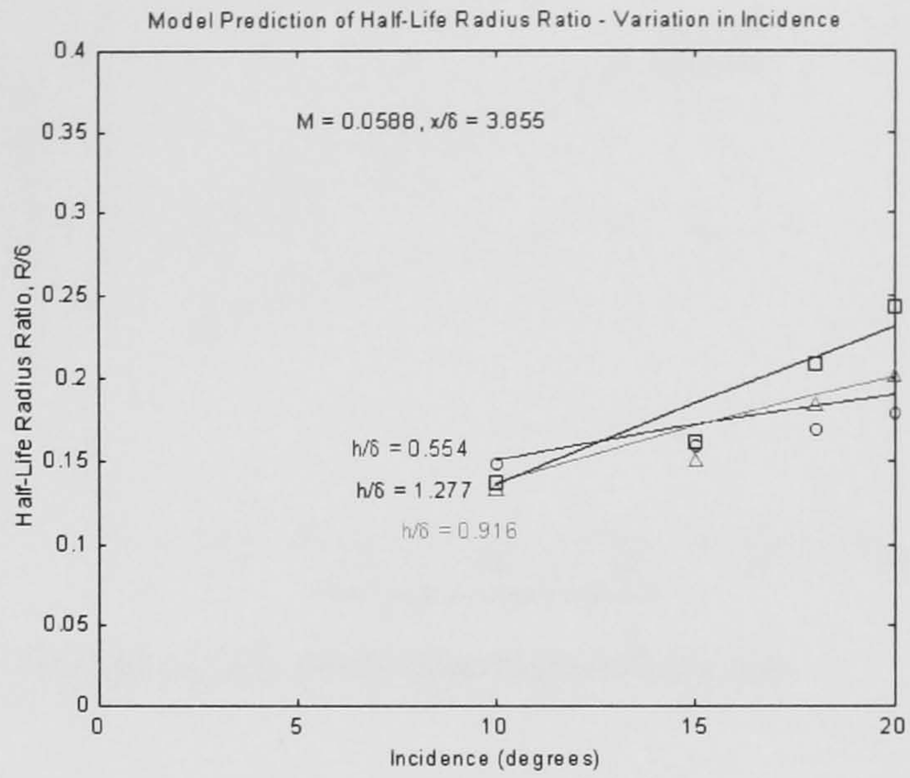

(b) Effect of α on Half-life Radius Prediction

Figure 68: Effect of Vane Height-to-Boundary Layer Thickness Ratio

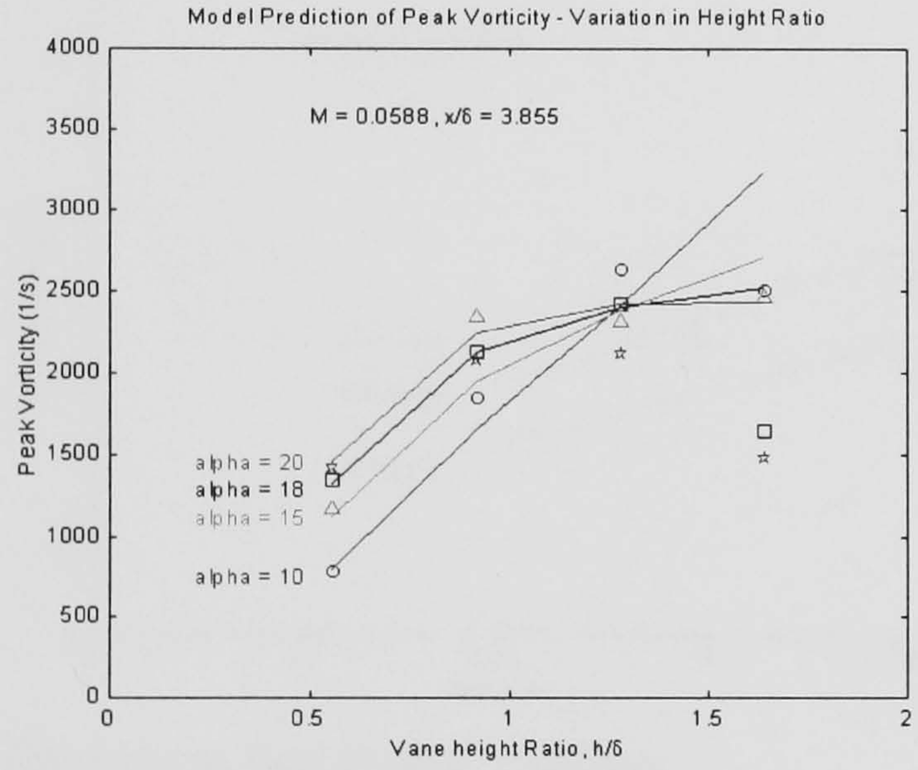

(a) Effect of h/δ on Peak Vorticity Prediction

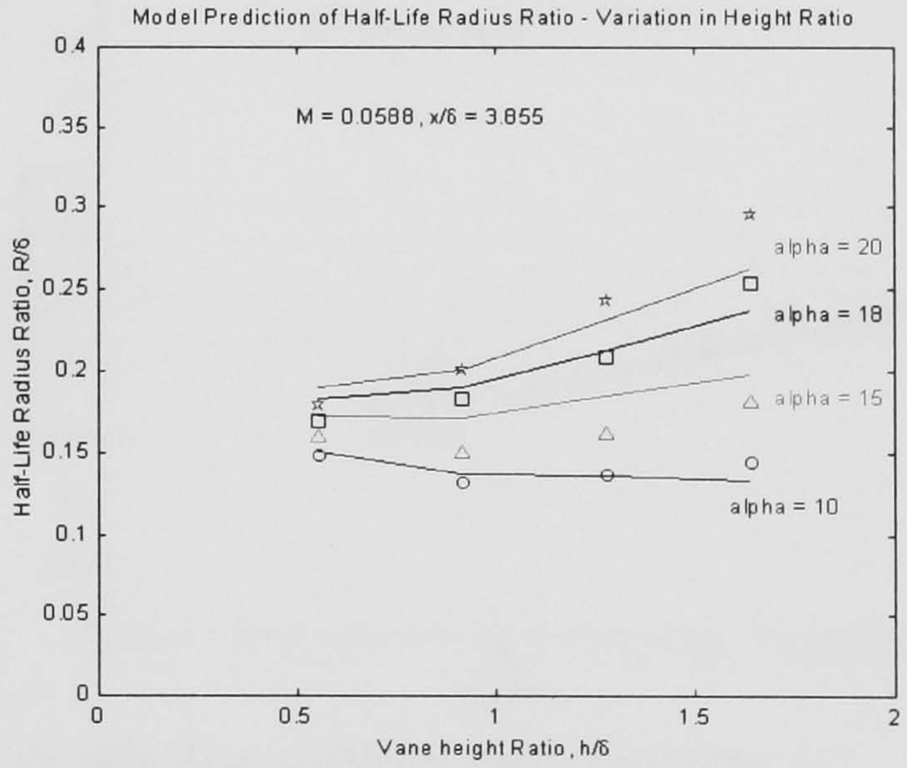

(b) Effect of h/δ on Half-life Radius Prediction

Figure 69: Streamwise Vortex Development

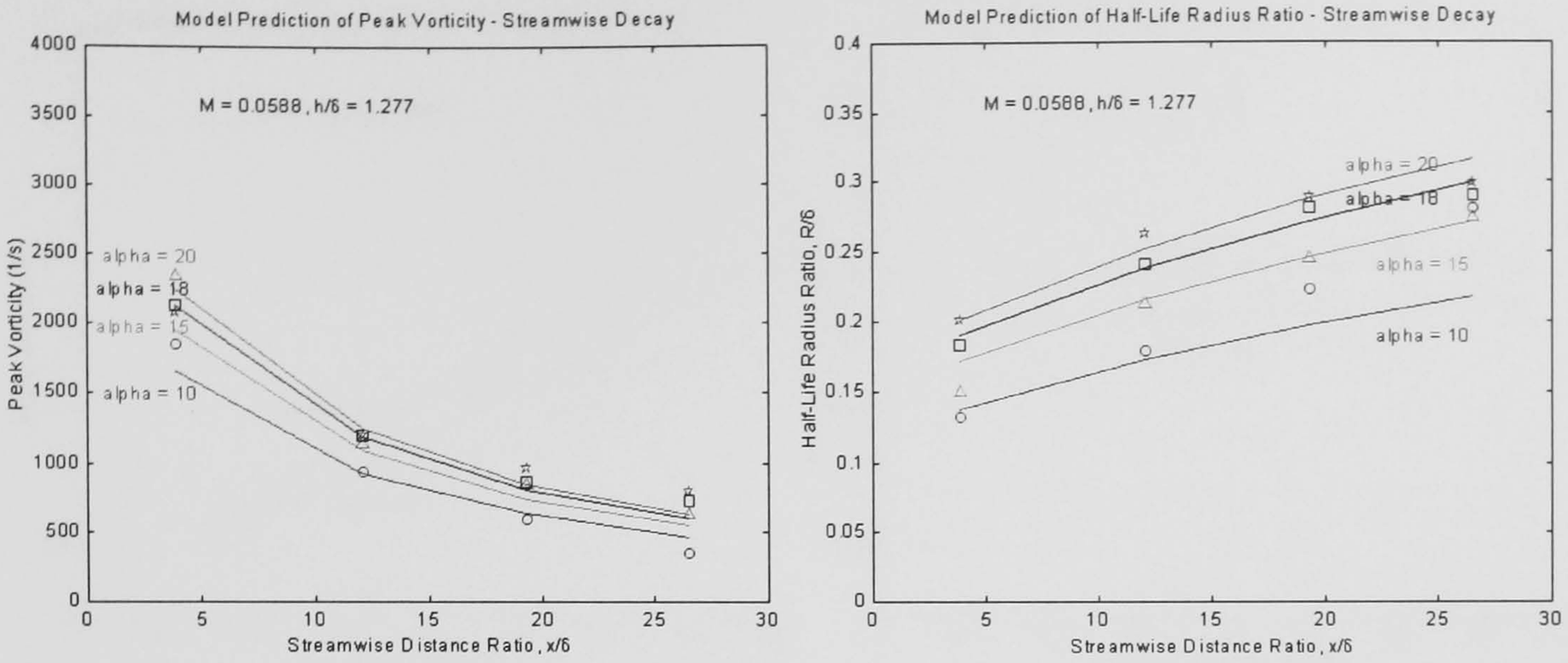

(a) Effect of x/δ on Peak Vorticity Prediction

(b) Effect of x/δ on Half-life Radius Prediction

Figure 70: Effect of Vane Incidence (Mach Number Cases)

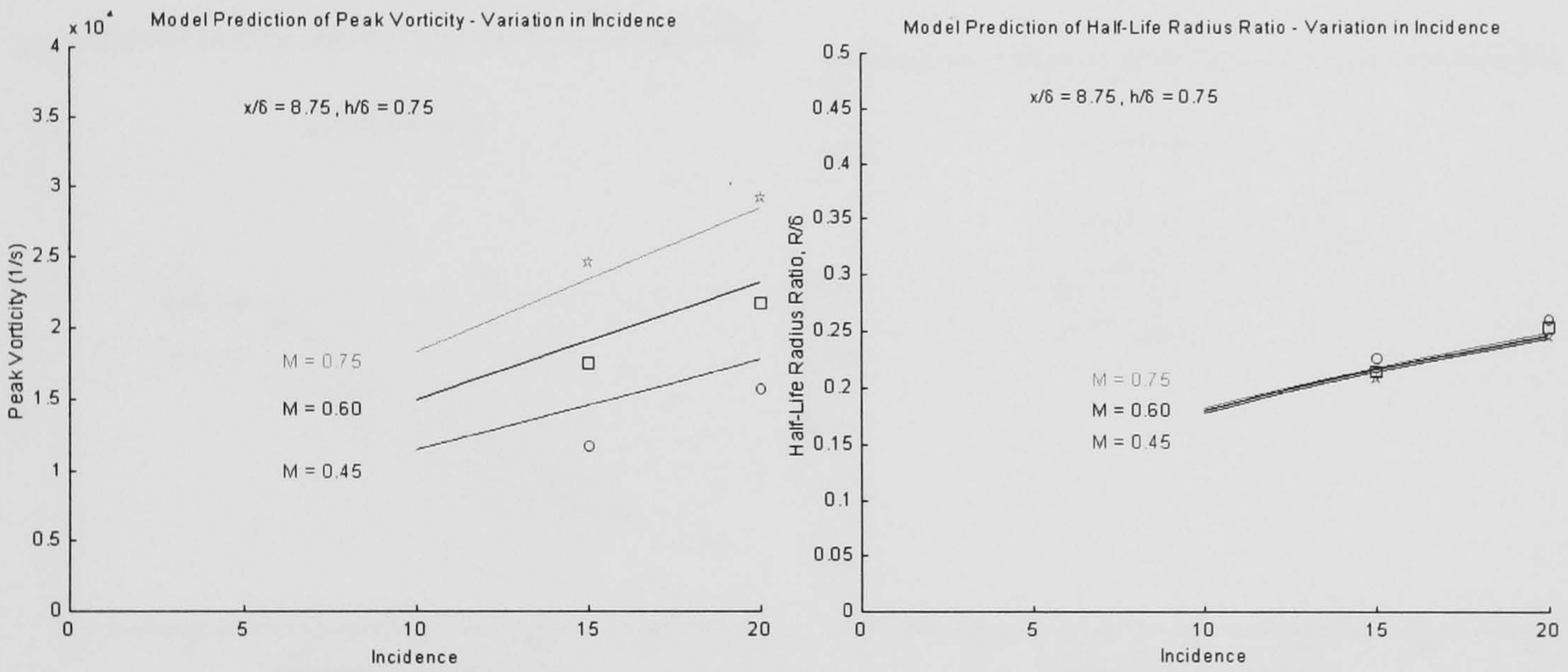

(a) Effect of α on Peak Vorticity Prediction

(b) Effect of α on Half-life Radius Prediction

Figure 71: Effect of Free-stream Mach Number

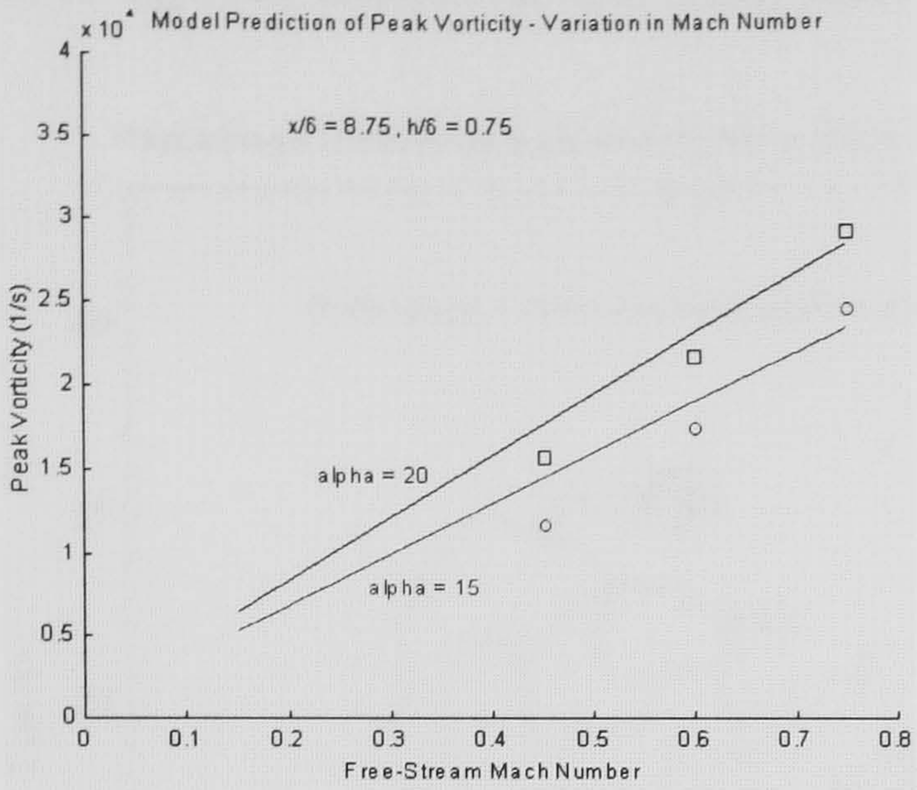

(a) Effect of Mach Number on Peak Vorticity Prediction

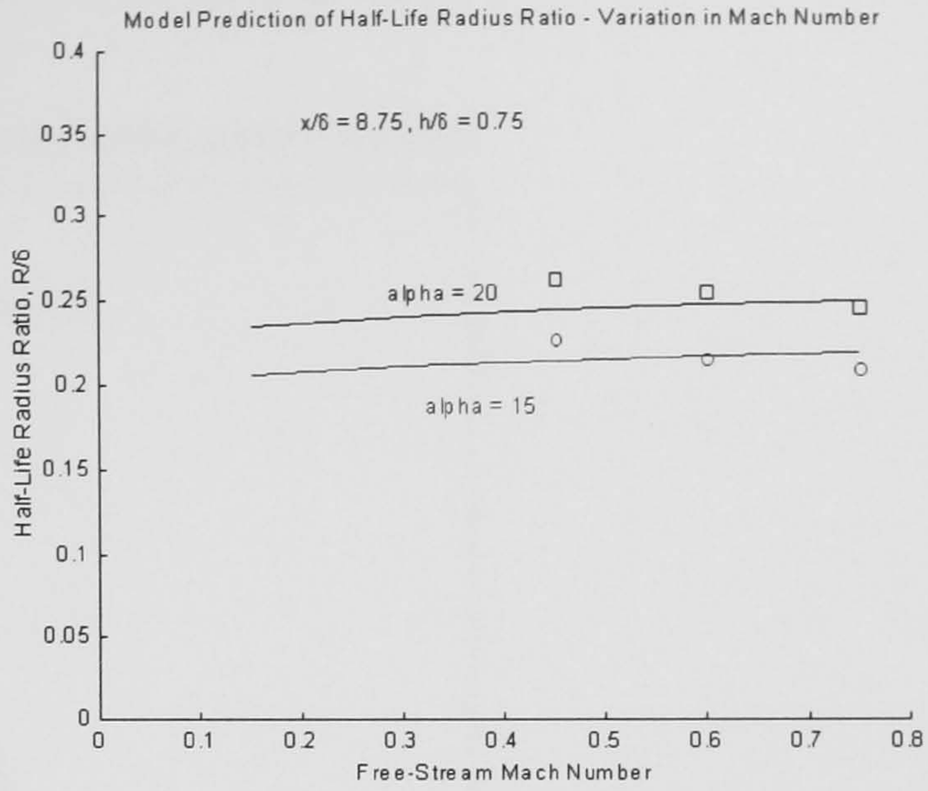

(b) Effect of Mach Number on Half-life Radius Prediction

Figure 72: Streamwise Vortex Development (Mach Number Cases)

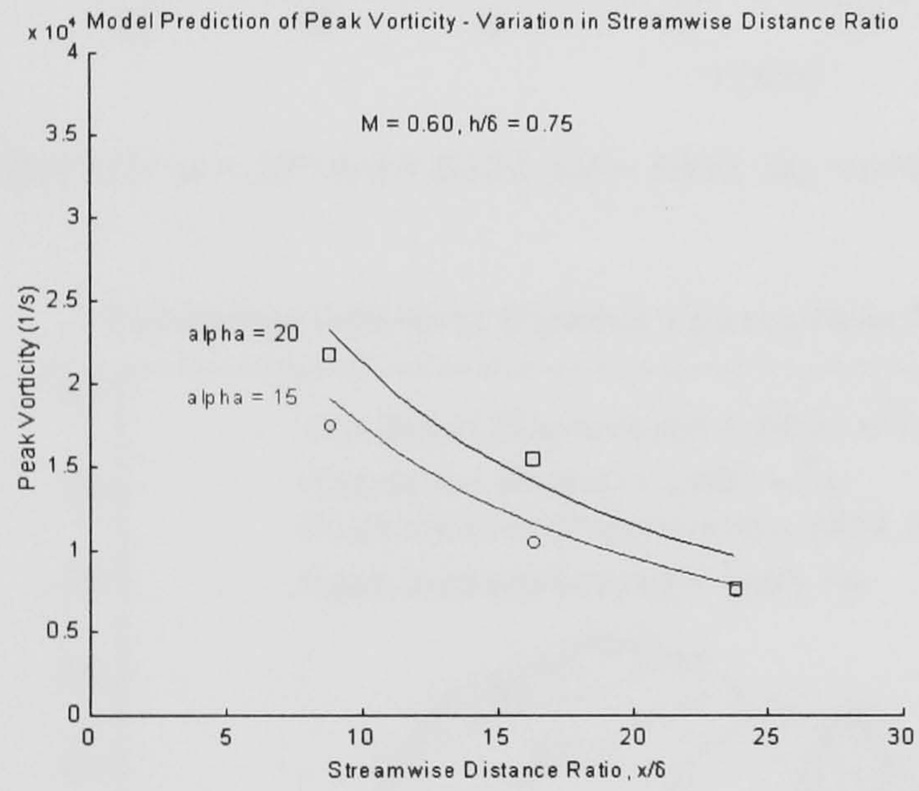

(a) Vortex Decay Prediction (with Mach Number)

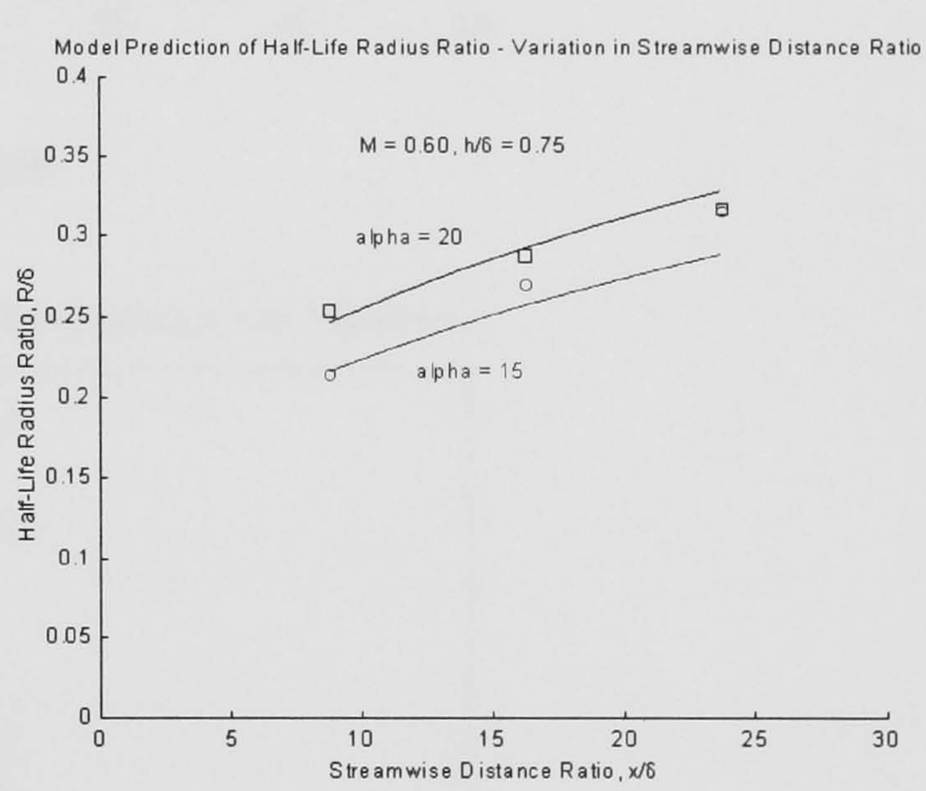

(b) Half-life Radius Prediction (with Mach Number)

8.7 - Vane Comparison between Prediction and Experiment

Figure 73: Difference Between Predictions and Experimental Vorticity Measurements

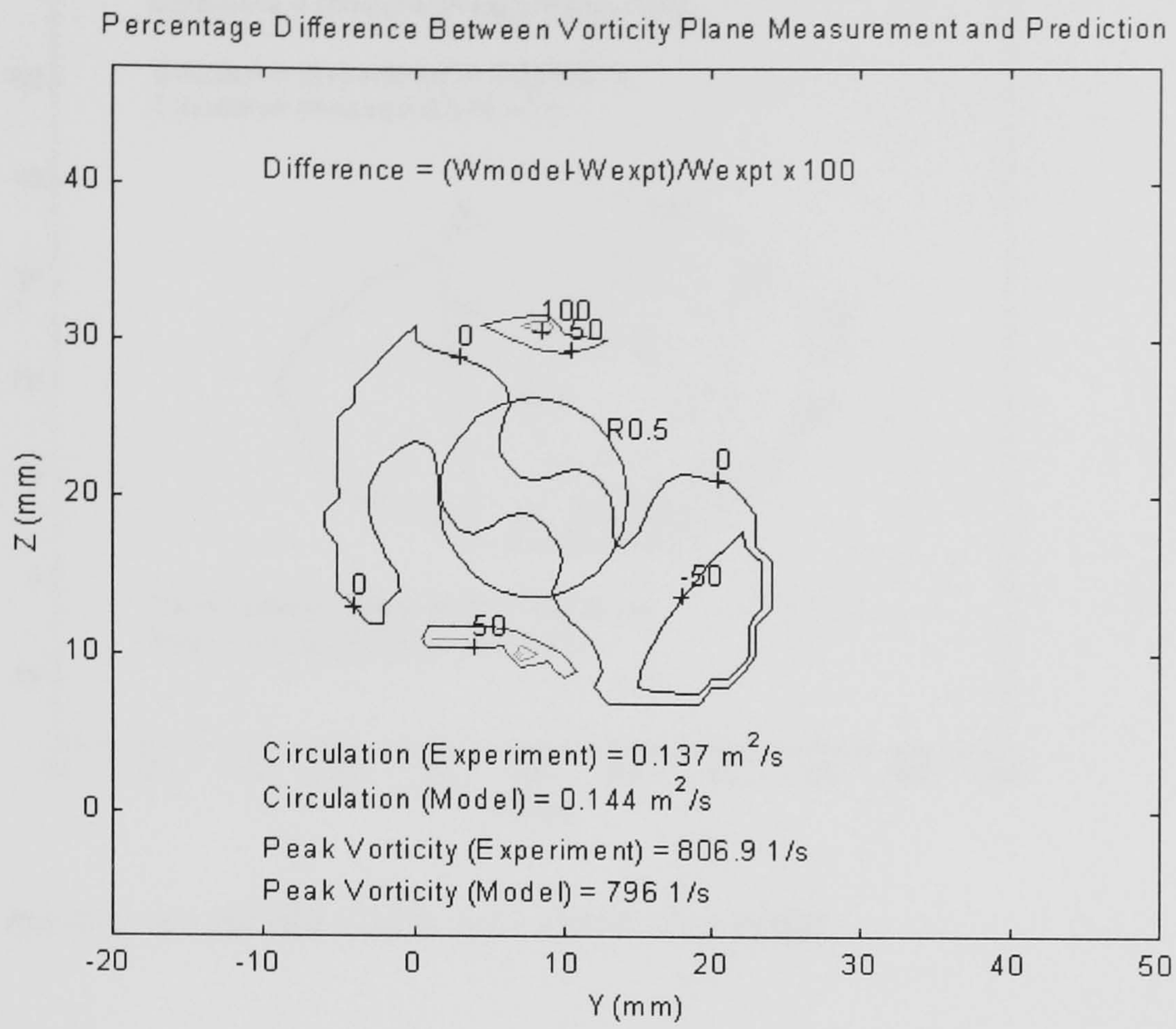

(a) Run 111: $\alpha = 10°$, $h/\delta = 0.554$, $x/\delta = 3.855$, $M_\infty = 0.0588$

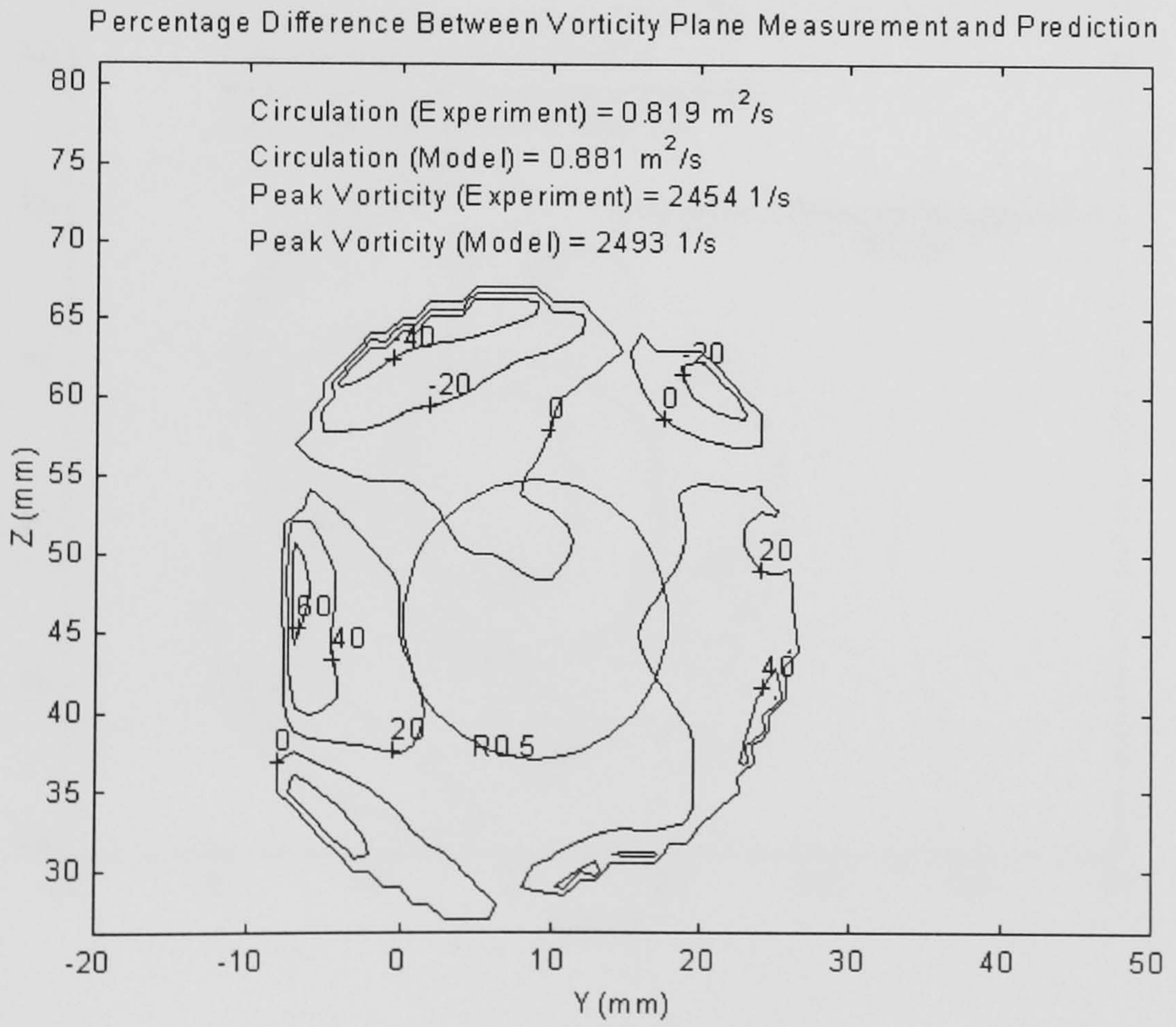

(b) Run 133: $\alpha = 18°$, $h/\delta = 1.277$, $x/\delta = 3.855$, $M_\infty = 0.0588$

Figure 73: Difference Between Predictions and Experimental Vorticity Measurements (Cont.)

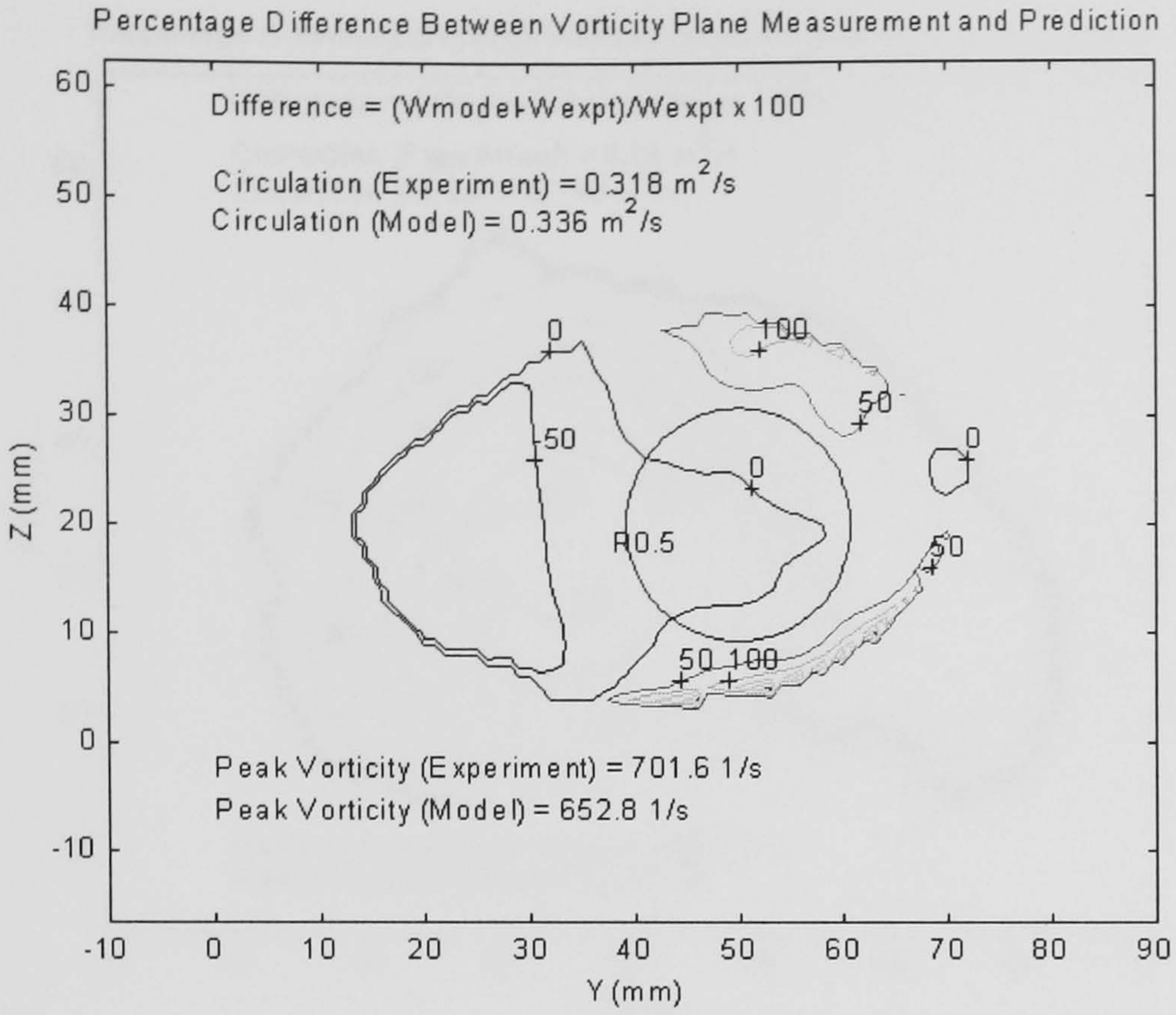

(c) Run 214: $\alpha = 20°$, $h/\delta = 0.554$, $x/\delta = 12.048$, $M_\infty = 0.0588$

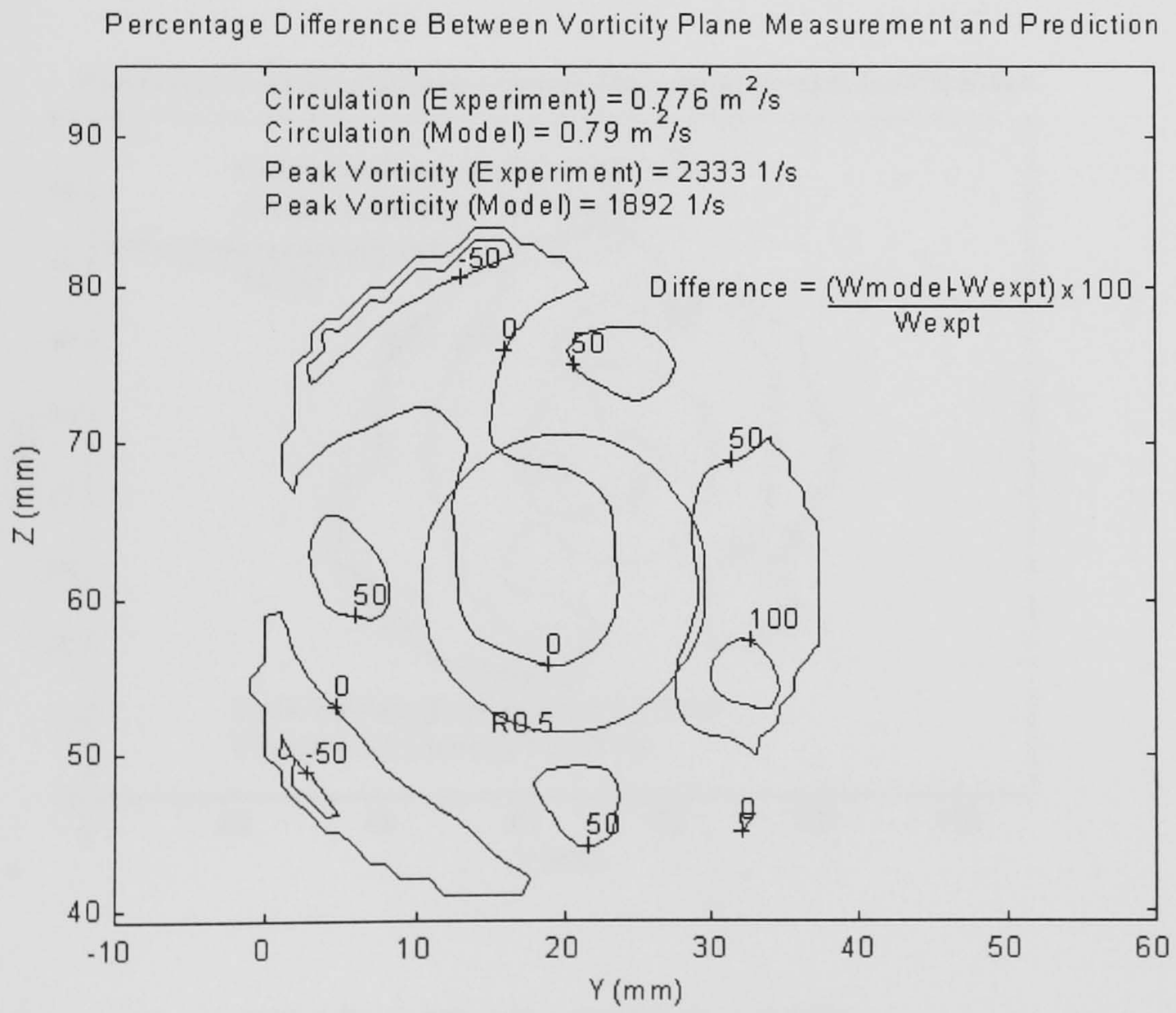

(d) Run 242: $\alpha = 15°$, $h/\delta = 16.39$, $x/\delta = 12.048$, $M_\infty = 0.0588$

Figure 73: Difference Between Predictions and Experimental Vorticity Measurements (Cont.)

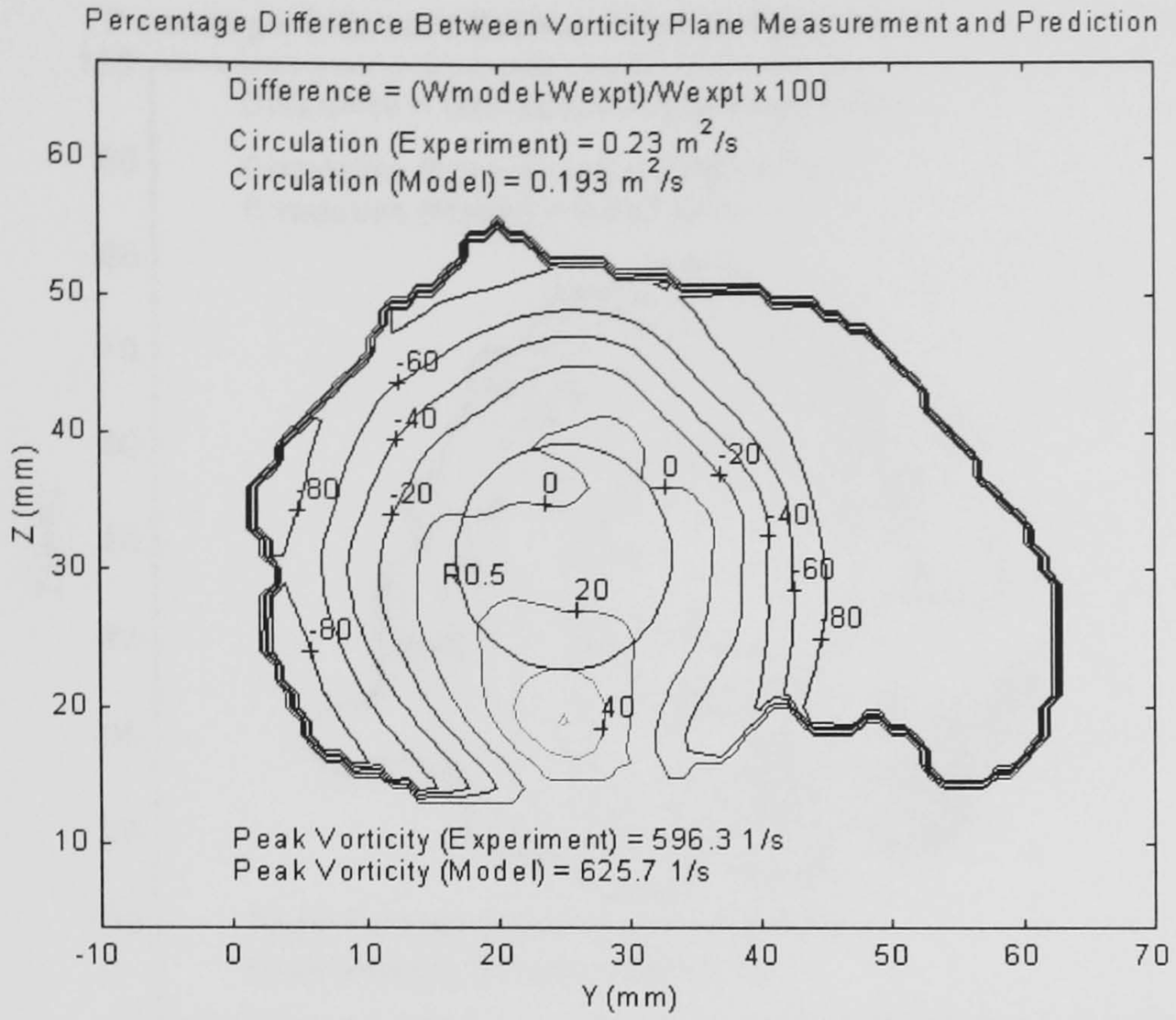

(e) Run 321: $\alpha = 10°$, $h/\delta = 0.916$, $x/\delta = 19.277$, $M_\infty = 0.0588$

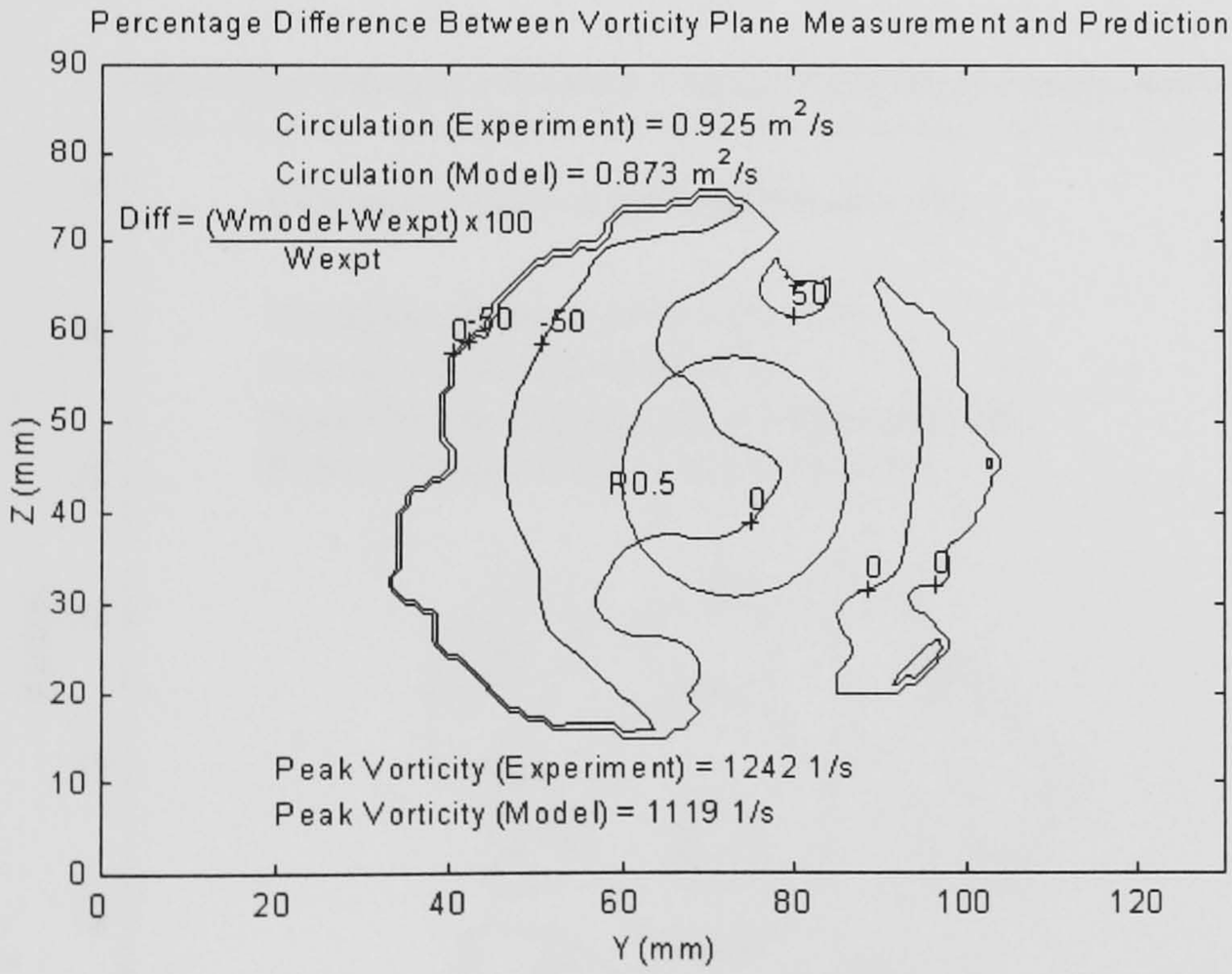

(f) Run 334: $\alpha = 20°$, $h/\delta = 1.277$, $x/\delta = 19.277$, $M_\infty = 0.0588$

Figure 73: Difference Between Predictions and Experimental Vorticity Measurements (Cont.)

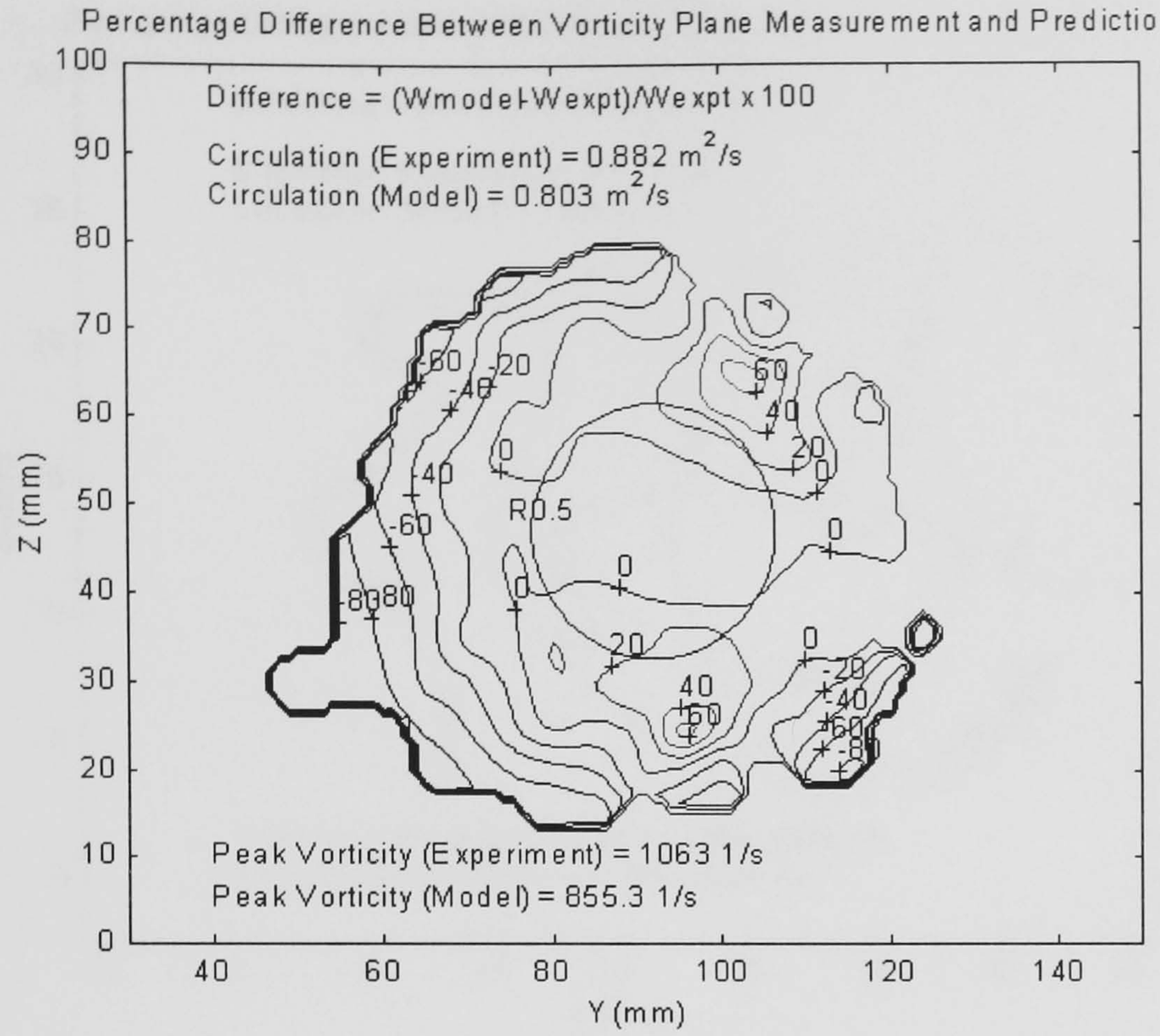

(g) Run 434: $\alpha = 20°$, $h/\delta = 1.277$, $x/\delta = 26.506$, $M_\infty = 0.0588$

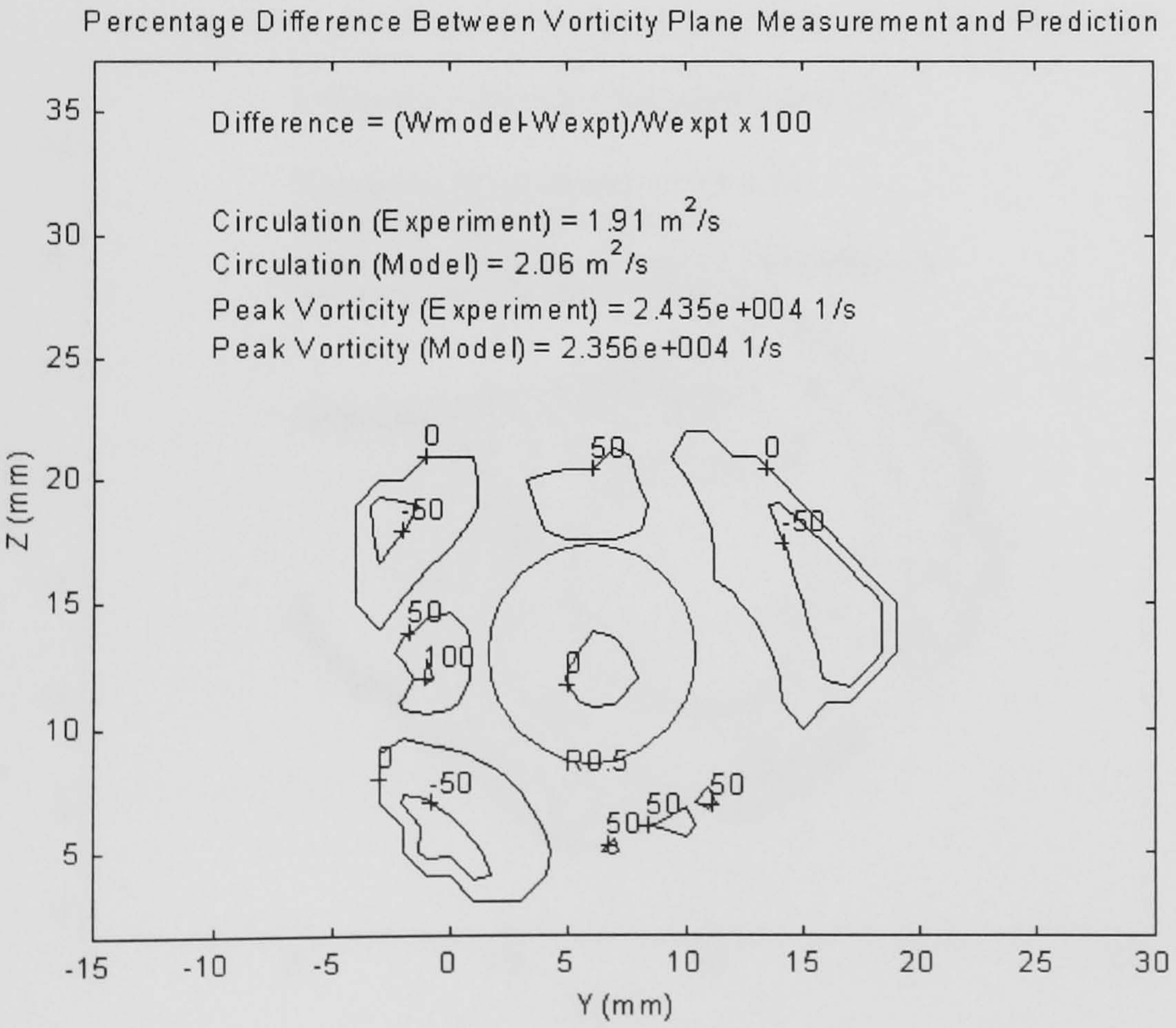

(h) Run v03: $\alpha = 15°$, $h/\delta = 0.75$, $x/\delta = 8.75$, $M_\infty = 0.743$

Figure 73: Difference Between Predictions and Experimental Vorticity Measurements (Cont.)

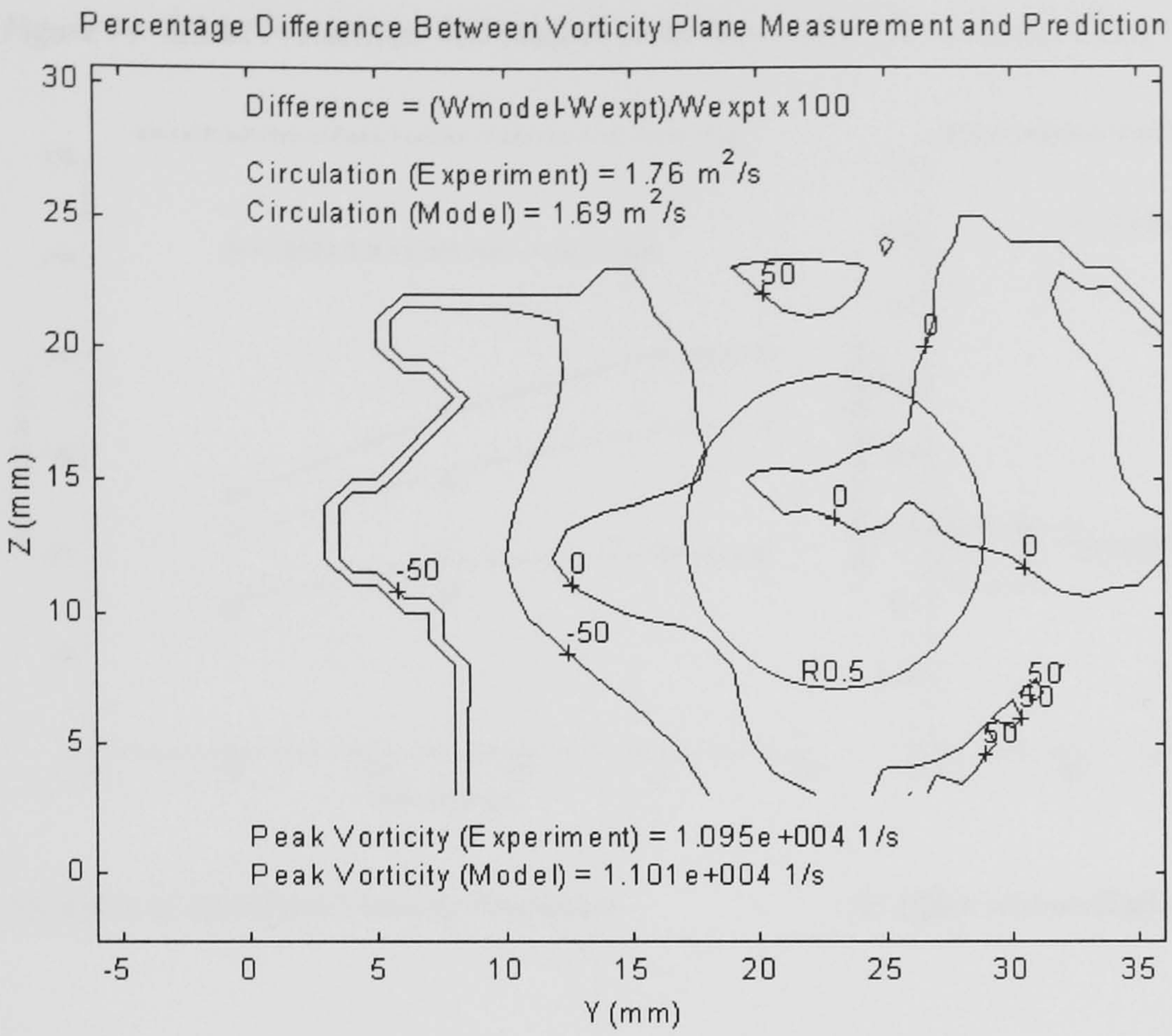

(i) Run v10: $\alpha = 20°$, $h/\delta = 0.75$, $x/\delta = 16.25$, $M_\infty = 0.454$

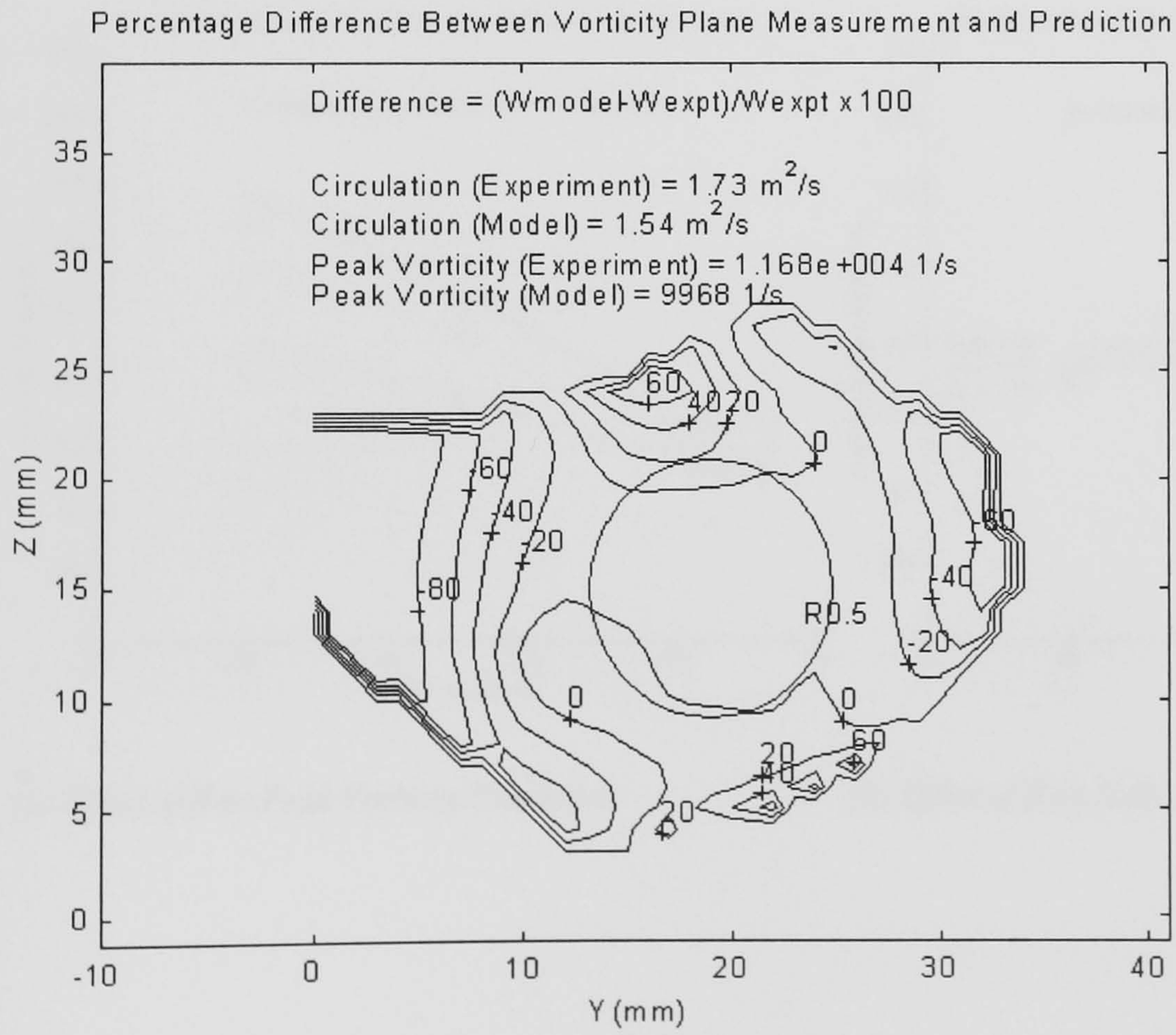

(j) Run v15: $\alpha = 15°$, $h/\delta = 0.75$, $x/\delta = 23.75$, $M_\infty = 0.752$

8.8 - Comparisons between the Air-jet Experimental Results and the Vane Predictions

Figure 74: Model Predictions with Respect to Jet Skew Angle (Jet Incidence Cases)

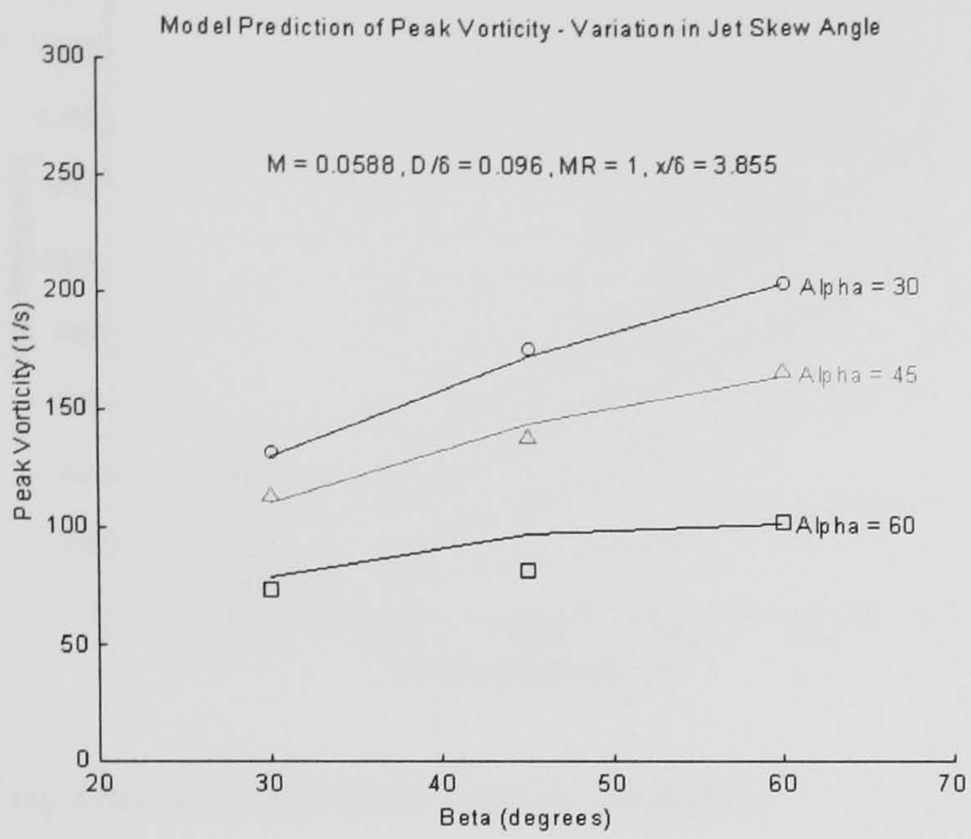

(a) Effect of α on Peak Vorticity Prediction

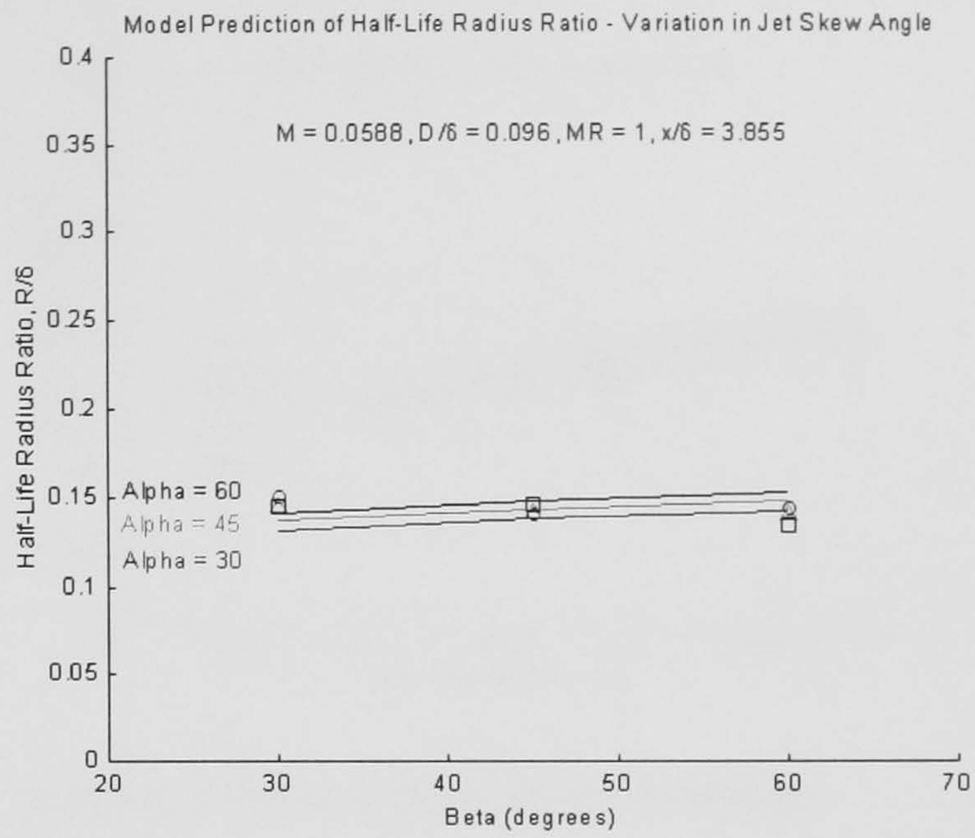

(b) Effect of α on Half-Life Radius Prediction

Figure 75: Model Predictions with Respect to Jet Incidence Angle (Jet Skew Cases)

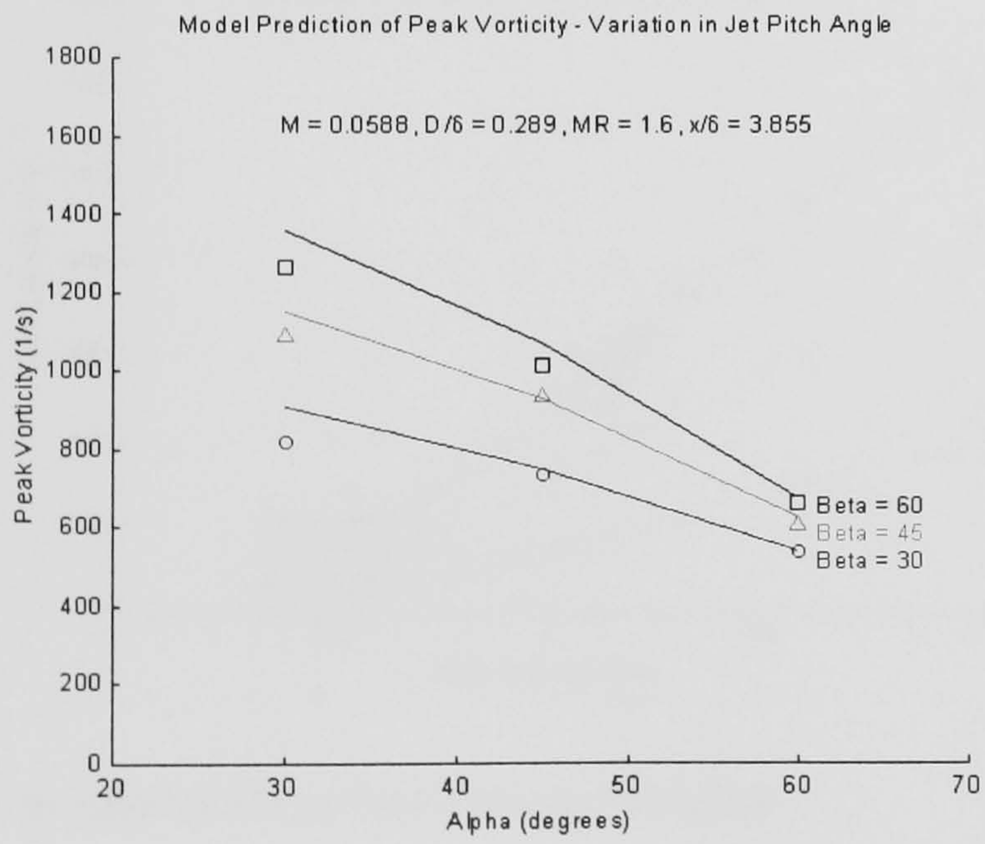

(a) Effect of β on Peak Vorticity Prediction

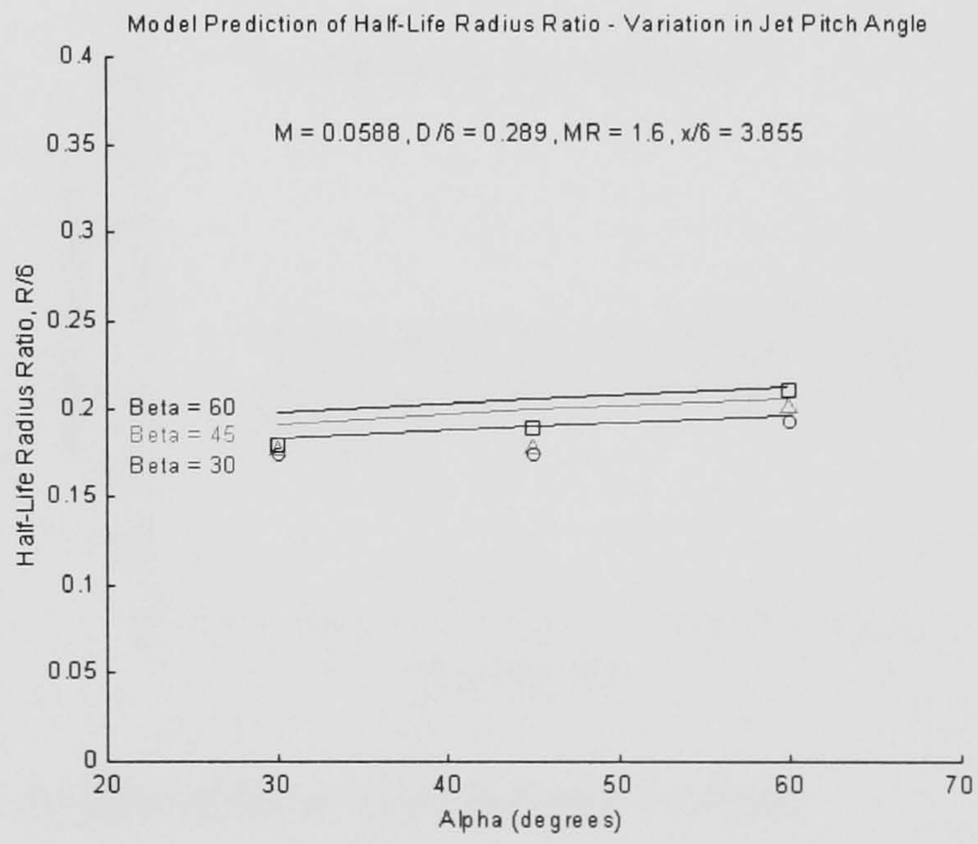

(b) Effect of β on Half-Life Radius Prediction

Figure 76: Model Predictions with Respect to Jet Hole Diameter Ratio (Mach No Ratio Cases)

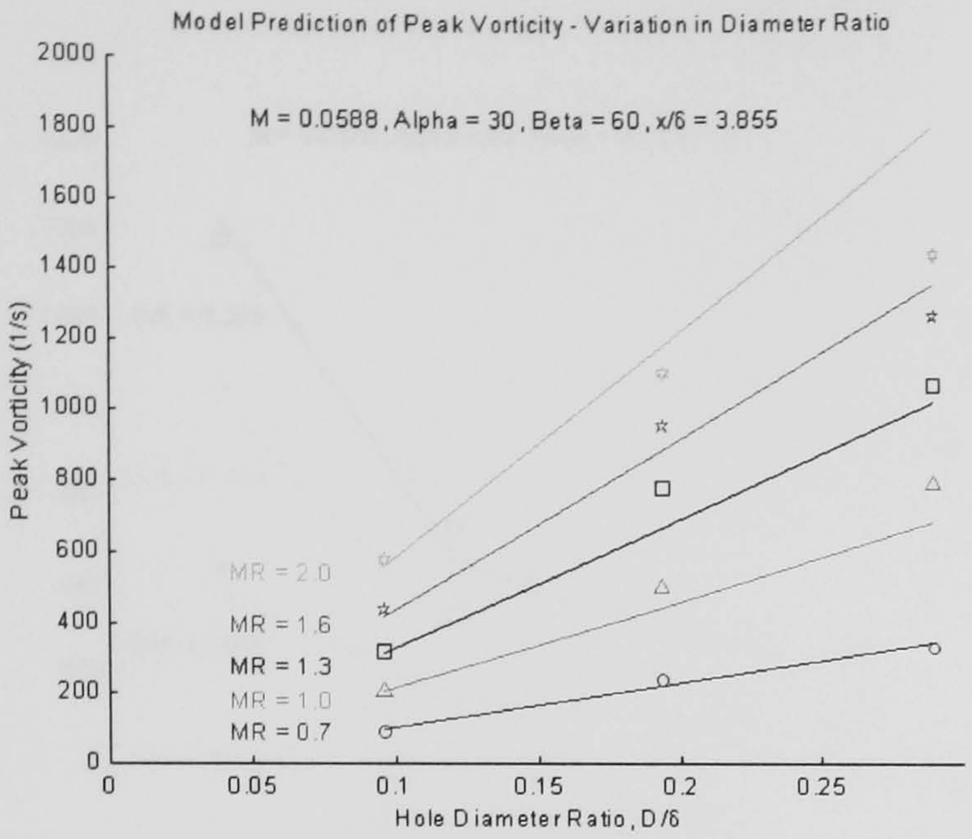

(a) Effect of D/δ on Peak Vorticity Prediction

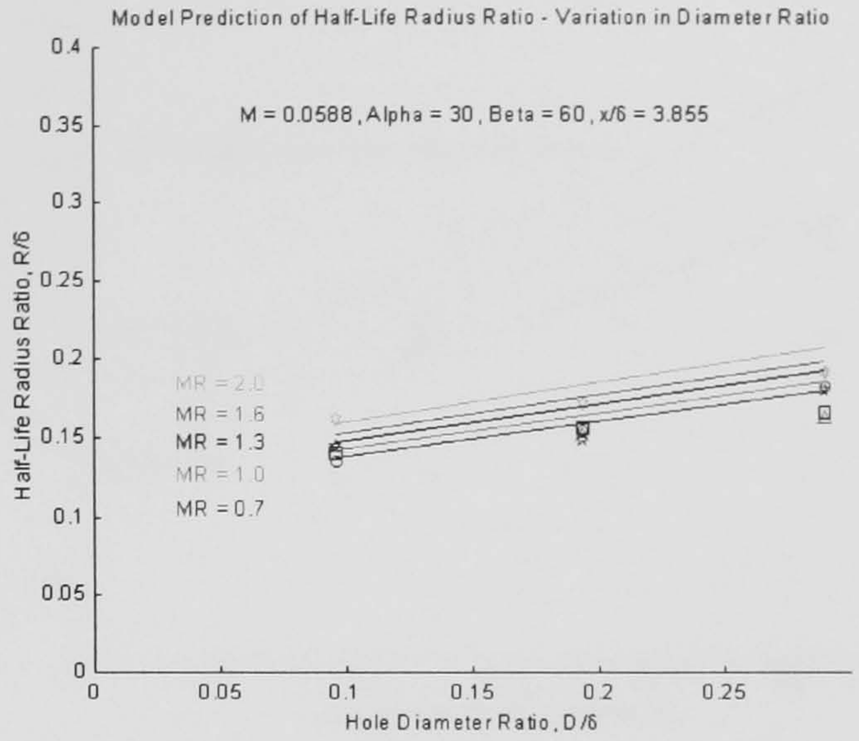

(b) Effect of D/δ on Half-Life Radius Prediction

Figure 77: Model Predictions with respect to Mach Number Ratio (Jet Hole Diameter Ratio Cases)

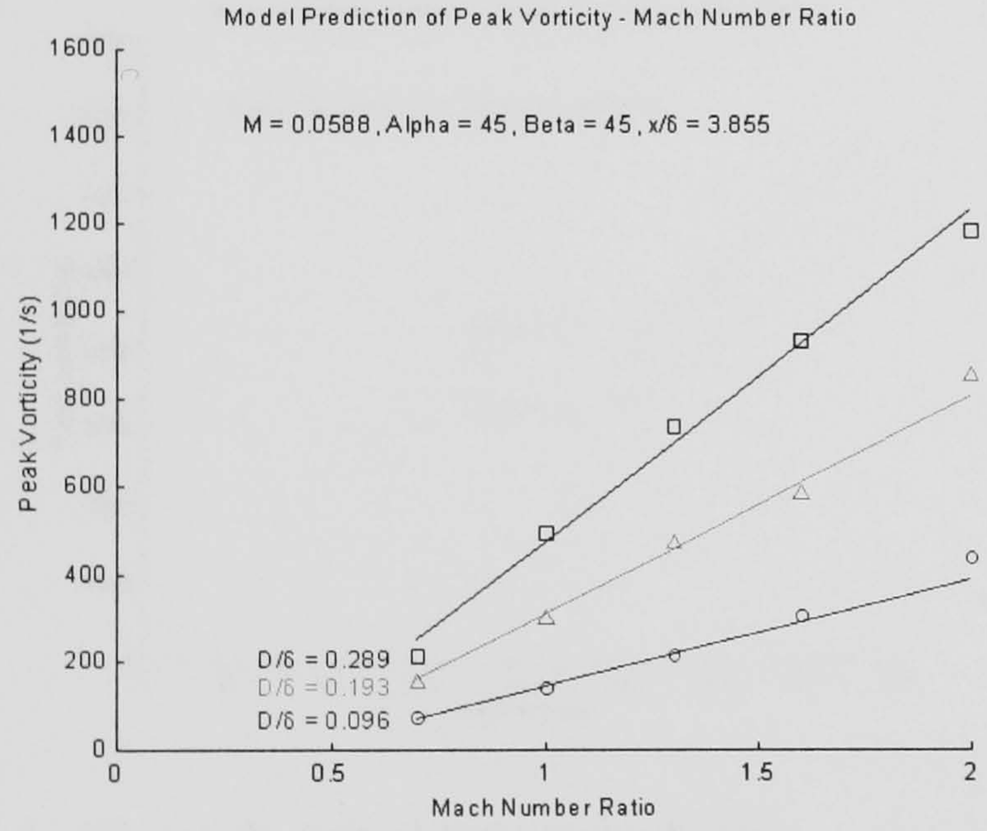

(a) Effect of MR on Peak Vorticity Prediction

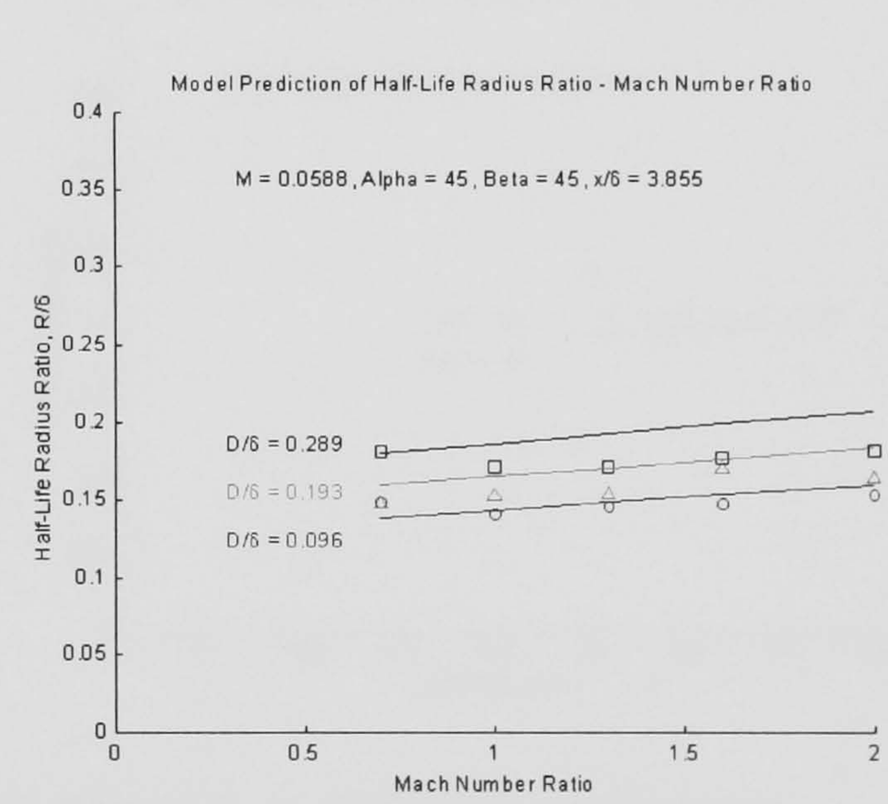

(b) Effect of MR on Half-Life Radius Prediction

Figure 78: Model Predictions with respect to Streamwise Distance Ratio (Jet Hole Diameter Ratio Cases)

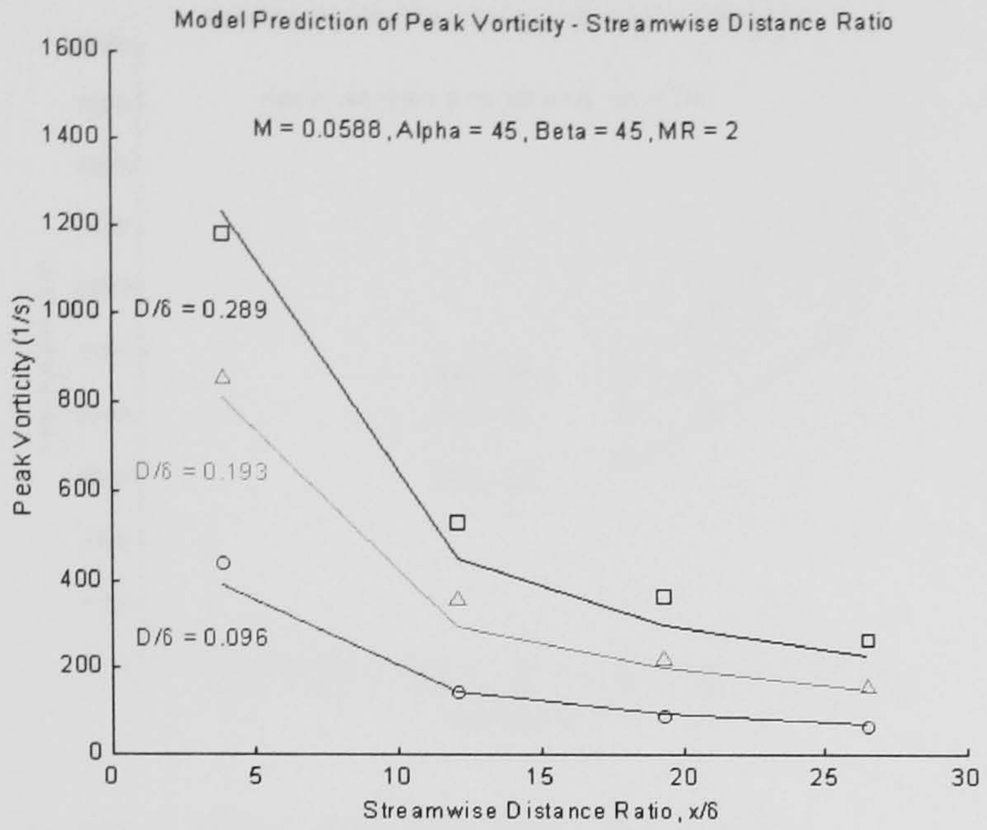

(a) Effect of x/δ on Peak Vorticity Prediction

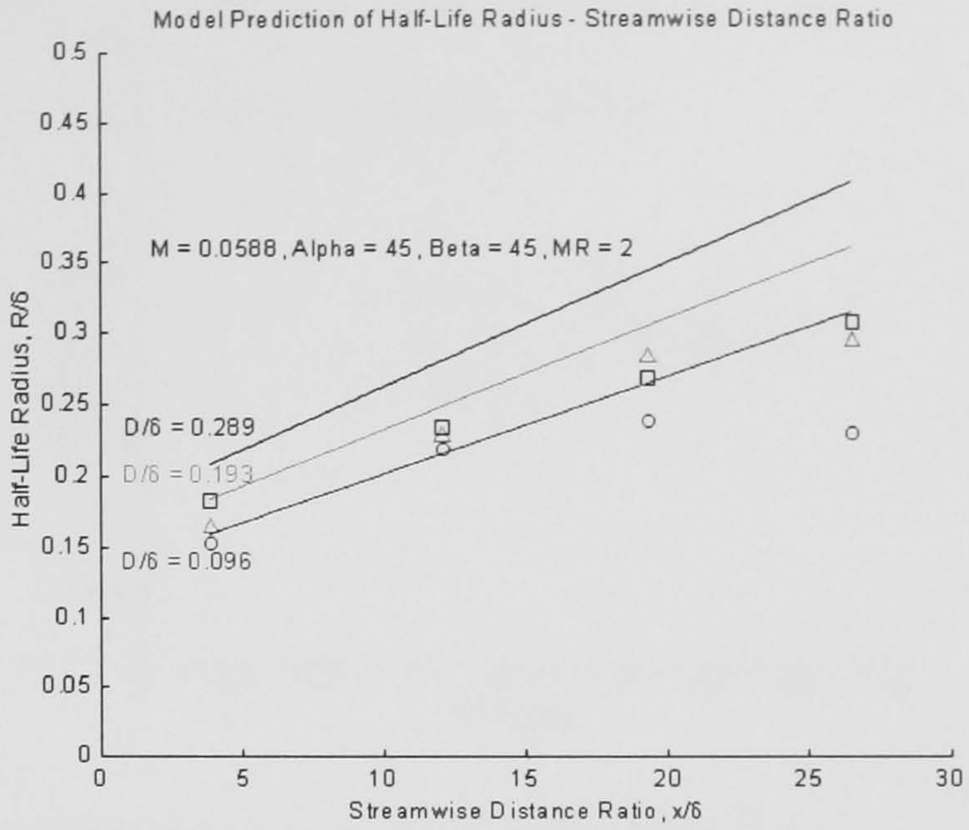

(b) Effect of x/δ on Half-Life Radius Prediction

Figure 79: Model Predictions with respect to Free-stream Mach Number (Jet Incidence Cases)

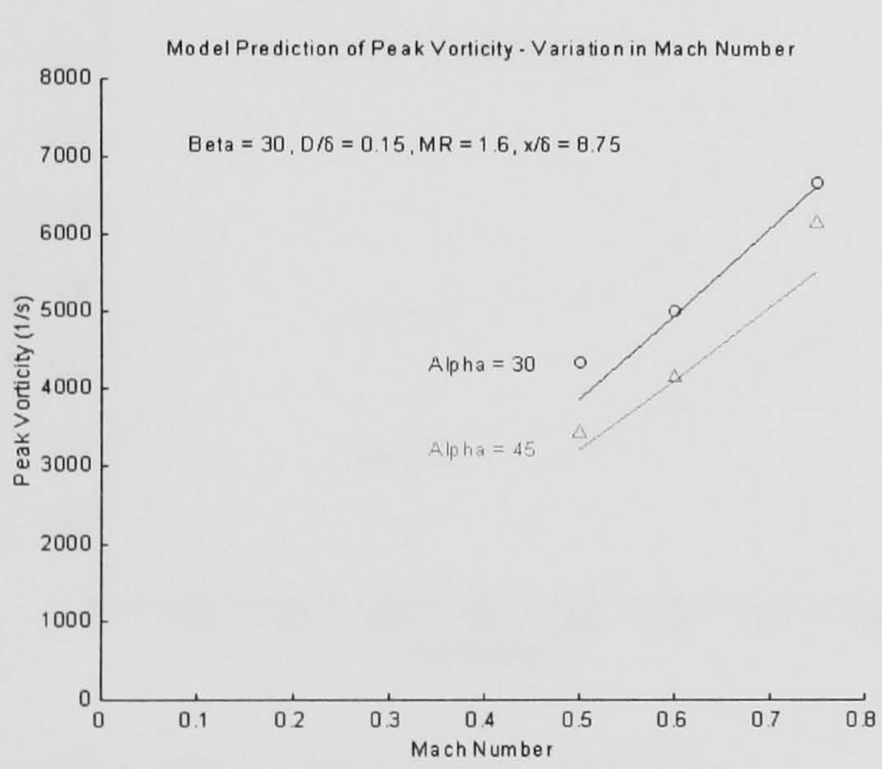

(a) Effect of M_∞ on Peak Vorticity Prediction

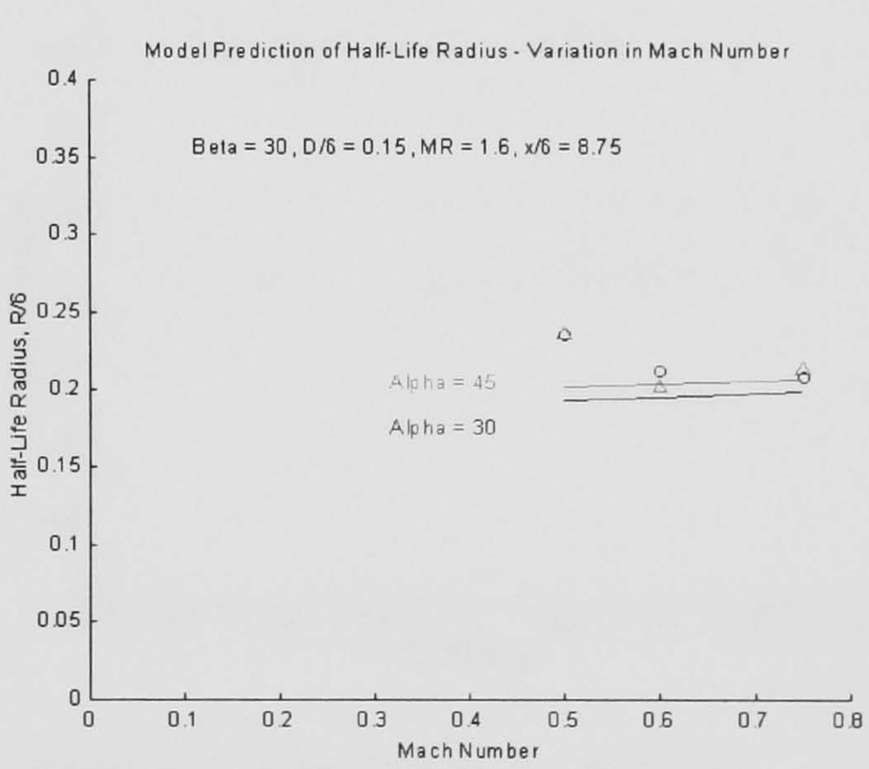

(b) Effect of M_∞ on Half-Life Radius Prediction

Figure 80: Model Predictions with respect to Free-stream Mach Number (Jet Skew Angle Cases)

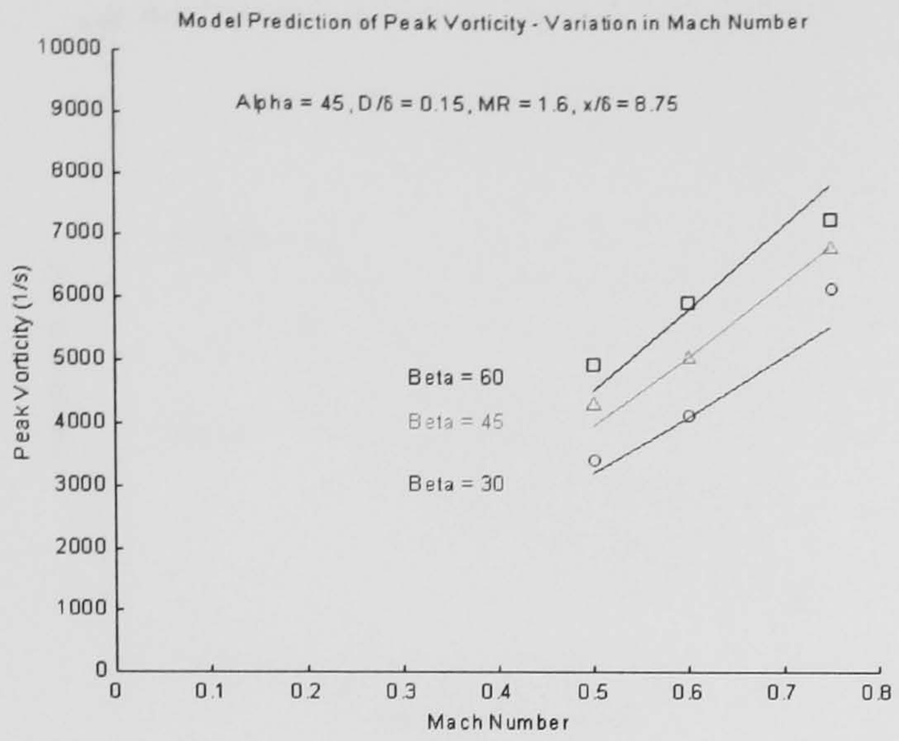

(a) Effect of M_∞ on Peak Vorticity Prediction

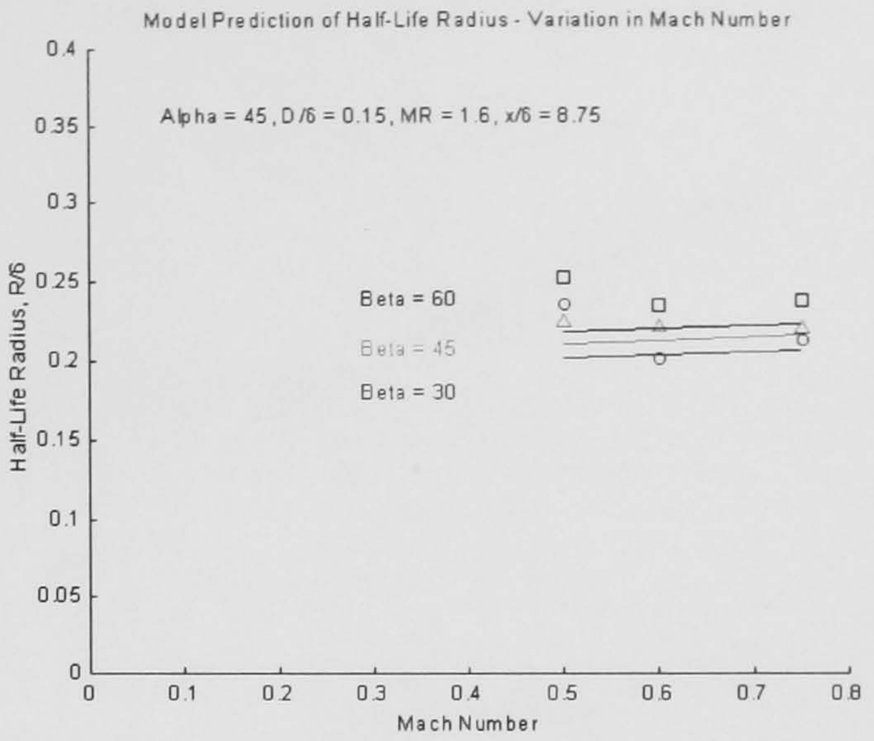

(b) Effect of M_∞ on Half-Life Radius Prediction

Figure 81: Model Predictions with respect to Free-stream Mach Number (Jet Diameter Ratio Cases)

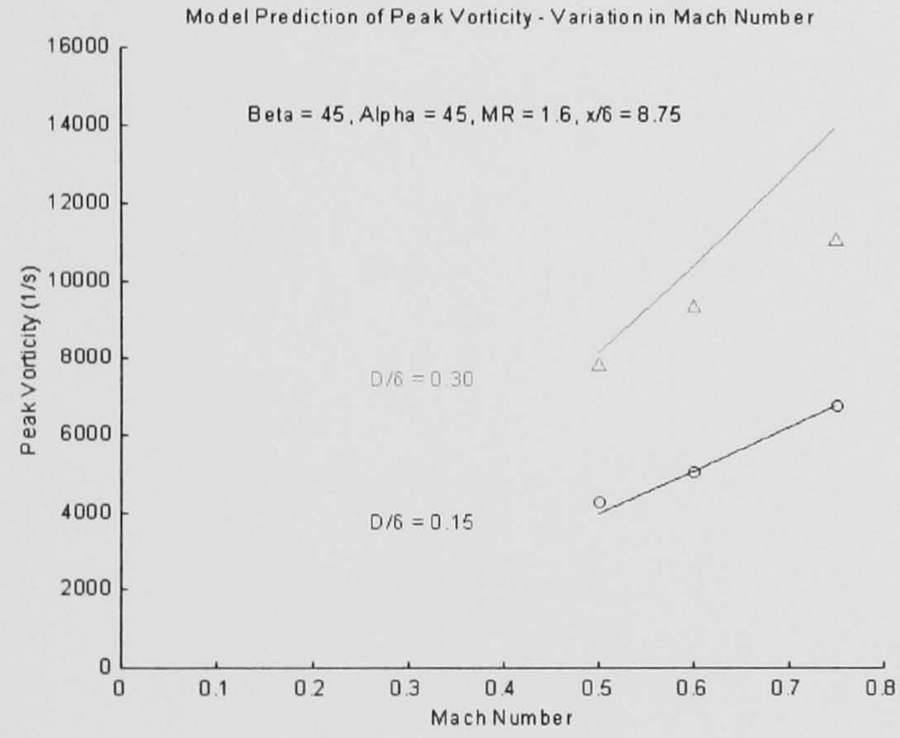

(a) Effect of M_∞ on Peak Vorticity Prediction

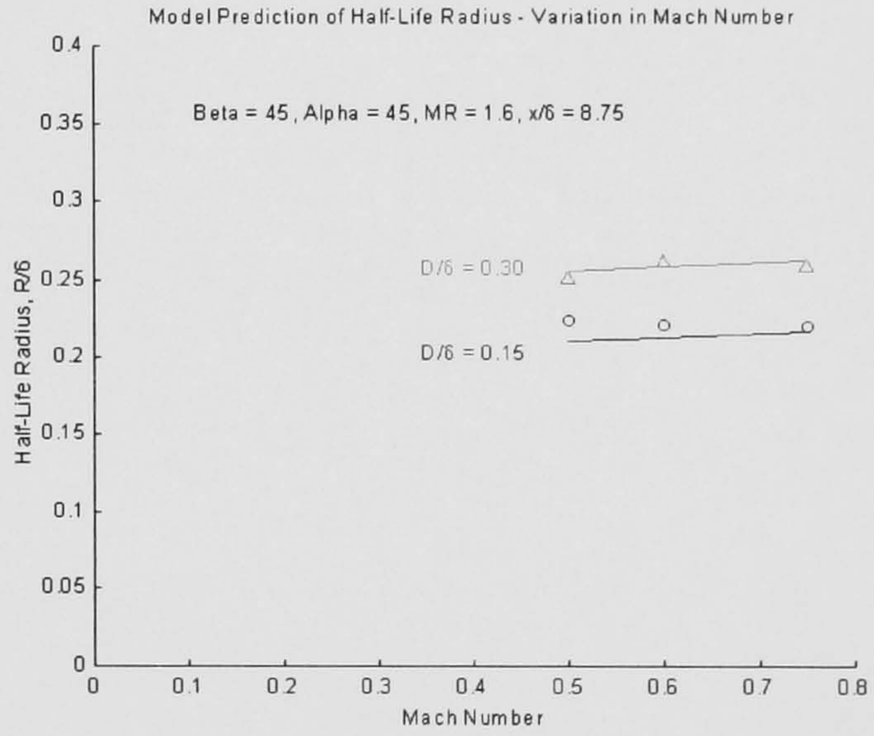

(b) Effect of M_∞ on Half-Life Radius Prediction

Figure 82: Model Predictions with respect to Streamwise Distance Ratio (Mach Number Cases)

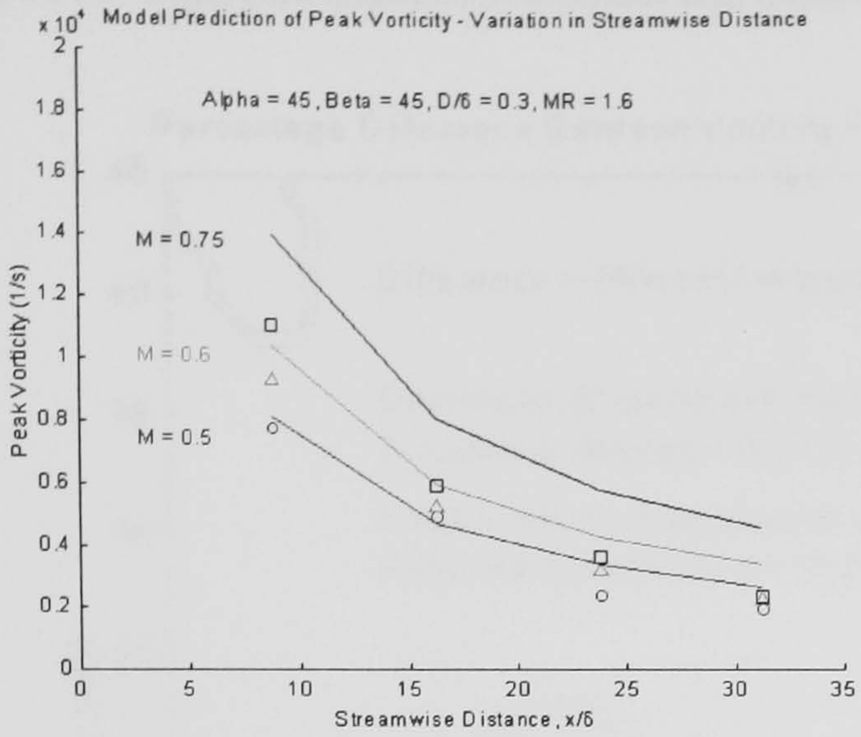

(a) Effect of x/δ on Peak Vorticity Prediction

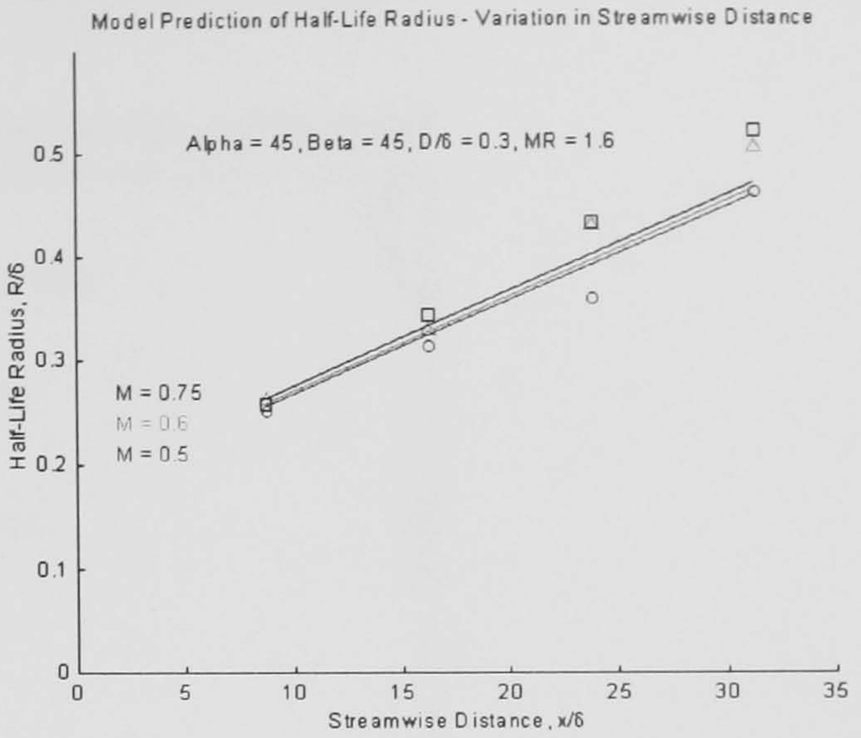

(b) Effect of x/δ on Half-Life Radius Prediction

8.9 - Vane Comparison between Prediction and Experiment

Figure 83: Difference Between Predictions and Experimental Vorticity Measurements

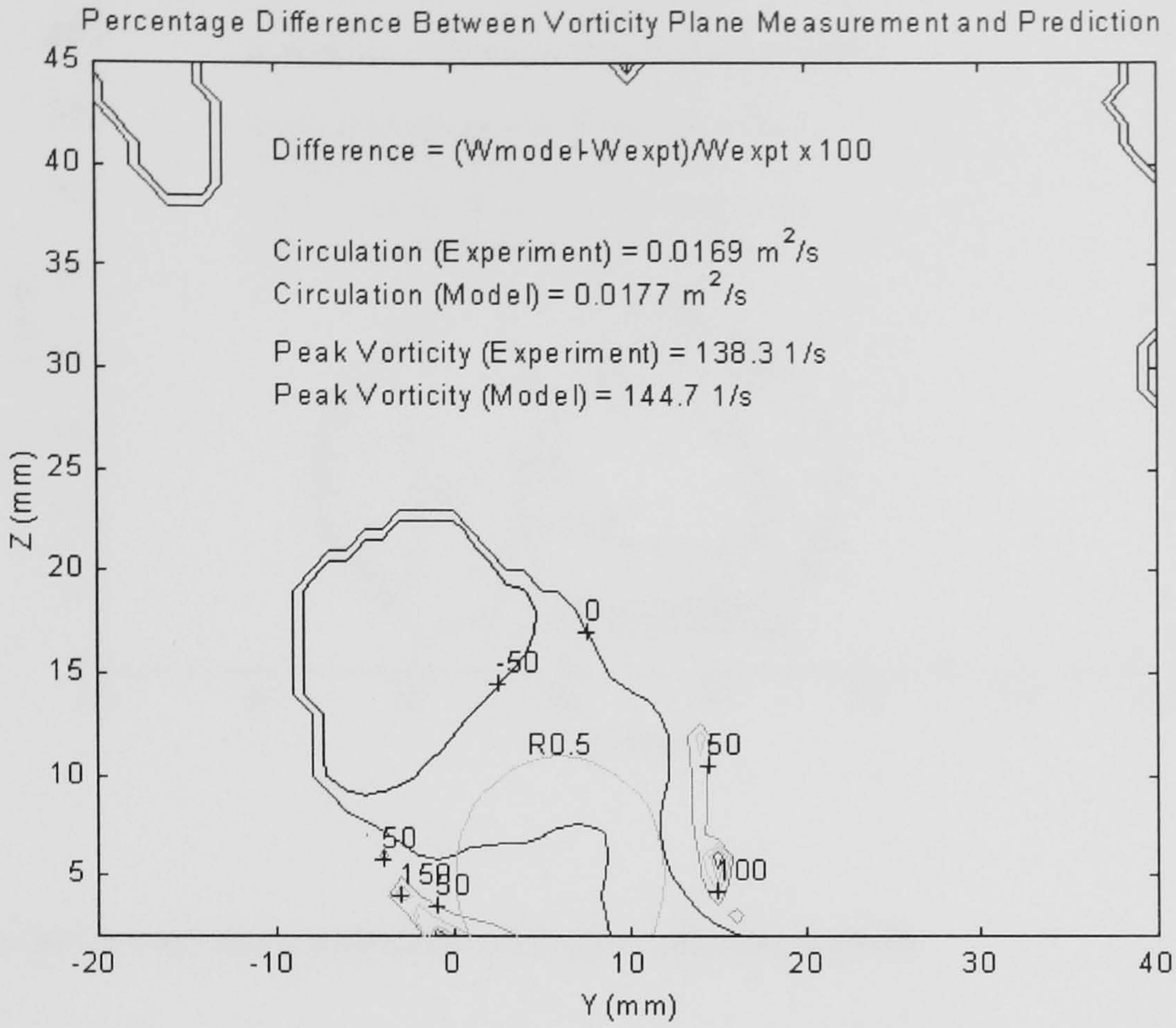

(a) α = 45°, β = 45°, D/δ = 0.096, MR = 1.0, x/δ = 3.855, M_∞ = 0.0588

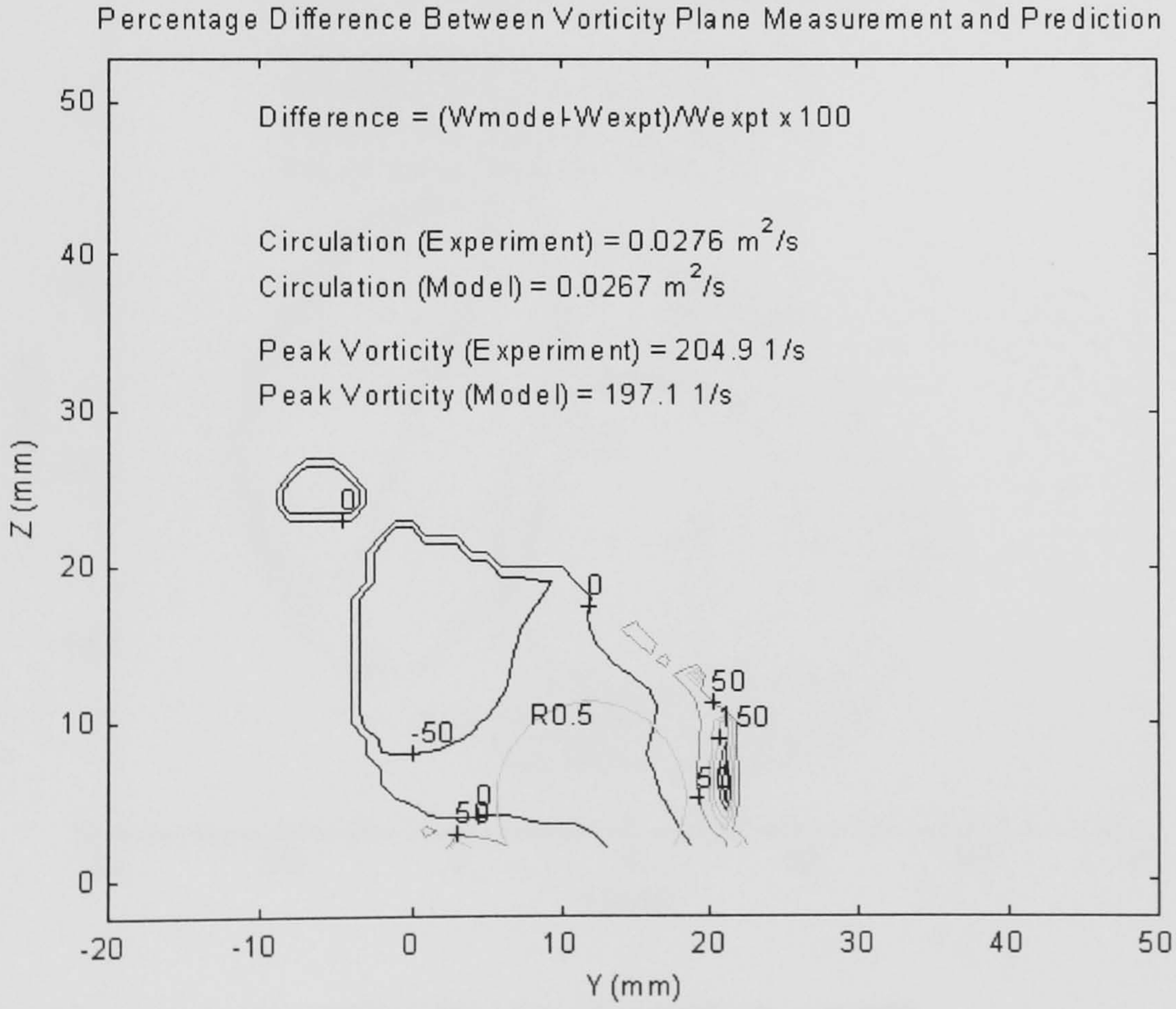

(b) α = 30°, β = 45°, D/δ = 0.193, MR = 0.7, x/δ = 3.855, M_∞ = 0.0588

Figure 83: Difference Between Predictions and Experimental Vorticity Measurements (Cont.)

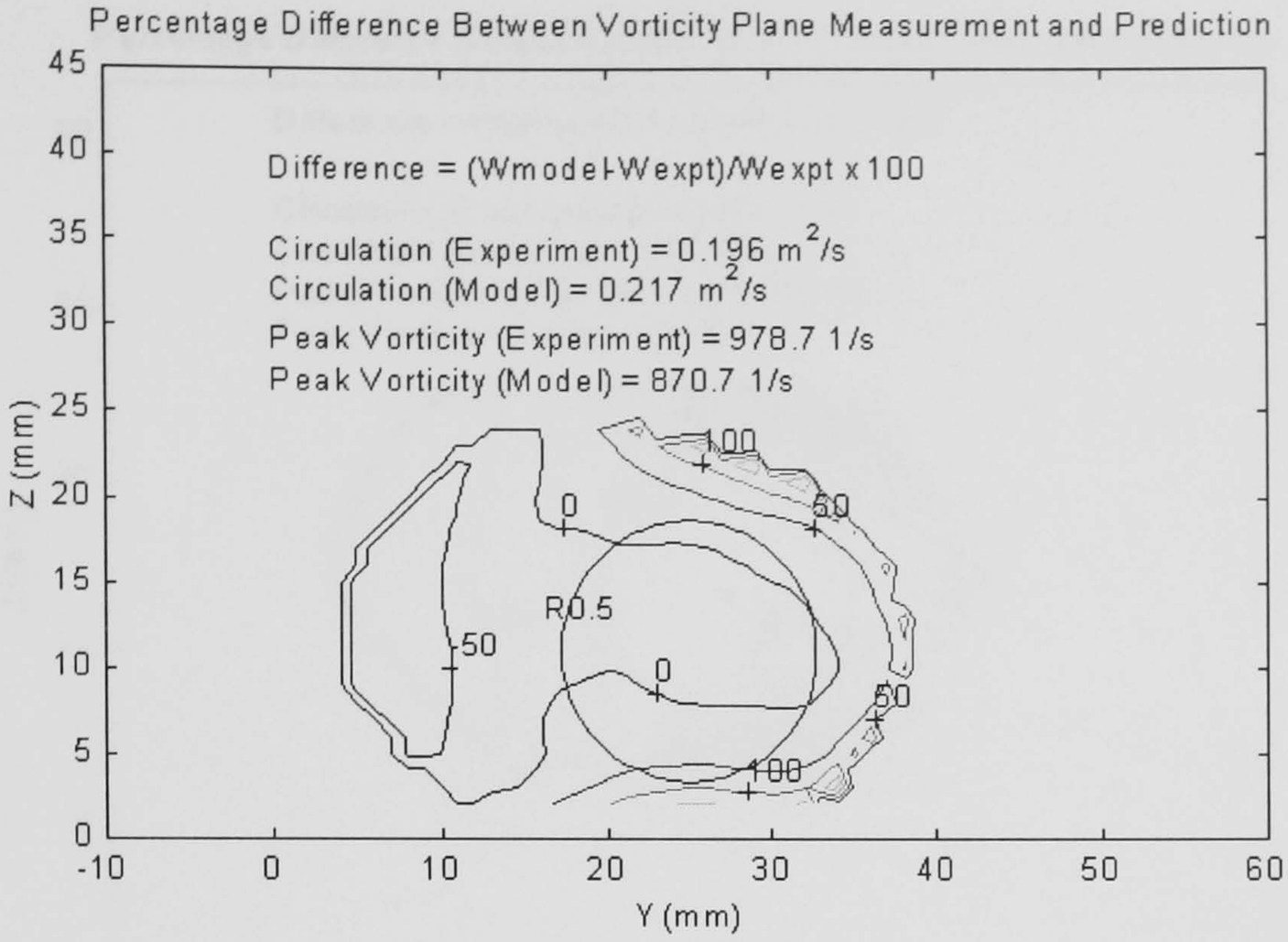

(c) $\alpha = 30°$, $\beta = 45°$, $D/\delta = 0.289$, MR = 1.3, $x/\delta = 3.855$, $M_\infty = 0.0588$

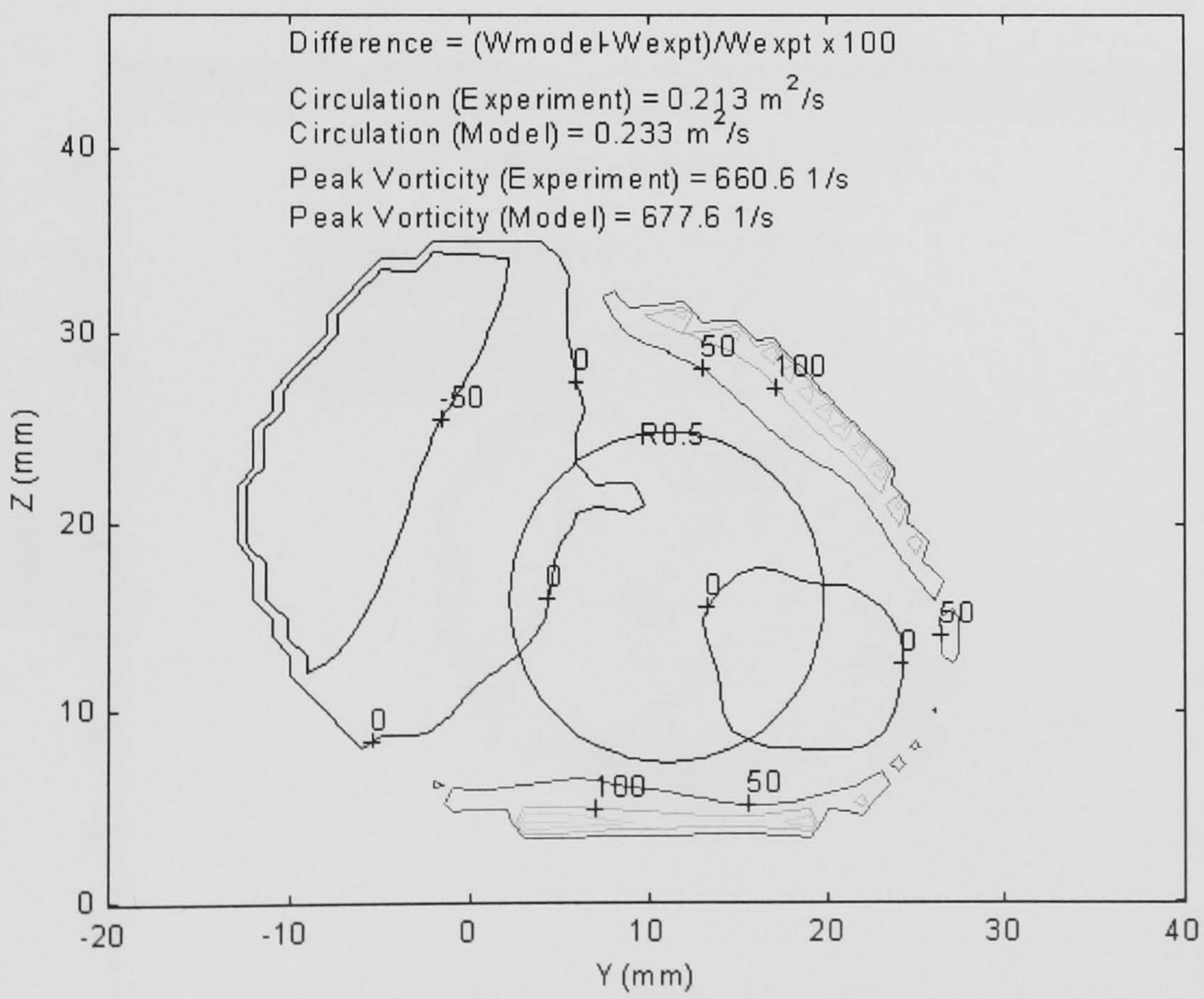

(d) $\alpha = 60°$, $\beta = 60°$, $D/\delta = 0.289$, MR = 1.6, $x/\delta = 3.855$, $M_\infty = 0.0588$

Figure 83: Difference Between Predictions and Experimental Vorticity Measurements (Cont.)

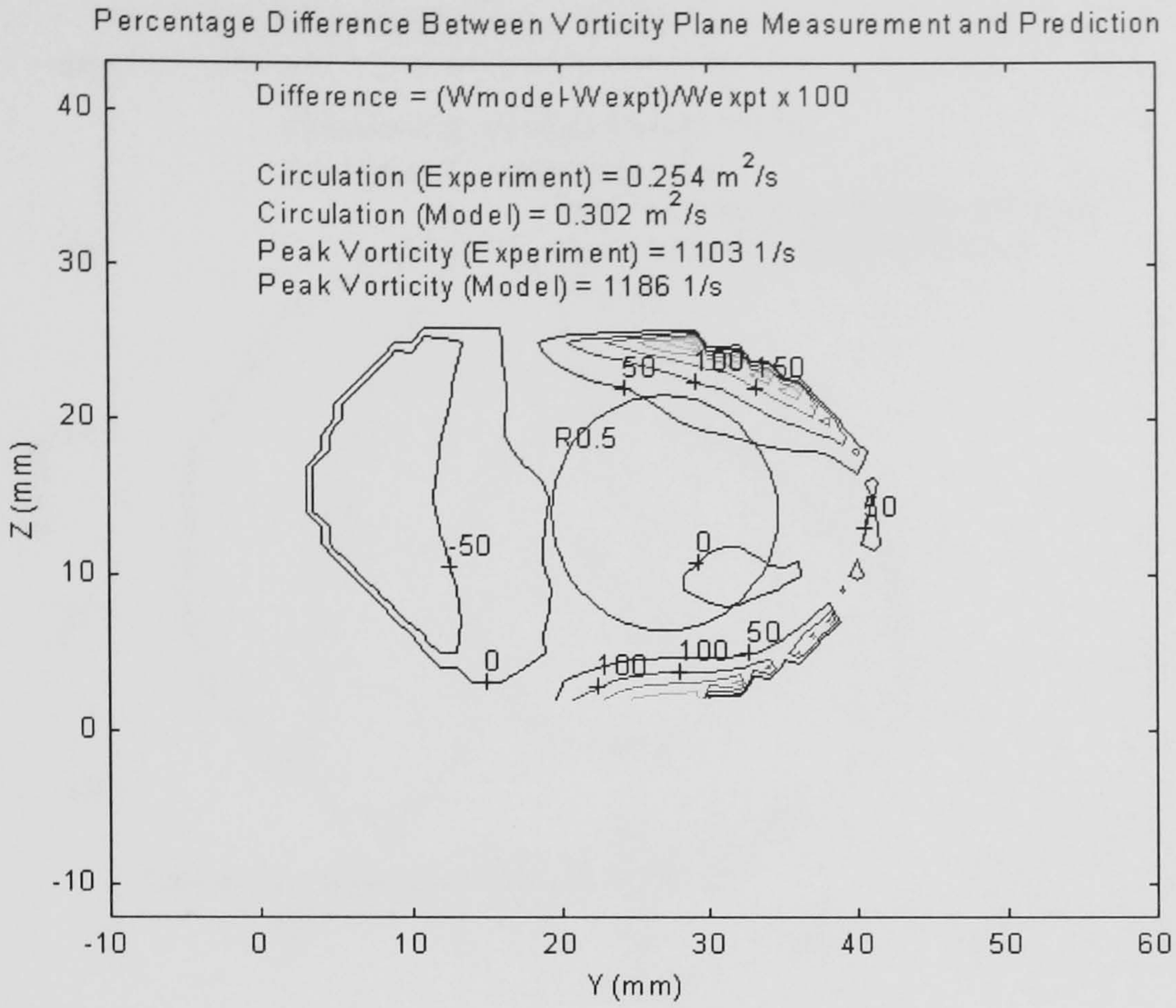

(e) $\alpha = 30°$, $\beta = 60°$, $D/\delta = 0.193$, MR = 2.0, $x/\delta = 3.855$, $M_\infty = 0.0588$

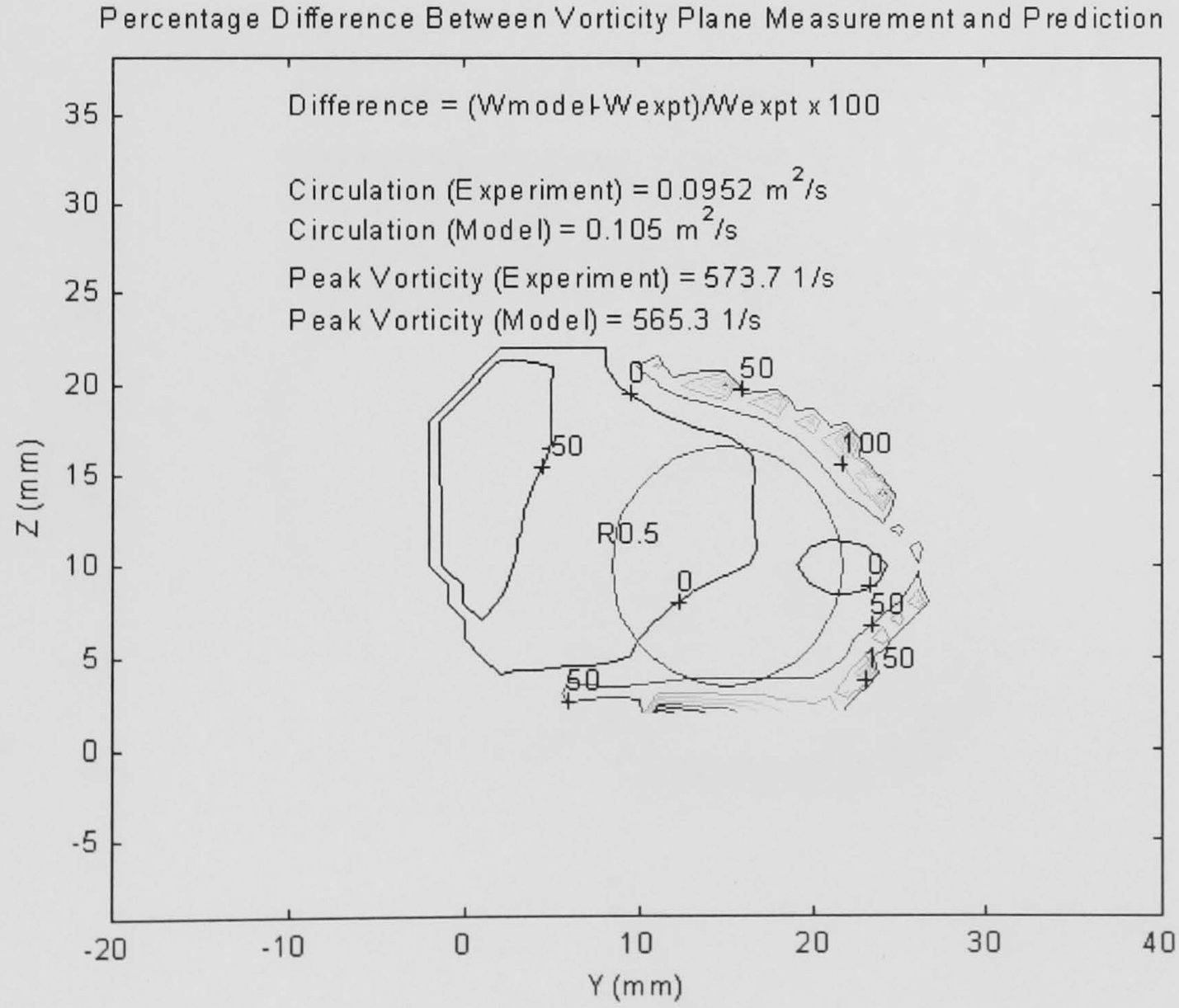

(f) $\alpha = 30°$, $\beta = 60°$, $D/\delta = 0.096$, MR = 2.0, $x/\delta = 3.855$, $M_\infty = 0.0588$

Figure 83: Difference Between Predictions and Experimental Vorticity Measurements (Cont.)

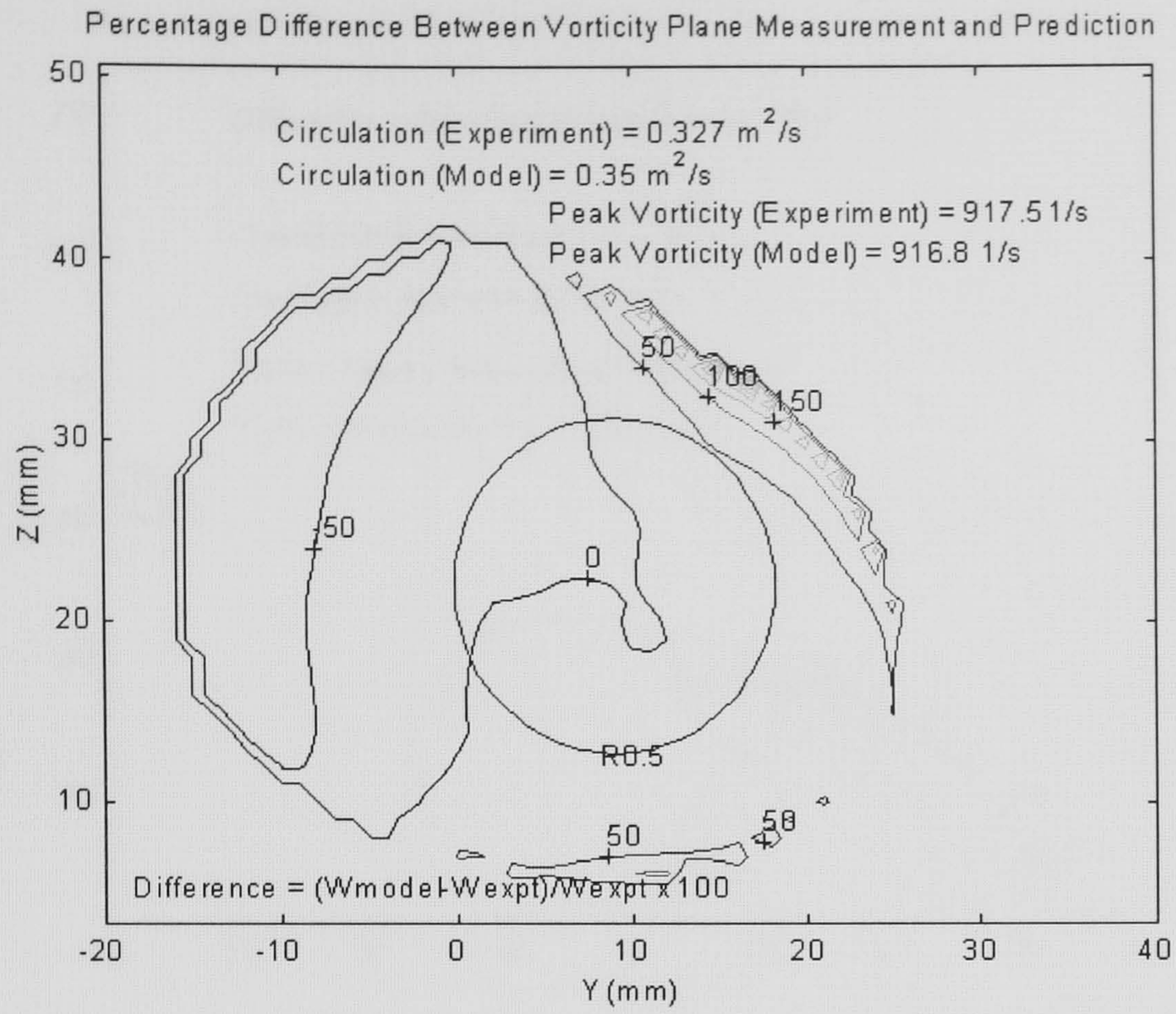

(g) $\alpha = 60°$, $\beta = 60°$, $D/\delta = 0.289$, MR = 2.0, $x/\delta = 3.855$, $M_\infty = 0.0588$

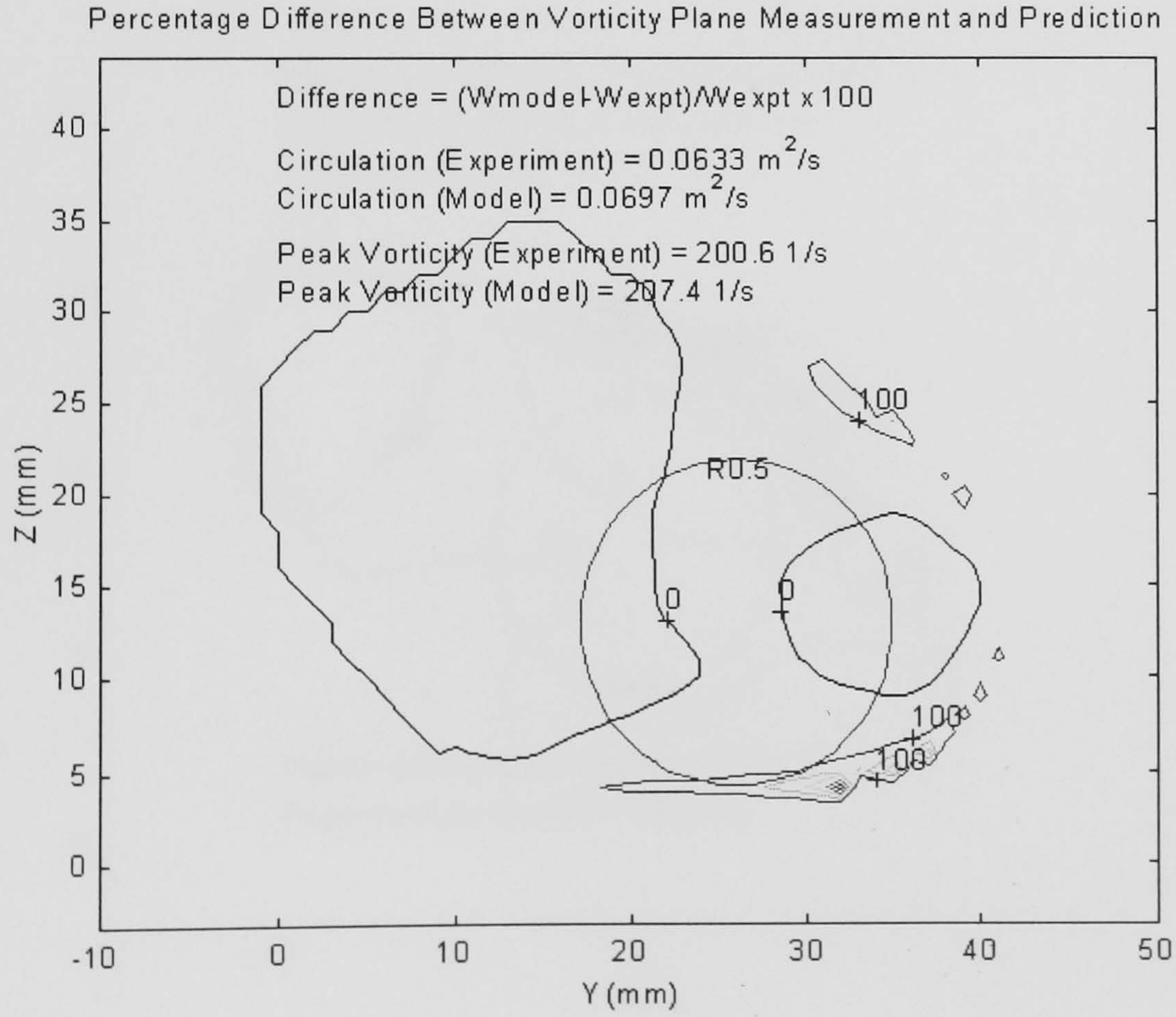

(h) $\alpha = 30°$, $\beta = 60°$, $D/\delta = 0.096$, MR = 2.0, $x/\delta = 12.048$, $M_\infty = 0.0588$

Figure 83: Difference Between Predictions and Experimental Vorticity Measurements (Cont.)

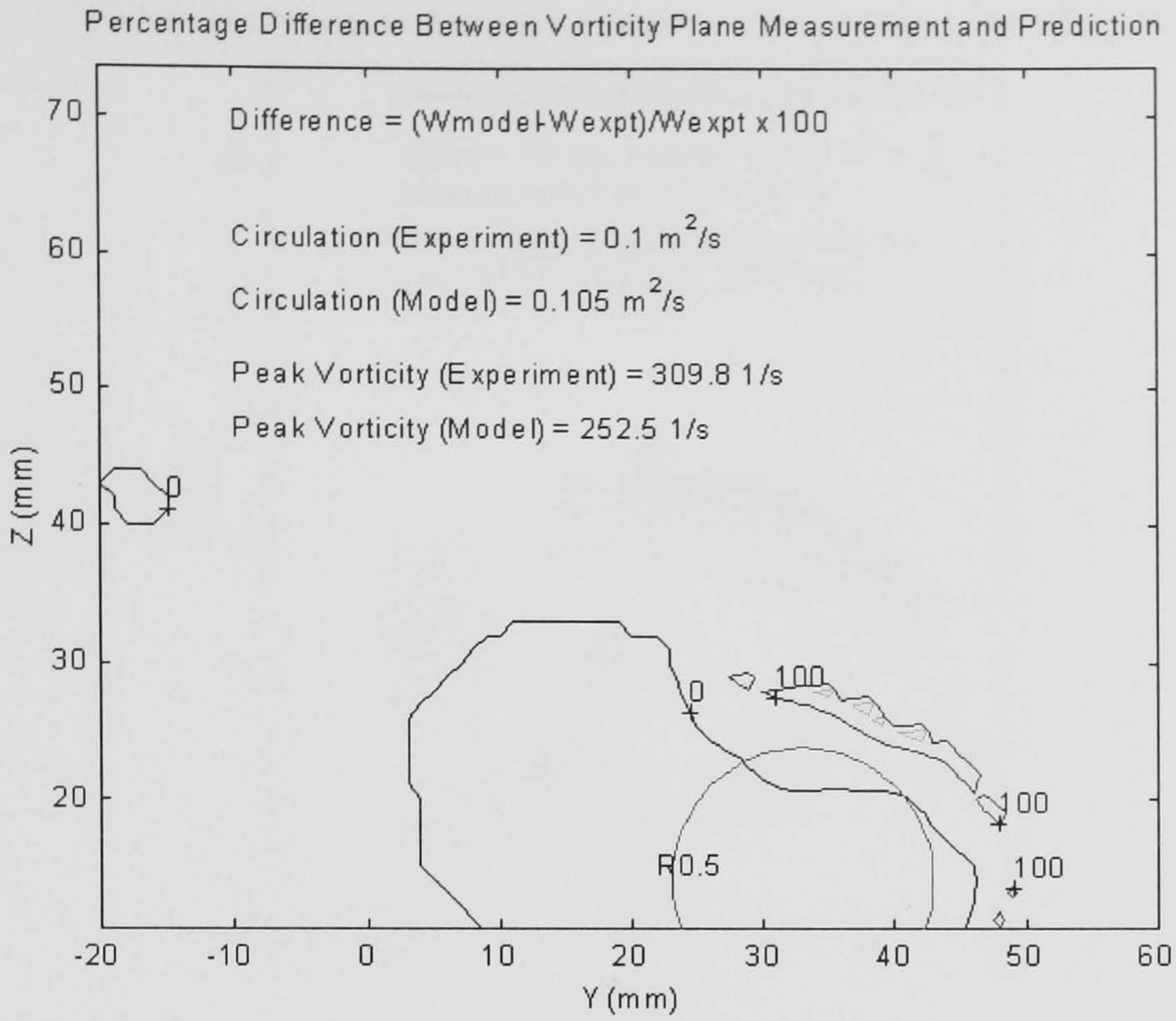

(i) $\alpha = 30°$, $\beta = 30°$, $D/\delta = 0.289$, MR = 1.3, $x/\delta = 12.048$, $M_\infty = 0.0588$

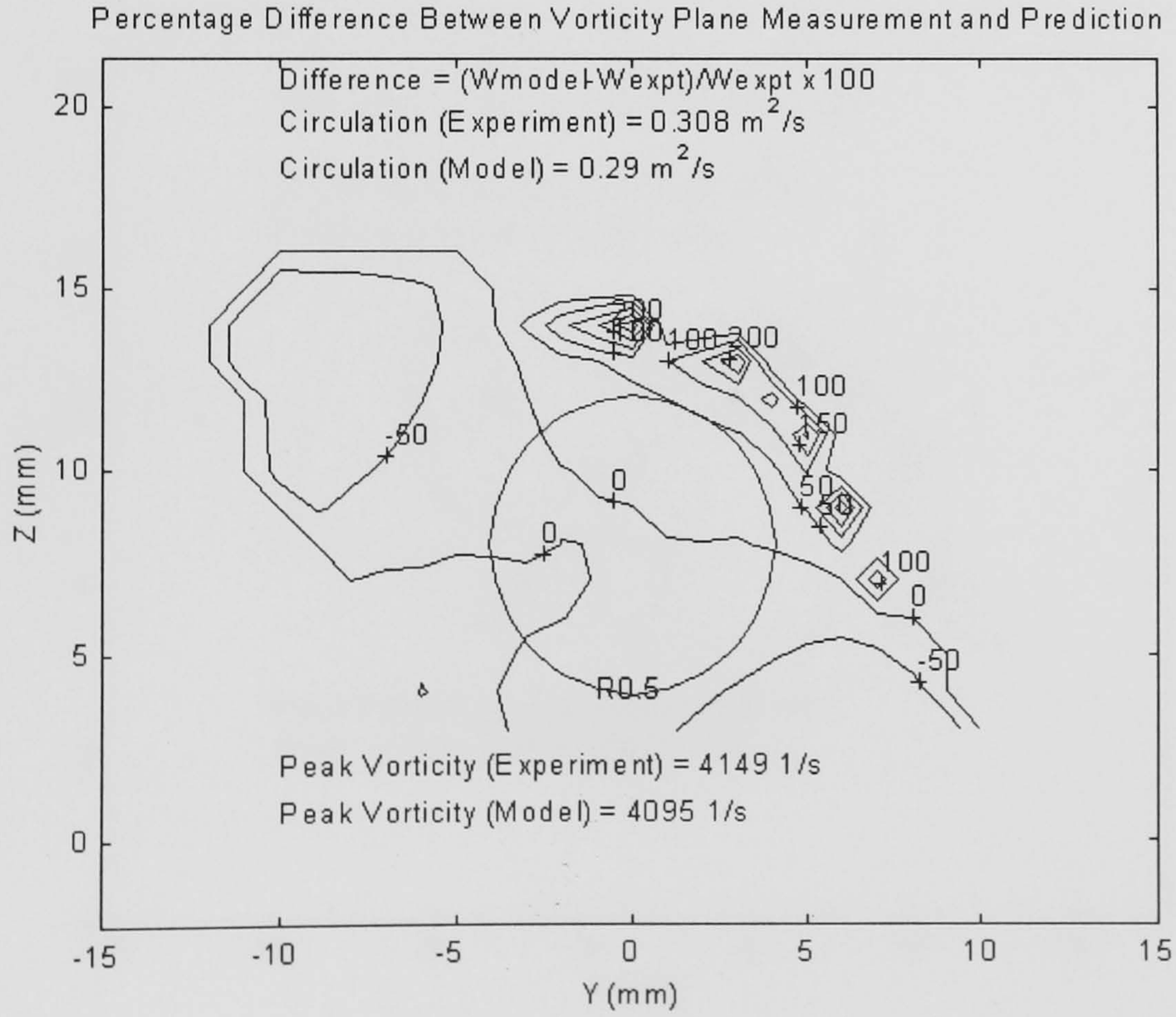

(j) $\alpha = 45°$, $\beta = 30°$, $D/\delta = 0.15$, MR = 1.6, $x/\delta = 8.75$, $M_\infty = 0.60$

Figure 83: Difference Between Predictions and Experimental Vorticity Measurements (Cont.)

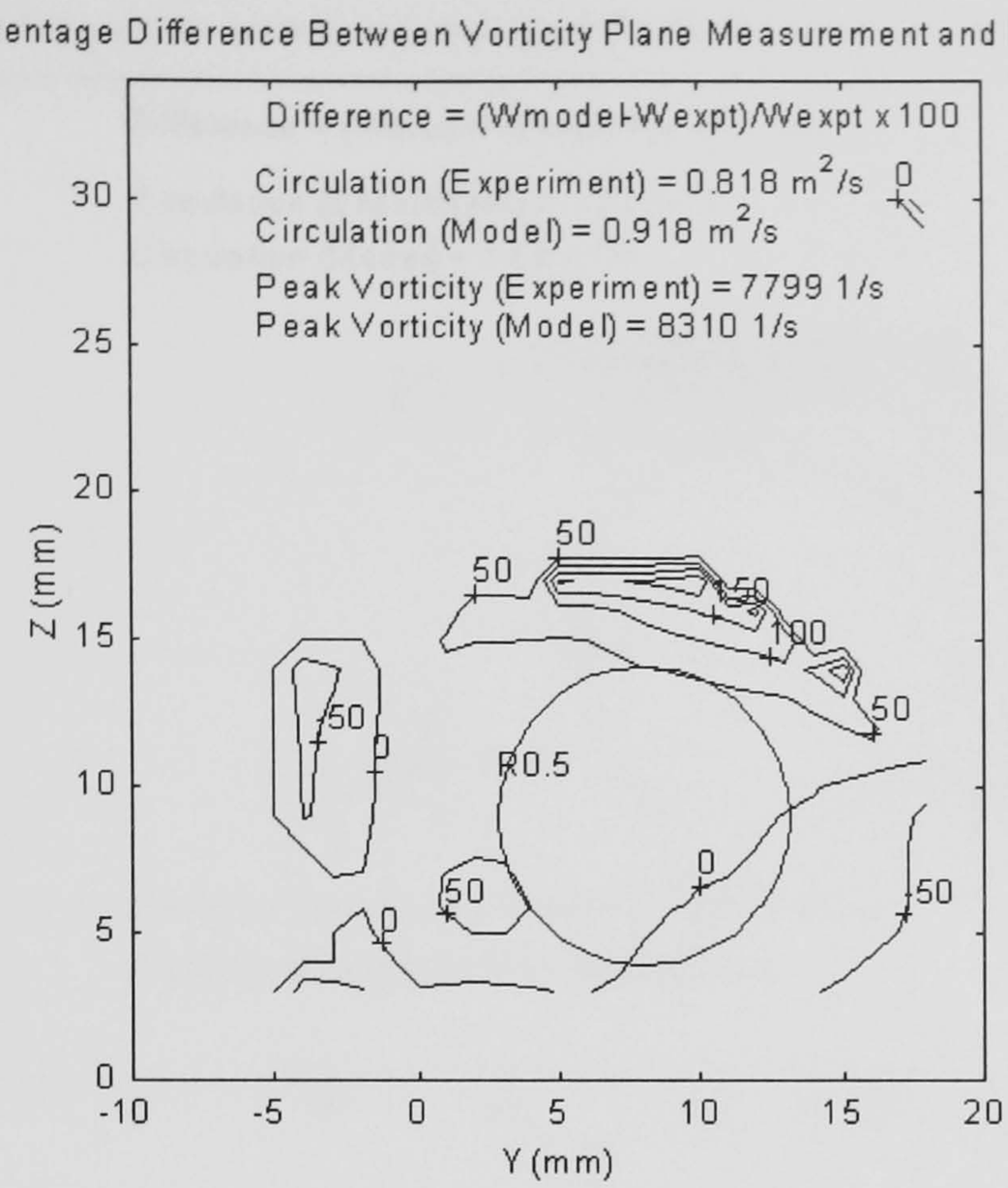

(k) $\alpha = 45°$, $\beta = 45°$, $D/\delta = 0.30$, MR = 1.6, $x/\delta = 8.75$, $M_\infty = 0.50$

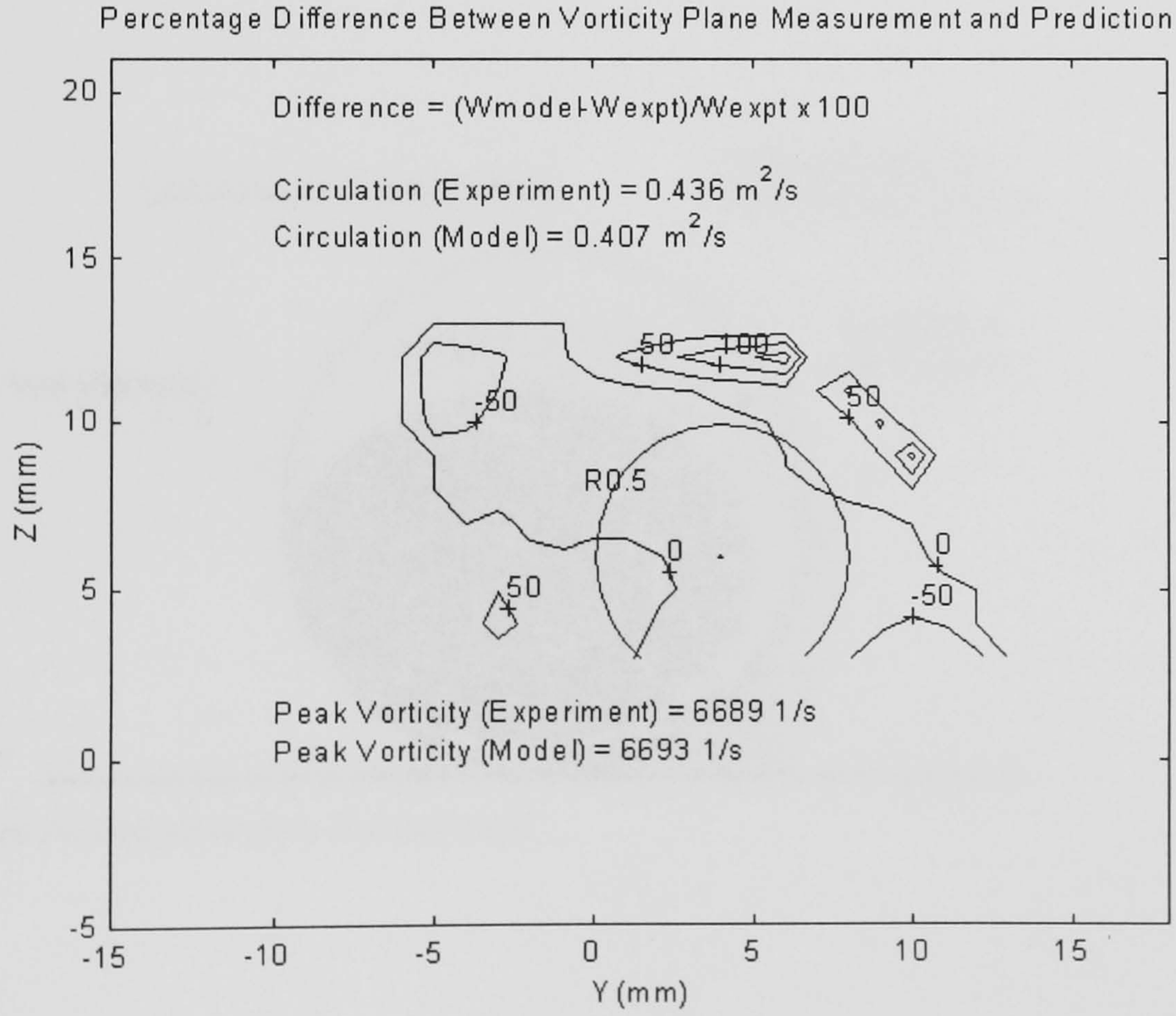

(l) $\alpha = 30°$, $\beta = 30°$, $D/\delta = 0.15$, MR = 1.6, $x/\delta = 8.75$, $M_\infty = 0.75$

Figure 83: Difference Between Predictions and Experimental Vorticity Measurements (Cont.)

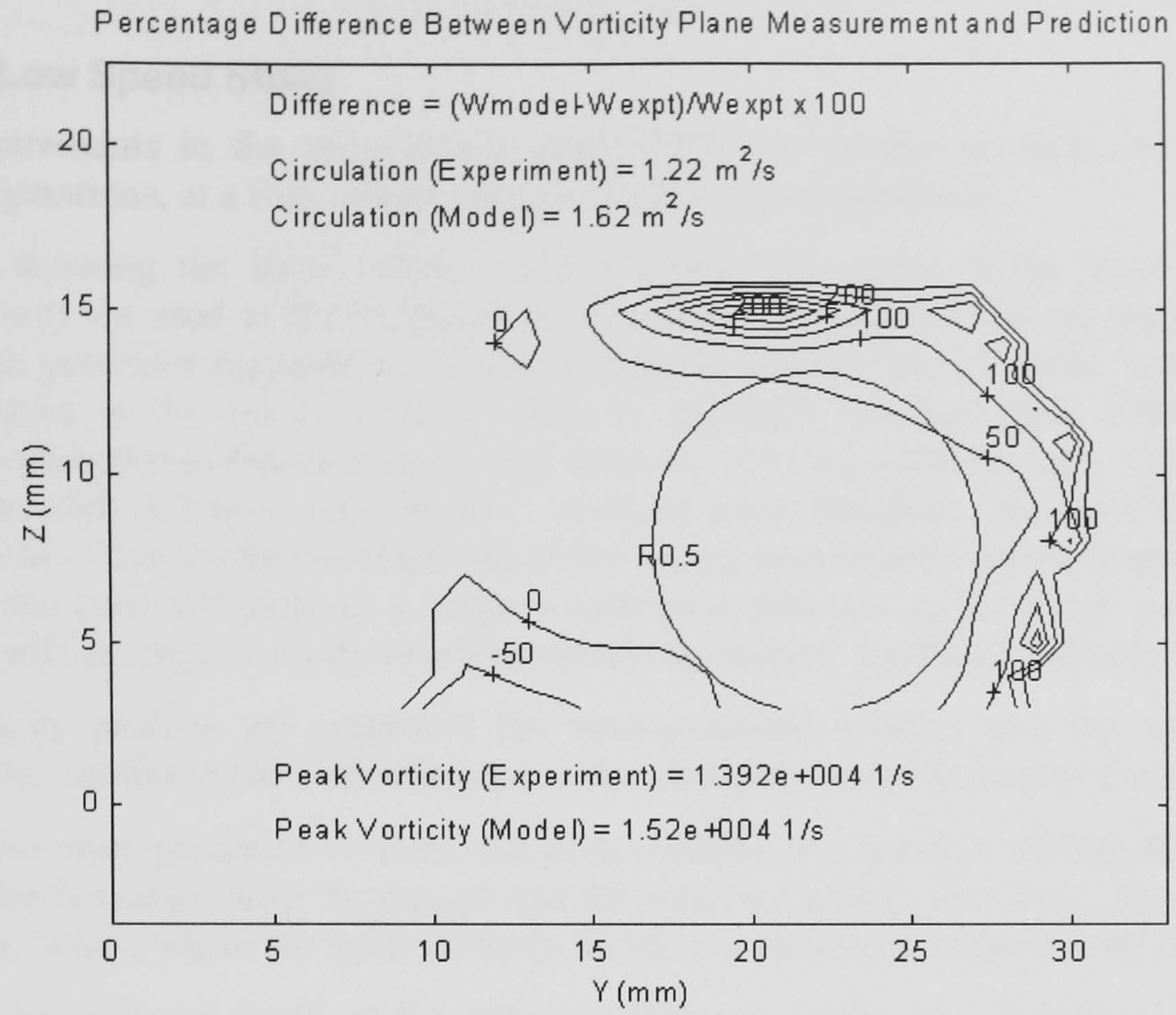

(n) $\alpha = 30°$, $\beta = 60°$, $D/\delta = 0.30$, MR = 1.6, $x/\delta = 8.75$, $M_\infty = 0.60$

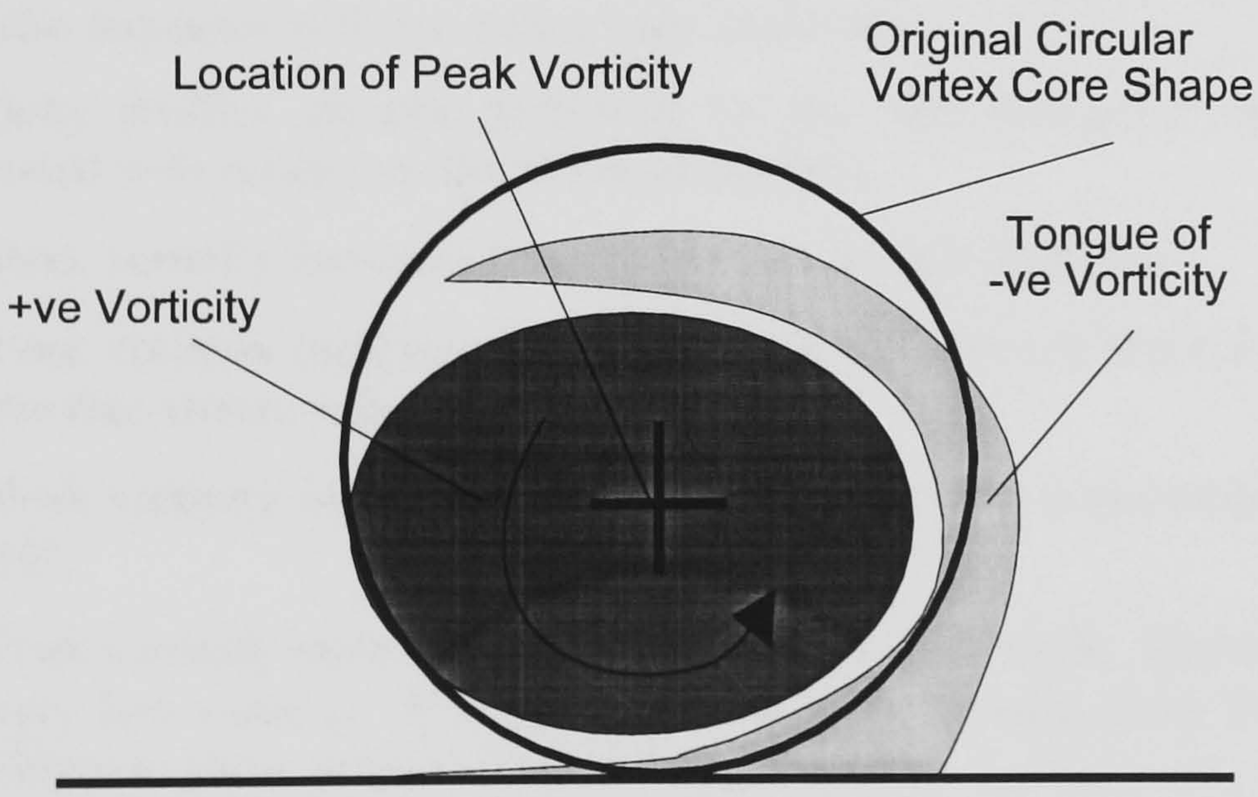

Figure 84: Distortion of the Vorticity Field

Chapter 9 - Conclusions

9.1 - Low Speed Study

Measurements in the cross-stream plane behind a variety of vane and air-jet vortex generator configurations, at a free-stream velocity of 20 m/s, are presented.

Data showing the local dynamic pressure ratio (the ratio of the local to free-stream dynamic pressure) are used to demonstrate the variation in boundary layer mixing with the variation of the vortex generator parameters. These data plots are also used to infer information about the axial velocities in the vortex core, in order to highlight one particular difference in the generation methods between the vane and air-jet devices. It is seen that the vane vortex generators produce a vortex with a lower core dynamic pressure (and therefore velocity) than the air-jet produced vortices. Thus in the development of the vortex immediately downstream of the vortex generator, the vane core will undergo a larger acceleration than that of the air-jet core. As a result, the vane core will undergo vorticity filament stretching, thereby yielding a different vorticity decay rate.

Vorticity profiles are presented for vane-produced vortices and the variations in the vorticity profiles are discussed with reference to the changing vortex generator parameters.

- For vane-produced vortices, the peak vorticity is a function of both the vane height (relative to the boundary layer thickness) and the vane incidence. However, the vanes exhibit a tendency to 'stall', where the peak vorticity varies in a non-linear manner with incidence.
- The angle of 'stall' of the vane is a function of the vane height-to-boundary-layer-thickness ratio, and thus a complex relationship is evident.
- The decay rate for a vane-produced vortex is in the form of an exponential function of the streamwise distance from the vortex generator and the height of the vortex from the wall. Since the height of the vortices from the wall does not change significantly with streamwise distance, the height of the vane can be used in place of the height of the vortex from the wall.
- As the peak vorticity of a vortex decays with streamwise distance, the radius of the vortex increases (as the vorticity is diffused in the cross-stream directions. The radius of the vortex also increases with increasing vane incidence.

Vorticity profiles are also presented for the vane produced vortices, and the observations are discussed with relation to the air-jet parameters.

- Peak vorticity increases linearly with the jet exit diameter,
- Peak vorticity increases linearly with the Velocity (or Mach number) ratio of the jet (related to the free-stream value),
- Peak vorticity increases with jet skew angle with a maximum value at an incidence close to 60°,
- Peak vorticity increases with decreasing jet pitch angle. However, reducing the pitch angle to a very low value (< 20°) must result in a vortex very close to the wall which has insufficient height to allow proper vortex development.
- The streamwise decay of peak vorticity is a good approximation to a power law function in streamwise distance to a power which is approximately constant (with a value of –0.88), regardless of the vortex generator configuration. Since the height of the vortex from the wall did not significantly change with varying parameters, no conclusion can be drawn as to whether this is the correct parameter to use for non-dimensionalisation (as with the case of the vanes), and the constant value must be used instead.
- Vortex radius is a strong function of the jet diameter and Velocity (or Mach number) ratio, but is a weak function of the jet pitch and skew angles.

9.2 - High Speed Study

Data are presented for the cross-stream measurements behind vane and air-jet vortex generators at free-stream Mach number from 0.45 to 0.75.

It was demonstrated that the trends in peak vorticity of a vortex with variation in the vortex generator parameters are largely independent of Mach number, regardless of the type of generator. Further, while the vortex circulation strength of the vortex varies linearly with Mach number, the compressibility effects in the vortex core cause an apparent stretching of the vorticity filaments. This yields an non-linear increase in peak vorticity with Mach number (with the vorticity varying with M^k (where k takes a value of approximately 1.3), and a corresponding decrease in the vortex radius.

Peak vorticity decay rates were observed as being independent of free-stream Mach number. Consistent with the low speed results, vorticity decay rates for the high speed tests were noted as being a function of the distance from the vortex generator and the distance of the vortex centre-line from the wall.

9.3 - Empirically Derived Vorticity Profile Predictions

The data for the low- and high- speed tests was used to provide a simple equation based technique for the prediction of the vorticity profiles from the vortex generator types. Two differing approaches were used for each vortex generator type. Both models employ the observation that the vorticity in the cross-stream plane can be approximated to an excellent degree of accuracy to a Gaussian distribution. It has been shown that the experimental data presented here supports this observation.

A vorticity model, based on a simple horseshoe vortex system has been proposed to model the vortex from a vane vortex generator. The vane may be considered as a thin aerofoil at moderate incidence, and the circulation from the vane can be found by relating the vortex circulation to the lift curve slope. Since the integration of the vorticity profile reveals the circulation, knowledge of the radius of the vortex can be used to define the peak vorticity. Thus, an empirically derived equation has been produced which relates the radius of the vortex to the vortex generator parameters, thereby allowing the vorticity profile to be predicted.

The experimental data set that was used to investigate the trends in peak vorticity and vortex radius was used to compare with predicted values of the same vortex generator parameters. Results are presented which show that the peak vorticity was predicted to better than 12% difference, while the vortex radius was predicted to better than 15% difference. The vortex was also compared in terms of the circulation strength (that is, a combination of the peak vorticity and vortex radius data), and differences of better than 15% are reported. With the simple nature of this modelling technique, these results are considered to be excellent, and require very low computational effort.

A vorticity prediction technique is also presented for the air-jet vortex generators. The low- and high-speed studies revealed that the flow field around the vortex generators was of a highly complex nature, especially as the jet parameters were varied. Since it was not possible to generate a simple theoretical model, a prediction technique was developed which modelled the effects of varying the air-jet parameters.

A simple equation was produced for both the peak vorticity and vortex radius values, which can be combined to predict the vorticity field using the vortex generator parameters. Agreement between predicted and experimental values of peak vorticity was seen to be better than 20%. While this agreement is worse than that for the vane cases, it should be recalled that the levels of peak vorticity measured in the air-jet produced vortices was significantly less. Those cases which exhibited lower levels of agreement were those with levels of vorticity where the experimental uncertainty would become more significant. Vortex radius was predicted to within 15% of the experimental value. Comparing the predicted vorticity field with the experimental one allowed an assessment of the prediction technique. Regions of lower experimental vorticity were noted on the upwash region of the vortex. Since the air-jet produced vortices are generally quite low in the boundary layer, negative vorticity is swept from the wall around the vortex. However, while the

difference (as expressed as a percentage) appears to be very large, the absolute levels of vorticity in this region are very low compared with the peak vorticity. Regardless of this observation, circulation is predicted to within 20%.

Thus, an air-jet vortex generator vorticity prediction technique is presented which gives good agreement with experimental data for very low computational effort.

Chapter 10 - Recommendations for Further Work

Extensions to this work could be broadly divided in to two main areas: extensions to the prediction techniques presented here, and the application of experimental data and these predictions.

10.1 - Further Modelling Work

The models as presented have some limits in their use, due to the bounds of the experimental data that was used to create them. For most of the experimental parameters that were varied, extensions beyond the current experimental limits will be subject to significant errors. Thus, more experimental data would increase the range of application of these equations directly.

Further, some parameters for both the vane and air-jet equations were not varied, since assumptions were made prior to the experimental testing about the types of devices under consideration. In the case of the vane vortex generators, both the planform and the aspect ratio of the vanes was held constant (as a rectangular vane with a vane-vortex-generator aspect ratio of unity). The equation could be easily extended to include different wing-type vortex generators, since the equation is based on circulation prediction. Thus the effects of vane sweep and taper ratio could be addressed. Further, the effect of vane profiles could be addressed. While this equation has been based on simple thin plates, some uses of vortex generators involve devices with thickness and planform. This will affect the vortex production through the incidence parameter, and thus the equation could be altered accordingly. Clearly, these modifications would require significant experimental data in order to give a sufficiently accurate extension to the current equation.

In the same vein, only air-jets with circular jet walls were used. This was considered to be a logical assumption, since the scale of an air-jet device on a real aircraft (around 2-mm) would require that the jet orifice was manufactured using a circular drill bit. Other investigators have suggested that rectangular slots produce stronger vortices[47], and thus in the case where the slot could be produced in the correct scale, this extension may be important.

All of the experimental data was taken using experiments with a zero streamwise pressure gradient. Vortex generators are most often used in regions where an adverse pressure gradient is present (e.g. engine inlet systems, rear sections of aerofoils, etc.). Thus this prediction technique should be expanded to include the effects of an adverse pressure gradient. The pressure gradient should only affect the development of the vortex in the streamwise development (through the peak vorticity and radial growth), and thus the values of peak vorticity at the point of generation should still be valid. Only in the case where the pressure gradient is sufficiently large in comparison with the device size would any significant difference be needed in the equations. This prediction technique extension would need significant experimental data taken in a wind tunnel that could allow close control of the pressure gradient.

10.2 - Further Modelling Applications

The task to produce the prediction techniques presented here was based on the need to simplify the calculations in Computational Fluid Dynamics (CFD) codes for flowfields including vortex generators. Since the flow field may be of a large and complex geometry incorporating many vortex generators, it would be mode efficient to place step inputs of vorticity in to the flow field at the location of the vortex generators. This would reduce the grid complexity needed to resolve the flow around the generators, while their effect was developed in the flowfield solution. This task is an important development of this work. In the first instant, a CFD solution should be set up which takes the equation input (in vorticity) in order to produce a vortex over a flat plate. This equation should then be validated against the experimental measurement. In order to model the vortex successfully, the effective streamwise position of vortex generation may need to be varied in order to achieve the correct predicted vorticity at some downstream location. With the CFD model validated, it would then be possible to extend the experimental database computationally in order to investigate the streamwise pressure gradient effects.

This data is also very important from a CFD code validation aspect. The modelling of vortices is challenging, not least since the turbulence in the vortex core is difficult to model. In the case of air-jet vortex generators, this is compounded by the difficulty in the modelling of the jet boundary-free-stream mixing turbulence models. The large amount of experimental data in this study allows many comparison cases for CFD validation studies.

Chapter 11 - References

1. Johnson, G. & Scholes, K. Exploring Corporate Strategy. Forth Edition, Prentice Hall Europe, 1997.
2. Augustine, N. Augustine's Laws and Major Systems Development Programs. American Institute of Aeronautics and Astronautics, Inc. New York, 1983.
3. Samson, P. (Corporate Development Advisor, LOT Polish Airlines) Personal Communication, 1994.
4. Gridley, S. Presentation on Advanced Compact Inlets, United States Air Force Wright Laboratory, November 1997.
5. Houghton, E. L. & Carruthers, N. B. Aerodynamics for Engineering Students. Third Edition. (Edward Arnold, 1990)
6. Morton, B. R. The Generation and Decay of Vorticity. Geophys. Fluid Dynamics, 1984, Vol. 28, pp 277 - 308.
7. Lighthill, M. J. Part II of Laminar Boundary Layers (ed. Rosenhead), Oxford University Press (1963)
8. Bushnell, D. M. Longitudinal Vortex Control - Techniques and Applications. The 32nd Lanchester Lecture. Aeronautical Journal, October 1992, pp 297 - 308.
9. Iverson, J. D. Inviscid to Turbulent Transition of Trailing Vortices. AIAA 75-0883
10. Delery, J. M. Aspects of Vortex Breakdown. Prog. Aerospace Sci. Vol. 30, pp 1-59, 1994.
11. Batchelor, G. K. Axial Flow in Trailing Line Vortices. Journal of Fluid Mechanics, Vol. 20, part 4, pp 645-658, 1964.
12. Shabaka, I. M. M. A., Mehta, R. D., & Bradshaw, P. Longitudinal Vortices Imbedded in Turbulent Boundary Layers. Part 1: Single Vortex. Journal of Fluid Mechanics, Vol. 155, pp 37 - 57.
13. Sarpkaya, T. Vortex Breakdown in Swirling Conical Flows. AIAA Journal, 9(9), pp 1792 - 1799, 1971.
14. Wendt, B. J., Greber, I. & Hingst, W. R. The Structure and Development of Streamwise Vortex Arrays Embedded in a Turbulent Boundary Layer. AIAA Paper 92-0551.
15. Schubauer, G. B. & Spangenberg, W. G. Forced Mixing in Boundary Layers. Journal or Fluid Mechanics, Vol. 8, 1960.
16. Taylor, H. D. The Elimination of Diffuser Separation by Vortex Generators. UAC Research Department Report R-4012-3, June 10, 1947.
17. ESDU Transonic Data Memorandum 93024 - Vortex Generators for Control of Shock-Induced Separation, Part 1: Introduction and Aerodynamics.
18. Freestone, M. M. Inviscid Theory Applied to Vortex-Induced Mixing. RAeS Conference on High Lift and Separation Control, Bath, 1995.
19. Cutler, A. & Bradshaw, P. Vortex/Boundary-Layer Interactions. AIAA 89-0083.
20. Hornung, H. Vorticity Generation and Transport. Keynote Paper KS-3, presented at the 10th Australian Fluid Mechanics Conference, University of Melbourne, December 1989.
21. Harvey, J. K. & Perry, F. J. Flowfield Produced by Trailing Vortices in the Vicinity of the Ground. Technical note from: AIAA Journal, Vol. 9, No. 8, 1971.
22. Jones, J. P. The Calculation of the Paths of Vortices from a System of Vortex Generators, and Comparison with Experiment. A.R.C. C.P. N°. 361, 1957.

23. Squire, H. B. The Growth of a Vortex in Turbulent Flow. The Aeronautical Quarterly, August 1965, PP 302 - 306.

24. Lamb, Sir H. Hydrodynamics. Cambridge University Press, 1932. Pp 591 - 592.

25. Wendt, B. J. & Hingst, W. R. Measurements and Modelling of Flow Structure in the Wake of a Low Profile "Wishbone" Vortex Generator. AIAA Paper 94-0620.

26. Shizawa, T. & Eaton, J. K. Interaction of a Longitudinal Vortex with a Three-dimensional Turbulent Boundary Layer. AIAA Journal, Vol. 30, N°. 5. May 1992.

27. Valentine, E. F. & Carroll, R. B. Effects of Some Primary Variables of Rectangular Vortex Generators on the Static-Pressure Rise through a Short Diffuser. NACA RM 152B13, May 1952.

28. Tanner, L. H., Pearcey, H. H. & Tracy, C. M. Vortex Generators: their Design and their Effects on Turbulent Boundary Layers. Preliminary Report. A.R.C. 16,487. January 1954.

29. Pearcey, H. H. Shock Induced Separation and its Prevention by Design and Boundary Layer Control. In 'Boundary Layer and Flow Control, its Principles and Application', Vol. 2, Ed. Lachmann, G. V., Pergamon Press, Oxford, 1961.

30. ESDU Transonic Data Memorandum 93025 - Vortex Generators for Control of Shock-Induced Separation, Part 2: Guide to Use of Vane Vortex Generator, June 1994.

31. Personal communication with B. H. Anderson, NASA Lewis Research Center.

32. Wheeler, G. O. Means for Maintaining Attached Flow of a Flowing Medium. Untied States Patent 4 455 045, June 1984.

33. Wallis, R. A. A preliminary Note on a Modified Type of Air Jet for Boundary Layer Control. A.R.C. C.P. N°. 513, 1960.

34. Keffer, J. F. & Baines, W. D. The Round Turbulent Jet in a Cross-Wind. Journal of Fluid Mechanics, Vol. 15, 1963. Pp 481 - 497.

35. Kamotani, Y. & Greber, I. Experiments on a Turbulent Jet in a Cross-Flow. AIAA Journal, Vol. 10, N°. 11, November 1972. Pp 1425 - 1429.

36. Karagozian, A. R., Nguyen, T. T. & Kim, C. N. Vortex Modelling of Single and Multiple Dilution Jet Mixing in a Cross Flow. Journal of Propulsion, Vol. 2, N°. 4, July 1986. Pp 354 - 360.

37. Fearn, R. & Weston, R. P. Vorticity Associated with a Jet in a Cross Flow. AIAA Journal, Vol. 12, N°. 12, December 1974. Pp 1666 - 1671.

38. Pearcey, H. H., Rao, K. & Sykes, D. M. Inclined Air-Jets used as Vortex Generators to Suppress Shock-Induced Separation. AGARD CP-534, Paper 40, April 1993.

39. Barberopoulos, A. A. Investigation of the Effects of a Vortex Generator Jet on a Turbulent Boundary Layer at High Subsonic Speed. MSc Thesis, College of Aeronautics, Cranfield University. 1995.

40. Johnston, J. & Nishi, M. Vortex Generator Jets - A Means for Passive and Active Control of Boundary Layer Separation. AIAA Paper 89-0564.

41. Compton, D. A. & Johnston, J. P. Streamwise Vortex Production by Pitched and Skewed Jets in a Turbulent Boundary Layer. AIAA Paper 91-0038.

42. Selby, G., Lin, J. & Howard, F. Jet Vortex Generators for Turbulent Flow Separation Control. Paper from 12th Symposium on Turbulence, September, 1990.

43. Zhang, S. Y. & Li, F. Experiments about the Air Jet Vortex Generator. Paper presented at 8th International Symposium on Air Breathing Engines, Cincinnati, June 1987.

44. Zhang, X. Computational Analysis of Co- and Contra- Rotating Streamwise Vortices in a Turbulent Boundary Layer. AIAA Paper 93-3035.

45. Henry, F. S. & Pearcey, H. H. Numerical Model of Boundary Layer Control Using Air-jet Generated Vortices. AIAA Journal, Vol. 32, N°. 12, December 1994.

46. Akanni, S. D. & Henry, F. S. Numerical Calculations for Air-Jet Vortex Generators in Turbulent Boundary Layers. Proceedings of RAeS High Lift and Separation Control Conference, Bath, March 1995. Paper 16.

47. Freestone, M. M. Preliminary Tests at Low Speeds on the Vorticity Produced by Air-Jet Vortex Generators. Research Memo Aero 85/01, Department of Aeronautics, City University, London. February 1985.

48. Rao, M. K. An Experimental Investigation of the Use of Air Jet Vortex Generators to Control Shock Induced Boundary Layer Separation. PhD Thesis, City University, 1988.

49. Anderson, B. H. & Gibb, J. Application of Computational Fluid Dynamics to the Study of Vortex Flow Control for the Management of Inlet Distortion. AIAA 92-3177, July 1992.

50. Gibb, J. & Jackson, M. Vortex Flow Control for the Management of Intake Distortion – Results of M2129 Phase 4 Tests in the DRA Bedford 13' x 9' Wind Tunnel. DRA/AS/HWA/CR/94212/1 (Restricted), August 1994.

51. Dewey, P. E. A Preliminary Investigation of Aerodynamic Characteristics of Small Inclined Air Outlets at Transonic Mach Numbers. NACA RM L53C10. April 1953

52. Nelson, W. J. & Dewey, P. E. A Transonic Investigation of the Aerodynamic Characteristics of Plate- and Bell-Type Outlets for Auxiliary Air. NACA RM L52H50, Sept. 1952.

53. Bolton, W. Measurement & Instrumentation Systems (Newnes, 1996).

54. Wendt, B, & Reighert, B. The Modelling of Symmetric Airfoil Vortex Generators. NASA CR-198501, June 1996.

55. ESDU Data Item Number 70015. Fluid Forces and Moments on Flat Plates. October 1972.

56. Bray, T. P. Calibration of the DERA Bedford 4" Wind Tunnel. DERA/AS/HWA/WP97513/1.0, March 1998.

57. Green, S. Chapter 1 of Fluid vortices, (ed. Sheldon Green) Dordrecht: Kluwer Academic Publishers, 1995.

Bryer, D. W. & Pankhurst, R. C. Pressure Probes for Determining Wind Speed and Flow Direction (NPL, London, 1971).

Chapter 12 - Acknowledgements

The topic of this research was suggested by Dr. Jim Gibb, DERA Bedford. Throughout the four years of the programme, he has provided unstinting support, enthusiasm, guidance, and confidence in me and for this, I am truly in his debt.

I also wish to thank Dr Kevin Garry, College of Aeronautics, for his unique supervision style, and for giving me the freedom to pursue my research in my own way. Further thanks go to the workshop staff at the College of Aeronautics for their assistance with the experimental facilities.

Finally, I must thank my family and friends for their support, without which I would never have finished.

Appendix A – Technology Strategy Methodology Questionnaire

Technology Ranking

A Future Air-Combat Engagement System (FACES) is proposed as a next generation air-superiority fighter. It is assumed that the aircraft will have an in-service date of around 2030, and will fulfil the role currently filled by aircraft such as Eurofighter 2000, F-22, Mig-33, and Sukhoi-35.

In order to assess the current state of technologies that might be applied to the aircraft, three proposed designs will be used as possible configurations on which to build. The configurations are to be assessed on various technology drivers, with the assessment being made on the Technology Risk involved with each driver.

The Technology Risk is defined as being the technology leap over existing aircraft technology to achieve a mature technology capable of being applied to FACES. The Technology Risk will be a function of such things as:

- required effort,
- technical maturity,
- obsolescence,
- complexity,
- possible acceptance of failure.

Cost should not be considered as part of this Technology Risk. While cost is a significant factor, the Technology Risk is concerned with the technical problems which may be overcome, should fair and reasonable funding be made. The Technology Risks are to be rated on a scale from 1 to 9, where 1 is a very low risk, and 9 is a very high risk.

Each of the next three pages will contain a set of high-level technology descriptions, with their effects on each of the aircraft types. Please rate the Technology Risk needed in each area to overcome the problems/outcomes of the technology drivers ***on the aircraft design under consideration***.

Example

Technology Driver: Pilot's Coffee Cup Holder

FACES-A (Stealth): The stealthy aspects of the coffee cup holder are irrelevant, as it will be located on the inside of the aircraft, which will have a canopy which radar energy cannot penetrate. Other aspects of the coffee cup holder technology are relatively mature, and the complexity is low. Therefore this Technology Driver would have a Technology Risk rating of 1 (that is the development technology is in place). The engineering aspects are the only problem to overcome.

FACES-B (Agility): The high agility of this aircraft suggest that the coffee cup holder may need to be self-levelling. This technology may not currently exist, which would drive up the Technology Risk value. The complexity of this item could be high, and therefore will have a similar effect. However, the acceptance of failure is not a significant issue (except to the pilot) as the mission will not be significantly affected. On balance, a Technology Risk of 2/3 may be appropriate.

FACES-C (Weapons): The coffee cup holder will have no affect on the weapons platform performance, will not have the added problems of manoeuvrability. It will therefore have a Technology Risk of 1.

Scenario A: Stealthy Aircraft

FACES scenario A is a piloted next-generation stealth design that achieves its mission success primarily on the basis that the aircraft is less 'visible' than the attacking aircraft. This will give FACES-A a longer 'reach' in the Beyond Visual Range (BVR) encounter, and present a more challenging target to the enemy aircraft. Whilst being fairly manoeuvrable (a naturally unstable configuration augmented with a Fly-By-Wire system) it is not envisaged that this aircraft will employ Thrust-Vectoring-Technology which would compromise its stealth characteristics.

Technology Risk Rating: 1 = very low, 9 = very high

Aerodynamics Technology Drivers	Scenario A Stealthy Aircraft	Technology Risk (1 to 9)
Configuration Performance (Multi-Varient Optimisation)	Studies required to further the database of stealth configurations and performance estimation	
Wing	Understand & predict performance of stealthy configs in manoeuvring, particularly buffet and flutter prediction	
Control Surfaces/Jet Reaction control	Stealthy control surfaces needed. Possible removal of deflecting control surfaces with control jets.	
Air Intake Design	Stealthy engine installation to reduce aircraft RCS	
Engine Exhaust Treatment	Reduction of IR signature and emissions	

Scenario B: Manoeuvrable Aircraft

FACES scenario B is a highly agile aircraft that achieves its mission success based on its extreme manoeuvrability to allow a first-shot capability and to evade incoming missiles. FACES-B would have a modern radar system which would extend the abilities of the current generation of intercept radar for a fair Beyond Visual Range (BVR) performance, but at close range would use agility to bring weapons to bare for the release of Infra-Red weapons. Some stealthy attributes would be included to reduce the target size (e.g. Radar Absorbent Materials, paints, etc.), but the primary performance concern would be for agility.

Technology Risk Rating: 1 = very low, 9 = very high

Aerodynamics Technology Drivers	Scenario B Agile Aircraft	Technology Risk (1 to 9)
Configuration Performance (Multi-Varient Optimisation)	Studies required to further the database of thrust vectoring options and to improve performance estimation	
Wing	Prediction techniques for extreme manoeuvres with non-linear and dynamic aerodynamics needed.	
Control Surfaces/Jet Reaction control	Control techniques needed for very high incidence manoeuvres where control surfaces become unresponsive: forebody blowing with air-jets, control jets	
Air Intake Design	Inlet capable of low engine distortion at engine during manoeuvres	
Engine Exhaust Treatment	Thrust vectoring though the use of jet efflux control: mechanical paddles, or fluidic control	

Scenario C: Weapons Up-Grade Scenario

FACES scenario C would be an extension to an existing platform, with a next-generation weapons system up-grade. The use of a more powerful and more reliable missile system would allow FACES-C to achieve its mission though a longer and more reliable missile 'reach'. It is envisaged that the aircraft would be structurally upgraded, and new engines would also be fitted, with a weight saving driver in mind. However, the lion's share of the development effort would be placed on the avionics/weapons system. Some stealth attributes may be included through the use of Radar Absorbent Materials, paints, and next generation low-IR engine exhausts. Suitable airframes might include Eurofighter 2000, F-22, and JSF.

Technology Risk Rating: 1 = very low, 9 = very high

Aerodynamics Technology Drivers	Scenario C Weapon Platform	Technology Risk (1 to 9)
Configuration Performance (Multi-Varient Optimisation)	Studies to reduce the aircraft weight.	
Wing	Studies on improved wing/missile integration	
Control Surfaces/Jet Reaction control	No significant work needed	
Air Intake Design	Reduction in duct size/weight	
Engine Exhaust Treatment	Reduction of weight of engine exhaust	

Appendix B – 5-Hole Probe Calibrations

Notation

Cp	Pressure coefficients
HWCR	Hot-Wire Calibration Rig
M	Mach number
P	Pressure (in Pa unless otherwise stated)
p	Static pressure (in Pa unless otherwise stated)
T	Temperature (K)

Subscripts

0	Free-stream
1,2,3,4,5	Conditions in probe tubes 1 to 5 respectively
atm	Atmospheric conditions
avg	Conditions averaged between tubes 1 to 4 of the pressure probe
HWCR	Hot-Wire Calibration Rig Conditions
W/S	Wind tunnel working section conditions

Introduction

Five-hole probes have long been a convenient tool with which to find the local pitch and yaw angles and the local total and static pressures at any point in a flowfield. The five hole probe is a name given to any probe which has 5 holes oriented at a probe tip where one hole is located along the centre-line of the probe has the end of the tube perpendicular to the tube axis. The other four tubes will be located at 90° sector spacings parallel to the centre tube, with the tube ends being at some angle to the tube axis, usually 45°. Typical examples are shown in Figure 85.

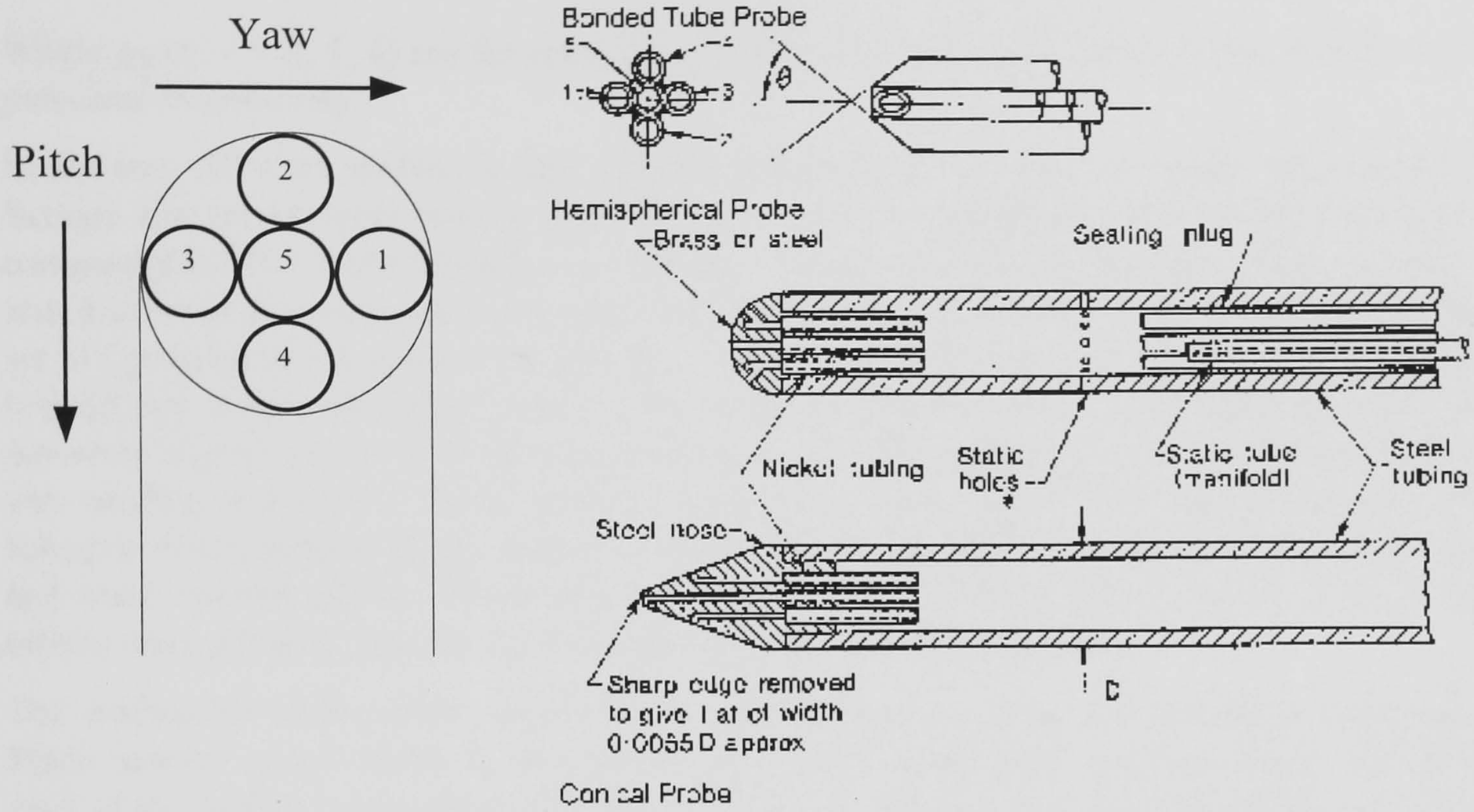

Figure 85: Five Hole Probes (Bryer, D. W. & Pankhurst, R. C. Pressure Probes for Determining Wind Speed and Flow Direction (NPL: London. HMSO 1971))

When using the probe, the pressures from each tube are measured. If the probe axis is aligned with the free-stream, the centre tube should sample a pressure value very close to the total pressure of the free-stream. Further, it would be expected that the chamfered tubes would sample a pressure which was could be related to the static pressure. Thus a measure of the Mach number and the dynamic pressure can be calculated if the probe is calibrated. The calibration is usually made with respect to the free-stream total and static pressures as follows:

$$Cp_5 = \frac{p_5 - p_0}{H_0 - p_0}$$

Equation 80

$$Cp_{avg} = \frac{p_{avg} - p_0}{H_0 - p_0}$$

Where p_5 is the pressure measured from the centre tube, p_{avg} is the average of the pressures measured from the four outer chamfered tubes, and H_0 and p_0 are the free-stream total and static pressures respectively.

Further, as the probe is pitched or yawed, one of the chamfered tubes will be angled to place the chamfer surface closer to a perpendicular angle with the free-stream, while the leeward side moves to a more parallel position. As a result, the windward tube will read a value of pressure closer to the total pressure, while the leeward tube would be at the free-stream static or less. Taking the difference

in pressure between these two tubes would allow the response of the probe to be mapped with flow angle. The following relations are used:

$$Cp_\theta = \frac{p_3 - p_1}{p_5 - p_{avg}}$$

$$Cp_\phi = \frac{p_2 - p_4}{p_5 - p_{avg}}$$

Equation 81

Where p_n (n = 1, 2, 3, 4) are the pressures at tube n, and H_0 and p_∞ are the free-stream total and static pressures respectively.

In the two different studies in this research programme (i.e. the low-speed tests carried out in the Brough low speed wind tunnel, and the Mach number dependant tests carried out in the 9" x 9" compressible flow wind tunnel), two different 5-hole pressure probes were used. In the low speed test, a 2.5-mm diameter probe was used, and was calibrated at only one flow speed, and thus only one set of *Cp* variations was taken for that flow speed. Since the range of velocities to be tested was from 0 to 20 m/s, it was considered that the Reynolds number changes in this range were not sufficient to introduce significant error in the measurements. For the high-speed test, the scale of the experiment was smaller, and so a 1.5-mm diameter probe was used. This probe was to be used over a wide subsonic Mach number range, and was calibrated to account for the relatively large Reynolds number and Mach number effects which may have been present. If any Mach number or Reynolds number effects were present, then the *Cp* values would vary with Mach number.

The calibration of the probe involves the simultaneous pitching and yawing of the probe over the Mach number range which is of expected use, and at each pitch and yaw angle, the pressure from each of the probes is measured and reduced to the coefficient form as outlined above. This produces a series of pressure response data sets. When the probe is used in a real flow, the pressure response of the probe is measured, converted to coefficient form, and these coefficients are then compared with the calibration data set. A simple interpolation method is needed to find the exact pitch and yaw angles.

The two probes were calibrated in different facilities and at different pressure ranges, and thus the results are presented as two reports.

Calibration of the 2.5-mm Probe for Low-Speed Testing

'Cranwell' Low-Speed Open Jet Wind Tunnel

The 2.5-mm five-hole pressure probe was calibrated for the low-Mach number tests in the College of Aeronautics Cranwell wind tunnel. This facility is a 0.457-m x 0.457-m open jet wind tunnel that is driven by a centrifugal fan, located upstream of the settling chamber. The probe was mounted in a pitch-yaw quadrant, which was located with the probe tip at the centre-line of the exit plane of the wind tunnel jet. The quadrant mount was a carriage-on-arc design, which allowed the probe tip to be located at the centre of rotation of both the pitch and yaw axes of rotation. A schematic of the experimental apparatus is shown in Figure 86.

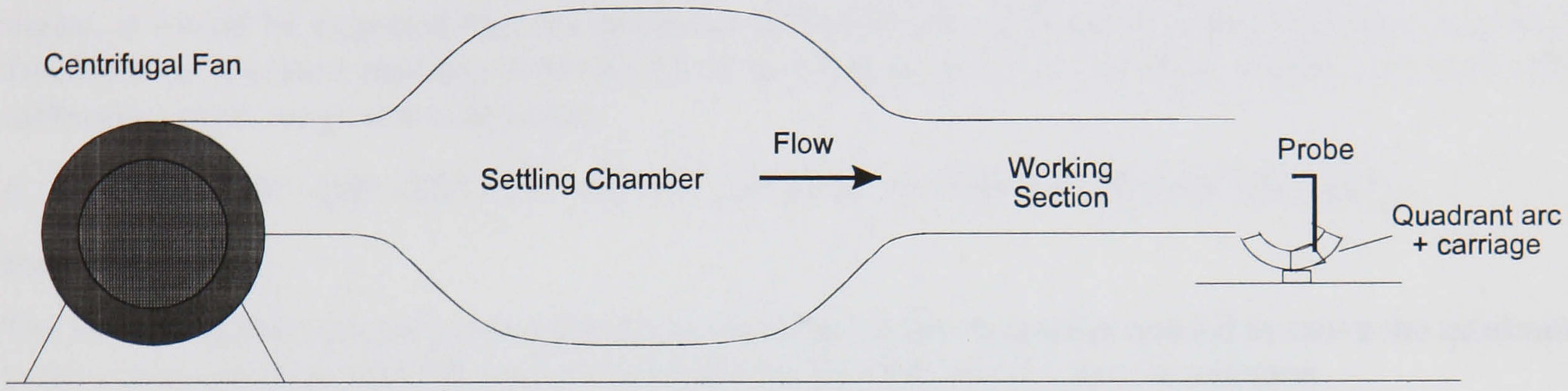

Figure 86: College of Aeronautics Cranwell Open Jet Tunnel as used for Probe Calibrations

A photograph of the calibration quadrant is shown in Figure 87, and illustrates the twin rotational axes nature of the device. The arc carriage allows the probe to be pitched around the probe tip. The whole assembly can then be yawed using the turntable on which the arc is mounted. The probe is mounted centrally on the turntable axis, and thus the probe is yawed about the probe tip.

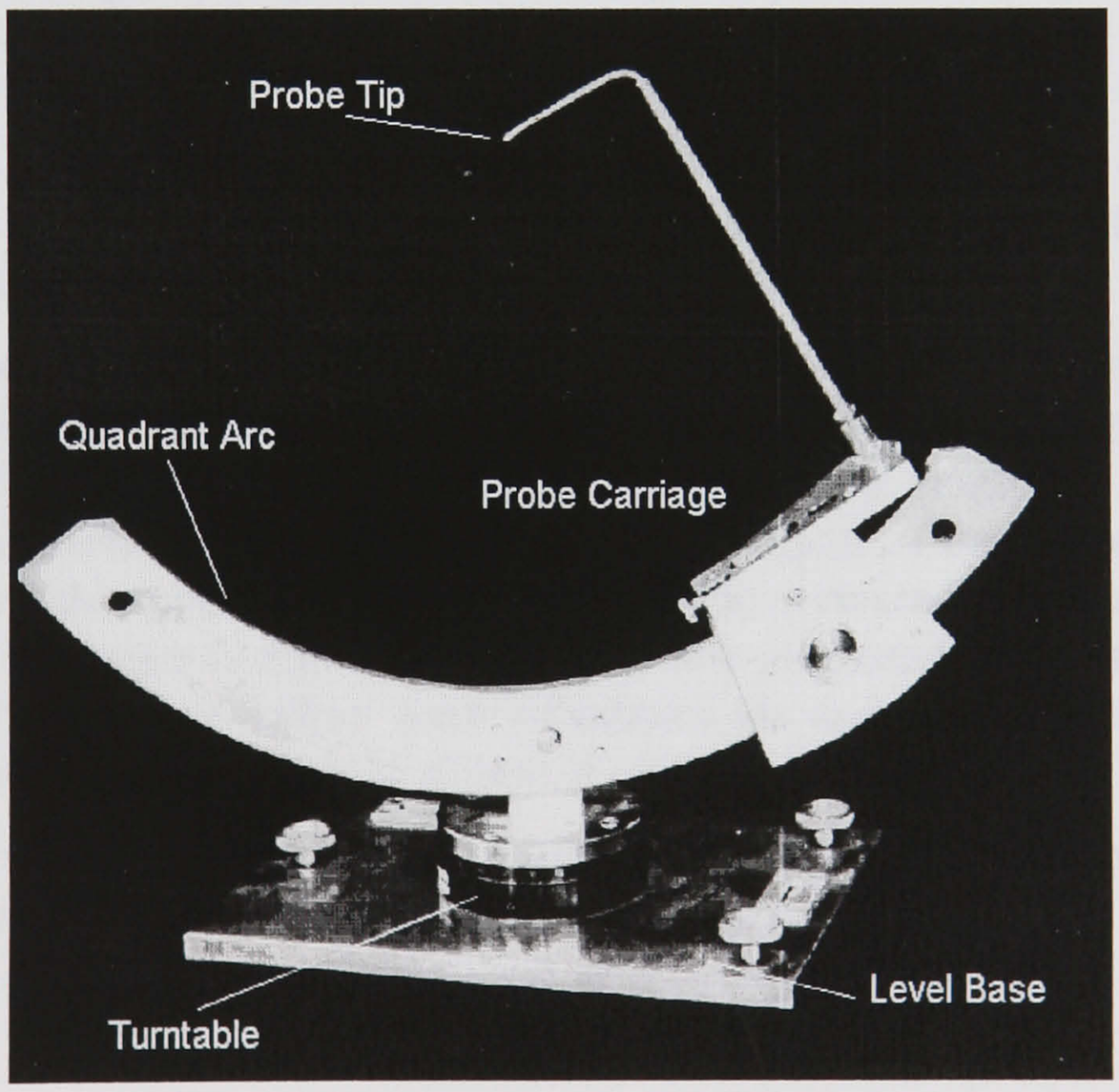

Figure 87: Probe Calibration Quadrant

The turntable was driven by a computer controlled stepper motor, and could rotated without restriction. Angles could be set to an accuracy of 0.01°. The pitch angle of the probe was set manually by sliding the probe carriage along the quadrant arc, and the angular range was ±40° from the centre of the quadrant arc. Use of a digital inclinometer allowed the pitch angle to be set to an accuracy of 0.1°.

The wind tunnel maximum speed is governed largely by the temperature of the day, but was around 18 m/s. This was used as the calibration speed for the probe, even though the probe was to be used at a free-stream speed of 20 m/s. The small difference in flow speeds was considered to be of small consequence in the calibration of the probe. The probe was also calibrated over the expected range of pitch and yaw angles. Previous investigations using 5-hole probes had suggested that maximum pitch and yaw angles of the flow in vortices would be around 25°[14]. As such, the probe was calibrated over the range ±32° in pitch and yaw simultaneously. In order to achieve good definition of the calibration data, it was decided to take more calibration data over the areas of the calibration range where either: (a) most of the flow field data points would lie, or (b) the largest changes in the trends of the calibration data occurs. It would be expected that most flow angles would be below 5° (over an entire grid of data), and thus extra definition would be warranted in this region. Also, at extreme angles, it would be expected that the probe would behave in a non-linear manner (in the same way that the total pressure readings from a Pitot tube increase in error with flow angle). As such, the calibration angle range was selected as:

θ, ϕ = [-32° -28° -24° -20° -15° -10° -5° -2° 0° 2° 5° 10° 15° 20° 24° 28° 32°]

Instrumentation

The instrumentation for the probe calibration consisted of the equipment needed to move the quadrant to the correct position, and the equipment needed to read the pressure instrumentation.

The pitch angle of the probe was set manually, and once at the required pitch angle, was left. The yaw angles were then stepped though using the automated system. The yaw-turntable stepper motor controller was Parker Hannifin Digiplan AT6400 personal computer controlled devices driving Digiplan PDS15-2 drives. This product allowed the easy control of the system through a set of Visual Basic libraries that could be used to construct a control program. The calibration quadrant was controlled such that a sweep in yaw was carried out at a given pitch angle. Once the sweep was finished, the probe was traversed back through the entire yaw range, and a new pitch angle was manually selected. Using this method, the effect of any backlash in the system was minimised.

Tunnel dynamic pressure was measured using a Pitot-static tube located in the exit plane of the wind tunnel (i.e. in the same plane as the probe tip), and the pressure was measured using a Furness FCO 16 ±200-mmH_2O differential pressure transducer.

The five probe pressures were sampled using Furness FCO 44 ±100-mmH_2O differential digital output pressure transducers (Serial Numbers: 9509141 to 9509145). The outputs from the pressure transducers were conditioned using College of Aeronautics voltage amplifiers set to a gain of 1, and with high bypass filters switched on. The negative pressure inputs of the transducers were connected to the static port of the Pitot static tube. The output from the pressure transducer system was sampled using a PC mounted analogue-to-digital converter, which measured samples for 3 seconds and a frequency of 100 Hz. Average values were calculated for each pressure, helping to reduce the experimental uncertainty and the effects of electrical noise in the system.

Control software was written using Microsoft Visual Basic. This software allowed the control of the stepper motor system (as mentioned above) and the interrogation of the transducers, with the subsequent storage to disk of the pressure data and probe angular position.

Results

The calibration results for the low-Mach number five-hole probe are presented. Tables give the values of the four pressure coefficients measured at a free-stream velocity of 18 m/s. This calibration was considered to be applicable over the speed range for 0 to 20 m/s without significant error being generated.

This data has also been plotted to give and indication of the non-linearity of the five-hole probe, and to highlight how the relatively large amount of experimental data helps to define the calibration. It is clear from these results that the five-hole has a cross coupling between the pitch and yaw axes, and thus simultaneous pitch and yaw angles must be used for the calibration process.

Non-linearities are largely due to manufacturing defects. Since the probe tip is only 2.5-mm in diameter, it may be expected that the chamfer angles on the tip may not be exactly equal, and that the probe tip may be twisted in its axis. These points are evident from the following close up photograph of the tip. It is important to note that there are no burs on the tip, which could cause large scale flow separations if present.

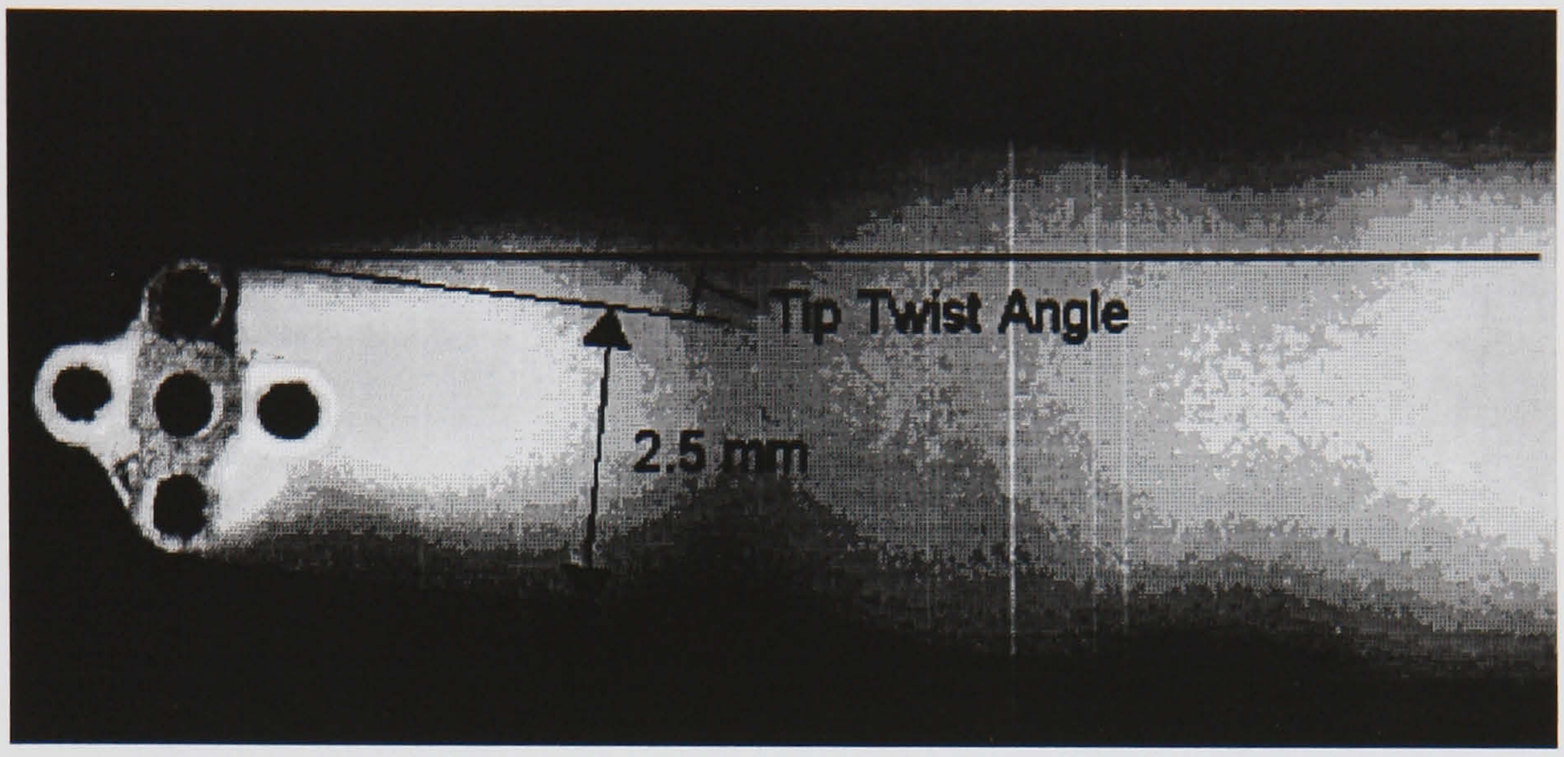

Figure 88: Close up view of the 2.5-mm Five-Hole Probe (blurred region in the probe shaft)

Derived Coefficients Plots

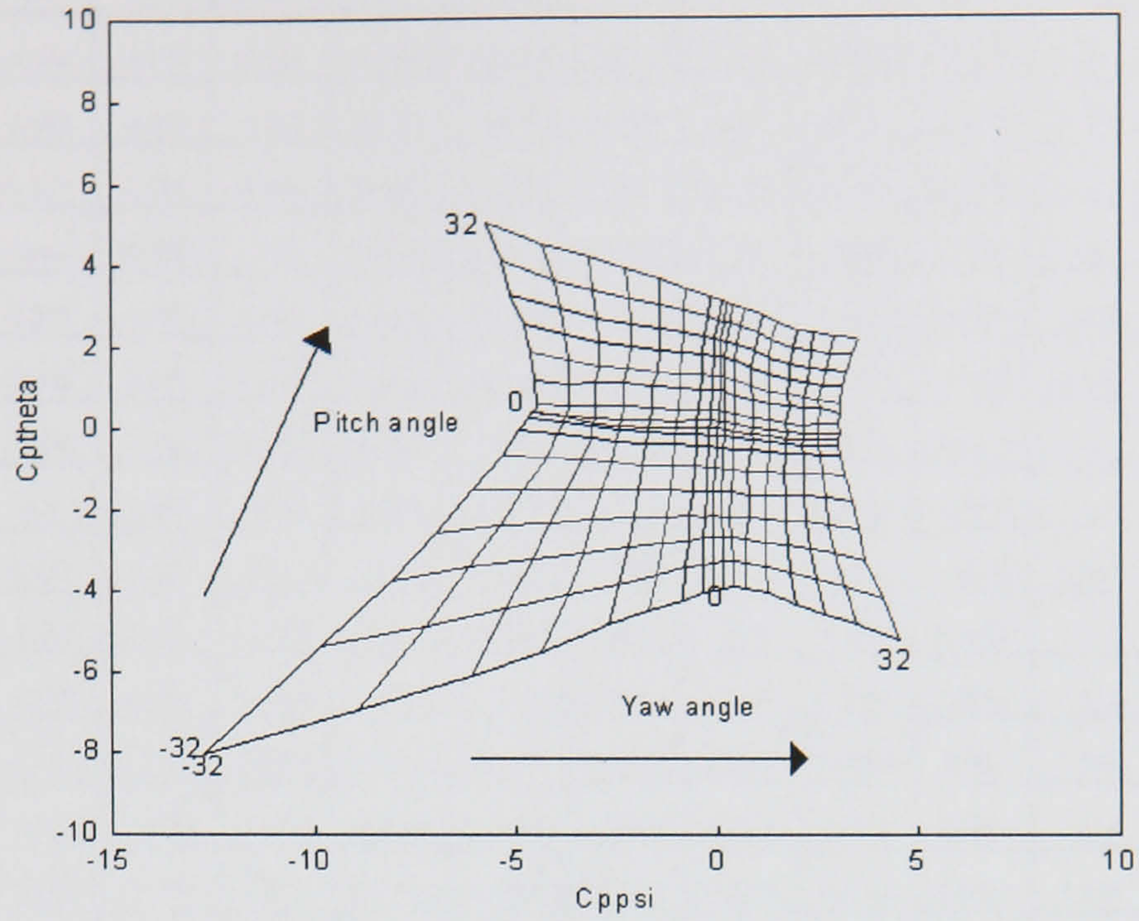

Figure 89: Pitch pressure Coefficient vs. Yaw Pressure Coefficient

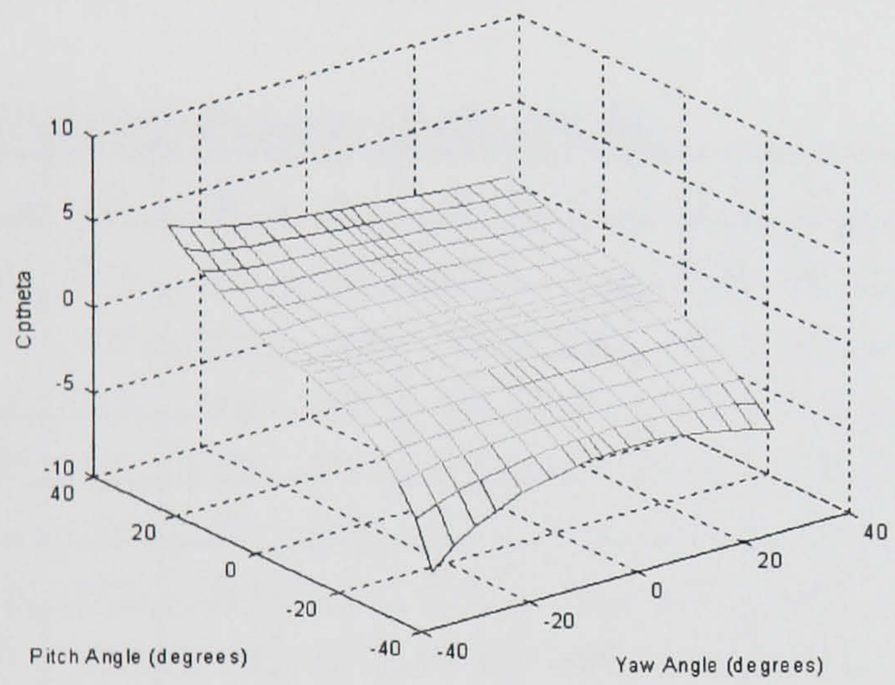

Figure 90: Cp_θ vs. Pitch Angle, θ

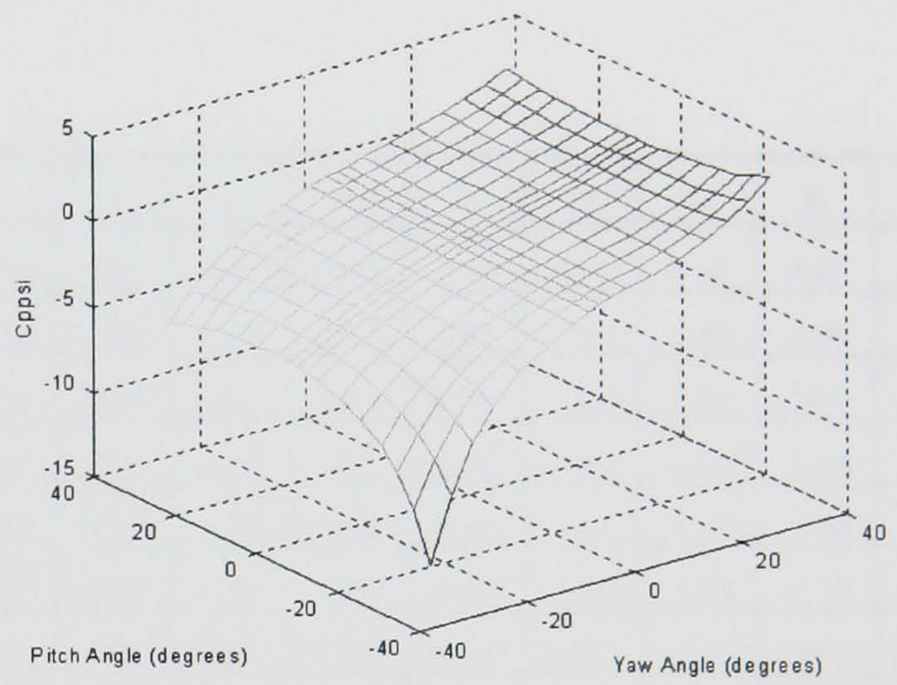

Figure 91: Cp_ϕ vs. Yaw Angle, ϕ

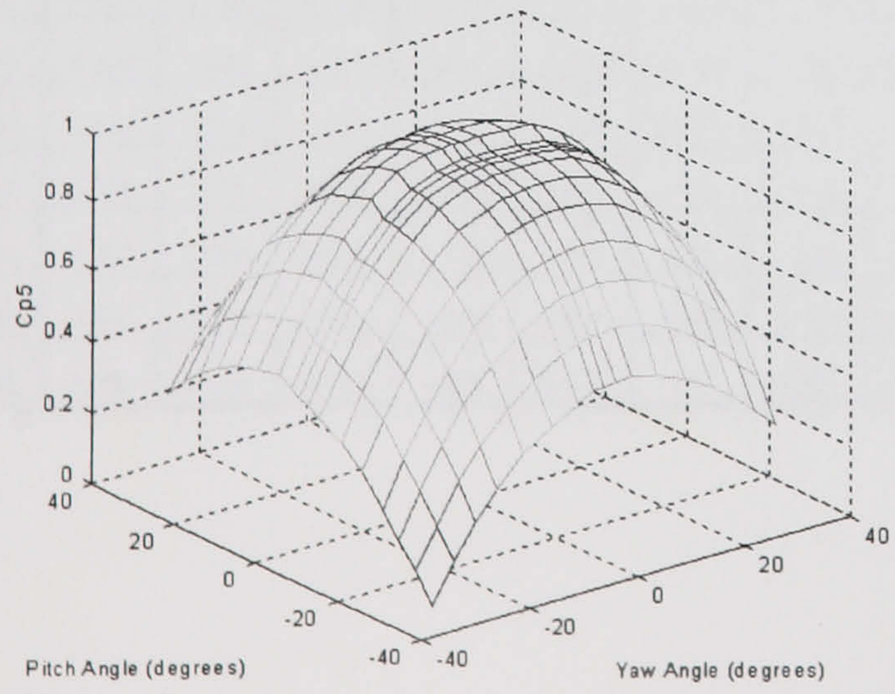

Figure 92: Cp_5 vs. Pitch (θ) and Yaw (ϕ) Angle

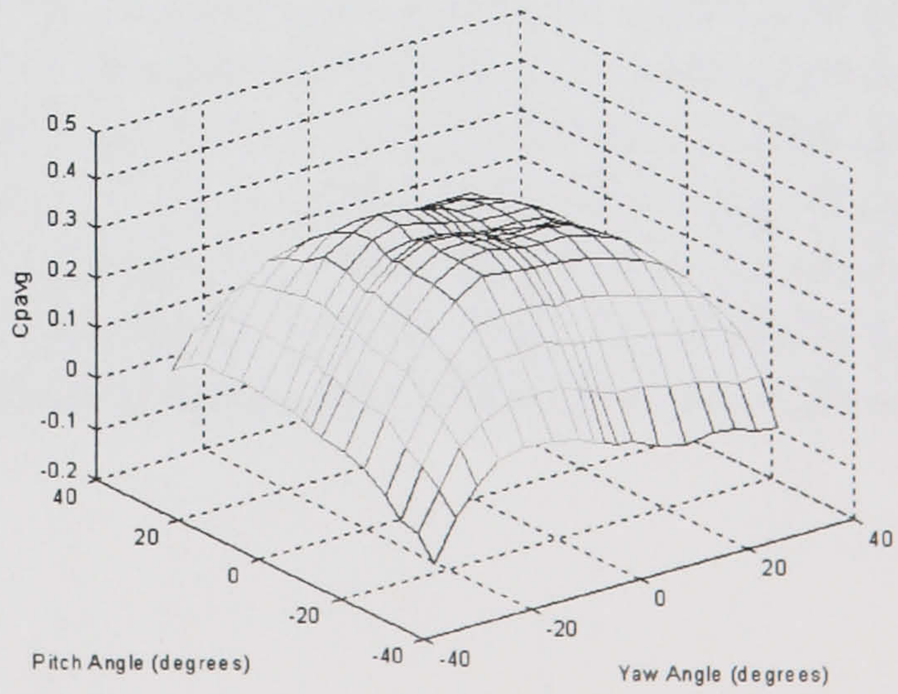

Figure 93: Cp_{avg} vs. Pitch (θ) and Yaw (ϕ) Angle

Yaw Angle Pressure Coefficient, Cp_{ϕ}

θ ϕ	-32	-28	-24	-20	-15	-10	-5	-2	0	2	5	10	15	20	24	28	32
-32	-12.76	-8.942	-6.083	-4.384	-2.702	-1.665	-0.8184	-0.3344	-0.09172	0.1386	0.4479	0.7305	1.231	1.976	2.673	3.467	4.513
-28	-9.844	-7.223	-5.237	-3.686	-2.463	-1.503	-0.7471	-0.3276	-0.0881	0.1444	0.4297	0.7246	1.224	1.845	2.479	3.194	4.128
-24	-8.1	-6.132	-4.582	-3.317	-2.203	-1.364	-0.6965	-0.3182	-0.07557	0.1222	0.3949	0.7376	1.22	1.775	2.321	2.942	3.692
-20	-6.97	-5.395	-4.115	-3.061	-2.048	-1.26	-0.6515	-0.2961	-0.09449	0.1079	0.3295	0.7955	1.207	1.722	2.201	2.8	3.537
-15	-6.067	-4.801	-3.719	-2.825	-1.929	-1.161	-0.5695	-0.2524	-0.07562	0.1104	0.3682	0.8095	1.209	1.739	2.18	2.719	3.387
-10	-5.343	-4.223	-3.371	-2.609	-1.811	-1.115	-0.522	-0.2189	-0.0342	0.16	0.4177	0.789	1.242	1.698	2.143	2.65	3.188
-5	-4.883	-3.919	-3.135	-2.478	-1.746	-1.074	-0.499	-0.1857	0.003877	0.162	0.4303	0.8451	1.277	1.75	2.144	2.609	3.058
-2	-4.678	-3.802	-3.071	-2.4	-1.68	-1.05	-0.4978	-0.1976	-0.01731	0.1865	0.4396	0.8952	1.313	1.746	2.139	2.54	3.018
0	-4.614	-3.749	-3.016	-2.381	-1.66	-1.01	-0.4848	-0.1884	0.01726	0.2116	0.4549	0.8894	1.304	1.747	2.141	2.564	3.029
2	-4.517	-3.705	-2.977	-2.357	-1.627	-1.005	-0.461	-0.1267	0.05695	0.2246	0.4845	0.9214	1.312	1.768	2.147	2.56	3.053
5	-4.469	-3.645	-2.959	-2.289	-1.582	-0.956	-0.4303	-0.1362	0.07007	0.2607	0.5004	0.9091	1.315	1.753	2.149	2.567	3.02
10	-4.538	-3.636	-2.979	-2.318	-1.578	-0.9321	-0.3847	-0.107	0.07442	0.2454	0.4988	0.902	1.337	1.803	2.161	2.592	3.054
15	-4.631	-3.666	-2.886	-2.2	-1.462	-0.8634	-0.3564	-0.07641	0.09676	0.2355	0.4732	0.8799	1.314	1.794	2.18	2.572	3.055
20	-4.768	-3.736	-2.879	-2.138	-1.399	-0.8213	-0.3361	-0.06969	0.09328	0.2526	0.4993	0.8829	1.329	1.829	2.238	2.657	3.122
24	-5.073	-3.867	-2.927	-2.129	-1.38	-0.7832	-0.2818	-0.02993	0.1176	0.2856	0.5299	0.959	1.358	1.815	2.291	2.74	3.238
28	-5.312	-3.999	-3.04	-2.165	-1.379	-0.7551	-0.2039	0.06449	0.225	0.3773	0.6073	1.037	1.409	1.913	2.344	2.854	3.388
32	-5.734	-4.305	-3.155	-2.236	-1.387	-0.6984	-0.1271	0.1442	0.2875	0.4489	0.6991	1.133	1.537	2.03	2.458	2.921	3.536

Pitch Angle Pressure Coefficient, Cp_{θ}

θ ϕ	-32	-28	-24	-20	-15	-10	-5	-2	0	2	5	10	15	20	24	28	32
-32	-8.058	-6.971	-6.087	-5.509	-4.831	-4.504	-4.233	-4.044	-3.983	-3.937	-3.893	-3.947	-4.067	-4.345	-4.585	-4.845	-5.213
-28	-5.384	-4.857	-4.418	-4.1	-3.842	-3.607	-3.432	-3.361	-3.297	-3.285	-3.248	-3.304	-3.407	-3.548	-3.698	-3.886	-4.204
-24	-3.732	-3.418	-3.199	-3.05	-2.931	-2.832	-2.764	-2.693	-2.69	-2.689	-2.691	-2.731	-2.806	-2.869	-2.959	-3.052	-3.247
-20	-2.564	-2.409	-2.334	-2.243	-2.203	-2.187	-2.16	-2.173	-2.163	-2.171	-2.171	-2.2	-2.254	-2.291	-2.293	-2.398	-2.497
-15	-1.493	-1.509	-1.494	-1.51	-1.505	-1.507	-1.543	-1.562	-1.572	-1.576	-1.582	-1.64	-1.661	-1.661	-1.669	-1.708	-1.795
-10	-0.701	-0.7318	-0.7737	-0.8335	-0.904	-0.923	-0.9489	-0.9659	-0.9923	-1.002	-1.027	-1.068	-1.094	-1.105	-1.106	-1.136	-1.193
-5	-0.03512	-0.1228	-0.2231	-0.3221	-0.3841	-0.4102	-0.4377	-0.4473	-0.4722	-0.4821	-0.5261	-0.5536	-0.5939	-0.6378	-0.6521	-0.6844	-0.7061
-2	0.2442	0.1477	0.05013	-0.05316	-0.1054	-0.1434	-0.1563	-0.1855	-0.1989	-0.2012	-0.2669	-0.3149	-0.3522	-0.3992	-0.4597	-0.4352	-0.4418
0	0.4122	0.3162	0.08041	0.03803	-0.00371	0.02292	0.02365	0.003066	-0.01488	-0.0285	-0.0879	-0.1528	-0.195	-0.2779	-0.2962	-0.2773	-0.2975
2	0.4071	0.3136	0.2405	0.206	0.1862	0.1454	0.2073	0.184	0.1631	0.1567	0.1036	0.01519	-0.03296	-0.1147	-0.1694	-0.123	-0.1518
5	0.6047	0.5402	0.5216	0.5248	0.4721	0.4323	0.4269	0.4259	0.4169	0.398	0.3406	0.2647	0.1958	0.114	0.04764	0.0943	0.08284
10	1.164	1.062	1.134	1.111	1.037	0.9557	0.9232	0.9276	0.9098	0.8901	0.8039	0.6934	0.5993	0.5317	0.4903	0.4856	0.3448
15	1.834	1.638	1.534	1.441	1.363	1.331	1.309	1.27	1.258	1.22	1.157	1.018	0.8962	0.8344	0.717	0.6919	0.5999
20	2.527	2.301	2.102	1.976	1.903	1.861	1.814	1.762	1.741	1.702	1.636	1.485	1.319	1.188	1.101	1.047	1.028
24	3.272	2.906	2.678	2.546	2.428	2.35	2.255	2.188	2.151	2.108	2.036	1.892	1.715	1.568	1.475	1.42	1.374
28	4.09	3.603	3.376	3.184	3.018	2.866	2.712	2.645	2.608	2.562	2.482	2.333	2.161	1.967	1.884	1.821	1.783
32	5.002	4.506	4.174	3.896	3.637	3.405	3.208	3.121	3.071	3.015	2.929	2.794	2.592	2.406	2.323	2.258	2.2

Centre Hole Pressure Coefficient, *Cp5*

θ ϕ	-32	-28	-24	-20	-15	-10	-5	-2	0	2	5	10	15	20	24	28	32
-32	0.01494	0.1279	0.2221	0.3002	0.3778	0.4319	0.4721	0.496	0.4992	0.5017	0.5059	0.4832	0.4554	0.4107	0.3652	0.3071	0.251
-28	0.09957	0.2091	0.3184	0.4001	0.478	0.5409	0.5897	0.6052	0.6169	0.6164	0.6201	0.6081	0.5764	0.5294	0.4776	0.4194	0.3629
-24	0.1594	0.2864	0.3988	0.4955	0.5813	0.6425	0.6914	0.7123	0.7163	0.7229	0.7265	0.7138	0.6851	0.637	0.5892	0.5336	0.4587
-20	0.2321	0.3532	0.4633	0.5664	0.6655	0.7291	0.7765	0.7958	0.7999	0.807	0.8134	0.804	0.7716	0.7244	0.6779	0.6126	0.5253
-15	0.3112	0.4362	0.5475	0.6452	0.7422	0.8166	0.8578	0.8749	0.8818	0.8913	0.8925	0.8829	0.8592	0.8081	0.7562	0.6847	0.5888
-10	0.3621	0.4884	0.5991	0.6983	0.7934	0.8652	0.9026	0.9229	0.9256	0.9315	0.936	0.9312	0.909	0.862	0.8127	0.7334	0.6488
-5	0.4034	0.5299	0.6419	0.7353	0.8263	0.8983	0.9351	0.9453	0.9512	0.9523	0.9561	0.951	0.9386	0.8956	0.844	0.7693	0.6847
-2	0.4207	0.5508	0.6636	0.7586	0.8474	0.914	0.944	0.9527	0.9565	0.9606	0.9589	0.9566	0.945	0.9119	0.858	0.7872	0.6925
0	0.4353	0.5567	0.6679	0.7583	0.8507	0.917	0.9502	0.9551	0.9573	0.9599	0.9606	0.9556	0.9442	0.9118	0.8614	0.7884	0.702
2	0.4481	0.5682	0.6802	0.7658	0.8558	0.9173	0.9485	0.9543	0.9606	0.9601	0.9595	0.9601	0.9525	0.9144	0.8645	0.7896	0.6961
5	0.4688	0.5989	0.7063	0.8018	0.893	0.9525	0.978	0.985	0.992	0.9892	0.9901	0.9876	0.9838	0.9446	0.8889	0.8115	0.7172
10	0.4538	0.5795	0.6897	0.7878	0.8714	0.9354	0.9682	0.9807	0.9841	0.9829	0.9852	0.9843	0.9644	0.9267	0.8754	0.8074	0.7128
15	0.4368	0.5596	0.6683	0.7571	0.8494	0.9042	0.9407	0.9549	0.963	0.964	0.97	0.9622	0.9414	0.9001	0.849	0.7727	0.6832
20	0.4038	0.526	0.6293	0.7189	0.7949	0.8539	0.893	0.9073	0.9128	0.9145	0.9251	0.9186	0.8999	0.8565	0.801	0.7323	0.652
24	0.3674	0.4947	0.5916	0.6745	0.7427	0.7901	0.8384	0.8535	0.8622	0.8645	0.8727	0.8697	0.8558	0.8213	0.7604	0.691	0.6039
28	0.3179	0.4275	0.5156	0.5894	0.6537	0.7123	0.7475	0.7668	0.7751	0.7817	0.7946	0.7917	0.7809	0.7543	0.7071	0.6297	0.5477
32	0.2614	0.3623	0.4403	0.5019	0.5595	0.6174	0.6592	0.6746	0.6862	0.6898	0.7021	0.7097	0.7046	0.684	0.6484	0.5857	0.4937

Averaged Pressure Coefficient, Cp_{avg}

θ ϕ	-32	-28	-24	-20	-15	-10	-5	-2	0	2	5	10	15	20	24	28	32
-32	-0.1046	-0.02272	0.02899	0.06915	0.07664	0.07322	0.06197	0.04769	0.03885	0.03125	0.0279	0.003524	-0.00846	0.001119	-0.0045	-0.02048	-0.02866
-28	-0.05896	0.01653	0.08954	0.1244	0.1494	0.1512	0.1472	0.1347	0.1249	0.1165	0.1076	0.105	0.08992	0.08191	0.06986	0.05709	0.05924
-24	-0.04673	0.04773	0.1253	0.1827	0.2156	0.2138	0.2216	0.2089	0.2015	0.1984	0.1933	0.1859	0.1753	0.1589	0.1565	0.1454	0.1155
-20	-0.01313	0.06955	0.1427	0.2109	0.2667	0.2726	0.2747	0.27	0.2602	0.2648	0.2651	0.2518	0.2371	0.2221	0.2099	0.1925	0.1413
-15	0.01785	0.1099	0.1841	0.2443	0.2976	0.3324	0.3243	0.3206	0.3175	0.3187	0.3152	0.3056	0.2894	0.271	0.2508	0.2123	0.1516
-10	0.03092	0.1123	0.1909	0.2547	0.3118	0.3398	0.3499	0.3421	0.338	0.3314	0.3313	0.3318	0.3182	0.2954	0.2574	0.204	0.1522
-5	0.03838	0.1228	0.2004	0.2633	0.3129	0.3429	0.3461	0.3414	0.3357	0.3286	0.3282	0.3301	0.3175	0.2884	0.2469	0.2024	0.1491
-2	0.0455	0.1349	0.2148	0.2772	0.3245	0.3501	0.3456	0.3364	0.3336	0.3247	0.3187	0.3182	0.3094	0.286	0.2452	0.2041	0.1286
0	0.05536	0.1355	0.2116	0.2698	0.3175	0.344	0.3422	0.3346	0.3278	0.3192	0.3203	0.3076	0.3045	0.2788	0.2414	0.1922	0.1258
2	0.06251	0.1479	0.2228	0.2768	0.3242	0.337	0.3343	0.3225	0.3179	0.3145	0.3111	0.3105	0.3068	0.2776	0.2417	0.1833	0.1104
5	0.06113	0.1528	0.2343	0.2925	0.3403	0.3548	0.3439	0.3331	0.3317	0.3243	0.3189	0.3157	0.3162	0.2845	0.2438	0.1859	0.101
10	0.06589	0.1477	0.2341	0.3007	0.3365	0.3576	0.3495	0.3413	0.3364	0.3315	0.3183	0.3167	0.309	0.2808	0.2388	0.1801	0.1078
15	0.07026	0.153	0.2226	0.2723	0.3162	0.3233	0.3155	0.3134	0.3131	0.3102	0.3101	0.3057	0.2908	0.2579	0.2187	0.1553	0.07101
20	0.0645	0.1486	0.2155	0.2594	0.2835	0.2836	0.2803	0.2795	0.2863	0.2851	0.2822	0.2817	0.2826	0.2366	0.1936	0.14	0.08328
24	0.06815	0.1523	0.2021	0.2394	0.249	0.2324	0.2471	0.2487	0.2496	0.2473	0.256	0.2572	0.2561	0.2445	0.1834	0.1256	0.06449
28	0.0489	0.1172	0.1667	0.1851	0.1756	0.1862	0.1776	0.1777	0.1747	0.1813	0.1947	0.1981	0.2018	0.2056	0.1793	0.1047	0.03866
32	0.02368	0.08622	0.1206	0.1273	0.1107	0.1115	0.1056	0.1091	0.1106	0.107	0.1201	0.1486	0.1565	0.1675	0.1615	0.1076	0.01684

Calibration of the 1.5-mm Probe for Mach Number Dependant Tests

DERA Bedford 0.1016 m Subsonic Wind Tunnel

The 1.5 mm 5 hole probe was calibrated in the DERA Bedford 0.1016 m (4") subsonic wind tunnel. This facility is an open return facility that is driven using two vacuum pumps located downstream. The inlet to the tunnel is through a circular cross-section bell-mouth intake that feeds a settling chamber containing anti-turbulence screens. After a 40:1 contraction ratio, the flow is passed though a 0.1016 m solid wall working section, after which it is passed to the Hot-Wire Calibration Rig (HWCR).

The HWCR is a plenum-chamber-enclosed jet/collector arrangement that is surrounded outside the jet area by a gimbal mount system which allows a probe to be inserted into the jet flow, and simultaneously pitched and yawed with the probe tip held at a single point in the flow. The angular motion is automated using stepper motors, and pressure tubing can be fed though the wall of the plenum.

Downstream of the HWCR is a stepper motor controlled 2-dimensional variable throat that controls the tunnel Mach number. The flow is then ejected through a series of open/closed safety valves to the vacuum pumps. Sufficient suction can be provided by the vacuum pumps to run the wind tunnel in a continuous mode.

Instrumentation

The instrumentation for the probe calibration consisted of the equipment needed to move the traverse to the correct positions, and the equipment needed to read the pressure instrumentation.

The stepper motors controllers were Parker Hannifin Digiplan AT6400 personal computer controlled devices driving Digiplan PDS15-2 drives. This product allowed the easy control of the system through a set of Visual Basic libraries that could be used to construct a control program. The HWCR was controlled such that a sweep in yaw was carried out at a given pitch angle. Once the sweep was finished, the probe was traversed back through the entire yaw range, and a new pitch angle was selected. Using this method, the effect of any backlash in the system was minimised.

The pressures were sampled using 7 Digiquartz 20-psi differential digital output pressure transducers (Serial Numbers: 33885, 32451, 34012, 33887, 32450, 33874, and 32442). These devices are pressure transducers which, when interrogated via an RS232 interface, output a digital format of the pressure converted to a user defined unit. The devices can be programmed to average the pressure samples from a selectable frequency and sample time. During their use, it was determined that a sample time of 0.5 seconds gave a good reading, once the input pressure had stabilised. Tests showed that a settling time of about 10 seconds was needed. Increases in sample time gave no significant increase in accuracy. The devices gave an accuracy of 0.0007% of the full-scale deflection, equivalent to 0.94 Pa. The reference port of the transducers were left open to the atmosphere, and the atmospheric pressure was sampled using a further Digiquartz transducer located in the tunnel control system.

Control software was written using Microsoft Visual Basic. This software allowed the control of the stepper motor system (as mentioned above) and the interrogation of the transducers, with the subsequent storage to disk of the pressure data and probe angular position. Pressure which were sampled were:

- Tunnel total pressure (measured in the tunnel settling chamber - calibration had shown this to be the same as the total pressure in the HWCR)
- HWCR Static pressure (taken as the average of four wall static pressures in the streamwise plane of the probe tip)
- The 5 probe tube pressures.

Calibration Parameters

Calibrations were carried out over the following angles:

Pitch	-25°	-20°	-15°	-12°	-9°	-6°	-3°	0°	3°	6°	9°	12°	15°	20°	25°
Yaw	-25°	-20°	-15°	-12°	-9°	-6°	-3°	0°	3°	6°	9°	12°	15°	20°	25°

Table A-1: Probe Calibration Angles

These angles were chosen to give as fine a calibration over the region where the probe would be expected to be used (i.e. ±15° pitch and yaw) while keeping the run time sufficiently low. The maximum angles were set by the travel of the HWCR.

Calibration Mach numbers were set using the tunnel working section Mach number as the desired Mach number as follows:

Mach Number	0.2	0.3	0.4	0.5	0.6	0.7

Table A-2: Tunnel Working Section Mach Numbers

A calibration of the HWCR had previously been carried out which allowed a correction to the working section Mach number to be applied in order to find the HWCR Mach number. The correction is in the form of a polynomial, as follows:

$$\left(M_{HWCR} - M_{W/S}\right) = 0.1129 M_{W/S}^{\ 4} - 0.0751 M_{W/S}^{\ 3} + 0.0253 M_{W/S}^{\ 2} + 0.0178 M_{W/S} \qquad \textit{Equation 82}$$

Where M_{HWCR} is the Mach number in the HWCR, and $M_{W/S}$ is the Mach number in the working section. Thus, for the working section Mach numbers above, the Mach numbers in the HWCR were as follows:

M_{HWCR}	0.20415	0.30650	0.40925	0.51289	0.61819	0.72620

Table A-3: HWCR Mach Number (corrected from working section Mach numbers)

Results

The derived pressure coefficient values are listed in Table 19 to Table 42. The derived data is plotted below for each Mach number in terms of Cp_{pitch}, Cp_{yaw}, Cp_5 and Cp_{avg} with respect to the pitch and yaw angles (Figure 94 to Figure 122)

Tests were carried out to ensure that the repeatability of the results was sufficient at the high and low Mach numbers. However, that data is not displayed here.

Comparison of the graphs thought the Mach number range reveals that the differences in the results with Mach number are small. Further, it may be seen that the number of data points is sufficient to allow accurate interpolation of the data, since the results can be easily linearised.

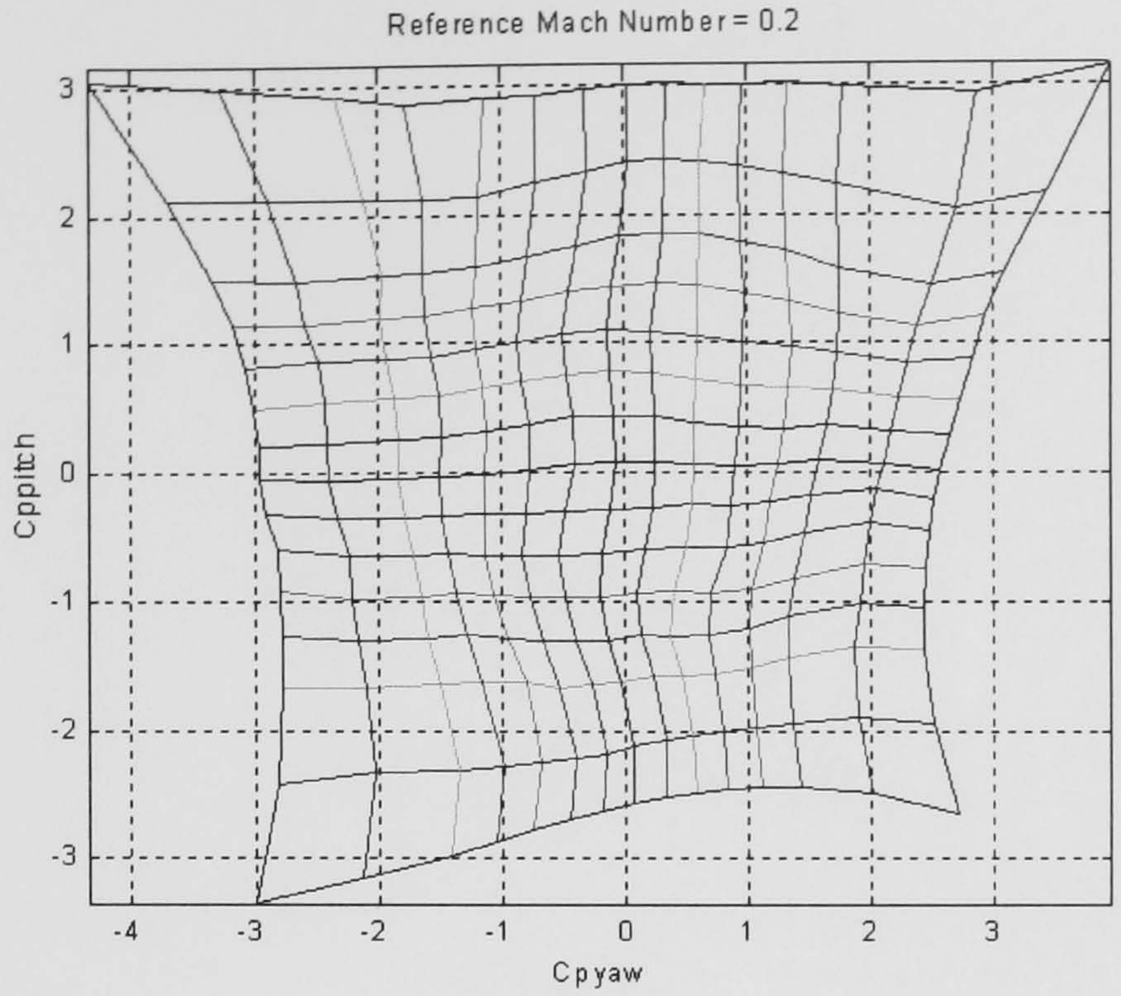

Figure 94: Cppitch vs. Cpyaw

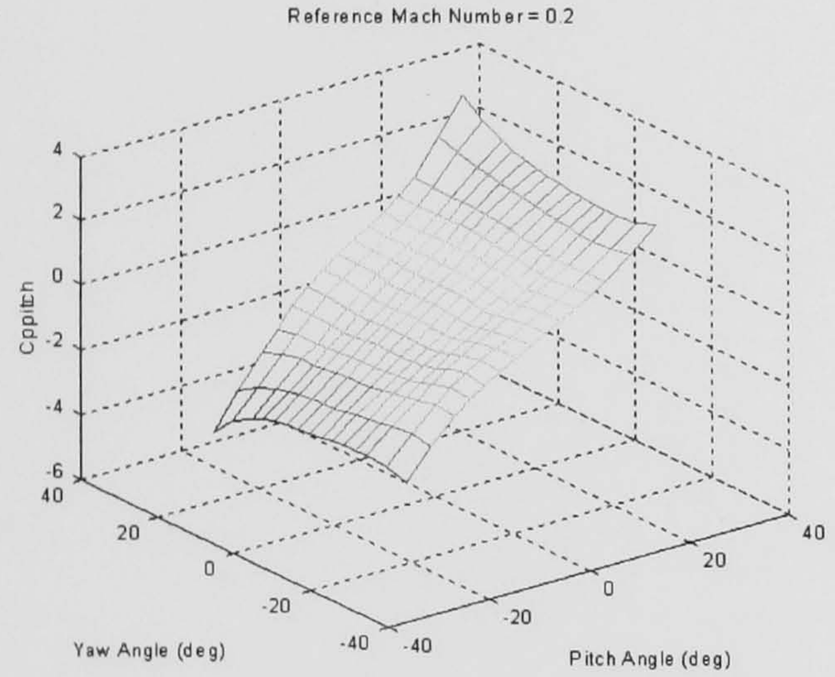

Figure 95: Cppitch vs. Pitch and Yaw

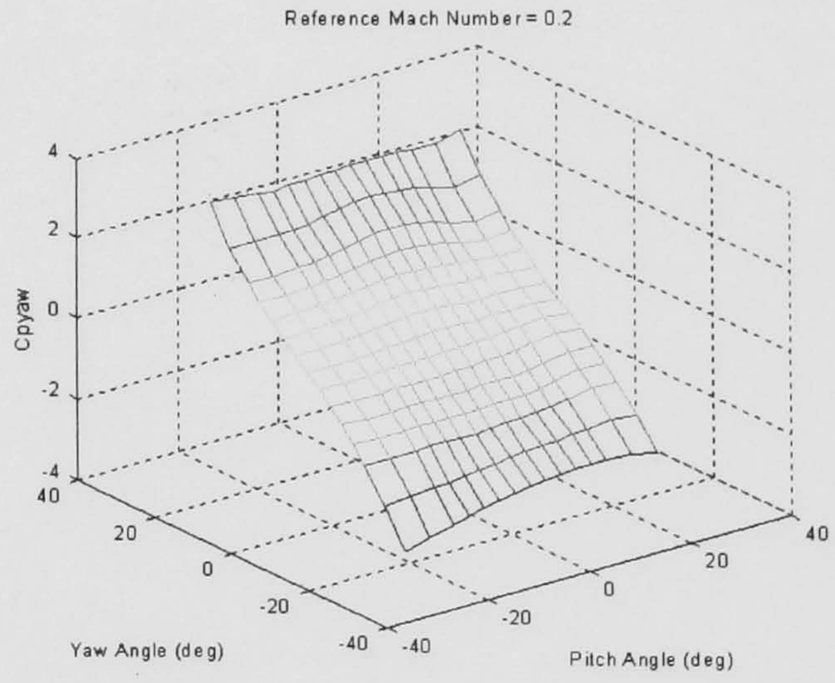

Figure 96: Cpyaw vs. Pitch and Yaw

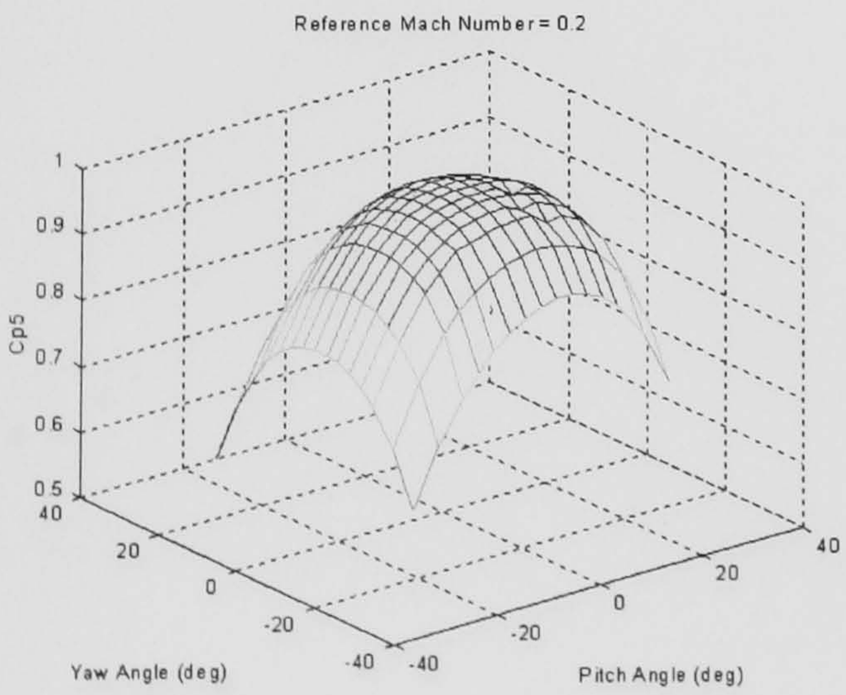

Figure 97: Cp5 vs. Pitch and Yaw

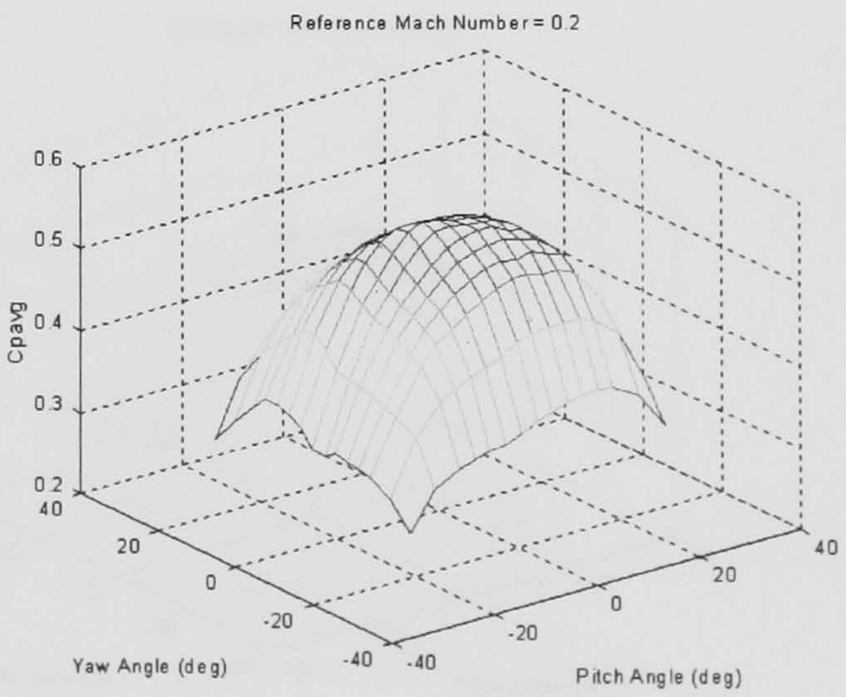

Figure 98: Cpavg vs. Pitch and Yaw

Derived Coefficients - Mach 0.307

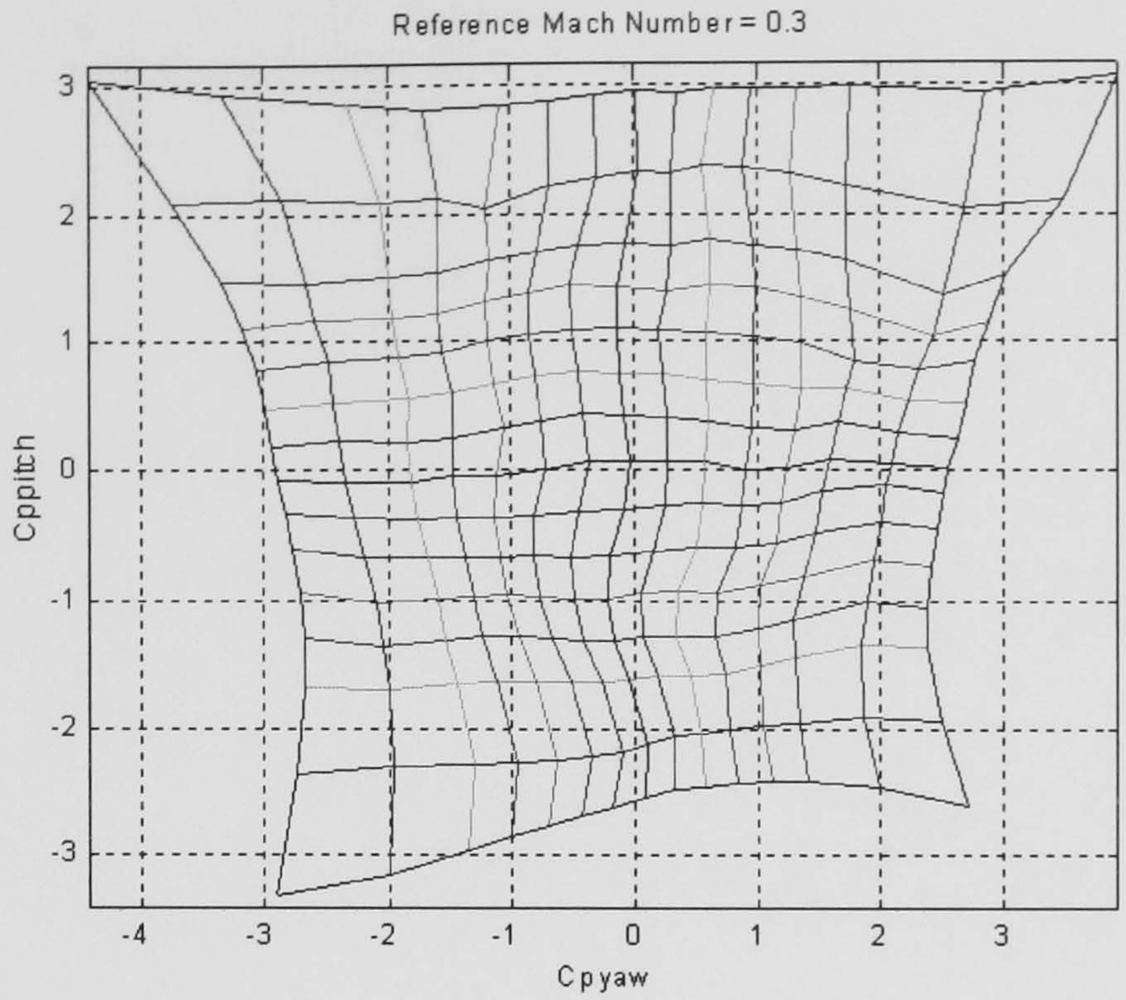

Figure 99: Cppitch vs. Cpyaw

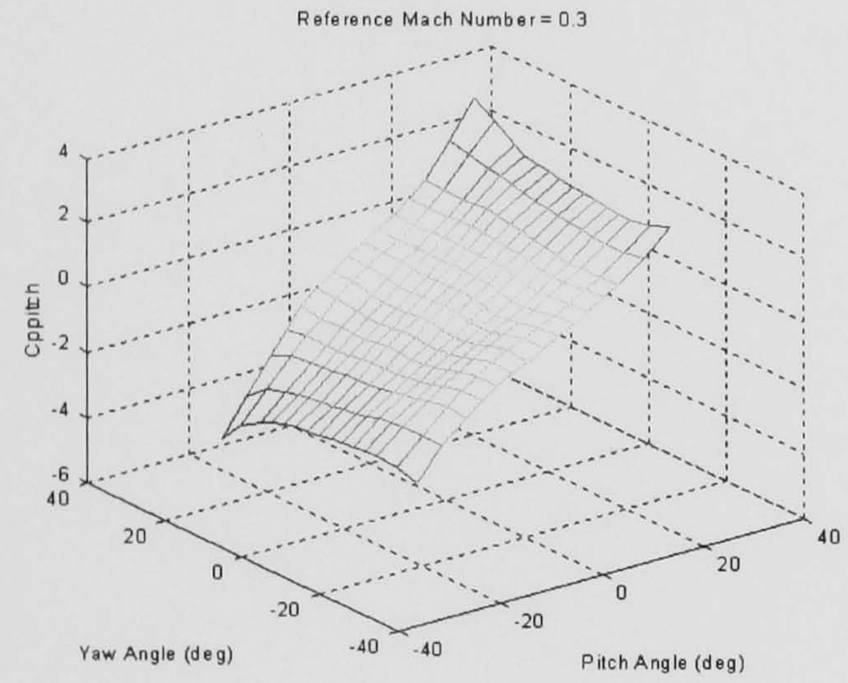

Figure 100: Cppitch vs. Pitch and Yaw

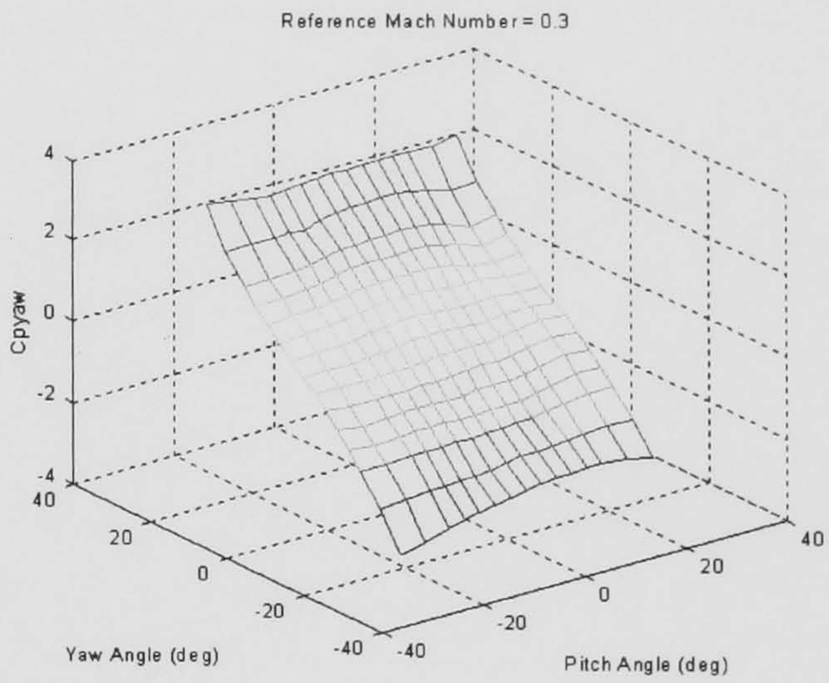

Figure 101: Cpyaw vs. Pitch and Yaw

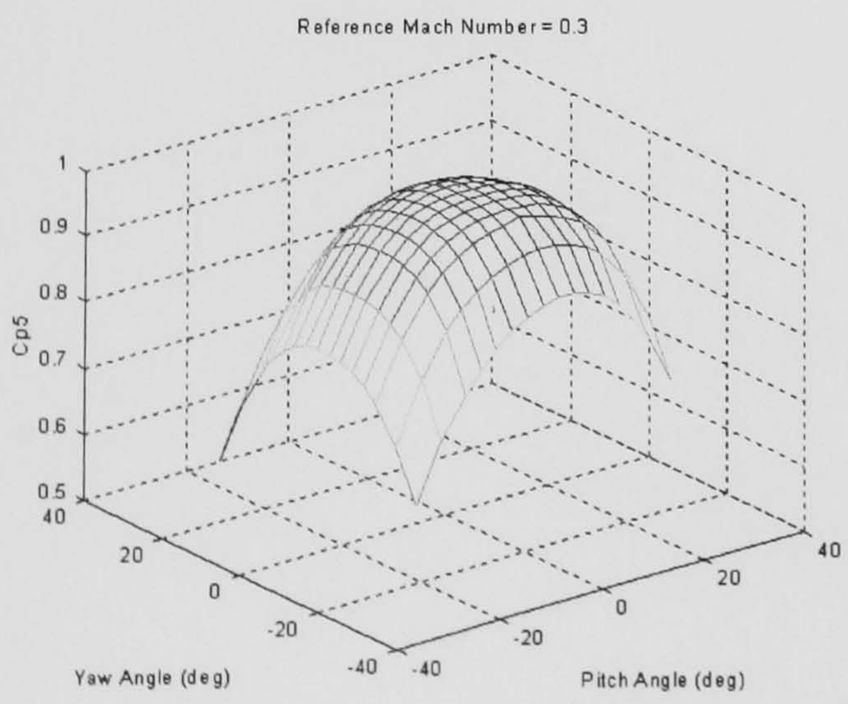

Figure 102: Cp5 vs. Pitch and Yaw

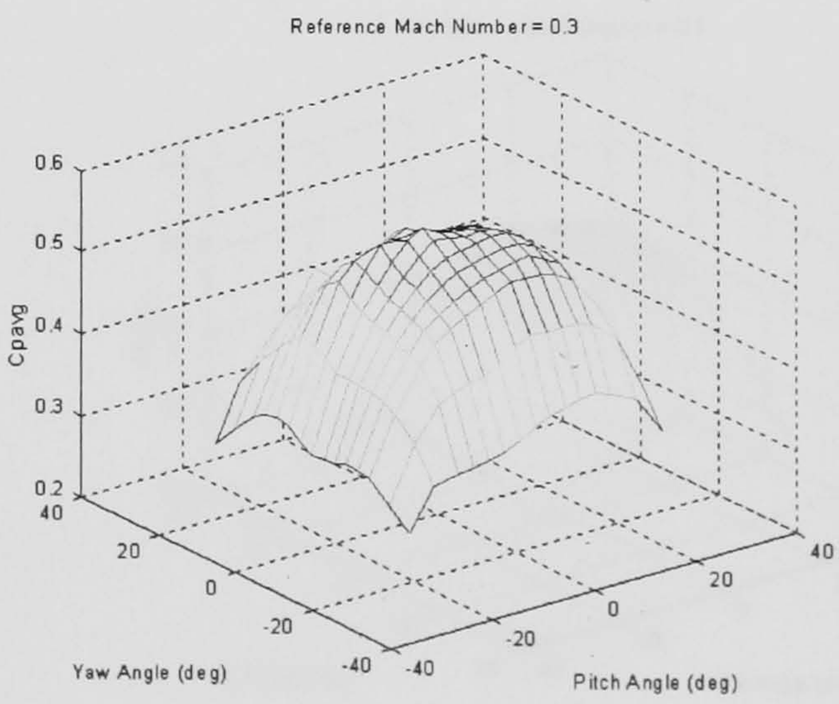

Figure 103: Cpavg vs. Pitch and Yaw

Derived Coefficients - Mach 0.409

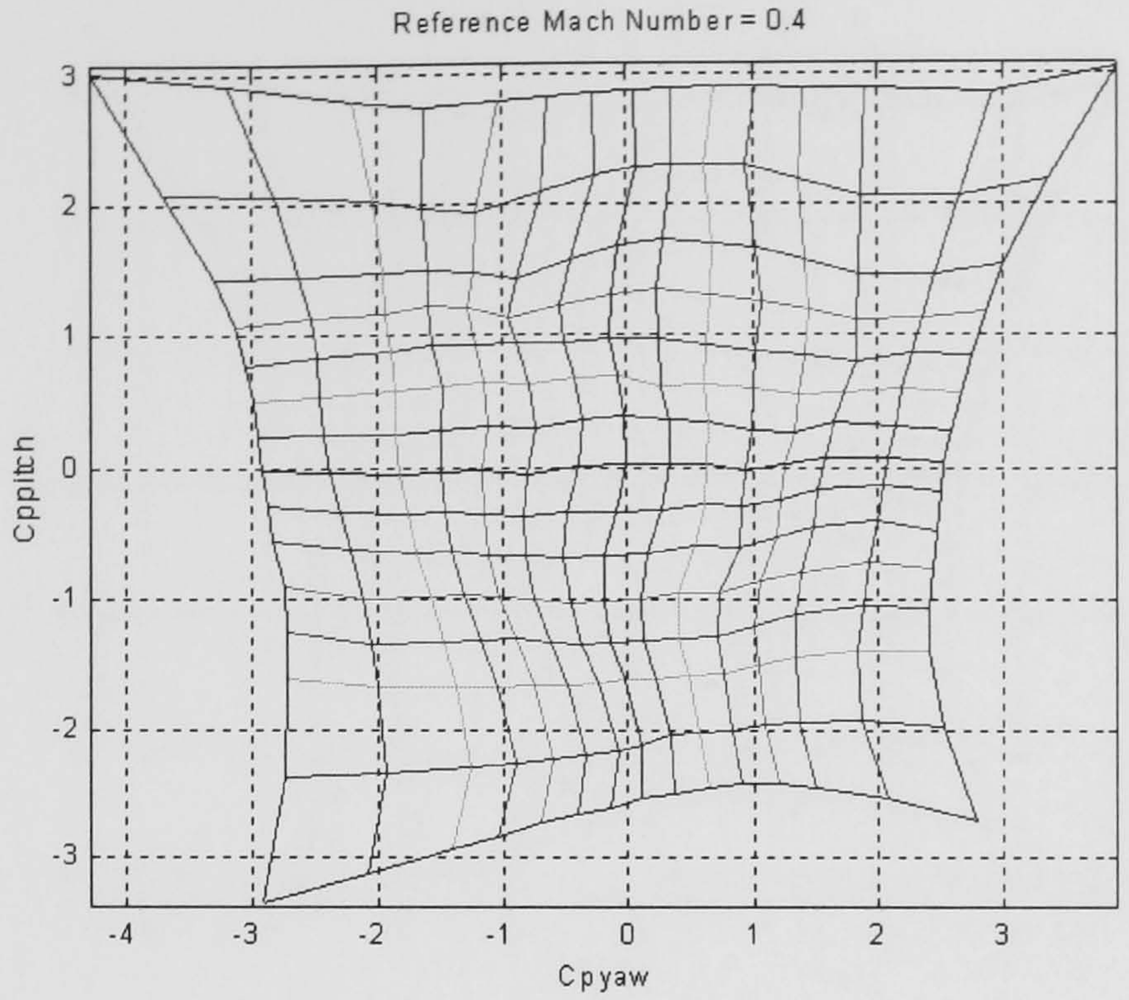

Figure 104: Cppitch vs. Cpyaw

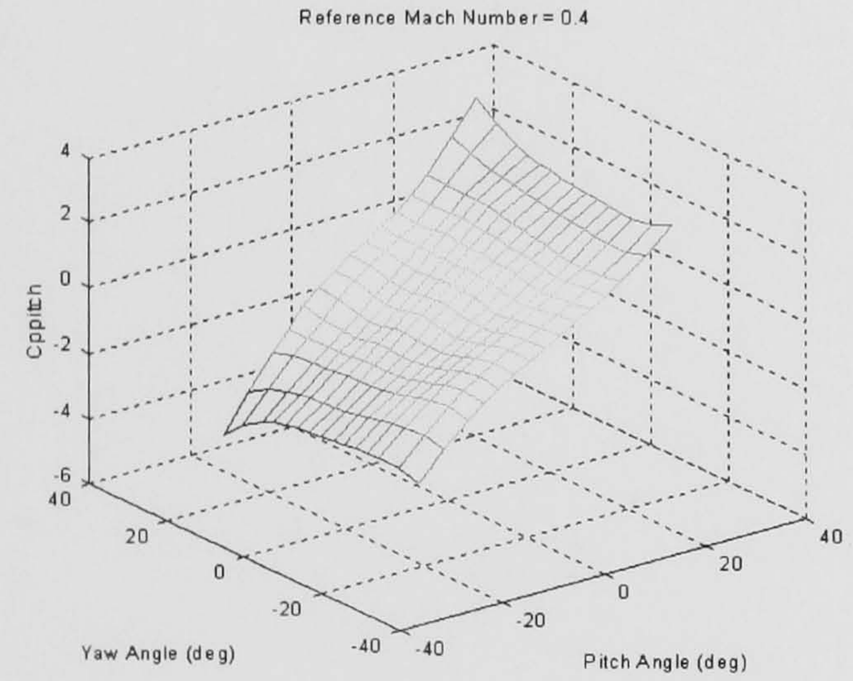

Figure 105: Cppitch vs. Pitch and Yaw

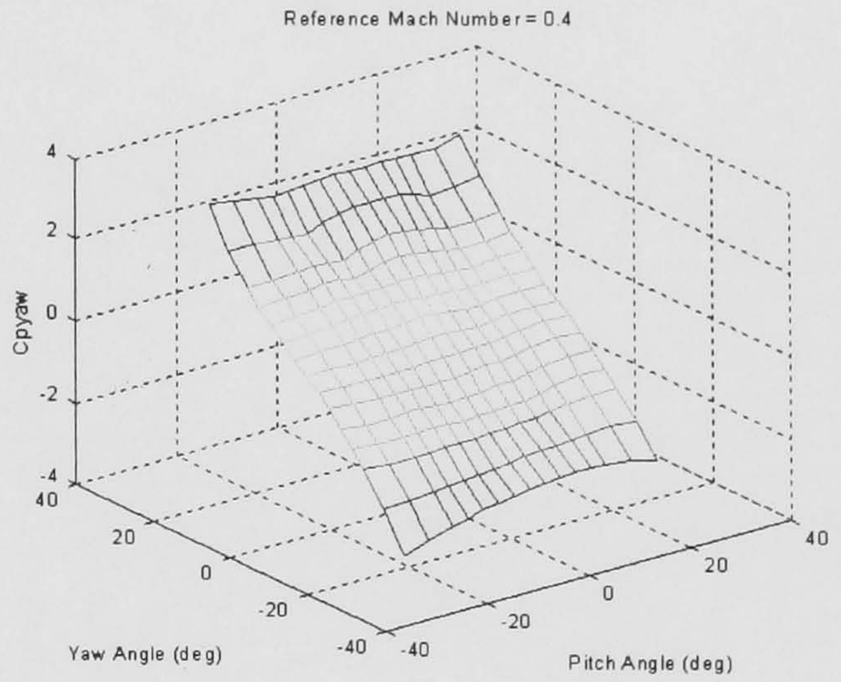

Figure 106: Cpyaw vs. Pitch and Yaw

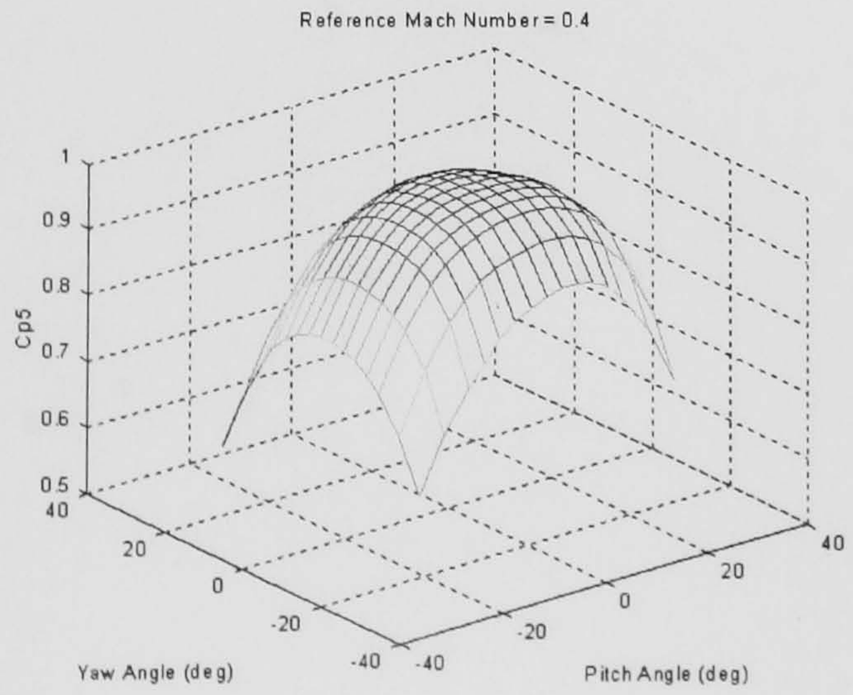

Figure 107: Cp5 vs. Pitch and Yaw

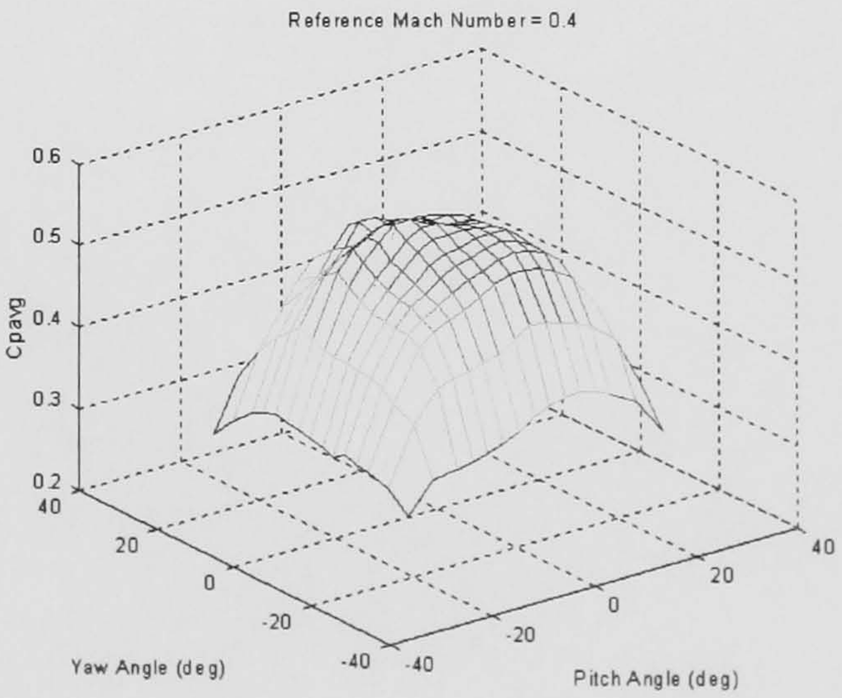

Figure 108: Cpavg vs. Pitch and Yaw

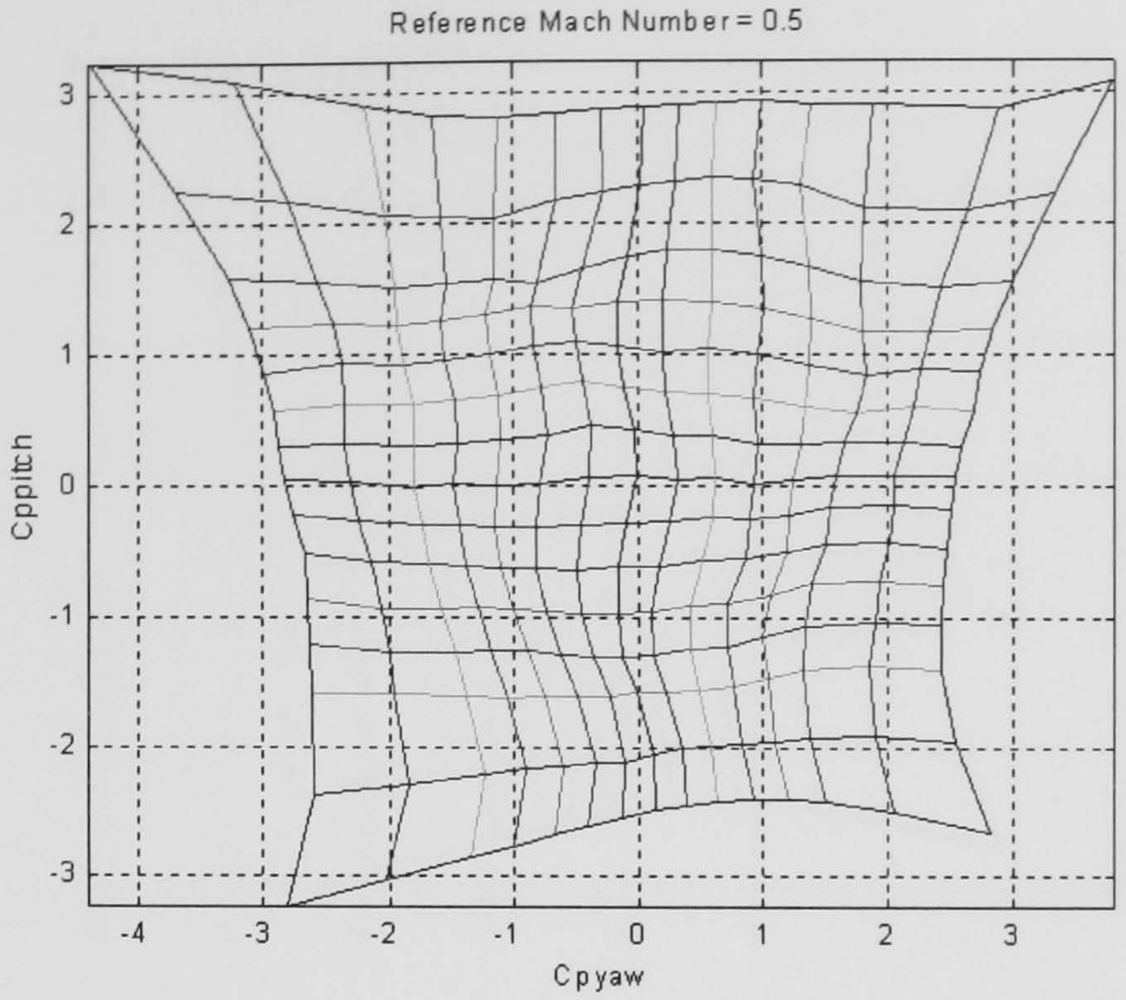

Figure 109: Cppitch vs. Cpyaw

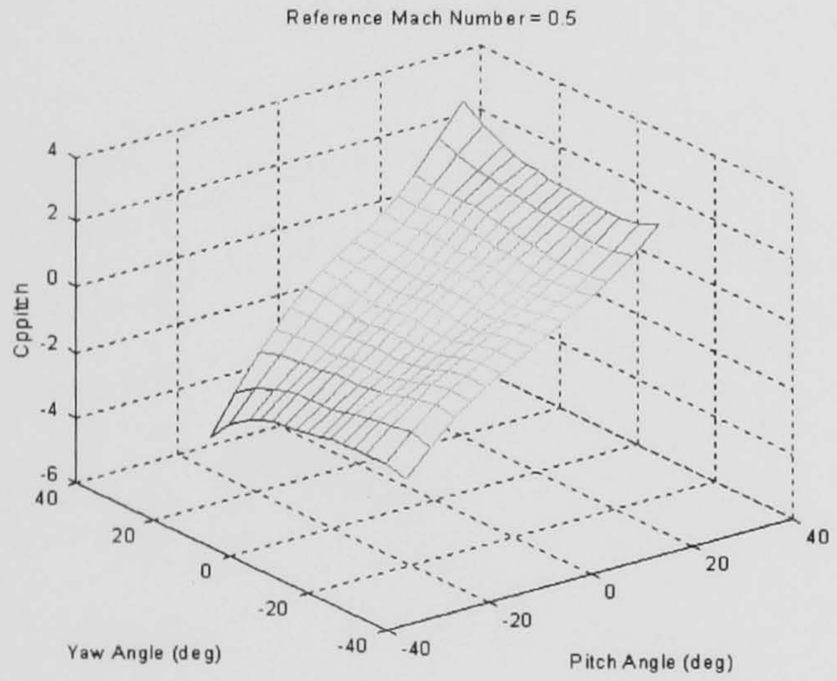

Figure 110: Cppitch vs. Pitch and Yaw

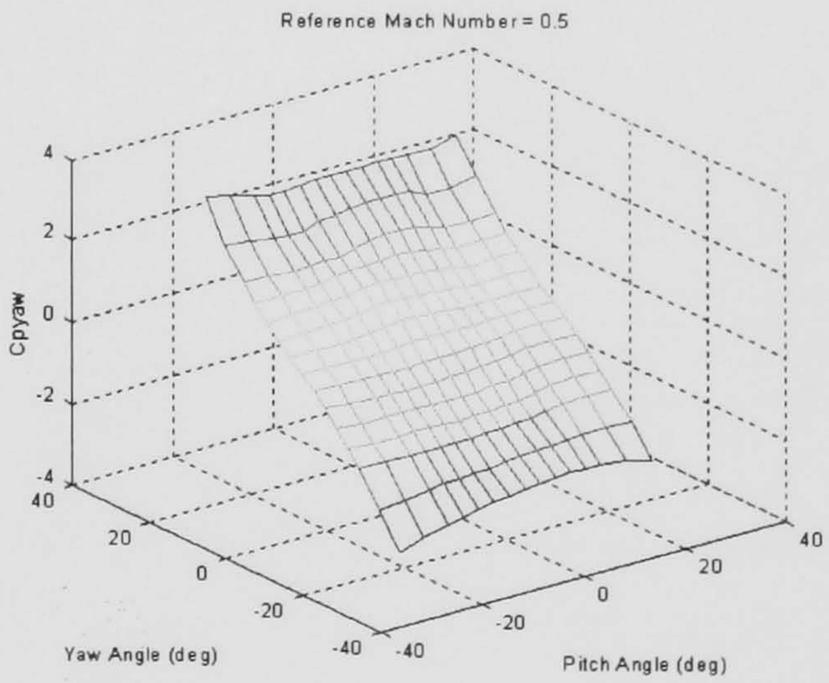

Figure 111: Cpyaw vs. Pitch and Yaw

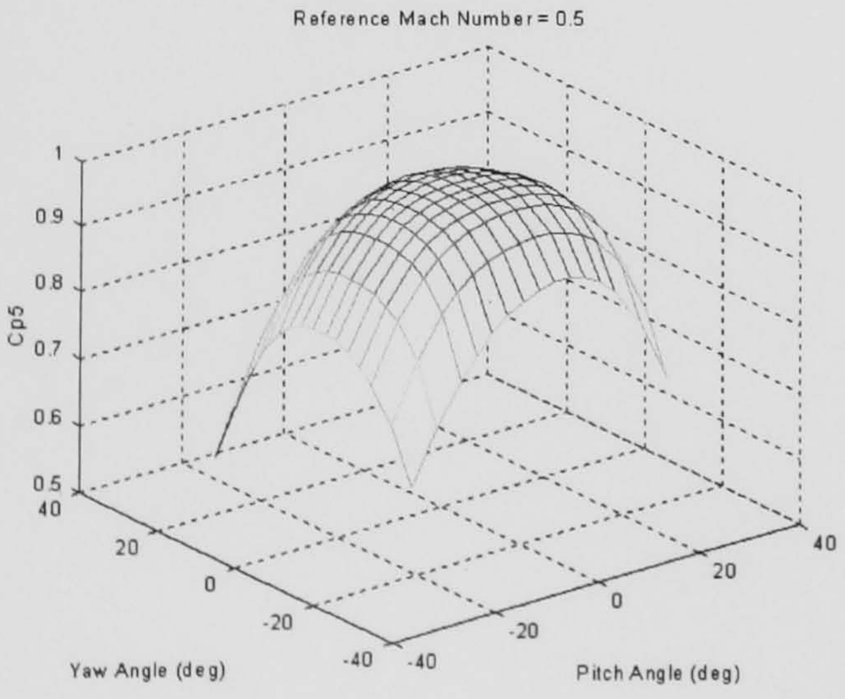

Figure 112: Cp5 vs. Pitch and Yaw

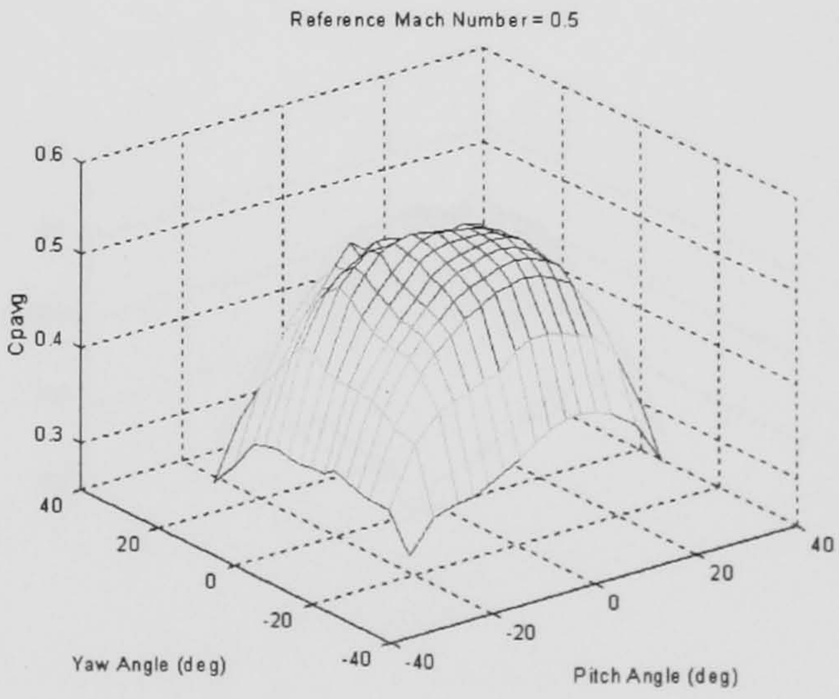

Figure 113: Cpavg vs. Pitch and Yaw

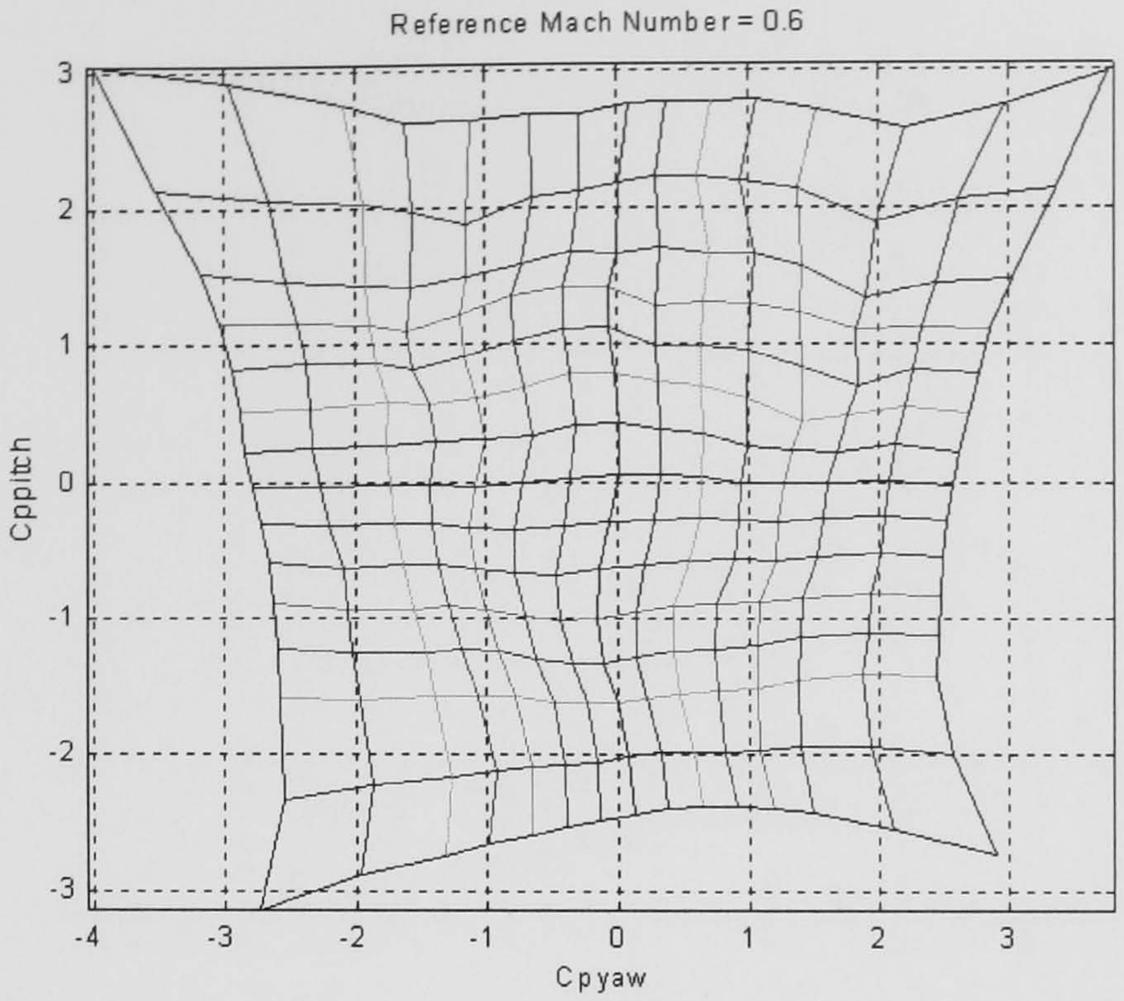

Figure 114: Cppitch vs. Cpyaw

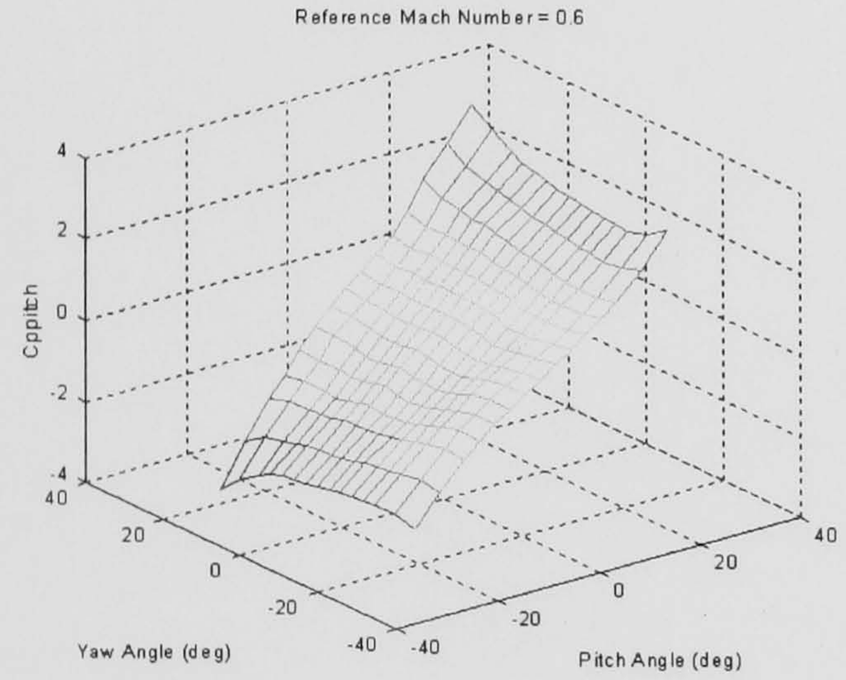

Figure 115: Cppitch vs. Pitch and Yaw

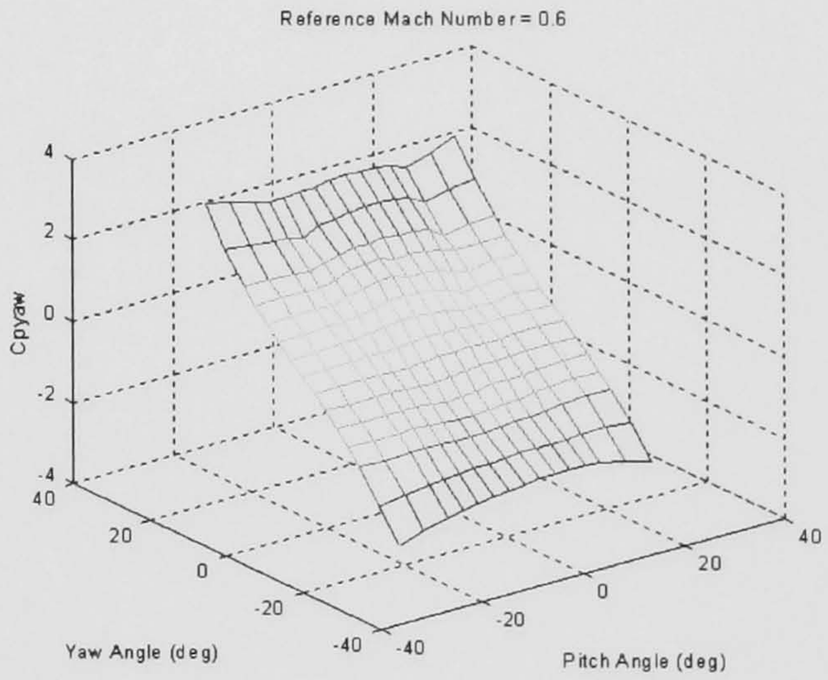

Figure 116: Cpyaw vs. Pitch and Yaw

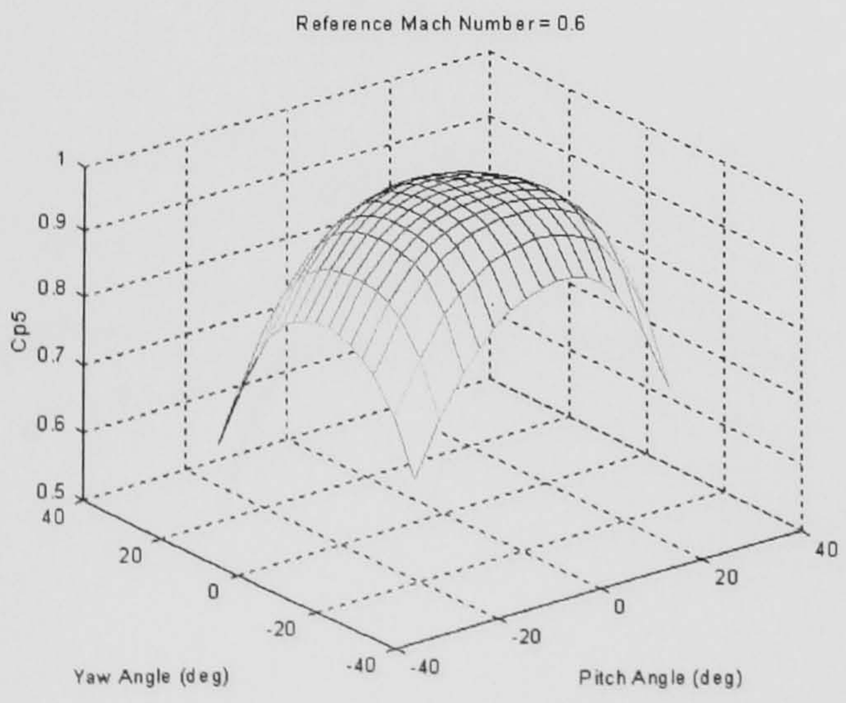

Figure 117: Cp5 vs. Pitch and Yaw

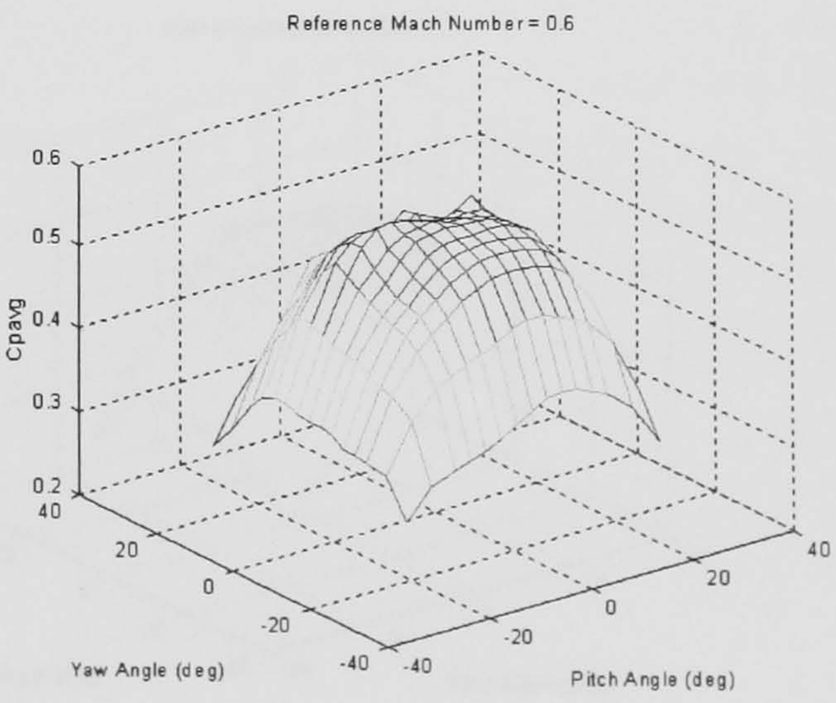

Figure 118: Cpavg vs. Pitch and Yaw

Derived Coefficients - Mach 0.726

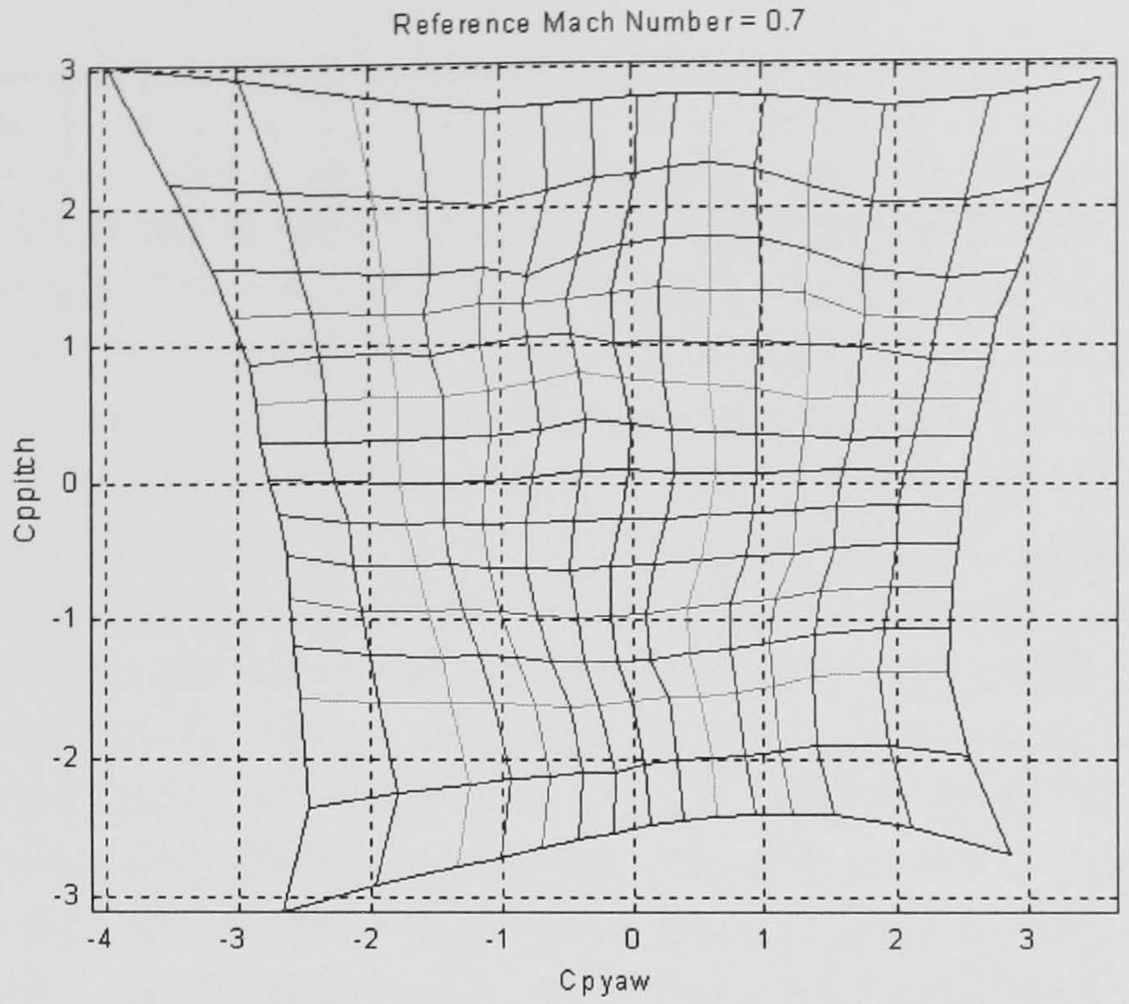

Figure 119: Cppitch vs. Cpyaw

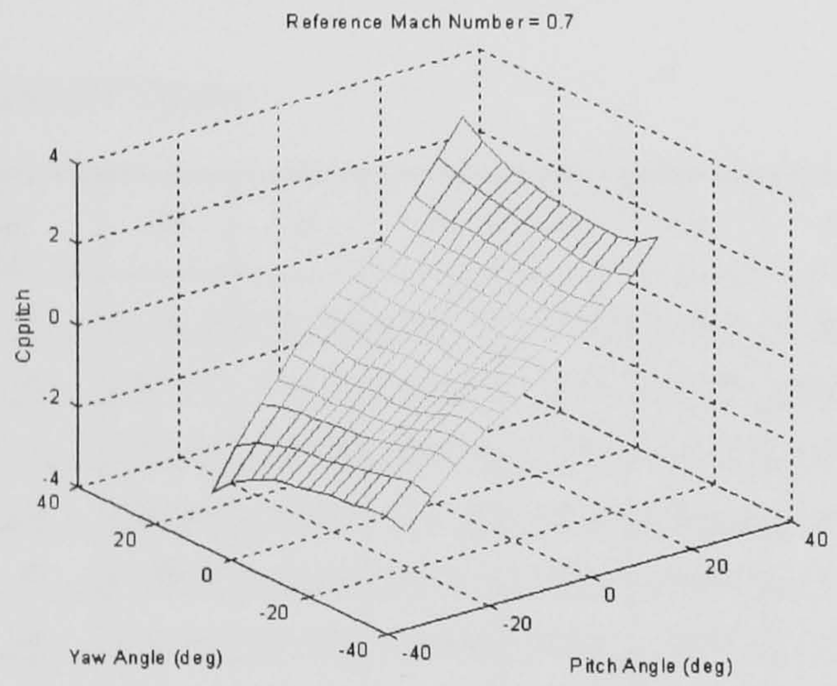

Figure 120: Cppitch vs. Pitch and Yaw

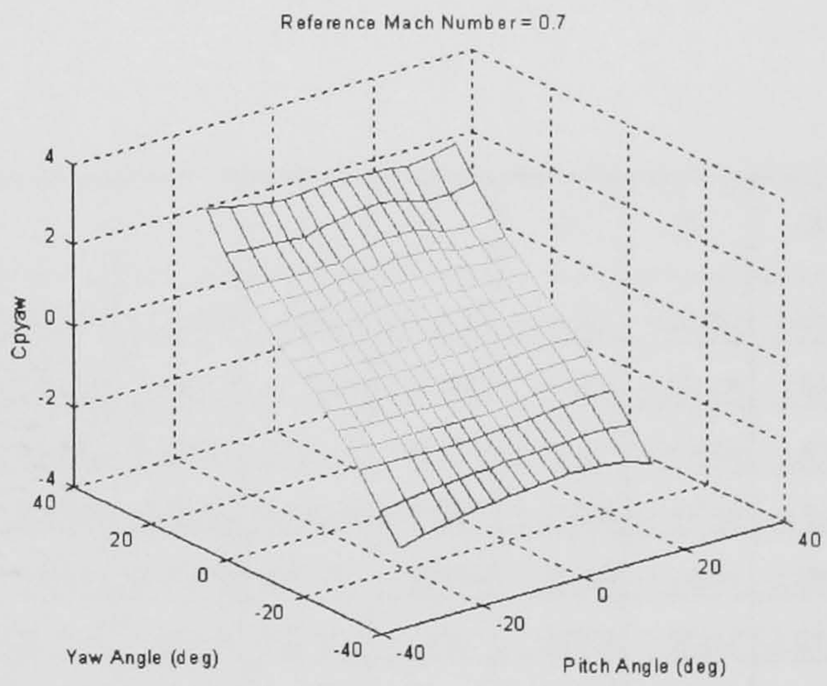

Figure 121: Cpyaw vs. Pitch and Yaw,

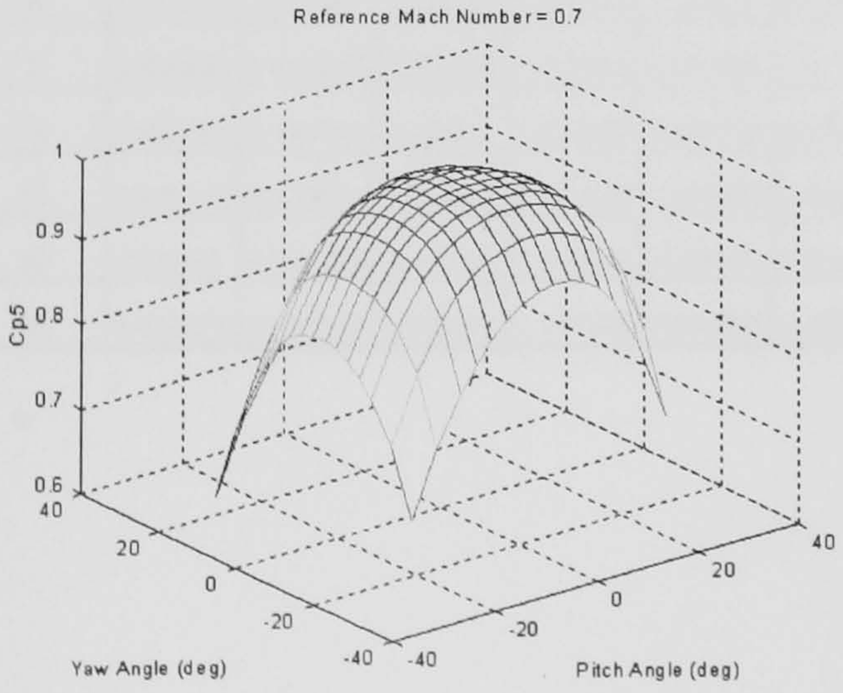

Figure 122: Cp5 vs. Pitch and Yaw

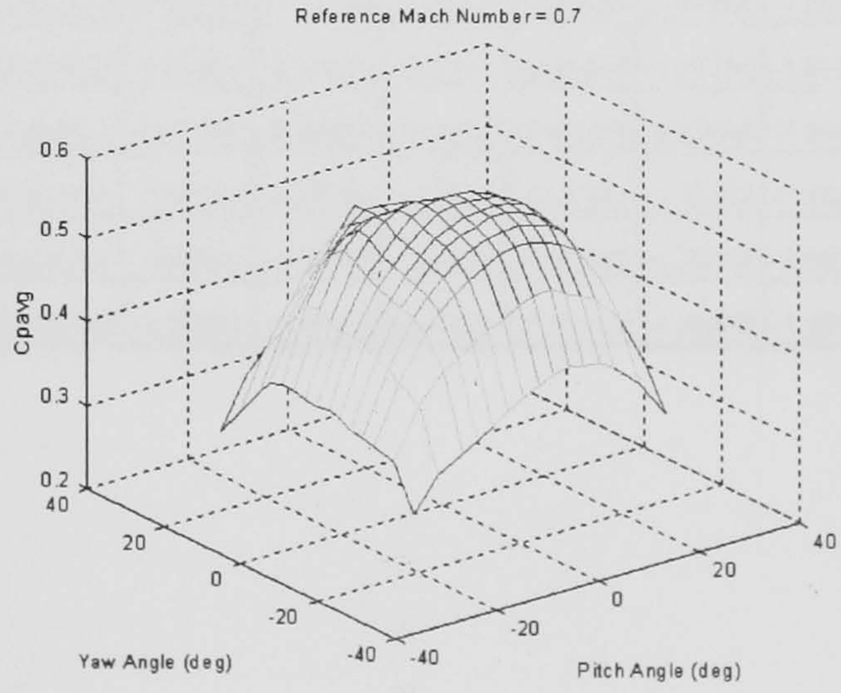

Figure 123: Cpavg vs. Pitch and Yaw

Data: M = 0.204

Table 19: Cppitch

Yaw Pitch	-25	-20	-15	-12	-9	-6	-3	0	3	6	9	12	15	20	25
-25	3.933913	3.424991	3.075766	2.937146	2.821745	2.730263	2.646126	2.569377	2.507186	2.471289	2.431988	2.41772	2.428465	2.508898	2.715395
-20	2.860786	2.686876	2.484249	2.373581	2.289541	2.229617	2.167382	2.100119	2.043169	1.999713	1.943502	1.913351	1.868564	1.897418	2.01484
-15	1.777781	1.731195	1.736157	1.740929	1.726313	1.698411	1.649102	1.585191	1.515185	1.471651	1.37237	1.325902	1.333555	1.36414	1.426758
-12	1.323708	1.288269	1.306193	1.336331	1.360098	1.33041	1.28928	1.240478	1.180851	1.134697	1.028392	1.003484	1.022008	1.074616	1.116836
-9	0.963205	0.921353	0.941754	0.971645	0.967352	0.947947	0.928125	0.901665	0.865745	0.830593	0.709996	0.678553	0.738597	0.79981	0.83256
-6	0.65722	0.605391	0.61423	0.600643	0.5882	0.574631	0.570206	0.561005	0.548498	0.505489	0.408108	0.364807	0.46189	0.548231	0.571163
-3	0.355969	0.330807	0.315018	0.259805	0.218052	0.232336	0.244315	0.245235	0.227784	0.163715	0.093783	0.128053	0.222096	0.318014	0.32311
0	0.037736	0.03023	-0.02496	-0.10168	-0.13452	-0.12409	-0.09299	-0.08045	-0.12292	-0.1911	-0.20698	-0.13609	-0.03242	0.076996	0.07674
3	-0.30931	-0.29879	-0.3833	-0.45214	-0.49898	-0.47167	-0.42622	-0.41512	-0.47959	-0.52764	-0.48823	-0.39302	-0.26793	-0.15212	-0.18765
6	-0.71343	-0.70664	-0.79081	-0.84299	-0.86617	-0.82958	-0.77351	-0.76104	-0.81038	-0.83729	-0.77286	-0.65615	-0.52758	-0.39717	-0.46038
9	-1.13865	-1.18211	-1.20826	-1.22865	-1.20516	-1.15845	-1.10405	-1.13179	-1.13996	-1.12095	-1.061	-0.95496	-0.80559	-0.67283	-0.74504
12	-1.77159	-1.63559	-1.64039	-1.615	-1.57444	-1.50947	-1.46878	-1.48725	-1.46781	-1.42431	-1.36763	-1.28947	-1.16716	-0.9784	-1.04805
15	-2.35518	-2.10337	-1.9713	-1.98	-1.93385	-1.85447	-1.8309	-1.82604	-1.78134	-1.70786	-1.64273	-1.59575	-1.49893	-1.34276	-1.41398
20	-3.27882	-2.89378	-2.67336	-2.58766	-2.47806	-2.43293	-2.40903	-2.39717	-2.33375	-2.24443	-2.20298	-2.15376	-2.09186	-2.02604	-2.13189
25	-4.33585	-3.71254	-3.34719	-3.17769	-3.07347	-3.01408	-2.97416	-2.95006	-2.90007	-2.80763	-2.78666	-2.77776	-2.77098	-2.80852	-3.00177

Table 20: Cpyaw

Yaw Pitch	-25	-20	-15	-12	-9	-6	-3	0	3	6	9	12	15	20	25
-25	3.136723	2.181232	1.534473	1.196298	0.86553	0.556322	0.278218	0.017479	-0.21138	-0.45001	-0.74268	-1.0438	-1.35728	-1.93488	-2.64015
-20	2.938712	2.04114	1.435537	1.12764	0.838357	0.563998	0.309012	0.062751	-0.12991	-0.39508	-0.70668	-1.01247	-1.33951	-1.8857	-2.48314
-15	2.990351	2.244158	1.575555	1.216445	0.921818	0.636307	0.355001	0.089566	-0.17564	-0.46354	-0.81001	-1.11031	-1.41699	-1.9317	-2.44504
-12	3.011914	2.321863	1.715289	1.316028	0.961663	0.640397	0.327132	0.055466	-0.22856	-0.54938	-0.89047	-1.20368	-1.49738	-1.9593	-2.44314
-9	3.008048	2.377156	1.792797	1.379354	1.000184	0.663379	0.336734	0.036134	-0.26342	-0.58147	-0.93578	-1.25388	-1.54316	-1.99626	-2.45521
-6	3.006868	2.414734	1.848628	1.435303	1.036296	0.702682	0.381591	0.061292	-0.25124	-0.57311	-0.9162	-1.26378	-1.56257	-2.02133	-2.48369
-3	3.013344	2.424279	1.852317	1.457099	1.077324	0.754427	0.420804	0.079079	-0.2707	-0.59807	-0.93175	-1.24623	-1.56861	-2.05073	-2.51823
0	3.003345	2.419669	1.841482	1.429784	1.087175	0.773451	0.425704	0.072839	-0.28803	-0.62389	-0.96537	-1.29599	-1.61141	-2.10146	-2.56268
3	2.961349	2.325531	1.7604	1.391546	1.053686	0.738153	0.41675	0.051234	-0.31535	-0.64597	-0.96189	-1.29816	-1.63387	-2.16428	-2.62971
6	2.913793	2.251967	1.668169	1.320865	1.00398	0.687017	0.352178	0.004434	-0.33175	-0.64573	-0.95686	-1.29369	-1.65518	-2.2057	-2.69969
9	2.899883	2.149213	1.591846	1.25962	0.953768	0.643455	0.316092	-0.01801	-0.33195	-0.6413	-0.94644	-1.27708	-1.61749	-2.24523	-2.77064
12	2.850253	2.125111	1.52933	1.198403	0.889755	0.583548	0.266941	-0.03169	-0.33808	-0.62005	-0.93269	-1.25358	-1.61652	-2.28344	-2.8644
15	2.921148	2.129643	1.523447	1.181649	0.868936	0.568051	0.247964	-0.05704	-0.36026	-0.6412	-0.96356	-1.27924	-1.62883	-2.30747	-2.98845
20	2.98155	2.123153	1.47517	1.146679	0.85041	0.535319	0.224297	-0.0646	-0.35462	-0.6485	-0.97142	-1.30186	-1.66109	-2.33123	-3.15288
25	3.056276	2.121318	1.484312	1.137629	0.800783	0.490729	0.207049	-0.05323	-0.32236	-0.59747	-0.91463	-1.26919	-1.65603	-2.4214	-3.33944

Table 21: Cp5

Yaw Pitch	-25	-20	-15	-12	-9	-6	-3	0	3	6	9	12	15	20	25
-25	0.609283	0.699807	0.766585	0.795148	0.818505	0.836004	0.850825	0.861564	0.867654	0.868167	0.866623	0.857955	0.841259	0.794994	0.71828
-20	0.695732	0.786807	0.84622	0.87208	0.892197	0.907533	0.919555	0.928603	0.933774	0.935177	0.933539	0.925696	0.91373	0.8757	0.802651
-15	0.749952	0.837272	0.898011	0.921051	0.939401	0.953201	0.96277	0.969784	0.974546	0.974562	0.971991	0.966916	0.955695	0.919658	0.854883
-12	0.770111	0.856466	0.914114	0.939473	0.957046	0.969285	0.978617	0.984628	0.987167	0.988088	0.98555	0.979511	0.969229	0.934966	0.874951
-9	0.782564	0.867505	0.925515	0.95176	0.96843	0.980272	0.988503	0.992566	0.994908	0.981339	0.992736	0.987237	0.964742	0.94526	0.885313
-6	0.789909	0.875456	0.932612	0.958059	0.974749	0.986451	0.99336	0.997064	0.998775	0.999417	0.996932	0.982404	0.982978	0.951851	0.891742
-3	0.791197	0.877262	0.936061	0.960182	0.977595	0.989629	0.996325	0.99857	0.999066	0.999563	0.998167	0.993663	0.98378	0.952382	0.892075
0	0.789368	0.874733	0.934102	0.959123	0.976788	0.988804	0.996022	0.997952	0.99886	0.998459	0.99756	0.991952	0.98157	0.948901	0.885414
3	0.784731	0.871665	0.92928	0.954278	0.972083	0.984718	0.991742	0.99531	0.996942	0.996337	0.994261	0.988045	0.97663	0.941263	0.875082
6	0.773151	0.862189	0.920857	0.945254	0.963937	0.977581	0.984911	0.989706	0.991228	0.990096	0.987973	0.980015	0.967862	0.92963	0.858164
9	0.759697	0.844819	0.90526	0.932335	0.952103	0.965973	0.973698	0.979311	0.98156	0.980739	0.976664	0.967678	0.963381	0.913543	0.838782
12	0.736037	0.826841	0.885445	0.913154	0.933891	0.948145	0.958928	0.962477	0.964078	0.963695	0.958978	0.95064	0.935719	0.892333	0.813097
15	0.706867	0.799401	0.86499	0.888655	0.908907	0.925244	0.935161	0.94045	0.942278	0.941241	0.93674	0.925543	0.911572	0.86352	0.779242
20	0.653377	0.741368	0.805052	0.832856	0.855165	0.871016	0.881065	0.884106	0.885945	0.884367	0.876243	0.864	0.848149	0.801941	0.718573
25	0.570336	0.659621	0.72373	0.754936	0.777165	0.792988	0.801348	0.80596	0.804819	0.804677	0.795887	0.781346	0.761584	0.709846	0.6302

Table 22: Cpavg

Yaw Pitch	-25	-20	-15	-12	-9	-6	-3	0	3	6	9	12	15	20	25
-25	0.305387	0.339162	0.359685	0.366687	0.368551	0.370856	0.376296	0.384268	0.389777	0.389657	0.390942	0.388488	0.382452	0.366417	0.320612
-20	0.361253	0.422461	0.445669	0.450592	0.449921	0.448954	0.454256	0.46164	0.469247	0.470558	0.47077	0.468184	0.463109	0.430703	0.365929
-15	0.348658	0.427373	0.480945	0.496828	0.502985	0.506962	0.512377	0.516854	0.520048	0.521633	0.519743	0.515045	0.499106	0.453044	0.383336
-12	0.340153	0.426085	0.480783	0.505744	0.518696	0.524532	0.531477	0.53395	0.536724	0.538087	0.532263	0.520765	0.508739	0.461204	0.387078
-9	0.339032	0.422453	0.483418	0.510081	0.52438	0.532419	0.539449	0.543178	0.547159	0.540838	0.53807	0.529788	0.508692	0.460219	0.385616
-6	0.336353	0.420916	0.483429	0.511243	0.526415	0.536045	0.543096	0.547894	0.549304	0.550797	0.542826	0.525322	0.514688	0.46101	0.381994
-3	0.332087	0.420394	0.48703	0.511833	0.526197	0.53374	0.544248	0.549878	0.552051	0.551581	0.541041	0.528391	0.513561	0.458673	0.375108
0	0.331049	0.424571	0.488469	0.514055	0.525348	0.534562	0.548526	0.555109	0.554942	0.548355	0.536474	0.523753	0.506643	0.453162	0.368964
3	0.342104	0.448555	0.490971	0.512992	0.524629	0.53732	0.551014	0.559386	0.554057	0.540976	0.52968	0.515077	0.497382	0.440862	0.357956
6	0.359995	0.448987	0.488306	0.507934	0.520645	0.534065	0.548546	0.552134	0.540447	0.52563	0.515183	0.503837	0.484775	0.433185	0.350363
9	0.375891	0.45985	0.483699	0.49912	0.51545	0.528368	0.538159	0.530573	0.51939	0.507138	0.498195	0.488544	0.472381	0.427063	0.348294
12	0.394558	0.444684	0.471191	0.488381	0.504608	0.517014	0.518712	0.505329	0.495376	0.487311	0.479993	0.470722	0.460875	0.417881	0.343172
15	0.379884	0.423657	0.458724	0.472307	0.483824	0.494968	0.49077	0.479942	0.470827	0.463718	0.458029	0.445529	0.438215	0.406236	0.335491
20	0.342483	0.380991	0.40874	0.421367	0.438097	0.438971	0.426313	0.408936	0.402583	0.402993	0.396739	0.389817	0.385262	0.37192	0.320241
25	0.275034	0.308797	0.339077	0.353848	0.355241	0.349594	0.339566	0.321179	0.317811	0.328345	0.324576	0.32232	0.318817	0.30496	0.274162

Data: M = 0.307

Table 23: Cppitch

Yaw Pitch	-25	-20	-15	-12	-9	-6	-3	0	3	6	9	12	15	20	25
-25	3.919692	3.487496	3.026264	2.875598	2.773915	2.704345	2.632891	2.557807	2.511294	2.464448	2.420129	2.380042	2.385278	2.495495	2.717596
-20	2.841109	2.680559	2.528502	2.431467	2.321419	2.243236	2.161266	2.098703	2.051721	2.009036	1.945443	1.89306	1.856376	1.869879	1.988674
-15	1.774839	1.729413	1.7307	1.747731	1.810954	1.727196	1.662698	1.592182	1.526159	1.483655	1.371405	1.296433	1.31285	1.336548	1.417527
-12	1.323778	1.282449	1.329419	1.354797	1.360904	1.346951	1.304495	1.24355	1.195055	1.154595	1.020982	0.994339	1.022009	1.0564	1.122561
-9	0.949591	0.888849	0.968296	0.987205	0.962743	0.96558	0.946416	0.902859	0.874045	0.832984	0.687852	0.661634	0.742822	0.776558	0.834366
-6	0.653607	0.559819	0.623627	0.620676	0.577222	0.59161	0.602379	0.575347	0.554317	0.497851	0.356318	0.349456	0.448698	0.5342	0.568653
-3	0.360316	0.314402	0.311887	0.259431	0.20632	0.228651	0.262433	0.261049	0.243453	0.14615	0.053054	0.071763	0.180924	0.321021	0.321689
0	0.029078	0.036345	-0.06394	-0.13459	-0.14471	-0.11426	-0.06748	-0.02879	-0.0878	-0.20267	-0.21822	-0.17165	-0.04005	0.100192	0.080598
3	-0.32055	-0.29588	-0.44334	-0.51398	-0.50162	-0.46215	-0.40681	-0.36441	-0.46198	-0.51873	-0.48279	-0.41069	-0.26312	-0.10404	-0.17754
6	-0.67933	-0.68823	-0.78531	-0.85333	-0.86629	-0.80132	-0.7449	-0.72221	-0.80776	-0.80938	-0.75726	-0.66968	-0.52584	-0.35085	-0.42989
9	-1.07988	-1.21929	-1.16566	-1.21021	-1.19382	-1.12487	-1.0478	-1.11012	-1.12621	-1.09073	-1.03562	-0.93397	-0.80231	-0.64117	-0.69444
12	-1.70396	-1.5896	-1.60112	-1.6002	-1.5528	-1.47095	-1.46098	-1.46477	-1.43896	-1.37778	-1.31072	-1.23653	-1.11721	-0.95192	-1.00022
15	-2.34051	-2.06573	-1.98974	-1.96036	-1.90032	-1.82645	-1.83567	-1.79779	-1.7494	-1.6738	-1.60426	-1.53276	-1.43491	-1.30867	-1.36306
20	-3.35241	-2.87131	-2.65946	-2.58526	-2.48609	-2.44805	-2.40454	-2.34446	-2.27308	-2.18434	-2.09442	-2.04649	-2.00276	-1.9644	-2.00542
25	-4.41812	-3.7492	-3.35151	-3.18882	-3.07658	-2.99827	-2.9484	-2.89816	-2.8333	-2.78143	-2.72151	-2.68723	-2.68233	-2.74399	-2.90741

Table 24: Cpyaw

Yaw Pitch	-25	-20	-15	-12	-9	-6	-3	0	3	6	9	12	15	20	25
-25	3.061887	2.104351	1.50927	1.147665	0.831713	0.52034	0.251744	0.017786	-0.17073	-0.44885	-0.73743	-1.04871	-1.36568	-1.94176	-2.61323
-20	2.945465	2.036843	1.347287	1.028107	0.773436	0.539291	0.290418	0.058359	-0.10996	-0.39025	-0.69154	-1.01395	-1.34119	-1.90382	-2.47376
-15	2.994527	2.219692	1.617543	1.243644	0.839426	0.628258	0.368519	0.082038	-0.16207	-0.47266	-0.80826	-1.15402	-1.44471	-1.94606	-2.42174
-12	2.974657	2.309656	1.700235	1.337704	0.980425	0.632925	0.313597	0.018398	-0.25126	-0.55587	-0.88353	-1.20745	-1.50714	-1.96526	-2.41818
-9	2.972136	2.36262	1.750526	1.414631	1.022647	0.66064	0.324775	0.006998	-0.27543	-0.59189	-0.94006	-1.27488	-1.56949	-2.00731	-2.43934
-6	2.977452	2.372509	1.795312	1.426551	1.056156	0.700452	0.374044	0.064339	-0.25396	-0.58863	-0.93097	-1.27296	-1.58445	-2.03544	-2.46503
-3	2.942169	2.316516	1.750454	1.387704	1.074971	0.743451	0.399694	0.070653	-0.27008	-0.61572	-0.94572	-1.28465	-1.59165	-2.04173	-2.47749
0	2.947492	2.328643	1.76515	1.409692	1.088269	0.747708	0.420556	0.07082	-0.29421	-0.65884	-0.99692	-1.31237	-1.61756	-2.10961	-2.55156
3	2.918196	2.280359	1.730535	1.424516	1.08256	0.761195	0.431283	0.07508	-0.31365	-0.67265	-0.99267	-1.31346	-1.62965	-2.17911	-2.62221
6	2.879801	2.215357	1.695362	1.373855	1.049932	0.720857	0.372687	0.009335	-0.34121	-0.65951	-0.96688	-1.29307	-1.62516	-2.21547	-2.68894
9	2.838219	2.03759	1.626882	1.305754	1.003698	0.664078	0.320786	-0.0368	-0.36366	-0.66963	-0.96261	-1.28672	-1.63066	-2.2364	-2.76349
12	2.817062	2.114479	1.535345	1.203106	0.904232	0.598887	0.250181	-0.04993	-0.36431	-0.67722	-0.97641	-1.27477	-1.62963	-2.25245	-2.85878
15	2.853095	2.081732	1.498972	1.177454	0.87363	0.556126	0.205402	-0.09473	-0.37923	-0.6758	-0.99593	-1.3092	-1.65275	-2.26815	-2.96239
20	2.94531	2.116009	1.451446	1.154296	0.840484	0.521636	0.220428	-0.08685	-0.3726	-0.66491	-1.02189	-1.35592	-1.69	-2.30707	-3.15005
25	3.052802	2.087035	1.470654	1.099403	0.777462	0.473924	0.183291	-0.08241	-0.33962	-0.60431	-0.9391	-1.29344	-1.68516	-2.37451	-3.31097

Table 25: Cp5

Yaw Pitch	-25	-20	-15	-12	-9	-6	-3	0	3	6	9	12	15	20	25
-25	0.615125	0.701832	0.771772	0.80419	0.827387	0.843516	0.856056	0.865172	0.868153	0.870699	0.869144	0.862551	0.84652	0.79857	0.721741
-20	0.697783	0.789216	0.850683	0.876613	0.895926	0.911348	0.923405	0.931239	0.93507	0.936472	0.935691	0.929941	0.916509	0.879052	0.808064
-15	0.751715	0.843049	0.898973	0.92286	0.941772	0.954674	0.964205	0.971106	0.974591	0.975705	0.973385	0.967552	0.957065	0.923203	0.858723
-12	0.772829	0.860783	0.917432	0.941404	0.958321	0.971353	0.9798	0.984776	0.987805	0.988432	0.986292	0.980839	0.970305	0.93878	0.879083
-9	0.786947	0.872978	0.929648	0.952509	0.969574	0.981892	0.988626	0.993423	0.995043	0.995168	0.994041	0.98867	0.979266	0.948566	0.889972
-6	0.791864	0.881735	0.936676	0.959725	0.975988	0.987435	0.994281	0.997639	0.998757	0.999265	0.997485	0.992939	0.98403	0.954167	0.897053
-3	0.79783	0.882418	0.938471	0.961347	0.978013	0.989789	0.996543	0.999173	0.999205	0.999302	0.998485	0.993709	0.990721	0.95606	0.896787
0	0.793853	0.879133	0.936205	0.959751	0.976836	0.989254	0.995911	0.998806	0.9994	0.999167	0.9973	0.992388	0.983166	0.952023	0.890518
3	0.7891	0.874771	0.930476	0.954312	0.972885	0.985306	0.993007	0.996179	0.997264	0.997171	0.994347	0.98863	0.978351	0.944041	0.878529
6	0.777438	0.866459	0.923323	0.947591	0.964851	0.978773	0.986385	0.99037	0.992326	0.991486	0.988588	0.981546	0.969905	0.933305	0.864585
9	0.767408	0.849358	0.909015	0.934219	0.953142	0.967424	0.975864	0.980388	0.982611	0.981279	0.977868	0.970007	0.957099	0.918278	0.844181
12	0.740419	0.832085	0.88956	0.915942	0.937558	0.951351	0.960423	0.964363	0.966262	0.966206	0.961569	0.952967	0.938829	0.898235	0.81834
15	0.709135	0.805316	0.865602	0.890439	0.913074	0.927522	0.937642	0.942383	0.944032	0.943252	0.938297	0.928911	0.914447	0.871158	0.786442
20	0.652307	0.743988	0.810082	0.832789	0.857649	0.878378	0.882579	0.888173	0.889234	0.887646	0.882399	0.870951	0.854525	0.809409	0.72837
25	0.569499	0.659362	0.724304	0.756447	0.779645	0.795898	0.805459	0.809671	0.809917	0.806368	0.800442	0.788915	0.767494	0.717005	0.640239

Table 26: Cpavg

Yaw Pitch	-25	-20	-15	-12	-9	-6	-3	0	3	6	9	12	15	20	25
-25	0.305294	0.340885	0.348535	0.352513	0.358228	0.364712	0.371305	0.380135	0.379756	0.381915	0.384799	0.384179	0.378869	0.361379	0.316889
-20	0.355622	0.421609	0.442341	0.445807	0.444595	0.445992	0.447409	0.455186	0.459528	0.462993	0.463684	0.462389	0.455003	0.428594	0.363682
-15	0.341455	0.425637	0.471022	0.492414	0.509075	0.501384	0.503863	0.50927	0.509358	0.512072	0.512816	0.508036	0.495178	0.451956	0.377316
-12	0.336853	0.422909	0.479211	0.49553	0.509836	0.516336	0.522055	0.523672	0.528073	0.532768	0.528177	0.518308	0.506544	0.458936	0.385126
-9	0.335173	0.419492	0.482847	0.498814	0.513009	0.520845	0.529663	0.534324	0.539895	0.54252	0.535381	0.527319	0.511297	0.458016	0.383168
-6	0.333634	0.418499	0.485473	0.505312	0.51313	0.522182	0.53142	0.538342	0.543606	0.542857	0.535477	0.52722	0.511592	0.458714	0.378445
-3	0.341257	0.436533	0.505329	0.517593	0.518009	0.524391	0.531784	0.539071	0.541443	0.538982	0.530553	0.52129	0.513415	0.460075	0.372174
0	0.339093	0.439288	0.494087	0.507808	0.517044	0.525408	0.536925	0.544863	0.544235	0.535672	0.526002	0.515372	0.505237	0.451379	0.365294
3	0.336414	0.448978	0.48667	0.497828	0.511119	0.523929	0.541125	0.554937	0.545508	0.532492	0.520759	0.508593	0.496091	0.4352	0.352678
6	0.346556	0.450401	0.476476	0.492635	0.507244	0.523414	0.537618	0.544917	0.531563	0.522122	0.511072	0.498796	0.486956	0.426597	0.344384
9	0.359746	0.470128	0.47045	0.48735	0.506605	0.524412	0.53802	0.523601	0.513562	0.505741	0.496412	0.486812	0.476315	0.422574	0.339301
12	0.380613	0.435147	0.465644	0.484311	0.503897	0.516819	0.511545	0.499968	0.4923	0.485797	0.477913	0.473137	0.464049	0.415258	0.335113
15	0.375571	0.423771	0.452463	0.469163	0.487407	0.497914	0.483023	0.474132	0.466938	0.463132	0.455667	0.450415	0.443565	0.406104	0.334415
20	0.341524	0.376465	0.405893	0.422201	0.432215	0.427068	0.419486	0.409442	0.407431	0.406715	0.404054	0.400781	0.391694	0.368576	0.326837
25	0.273644	0.303497	0.330476	0.339512	0.342276	0.338344	0.325989	0.31714	0.318001	0.319309	0.326307	0.324595	0.323395	0.301014	0.278315

Data: M = 0.409

Table 27: Cppitch

Yaw Pitch	-25	-20	-15	-12	-9	-6	-3	0	3	6	9	12	15	20	25
-25	3.892225	3.365711	2.997301	2.849251	2.73974	2.666888	2.588204	2.531381	2.501681	2.464048	2.428439	2.396984	2.395886	2.509658	2.785283
-20	2.923252	2.655301	2.44381	2.348176	2.27123	2.201832	2.129344	2.065852	2.037862	1.999127	1.924953	1.886785	1.837627	1.86852	2.063272
-15	1.901623	1.863358	1.850455	1.833592	1.841909	1.729403	1.653387	1.586994	1.522115	1.493566	1.380871	1.329074	1.3295	1.362043	1.506089
-12	1.402456	1.368267	1.419003	1.459035	1.418303	1.368599	1.330394	1.260744	1.215401	1.196242	1.05116	1.00572	1.041766	1.102498	1.199631
-9	1.0253	0.936544	1.026174	1.074032	1.021177	0.995068	0.9904	0.938359	0.906018	0.890018	0.733213	0.713852	0.762756	0.828197	0.908436
-6	0.681728	0.616355	0.669455	0.663901	0.624971	0.61621	0.648283	0.630819	0.605929	0.524926	0.410876	0.404604	0.478727	0.569355	0.634174
-3	0.365099	0.357968	0.27962	0.231199	0.241912	0.26894	0.319211	0.329306	0.265638	0.155236	0.100616	0.123547	0.214228	0.340652	0.367459
0	0.066916	0.080178	-0.08334	-0.13491	-0.14822	-0.07945	-0.01456	0.002969	-0.1008	-0.18982	-0.19042	-0.1428	-0.01781	0.114328	0.104259
3	-0.26719	-0.25632	-0.46383	-0.53738	-0.50408	-0.42308	-0.34961	-0.39232	-0.48633	-0.51684	-0.46019	-0.36086	-0.24591	-0.08531	-0.15018
6	-0.63628	-0.68163	-0.88433	-0.93901	-0.88098	-0.78921	-0.71983	-0.8107	-0.83808	-0.82729	-0.74041	-0.61601	-0.4858	-0.33804	-0.41772
9	-1.02596	-1.20893	-1.23487	-1.27095	-1.21709	-1.14477	-1.11202	-1.1699	-1.15718	-1.10915	-1.01781	-0.90531	-0.7528	-0.60731	-0.69698
12	-1.62058	-1.63135	-1.58452	-1.58322	-1.55609	-1.46157	-1.48782	-1.49065	-1.45233	-1.40216	-1.30136	-1.18218	-1.04502	-0.90428	-1.03441
15	-2.2047	-2.03367	-1.94505	-1.9386	-1.88832	-1.85303	-1.85698	-1.81074	-1.74938	-1.6856	-1.58104	-1.47553	-1.37656	-1.25329	-1.40693
20	-3.19937	-2.808	-2.62682	-2.51848	-2.46179	-2.45576	-2.42587	-2.36882	-2.30147	-2.21545	-2.10759	-2.05	-2.00602	-1.92782	-2.08156
25	-4.27504	-3.71251	-3.30562	-3.13448	-3.05491	-2.99259	-2.95876	-2.91307	-2.86558	-2.8274	-2.73562	-2.72629	-2.72509	-2.74234	-2.91771

Table 28: Cpyaw

Yaw Pitch	-25	-20	-15	-12	-9	-6	-3	0	3	6	9	12	15	20	25
-25	3.03829	2.19523	1.534458	1.168599	0.846074	0.553357	0.274661	0.046459	-0.18792	-0.47112	-0.76606	-1.06197	-1.39477	-1.97038	-2.7071
-20	2.857542	2.071482	1.453048	1.128675	0.855499	0.586336	0.313921	0.067533	-0.12846	-0.40526	-0.7212	-1.05012	-1.38416	-1.92002	-2.52986
-15	2.879395	2.05884	1.4571	1.108292	0.793472	0.557098	0.332845	0.070244	-0.16882	-0.45445	-0.78617	-1.11067	-1.43508	-1.94094	-2.45391
-12	2.891032	2.184651	1.571138	1.186079	0.840372	0.540964	0.260253	0.019391	-0.23902	-0.52931	-0.861	-1.19645	-1.50187	-1.96223	-2.42747
-9	2.901142	2.294652	1.655419	1.247199	0.875564	0.589211	0.269126	-0.02714	-0.28812	-0.59776	-0.94359	-1.28521	-1.56371	-2.00066	-2.4331
-6	2.893779	2.303858	1.71221	1.292738	0.925251	0.622225	0.335396	0.016582	-0.27421	-0.5831	-0.94233	-1.29314	-1.58341	-2.02245	-2.45696
-3	2.878297	2.307511	1.736685	1.344872	0.961732	0.598457	0.361335	0.018967	-0.31559	-0.6518	-0.99086	-1.31245	-1.60896	-2.03527	-2.50028
0	2.87073	2.281267	1.689437	1.303996	0.966434	0.676569	0.37778	0.021584	-0.3369	-0.66477	-1.01717	-1.33273	-1.6074	-2.11964	-2.54298
3	2.848907	2.228122	1.568334	1.222115	0.932802	0.666977	0.359936	0.007839	-0.33705	-0.6879	-1.02311	-1.34347	-1.6437	-2.16609	-2.60931
6	2.825087	2.104707	1.427818	1.124618	0.930006	0.625125	0.291462	-0.04669	-0.36615	-0.67441	-1.0009	-1.33065	-1.65153	-2.19279	-2.65781
9	2.789337	1.946093	1.461657	1.201658	0.927295	0.632037	0.307073	-0.01991	-0.34632	-0.65957	-0.98132	-1.30287	-1.65506	-2.22391	-2.72144
12	2.747678	1.972079	1.491918	1.213552	0.913039	0.607462	0.26823	-0.03698	-0.3432	-0.64181	-0.96711	-1.31515	-1.67642	-2.26921	-2.82968
15	2.794935	2.029635	1.46406	1.149164	0.868719	0.566442	0.237243	-0.05617	-0.35143	-0.65928	-0.98828	-1.3263	-1.67938	-2.30581	-2.93042
20	2.918639	2.073113	1.434624	1.124464	0.828983	0.521729	0.245878	-0.03696	-0.33145	-0.61584	-0.99034	-1.33874	-1.67475	-2.34603	-3.11367
25	3.002022	2.077162	1.417623	1.066262	0.769332	0.487903	0.227232	-0.02761	-0.29624	-0.55594	-0.90252	-1.24729	-1.61554	-2.37736	-3.33578

Table 29: Cp5

Yaw Pitch	-25	-20	-15	-12	-9	-6	-3	0	3	6	9	12	15	20	25
-25	0.610889	0.69629	0.768966	0.803446	0.82962	0.845125	0.859363	0.866252	0.870778	0.872736	0.870431	0.863167	0.845417	0.793417	0.709293
-20	0.695611	0.784818	0.848383	0.877274	0.897351	0.912793	0.924948	0.933009	0.935839	0.937761	0.936889	0.931753	0.918193	0.878609	0.797749
-15	0.748313	0.844339	0.90027	0.924573	0.941886	0.956386	0.965456	0.971888	0.97546	0.976168	0.974887	0.96962	0.958866	0.924464	0.855162
-12	0.772859	0.862867	0.919266	0.942915	0.96026	0.97202	0.979732	0.985094	0.9883	0.989201	0.98743	0.982126	0.972145	0.940765	0.880801
-9	0.791414	0.877035	0.932445	0.955194	0.971169	0.982236	0.988932	0.993233	0.995399	0.996098	0.994623	0.989471	0.980055	0.950264	0.893739
-6	0.799674	0.885294	0.940239	0.961688	0.977286	0.98806	0.994225	0.997567	0.998792	0.999016	0.99773	0.993077	0.984016	0.954683	0.899031
-3	0.803353	0.887739	0.942561	0.963522	0.979781	0.990537	0.996571	0.998994	0.999738	0.999487	0.998358	0.993759	0.984394	0.955665	0.898302
0	0.800622	0.885846	0.939664	0.962254	0.978564	0.989932	0.996093	0.998792	0.999228	0.999203	0.9975	0.992153	0.982772	0.95169	0.89275
3	0.795551	0.881289	0.934603	0.956891	0.974539	0.986532	0.993321	0.996517	0.997369	0.997023	0.994368	0.98841	0.977717	0.944929	0.881321
6	0.782905	0.872714	0.924715	0.948177	0.965857	0.979227	0.986986	0.99093	0.99215	0.991792	0.988382	0.981611	0.970255	0.935318	0.868543
9	0.772694	0.856679	0.91219	0.935361	0.954488	0.968299	0.976708	0.981499	0.982636	0.981867	0.978263	0.970561	0.958157	0.920956	0.848775
12	0.747491	0.837513	0.894162	0.919389	0.939305	0.953544	0.961605	0.966339	0.96758	0.966521	0.962309	0.954021	0.940069	0.900353	0.817521
15	0.718197	0.810467	0.873748	0.897456	0.91659	0.93172	0.940563	0.944943	0.946061	0.944028	0.940397	0.931298	0.916808	0.873266	0.78526
20	0.660106	0.75209	0.815611	0.844617	0.86415	0.878952	0.887865	0.892215	0.89348	0.891033	0.884759	0.873356	0.856819	0.81173	0.727466
25	0.580101	0.663284	0.732708	0.766564	0.787695	0.803263	0.811836	0.816391	0.815201	0.810389	0.805457	0.791276	0.771788	0.721868	0.643996

Table 30: Cpavg

Yaw Pitch	-25	-20	-15	-12	-9	-6	-3	0	3	6	9	12	15	20	25
-25	0.286361	0.308217	0.332567	0.339857	0.344578	0.352766	0.36208	0.368996	0.371639	0.374208	0.378822	0.377216	0.371361	0.352904	0.308732
-20	0.344672	0.401678	0.415014	0.421953	0.429712	0.435705	0.441578	0.449069	0.451193	0.456193	0.456336	0.454027	0.447497	0.41771	0.352524
-15	0.337089	0.439329	0.481486	0.496277	0.50524	0.507596	0.501983	0.505382	0.50542	0.504404	0.502631	0.504533	0.490912	0.442271	0.370743
-12	0.320667	0.430202	0.482708	0.508389	0.517155	0.517649	0.518166	0.521545	0.52361	0.52579	0.520632	0.518727	0.504096	0.451245	0.379858
-9	0.323751	0.412967	0.490721	0.514955	0.521632	0.520074	0.528395	0.533421	0.535665	0.538738	0.532583	0.526807	0.51132	0.457253	0.384083
-6	0.322306	0.413041	0.497212	0.518544	0.521502	0.521028	0.52617	0.536249	0.539281	0.538823	0.5363	0.52981	0.515011	0.462397	0.382715
-3	0.329059	0.422814	0.496402	0.517261	0.528139	0.533382	0.531232	0.541461	0.542804	0.538888	0.534088	0.525667	0.514935	0.464489	0.377539
0	0.34057	0.437408	0.504352	0.524235	0.53348	0.532451	0.54115	0.547564	0.540803	0.5328	0.526926	0.518182	0.509349	0.453038	0.370233
3	0.343886	0.44757	0.513655	0.53263	0.5329	0.540461	0.552695	0.54906	0.541332	0.529848	0.522268	0.511763	0.497092	0.43793	0.356991
6	0.349343	0.458282	0.522103	0.533495	0.527674	0.542808	0.550364	0.537327	0.531005	0.520799	0.512301	0.502047	0.488028	0.434548	0.347654
9	0.3516	0.476008	0.498191	0.506611	0.516385	0.532147	0.534543	0.518328	0.512133	0.503801	0.497394	0.49137	0.479917	0.428919	0.340943
12	0.371639	0.452931	0.471621	0.487062	0.505533	0.523263	0.514039	0.502921	0.495544	0.489161	0.486821	0.478551	0.470797	0.425575	0.334544
15	0.364482	0.426243	0.457308	0.470841	0.490664	0.501665	0.489384	0.478671	0.471498	0.467574	0.465593	0.466086	0.456398	0.418491	0.330927
20	0.338645	0.380173	0.408829	0.424346	0.436346	0.428496	0.421177	0.418906	0.419598	0.416273	0.414845	0.410417	0.397983	0.384728	0.328145
25	0.277422	0.303755	0.326743	0.334111	0.338012	0.335336	0.332582	0.329891	0.324929	0.319507	0.330219	0.324895	0.322266	0.315821	0.292004

Data: M = 0.513

Table 31: Cppitch

Yaw Pitch	-25	-20	-15	-12	-9	-6	-3	0	3	6	9	12	15	20	25
-25	3.79675	3.33904	2.998146	2.846702	2.737655	2.680842	2.593442	2.547228	2.517776	2.476948	2.44802	2.427458	2.424745	2.540387	2.824779
-20	2.890494	2.643642	2.428028	2.336945	2.259909	2.208912	2.135945	2.064094	2.040125	2.0022	1.932501	1.89746	1.849244	1.894385	2.062377
-15	1.879351	1.825984	1.790255	1.801596	1.832296	1.750331	1.653938	1.591068	1.532681	1.505209	1.394935	1.339096	1.334944	1.379863	1.505928
-12	1.388201	1.293749	1.371358	1.395892	1.385098	1.345176	1.298742	1.243771	1.211584	1.196698	1.0575	1.000769	1.041385	1.094955	1.203006
-9	1.00447	0.914117	1.005558	1.010139	0.966185	0.926364	0.950974	0.917471	0.886309	0.86571	0.723339	0.711201	0.764348	0.83051	0.916095
-6	0.634324	0.598185	0.609354	0.582262	0.554913	0.556346	0.606019	0.613777	0.583931	0.513694	0.412901	0.410372	0.477207	0.581992	0.642911
-3	0.341422	0.306574	0.248452	0.203129	0.193725	0.217375	0.288709	0.326361	0.255228	0.16491	0.104758	0.118336	0.213192	0.349117	0.388835
0	0.061214	0.018926	-0.0709	-0.16029	-0.16731	-0.1022	-0.02587	-0.00275	-0.09318	-0.16529	-0.17235	-0.12208	-0.01448	0.111256	0.125107
3	-0.286	-0.28377	-0.43669	-0.52694	-0.48734	-0.43812	-0.36725	-0.39113	-0.4549	-0.4876	-0.4536	-0.35341	-0.23416	-0.10168	-0.14105
6	-0.6608	-0.6504	-0.79695	-0.84577	-0.8341	-0.77415	-0.71343	-0.77982	-0.81814	-0.80589	-0.73421	-0.61878	-0.48127	-0.33929	-0.40172
9	-1.11762	-1.14502	-1.13899	-1.21525	-1.18111	-1.11714	-1.0907	-1.13383	-1.14256	-1.10015	-1.00306	-0.89718	-0.75814	-0.60619	-0.67691
12	-1.64218	-1.58496	-1.51762	-1.58127	-1.54178	-1.45928	-1.4444	-1.47235	-1.43646	-1.38731	-1.28641	-1.18369	-1.04647	-0.91437	-0.9982
15	-2.19281	-2.02224	-1.94826	-1.9204	-1.86705	-1.79863	-1.79416	-1.78567	-1.73267	-1.67854	-1.57738	-1.46161	-1.38154	-1.24472	-1.35664
20	-3.22875	-2.801	-2.56236	-2.43739	-2.37576	-2.35585	-2.36351	-2.31126	-2.22864	-2.13397	-2.05876	-2.00079	-1.96706	-1.8423	-2.02323
25	-4.38314	-3.69792	-3.27951	-3.11267	-2.98303	-2.91831	-2.88356	-2.82703	-2.7647	-2.66434	-2.63931	-2.62741	-2.61343	-2.58921	-2.81196

Table 32: Cpyaw

Yaw Pitch	-25	-20	-15	-12	-9	-6	-3	0	3	6	9	12	15	20	25
-25	3.077411	2.23123	1.545644	1.192396	0.870222	0.571871	0.301275	0.080973	-0.16441	-0.46187	-0.75242	-1.05348	-1.39562	-1.95273	-2.65419
-20	2.878915	2.10115	1.49832	1.173841	0.889998	0.601495	0.332006	0.087335	-0.13276	-0.41423	-0.71676	-1.04017	-1.36878	-1.90189	-2.49672
-15	2.905414	2.120443	1.543592	1.166899	0.833347	0.562278	0.341289	0.086127	-0.1517	-0.43012	-0.74151	-1.0623	-1.39986	-1.92058	-2.42117
-12	2.908261	2.288248	1.662741	1.270255	0.921005	0.606837	0.312974	0.055916	-0.21236	-0.50557	-0.82926	-1.15458	-1.46625	-1.95028	-2.40471
-9	2.935774	2.331768	1.737118	1.337625	0.991891	0.660642	0.321381	0.025482	-0.24243	-0.54858	-0.89893	-1.2336	-1.52535	-1.97016	-2.40109
-6	2.919984	2.34845	1.787899	1.396731	1.043992	0.700035	0.379225	0.061894	-0.24033	-0.55924	-0.90785	-1.24934	-1.55067	-1.98995	-2.41715
-3	2.907602	2.316745	1.780217	1.411705	1.020382	0.706529	0.380821	0.058403	-0.27133	-0.60333	-0.95979	-1.28733	-1.57742	-2.00571	-2.45324
0	2.885433	2.286968	1.737758	1.385411	1.059899	0.748301	0.427081	0.07611	-0.27418	-0.61762	-0.97103	-1.2987	-1.57647	-2.04262	-2.49376
3	2.868858	2.240687	1.649588	1.350861	1.093846	0.798392	0.461025	0.063041	-0.29762	-0.64328	-0.98118	-1.30737	-1.60376	-2.12141	-2.55285
6	2.84175	2.178943	1.5305	1.35861	1.060887	0.738733	0.374966	0.020061	-0.30688	-0.63088	-0.96242	-1.28572	-1.60676	-2.12812	-2.61553
9	2.819043	2.04063	1.558242	1.304427	1.003294	0.688046	0.352693	0.006153	-0.31658	-0.62804	-0.94235	-1.26162	-1.60266	-2.1613	-2.6824
12	2.824127	2.056265	1.539384	1.242398	0.948712	0.653555	0.322201	0.01268	-0.29975	-0.60373	-0.92902	-1.25774	-1.6146	-2.17099	-2.76523
15	2.912791	2.077264	1.498967	1.222102	0.918589	0.623785	0.29955	-0.00716	-0.2984	-0.60244	-0.93541	-1.27545	-1.60977	-2.21863	-2.85468
20	3.088428	2.186768	1.555183	1.238926	0.93751	0.62024	0.321588	0.02934	-0.26461	-0.58541	-0.93975	-1.27703	-1.58986	-2.29413	-3.02577
25	3.237047	2.264955	1.588601	1.204449	0.859743	0.571175	0.306218	0.045258	-0.21935	-0.5118	-0.856	-1.20424	-1.58535	-2.37404	-3.22896

Table 33: Cp5

Yaw Pitch	-25	-20	-15	-12	-9	-6	-3	0	3	6	9	12	15	20	25
-25	0.614182	0.699765	0.772983	0.80709	0.833405	0.848123	0.86193	0.86803	0.872197	0.874754	0.872865	0.865995	0.850583	0.79812	0.714622
-20	0.696846	0.786733	0.84992	0.879091	0.900065	0.915155	0.926024	0.934149	0.936671	0.938344	0.937797	0.93351	0.92037	0.881923	0.805731
-15	0.748358	0.844332	0.902257	0.925856	0.943136	0.95637	0.96579	0.972127	0.975693	0.976468	0.975943	0.971093	0.960601	0.92771	0.86287
-12	0.773283	0.863125	0.919345	0.942626	0.959778	0.971523	0.979708	0.984911	0.988076	0.989151	0.987946	0.982847	0.973818	0.943463	0.884927
-9	0.786841	0.874313	0.930844	0.9537	0.969789	0.981525	0.988532	0.993035	0.995122	0.996012	0.994795	0.990385	0.981858	0.953789	0.899135
-6	0.7939	0.881911	0.937649	0.959717	0.975937	0.987097	0.993738	0.997382	0.998626	0.999122	0.998066	0.994016	0.986059	0.958813	0.905671
-3	0.796213	0.883302	0.939608	0.96166	0.978268	0.989455	0.996044	0.999033	0.999561	0.999469	0.998735	0.995	0.986727	0.960029	0.904553
0	0.795263	0.881631	0.938168	0.960428	0.977377	0.989151	0.995827	0.998677	0.999368	0.999272	0.998089	0.993705	0.985406	0.957505	0.899626
3	0.788575	0.877042	0.93281	0.955587	0.972904	0.985398	0.993015	0.996437	0.997633	0.997624	0.995568	0.990194	0.980683	0.949968	0.88845
6	0.776576	0.867845	0.923703	0.947887	0.965538	0.97893	0.987354	0.991473	0.992994	0.992807	0.990102	0.983875	0.973293	0.940884	0.874212
9	0.757987	0.852083	0.910945	0.935561	0.954719	0.968718	0.977688	0.982302	0.984212	0.983433	0.980475	0.973614	0.9619	0.927496	0.853569
12	0.736149	0.831306	0.894013	0.918727	0.939608	0.953685	0.962519	0.967959	0.969778	0.968972	0.96539	0.958277	0.945535	0.908431	0.826247
15	0.703852	0.803438	0.870027	0.896084	0.918304	0.933514	0.94208	0.94731	0.948906	0.947587	0.943954	0.937301	0.923064	0.881454	0.795218
20	0.643744	0.742333	0.812122	0.844409	0.867268	0.883137	0.892386	0.896728	0.898425	0.897518	0.891918	0.882097	0.867643	0.822248	0.736152
25	0.562765	0.653459	0.726339	0.761241	0.791225	0.809478	0.819966	0.824214	0.824966	0.823554	0.815331	0.802676	0.784951	0.737104	0.655896

Table 34: Cpavg

Yaw Pitch	-25	-20	-15	-12	-9	-6	-3	0	3	6	9	12	15	20	25
-25	0.281333	0.312067	0.334842	0.342869	0.34925	0.361759	0.368927	0.37449	0.377917	0.381908	0.387037	0.384629	0.380134	0.358403	0.311965
-20	0.339488	0.403087	0.42015	0.425356	0.434908	0.44275	0.447925	0.454092	0.456285	0.462245	0.46159	0.460395	0.453985	0.422136	0.356733
-15	0.329654	0.43383	0.476102	0.494123	0.510112	0.511717	0.508952	0.512778	0.513142	0.513193	0.507997	0.508051	0.494912	0.448806	0.376808
-12	0.314573	0.407649	0.477568	0.502268	0.515325	0.518088	0.522046	0.527688	0.527616	0.529728	0.521372	0.518083	0.505189	0.454238	0.382719
-9	0.308344	0.402198	0.485737	0.505518	0.511417	0.513879	0.524395	0.533862	0.535296	0.536078	0.531186	0.524386	0.512308	0.461115	0.385299
-6	0.311642	0.403199	0.48364	0.50439	0.50976	0.513689	0.52372	0.537337	0.537971	0.537308	0.534368	0.528275	0.51458	0.464847	0.383685
-3	0.314773	0.41139	0.485019	0.50692	0.518575	0.519127	0.528164	0.539447	0.537269	0.534036	0.532741	0.524496	0.512566	0.463652	0.377363
0	0.323587	0.419999	0.490462	0.511592	0.516337	0.521095	0.536083	0.54242	0.537666	0.531052	0.526653	0.51709	0.507361	0.456094	0.36862
3	0.324652	0.428674	0.497688	0.512991	0.507316	0.522665	0.539276	0.539951	0.534432	0.527133	0.521318	0.511977	0.498866	0.437719	0.356641
6	0.329279	0.443491	0.510738	0.501467	0.511791	0.52417	0.535172	0.528389	0.524475	0.515357	0.510343	0.502082	0.488611	0.434446	0.347192
9	0.347719	0.458884	0.48951	0.492003	0.509427	0.524118	0.527946	0.512366	0.50524	0.497224	0.493997	0.48654	0.475719	0.425399	0.337202
12	0.357828	0.44029	0.467351	0.479736	0.499072	0.512208	0.508999	0.49554	0.487567	0.479382	0.477338	0.471749	0.460931	0.421331	0.329865
15	0.347993	0.418853	0.44499	0.465183	0.482858	0.494729	0.488115	0.473907	0.465469	0.458033	0.456238	0.454362	0.444204	0.41323	0.327735
20	0.324464	0.368071	0.396535	0.416184	0.433713	0.43135	0.419431	0.415068	0.415308	0.414994	0.411428	0.405352	0.393969	0.387971	0.321251
25	0.265015	0.291833	0.32482	0.329291	0.332642	0.32918	0.327733	0.329905	0.330021	0.340229	0.334652	0.330369	0.326965	0.326588	0.285753

Data: M = 0.618

Table 35: Cppitch

Yaw Pitch	-25	-20	-15	-12	-9	-6	-3	0	3	6	9	12	15	20	25
-25	3.745103	3.360908	3.024837	2.863072	2.765372	2.694069	2.62042	2.568378	2.529658	2.494662	2.463536	2.444462	2.430111	2.573488	2.897795
-20	2.95718	2.62296	2.435431	2.334146	2.270039	2.206345	2.139247	2.077546	2.047535	2.020224	1.939335	1.919644	1.872935	1.934306	2.098283
-15	2.2064	1.978569	1.912865	1.833032	1.851079	1.760639	1.689917	1.599545	1.57101	1.53287	1.431126	1.399036	1.374571	1.388963	1.503492
-12	1.525387	1.379257	1.417454	1.389714	1.405017	1.411001	1.329096	1.274582	1.236436	1.210134	1.093077	1.058275	1.061532	1.094198	1.203184
-9	1.060238	0.948741	1.051923	1.016806	1.007505	0.994321	0.992374	0.939471	0.92314	0.894524	0.760857	0.747998	0.772735	0.822749	0.918082
-6	0.736675	0.619174	0.707785	0.663112	0.646753	0.642544	0.662174	0.635878	0.620274	0.554074	0.436824	0.430385	0.478414	0.580302	0.64055
-3	0.380393	0.301254	0.326693	0.291658	0.288847	0.314225	0.332688	0.33113	0.278561	0.207138	0.139862	0.146129	0.221034	0.329044	0.387298
0	0.104892	0.01147	-0.01316	-0.07152	-0.06929	-0.01976	0.01043	0.002723	-0.06231	-0.1348	-0.15689	-0.11212	-0.01237	0.080172	0.126878
3	-0.27473	-0.28464	-0.34843	-0.40589	-0.41494	-0.37248	-0.30652	-0.36968	-0.41893	-0.46598	-0.43885	-0.35058	-0.22655	-0.15858	-0.13818
6	-0.65208	-0.64147	-0.72865	-0.80821	-0.78601	-0.72	-0.63983	-0.7367	-0.79427	-0.78992	-0.71751	-0.61725	-0.49345	-0.40728	-0.39428
9	-1.12559	-1.15437	-1.14622	-1.19575	-1.16925	-1.07949	-1.00025	-1.09535	-1.13619	-1.08592	-1.00117	-0.90354	-0.784	-0.65548	-0.6645
12	-1.62392	-1.55506	-1.5667	-1.59873	-1.55866	-1.44392	-1.38943	-1.43912	-1.42096	-1.37692	-1.29226	-1.19519	-1.08034	-0.92922	-0.97926
15	-2.10385	-1.93655	-1.92249	-1.88996	-1.85003	-1.76181	-1.77363	-1.73937	-1.69401	-1.63345	-1.55454	-1.47227	-1.40637	-1.26806	-1.32459
20	-2.97283	-2.6626	-2.53678	-2.44426	-2.37152	-2.33899	-2.3284	-2.26935	-2.21027	-2.10684	-2.06641	-2.02547	-1.95886	-1.86962	-1.97209
25	-3.99841	-3.52631	-3.18063	-3.02926	-2.9399	-2.87856	-2.85534	-2.79543	-2.72284	-2.65539	-2.63594	-2.60388	-2.57668	-2.54813	-2.7372

Table 36: Cpyaw

Yaw Pitch	-25	-20	-15	-12	-9	-6	-3	0	3	6	9	12	15	20	25
-25	2.982937	2.14191	1.465893	1.111383	0.793089	0.505585	0.225657	-0.02036	-0.26932	-0.55159	-0.83065	-1.1249	-1.4241	-1.99966	-2.72618
-20	2.736399	2.054857	1.446915	1.130056	0.820112	0.555613	0.278005	0.015203	-0.24434	-0.51785	-0.81487	-1.108	-1.40952	-1.92908	-2.55047
-15	2.579234	1.900284	1.333489	1.107902	0.710731	0.488445	0.222009	-0.00346	-0.25513	-0.55072	-0.84746	-1.13012	-1.4461	-1.93735	-2.43094
-12	2.712481	2.129567	1.560749	1.227574	0.841325	0.446143	0.235778	-0.00905	-0.28419	-0.58251	-0.87865	-1.19477	-1.50415	-1.96356	-2.4009
-9	2.783164	2.196447	1.646855	1.294681	0.96508	0.614196	0.267924	-0.00351	-0.27555	-0.56441	-0.89724	-1.23203	-1.52855	-1.98103	-2.38301
-6	2.770942	2.227112	1.660703	1.305319	0.996264	0.698755	0.354101	0.034931	-0.2643	-0.56958	-0.90309	-1.24649	-1.55247	-1.97593	-2.38646
-3	2.774058	2.231229	1.710265	1.280515	0.988982	0.736182	0.391363	0.053168	-0.28219	-0.61013	-0.95286	-1.28911	-1.58659	-1.9802	-2.39491
0	2.747761	2.182096	1.653491	1.417346	1.128525	0.790327	0.43401	0.059666	-0.29303	-0.64391	-1.00112	-1.33297	-1.61192	-2.016	-2.44093
3	2.678498	2.128508	1.675844	1.408839	1.114787	0.792937	0.416165	0.032502	-0.32679	-0.68022	-1.02014	-1.33518	-1.6211	-2.05529	-2.48796
6	2.678769	2.079292	1.575691	1.349925	1.024797	0.687734	0.344269	-0.00865	-0.34836	-0.66465	-0.97985	-1.29752	-1.61042	-2.0622	-2.5327
9	2.628816	1.87925	1.488201	1.209961	0.915875	0.614471	0.307901	-0.03676	-0.34322	-0.63472	-0.93463	-1.2409	-1.57766	-2.09303	-2.59512
12	2.624266	1.968585	1.408963	1.098544	0.817788	0.561326	0.292414	-0.0158	-0.30984	-0.61277	-0.91409	-1.23018	-1.57477	-2.13442	-2.65616
15	2.752167	2.025075	1.433686	1.149195	0.870232	0.582282	0.274026	-0.02064	-0.31003	-0.60419	-0.93532	-1.25175	-1.56865	-2.17524	-2.74514
20	2.922662	2.067831	1.45954	1.161556	0.867977	0.545005	0.259562	-0.03758	-0.31527	-0.63611	-0.94493	-1.25318	-1.59537	-2.23376	-2.8811
25	3.041179	2.134525	1.512758	1.151393	0.822691	0.518659	0.229241	-0.03144	-0.31257	-0.59233	-0.89342	-1.21965	-1.59055	-2.33624	-3.13968

Table 37: Cp5

Yaw Pitch	-25	-20	-15	-12	-9	-6	-3	0	3	6	9	12	15	20	25
-25	0.617598	0.702577	0.778463	0.81427	0.83793	0.852313	0.865436	0.87169	0.876134	0.879216	0.878023	0.870331	0.853267	0.796663	0.704361
-20	0.7023	0.78796	0.852595	0.882654	0.902981	0.916926	0.926858	0.933196	0.936737	0.939255	0.94076	0.934792	0.92237	0.881071	0.801467
-15	0.758906	0.848646	0.904977	0.92716	0.944878	0.957471	0.966468	0.972262	0.975624	0.977736	0.976734	0.97152	0.960818	0.930028	0.866502
-12	0.784509	0.867359	0.921321	0.9438	0.960701	0.972499	0.980058	0.985281	0.9881	0.989517	0.988048	0.98319	0.974142	0.945413	0.890201
-9	0.798994	0.883735	0.933067	0.954873	0.970648	0.981689	0.988788	0.993185	0.995167	0.996075	0.994762	0.990442	0.982258	0.955142	0.905016
-6	0.807611	0.888287	0.940626	0.961226	0.97657	0.987314	0.993826	0.997275	0.998661	0.999063	0.99797	0.994168	0.986283	0.960891	0.911276
-3	0.807159	0.890392	0.943363	0.963628	0.979175	0.988905	0.996085	0.999038	0.9995	0.999485	0.999004	0.995337	0.987359	0.964843	0.912359
0	0.809457	0.889299	0.941329	0.962618	0.978823	0.989725	0.996275	0.998935	0.99935	0.999515	0.998374	0.994205	0.986155	0.959888	0.908169
3	0.805833	0.885142	0.937457	0.959273	0.974479	0.986976	0.994218	0.997238	0.998024	0.998125	0.99615	0.990994	0.981968	0.954073	0.898706
6	0.792675	0.876542	0.930465	0.951644	0.969002	0.981389	0.98901	0.992879	0.993879	0.993646	0.991096	0.985275	0.975116	0.945698	0.887862
9	0.774696	0.862937	0.917492	0.941319	0.959339	0.972252	0.980339	0.984694	0.986147	0.985695	0.982543	0.976126	0.96496	0.931778	0.868486
12	0.756113	0.841751	0.901689	0.92641	0.945338	0.95869	0.966649	0.971771	0.973416	0.972555	0.968865	0.962022	0.949645	0.913544	0.844177
15	0.723918	0.817941	0.879961	0.906045	0.92531	0.939222	0.948074	0.953011	0.954639	0.954016	0.949568	0.943068	0.929014	0.888275	0.813976
20	0.666537	0.763664	0.828728	0.856779	0.878297	0.894191	0.902433	0.907398	0.909033	0.908643	0.902768	0.894226	0.879239	0.834203	0.757766
25	0.592645	0.6798	0.749264	0.782925	0.807909	0.825708	0.834813	0.840472	0.841844	0.840144	0.833533	0.82266	0.804866	0.757525	0.678729

Table 38: Cpavg

Yaw Pitch	-25	-20	-15	-12	-9	-6	-3	0	3	6	9	12	15	20	25
-25	0.269323	0.304141	0.340763	0.356586	0.364734	0.372911	0.382454	0.388949	0.390027	0.389674	0.390712	0.387356	0.375334	0.349584	0.298746
-20	0.341552	0.380688	0.413713	0.428355	0.447953	0.453007	0.461003	0.466305	0.467722	0.468717	0.46377	0.459339	0.449691	0.41396	0.346779
-15	0.383796	0.446311	0.497801	0.49514	0.524428	0.526198	0.522791	0.524456	0.525692	0.526169	0.516342	0.508755	0.495254	0.445224	0.372617
-12	0.342626	0.416074	0.483358	0.504316	0.528311	0.548321	0.538693	0.535958	0.537646	0.537838	0.530395	0.523748	0.507877	0.456684	0.379084
-9	0.318122	0.405907	0.485845	0.50818	0.519048	0.534447	0.53895	0.540565	0.544165	0.544323	0.535362	0.528796	0.514624	0.463989	0.388888
-6	0.311276	0.405749	0.496565	0.519049	0.52537	0.529919	0.53841	0.545015	0.548251	0.545072	0.539317	0.531592	0.518006	0.470243	0.389607
-3	0.308678	0.407689	0.49667	0.532103	0.534231	0.529315	0.540449	0.544825	0.547663	0.542369	0.538895	0.532182	0.517643	0.471023	0.389298
0	0.317992	0.424903	0.509142	0.509385	0.518258	0.52899	0.545188	0.551067	0.549236	0.542905	0.537782	0.529396	0.515328	0.464539	0.378306
3	0.34036	0.438862	0.499712	0.508676	0.514776	0.532454	0.550708	0.548326	0.546705	0.5406	0.533013	0.523161	0.507453	0.453341	0.36709
6	0.346843	0.445681	0.503255	0.507148	0.522719	0.541105	0.553704	0.545054	0.542078	0.531892	0.523375	0.512858	0.497058	0.446463	0.354901
9	0.370762	0.475245	0.496525	0.513041	0.528651	0.54006	0.549864	0.532283	0.524431	0.513278	0.506802	0.497867	0.482087	0.437463	0.346311
12	0.371923	0.442086	0.482435	0.502592	0.521	0.532513	0.532874	0.513738	0.50289	0.491809	0.487691	0.48184	0.468166	0.428481	0.341011
15	0.347595	0.411933	0.451406	0.476604	0.494554	0.513054	0.502758	0.493051	0.484658	0.475887	0.470644	0.464704	0.451331	0.419962	0.333072
20	0.315579	0.367203	0.408037	0.427853	0.447727	0.445919	0.439607	0.435507	0.430382	0.429932	0.420268	0.411729	0.40826	0.388836	0.322062
25	0.266837	0.298233	0.336686	0.352681	0.359528	0.359803	0.353642	0.352895	0.351516	0.350642	0.339343	0.339226	0.337871	0.332822	0.289549

Data: M = 0.726

Table 39: Cppitch

Yaw Pitch	-25	-20	-15	-12	-9	-6	-3	0	3	6	9	12	15	20	25
-25	3.554484	3.184974	2.921715	2.783175	2.700792	2.644941	2.583807	2.534982	2.504012	2.471537	2.440867	2.422161	2.407083	2.558273	2.87551
-20	2.727899	2.535884	2.399843	2.315863	2.262157	2.211821	2.141943	2.075281	2.035263	2.010799	1.949546	1.909815	1.868598	1.940941	2.116157
-15	1.93104	1.831673	1.766413	1.768325	1.745669	1.714053	1.663776	1.595342	1.551279	1.53601	1.43422	1.378792	1.365836	1.402972	1.525563
-12	1.425324	1.356074	1.349081	1.324873	1.349248	1.342859	1.301787	1.264733	1.229325	1.215937	1.090967	1.043709	1.066036	1.11396	1.201387
-9	1.023186	0.936486	0.972504	0.98989	0.955446	0.942506	0.93765	0.934306	0.91053	0.863599	0.747063	0.744156	0.785279	0.845084	0.922285
-6	0.637741	0.597178	0.59071	0.590586	0.576243	0.570794	0.619965	0.619791	0.573102	0.520772	0.418019	0.427473	0.501324	0.596492	0.643325
-3	0.350402	0.295412	0.240854	0.200908	0.21088	0.238958	0.308188	0.315398	0.249552	0.163209	0.099828	0.128213	0.263672	0.341657	0.379847
0	0.057753	0.035081	-0.07602	-0.15498	-0.14094	-0.07694	-0.01439	-0.01877	-0.1016	-0.17912	-0.1728	-0.12472	-0.00581	0.086927	0.12224
3	-0.28758	-0.27931	-0.40792	-0.50011	-0.46488	-0.40496	-0.3463	-0.38733	-0.46338	-0.48804	-0.43173	-0.36292	-0.26292	-0.13848	-0.1503
6	-0.66407	-0.63314	-0.79627	-0.83106	-0.80162	-0.73934	-0.69118	-0.76989	-0.81917	-0.80954	-0.72329	-0.61818	-0.48359	-0.37959	-0.42629
9	-1.11541	-1.12921	-1.13837	-1.16588	-1.1628	-1.09213	-1.0677	-1.12396	-1.14641	-1.09758	-1.00406	-0.89225	-0.76169	-0.63947	-0.69716
12	-1.62648	-1.54432	-1.54013	-1.5807	-1.52834	-1.44553	-1.42987	-1.45272	-1.43491	-1.38615	-1.29253	-1.18165	-1.05526	-0.93695	-1.01682
15	-2.13658	-1.96593	-1.89974	-1.87781	-1.83788	-1.78183	-1.77692	-1.76052	-1.71429	-1.64662	-1.56132	-1.45392	-1.38205	-1.25174	-1.34818
20	-2.98858	-2.67641	-2.53622	-2.43266	-2.36759	-2.33433	-2.32323	-2.27058	-2.16817	-2.11681	-2.06108	-2.00099	-1.93581	-1.80651	-1.9771
25	-3.98961	-3.50999	-3.19872	-3.04821	-2.92	-2.86799	-2.83873	-2.77041	-2.68271	-2.63578	-2.61601	-2.58918	-2.54257	-2.46299	-2.66928

Table 40: Cpyaw

Yaw Pitch	-25	-20	-15	-12	-9	-6	-3	0	3	6	9	12	15	20	25
-25	2.903816	2.161436	1.519622	1.195182	0.899429	0.609032	0.333083	0.087258	-0.17335	-0.44629	-0.752	-1.05555	-1.37146	-1.96648	-2.69248
-20	2.776562	2.049996	1.477013	1.178092	0.889483	0.607985	0.340557	0.082254	-0.16006	-0.43667	-0.7477	-1.05637	-1.36392	-1.8991	-2.49768
-15	2.722518	2.035224	1.534041	1.202603	0.979486	0.629391	0.316413	0.102134	-0.1688	-0.47495	-0.78428	-1.09146	-1.40515	-1.89943	-2.40527
-12	2.761316	2.154317	1.672538	1.367057	1.001681	0.615389	0.345539	0.091018	-0.19962	-0.51214	-0.84366	-1.15616	-1.46629	-1.94495	-2.40459
-9	2.789938	2.26893	1.784714	1.385714	1.031648	0.690374	0.353792	0.075646	-0.21022	-0.52677	-0.86965	-1.20135	-1.51313	-1.96483	-2.40017
-6	2.803897	2.318167	1.793632	1.390691	1.020701	0.707795	0.368433	0.062462	-0.23395	-0.5572	-0.90052	-1.23342	-1.54548	-1.97983	-2.41437
-3	2.804148	2.279752	1.778202	1.419015	1.031621	0.724769	0.387017	0.065472	-0.26022	-0.59272	-0.94679	-1.27701	-1.54811	-1.99871	-2.44335
0	2.800494	2.248097	1.731323	1.370472	1.019005	0.761214	0.436183	0.094032	-0.25892	-0.60495	-0.96115	-1.28719	-1.57961	-2.03185	-2.47867
3	2.769129	2.205701	1.647407	1.322671	1.078928	0.797307	0.454465	0.080057	-0.27929	-0.63146	-0.9779	-1.2973	-1.60248	-2.09796	-2.52948
6	2.737199	2.125789	1.492424	1.304426	1.055585	0.726937	0.379569	0.047055	-0.29209	-0.62387	-0.96269	-1.28773	-1.62471	-2.10286	-2.58375
9	2.704452	2.011014	1.547737	1.290778	0.996127	0.673106	0.337323	0.007208	-0.30085	-0.61699	-0.93736	-1.26612	-1.6059	-2.12711	-2.64077
12	2.750876	2.043022	1.504964	1.224239	0.922971	0.624373	0.320179	0.002316	-0.29495	-0.59317	-0.9209	-1.25058	-1.59571	-2.14782	-2.71015
15	2.806039	2.093976	1.507118	1.222902	0.933371	0.621436	0.311034	-0.00362	-0.30448	-0.60682	-0.92954	-1.26227	-1.59103	-2.18889	-2.77791
20	2.928892	2.125526	1.537542	1.236871	0.922692	0.607847	0.294165	0.003385	-0.28529	-0.60101	-0.92858	-1.25406	-1.58917	-2.25611	-2.91641
25	3.035828	2.178674	1.55164	1.210473	0.870165	0.576492	0.288183	0.021977	-0.23136	-0.52854	-0.84666	-1.18326	-1.56464	-2.35706	-3.10591

Table 41: Cp5

Yaw Pitch	-25	-20	-15	-12	-9	-6	-3	0	3	6	9	12	15	20	25
-25	0.646386	0.73019	0.797956	0.829471	0.85072	0.8645	0.875416	0.88171	0.884905	0.887543	0.887959	0.881403	0.866818	0.810639	0.723107
-20	0.72406	0.809425	0.864429	0.891439	0.910361	0.92408	0.933594	0.940084	0.943074	0.944166	0.943773	0.940128	0.929288	0.888045	0.813404
-15	0.777123	0.861499	0.912635	0.933757	0.948544	0.960219	0.968824	0.974409	0.978179	0.978789	0.978444	0.973701	0.964301	0.935224	0.874679
-12	0.801957	0.878097	0.927263	0.948271	0.963551	0.974168	0.981298	0.985648	0.989077	0.989938	0.988828	0.984344	0.976179	0.95038	0.897619
-9	0.818396	0.890065	0.938348	0.958089	0.972882	0.983066	0.989444	0.993438	0.995447	0.996228	0.99516	0.991172	0.983537	0.959161	0.910787
-6	0.823794	0.897822	0.945374	0.964562	0.978817	0.98848	0.994349	0.997478	0.998608	0.999005	0.998043	0.994666	0.987532	0.964172	0.918115
-3	0.826854	0.90032	0.948315	0.967349	0.981193	0.990721	0.996497	0.998885	0.999516	0.999531	0.998866	0.995599	0.988721	0.965159	0.917877
0	0.824694	0.899642	0.947776	0.966745	0.981011	0.990772	0.996581	0.999006	0.999408	0.999348	0.998252	0.994775	0.987582	0.963661	0.914151
3	0.820694	0.895849	0.943528	0.963256	0.977986	0.988323	0.994509	0.99725	0.998466	0.998007	0.996433	0.99192	0.983529	0.957793	0.904679
6	0.808476	0.887288	0.935708	0.956244	0.971551	0.982713	0.989818	0.992931	0.994225	0.993923	0.991632	0.98634	0.977261	0.949724	0.891196
9	0.788373	0.870404	0.922907	0.945208	0.961574	0.973752	0.981279	0.985426	0.986855	0.986422	0.9836	0.977631	0.967396	0.938255	0 873478
12	0.759903	0.849574	0.908611	0.930378	0.948467	0.961449	0.968671	0.973255	0.975034	0.973642	0.970637	0.964612	0.953025	0.919983	0.848158
15	0.732739	0.822054	0.885724	0.911477	0.930735	0.94389	0.950791	0.955409	0.956685	0.955565	0.952343	0.946475	0.933139	0.895979	0.820648
20	0.678509	0.768007	0.831537	0.862039	0.885409	0.899444	0.907277	0.91113	0.91312	0.911197	0.906274	0.897045	0.883575	0.841664	0.762754
25	0.604577	0.689785	0.756503	0.788986	0.818003	0.835722	0.844033	0.848989	0.850189	0.848295	0.840163	0.828088	0.810176	0.76464	0.686544

Table 42: Cpavg

Yaw Pitch	-25	-20	-15	-12	-9	-6	-3	0	3	6	9	12	15	20	25
-25	0.283099	0.324169	0.353786	0.366973	0.378546	0.392599	0.402339	0.408401	0.410538	0.413319	0.415601	0.411568	0.39911	0.371762	0.322627
-20	0.337497	0.404643	0.43225	0.444409	0.459075	0.469394	0.475387	0.481374	0.483323	0.485174	0.483314	0.481092	0.469942	0.433645	0.366774
-15	0.363905	0.44509	0.486234	0.506646	0.514086	0.522876	0.535353	0.536208	0.538616	0.53799	0.53111	0.529462	0.513329	0.464692	0.39546
-12	0.349465	0.43781	0.489739	0.506373	0.530406	0.542299	0.548279	0.549848	0.553348	0.55523	0.547983	0.541494	0.525798	0.474924	0.405457
-9	0.336062	0.423169	0.491088	0.51715	0.528616	0.535851	0.551434	0.55966	0.56182	0.561082	0.5558	0.547079	0.533037	0.482932	0.407739
-6	0.334577	0.419825	0.495116	0.521922	0.53422	0.540393	0.55537	0.567982	0.565121	0.563893	0.5612	0.5531	0.539306	0.492811	0.413758
-3	0.337637	0.430496	0.505034	0.52828	0.539062	0.543838	0.559306	0.568684	0.566843	0.562645	0.561037	0.550526	0.538846	0.489816	0.408483
0	0.340071	0.436839	0.510002	0.534825	0.544561	0.546423	0.560903	0.569899	0.566657	0.559908	0.555156	0.547561	0.534325	0.483865	0.401539
3	0.343602	0.447162	0.518043	0.539147	0.534104	0.549751	0.564476	0.56645	0.562008	0.553476	0.549355	0.539744	0.52396	0.472163	0.392017
6	0.355767	0.460153	0.536661	0.537643	0.539023	0.548906	0.558226	0.55694	0.549576	0.54478	0.53976	0.529322	0.513885	0.465212	0.380854
9	0.375011	0.474475	0.51137	0.525638	0.53552	0.547834	0.549915	0.539766	0.534367	0.528247	0.523707	0.516199	0.500884	0.454557	0.367756
12	0.376955	0.449952	0.488137	0.50543	0.524513	0.538547	0.534349	0.520466	0.514167	0.508136	0.503313	0.498499	0.485238	0.44166	0.356201
15	0.365713	0.422568	0.461337	0.484679	0.506076	0.519031	0.511723	0.499794	0.492615	0.486167	0.481576	0.476943	0.465324	0.432746	0.345859
20	0.332426	0.37734	0.410622	0.433657	0.452809	0.455281	0.447456	0.442789	0.44487	0.440611	0.433503	0.426116	0.415851	0.401229	0.33001
25	0.27753	0.310646	0.345981	0.363559	0.369375	0.368726	0.364439	0.362834	0.366774	0.362751	0.355315	0.352741	0.349313	0.342532	0.291294

Appendix C – Experimental Raw Data (Vanes)

Run No	α (°)	M	h/δ	x/δ	c (mm)	Reδ	ω_{peak} (s^{-1})	Γ (m^2/s)	$R_{0.5}/\delta$	y_{centre} (mm)	ω_{peak} model	% diff	$R_{0.5}/\delta$ model	% diff
111	10	0.0588	0.554	3.855	0.046	62971	791.2	0.1370	0.149	8.5	803.1	1.5	0.1511	1.4
112	15	0.0588	0.554	3.855	0.046	62971	1174.1	0.2352	0.157	14.0	1123.5	4.3	0.1728	7.9
114	20	0.0588	0.554	3.855	0.046	62971	1427.5	0.3578	0.183	20.5	1461.1	2.4	0.1900	6.0
121	10	0.0588	0.916	3.855	0.076	104038	1855.2	0.2541	0.116	5.0	1660.4	10.5	0.1379	4.1
122	15	0.0588	0.916	3.855	0.076	104038	2344.1	0.4119	0.137	10.0	1951.7	16.7	0.1720	14.6
123	18	0.0588	0.916	3.855	0.076	104038	2122.8	0.5559	0.165	14.0	2126.5	0.2	0.1900	3.7
124	20	0.0588	0.916	3.855	0.076	104038	2082.8	0.6547	0.192	16.5	2242.6	7.7	0.2012	0.3
131	10	0.0588	1.277	3.855	0.106	145106	2638.1	0.3883	0.123	2.0	2408.4	8.7	0.1364	0.7
132	15	0.0588	1.277	3.855	0.106	145106	2309.1	0.4711	0.132	5.5	2383.0	3.2	0.1855	14.7
133	18	0.0588	1.277	3.855	0.106	145106	2424.1	0.8212	0.189	9.0	2402.0	0.9	0.2130	2.2
134	20	0.0588	1.277	3.855	0.106	145106	2119.5	0.9730	0.229	12.0	2421.5	14.3	0.2308	4.8
141	10	0.0588	1.639	3.855	0.136	186174	2508.4	0.4150	0.117	-0.5	3235.7	29.0	0.1340	8.0
142	15	0.0588	1.639	3.855	0.136	186174	2457.9	0.6306	0.142	1.0	2699.6	9.8	0.1984	9.4
143	18	0.0588	1.639	3.855	0.136	186174	1651.7	0.8306	0.215	4.0	2518.2	52.5	0.2368	6.7
144	20	0.0588	1.639	3.855	0.136	186174	1484.6	1.0144	0.247	7.5	2427.1	63.5	0.2624	11.3
211	10	0.0588	0.554	12.048	0.046	62971	293.2	0.1268	0.285	19.5	359.5	22.6	0.2019	14.2
212	15	0.0588	0.554	12.048	0.046	62971	447.5	0.2053	0.272	32.5	507.1	13.3	0.2302	5.1
213	18	0.0588	0.554	12.048	0.046	62971	581.9	0.2740	0.266	42.0	597.6	2.7	0.2445	0.5
214	20	0.0588	0.554	12.048	0.046	62971	702.5	0.3197	0.261	49.5	659.5	6.1	0.2531	4.8
221	10	0.0588	0.916	12.048	0.076	104038	945.4	0.2380	0.156	15.0	927.3	1.9	0.1725	3.9
222	15	0.0588	0.916	12.048	0.076	104038	1140.8	0.4018	0.180	28.5	1090.0	4.5	0.2152	1.3
223	18	0.0588	0.916	12.048	0.076	104038	1203.3	0.5434	0.219	39.5	1187.5	1.3	0.2377	1.2
224	20	0.0588	0.916	12.048	0.076	104038	1201.0	0.6477	0.255	49.0	1252.4	4.3	0.2518	4.2
231	10	0.0588	1.277	12.048	0.106	145106	1762.2	0.3399	0.132	11.0	1520.2	13.7	0.1636	4.1
232	15	0.0588	1.277	12.048	0.106	145106	1924.8	0.5852	0.169	25.0	1504.2	21.9	0.2225	12.7
234	20	0.0588	1.25	12.048	0.106	145106	1479.0	0.7859	0.256	44.5	1547.9	4.7	0.2746	5.3
241	10	0.0588	1.639	12.048	0.136	186174	2374.8	0.4607	0.133	7.0	2212.6	6.8	0.1561	1.0
242	15	0.0588	1.639	12.048	0.136	186174	2316.3	0.7820	0.171	19.5	1846.0	20.3	0.2311	11.1
243	18	0.0588	1.639	12.048	0.136	186174	1684.9	1.0486	0.250	30.0	1722.0	2.2	0.2758	2.3
244	20	0.0588	1.639	12.048	0.136	186174	1568.8	1.2593	0.280	39.0	1659.7	5.8	0.3056	4.7
311	10	0.0588	0.55	19.277	0.046	62971	177.7	0.1127	0.376	31.0	222.0	25.0	0.2328	18.3
312	15	0.0588	0.554	19.277	0.046	62971	302.1	0.1854	0.314	47.5	313.6	3.8	0.2654	5.4
313	18	0.0588	0.554	19.277	0.046	62971	393.7	0.2388	0.290	58.5	369.6	6.1	0.2819	1.1
314	20	0.0588	0.554	19.277	0.046	62971	485.6	0.2744	0.272	67.0	407.9	16.0	0.2919	8.5
321	10	0.0588	0.916	19.277	0.076	104038	590.4	0.2310	0.196	25.0	631.3	6.9	0.1971	12.0
322	15	0.0588	0.916	19.277	0.076	104038	851.5	0.3978	0.211	46.0	742.0	12.9	0.2458	0.5
323	18	0.0588	0.916	19.277	0.076	104038	865.5	0.5323	0.263	62.0	808.5	6.6	0.2716	3.3
324	20	0.0588	0.916	19.277	0.076	104038	969.3	0.6290	0.273	75.0	852.7	12.0	0.2876	0.2
331	10	0.0588	1.277	19.277	0.106	145106	1346.3	0.3368	0.146	21.0	1102.5	18.1	0.1842	2.9
332	15	0.0588	1.277	19.277	0.106	145106	1485.3	0.5849	0.184	41.5	1090.9	26.6	0.2504	11.5

Low-Mach Number Vane Test Results (Cont.)

Run No	α (°)	M	h/δ	x/δ	c (mm)	Reδ	ω_{peak} (s^{-1})	Γ (m^2/s)	$R_{0.5}/\delta$	y_{centre} (mm)	ω_{peak} model	% diff	$R_{0.5}/\delta$ model	% diff
333	18	0.0588	1.277	19.277	0.106	145106	1247.1	0.7827	0.260	59.0	1099.6	11.8	0.2876	1.4
334	20	0.0588	1.277	19.277	0.106	145106	1222.1	0.9231	0.290	73.0	1108.6	9.3	0.3115	0.1
341	10	0.0588	1.639	19.277	0.136	186174	1473.7	0.3396	0.129	17.0	1679.5	14.0	0.1733	0.9
342	15	0.0588	1.639	19.277	0.136	186174	1388.9	0.5493	0.168	36.0	1401.2	0.9	0.2566	14.0
343	18	0.0588	1.639	19.277	0.136	186174	984.0	0.7178	0.241	52.0	1307.1	32.8	0.3063	0.2
344	20	0.0588	1.639	19.277	0.136	186174	968.0	0.8648	0.269	65.0	1259.8	30.1	0.3394	0.3
411	10	0.0588	0.55	26.506	0.046	62971	118.5	0.0992	0.462	38.5	152.2	28.4	0.2547	22.2
412	15	0.0588	0.554	26.506	0.046	62971	203.3	0.1608	0.365	55.5	215.3	5.9	0.2905	8.8
413	18	0.0588	0.554	26.506	0.046	62971	270.9	0.2084	0.340	69.0	253.7	6.3	0.3085	1.7
414	20	0.0588	0.554	26.506	0.046	62971	306.0	0.2278	0.319	75.5	279.9	8.5	0.3194	3.4
421	10	0.0588	0.916	26.506	0.076	104038	353.3	0.2175	0.259	33.5	462.3	30.8	0.2171	22.7
422	15	0.0588	0.916	26.506	0.076	104038	621.7	0.3657	0.239	58.5	543.3	12.6	0.2708	1.4
423	18	0.0588	0.916	26.506	0.076	104038	728.8	0.4783	0.263	78.0	592.0	18.8	0.2991	3.2
424	20	0.0588	0.916	26.506	0.076	104038	803.0	0.5603	0.279	91.0	624.3	22.2	0.3168	6.0
431	10	0.0588	1.277	26.506	0.106	145106	1029.2	0.3229	0.162	28.5	842.9	18.1	0.2019	0.7
432	15	0.0588	1.277	26.506	0.106	145106	1215.1	0.5487	0.197	54.5	834.0	31.4	0.2745	14.1
433	18	0.0588	1.277	26.506	0.106	145106	1018.6	0.7412	0.281	75.5	840.6	17.5	0.3152	3.2
434	20	0.0588	1.277	26.506	0.106	145106	1045.2	0.8849	0.306	93.0	847.4	18.9	0.3415	3.7
441	10	0.0588	1.639	26.506	0.136	186174	1722.2	0.4147	0.139	25.5	1326.3	23.0	0.1887	7.4
442	15	0.0588	1.639	26.506	0.136	186174	1201.1	0.5306	0.175	51.5	1106.6	7.9	0.2793	17.4
443	18	0.0588	1.639	26.506	0.136	186174	1163.0	1.0046	0.302	73.0	1032.2	11.2	0.3335	0.2
444	20	0.0588	1.639	26.506	0.136	186174	1152.7	1.1985	0.349	89.0	994.9	13.7	0.3695	1.2

High-Mach Number Vane Test Results

Run No	α (°)	M	h/δ	x/δ	c (mm)	Reδ	ω_{peak} (s^{-1})	Γ (m^2/s)	$R_{0.5}/\delta$	y_{centre} (mm)	ω_{peak} model	% diff	$R_{0.5}/\delta$ model	% diff
v01	15	0.4481	0.75	8.75	0.03	186800	11760.0	1.0918	0.203	5.7	14587.2	24.0	0.2141	5.4
v02	15	0.5920	0.75	8.75	0.03	223200	17530.0	1.4630	0.206	5.8	18840.7	7.5	0.2165	0.9
v03	15	0.7434	0.75	8.75	0.03	249200	24540.0	1.9307	0.180	6.0	23212.6	5.4	0.2186	4.9
v04	20	0.4502	0.75	8.75	0.03	182700	15830.0	1.9619	0.249	11.8	17816.3	12.5	0.2435	6.9
v05	20	0.6015	0.75	8.75	0.03	223300	21780.0	2.5416	0.249	12.2	23249.7	6.7	0.2464	2.9
v06	20	0.7545	0.75	8.75	0.03	251200	29130.0	3.1750	0.236	13.3	28614.9	1.8	0.2487	1.4
v07	15	0.4490	0.75	16.25	0.03	181800	7057.0	1.0350	0.281	12.7	8908.8	26.2	0.2544	10.6
v08	15	0.5930	0.75	16.25	0.03	212100	10580.0	1.4024	0.264	12.7	11503.1	8.7	0.2573	4.9
v09	15	0.7486	0.75	16.25	0.03	241900	15590.0	1.8087	0.234	13.5	14240.9	8.7	0.2598	2.7
v10	20	0.4536	0.75	16.25	0.03	178000	10970.0	1.8253	0.279	23.2	10936.2	0.3	0.2894	4.5
v11	20	0.6050	0.75	16.25	0.03	217600	15530.0	2.3362	0.264	23.7	14248.7	8.3	0.2928	1.7
v12	20	0.7524	0.75	16.25	0.03	243700	21970.0	2.9116	0.245	24.0	17399.2	20.8	0.2955	9.3
v13	15	0.4559	0.75	23.75	0.03	184400	5165.0	1.0396	0.351	18.8	6175.4	19.6	0.2856	14.3
v14	15	0.5977	0.75	23.75	0.03	211000	7611.0	1.3752	0.319	18.8	7919.8	4.1	0.2888	8.5
v15	15	0.7521	0.75	23.75	0.03	239000	11680.0	1.7163	0.289	19.0	9775.6	16.3	0.2916	2.4
v16	20	0.4676	0.75	23.75	0.03	191600	5661.0	1.0684	0.286	31.3	7687.1	35.8	0.3252	0.8
v17	20	0.6027	0.75	23.75	0.03	226400	7685.0	1.3991	0.263	31.0	9705.3	26.3	0.3285	3.7
v18	20	0.7551	0.75	23.75	0.03	257200	10950.0	1.7259	0.253	30.2	11931.8	9.0	0.3317	12.5

Appendix D – Experimental Raw Data (Air-jets)

Low-Mach Number Air-jet Test Results

Run No	δ	D/δ	α	β	*MR*	M	x/δ	Reδ	ωpeak	$R_{0.5}$/δ	ycentre (mm)	zcentre (mm)	ωpeak (model)	% diff	$R_{0.5}$/δ (model)	% diff
1	41.5	0.0964	30	30	0.7	0.0588	3.855	5476	52.9	0.116	4.0	4.8	49.8	5.9	0.128	10.0
2	41.5	0.0964	30	30	1.0	0.0588	3.855	5476	132.1	0.138	6.6	4.2	127.9	3.2	0.132	4.2
3	41.5	0.0964	30	30	1.3	0.0588	3.855	5476	208.5	0.145	8.4	4.8	206.0	1.2	0.137	5.8
4	41.5	0.0964	30	30	1.6	0.0588	3.855	5476	262.9	0.145	8.6	6.8	284.0	8.0	0.141	2.6
5	41.5	0.0964	30	45	0.7	0.0588	3.855	5476	80.27	0.128	5.2	4.8	78.5	2.2	0.134	4.4
6	41.5	0.0964	30	45	1.0	0.0588	3.855	5476	176.2	0.138	9.4	4.4	170.8	3.1	0.138	0.0
7	41.5	0.0964	30	45	1.3	0.0588	3.855	5476	275.5	0.150	10.8	5.6	263.0	4.5	0.143	4.6
8	41.5	0.0964	30	45	1.6	0.0588	3.855	5476	359.3	0.157	12.8	8.2	355.3	1.1	0.148	5.8
9	41.5	0.0964	30	60	0.7	0.0588	3.855	5476	94.44	0.131	7.0	4.8	94.1	0.4	0.138	5.6
10	41.5	0.0964	30	60	1.0	0.0588	3.855	5476	204.1	0.149	10.4	5.2	201.0	1.5	0.143	3.8
11	41.5	0.0964	30	60	1.3	0.0588	3.855	5476	319	0.150	14.0	7.0	308.0	3.5	0.148	1.4
12	41.5	0.0964	30	60	1.6	0.0588	3.855	5476	440	0.159	15.2	8.8	414.9	5.7	0.153	4.0
13	41.5	0.0964	45	30	0.7	0.0588	3.855	5476	52.52	0.125	2.8	5.0	42.8	18.5	0.133	6.0
14	41.5	0.0964	45	30	1.0	0.0588	3.855	5476	113.5	0.147	3.8	5.2	108.8	4.1	0.138	6.5
15	41.5	0.0964	45	30	1.3	0.0588	3.855	5476	167.4	0.141	3.8	5.4	174.8	4.4	0.142	1.0
16	41.5	0.0964	45	30	1.6	0.0588	3.855	5476	237.1	0.153	3.2	8.8	240.8	1.6	0.147	4.2
17	41.5	0.0964	45	45	0.7	0.0588	3.855	5476	72.76	0.141	4.2	5.0	67.7	7.0	0.139	1.4
18	41.5	0.0964	45	45	1.0	0.0588	3.855	5476	138.6	0.146	6.0	5.2	142.5	2.8	0.144	1.2
19	41.5	0.0964	45	45	1.3	0.0588	3.855	5476	213.6	0.153	6.2	6.0	217.4	1.8	0.149	3.0
20	41.5	0.0964	45	45	1.6	0.0588	3.855	5476	307.1	0.163	5.6	9.0	292.2	4.8	0.154	5.9
21	41.5	0.0964	45	60	0.7	0.0588	3.855	5476	86.92	0.142	5.2	5.2	78.6	9.6	0.144	0.9
22	41.5	0.0964	45	60	1.0	0.0588	3.855	5476	165.9	0.139	8.2	5.0	162.6	2.0	0.149	7.1
23	41.5	0.0964	45	60	1.3	0.0588	3.855	5476	246.4	0.158	7.8	7.0	246.7	0.1	0.154	2.7
24	41.5	0.0964	45	60	1.6	0.0588	3.855	5476	359.3	0.163	8.4	9.4	330.7	8.0	0.159	2.7
63	41.5	0.0964	60	30	0.7	0.0588	3.855	5476	31.35	0.144	1.0	5.6	27.6	11.8	0.137	4.8
64	41.5	0.0964	60	30	1.0	0.0588	3.855	5476	73.93	0.142	-0.2	5.2	78.1	5.6	0.142	0.2
65	41.5	0.0964	60	30	1.3	0.0588	3.855	5476	114.4	0.135	0.2	6.0	128.5	12.3	0.147	8.3
66	41.5	0.0964	60	30	1.6	0.0588	3.855	5476	158.2	0.149	0.2	8.4	178.9	13.1	0.151	1.6
68	41.5	0.0964	60	45	1.0	0.0588	3.855	5476	82.16	0.142	0.8	6.6	97.3	18.4	0.148	4.7
69	41.5	0.0964	60	45	1.3	0.0588	3.855	5476	132.3	0.141	2.8	5.6	149.5	13.0	0.153	9.2
70	41.5	0.0964	60	45	1.6	0.0588	3.855	5476	202.5	0.155	2.0	9.0	201.7	0.4	0.158	2.1
71	41.5	0.0964	60	45	0.7	0.0588	3.855	5476	47.55	0.141	1.2	5.8	45.1	5.2	0.143	1.7
72	41.5	0.0964	60	60	0.7	0.0588	3.855	5476	48.74	0.143	1.4	7.0	47.6	2.3	0.148	3.7
73	41.5	0.0964	60	60	1.0	0.0588	3.855	5476	102.5	0.135	3.8	5.2	101.8	0.7	0.153	13.8
74	41.5	0.0964	60	60	1.3	0.0588	3.855	5476	152.2	0.142	4.6	5.2	155.9	2.5	0.159	12.1
75	41.5	0.0964	60	60	1.6	0.0588	3.855	5476	145.7	0.153	4.2	6.2	210.1	44.2	0.164	6.8
134	41.5	0.0964	30	30	2.0	0.0588	3.855	5476	376.8	0.158	6.8	10.0	388.1	3.0	0.147	7.0
135	41.5	0.0964	30	45	2.0	0.0588	3.855	5476	527.7	0.161	11.2	10.0	478.3	9.4	0.154	4.5
136	41.5	0.0964	30	60	2.0	0.0588	3.855	5476	578.1	0.179	14.6	10.4	557.5	3.6	0.159	10.9
137	41.5	0.0964	45	30	2.0	0.0588	3.855	5476	347.2	0.153	2.8	10.2	328.8	5.3	0.153	0.0
138	41.5	0.0964	45	45	2.0	0.0588	3.855	5476	439.8	0.163	5.2	10.6	392.1	10.9	0.160	1.8
140	41.5	0.0964	60	60	2.0	0.0588	3.855	5476	245.6	0.149	0.0	10.0	282.3	15.0	0.171	14.9
141	41.5	0.0964	60	30	2.0	0.0588	3.855	5476	290.4	0.151	2.4	9.8	246.2	15.2	0.158	4.5
142	41.5	0.0964	60	45	2.0	0.0588	3.855	5476	321.2	0.171	4.2	9.6	271.3	15.5	0.165	3.4
143	41.5	0.0964	45	60	2.0	0.0588	3.855	5476	521.7	0.160	9.0	10.2	442.8	15.1	0.166	3.6
25	41.5	0.1928	30	30	0.7	0.0588	3.855	10951	155	0.149	8.6	4.6	154.6	0.3	0.147	1.5
27	41.5	0.1928	30	30	1.3	0.0588	3.855	10951	477.3	0.165	12.6	9.4	451.2	5.5	0.157	5.0

Low-Mach Number Air-jet Test Results (Cont.)

Run No.	δ	D/δ	α	β	*MR*	M	x/δ	Reδ	ωpeak	$R_{0.5}$/δ	ycentre (mm)	zcentre (mm)	ωpeak (model)	% diff	$R_{0.5}$/δ (model)	% diff
28	41.5	0.1928	30	30	1.6	0.0588	3.855	10951	584.4	0.173	12.8	10.2	599.5	2.6	0.162	6.4
29	41.5	0.1928	30	45	0.7	0.0588	3.855	10951	205	0.150	11.6	5.2	202.2	1 4	0.153	2.0
30	41.5	0.1928	30	45	1.0	0.0588	3.855	10951	427	0.159	15.8	8.4	389.5	8.8	0.159	0.3
31	41.5	0.1928	30	45	1.3	0.0588	3.855	10951	666	0.164	19.4	9.6	576.9	13.4	0.164	0.0
32	41.5	0.1928	30	45	1.6	0.0588	3.855	10951	797.1	0.178	20.2	10.2	764.2	4.1	0.170	4.5
33	41.5	0.1928	30	60	0.7	0.0588	3.855	10951	238.1	0.163	14.8	5.2	226.5	4.9	0.159	3.0
34	41.5	0.1928	30	60	1.0	0.0588	3.855	10951	502.1	0.169	20.2	8.8	453.3	9.7	0.164	3.1
35	41.5	0.1928	30	60	1.3	0.0588	3.855	10951	969.9	0.169	25.6	10.6	680.2	29.9	0.170	0.3
36	41.5	0.1928	30	60	1.6	0.0588	3.855	10951	799.5	0.161	24.4	9.8	907.0	13.4	0.175	8.7
37	41.5	0.1928	45	30	0.7	0.0588	3.855	10951	125.6	0.144	4.6	4.8	122.6	2.4	0.153	6.0
38	41.5	0.1928	45	30	1.0	0.0588	3.855	10951	231.3	0.162	5.4	8.0	247.7	7.1	0.158	2.6
39	41.5	0.1928	45	30	1.3	0.0588	3.855	10951	366.7	0.175	6.0	9.6	372.7	1.6	0.163	6.7
40	41.5	0.1928	45	30	1.6	0.0588	3.855	10951	475.8	0.173	5.2	12.2	497.7	4.6	0.169	2.1
42	41.5	0.1928	45	45	0.7	0.0588	3.855	10951	152.8	0.151	8.0	5.2	161.8	5.9	0.160	6.1
43	41.5	0.1928	45	45	1.0	0.0588	3.855	10951	300.2	0.156	10.0	8.2	314.8	4.9	0.165	6.3
44	41.5	0.1928	45	45	1.3	0.0588	3.855	10951	474	0.176	11.2	9.6	467.8	1.3	0.171	2.6
45	41.5	0.1928	45	45	1.6	0.0588	3.855	10951	586.3	0.188	11.0	11.4	620.8	5.9	0.177	6.1
47	41.5	0.1928	45	60	0.7	0.0588	3.855	10951	172.3	0.171	10.0	5.2	176.0	2.2	0.165	3.2
48	41.5	0.1928	45	60	1.0	0.0588	3.855	10951	355.1	0.184	14.4	8.8	357.3	0.6	0.171	6.9
49	41.5	0.1928	45	60	1.3	0.0588	3.855	10951	561.7	0.183	15.8	9.8	538.7	4.1	0.177	3.6
50	41.5	0.1928	45	60	1.6	0.0588	3.855	10951	693.7	0.180	16.0	11.6	720.0	3.8	0.183	1.5
51	41.5	0.1928	60	30	0.7	0.0588	3.855	10951	97.91	0.145	2.8	6.2	74.4	24.0	0.157	8.2
52	41.5	0.1928	60	30	1.0	0.0588	3.855	10951	192.4	0.163	1.6	8.8	169.1	12.1	0.163	0.1
53	41.5	0.1928	60	30	1.3	0.0588	3.855	10951	280.5	0.145	4.0	10.0	263.9	5.9	0.168	16.5
54	41.5	0.1928	60	30	1.6	0.0588	3.855	10951	443.8	0.170	0.0	14.6	358.7	19.2	0.174	2.4
55	41 5	0.1928	60	45	0.7	0.0588	3.855	10951	115.9	0.152	4.6	5.6	97.7	15.7	0.165	8.5
56	41.5	0.1928	60	45	1.0	0.0588	3.855	10951	228.8	0.184	5.0	8.8	205.9	10.0	0.170	7.3
57	41.5	0.1928	60	45	1.3	0.0588	3.855	10951	375.3	0.178	5.0	10.0	314.1	16.3	0.176	0.9
58	41.5	0.1928	60	45	1.6	0.0588	3.855	10951	486.8	0.180	4.2	13.8	422.3	13.2	0.182	1.4
59	41.5	0.1928	60	60	0.7	0.0588	3.855	10951	117.5	0.169	5.0	6.4	94.7	19.4	0.170	0.5
60	41.5	0.1928	60	60	1.0	0.0588	3.855	10951	239.4	0.198	7.4	8.6	216.5	9.6	0.176	11.1
61	41.5	0.1928	60	60	1.3	0.0588	3.855	10951	384.8	0.203	8.6	10.0	338.4	12.1	0.182	10.2
62	41.5	0.1928	60	60	1.6	0.0588	3.855	10951	482.7	0.205	7.4	13.6	460.2	4.7	0.188	8.0
125	41.5	0.1928	30	30	2.0	0.0588	3.855	10951	627.2	0.181	11.2	11.6	797.2	27.1	0.169	6.4
126	41 5	0.1928	30	45	2.0	0.0588	3.855	10951	964	0.183	19.8	13.6	1013.9	5.2	0.177	3.3
127	41.5	0.1928	30	60	2.0	0.0588	3.855	10951	1107	0.187	26.6	13.6	1209.5	9.3	0.183	2.3
128	41.5	0.1928	45	30	2.0	0.0588	3.855	10951	715.4	0.164	1.8	19.6	664.5	7.1	0.176	7.7
129	41.5	0.1928	45	45	2.0	0.0588	3.855	10951	855.2	0.169	6.8	18.2	824.8	3.6	0.184	9.1
130	41.5	0.1928	45	60	2.0	0.0588	3.855	10951	955.2	0.176	12.0	17.0	961.8	0.7	0.190	8.2
131	41.5	0.1928	60	30	2.0	0.0588	3.855	10951	539.4	0.168	-1.8	20.0	485.0	10.1	0.181	7.7
132	41 5	0.1928	60	45	2.0	0.0588	3.855	10951	578.4	0.194	2.0	18.2	566.6	2.0	0.190	2.1
133	41.5	0.1928	60	60	2.0	0.0588	3.855	10951	613.2	0.205	5.2	17.4	622.6	1.5	0.196	4 3
76	41.5	0.2892	30	30	0.7	0.0588	3.855	16427	247.6	0.167	10.6	8.4	259.4	4.8	0.166	0.7
77	41.5	0.2892	30	30	1.0	0.0588	3.855	16427	528	0.164	16.2	9.6	477.9	9.5	0.171	4 2
78	41 5	0.2892	30	30	1.3	0.0588	3.855	16427	699.9	0.175	17.6	10.6	696 4	0.5	0.177	1.6
79	41 5	0.2892	30	30	1.6	0.0588	3.855	16427	819.7	0.182	15.6	14 4	914.9	11.6	0.183	0 4
80	41 5	0.2892	30	45	0.7	0.0588	3.855	16427	313.9	0.182	15.0	7 8	326.0	3.8	0.173	5.0
81	41.5	0.2892	30	45	1.0	0.0588	3.855	16427	721.6	0.164	23 4	9.8	608.3	15.7	0.179	9.6

Low-Mach Number Air-jet Test Results (Cont.)

Run No.	δ	D/δ	α	β	*MR*	M	x/δ	Reδ	ωpeak	R0.5/δ	ycentre (mm)	zcentre (mm)	ωpeak (model)	% diff	R0.5/δ (model)	% diff
82	41.5	0.2892	30	45	1.3	0.0588	3.855	16427	979.3	0.176	25.2	11.0	890.7	9.0	0.186	5.5
83	41.5	0.2892	30	45	1.6	0.0588	3.855	16427	1090	0.192	25.6	14.2	1173.1	7.6	0.192	0.0
84	41.5	0.2892	30	60	0.7	0.0588	3.855	16427	333.6	0.216	19.4	8.4	358.8	7.6	0.179	17.2
85	41.5	0.2892	30	60	1.0	0.0588	3.855	16427	790.7	0.179	28.8	10.0	705.6	10.8	0.186	3.5
86	41.5	0.2892	30	60	1.3	0.0588	3.855	16427	1070	0.180	31.8	11.6	1052.4	1.6	0.192	6.4
87	41.5	0.2892	30	60	1.6	0.0588	3.855	16427	1263	0.192	34.4	14.4	1399.1	10.8	0.198	3.2
88	41.5	0.2892	45	30	0.7	0.0588	3.855	16427	180.5	0.171	5.8	6.8	202.5	12.2	0.172	0.9
89	41.5	0.2892	45	30	1.0	0.0588	3.855	16427	405.8	0.181	9.6	9.4	386.5	4.7	0.179	1.1
90	41.5	0.2892	45	30	1.3	0.0588	3.855	16427	582.7	0.183	9.8	11.2	570.6	2.1	0.185	1.0
91	41.5	0.2892	45	30	1.6	0.0588	3.855	16427	737	0.182	7.2	15.8	754.7	2.4	0.191	5.1
92	41.5	0.2892	45	45	0.7	0.0588	3.855	16427	212.4	0.203	10.6	7.2	255.8	20.5	0.180	11.3
93	41.5	0.2892	45	45	1.0	0.0588	3.855	16427	495.8	0.199	15.4	9.6	487.0	1.8	0.187	6.0
94	41.5	0.2892	45	45	1.3	0.0588	3.855	16427	737.3	0.188	15.6	11.8	718.2	2.6	0.193	2.8
95	41.5	0.2892	45	45	1.6	0.0588	3.855	16427	934.3	0.186	14.6	15.2	949.3	1.6	0.200	7.2
96	41.5	0.2892	45	60	0.7	0.0588	3.855	16427	214.4	0.230	13.0	7.6	273.5	27.6	0.187	19.0
97	41.5	0.2892	45	60	1.0	0.0588	3.855	16427	542.8	0.227	21.8	9.8	552.1	1.7	0.193	15.1
98	41.5	0.2892	45	60	1.3	0.0588	3.855	16427	791.2	0.203	20.2	12.6	830.7	5.0	0.200	1.3
99	41.5	0.2892	45	60	1.6	0.0588	3.855	16427	1015	0.198	20.2	15.6	1109.3	9.3	0.206	4.2
100	41.5	0.2892	60	30	0.7	0.0588	3.855	16427	118.4	0.156	2.2	9.0	121.1	2.3	0.178	13.7
101	41.5	0.2892	60	30	1.0	0.0588	3.855	16427	259.9	0.182	5.2	9.4	260.2	0.1	0.184	1.2
102	41.5	0.2892	60	30	1.3	0.0588	3.855	16427	395.7	0.190	4.8	11.6	399.3	0.9	0.190	0.1
103	41.5	0.2892	60	30	1.6	0.0588	3.855	16427	539.5	0.191	2.6	16.8	538.4	0.2	0.197	2.8
104	41.5	0.2892	60	45	0.7	0.0588	3.855	16427	140.6	0.183	5.4	8.8	150.4	7.0	0.186	1.9
105	41.5	0.2892	60	45	1.0	0.0588	3.855	16427	297.3	0.222	9.4	9.4	314.6	5.8	0.193	13.2
106	41.5	0.2892	60	45	1.3	0.0588	3.855	16427	460.7	0.214	10.0	11.4	478.8	3.9	0.199	7.0
107	41.5	0.2892	60	45	1.6	0.0588	3.855	16427	607.7	0.212	7.0	16.6	643.0	5.8	0.206	2.8
108	41.5	0.2892	60	60	0.7	0.0588	3.855	16427	150.4	0.198	6.6	8.6	141.8	5.7	0.192	3.1
109	41.5	0.2892	60	60	1.0	0.0588	3.855	16427	304.3	0.256	12.0	9.6	331.3	8.9	0.199	22.2
110	41.5	0.2892	60	60	1.3	0.0588	3.855	16427	498.8	0.235	14.0	11.0	520.8	4.4	0.206	12.4
111	41.5	0.2892	60	60	1.6	0.0588	3.855	16427	661.1	0.225	11.4	15.8	710.3	7.4	0.213	5.5
144	41.5	0.2892	30	30	2.0	0.0588	3.855	16427	1015	0.183	15.0	18.8	1206.2	18.8	0.191	4.5
145	41.5	0.2892	30	45	2.0	0.0588	3.855	16427	1265	0.197	25.2	17.0	1549.6	22.5	0.200	1.4
146	41.5	0.2892	30	60	2.0	0.0588	3.855	16427	1438	0.206	35.2	17.4	1861.4	29.4	0.207	0.3
148	41.5	0.2892	45	30	2.0	0.0588	3.855	16427	1026	0.177	5.0	22.4	1000.1	2.5	0.199	12.2
149	41.5	0.2892	45	45	2.0	0.0588	3.855	16427	1182	0.183	11.8	21.0	1257.5	6.4	0.208	13.6
150	41.5	0.2892	45	60	2.0	0.0588	3.855	16427	1259	0.197	19.0	20.4	1480.7	17.6	0.215	9.1
151	41.5	0.2892	60	30	2.0	0.0588	3.855	16427	808.2	0.183	-0.6	24.8	723.9	10.4	0.205	12.0
152	41.5	0.2892	60	45	2.0	0.0588	3.855	16427	907.6	0.192	4.4	23.8	861.9	5.0	0.214	11.6
153	41.5	0.2892	60	60	2.0	0.0588	3.855	16427	918.5	0.218	9.0	22.4	962.9	4.8	0.222	1.9
156	41.5	0.0964	30	30	1.3	0.0588	12.048	5476	73.49	0.203	12.6	9.8	73.9	0.5	0.184	9.1
157	41.5	0.0964	30	30	2.0	0.0588	12.048	5476	144	0.219	16.4	10.6	139.2	3.3	0.198	9.4
160	41.5	0.0964	30	45	1.3	0.0588	12.048	5476	94.92	0.242	17.8	10.0	94.3	0.6	0.193	20.5
159	41.5	0.0964	30	45	2.0	0.0588	12.048	5476	181.4	0.242	24.0	11.4	171.5	5.4	0.208	14.2
161	41.5	0.0964	30	60	1.3	0.0588	12.048	5476	101.9	0.230	20.2	10.4	110.4	8.4	0.199	13.4
162	41.5	0.0964	30	60	2.0	0.0588	12.048	5476	201	0.255	26.0	12.4	199.9	0.5	0.215	15.7
163	41.5	0.0964	45	30	1.3	0.0588	12.048	5476	69.41	0.193	7.0	10.2	62.7	9.7	0.192	0.4
164	41.5	0.0964	45	30	2.0	0.0588	12.048	5476	126.4	0.221	10.6	11.2	117.9	6.7	0.207	6.4
165	41.5	0.0964	45	45	1.3	0.0588	12.048	5476	85.53	0.201	12.6	10.0	78.0	8.9	0.201	0.4

Low-Mach Number Air-jet Test Results (Cont.)

Run No.	δ	D/δ	α	β	*MR*	M	x/δ	Reδ	ω_{peak}	$R_{0.5}/\delta$	y_{centre} (mm)	z_{centre} (mm)	ω_{peak} (model)	% diff	$R_{0.5}/\delta$ (model)	% diff
166	41.5	0.0964	45	45	2.0	0.0588	12.048	5476	143.9	0.266	15.6	11.2	140.6	2.3	0.216	18.7
167	41.5	0.0964	60	30	1.3	0.0588	12.048	5476	48.54	0.165	2.8	10.2	46.1	5.1	0.198	19.7
168	41.5	0.0964	60	30	2.0	0.0588	12.048	5476	85.27	0.211	4.6	10.6	88.3	3.5	0.213	0.8
169	41.5	0.0964	60	45	1.3	0.0588	12.048	5476	56.04	0.190	6.4	10.0	53.6	4.3	0.207	8.6
170	41.5	0.0964	60	45	2.0	0.0588	12.048	5476	98.08	0.248	9.2	10.8	97.3	0.8	0.223	10.1
171	41.5	0.0964	60	60	1.3	0.0588	12.048	5476	57.11	0.207	8.4	10.0	55.9	2.1	0.214	3.5
172	41.5	0.0964	60	60	2.0	0.0588	12.048	5476	109.3	0.248	13.6	10.4	101.3	7.4	0.230	7.1
173	41.5	0.0964	45	60	1.3	0.0588	12.048	5476	86.85	0.216	15.6	9.8	88.5	1.9	0.207	4.0
174	41.5	0.0964	45	60	2.0	0.0588	12.048	5476	170	0.257	18.6	11.4	158.8	6.6	0.223	13.2
175	41.5	0.1928	30	30	1.3	0.0588	12.048	10951	181.3	0.244	25.2	10.6	161.8	10.8	0.212	13.4
176	41.5	0.1928	30	30	2.0	0.0588	12.048	10951	286.3	0.290	23.4	15.8	285.9	0.1	0.228	21.3
177	41.5	0.1928	30	45	1.3	0.0588	12.048	10951	239.2	0.226	33.8	11.4	206.9	13.5	0.221	2 2
178	41.5	0.1928	30	45	2.0	0.0588	12.048	10951	459.1	0.237	39.4	15.6	363.6	20.8	0.238	0.5
179	41.5	0.1928	30	60	1.3	0.0588	12.048	10951	262.1	0.252	40.0	12.6	243.9	6.9	0.229	9.1
180	41.5	0.1928	30	60	2.0	0.0588	12.048	10951	544.7	0.237	49.4	17.4	433.7	20.4	0.247	4.0
181	41 5	0.1928	45	30	1.3	0.0588	12.048	10951	151.7	0.257	13.6	11.6	133.7	11.9	0.220	14.1
182	41.5	0.1928	45	30	2.0	0.0588	12.048	10951	259.9	0.252	9.2	23.2	238.3	8.3	0.237	5.7
183	41.5	0.1928	45	45	1.3	0.0588	12.048	10951	182.9	0.271	20.6	12.4	167.8	8 3	0.231	14.9
184	41.5	0.1928	45	45	2.0	0.0588	12.048	10951	357.6	0.248	16.6	20.0	295.8	17.3	0.248	0.2
185	41.5	0.1928	45	60	1.3	0.0588	12.048	10951	217	0.265	27.8	12.2	193.2	11.0	0.238	10.1
186	41.5	0.1928	45	60	2.0	0.0588	12.048	10951	400	0.274	26.8	18.8	344.9	13.8	0.257	6.2
187	41.5	0.1928	60	30	1.3	0.0588	12.048	10951	108.9	0.240	10.0	11.2	94.6	13.1	0.227	5.3
188	41.5	0.1928	60	30	2.0	0.0588	12.048	10951	178.3	0.278	4.6	20.4	173.9	2.4	0.245	12.1
189	41.5	0.1928	60	45	1.3	0.0588	12.048	10951	135.7	0.267	16.2	11.2	112.7	17.0	0.238	11.0
190	41.5	0.1928	60	45	2.0	0.0588	12.048	10951	203.5	0.310	13.0	19.0	203.2	0.2	0.256	17.6
191	41.5	0.1928	60	60	1.3	0.0588	12.048	10951	146.4	0.287	19.6	11.6	121.3	17.1	0.246	14.6
192	41.5	0.1928	60	60	2.0	0.0588	12.048	10951	230.7	0.315	17.0	19.0	223.3	3.2	0.265	16.0
193	41.5	0.2892	30	30	1 3	0.0588	12.048	16427	310.9	0.240	33.2	14.6	249.7	19.7	0.239	0.4
194	41.5	0.2892	30	30	2.0	0.0588	12.048	16427	413.4	0.298	30.0	20.4	432.6	4.6	0.257	13.6
195	41.5	0.2892	30	45	1.3	0.0588	12.048	16427	454.1	0.226	45.4	15.4	319.4	29.7	0.250	10.8
196	41.5	0.2892	30	45	2.0	0.0588	12.048	16427	638.3	0.257	49.0	20.4	555.7	12.9	0.269	4.9
197	41.5	0.2892	30	60	1.3	0.0588	12.048	16427	492.1	0.230	54.0	16.0	377.4	23.3	0.259	12.2
198	41.5	0.2892	30	60	2.0	0.0588	12.048	16427	861.3	0.238	64.2	21.0	667.6	22.5	0.279	17.2
199	41.5	0.2892	45	30	1.3	0.0588	12.048	16427	239.6	0.264	23.6	14.0	204.6	14.6	0.249	5.8
200	41.5	0.2892	45	30	2.0	0.0588	12.048	16427	415	0.244	14.4	24.6	358.6	13.6	0.268	9.7
201	41.5	0.2892	45	45	1.3	0.0588	12.048	16427	313.4	0.264	33.4	15.0	257.5	17.8	0.260	1.5
202	41.5	0.2892	45	45	2.0	0.0588	12.048	16427	536.4	0.252	26.8	23.6	451.0	15.9	0.280	11 3
203	41 5	0.2892	45	60	1.3	0.0588	12.048	16427	327.9	0.301	40.2	16.4	297.9	9.2	0.269	10.5
204	41.5	0.2892	45	60	2.0	0.0588	12.048	16427	605.9	0.272	35.8	24.4	531.0	12.4	0.290	6.8
205	41.5	0.2892	60	30	1.3	0.0588	12.048	16427	129	0.315	12.8	13.6	143.2	11.0	0.256	18.5
206	41.5	0.2892	60	30	2.0	0.0588	12.048	16427	269.7	0.277	3.8	28.8	259.6	3 7	0.276	0.1
207	41.5	0.2892	60	45	1 3	0.0588	12.048	16427	163.5	0.332	21.4	13.0	171.7	5.0	0.268	19.2
208	41.5	0.2892	60	45	2.0	0.0588	12.048	16427	325.3	0.293	12.8	25.4	309.1	5.0	0.289	1 2
209	41 5	0.2892	60	60	1.3	0.0588	12.048	16427	176.4	0.359	29.4	13.4	186.8	5.9	0.277	22 6
210	41 5	0.2892	60	60	2.0	0.0588	12.048	16427	368.8	0.313	20.0	25 4	345 3	6.4	0.299	4 5
213	41 5	0.0964	30	30	1 3	0.0588	19.277	5476	51 22	0.198	15.2	10.0	48.4	5 5	0.226	14 3
214	41 5	0.0964	30	30	2 0	0.0588	19.277	5476	85.79	0.270	21 4	11.2	91.2	6.3	0 244	9.8
215	41 5	0.0964	30	45	1.3	0.0588	19.277	5476	59.99	0.193	22.8	10.2	61.8	3.0	0.237	22 6

Low-Mach Number Air-jet Test Results (Cont.)

Run No	δ	D/δ	α	β	*MR*	M	x/δ	Reδ	ω_{peak}	$R_{0.5}/\delta$	y_{centre} (mm)	z_{centre} (mm)	ω_{peak} (model)	% diff	$R_{0.5}/\delta$ (model)	% diff
216	41.5	0.0964	30	45	2.0	0.0588	19.277	5476	101.9	0.293	29.2	12.8	112.4	10.3	0.255	13.1
217	41.5	0.0964	30	60	1.3	0.0588	19.277	5476	61.28	0.245	25.0	11.2	72.4	18.1	0.245	0.0
218	41.5	0.0964	30	60	2.0	0.0588	19.277	5476	117.7	0.288	33.8	13.8	131.0	11.3	0.263	8.5
219	41.5	0.0964	45	30	1.3	0.0588	19.277	5476	44.41	0.172	14.4	10.4	41.1	7.5	0.235	36.9
220	41.5	0.0964	45	30	2.0	0.0588	19.277	5476	81.43	0.253	14.8	12.4	77.3	5.1	0.254	0.2
221	41.5	0.0964	45	45	1.3	0.0588	19.277	5476	54.3	0.183	18.2	10.2	51.1	5.9	0.246	34.6
222	41.5	0.0964	45	45	2.0	0.0588	19.277	5476	91.59	0.274	20.2	12.0	92.1	0.6	0.265	3.2
223	41.5	0.0964	45	60	1.3	0.0588	19.277	5476	57.71	0.212	19.8	10.6	57.9	0.4	0.255	20.2
224	41.5	0.0964	45	60	2.0	0.0588	19.277	5476	94.56	0.307	22.2	13.4	104.0	10.0	0.274	10.7
225	41.5	0.0964	60	30	1.3	0.0588	19.277	5476	30.78	0.213	9.2	12.4	30.2	1.9	0.243	13.7
226	41.5	0.0964	60	30	2.0	0.0588	19.277	5476	60.93	0.242	9.0	11.4	57.8	5.1	0.261	8.0
227	41.5	0.0964	60	45	1.3	0.0588	19.277	5476	30.09	0.242	9.0	19.0	35.1	16.7	0.254	4.9
228	41.5	0.0964	60	45	2.0	0.0588	19.277	5476	70.59	0.240	14.2	10.8	63.7	9.7	0.273	14.0
229	41.5	0.0964	60	60	1.3	0.0588	19.277	5476	34.69	0.317	13.6	18.8	36.6	5.6	0.263	17.2
230	41.5	0.0964	60	60	2.0	0.0588	19.277	5476	72.02	0.272	15.2	11.0	66.3	7.9	0.283	4.0
231	41.5	0.1928	30	30	1.3	0.0588	19.277	10951	101.4	0.267	30.2	11.2	106.0	4.5	0.260	2.7
232	41.5	0.1928	30	30	2.0	0.0588	19.277	10951	175.7	0.337	34.4	17.2	187.3	6.6	0.280	17.0
233	41.5	0.1928	30	45	1.3	0.0588	19.277	10951	123.9	0.298	40.6	12.8	135.5	9.4	0.272	8.9
234	41.5	0.1928	30	45	2.0	0.0588	19.277	10951	262.4	0.289	50.2	18.8	238.2	9.2	0.293	1.2
235	41.5	0.1928	30	60	1.3	0.0588	19.277	10951	135.3	0.308	47.8	14.2	159.8	18.1	0.281	8.7
236	41.5	0.1928	30	60	2.0	0.0588	19.277	10951	333.9	0.267	60.8	19.6	284.1	14.9	0.303	13.6
237	41.5	0.1928	45	30	1.3	0.0588	19.277	10951	92.32	0.291	15.4	13.8	87.6	5.2	0.271	7.1
238	41.5	0.1928	45	30	2.0	0.0588	19.277	10951	146.0008	0.366	12.0	23.0	156.1	6.9	0.291	20.5
239	41.5	0.1928	45	45	1.3	0.0588	19.277	10951	108.1	0.319	27.8	12.4	109.9	1.7	0.283	11.3
240	41.5	0.1928	45	45	2.0	0.0588	19.277	10951	218.2	0.329	26.0	20.2	193.8	11.2	0.305	7.3
241	41.5	0.1928	45	60	1.3	0.0588	19.277	10951	119.3	0.328	36.2	13.8	126.5	6.1	0.293	10.9
242	41.5	0.1928	45	60	2.0	0.0588	19.277	10951	278	0.301	39.6	20.0	225.9	18.7	0.315	4.6
243	41.5	0.1928	60	30	1.3	0.0588	19.277	10951	71.91	0.271	13.8	11.0	62.0	13.8	0.279	2.8
244	41.5	0.1928	60	30	2.0	0.0588	19.277	10951	108.8	0.342	8.8	20.8	113.9	4.7	0.300	12.2
245	41.5	0.1928	60	45	1.3	0.0588	19.277	10951	72.64	0.307	11.6	11.6	73.8	1.6	0.292	4.9
246	41.5	0.1928	60	45	2.0	0.0588	19.277	10951	108	0.350	6.6	22.8	133.1	23.2	0.314	10.3
247	41.5	0.1928	60	60	1.3	0.0588	19.277	10951	87.98	0.310	19.4	12.4	79.5	9.7	0.302	2.6
248	41.5	0.1928	60	60	2.0	0.0588	19.277	10951	134.9	0.403	19.2	20.2	146.3	8.4	0.325	19.5
251	41.5	0.2892	30	30	1.3	0.0588	19.277	16427	176.1	0.306	41.2	15.6	163.6	7.1	0.293	4.2
252	41.5	0.2892	30	30	2.0	0.0588	19.277	16427	286.6	0.316	43.8	20.4	283.4	1.1	0.316	0.1
253	41.5	0.2892	30	45	1.3	0.0588	19.277	16427	237.8	0.290	55.2	17.2	209.3	12.0	0.307	5.9
254	41.5	0.2892	30	45	2.0	0.0588	19.277	16427	481.3	0.268	64.0	22.0	364.0	24.4	0.331	23.5
255	41.5	0.2892	30	60	1.3	0.0588	19.277	16427	278.5	0.277	65.4	17.8	247.2	11.2	0.317	14.5
256	41.5	0.2892	30	60	2.0	0.0588	19.277	16427	633.1	0.259	79.6	25.2	437.3	30.9	0.342	32.2
257	41.5	0.2892	45	30	1.3	0.0588	19.277	16427	139.8	0.353	30.0	15.2	134.0	4.1	0.306	13.4
258	41.5	0.2892	45	30	2.0	0.0588	19.277	16427	254	0.325	20.0	25.0	234.9	7.5	0.329	1.2
259	41.5	0.2892	45	45	1.3	0.0588	19.277	16427	172.3	0.337	40.8	16.2	168.7	2.1	0.320	5.2
260	41.5	0.2892	45	45	2.0	0.0588	19.277	16427	365.8	0.294	39.4	21.6	295.4	19.2	0.344	17.2
261	41.5	0.2892	45	60	1.3	0.0588	19.277	16427	185.7	0.349	50.4	18.0	195.1	5.1	0.331	5.2
262	41.5	0.2892	45	60	2.0	0.0588	19.277	16427	392.5	0.320	49.2	25.2	347.9	11.4	0.356	11.4
263	41.5	0.2892	60	30	1.3	0.0588	19.277	16427	81.42	0.332	20.6	13.6	93.8	15.2	0.315	5.2
264	41.5	0.2892	60	30	2.0	0.0588	19.277	16427	158.4	0.356	8.8	30.4	170.1	7.4	0.339	4.7
265	41.5	0.2892	60	45	1.3	0.0588	19.277	16427	101.1	0.367	29.0	15.4	112.5	11.3	0.329	10.1

Low-Mach Number Air-jet Test Results (Cont.)

Run No.	δ	D/δ	α	β	MR	M	x/δ	Reδ	ωpeak	R0.5/δ	ycentre (mm)	zcentre (mm)	ωpeak (model)	% diff	R0.5/δ (model)	% diff
266	41.5	0.2892	60	45	2.0	0.0588	19.277	16427	200.8	0.373	22.2	25.8	202 5	0.8	0.355	4 7
267	41.5	0.2892	60	60	1.3	0.0588	19.277	16427	117.9	0.394	36.0	15.6	122.3	3.8	0.341	13.6
268	41.5	0.2892	60	60	2.0	0.0588	19.277	16427	239.1	0.373	30.6	25.8	226.2	5.4	0.367	1.7
269	41.5	0.0964	30	30	1.3	0.0588	26.506	5476	39.66	0.218	16.8	11.2	36.3	8.4	0.268	22.9
270	41.5	0.0964	30	30	2.0	0.0588	26.506	5476	64.06	0.295	23.2	13 2	68.5	6.9	0.289	2.1
271	41.5	0.0964	30	45	1.3	0.0588	26.506	5476	48.72	0.255	22.8	10.2	46.4	4.8	0.280	10.0
272	41.5	0.0964	30	45	2.0	0.0588	26.506	5476	69.4	0.318	30.8	15.2	84.4	21.6	0.302	4.9
273	41.5	0.0964	30	60	1.3	0.0588	26.506	5476	45.29	0.242	25.2	11.0	54.3	19.9	0.290	19.9
274	41.5	0.0964	30	60	2.0	0.0588	26.506	5476	78.34	0.339	36.4	14.8	98.3	25.5	0.312	7 9
275	41.5	0.0964	45	30	1.3	0.0588	26.506	5476	31.61	0.242	11.4	14.4	30.8	2 5	0.279	15.5
276	41.5	0.0964	45	30	2.0	0.0588	26.506	5476	62.83	0.258	18.6	10.6	58.0	7 7	0.301	16.4
277	41.5	0.0964	45	45	1.3	0.0588	26.506	5476	40.22	0.237	15.8	11.4	38 3	4.7	0.292	23.3
278	41.5	0.0964	45	45	2.0	0.0588	26.506	5476	66.6	0.263	20.8	14.2	69.2	3.8	0.315	19.6
279	41.5	0.0964	45	60	1.3	0.0588	26.506	5476	45.03	0.195	20.0	10.2	43 5	3.4	0.302	54.6
280	41.5	0.0964	45	60	2.0	0.0588	26.506	5476	71.9	0.315	25.0	14.4	78.1	8.6	0.325	3.2
281	41.5	0.0964	60	30	1.3	0.0588	26.506	5476	34.02	0.165	4.8	11.2	22.7	33.4	0.288	74.3
282	41.5	0.0964	60	30	2.0	0.0588	26.506	5476	48.45	0.278	9.8	13.6	43.4	10.4	0.310	11.4
283	41.5	0.0964	60	45	1.3	0.0588	26.506	5476	38.35	0.205	9.0	10.2	26.4	31.2	0.301	46.9
284	41.5	0.0964	60	45	2.0	0.0588	26.506	5476	59.22	0.209	15.0	11.4	47.9	19.2	0.324	55.5
285	41.5	0.0964	60	60	1.3	0.0588	26.506	5476	37.21	0.202	5.2	10.0	27.5	26.1	0.311	53.9
286	41.5	0.0964	60	60	2.0	0.0588	26.506	5476	56.9	0.265	14.8	10.0	49.8	12.5	0.335	26.5
287	41.5	0.1928	30	30	1.3	0.0588	26.506	10951	72.83	0.276	34.0	11.4	79.6	9.3	0.308	11.6
288	41.5	0.1928	30	30	2.0	0.0588	26.506	10951	124.1	0.380	36.2	18.0	140.6	13.3	0.332	12.7
289	41.5	0.1928	30	45	1.3	0.0588	26.506	10951	81.89	0.315	41.2	14.8	101.7	24.3	0.322	2.2
290	41.5	0.1928	30	45	2.0	0.0588	26.506	10951	170.8	0.353	57.0	19.2	178.8	4.7	0.347	1.7
291	41.5	0.1928	30	60	1.3	0.0588	26.506	10951	96.38	0.335	49.6	15.0	120.0	24.5	0.333	0.5
292	41.5	0.1928	30	60	2.0	0.0588	26.506	10951	224.7	0.293	68.8	20.6	213.3	5.1	0.359	22.3
293	41.5	0.1928	45	30	1.3	0.0588	26.506	10951	66.09	0.381	23.2	13.8	65.7	0.5	0.321	15.8
294	41.5	0.1928	45	30	2.0	0.0588	26.506	10951	109.1	0.463	20.2	23.2	117 2	7.4	0.345	25.4
295	41 5	0.1928	45	45	1.3	0.0588	26.506	10951	82.88	0.307	33.0	14.4	82.5	0.5	0.336	9.4
296	41.5	0.1928	45	45	2.0	0.0588	26.506	10951	155.1	0.341	34.2	22.4	145.5	6.2	0.361	6.1
297	41.5	0.1928	45	60	1.3	0.0588	26.506	10951	90.06	0.353	35.8	15.2	95.0	5.5	0.347	1.9
298	41.5	0.1928	45	60	2.0	0.0588	26.506	10951	174	0.389	49.0	20.6	169.6	2.5	0.374	3.9
299	41.5	0.1928	60	30	1.3	0.0588	26.506	10951	64.87	0.252	14.6	14.8	46.5	28.2	0.330	31.4
300	41.5	0.1928	60	30	2.0	0.0588	26.506	10951	78.06	0.368	9.8	23.6	85.5	9.6	0.356	3.4
301	41.5	0.1928	60	45	1.3	0.0588	26.506	10951	63.02	0.318	20.8	13.8	55.4	12.1	0.346	8.6
302	41.5	0.1928	60	45	2.0	0.0588	26.506	10951	99.3	0.414	20.2	20.6	99.9	0.6	0.372	10.0
303	41.5	0.1928	60	60	1.3	0.0588	26.506	10951	64.41	0.370	21.0	14.8	59.7	7.3	0.358	3.4
304	41.5	0.1928	60	60	2.0	0.0588	26.506	10951	106.2	0.434	29.8	23.6	109.8	3.4	0.385	11.3
305	41.5	0.2892	30	30	1 3	0.0588	26.506	16427	113.1	0.347	46.0	17.6	122.8	8.6	0.348	0.3
306	41.5	0.2892	30	30	2.0	0.0588	26.506	16427	200	0.384	47.2	22.8	212.8	6.4	0.375	2.5
307	41.5	0.2892	30	45	1.3	0.0588	26.506	16427	147.8	0.327	64.2	19.6	157.1	6.3	0.364	11.5
308	41.5	0.2892	30	45	2.0	0.0588	26 506	16427	341.3	0.294	74.6	22 2	273.3	19.9	0.392	33.2
309	41.5	0.2892	30	60	1.3	0.0588	26 506	16427	167.6	0.358	74 6	20.2	185.6	10.7	0 376	5.2
310	41.5	0.2892	30	60	2 0	0.0588	26.506	16427	460 9	0.260	89.4	29 4	328.3	28.8	0.405	56.2
311	41 5	0.2892	45	30	1.3	0.0588	26.506	16427	93 35	0.390	35 4	16.0	100.6	7.8	0 362	7 1
312	41 5	0 2892	45	30	2.0	0.0588	26 506	16427	172 1	0 423	29 2	24 6	176 4	2.5	0 390	7 8
314	41 5	0 2892	45	45	1.3	0.0588	26.506	16427	116.9	0.391	49 0	16.8	126.7	8 4	0.379	3.0

Low-Mach Number Air-jet Test Results (Cont.)

Run No.	δ	D/δ	α	β	*MR*	M	x/δ	Re_δ	ω_{peak}	$R_{0.5}/\delta$	y_{centre} (mm)	z_{centre} (mm)	ω_{peak} (model)	% diff	$R_{0.5}/\delta$ (model)	% diff
315	41.5	0.2892	45	45	2.0	0.0588	26.506	16427	264.7	0.342	44.8	25.2	221.8	16.2	0.408	19.4
316	41.5	0.2892	45	60	1.3	0.0588	26.506	16427	138.2	0.372	55.6	19.0	146.5	6.0	0.392	5.3
317	41.5	0.2892	45	60	2.0	0.0588	26.506	16427	319.7	0.325	59.4	26.0	261.2	18.3	0.422	29.9
318	41.5	0.2892	60	30	1.3	0.0588	26.506	16427	64.79	0.375	26.8	11.2	70.4	8.7	0.373	0.4
319	41.5	0.2892	60	30	2.0	0.0588	26.506	16427	110.6	0.507	14.0	30.4	127.7	15.4	0.402	20.7
320	41.5	0.2892	60	45	1.3	0.0588	26.506	16427	75.99	0.499	35.0	15.0	84.5	11.1	0.391	21.8
321	41.5	0.2892	60	45	2.0	0.0588	26.506	16427	153.3	0.451	22.0	29.6	152.0	0.8	0.421	6.6
322	41.5	0.2892	60	60	1.3	0.0588	26.506	16427	95.43	0.451	39.0	15.2	91.9	3.7	0.404	10.5
323	41.5	0.2892	60	60	2.0	0.0588	26.506	16427	172.7	0.455	35.6	30.0	169.8	1.7	0.435	4.4

High-Mach Number Air-jet Test Results

Run No.	δ	D/δ	α	β	*MR*	M	x/δ	Re_δ	ω_{peak}	$R_{0.5}/\delta$	y_{centre} (mm)	z_{centre} (mm)	ω_{peak} (model)	% diff	$R_{0.5}/\delta$ (model)	% diff
a03	20	0.1500	45	45	1.588	0.493	8.750	214900	4306	0.224	4.7	5.8	3644.4	15.4	0.210	6.1
a04	20	0.1500	45	45	1.584	0.595	8.750	241100	5060	0.222	3.8	6.0	4645.6	8.2	0.213	4.1
a05	20	0.1500	45	45	1.606	0.743	8.750	267300	6791	0.220	2.3	8.0	6324.1	6.9	0.216	1.7
a06	20	0.1500	45	60	1.599	0.494	8.750	199300	4960	0.252	7.7	4.7	4243.1	14.5	0.218	13.7
a07	20	0.1500	45	60	1.624	0.584	8.750	229500	5929	0.235	6.7	5.8	5401.5	8.9	0.221	6.3
a08	20	0.1500	45	60	1.612	0.736	8.750	263500	7249	0.238	5.0	7.3	7239.4	0.1	0.224	6.0
a09	20	0.1500	45	30	1.598	0.497	8.750	202100	3439	0.236	0.8	5.8	3001.1	12.7	0.201	14.7
a10	20	0.1500	45	30	1.593	0.602	8.750	234000	4155	0.202	0.0	7.8	3836.5	7.7	0.204	0.6
a11	20	0.1500	45	30	1.597	0.754	8.750	263800	6147	0.213	-0.2	8.7	5169.3	15.9	0.207	3.0
a12	20	0.3000	45	30	1.522	0.486	8.750	197100	5923	0.247	3.5	8.7	5587.2	5.7	0.242	2.0
a14	20	0.3000	45	30	1.587	0.594	8.750	223000	7515	0.203	1.5	11.7	7659.4	1.9	0.247	21.3
a15	20	0.3000	45	30	1.584	0.747	8.750	255600	9971	0.232	0.0	12.5	10323.9	3.5	0.251	8.2
a16	20	0.3000	45	45	1.618	0.502	8.750	199000	7808	0.251	8.2	8.8	7940.9	1.7	0.257	2.2
a17	20	0.3000	45	45	1.593	0.604	8.750	230800	9330	0.262	7.0	9.5	9904.9	6.2	0.259	1.2
a18	20	0.3000	45	45	1.595	0.755	8.750	256300	11060	0.258	4.7	11.3	13289.6	20.2	0.263	1.7
a19	20	0.3000	45	60	1.6	0.500	8.750	193400	8649	0.300	12.7	8.5	9100.2	5.2	0.265	11.9
a20	20	0.3000	45	60	1.595	0.605	8.750	227600	9955	0.265	11.7	9.2	11630.1	16.8	0.267	1.0
a22	20	0.1500	30	30	1.593	0.503	8.750	196400	4353	0.237	6.0	4.3	3630.4	16.6	0.193	18.2
a23	20	0.1500	30	30	1.608	0.604	8.750	227300	5015	0.213	5.5	5.0	4680.6	6.7	0.196	7.9
a24	20	0.1500	30	30	1.591	0.759	8.750	261300	6689	0.209	4.0	6.0	6216.3	7.1	0.199	5.0
a25	20	0.1500	30	45	1.584	0.505	8.750	196700	5133	0.216	9.5	4.7	4596.3	10.5	0.202	6.3
a26	20	0.1500	30	45	1.592	0.605	8.750	221300	6874	0.216	9.2	4.8	5869.5	14.6	0.205	5.4
a27	20	0.1500	30	45	1.597	0.754	8.750	259000	9614	0.197	8.8	5.3	7861.7	18.2	0.208	5.5
a28	20	0.1500	30	60	1.589	0.508	8.750	216100	6539	0.225	12.5	5.2	5497.7	15.9	0.209	7.1
a29	20	0.1500	30	60	1.6	0.615	8.750	236700	8157	0.218	12.7	5.2	7124.9	12.7	0.212	2.6
a30	20	0.1500	30	60	1.597	0.756	8.750	262600	11450	0.194	12.5	5.3	9309.5	18.7	0.215	10.6
a31	20	0.3000	30	30	1.661	0.506	8.750	202900	8340	0.250	9.2	8.5	7977.4	4.3	0.237	5.2
a32	20	0.3000	30	30	1.666	0.617	8.750	224800	10250	0.238	9.0	8.5	10405.7	1.5	0.240	0.7
a33	20	0.3000	30	30	1.66	0.767	8.750	259300	15550	0.209	6.0	9.3	13773.2	11.4	0.243	16.6
a34	20	0.3000	30	45	1.608	0.502	8.750	200100	11810	0.219	17.7	7.5	9721.0	17.7	0.246	12.6
a35	20	0.3000	30	45	1.599	0.600	8.750	235800	13750	0.218	17.8	7.2	12193.7	11.3	0.248	14.1
a36	20	0.3000	30	45	1.596	0.757	8.750	269100	18320	0.221	15.5	8.0	16500.7	9.9	0.252	14.1
a37	20	0.3000	30	60	1.603	0.503	8.750	201800	11240	0.236	21.8	8.5	11610.0	3.3	0.254	7.7
a38	20	0.3000	30	60	1.591	0.605	8.750	226900	14000	0.234	21.7	8.2	14619.2	4.4	0.257	9.8
a39	20	0.3000	30	60	1.6	0.756	8.750	263100	18910	0.234	21.0	8.5	19729.4	4.3	0.261	11.6
a40	20	0.3000	45	45	1.595	0.508	16.250	208100	4955	0.312	11.8	11.7	4530.7	8.6	0.324	3.6
a41	20	0.3000	45	45	1.594	0.606	16.250	232000	5283	0.327	11.3	11.4	5708.2	8.0	0.327	0.1
a42	20	0.3000	45	45	1.593	0.757	16.250	263300	5973	0.343	7.8	12.5	7626.9	27.7	0.332	3.3
a43	20	0.3000	45	45	1.586	0.504	23.750	209100	2387	0.359	17.8	12.0	3167.4	32.7	0.391	8.7
a44	20	0.3000	45	45	1.584	0.603	23.750	231400	3155	0.429	16.5	9.5	4000.2	26.8	0.395	8.1
a45	20	0.3000	45	45	1.593	0.750	23.750	254900	3678	0.432	11.3	12.3	5360.3	45.7	0.401	7.1
a46	20	0.3000	45	45	1.596	0.505	31.250	210400	1935	0.461	20.8	10.5	2498.4	29.1	0.459	0.6
a47	20	0.3000	45	45	1.598	0.603	31.250	229800	2253	0.505	20.5	9.5	3157.9	40.2	0.463	8.2
a48	20	0.3000	45	45	1.596	0.755	31.250	264600	2364	0.521	14.0	12.2	4230.4	79.0	0.470	9.7